

Springer Series in MATERIALS SCIENCE

Editors: R. Hull R. M. Osgood, Jr. J. Parisi H. Warlimont

The Springer Series in Materials Science covers the complete spectrum of materials physics, including fundamental principles, physical properties, materials theory and design. Recognizing the increasing importance of materials science in future device technologies, the book titles in this series reflect the state-of-the-art in understanding and controlling the structure and properties of all important classes of materials.

- | | |
|---|--|
| 61 Fatigue in Ferroelectric Ceramics and Related Issues
By D.C. Lupascu | 69 Chemical-Mechanical Planarization of Semiconductor Materials
Editor: M.R. Oliver |
| 62 Epitaxy
Physical Principles and Technical Implementation
By M.A. Herman, W. Richter, and H. Sitter | 70 Applications of the Isotopic Effect in Solids
By G.V. Plekhanov |
| 63 Fundamentals of Ion-Irradiated Polymers
By D. Fink | 71 Dissipative Phenomena in Condensed Matter
Some Applications
By S. Dattagupta and S. Puri |
| 64 Morphology Control of Materials and Nanoparticles
Advanced Materials Processing and Characterization
Editors: Y. Waseda and A. Muramatsu | 72 Predictive Simulation of Semiconductor Processing
Status and Challenges
Editors: J. Dabrowski and E.R. Weber |
| 65 Transport Processes in Ion-Irradiated Polymers
By D. Fink | 73 SiC Power Materials
Devices and Applications
Editor: Z.C. Feng |
| 66 Multiphased Ceramic Materials
Processing and Potential
Editors: W.-H. Tuan and J.-K. Guo | 74 Plastic Deformation in Nanocrystalline Materials
By M.Yu. Gutkin and I.A. Ovid'ko |
| 67 Nondestructive Materials Characterization
With Applications to Aerospace Materials
Editors: N.G.H. Meyendorf, P.B. Nagy, and S.I. Rokhlin | 75 Wafer Bonding
Applications and Technology
Editors: M. Alexe and U. Gösele |
| 68 Diffraction Analysis of the Microstructure of Materials
Editors: E.J. Mittemeijer and P. Scardi | 76 Spirally Anisotropic Composites
By G.E. Freger, V.N. Kestelman, and D.G. Freger |

Volumes 10–60 are listed at the end of the book.

Zhe Chuan Feng (Ed.)

SiC Power Materials

Devices and Applications

With 227 Figures and 26 Tables



Springer

Professor Zhe Chuan Feng
Graduate Institute of Electro-Optical Engineering
Department of Electrical Engineering
National Taiwan University
Taipei, Taiwan, ROC
E-mail: zcfeng@cc.ee.ntu.edu.tw

Series Editors:

Professor Robert Hull
University of Virginia
Dept. of Materials Science and Engineering
Thornton Hall
Charlottesville, VA 22903-2442, USA

Professor R. M. Osgood, Jr.
Microelectronics Science Laboratory
Department of Electrical Engineering
Columbia University
Seeley W. Mudd Building
New York, NY 10027, USA

Professor Jürgen Parisi
Universität Oldenburg, Fachbereich Physik
Abt. Energie- und Halbleiterforschung
Carl-von-Ossietzky-Strasse 9–11
26129 Oldenburg, Germany

Professor Hans Warlimont
Institut für Festkörper-
und Werkstoffforschung,
Helmholtzstrasse 20
01069 Dresden, Germany

ISSN 0933-033X

ISBN 978-3-642-05845-5

Library of Congress Cataloging-in-Publication Data.

SiC power materials : devices and applications / Z.C. Feng (ed.) p. cm. – (Springer series in materials science, ISSN 0933-033X)

ISBN 978-3-642-05845-5 ISBN 978-3-662-09877-6 (eBook)

DOI 10.1007/978-3-662-09877-6

1. Silicon carbide—Electric properties. 2. Semiconductors. I. Feng, Zhe Chuan. II. Series.
TK7871.15.S56S53 2004
621.3815'2-dc22

2004042933

This work is subject to copyright. All rights are reserved, whether the whole or part of the material is concerned, specifically the rights of translation, reprinting, reuse of illustrations, recitation, broadcasting, reproduction on microfilm or in any other way, and storage in data banks. Duplication of this publication or parts thereof is permitted only under the provisions of the German Copyright Law of September 9, 1965, in its current version, and permission for use must always be obtained from Springer-Verlag Berlin Heidelberg GmbH.

Violations are liable for prosecution under the German Copyright Law.

springeronline.com

© Springer-Verlag Berlin Heidelberg 2004

Originally published by Springer-Verlag Berlin Heidelberg New York in 2004

The use of general descriptive names, registered names, trademarks, etc. in this publication does not imply, even in the absence of a specific statement, that such names are exempt from the relevant protective laws and regulations and therefore free for general use.

Production and Typesetting: Data conversion LE-T_EX Jelonek, Schmidt & Vöckler GbR, Leipzig
using a Springer L_ET_EX macro package

Cover concept: eStudio Calamar Steinen

Cover production: *design & production* GmbH, Heidelberg

Printed on acid-free paper

SPIN: 10867307

57/3141/YL

5 4 3 2 1 0

Preface

Silicon carbide (SiC) is an important wide gap semiconductor which has a large band gap and other excellent properties, such as a large thermal conductivity, high breakdown voltage, and outstanding mechanical and chemical stability. SiC is the first semiconductor material to lead to the creation of blue LEDs. In the last few years research and development (R&D) on SiC has attracted much attention and effort across the world. It is recognized as the power semiconductor of the 21st century and is very suitable for the fabrication of various electronic and optoelectronic devices in use of high-power, high-temperature, high-frequency and high-resistance-to-radiation applications and systems.

The rapid developments in SiC research and SiC related industry have highlighted the need for a proper book for engineers working in the field of SiC related materials, engineering and technologies; which is the goal of this book. This review book focus on the general topics of SiC growth, material characterization, processing and device fabrication, in particular for high power and high speed (but not limited to) electronic and optoelectronic applications. The book is suitable for a wide range of audiences and covers each of the basic and critical aspects of SiC science and technology. Each chapter, written by experts in the field, reviews works in the field, describe the basics, discusses progresses made by different groups, and suggests further works needed.

The topics of the book include in 11-chapters: (1) Materials science and engineering of bulk silicon carbides; (2) Fundamental properties of silicon carbides; (3) Sublimation growth of SiC materials; (4) Modeling and evaluation of crystal growth of silicon carbide; (5) Structural, dynamical, thermal and defect properties of 3C-SiC; (6) Characterization of cubic SiC on Si grown by chemical vapor deposition; (7) Electron paramagnetic resonance characterization of SiC; (8) Material selection and interfacial reaction in ohmic contact formation on SiC; (9) SiC oxidation, MOS capacitors, and MOSFETs; (10) 4H-SiC power switching devices for extreme environment applications; and (11) SiC nuclear radiation detectors.

This book acts as a sister book of Feng and Zhao ed., silicon carbide materials, processing and devices (Taylor & Francis, 2004). The topics are not repeated but complement each other. The current book addressed more to engineers and also complements the book of Choyke, Matsunami and Pensl ed. *Silicon Carbide Recent Major Advances* (Springer 2004) that is written for scientists and researchers.

As can be seen, the current book presents the key properties of SiC materials and describes key SiC devices as well as demonstrates the remaining challenging issues in material growth and device fabrication for future R&D in the 21st century. This book can well serve material growers and evaluators, device design and processing engineers as well as potential users of SiC technologies, including newcomers, graduate students, engineers and scientists in the SiC field.

Taipei,
February 2004

Zhe Chuan Feng

Contents

1 Materials Science and Engineering of Bulk Silicon Carbides	
<i>T. Sudarshan</i>	1
1.1 Introduction	1
1.2 Historical Perspective	2
1.2.1 Construction Materials	5
1.2.2 Growth of SiC from Solution	6
1.2.3 First Demonstration of Single Crystal SiC Ingot or Boule Growth	7
1.3 Fundamental Physics and Chemistry Issues	
Related to Bulk Crystal Growth	8
1.3.1 Source Material and Vapor Composition	8
1.3.2 Mechanism of Growth	10
1.3.3 Seed Surface Effects	14
1.3.4 Polytype Control	14
1.3.5 Bulk Crystal Doping	16
1.4 Theoretical Considerations and Influence	
of Independent Parameters on Growth Rate	17
1.4.1 Theoretical Considerations Relevant to Growth	17
Supersaturation	17
Mass Transport Process	18
Kinetic Processes	22
Thermal Stresses in the Growing Boule and Defect Initiation	23
1.4.2 Crystal Growth Rate: Influence of Independent Parameters	24
Influence of Temperature on the Growth Rate	25
Source-to-Seed Distance	25
Growth Pressure	26
Temperature Gradient	27
1.5 Defect Generation Processes in Silicon Carbide Crystal Growth . . .	28
1.5.1 Micropipe Generation	28
1.5.2 Planar Defects	30
1.5.3 Inclusions, Dendrites, and Polytype Inclusions	31

VIII Contents

1.6	Development of Industrial Production of SiC Wafers and Current Status	32
1.6.1	Early Stage Developments	33
1.6.2	Intermediate Stage Development	34
1.6.3	Recent Developments and Current Status of SiC Wafers ...	36
1.6.4	Bulk Crystal Growth of Semi-Insulating SiC	37
1.6.5	SiC Bulk Crystal Growth with p-Type Doping.....	39
1.7	Evaluation and Characterization of SiC Wafers	42
1.7.1	Material Evaluation	42
1.7.2	Defect Characterization	44
1.7.3	Evaluation of Crystalline Quality by Chemical Etching: Destructive Method	47
1.8	Market and Application Needs and Future Prospects	52
	Acknowledgements	55
	References	56

2 Fundamental Properties of SiC: Crystal Structure, Bonding Energy, Band Structure, and Lattice Vibrations

<i>J. Dong, A.-B. Chen</i>	63	
2.1	Introduction	63
2.2	Crystal Structure and Bonding Energy	64
2.3	Electronic Band Structure	70
2.4	Lattice Vibration	75
2.5	Conclusion.....	83
	Acknowledgements	83
	References	83

3 Sublimation Growth of SiC Single Crystals

<i>N. Ohtani, T. Fujimoto, M. Katsuno, H. Yashiro</i>	89	
3.1	Introduction	89
3.2	Polytypism of SiC	91
3.3	Sublimation Growth of SiC	94
3.4	Crystal Diameter Enlargement	96
3.5	Reduction of Micropipe Defects	98
3.6	Improved Mosaicity of Bulk SiC Crystals	104
3.7	SiC Bulk Crystal Growth in Directions Perpendicular to the <i>c</i> -Axis	109
3.8	Summary	116
	Acknowledgements	117
	References	117

4 Crystal Growth of Silicon Carbide: Evaluation and Modeling

<i>E. Pernot, M. Pons, R. Madar</i>	123	
4.1	Introduction	123
4.2	History of Crystal Growth	124

4.3	Modeling and Simulation of the Growth Procedure	126
4.3.1	Introduction	126
4.3.2	Modeling and Databases	127
	Thermodynamic Modeling	127
	Gas and Surface Chemistry	128
	Induction Heating and Temperature Distribution	128
	Multicomponent Fluid Transport	129
4.3.3	Selected Results for Heat Transfer	129
	A General Overview of the Simulation Results	129
	Heat Transfer: Influence of the Diameter of the Pyrometric Holes	131
	Heat Transfer: Influence of the Growing Crystal	133
	Heat Transfer and the Scaling Up of the Reactor	133
4.4	Crystal Evaluation Methods	134
4.4.1	Optical Microscopy	134
	The Polarized-Light Technique	134
	The Rotating-Polarizer Technique	134
4.4.2	X-Ray Diffraction Imaging (Also Called Topography)	135
	Investigation of Ingots	136
	Investigation of Wafers	137
4.4.3	Raman Spectroscopy Imaging	138
4.4.4	Some Conclusions	138
4.5	Results of Modeling and Characterization	138
4.5.1	Introduction	138
4.5.2	Multicomponent Mass Transport and Crystal Growth Rate Evaluation of Mass Transfer	139
	Geometry Modification and Crystal Shape	140
4.5.3	Ingots Evaluation	140
	Surface Polarity and Polype	141
	Enlargement Process	142
	Growth of the Polycrystal and Cracks	143
	Defect Propagation	144
4.5.4	Wafer Evaluation	147
	Relations Between Defects and Macroscopic Modeling	147
	Density of Dislocations and Micropipes	151
4.5.5	Evaluation of Stress Patterns	152
	Birefringence Imaging	153
	Raman Imaging	154
	Model Development	155
4.6	Conclusions	156
	References	157

5 Lattice Dynamics of Defects and Thermal Properties of 3C-SiC

<i>D.N. Talwar</i>	161
5.1 Introduction	161
5.1.1 Polymorphic Forms of SiC	162
5.1.2 Issues Related to Defects and Polytypism	162
5.1.3 Structural and Dynamical Properties of 3C-SiC	163
5.2 Theoretical Background	165
5.2.1 Atomic Configuration of Defects	166
5.2.2 Geometrical Configuration of Defects	167
5.2.3 Lattice Relaxation and Distortion	171
5.3 Lattice Dynamical Models	172
5.3.1 The Second-Neighbor Rigid-Ion Model	173
5.3.2 The Phonon-Model Parameters	176
5.3.3 Pressure Dependent and Thermo-Dynamical Properties	176
5.4 The Green's Function Method	177
5.4.1 The Lattice Green's Function	178
5.4.2 The Impurity Green's Function	178
5.4.3 Impurity Perturbation	179
Substitutional Defects	180
Complex Defect Centers	181
Interstitial Defect Centers	183
Lattice Distortion	183
5.5 Numerical Computations and Results	183
5.5.1 Dynamical Properties of Perfect 3C-SiC	184
5.5.2 Debye Temperature, Mode Grüneisen Parameters and Thermal Expansion	187
5.5.3 Dynamical Properties of Defects in 3C-SiC	190
Isolated Single Substitutional Defect	191
Dynamical Properties of Pair and Complex Defects in 3C-SiC	194
5.6 Summary and Conclusion	198
Acknowledgments	201
References	202

6 Optical and Interdisciplinary Analysis of Cubic SiC Grown on Si by Chemical Vapor Deposition

<i>Z.C. Feng</i>	209
6.1 Introduction	209
6.2 Experiment	211
6.2.1 Sample Growth	211
6.2.2 Materials Analysis Techniques	212
6.2.3 Absorption Coefficients	212
6.3 General Materials Characterization of 3C-SiC	213
6.3.1 X-ray Diffraction	213

6.3.2	Photoluminescence	214
6.3.3	Raman Scattering	216
6.3.4	UV-Vis Optical Spectroscopy	217
6.3.5	Infrared Transmission and Reflectance	217
6.4	Surface Science and Nuclear-Physics Analysis	219
6.4.1	X-Ray Photoelectron Spectroscopy	219
6.4.2	Secondary-Ion Mass Spectrometry	221
6.4.3	Rutherford Backscattering	222
6.4.4	Ion Channeling	223
6.5	Theoretical Aspects of Layer Stress and Strain in 3C-SiC/Si	223
6.5.1	Generalized Axial Stress and Strain	223
	Stress Tensor	223
	Strain Tensor	224
	Conversion Between S_{ij} and C_{ij}	225
	Poisson Ratio	225
	Volume Dilatation	226
6.5.2	Axial-Stress-Induced Raman Shifts	226
	Secular Equation	226
	Raman Optical-Phonon Frequencies from Axial Strains	227
	Raman Stress Coefficients η_S and η_H	227
	Mode Grüneisen Parameter	228
	General Raman Stress Coefficients η	228
	LO-TO Phonon Splitting	228
6.5.3	Axial-Strain-Induced Energy Gap Variations	230
	Strain Hamiltonian	230
	Axial-Strain Hamiltonian	230
	Energy Band Splitting	231
6.6	Raman Analysis of the 3C-SiC/Si Structure	232
6.6.1	Evaluation of Raman Stress Coefficients and Elastic Constants of 3C-SiC	232
6.6.2	Raman Determination of Stress and Strain in 3C-SiC/Si	233
6.6.3	Active Raman Studies of 3C-SiC/Si	235
6.6.4	Raman Mode Intensity Variation of 3C-SiC with and Without Si Substrate	236
	Raman Selection Rule for 3C-SiC/Si	237
	Selection Rule Broken	238
	Enhancements of Si and SiC Raman Signals	238
	Multiple Reflections and Forward Scattering	239
6.6.5	Raman Cross Section of 3C-SiC	241
	The Variation of Raman Signal Strength with Excitation Intensity	241
	A Simple Experimental Determination of the Raman Cross Section	242
6.6.6	Raman Defect Modes	242
6.6.7	Second-Order Raman Scattering of 3C-SiC	244

6.7	Penetrative Luminescence Analysis	246
6.7.1	Effects of a Tensile Biaxial Stress on Bound-Exciton Transitions	246
	Shifts of N-BE Lines	246
	Layer Stress and Deformation Potentials	247
	Influence of Spin-Orbit Splitting on the Energy Gap Shift	248
	Effects on the BE Line Intensities	250
6.7.2	Crystallinity Dependent Luminescence Characteristics and Defect Bands	250
	TEM and Defect W-band at 2.15 eV	251
	Intensity Ratio ρ – a Figure of Merit of Film Quality	251
	Spectral Comparison of Luminescence from 3C-SiC Films with and Without Si Substrate	252
	D _I Line at 1.972 eV	252
	Dislocation- and Extended-Defect-Related G Band	254
6.7.3	Photoluminescence Excitation, Time-Resolved, and Infrared Transmission Studies	256
6.7.4	Bound Electronic States of Isolated Single and Paired Native Defects	258
	Native Defects and DLTS Results	258
	Tight-Binding Calculation in the Framework of the Green's Function	259
	Other Theoretical Calculations	259
	Interpretation of PL and DLTS Data on Native Defect Centers	260
	Sharp 1.913 eV PL Line from Electron-Irradiated 3C-SiC .	261
6.8	Infrared Reflectance Spectroscopy Analysis	261
6.8.1	Basic Theoretical Model	261
6.8.2	Effect of Surface Roughness	263
6.8.3	Damping of Interference Fringes	264
6.9	Additional Issues	264
6.9.1	Combined PL–Raman Spectroscopy under UV Excitation .	264
6.9.2	Large-Diameter Thick 3C-SiC Epitaxially Grown on Si .	265
6.9.3	Epitaxial Lateral Overgrowth of 3C-SiC on Si	266
6.9.4	Excellent Reviews of Materials Characterization of SiC .	267
6.10	Conclusion	267
	Acknowledgments	268
	References	268
7	Electron Paramagnetic Resonance Characterization of SiC	
<i>M.E. Zvanut</i>	277
7.1	Introduction	277
7.1.1	The Technique	278
7.1.2	Collaborative Techniques	283

7.2	Intrinsic Defects	285
7.2.1	As-Grown SiC	285
7.2.2	Implantation-Induced Defects	291
7.3	Impurity-Related Defects	293
7.3.1	Shallow Impurities	293
7.3.2	Transition Metal Impurities: Vanadium and Other Elements	296
7.4	Concluding Comments	298
	References	299

8 Material Selection and Interfacial Reaction in Ohmic-Contact Formation on SiC

<i>W. Lu, W.E. Collins, W.C. Mitchel</i>	303	
8.1	Introduction	303
8.2	Classical Theory and the Critical Factors in Ohmic Contact Formation on SiC	304
8.3	Interfacial Reactions of Ohmic Contact Metals on SiC	307
8.3.1	Silicides and Carbon in Metal/SiC	307
8.3.2	Silicides and Carbides in Metal/SiC	312
8.3.3	Silicon and Carbides in Al/SiC and Al-Alloy/SiC	315
8.4	Compounds Used for Ohmic Contacts	319
8.4.1	Silicides	319
8.4.2	Carbides	320
8.4.3	Nitrides	321
8.4.4	Borides	322
8.4.5	Composite Structures	322
8.5	Recent Advances and Challenging Issues	324
8.5.1	Toward Understanding in the Ohmic Contact Mechanism	324
8.5.2	Catalytic Graphitization Effects of Metals	326
8.5.3	Structural Characterizations at Atomic and Nanometer Scales	335
8.5.4	Thermal Stability	336
8.6	Conclusion	338
	Acknowledgments	338
	References	338

9 Oxidation, MOS Capacitors, and MOSFETs

<i>S. Dimitrijev, H.B. Harrison, P. Tanner, K.Y. Cheong, J. Han</i>	345	
9.1	Introduction	345
9.2	Gate Oxides on SiC	346
9.2.1	Gate Dielectric Requirements	347
9.2.2	Interface and Near-Interface Traps	348
9.2.3	Electrical Characterization of SiO ₂ –SiC Interfaces	350
	Termaan's High-Frequency Capacitance–Voltage (HF C–V) Technique	350

Simultaneous High-Low Capacitance-Voltage (Hi-Lo $C-V$) Technique	350
AC Conductance Technique	351
Room Temperature Photo- CV Technique	351
Hall Effect Technique	353
MOSFET Subthreshold Current Technique	353
Other Techniques	355
9.2.4 Electrical Characterization of Defects	
Near the $\text{SiO}_2\text{-SiC}$ Interface	355
Low-Temperature CV Technique	355
Slow-Trap Profiling Technique	356
9.2.5 Processing Techniques for Improvement of Interface Quality	356
9.3 Nitrided Gate Oxides	358
9.3.1 Effects of Nitrogen at the $\text{SiO}_2\text{-SiC}$ Interface	358
9.3.2 Physical Characteristics of Nitrided $\text{SiO}_2\text{-SiC}$ Interfaces	358
9.3.3 Electrical Characteristics of MOS Capacitors with Nitrided Gate Oxides	360
9.3.4 Channel-Carrier Mobility in MOSFETs with Nitrided Gate Oxides	361
9.4 Power MOSFETs	365
9.4.1 Device Structures	366
9.4.2 Performance of Power SiC MOSFETs	367
References	368

10 4H-SiC Power-Switching Devices for Extreme-Environment Applications

Z. Luo, T. Chen, D.C. Sheridan, J.D. Cressler	375
10.1 Introduction	375
10.1.1 Fundamentals of Power Schottky Barrier Diodes	376
10.1.2 The Fundamentals of Radiation	378
10.2 SiC Power Diode Structures	379
10.2.1 SBD, pn and JBS diodes	379
10.2.2 Edge Termination for Power Diodes	380
Edge Termination Techniques	381
Guard Ring (GR) Structure Optimization	383
10.3 Device Fabrication	384
10.3.1 Fabrication of SBD/JBS Diodes with Guard Ring Termination	384
10.3.2 Fabrication of SiC MOS Capacitors	385
10.4 Radiation Effects in SiC Power Switching Diodes and Capacitors	386
10.4.1 SiC SBD Under Gamma Irradiation	387
10.4.2 Gamma Irradiation of SiC MOS Capacitors	389

10.4.3 SiC SBD/JBS Diodes Under Proton Irradiation	398
DC Performance Under Proton Irradiation	399
AC Performance Under Proton Irradiation	404
10.5 Summary	407
Acknowledgments	408
References	408
11 SiC Nuclear-Radiation Detectors	
<i>N.B. Strokan, A.M. Ivanov, A.A. Lebedev</i>	411
11.1 Introduction	411
11.2 Detector Material Properties	412
11.3 Detection of Short-Range Particles	413
11.3.1 Measurement of SiC Detectors	413
11.3.2 Determining the Average Energy per Electron–Hole Pair	415
11.3.3 Determining the Hole Diffusion Length	415
11.3.4 Shape of Amplitude Spectrum for Diffusion and Its Relationship to the Hole Lifetime τ	417
Calculation	417
Experiment	419
11.3.5 Drift Transport and Carrier Capture Times	419
Calculation	419
Experiment	422
Conclusion	422
11.4 Spectrometry of X-Ray Radiation	423
11.5 Response of SiC Detectors to Electron and Photon Irradiation	425
11.6 SiC Detectors for High-Energy Physics Experiments	426
11.7 Operation of SiC Detectors in a Reactor Channel	427
11.8 Radiation Hardness of the SiC Detectors	429
11.8.1 Introduction	429
11.8.2 Experimental Procedure	430
11.8.3 Experimental Results	431
11.8.4 Estimation of the Drift Parameters	435
11.9 Signal Amplification	436
11.9.1 Principle of “Through-Conducting Channel”	436
11.9.2 Amplification in a Triode Structure	437
Experimental Results	438
Phototransistor Model	440
Conclusion	441
11.10 Summary	442
References	442
Index	447

List of Contributors

An-Ban Chen

Physics Department,
Auburn University,
Auburn, AL 36849-5311, USA
abchen@physics.auburn.edu

Tianbing Chen

School of Electrical
and Computer Engineering,
Georgia Institute of Technology,
Atlanta, GA 30332 USA
tianbing@ece.gatech.edu

Kuan Yew Cheong

Universiti Sains Malaysia,
School of Materials and
Mineral Resources Engineering,
Engineering Campus,
14300 Nibong Tebal,
Seberang Perai Selatan,
Penang, Malaysia
ckuanyew@catcha.com,
K.Cheong@griffith.edu.au

Warren Eugene Collins

Department of Physics,
Fisk University,
Nashville, TN 37208 USA
ecollins@fisk.edu

John D. Cressler

School of Electrical
and Computer Engineering
Georgia Institute of Technology,
Atlanta, GA 30332 USA
cressler@ece.gatech.edu

Sima Dimitrijev

School of Microelectronic
Engineering,
Griffith University, Nathan Campus,
Queensland, QLD4111 Australia
s.dimitrijev@griffith.edu.au

Jianjun Dong

Physics Department,
Auburn University,
Auburn, AL 36849-5311, USA
jjdong@physics.auburn.edu

Zhe Chuan Feng

Graduate Institute of Electro-Optical
Engineering and Department of
Electrical Engineering,
National Taiwan University,
Taipei, Taiwan, ROC
zcfeng@cc.ee.ntu.edu.tw,
zhe_chuan_feng@hotmail.com

XVIII List of Contributors

Tatsuo Fujimoto

Nippon Steel Corporation,
Advanced Technology
Research Laboratories,
20-1 Shintomi, Futtsu,
Chiba 293-8511, Japan
tfuji@re.nsc.co.jp

Jisheng Han

School of Microelectronic
Engineering,
Griffith University, Nathan Campus,
Queensland, QLD4111 Australia
J.Han@griffith.edu.au

H. Barry Harrison

School of Microelectronic
Engineering,
Griffith University, Nathan Campus,
Queensland, QLD4111 Australia
Barry.Harrison@griffith.edu.au

Alexander Ivanov

A.F. Ioffe Physico-Technical
Institute, Russian Academy of
Science,
St. Petersburg 194021, Russia
alexandr.ivanov@pop.ioffe.rssi.ru

Masakazu Katsuno

Nippon Steel Corporation,
Advanced Technology
Research Laboratories,
20-1 Shintomi, Futtsu,
Chiba 293-8511, Japan
katsuno@re.nsc.co.jp

Alexander Lebedev

A.F. Ioffe Physico-Technical
Institute, Russian Academy of
Science,
St. Petersburg 194021, Russia
shura.lebe@pop.ioffe.rssi.ru

Weijie Lu

Department of Physics,
Fisk University,
Nashville, TN 37208 USA
wlu@fisk.edu

Zhiyun Luo

Department of Electrical
and Computer Engineering
Auburn University,
Auburn, AL 36849 USA
lozhiyu@eng.auburn.edu

Roland Madar

Institut National
Polytechnique de Grenoble,
LMGP-ENSPG, BP 46,
38402 Saint Martin-d'Hères,
France
Roland.Madar@inpg.fr

W.C. Mitchel

Air Force Research Laboratory,
Materials and Manufacturing
Directorate,
Wright-Patterson Air Force Base,
OH 45433, USA

Noboru Ohtani

Nippon Steel Corporation,
Advanced Technology
Research Laboratories,
20-1 Shintomi, Futtsu,
Chiba 293-8511, Japan
ohtani@re.nsc.co.jp

Etienne Pernot

Institut National
Polytechnique de Grenoble,
Laboratoire de Matériaux
et de Génie Physique,
UNR CNRS/INPG 5628,
ENSPG, BP 46,
38402 Saint Martin-d'Hères,
France
Etienne.Pernot@inpg.fr

Michel Pons

Institut National
Polytechnique de Grenoble,
Laboratoire de Thermodynamique
et Physicochimie Métallurgiques,
UMR CNRS/INPG/UJF 5614,
ENSEEG, BP 75,
38402 Saint Martin-d'Hères,
France

Michel.Pons@ltpcm.inpg.fr

David C. Sheridan

IBM Microelectronics
1000 River Street, Essex Junction,
VT 05452 USA
davsheri@us.ibm.com

Nikita Strokan

A.F. Ioffe Physico-Technical
Institute, Russian Academy of
Science,
St. Petersburg 194021, Russia
nikita.strokan@pop.ioffe.rssi.ru

Tangali Sudarshan

Department of
Electrical Engineering,
University of South Carolina,
Columbia,
SC 29208 USA
ts@sc.edu

Devki N. Talwar

Department of Physics,
56 Weyandt Hall,
975 Oakland Avenue,
Indiana University
of Pennsylvania,
Indiana, PA 15705-1087 USA
talwar@iup.edu

Philip Tanner

School of Microelectronic
Engineering,
Griffith University, Nathan Campus,
Queensland, QLD4111 Australia
P.Tanner@griffith.edu.au

Hirokatsu Yashiro

Nippon Steel Corporation,
Advanced Technology
Research Laboratories,
20-1 Shintomi, Futtsu,
Chiba 293-8511, Japan
yashiro@re.nsc.co.jp

Mary Ellen Zvanut

Department of Physics,
1530 3rd Ave. S.,
University of Alabama
at Birmingham,
Birmingham,
AL 35294-1170, USA
mezvanut@uab.edu

Materials Science and Engineering of Bulk Silicon Carbides

T. Sudarshan

This chapter highlights the main topics related to bulk silicon carbide growth and characterization, specifically for high-power electronics applications, with an emphasis on the practical issues faced by crystal growers. A brief summary is presented of the historical development of SiC from its initial use and method of growth through the evolution of new growth methods and the difficulties encountered in the production of this material. We then focus in detail on the most common method of crystal growth, the modified Lely method or physical vapor transport (PVT). The experimental aspects, in terms of furnace design, etc., are covered in addition to discussions of the primary parameters of crystal growth and their influence on growth rate and crystal quality. Theoretical considerations are presented to describe the PVT process and to provide the theoretical foundation for SiC crystal growth. The dominant defects that occur during growth and their mechanism of generation are discussed. Information is provided on the historical development of crystal growth from inception to commercial production. In addition to the growth of the commonly used n-doped SiC, the growth of p-doped and semi-insulating SiC boules is also presented. Also, the growth of SiC boules using a high-temperature chemical vapor deposition (HTCVD) process is discussed. The principal methods for material analysis (to analyze crystal quality) and defect characterization (to evaluate the nature, density, etc. of defects) are presented. Finally, the state of the art, future trends, and potential market applications are discussed to complete the overview of SiC growth and characterization.

1.1 Introduction

In the past sixteen years, there has been a significant interest in the development of microelectronic devices for blue and UV emission, solar blind UV detection, high power, high temperature, high frequency, and radiation hard applications, and sensors that operate in harsh environments [1]. The need for such devices has led to substantial research and development efforts in wide

bandgap semiconductor materials, specifically SiC and GaN. The unique electronic, physical, and thermal properties of SiC make it a particularly suitable choice as an electronic semiconductor material for the above-mentioned device applications.

Silicon carbide, in addition to providing the platform (substrate for epitaxy and subsequent device fabrication) for SiC homoepitaxial device structures, is also a substrate of choice for heteroepitaxy of GaN device structures due to its close lattice match to GaN and its excellent thermal conductivity. The thermal conductivity of the substrate is critical for heat dissipation in high power density devices. It is shown that the thermal conductivity approaches 5 W/cmK for SiC with low impurity content, i.e., semi-insulating SiC with electrical resistivity greater than $10^7 \Omega \text{ cm}$ [2]. The commercial availability of semi-insulating SiC wafers with high thermal conductivity has enabled the development of SiC high power microwave devices and monolithic integrated circuits.

As a wide bandgap semiconductor, the potential advantages of SiC include higher junction temperatures and narrower drift regions (due to a high critical electrical breakdown field value ten times higher than Si) that can result in much lower device on-resistance than is possible in Si [3–6]. Another important advantage of SiC as a power electronic device material is that its coefficient of thermal expansion (CTE) is better suited to the ceramics used today in packaging technology [3]. Further, evaluation of the thermomechanical properties (thermal conductivity and CTE) of various semiconductors, and comparing those semiconductors with the electrical properties of the best semiconductors for high voltage, unipolar (majority carrier) power devices indicates that 4H-SiC is one of the best materials for unipolar power devices that meets the critical packaging requirements using existing packaging ceramics. We can therefore envision an entirely SiC based power module from device (SiC or GaN epitaxy on SiC substrate) down to the insulating packaging substrate (AlSiC).

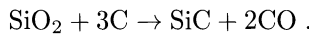
Solid state high frequency power devices are transit-time limited and require more compact designs to promote improved gain, frequency response, and efficiency [7]. Using conventional semiconductors, more compact devices lead to increased temperatures of operation due to increased power density. The above self-heating in compact Si devices degrades transistor gain and efficiency; hence, the devices are designed to be less compact to reduce heating effects. However, adoption of 4H-SiC offers higher electron velocity, higher breakdown field strength, and higher thermal conductivity than Si and hence, 4H-SiC permits transistor performances that exceed the power limits by a factor of as much as four [7].

1.2 Historical Perspective

Silicon carbide has been a part of human civilization for a long time; the technical importance of this hard and stable compound was realized by Cowless

(1885) and Acheson (1892) for grinding and cutting purposes [8], leading to its manufacture on a large scale.

One of the major problems encountered in the growth of SiC is the lack of a SiC liquid phase. This limitation implies that the traditional methods used for the growth of silicon cannot be used for the growth of SiC. Using spontaneous nucleation, Acheson (1892) was the first to attempt the growth of monocrystalline SiC, employing a reaction mixture of silica and carbon. The heating of this mixture as per a temperature-time cycle in air (maximum temperature $\sim 2700^{\circ}\text{C}$) yielded small size crystals of rather poor quality, although adequate for use as abrasives. The SiC grown by this process was in the form of an intergrown crystalline mass, consisting of arrays of long crystallites of diameter $\sim 1\text{ mm}$. The crystalline mass was then crushed into a powder, a process which is in use even today. The reaction occurring by heating the above mixture follows the gross equation



The revolutionary discovery of SiC has had a great impact on the modern mechanical industry, in the cutting and abrasion process, due to the superior hardness and corrosion resistance of SiC. The first demonstration of SiC as a viable electronic material took place in 1907 when electronics engineer Henry Round produced the first light-emitting diode (LED) by applying 10 volts to contacts placed on an SiC crystal, observing yellow, green, and orange luminescence. Further investigation of SiC as a semiconductor was hampered by the lack of an effective method to produce single crystal SiC. The above situation changed appreciably with the advent of the Lely method of growth in 1955 [9].

Lely developed the sublimation method as shown by the schematic representation of the growth cell in Fig. 1.1 [8]. A pseudo-closed vessel was constructed to result in a larger net vapor transport from the hot to the cooler parts of the vessel. A hollow cylinder was constructed from lumps of technical grade SiC (obtained from the Acheson method) in a graphite crucible. The above SiC charge was sintered at 2300°C from crystals grown by gas phase reactions to form a rigid SiC cylinder. The SiC cylinder was placed inside the furnace crucible (Fig. 1.1) and heated in 1 atm argon. A temperature of $\sim 2550^{\circ}\text{C}$ was reached in ~ 1 hour and held fixed for ~ 6 hours. The temperature distribution over the SiC cylinder was chosen so that the cylinder had its highest temperature at the outside surface. The center of the cylinder also had a higher temperature than the top and the bottom. The SiC sublimated from the outer part of the cylinder where the temperature was highest and condensed on the cooler inner face of the cylinder. As shown in Fig. 1.1, colorless transparent platelets were formed, attached to the cylinder inner wall, leaving behind a graphitized outer part of the original cylinder charge. At the top and bottom graphite lids, a mass of greenish hexagonal platelets was formed loosely attached to the graphite plates. Often, these platelets were intergrown with yellow cubic SiC. The platelets formed on the inner walls of the SiC

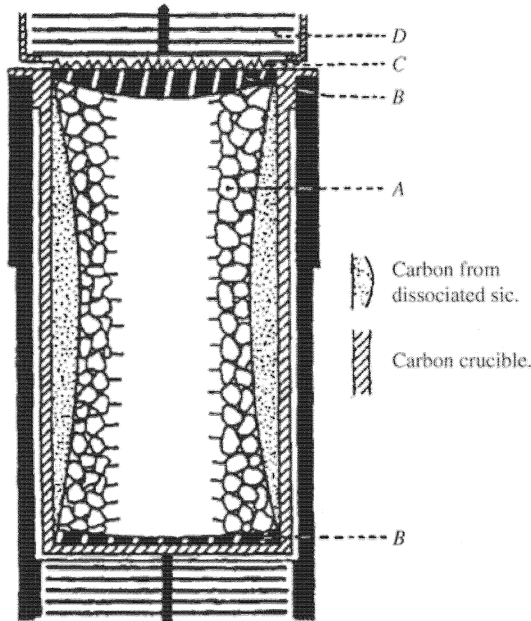


Fig. 1.1. Schematic cross section of growth geometry used in the Lely process. (A) Original SiC lumps, with growth of new platelike crystals; (B) dense layers of SiC; (C) intergrown and twinned mass of SiC platelets with cubic overgrowth; (D) hexagonal and cubic whiskers on radiation shields and further furnace parts ([8], reprinted with permission from Philips Research)

cylinder charge are the most useful, with a hexagonal tabular development having dimensions of 5 mm diameter and 2 mm thickness. For the formation of the above hexagonal platelets, radial temperature gradient is the driving force for SiC vapor diffusion from the source material. The latent heat of crystallization is transferred to the top and bottom lids by radiation. The growth rate greatly depends on temperature and is also influenced by the argon pressure. Lely's work that resulted in the formation of "Lely" SiC platelets led to its great interest for electronic and optoelectronic applications.

The availability of SiC Lely platelet single crystals led to the fabrication of SiC LEDs as the main focus of interest in the ensuing years. The fabrication of SiC based rectifiers, transistors, and detectors were also reported. Absence of a bulk growth process was the main barrier for further development. There was a lull in significant development from the time Lely developed platelet growth in 1955 until seeded sublimation growth was reported in 1978 by Tairov and Tsvetkov [10]. A status report of the progress of work in the intermediate period was discussed in the proceedings of the 1968 International Conference on SiC.

At the 1968 International Conference on SiC [11], Schaffer, in discussing problems in SiC device development, reviewed the status of SiC crystal growth. Various approaches were reported including growth by sublimation or vapor phase, pyrolysis (or CVD), sublimation analog to the liquid phase Czochralski technique, and from the liquid phase using a Si or Cr-Si solvent. Quoting proprietary concerns (a situation that continues to occur today), details regarding the above approaches were not given. In addition to the problem of making crystals grow to sufficient size, other issues cited included “controlling twinning and structure and preventing excess nucleation which leads to crystal interactions during growth.” A dense polycrystalline boule of 8 cm diameter and 2 cm thick, weighing \sim 400 gms. was demonstrated. Another primary challenge discussed by Schaffer relates to the growth of a single polytype SiC crystal: “if the semiconductor properties are to be controlled, and predictable, the energy gap and therefore the polytype must be controllable and predictable.” None of the available theories could predict in advance the specific polytype crystal that would form in a furnace. A way of growing a specific polytype on demand was shown to be by means of the “traveling solvent method” on a substrate of the desired polytype [12]. The key was to use a seed of a specific polytype in order to grow a bulk crystal of the same polytype as that of the seed, an idea developed by Tairov and Tsvetkov [10] to grow bulk crystals using the seeded sublimation growth technique which will be described later.

1.2.1 Construction Materials

The challenge in the use of appropriate materials for construction of the SiC growth furnace was well recognized in the article by Schaffer in 1969 [11]; the challenge arising from the extreme conditions required to work with SiC: “As a consequence, the problem of construction, heating, control of thermal gradients, and mechanical manipulation becomes more difficult. Instead of the quartz or platinum crucibles used to grow II-VI crystals, garnets, etc. there are only a few materials not molten at SiC growth temperatures ($> 1800^{\circ}\text{C}$). Further, most of these, refractory metals, carbides and silicides, are not chemically compatible with SiC at these temperatures. Formation of metal-silicon-carbon binary and ternary eutectics and low melting compounds rule out practically everything but graphite for the crystal growing zone. Graphite porosity, adsorption, and permeability to a wide variety of impurities at the use temperatures require the use of totally clean systems to prevent contamination.” It is noteworthy that the issues related to “construction materials” as presented by Schaffer in 1968 are still the dominant challenges faced by this generation of SiC crystal growers. The primary solution is the use of graphite of maximum simplicity and purity.

1.2.2 Growth of SiC from Solution

With regard to the difficulties faced in SiC bulk growth, it is appropriate to quote Tanenbaum “[one] can appreciate how distressing it can be to attempt to grow a crystal of semiconductor quality while the solvent is evaporating at a great rate and the crucible is liable to disappear at any moment” [13]. The main approaches utilized to grow large high quality single crystals were: (a) utilization of silicon in carbon crucibles, (b) investigation of various crucible materials, (c) increase of C solubility through increase in temperature, and (d) increase C solubility through additives to melt. The highest purity and largest crystals of β -SiC (cubic SiC) grown by the solution technique using high purity Si in a high density, high purity carbon crucible resulted in crystals 1 cm long, 2 mm wide, and 200 μm thick with resistivities up to $10 \Omega\text{ cm}$. Growth from pure silicon melt is expensive, time consuming, with very low yield and crucible failure is a major problem. Various crucibles including quartz, boron nitride, silicon nitride, and aluminum nitride were investigated, but none was found satisfactory and provided any distinct advantage over carbon. The solubility of carbon in silicon is ~ 0.1 atomic percent at 2000 K and $\sim 1\%$ at 2500 K. Low solubility and high supersaturation lead to uncontrolled nucleation and limits the crystal size.

An alternative method of increasing carbon solubility in silicon is through the addition of a constituent to the melt, such as iron, nickel, chromium, silver, etc. The primary considerations for the selection of the appropriate solvent includes: (a) increase the solubility of carbon in the melt at the desired growth temperature, (b) no formation of undesirable carbides, (c) electrically inactive when incorporated in the crystal, and (d) promote and sustain stable growth. Cobalt (Co) was chosen as an additive since CoSi with a melting point of $\sim 1460^\circ\text{C}$ did not form silicides above this temperature. Further, the solubility of carbon in Co is high at ~ 12.75 atomic percent at $\sim 1310^\circ\text{C}$. Growth occurred on both beta and alpha SiC seeds immersed in the melt at growth temperatures from 1600°C to 2200°C . The morphology and other characteristics of the grown film was rather poor and the method of melt growth was not suitable for bulk growth. The main problems of this method for Czochralski growth were: (a) a crust forming on the surface of the melt or at the crucible-melt surface interface and (b) melt traveling up the seed wetting the graphite seed holder [13].

In consideration of the possibility of single crystal SiC growth from melt, thermodynamic analysis indicated that the intrinsic melt of SiC can exist at $T > 3460$ K and pressures $> 10^4$ MPa, which does not allow the commonly used growth-form-melt techniques for the production of SiC boules [14].

J. Smiltens reported the first successful attempt to grow a boule of SiC from vapor by the Bridgman-Stockbarger method [15]. A dense boule 1.9 cm in diameter, 2.5 cm long, consisting of large grains oriented in nearly a common direction was obtained in a sublimation of ~ 28 hours in duration.

1.2.3 First Demonstration of Single Crystal SiC Ingot or Boule Growth

Tairov and Tsvetkov were the first to produce SiC single crystal ingots grown from SiC seeds [10]. The problems inherent to the Lely technique were uncontrolled nucleation, dendrite like growth, and most importantly, formation of platelets instead of the desired formation of ingots. The above difficulties were overcome by the authors by using a single crystal SiC seed, placed in a graphite crystallization cylinder, to which vapor was delivered by a sublimating SiC source. The approach for producing bulk ingots (boules) was based on the classical scheme of supersaturated vapor condensation on a single crystal seed in a quasi-closed crucible volume, shown in Fig. 1.2.

Single crystal Lely platelets of SiC with {0001} faces were used as seeds. Polycrystalline SiC grains synthesized from high purity Si and C are used as the vapor source (charge) placed either inside or outside the thin walled graphite cylinder (marked 3 in Fig. 1.2). Investigations of the boule growth process were carried out in the 1800 °C to 2600 °C range at partial Ar pressures from 0.1 mTorr to 760 Torr [10]. With the growth of ~ 8 mm long and ~ 8 mm diameter boules by the above process, Tairov and Tsvetkov were the first to demonstrate seeded single crystal boule growth of SiC and laid the foundation for modern SiC boule production and wafer fabrication for the SiC based semiconductor industry. The growth rate of the boules was determined by the growth temperature, axial temperature gradient, and the pressure of the inert gas. The boule diameter depended on the starting seed diameter and its length was determined by the volume of the SiC starting material and its complete decomposition. The primary impurities in the grown material were nitrogen (donor) and boron (acceptor), the source for both of the above was primarily the graphite used in the furnace for the crucible and thermal insulation. The authors suggested that the purity of the grown crystal could

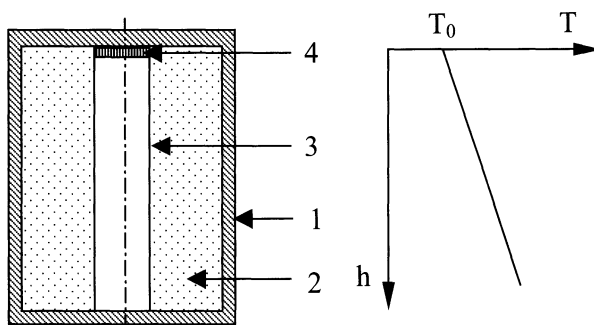


Fig. 1.2. Diagram of production of silicon carbide single-crystal ingots in a quasi-closed volume: (1) graphite crucible; (2) starting polycrystalline silicon carbide; (3) thin-wall shaping graphite cylinder; (4) single-crystalline SiC seed ([10], reprinted with permission from Elsevier)

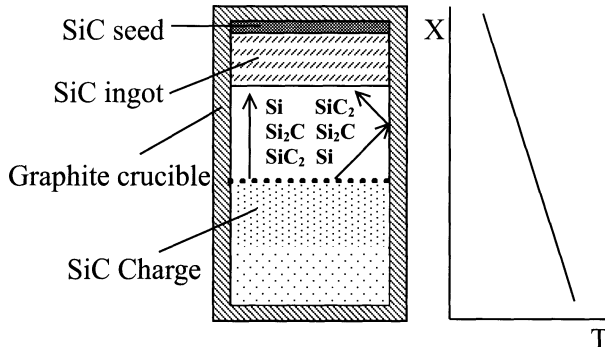


Fig. 1.3. Growth cell for growing bulk SiC single crystals. Reactions of charge dissociation: $\text{SiC}(\text{s}) \rightarrow \frac{1}{2}\text{Si}_2\text{C}(\text{v}) + \frac{1}{2}\text{C}(\text{s})$; $\text{SiC}(\text{s}) \rightarrow \frac{1}{2}\text{SiC}_2(\text{v}) + \frac{1}{2}\text{Si}(\text{v})$. Reactions on the crucible surface: $\text{C}(\text{s}) + 2\text{Si}(\text{v}) \rightarrow \text{Si}_2\text{C}(\text{v})$; $2\text{C}(\text{s}) + \text{Si}(\text{v}) \rightarrow \text{SiC}_2(\text{v})$ ([14], reprinted with permission from Elsevier)

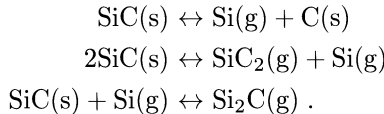
be improved by lowering the crystal growth temperature (to reduce boron) and to carry out growth in vacuum conditions (to reduce nitrogen). Analysis by the authors indicated the amount of SiC crystal grown per unit mass of the graphite heater evaporated increased 4.5 times when the growth temperature was reduced from 2707 °C to 1707 °C. Based on the above considerations, SiC crystals were grown at ~ 1800 °C in 0.1 to 1 mTorr vacuum, at 30 °C/cm axial temperature gradient, resulting in ~ 8 mm long boules grown at ~ 2 mm/hour. The ingots grown were of a single polytype, including 6H, 4H, and 15R, using the respective type seeds to initiate growth. The pure ingots grown exhibited an effective carrier concentration of $(N_d - N_a) = 1 \times 10^{16} / \text{cm}^3$.

In a later investigation, Tairov noted that depending on the composition and pressure of the gaseous medium in the growth region, SiC boules could be grown at high growth rates up to 10 mm/hour [14]. However, it is generally known the quality of the boule grown in terms of defect density degrades at high growth rates. The primary stages of bulk crystal growth are: dissociative sublimation of the source charge, mass transfer of evaporated Si and C species in the gas phase, crystallization of the species onto a seed, and removal of the heat of crystallization. Figure 1.3 shows this process schematically.

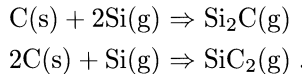
1.3 Fundamental Physics and Chemistry Issues Related to Bulk Crystal Growth

1.3.1 Source Material and Vapor Composition

The driving force for bulk SiC growth is provided by applying a temperature gradient such that the SiC source is at a higher temperature relative to the seed. The main components or species in the sublimed vapor present in the gas phase, are: Si, SiC₂, and Si₂C. The reactions are according to the following:



In the equilibrium vapor, the pressure of that component with the highest partial vapor pressure determines the total vapor pressure [16]. At the growth temperatures, Si has the highest vapor pressure of all the species. As noted earlier, since the growth occurs in a quasi-closed crucible, there is effective loss of Si from the decomposing SiC source resulting in graphitization of the source which creates unfavorable growth conditions. An even more serious issue is that the higher partial pressure of Si in the vapor, which implies a Si rich mass transport region, results in a higher ratio of silicon and carbon atoms, $N_{\text{Si}}/N_{\text{C}}$, or simply Si/C ratio. The Si/C ratio is an important parameter since it determines the stoichiometry of the grown crystal. Further, excess Si, when it reaches supersaturation at the crystallization surface, leads to a liquid phase at the growth surface, resulting in the generation of various defects, specifically micropipes. At long source to seed distances, typical of practical growth systems, there will be additional fluxes from the graphite wall constituting the crucible. Mass transport from the source to seed is given by fluxes of the Si and C containing gas phase components [16]. The Si vapor will react with the graphite wall as per:



The above reactions result in the generation of additional Si_2C and SiC_2 species, and thus points to the importance of the purity and density of the graphite crucible as a source of C and different types of impurities.

Investigations by Tairov [14] related to sublimation of the SiC charge demonstrated that the composition of the sublimated vapor, specifically the Si/C ratio, depends significantly on the polytype composition and preparation conditions of the source charge. It is shown that if the source is obtained by milling previously synthesized SiC platelets, the total vapor pressure and the Si/C ratio in the vapor strongly depend on the charge grain size with the ratio increasing with decreasing grain size at a given temperature. The results are explained in terms of plastic strain during milling. In addition to mechanochemical activation of the source charge, its polytype structure also influences the Si/C ratio. A main problem is the difficulty in maintaining this ratio constant during the entire duration of growth of large boules. Based on studies of vapor composition above the SiC source charge, Tairov concluded that “reproducible production of SiC single crystals of a specified geometry, growth rate, polytype, stoichiometric composition, doping level, etc. requires careful control of the preparation of the original charge and its composition.” Due to sintering and graphitization of the source powder, the relative vapor pressures of the gas species, and therefore the Si/C ratio, varies during the prolonged growth period of $\geq 24\text{ h}$.

In their investigation of 6H bulk growth, Nishino et al. [17] found that the crystal growth rate was influenced by the grade of graphite used for the crucible. For a given growth temperature, the growth rate decreased with an increase in the graphite density which was attributed to the existence of different partial pressures in the growth cavity for different grades of graphite. The results indicate that the growth rate is enhanced by the excess carbon species available with the lower density graphite.

The total pressure in the growth zone is highly dependent on temperature; the partial pressure of gaseous Si dominates below 2400 °C in both SiC-C and SiC-Si systems and hence the amount of Si is greater than C [16]. The vapor phase stoichiometry, which is essential for the growth of good quality SiC crystals, improves at higher temperatures of growth since the Si/C ratio in the vapor approaches unity at ~ 2800 °C (Fig. 1.4). However, at such high growth temperatures the introduction of unintended impurities arising from the graphite and the lifetime of the crucible and other graphite components constituting the growth furnace become serious issues. In general, the main challenge for crystal growers is the difficulty in maintaining constant or equilibrium stoichiometric conditions (i.e. Si/C ratio = constant) during the entire duration of ≥ 24 hours of growth of large bulk crystals. It is worth noting that in the case of intentional doping in bulk growth the partial pressure of the impurity could dominate and maintaining equilibrium stoichiometric conditions of Si, C, and the impurity during growth becomes a primary challenge [16].

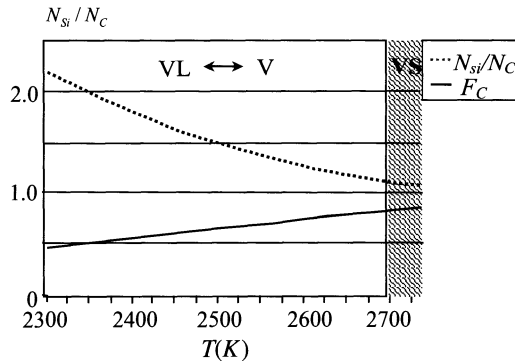


Fig. 1.4. Vapor composition N_{Si}/N_C and efficiency F of conversion of SiC vapor source to bulk crystal

1.3.2 Mechanism of Growth

Of the several readings available to understand the crystal growth mechanism, the one by M. Syväjärvi [16] is particularly useful to the understanding of the growth of bulk SiC and the material for this section is mostly derived from the above reference. Orientation of the seed or substrate surface is one

of the most important parameters that controls the growth process. The seed surface may be divided into several classifications as illustrated in Fig. 1.5: low-index facet, near-facet, terrace, and terrace-free regions [16]. The [100]-direction of Si or GaAs crystal or the [0001]-direction of SiC are examples of low-index or facet directions. Depending on the surface orientation of the seed (measured from the low-index direction), one can expect facet growth, near facet growth, etc. In the case of a perfect crystal with a low-index surface, there is only one way to start or nucleate crystal growth: two-dimensional (or 2D) nucleation, for which a nucleation site or an island that exceeds a critical radius must be formed, and the radius of this nucleation site is a function of supersaturation. The nucleus thus formed expands two dimensionally to cover the entire surface of the seed surface. In practice, the crystal is not perfect, and the above 2D growth is provided by the presence of an emerging imperfection on the surface, typically a dislocation, which can act as a step at which nucleation can occur [18]. Experimental evidence clearly shows the existence of growth spirals at the SiC growth front [17] as seen in Fig. 1.6. Hence, it is accepted that SiC bulk growth occurs via spiral growth initiated at screw dislocations, an excellent description of which is presented in [16]. Figure 1.7 shows a schematic illustration of growth arising from a screw dislocation. Crystal growth arises by the Si and C species from the sublimated vapor arriving at the seed surface. Any of the species that lands on the surface, away from the steps will eventually diffuse towards the stepped regions and get attached either at a kink or at a step and eventually migrate along the step to a kink, contributing to the propagation of the spiral and thus to

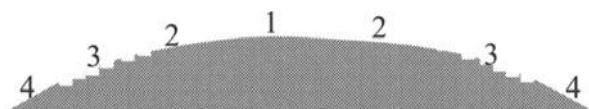


Fig. 1.5. Different substrate surface orientations on which different growth processes take place. (1) Facet growth; (2) near-facet growth; (3) terrace growth; (4) terrace free growth ([16], reprinted with permission from author)

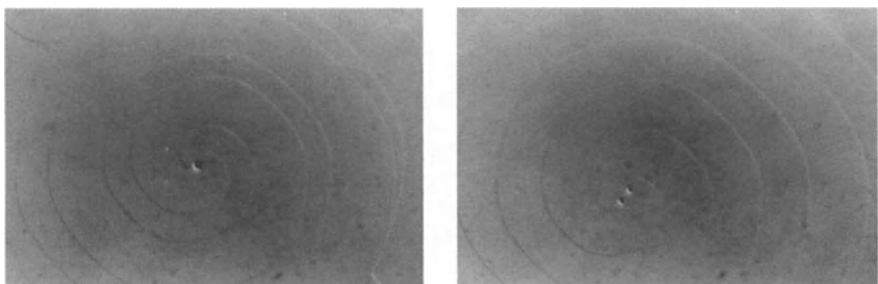


Fig. 1.6. Two noninteracting growth spirals emerging from neighboring screw dislocations ([16], reprinted with permission from author)

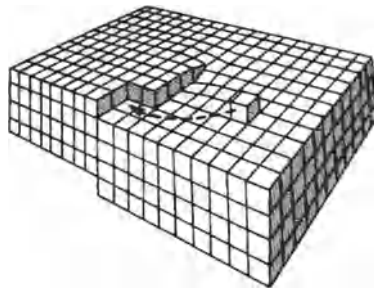


Fig. 1.7. Schematic illustration of growth with a screw dislocation ([19], in the public domain)

crystal growth. As the species continue to arrive at the seed surface, the step will move or sweep across the surface of the seed area. The step is pinned at the core of the screw dislocation, the surface emergence point, where the step will form a helicoidal surface. Ideally, under steady state conditions, the step will rotate and in the process build new steps in a spiral staircase fashion with the bottom-most stair moving outwards and the subsequent higher steps also moving outwards simultaneously, forming a spiral hillock. The outward moving spiral steps are nearly equidistant at the growth front, under ideal growth conditions, which indeed is rare in practice. For growth proceeding from a single nucleation screw dislocation site, in an ideal situation, a mesa structure is formed at the top of the growth front (hillock) with nearly equidistant growth spirals extending out such that the bottom platform of the staircase or spiral hillock extends to cover the entire diameter of the seed surface. However, in practice a large number of screw dislocations are present on the seed surface. Multiple steps will develop from the many dislocations, and in practice, the spiral fronts will interact with each other (Fig. 1.8) breaking the symmetry of equidistant steps formed from a single spiral (Fig. 1.6). Hence the spiral

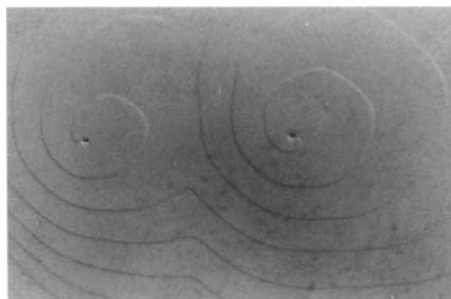


Fig. 1.8. Two interacting growth spirals emerging from neighboring screw dislocations ([16], reprinted with permission from author)

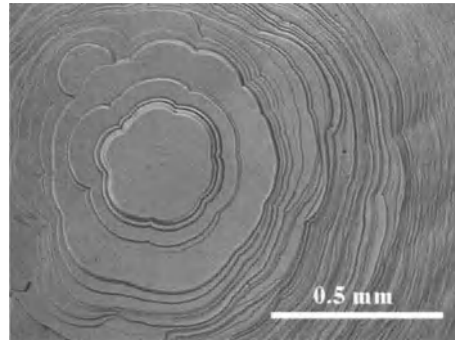


Fig. 1.9. Top of a SiC boule with steps advancing out from the mesa ([16], reprinted with permission from author)

fronts are no longer circular and further, in practice, the developed steps are bunched, i.e., the height of the step, at the edge of a spiral, increases during growth (Fig. 1.9) [16]. This situation is similar to a traffic jam where the propagating fronts will pile on top of the other; known as step-bunching. The above phenomena are clearly delineated in Fig. 1.9. At the northwestern corner of Fig. 1.9, one can observe the overlap of growth fronts arising from two sites – the dominant spiral from the center and a secondary spiral developing simultaneously from a nucleation site far away from the main spiral. The region where they overlap could result in a grain boundary. Figure 1.10 illustrates a situation where an obstacle pins the step front; the created disturbance causes macrodefects, which degrade crystal quality [16, 17]. The primary obstacles are agglomerates of carbon (from the graphite walls or the SiC source charge), impurities (Al, B, etc.), or silicon. The existence of obstacles, caused by impurities, were

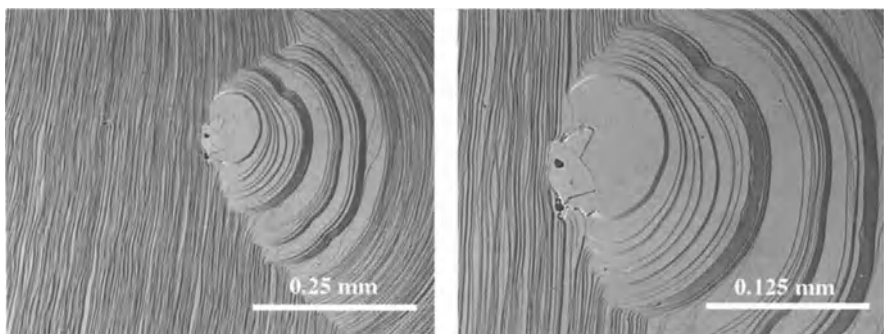


Fig. 1.10. A disturbance of advancing steps outside the mesa (*left*) and a magnified view (*right*); step direction from left to right ([16], reprinted with permission from author)

proposed to be the cause for the formation of micropipes [20] and planar defects [17], the major structural defects in SiC – to be discussed in Sect. 1.7. The profile or shape of the crystal growth front (crown) contains valuable information regarding the boule growth process since it is a result of the complex growth processes. Hence, the boule profile is an important barometer of the effectiveness of the growth process and the overall quality of the grown boule. Instabilities during the growth process are reflected in non uniform features present on the boule crown. Nearly flat, slightly convex growth front is beneficial for producing crystals of good quality [21].

1.3.3 Seed Surface Effects

One important process that occurs during seeding is that in a manner similar to sublimation of the source, the seed surface also undergoes sublimation before crystallization begins at the seed surface. This is referred to as the breaking up of the seed surface. Since the partial pressure of Si over the SiC seed surface is high compared to that of C, Si evaporation can take place leading to surface graphitization. It is shown by Heydemann and colleagues [22, 23] that seed surface degradation occurs at 1800 °C at an ambient pressure of 650 Torr in the absence of source material. However, seed degradation occurred at ~ 2150 °C at 650 Torr in the presence of source material. Generation of voids and silicon droplets is common during the temperature ramp-up stage.

Hence, in order to avoid seed surface graphitization, the pressure and temperature profile during the early non-equilibrium stage of growth must be controlled. Specifically, growth is initiated by lowering the system pressure from the starting value of ~ 800 mbar to the end pressure of 5–40 mbar [24].

Sublimation etching of the seed surface prior to the initiation of bulk growth is suggested to be an important step for defect-free crystal growth [25].

1.3.4 Polytype Control

An important aspect of single crystal SiC is the existence of more than 170 polytypes [26]. Different polytypes arise from the different stacking sequences of the Si-C bilayer producing crystals with different unit cell dimensions along the [0001] or *c*-axis, with the longest unit cell of a polytype identified thus far being 120 nm. The reason for the stability of so many polytypes in SiC is not well understood and is a matter of current study. It is noteworthy that each polytype differs from the other in terms of bandgap, and other fundamental electronic and electrical properties. Hence, SiC can be thought of as a family of a large number of semiconductors. For further reading on this subject, the reader is referred to references [16, 27]. The dominant polytypes, however, are 3C (cubic or β SiC), 4H and 6H (hexagonal or α SiC), and 15R (rhombohedral). During bulk growth of a given desired polytype (e.g. 4H or 6H) other polytypes can be simultaneously grown and they can be considered

as defects in the host polytype semiconductor. Hence, control of polytype is a major challenge in SiC bulk growth.

Knippenberg [8] presented the temperature versus structure relationship of a few important SiC polytypes, as shown in Fig. 1.11, and he considered the hexagonal polytypes to be a series of allotropic modifications. It is to be noted that the probability plot in Fig. 1.11 is derived for growth from the Acheson process and undoubtedly is modified for seeded bulk growth. It is noteworthy from the above figure that, other than 2H, it is difficult to establish conditions for the stable growth of other polytypes; the narrow regime available for the growth of the 4H polytype makes it an extremely challenging material to grow in the bulk form. Also noteworthy is the occurrence of 3C over a very wide temperature range. As noted from Fig. 1.11, the polytypes with the highest probability of occurrence are 6H, 4H, 15R, and 3C. Other polytypes are often found at the phase boundaries between the stable polytypes [16]. The 3C is not stable but can be favored during particular growth conditions.

Growth of several different polytypes can occur during the growth of a long SiC boule. Nucleation control, especially at the initial stage of growth is difficult and very important since the growth process is not stable at this early stage of growth. Polytypes other than that of the seed can easily be formed by phase transitions. Fluctuations in the vapor supersaturation at the non-equilibrium stage of initial growth (~ 1 to 2 hours of initial growth) can result in secondary polytype nucleation. Yakimova et al. [28] have shown that single polytype SiC boule growth can be enhanced by using a seed which is slightly off-axis from the low-index (0001) plane (Fig. 1.5) and by establishing low

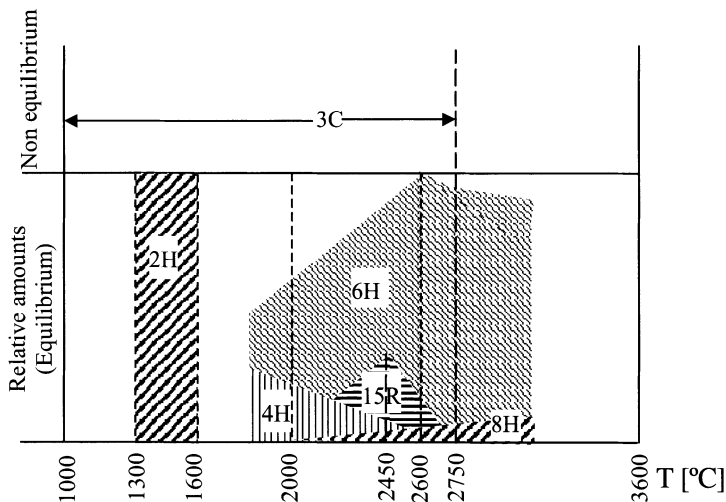


Fig. 1.11. Relation between structure and temperature of occurrence. The relative amounts of the different hexagonal structures are shown ([8], reprinted with permission from Philips Research)

growth rates at the initial stages of growth. By establishing growth of the same polytype as that of the seed in the initial non-equilibrium stage, the growth rates can be enhanced to reasonable values (~ 1 mm/h) after the stable conditions of growth are reached. This approach avoids phase transitions at the critical initial stage and hence single polytype boule growth of good quality can be grown. It will be shown later that control of the initial stage of boule growth is critical since most of the defects (dendrites, inclusions, micropipes, stacking faults, and dislocations) are formed in the initial transition layer of the boule next to the seed.

Another very important factor essential for polytype homogeneity in the grown boule relates to the ‘seed’ and the ‘seed surface.’ Stein, Yakimova, and others have shown that growth of 4H-SiC can only be accomplished from the carbon- (C-) face of 4H-SiC seed and not its Si-face [16, 28–31], and growth of 6H-SiC boules can be achieved from both the Si- and C-faces of the 6H-seeds. Further, 4H-SiC can also be grown from the C-face of a 6H-seed. It is believed that the difference in the surface free energies of the Si and C faces of 4H is the reason why 4H-SiC can only be grown on its C-face [28, 29]. As noted earlier, nucleation, also called seeding, is a key primary step in forming a transition layer (~ 1 mm thick layer adjacent to the seed) with minimum defect generation, and if not controlled properly, will lead to generation of dendrites, inclusions, and polytype phase transitions. This initial stage of seeding is influenced by the seed surface orientation, surface quality, etc.

1.3.5 Bulk Crystal Doping

SiC boules can be doped n- or p-type during growth with nitrogen and aluminum being the main n- and p-type dopants, respectively; the above dopants create relatively shallow donor and acceptor levels within the bandgap. There are no major distinctions for the doping processes between 6H and 4H crystals [32]. There is significant anisotropy for N and Al incorporation in PVT boule growth from the (0001) Si versus (000 $\bar{1}$) C faces, the nitrogen incorporation is higher on the C face versus the Si face, while for Al, the reverse is true. While the Al incorporation into the boule is roughly a linear function of Al concentration in the source for concentrations up to $10^{20}/\text{cm}^3$, nitrogen incorporation is approximately a function of the square root of the nitrogen partial pressure in the growth cell. Interestingly, nitrogen incorporation decreases with growth temperature while that of Al increases [32].

In summary, in order to produce good quality SiC boules, the important factors to keep in mind include: (a) growth to start from a minimum number of nucleation sites on the seed which implies very good seed quality and surface preparation, (b) growth under very pure conditions of the system to avoid formation of obstacles arising from impurities and silicon droplets, (c) maintenance of growth under constant conditions of stoichiometry which implies constant and uniform Si/C ratio of the vapor species impinging at the growth front, and (d) establishment and maintenance of appropriate radial and axial

temperature profiles to assure steady and uniform flow of the growth spirals to avoid step bunching. The primary challenge in bulk growth, especially that of large diameter and long boules, is the maintenance of some of the above factors constant throughout the long period (≥ 24 hours) of growth.

1.4 Theoretical Considerations and Influence of Independent Parameters on Growth Rate

In this section, we will first present some basic theoretical considerations useful for the understanding of SiC boule growth by the Physical Vapor Transport phenomena. Because of the high growth temperatures and the corrosive atmosphere of the SiC crystal growth reactor, the temperature profiles and thermophysical conditions inside the crucible are not accessible for measurements during PVT growth. Hence, analytical modeling or numerical simulations of heat and mass transport mechanisms can provide a valuable tool to understand the growth phenomena and hence to improve the growth process [33].

1.4.1 Theoretical Considerations Relevant to Growth

Supersaturation

One of the main kinetic phenomena that controls the crystal growth process is the formation of “new phase nucleation centers” at the surface of condensation of a perfect crystal that is assumed not to contain preferential nucleation centers. In order to initiate crystallization the radius of a nucleation center that gets formed on the surface must be stable, i.e., its radius must exceed a critical value:

$$r_c = \Omega \cdot \frac{\gamma}{kT \ln(P_v/P_s)} , \quad (1.1)$$

where Ω is the molecular (atomic) volume; γ represents the specific surface energy of the condensing solid surface; k and T are the Boltzmann constant and average temperature in the growth cell, respectively; P_v is the total vapor pressure of the system at the evaporation (SiC) temperature and P_s denotes the equilibrium or saturation vapor pressure at the temperature of crystallization, T_s .

The pressure ratio P_v/P_s is indicative of the vapor supersaturation at the surface of condensation. In the absence of preferential nucleation centers on the surface, P_v must be at least 10% above P_s , i.e., $P_v = 1.1 P_s$. However, in practice, due to the presence of kink sites (e.g., screw dislocations intersecting the crystal seed surface) that serve as nucleation or crystallization centers, crystallization takes place at much less supersaturation than 10%.

Supersaturation is defined by

$$\varepsilon = \frac{P_v - P_s}{P_v} . \quad (1.2)$$

The vapor pressure of the evaporating material (SiC) is $P_v = A \exp\left(-\frac{H}{RT}\right)$ where R = Gas constant and H = Enthalpy of sublimation.

For small values of H/RT , $P_v \cong A(1 - H/RT)$ and from this, it can be shown that

$$\varepsilon = \frac{P_v - P_s}{P_v} = \frac{\Delta P}{P_v} = \frac{H}{RT_v T_s} \times \Delta T = \frac{H}{RT^2} \times \Delta T \quad (1.3)$$

Hence, supersaturation (ε) is proportional to $\Delta T = T_V - T_S$, the temperature difference between the source and the seed or growth surface, and T is the average temperature in the growth cell.

If $\Delta T = 0$ and $\varepsilon = 0$, crystallization or growth does not take place. Hence, a certain supersaturation (or ΔT between the source and seed) is needed to initiate growth. If ε is large, the growth rate becomes very large. In this case, even before one layer spreads out completely on the seed (or growth) surface, new nucleation centers with critical size appear on the surface of the non-completed layer leading to step bunching and even 3D growth. It is possible to create second phase at the surface of condensation, e.g. Si liquid phase at very high ε arising from large ΔT , leading to macrodefects (e.g. micropipes and planars) in the crystal. If ε is very low, no growth is initiated. Hence, the optimum value of ε needs to be maintained during growth. During growth, the source to growth front spacing decreases and hence, ΔT between the source and seed changes continually, and hence ε is not constant during growth. For large diameter seed surfaces, maintaining a constant value of ε across the entire surface becomes difficult, i.e., the growth rates are different at different points on the surface and this creates thermal stress in the crystal.

Mass Transport Process

For purposes of modeling, the crucible where the PVT process takes place is considered as a closed system [34]. The different phenomena that can result in a gaseous flux containing Si and C species include: concentration gradients (diffusion), density gradients (natural convection), and interfacial heterogeneous chemical reactions (Stefan flow). Although the phenomenon of Stefan flow takes place during SiC PVT growth [35], its participation in the mass transport process is of second order importance [34]. Since SiC PVT bulk growth typically is conducted in the presence of an inert gas (argon), the SiC vapor and argon gas mixture in the growth cell is considered as the media where SiC mass transport phenomena takes place. An estimation of the heat and mass transport phenomena (convection versus diffusion) in the gas

mixture is typically performed through calculation of the magnitude of the dimensionless Grashof, Prandtl, and Rayleigh numbers that are respectively defined as:

$$\begin{aligned} Gr &= \frac{d^3 \cdot g \cdot \beta \cdot \Delta T}{\nu^2}, \\ Pr &= \frac{\nu}{\alpha}, \\ Ra &= Gr \cdot Pr, \end{aligned} \quad (1.4)$$

where β is the volume expansion coefficient of the gaseous media, g stands for the acceleration due to the gravity, d is the characteristic length (source-seed distance, see Fig. 1.12), ΔT represents the temperature difference between the source and the front of crystal growth, ν denotes the kinematic viscosity and α is the thermal diffusivity of the gas mixture.

Since the above mentioned parameters for SiC vapor are unknown, the reference data for argon are usually used in the calculations [34, 36]. All other parameters necessary for the estimation include typical characteristics of the mass transport zone $d \leq 5.0$ cm, $\partial T/\partial z = \Delta T/d \leq 30$ K/cm. In such a case, the Rayleigh parameter yields a value lower than 10, which is far below the value needed for the occurrence of natural convection ($Ra > 1000$). Therefore, mass transport is mainly driven by diffusion.

In order to find an expression for total SiC mass flux across the mass transport gap in the growth cell, a multicomponent diffusive flux equation for each component of the SiC vapor + argon system is solved, using Fick's law. A 1D model of ordinary diffusion in the binary SiC vapor + argon system is used, assuming a one component (SiC) composition of the vapor. In order to complete the problem formulation, the effective binary diffusion (effective diffusion) coefficient D of SiC in argon is defined [36]. The Chapman-Enskoog Kinetic Theory of Diffusion, for practical considerations, can be written in

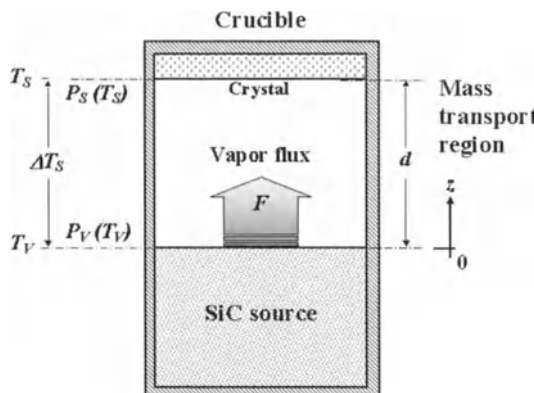


Fig. 1.12. Schematic representation of SiC PVT growth cell

a more convenient form as indicated below. For the SiC vapor and argon system, the diffusion coefficient approximation is given by [37]:

$$D(p_{\text{Ar}}, T) = D_0 \left(\frac{T}{T_0} \right)^n \frac{p_0}{p_{\text{Ar}} + p_{\text{SiC}}(T)}, \quad (1.5)$$

where T is the absolute average temperature in the growth cell, p_{Ar} represents the argon partial pressure and $p_{\text{SiC}}(T)$ is the partial pressure of SiC vapor in the SiC vapor + argon system under the assumption of one component composition of SiC vapor, parameters n , D_0 , T_0 and p_0 are equal to 1.8, $1 \times 10^{-1} \text{ cm}^2/\text{s}$, 273 K and 1 atm (760 Torr), respectively (D_0 is a function of size and mass of diffused atoms).

Graphically, the dependence of $D(p_{\text{Ar}}, T)$ in the range of argon partial pressure 1–50 Torr (typical range of argon partial pressure during SiC growth [36] is shown in Fig. 1.13). As can be seen from the plots, even at the “low end” limit, the effective diffusion coefficient of SiC vapor in argon yields the value of $D(p_{\text{Ar}}, 3150) \approx 20 \text{ cm}^2/\text{s}$. For this value of the effective diffusion coefficient, the velocity of the vapor front $V_f \cong D/d$ is more than 4 cm/s and the average flight time of SiC species from the source to the seed yields the value of $\tau \cong d^2/D$, which is less than 1.25 s for the typical source-seed distance $d \leq 5.0 \text{ cm}$. Such a small value of τ in comparison to the practical growth rate values $\leq 1.0 \text{ mm/h}$ ($3 \times 10^{-4} \text{ mm/s}$) and temperature rise rate during the furnace heat-up stage $dT/dt \leq 1 \text{ K/s}$ makes it possible to consider the problem in the steady state approximation.

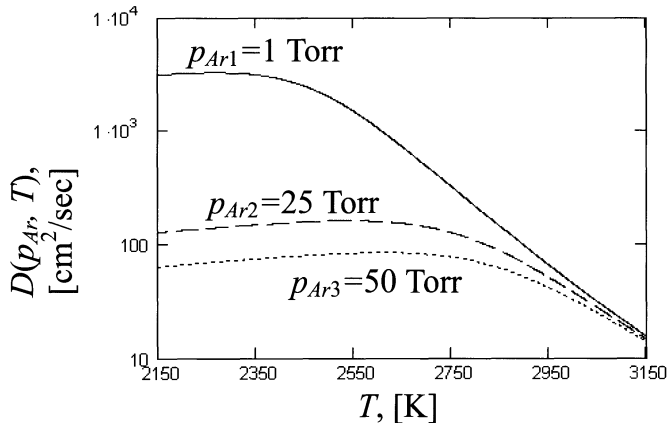


Fig. 1.13. Temperature dependence of SiC effective binary diffusion coefficient at different values of argon partial pressure p_{Ar}

It can be shown that the total diffusive mass flux of SiC vapor across the mass transport gap can be written as:

$$F = \frac{D}{d k T} (P_V - P_S) \cong \frac{P_V - P_S}{R_D}, \quad (1.6)$$

where $R_D = d k T / D$ stands for the diffusive resistance of the mass transport region; P_V and P_S represent the total equilibrium pressure of SiC vapor at the source top surface at temperature T_V and at the growth front with temperature T_S , respectively (see Fig. 1.13) and k is Boltzmann constant and $T = \sqrt{T_V T_S}$ is the average temperature in the growth cell.

Using the exponential approximation of SiC vapor pressure in the form of $P_i = A \exp(-W/R \cdot T_i)$ (where i can take either V or S, $A = 4.3323 \times 10^8 \text{ J/m}^3$, $W = 5.6 \times 10^5 \text{ J/mol}$ represents the evaporation energy of SiC and R is the gas constant) [38, 39], the net SiC vapor flux across the mass transport gap can be expressed in terms of the *source-growth front* temperature difference $\Delta T_S = T_V - T_S$:

$$F = \frac{P_V}{R T^2 R_D} \Delta T_S, \quad (1.7)$$

In (1.7), R_D , the resistance for diffusion, is dependent on d , the gap spacing between the source and the growth front; T , the average temperature in the crucible; and D . Temperature T determines the average collision distance or mean free path (MFP) in the growth gap region. An increase in T decreases the MFP, and understandably, this should increase R_D (it is to be noted that this is a rather simplistic picture). If R_D is very large, the growth will be very slow or can even stop. But too small of a R_D value will lead to very high growth velocity, increase in 3D growth, thermal stresses, defect generation, etc. Now, looking at the dependence of R_D on ' d ', an increase of d leads to significant number of collisions with the crucible wall, which implies additional resistance to the diffusive flux. But if d is very small, the small value of R_D will lead to high growth rate with its implications as discussed before. Further, for very small d , the exchange of heat between source and seed is very large and this creates additional instability of growth.

The diffusivity of vapor species in argon, D , is a sensitive function of temperature T in the growth cell and argon pressure as indicated by (1.5). A very low argon pressure leads to a very high value of D , which implies intense vapor flux arriving at the growth surface, and hence a very large growth rate or uncontrolled nucleation. Hence, the growth process is not limited by diffusive flow and surface kinetics at the growth front becomes the rate limiting process. Hence, from the above analysis, we conclude that crystal growth rate in the PVT process can be controlled either by ' T and d ' or p_{Ar} (the argon pressure). Growth control is more difficult and/or less practical to achieve by controlling ' d ' or ' T ', especially during growth. By changing T , the temperature of many points in the reactor will change: source, seed, growth front, seed holder, etc.

Hence, achieving control of growth via argon pressure is appropriate and easy to implement. The above discussion clearly points to the importance of using an inert gas such as argon for bulk SiC growth using the PVT process. The diffusion resistance R_D can be varied over a wide range in the growth reactor by varying D , i.e., by varying $(p_{\text{SiC}} + p_{\text{Ar}})$, the pressure of the (SiC vapor + argon) system.

Kinetic Processes

The above discussed diffusive flow describes the processes which control the transport of the chemical species (velocity, etc.) that result in crystal growth. But to determine the growth rate, we have to investigate the kinetics of the crystal growth process, which is determined by both the physical and chemical processes taking place in the reactor and on the crystallization surface. The *average rate* of chemical reaction is the variation in the amount of species taking part in the chemical reaction or alternatively it can be described in terms of the build up of the product of the chemical reaction (material deposited on the growth surface), during the time of reaction Δt . In the case of SiC, the rate of growth is determined by the rate of physical and chemical atomic level processes taking place on the crystallization or condensing surface.

The PVT process of SiC crystal growth is determined by several simultaneous physical and chemical processes taking place in the growth reactor. Material sublimation from the source determines the composition and the total pressure of the vapor. The kinetic parameters characterizing the process of sublimation is determined by the temperature of sublimation, the equilibrium or saturated vapor pressure, and the vapor stoichiometry (composition) coefficient at the given sublimation temperature. The mechanism of vapor transport from the source to seed must also be included to describe the kinetics of the SiC growth process. As discussed earlier, when diffusion is the dominant transport (of the chemical species) process, the diffusion coefficient, D , the pressure gradient, dP/dz , and the diffusion resistance, R_D , characterize the kinetic parameters of mass transport. Both physical and chemical processes (at the atomic level) take place at the surface of condensation receiving chemical species from the vapor transport region. The primary processes at the crystallization surface include: vapor condensation (adsorption and desorption of chemical species at the surface), surface diffusion processes, growth initiation at nucleation centers and formation of additional nucleation centers, and subsequent 2D development of the growing atomic layer. The main kinetic parameters that determine (or control) growth include supersaturation of the vapor, the parameters of atom accommodation at the surface, the coefficient of surface diffusion, specific surface energy, and the enthalpy of phase transformation (vapor to solid) reaction. Heat released at the surface of crystallization, as a result of chemical reaction, also influences the kinetic processes at the growth surface that controls crystal growth. This heat can influence the crystallization surface temperature; changing the supersatura-

tion condition. The heat dissipation process through the growing boule can initiate thermal stresses in the crystal volume and, as a result, plastic deformation leading to defect generation. The origin of the above process is not directly dependent on the composition or other parameters of the vapor system (pressure, stoichiometry, etc.)

Hence, the conditions of heat dissipation through the growing boule must be considered in conjunction with that of growth. The above discussion points out the existence of a large number of processes that determine the quality of the grown crystal and the interdependence of the different processes makes bulk growth of SiC by physical vapor transport a rather complex undertaking.

Thermal Stresses in the Growing Boule and Defect Initiation

During growth, heat is released as a result of chemical reaction at the surface of phase transformation. This heat must be removed from the crystal growth surface through the crystal body, to maintain the growth process. In addition to the above heat, the total heat flux irradiated from different parts of the growth cell, that is absorbed by the crystal body, must also be removed. Non-uniform temperature distribution in the crystal volume due to the above process creates thermal stresses within the growing boule.

Theoretical analysis [40] shows that the thermal stress generation is determined by two heat exchange factors: (a) the latent heat of crystallization which depends on the enthalpy of chemical reaction and the rate of crystal growth and (b) heat absorbed by the crystal due to heat irradiation from the inner walls of the crucible. This portion of the heat generated in the crystal can be considered as ‘parasitic’ heat, which must be minimized by appropriate furnace design.

Numerical simulation of the thermal field distribution in the crucible [41] shows that the significantly varying radial T gradient in the growing crystal represents a major factor in the development of excessive thermal stresses. The thermal stress field exhibits a complicated distribution with the stress components undergoing change of sign [compressive (negative) to expansion (positive)]. The ratio of maximal magnitude of the radial stress component to the maximum axial stress is close to 5.0. The simulated Von Mises stress distribution is shown in Fig. 1.14. As the figure indicates, the stress can be extremely non-uniform and can significantly exceed the value of the critically resolved shear stress, τ , at the temperature of SiC bulk growth, with $\tau \gg 1 \text{ MPa}$ [32].

The presence of a non-uniform thermal stress distribution, which exceeds the critically resolved shear stress by a factor of two implies intense plastic flow in the growing boule that would result in the generation of dislocations of high density. Since the latent heat of crystallization depends on the crystal growth rate, the boule growth rate directly influences crystal quality.

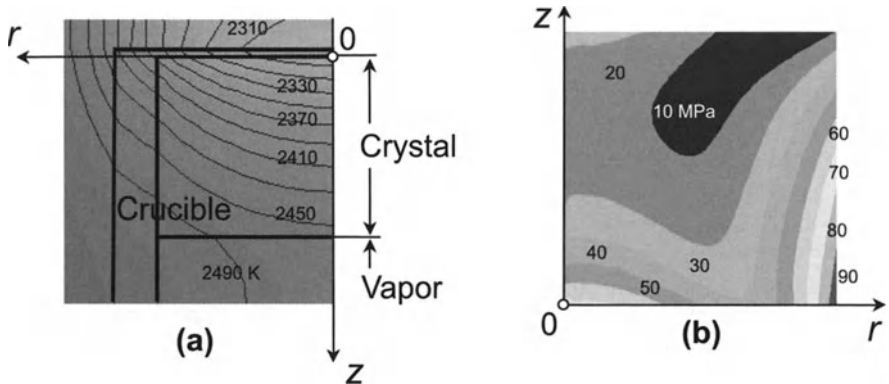


Fig. 1.14. (a) FIDAP-generated temperature field and (b) ANSYS-generated Von Mises stress distribution in a 2" diameter and 1" long SiC ingot during PVT growth (the numbers shown are in MPa) ([42], reprinted with permission from author)

1.4.2 Crystal Growth Rate: Influence of Independent Parameters

In the previous sections, we studied the primary mechanisms by which bulk crystal growth proceeds by physical vapor transport of the Si and C species emanating from the sublimating SiC source. The issues of importance include the composition of the physical vapor being transported to the crystallization surface; the primary mass transport mechanism; the kinetic processes at the source evaporation, graphite wall, and crystallization surfaces; issues related to seed, Si/C ratio, initial stage of growth, heat conduction through the growing boule, etc.; and the mechanism of defect generation in the boule. In this section, we will review how the most important parameter of growth, the growth rate or velocity, generally measured in mm/h, is influenced by specific independent parameters that can be controlled in a growth system (and its influence on crystal quality).

Besides the temperature and system pressure, very few parameters of growth can be directly measured. They include the size and weight of the grown material, the source-to-seed distance at the beginning of growth and the source to boule front at the end of growth. Because of the high temperature environment of the growth cell, other parameters such as temperature difference between the source surface and the growth front, the temperature difference across the source during growth, the temperature gradient in the crucible, vapor composition, etc., cannot be measured. Hence, computer models are employed to estimate the temperature gradient and other parameters of importance to growth, and to predict the growth rate. An average value of growth rate is derived from experiments and used to verify the model [43].

Influence of Temperature on the Growth Rate

Tairov reported that depending on the composition and pressure of the gaseous medium in the growth region, the production of SiC single crystals with high deposition rates of up to 10 mm/h is possible [14]. However, a growth rate of 0.5 to 2 mm/h appears to be the norm to obtain bulk crystals of acceptable quality. The crystal growth rate generally increases with increasing temperature, increasing source to seed temperature difference, ΔT , decreasing pressure, and decreasing crystal-to-source distance [44]. Figure 1.15 shows how the growth rate varies with source temperature and system pressure. At a fixed source temperature, the increase in growth rate at lower system pressures is noteworthy, consistent with theoretical predictions (Sect. 1.4.1).

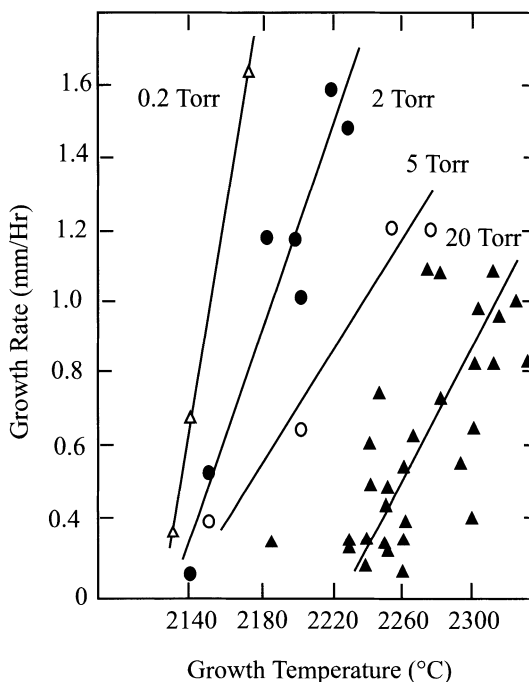


Fig. 1.15. The crystal growth rate increases with temperature (at constant source-to-seed temperature difference ΔT) and decreases with system pressure. Below 20 Torr, vapor transport is diffusive, while scatter in the data at 20 Torr indicates gaseous convective effects ([44], reprinted with permission from Elsevier)

Source-to-Seed Distance

More recent data, as shown in Fig. 1.16 confirms the trend presented in Fig. 1.15, and indicates that the growth rate is a strong function of temperature (Fig. 1.16a) and source-to-seed distance (Fig. 1.16b). The above

dependencies indicate a diffusion limited mass transfer process. At a given temperature, as Fig. 1.16b indicates, the growth rate increases as the spacing between source and seed decrease; this is understandable since the temperature gradient increases as the gap distance decreases. Likewise, at a given spacing, the growth rate increases as the temperature increases.

For small source-to-seed spacings the influence of the graphite walls of the crucible on the vapor composition and its transport process is minimized; hence, the purity and the quality of the crystals grown at small spacings may be superior to those grown at long source-to-seed spacings.

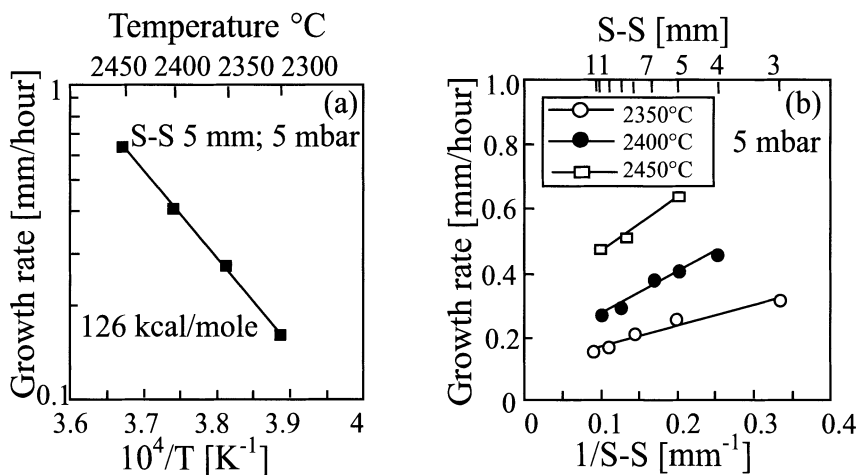


Fig. 1.16. Growth rate dependences versus (a) temperature and (b) source-to-seed distance ([43], reprinted with permission from Elsevier)

Growth Pressure

The rate of crystallization is often diffusion limited as the system growth pressure increases. However, if the system pressure is reduced the growth mechanism will not be limited by diffusion of the C and Si species from the source to the growth surface. In this case, the surface kinetics (surface diffusion, etc.) will be the mechanism that will limit the growth rate. Figure 1.17 shows the dependence of growth rate on growth pressure [16]. At low growth pressures below ~ 8 mbar (6 Torr) the growth rate is nearly constant, while the growth rate decreases by increasing the growth pressure. This is understandable since when the argon pressure is increased above 6 Torr, the dilution of the reactive species is increased, the growth rate decreases [34,45], and growth is less sensitive to temperature as indicated in Fig. 1.15. At lower pressures, according to Fig. 1.15, the growth can be performed at lower temperatures while still maintaining high growth rates (according to Fig. 1.17). Growth at

lower temperatures is beneficial for system purity since the injection of boron, a common impurity in the graphite, into the growth area will be suppressed at lower temperatures. Another advantage of lower system pressure is that the mean free path of the species in the vapor transport gap will be greater than the dimensions of the growth cell resulting in superior crystal stoichiometry [16]. But too low a pressure will result in increased Si/C ratio and rapid graphitization of the SiC source powder.

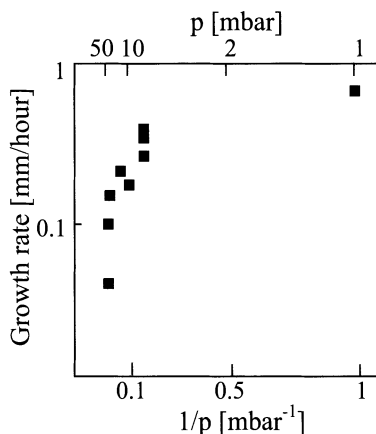


Fig. 1.17. Growth rate versus pressure in sublimation bulk growth ([16], reprinted with permission from author)

Temperature Gradient

The temperature gradient in the growth crucible creates the motive force, i.e., the pressure difference of the Si and C species in the source to seed gap that drives the vapor flow from the source to the growth front (crystallization surface). The temperature of the source and that of the seed which establishes the temperature gradient in the growth region is a very important crystal growth parameter that needs to be correctly determined for establishing the optimum crystal growth condition. However, the gradient which is established at the beginning of crystal growth (crystal thickness $t = 0$) will vary steadily during growth as the crystal thickness increases and the source-to-crystal spacing decreases. Hence, either maintaining a temperature gradient that is constant throughout the long growth period or varying the gradient during growth according to a predetermined profile offer extreme challenges in SiC crystal growth. Further, the temperature of the source (and that of the seed) varies in the radial direction resulting in local fluctuations and hence results in non-uniform source evaporation (or condensation on the seed). Such fluctuations can easily result in the onset of different polytypes and local fluctuation in

the thermoelastic stress can lead to defect generation. Further, as growth proceeds, the growth front approaches that of the source, the temperature of the crystallization surface increases, approaching that of the source surface, and as a consequence, the growth rate decreases with the time of growth, and eventually growth can completely stop. Hence, the growth rate steadily decreases during the long period of crystal growth, a major limitation of the current PVT method of crystal growth.

1.5 Defect Generation Processes in Silicon Carbide Crystal Growth

1.5.1 Micropipe Generation

Micropipes are the most common and harmful of structural defects in SiC. In 1993, Stein reported the existence of macrodefects in the region of the seed [46]. The hexagonal tube-like cavities were called channels, with diameter of 10 to 50 μm parallel to the growth direction. The diameter of the channels was found to enlarge up to ten times in diameter after a propagation length of 4–6 mm. At the end of the channel, the hexagonal cavities were sometimes partially filled with SiC of the same orientation as the surrounding crystal. It was concluded that the channels originated by secondary evaporation of SiC due to irregularity of contact between the seed and its graphite holder. Micropipes in 6H-SiC crystals grown by the modified sublimation method were extensively investigated by Yang and Pirouz using optical microscopy and TEM [20]. The diameters of micropipes ranged from submicron to a few microns. Most micropipes were shown to be hollow structures that propagated the entire boule along the growth direction, and a few stopped in the middle of the boule. Their density ranged from 100 to 1000/cm². Most micropipes were roughly perpendicular to the substrate surface and hence, were the predominant gross surface defects in SiC substrates and led to the growth of polycrystals on the top of micropipes during growth of SiC films on the SiC substrates [47]. Cross sectional TEM indicated a high density of partial dislocation loops generated from a site on the wall of the micropipe. As discussed earlier, during bulk growth, impurity particles may become accumulated at the growth surface. During the step-mediated growth of SiC, as the SiC steps impinge the edges of the impurity particles one after another, a wedge force builds up on the boundary of the particles, as shown in Fig. 1.18, and lifts them up a little bit each time since the bonding between SiC crystal and the impurity particle is very weak. As the SiC growth proceeds, the particles rise up with the growth surface and simultaneously, a hollow pipe forms underneath the particle, resulting in micropipe formation. The above description is one of the earliest models of micropipe formation.

To study defect generation at the beginning of growth, seed crystals with and without micropipes were used [24]. Micropipes present in the seed penetrated into the growing crystal and no new micropipes were generated at the

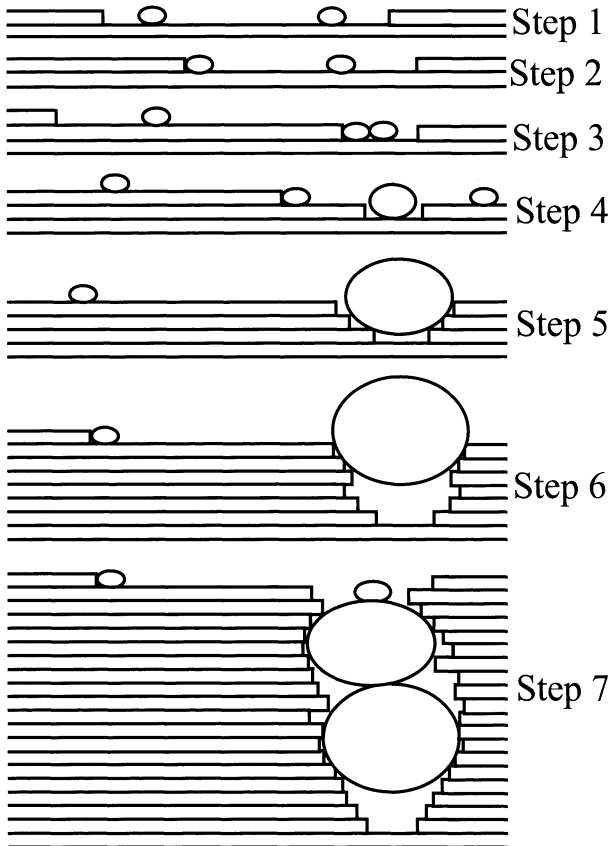


Fig. 1.18. A schematic illustration of the proposed micropipe formation mechanism. (1) SiC and impurity atoms are deposited on the substrate; (2) the SiC growth front drives the impurity atoms; (3) impurity atoms meet each other; (4) impurity atoms form a stable nucleus; (5) owing to the wedge force, the impurity particle is lifted by the growing SiC front; (6) a micropipe forms under the impurity particle; (7) continuing lengthening of the micropipe. *Small circles* represent impurity atoms; the *large circle* is a growing impurity particle ([47], reprinted with permission from author)

seed-crystal interface. Based on Auger analysis, both C and Si inclusions were observed, the density of C inclusions being much higher. Although no direct correlation between the density of inclusions and micropipe density was found since a number of inclusions did not cause micropipe formation, in general, new micropipe generation was attributed to the formation of second phases, especially carbon.

It has been demonstrated that micropipes could be generated if the seed surface is disintegrated by parasitic sublimation during the preheating stage of growth [48, 49]. Significant micropipe generation was observed emerging

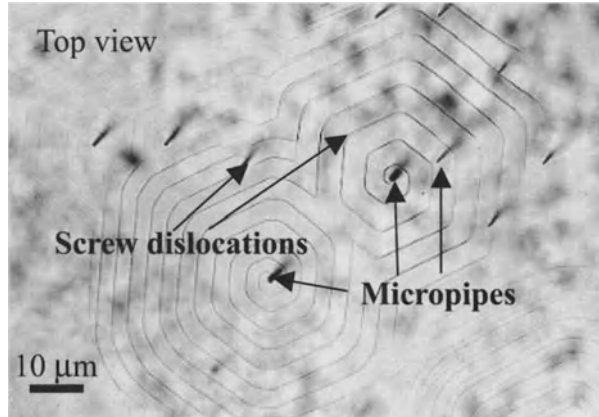


Fig. 1.19. Micropipes centered on growth spirals

from a graphitized seed/bulk crystal interface. A significant reduction of micropipe generation was observed when growth was initiated from a clean seed surface [21]. It is further noted that in SiC sublimation growth, the vapor supersaturation is high and temperature fluctuations during growth may result in deviation from optimal growth conditions and lead to micropipe generation.

Micropipes are generally considered as empty-core or Frank-type hollow-core super screw dislocations with Burgers vectors typically equal to 3–7 times the lattice parameter along the *c*-axis [50]. Micropipes are found to coincide with the positions of the axes of growth spirals, as shown in Fig. 1.19. It has also been shown that micropipes arise from stacking-related defects during growth.

There have been various demonstrations of ‘micropipe healing’ or ‘micropipe closing’ [21,51] using PVT epitaxy or liquid-phase epitaxy. In addition to micropipes, a large number of other defects exist in SiC wafers including planar defects, low-angle boundaries, stacking faults, and dislocations. Most of the defects present in the wafer or substrate propagate into the grown epitaxial layer, in turn degrading device characteristics and performance. Hence, it is essential to gain basic understanding of the mechanisms or processes that initiate a variety of defects during SiC bulk growth.

1.5.2 Planar Defects

There is yet another kind of structural defect that is quite prevalent in sublimation grown SiC crystals. It is variously called the planar defect or the hexagonal void which is a flat, hexagonal, platelet-shaped cavity with lateral dimensions significantly larger than its thickness [52]. It is shown that the void lies parallel to the basal plane. The void is typically 6 μm in thickness with trench-like depressions at the edges. Voids are shown to form at the interface between the seed and the graphite seed attachment. The temperature

gradient across the void thickness results in secondary evaporation from the higher temperature region of the void and condensation at the lower temperature side of the void next to the seed attachment. As a result, the void moves along the temperature gradient within the growing boule. Hence, the void will move from the seed to the crown end of the boule. Dislocations line up along the trace of the void path, and screw dislocations superimpose to form micropipes at the lower corners of the moving void. It is further suggested that the above process is the primary micropipe formation mechanism in SiC [52].

1.5.3 Inclusions, Dendrites, and Polytype Inclusions

An example of poor seeding conditions that will lead to significant defect generation of different types is provided by Fig. 1.20. During seeding, if the conditions of growth are not adequately controlled, a transition layer adjacent to the seed approximately 1 mm in thickness is formed where new defects (not those propagating from the seed) will be generated. In this early stage of growth, the high Si/C ratio, i.e., the silicon rich vapor, will result in liquid droplet formation at the growth surface and the reaction of the excess silicon with the graphite wall of the crucible will cause excess carbon in the form of clusters that will become incorporated at the growth front. Further, the non-stable thermal conditions will result in solid phase transformations leading to polytype transformations. All of the above factors will result in significant defect generation in the transition layer as shown in Fig. 1.20. Formation of dendrites (whisker growth) indicates the existence of a condensed liquid phase [54]. Figure 1.20 shows that the dendrites are occluded within the bulk crystal. A large number of micropipes were seen to emanate from the majority of the whisker branches. The presence of carbon inclusions was also evident. It is noteworthy from Fig. 1.20 that micropipes propagate through the boundary between two polytype phases, and often, new micropipes are generated at the

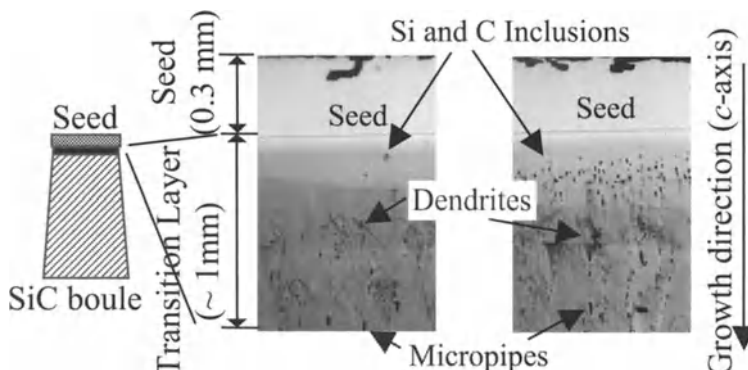


Fig. 1.20. Defect generation within the transition layer ([53], reprinted with permission from author)

interface between the two polytypes. The transition layer thickness and the density of defects initiated in the above layer was shown to depend on the kinetic growth process parameters (temperature, pressure, etc.) during the initial layer growth, and to a lesser extent, on the seed quality. The above illustration (Fig. 1.20) and discussion clearly demonstrates the importance of establishing good (optimum) growth conditions, especially at the early, non-equilibrium, stage of bulk PVT growth.

1.6 Development of Industrial Production of SiC Wafers and Current Status

After the first demonstration of ingot growth of SiC single crystals in 1976 [55] by the seeded sublimation process, also called the modified Lely method, Tairov and Tsvetkov outlined the general principles of growing bulk crystals of different polytypes [56], in turn enabling the fabrication of various SiC based devices. The model presented in Fig. 1.21 illustrates the essence of the processes associated with the seeded physical vapor transport (PVT) or sublimation crystal growth method. Contrary to the Lely method, the primary advantage is that this method employs a seed so that control of the nucleation process becomes possible.

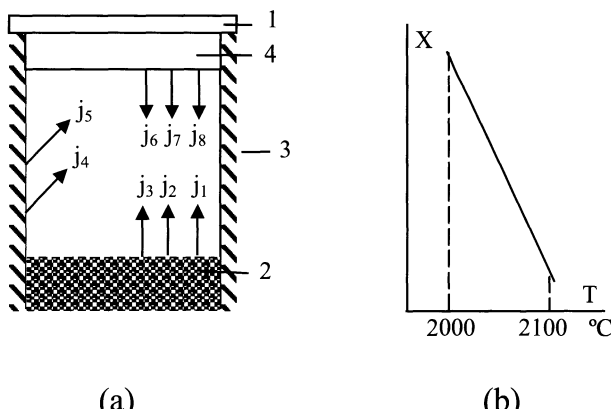


Fig. 1.21. (a) Schematic diagram of the various fluxes in the crystallization cell: (1) seed; (2) starting material to be recrystallized; (3) walls of graphite growth cavity; (4) growing silicon carbide crystal; (j_1, j_6) silicon fluxes from the source and growing crystal; (j_2, j_4, j_7) Si_2C fluxes; (j_3, j_5, j_8) SiC_2 fluxes. (b) Temperature profile along the cell. Optimal temperature of seed 1800–2000 °C. Temperature gradient 30 °C/cm ([56], reprinted with permission from Elsevier)

1.6.1 Early Stage Developments

Calculations based on Knudsen-Langmuir molecular-kinetic theory showed that high growth rates of ~ 1 mm/h can be achieved for initial source-to-seed separations of larger than 10 mm due to additional fluxes from the sidewall of the growth cavity (Fig. 1.21), whereas at smaller separations (0.5–10 mm), the principal contribution to the flux arriving at the growth surface is by the fluxes that arise due to the dissociative evaporation of the source. The primary drawback of the seeded PVT method was that simultaneously, several polytype modifications grew in one and the same crystal (called syntaxy). The most frequently coexisting types are 3C and 6H. Analysis indicated a lower energy barrier for 3C nucleation and hence, a smaller value of critical supersaturation required for its nucleation which results in a higher rate of formation of 3C. In the course of growth, the 3C nuclei acquire a metastable structure and a phase transition starts, which is responsible for the formation of a range of different polytypes. Dislocations and other defects accompanying the phase transition emerge on the growth surface and continue into the growing boule. The presence of impurities and deviations from the stoichiometry in the vapor phase exert an appreciable effect on the above process of polytype transformation. Since supersaturation fluctuations during crystal growth may cause 3C nucleation on the growth surface, it is essential to eliminate such fluctuations in the course of crystal growth [56]. Since the growth rate is dependent on supersaturation, in order to prevent 3C nucleation, it is important to transition from low supersaturation in the early non-equilibrium growth stage to high supersaturation when equilibrium conditions are reached to effect high growth rates.

Polytype structure control is also possible by selecting seeds of the required polytype or by growing the crystal on faces forming an angle to the (0001) basal plane (terrace growth). Since these faces contain information about the superstructure of the seed polytype, they can be used as templates for bulk growth. Due to step-like surface structure, growth on these faces proceeds by way of tangential displacement of growth steps so that the seed structure is reproduced [56]. Growth of the 4H-SiC polytype is feasible on the basal plane by introducing, at the initial growth stage, a low concentration ($\sim 10^{17} / \text{cm}^3$) of scandium, which appears to retard, at the nucleation stage, the 3C \rightarrow 6H phase transition, on the 4H seed. This retardation can also be achieved by appropriately changing the Si/C ratio or by selecting an appropriate time constant for supersaturation during the seeding phase.

Using the crystallization cell shown diagrammatically in Fig. 1.21, SiC ingot growth was carried out in the temperature range of 1800–2000 °C under a vacuum of 0.1 Torr–0.1 mTorr. The initial growth rates were 5–10 $\mu\text{m}/\text{h}$ and the atmosphere in the cell was ~ 100 Torr argon. The system was evacuated with a time constant of ~ 7 min after which the growth rate increased to ~ 2 mm/h. In the growth zone, the axial temperature gradient was 30–40 °C/cm. Boules of 14 mm diameter and 18 mm length were achieved with

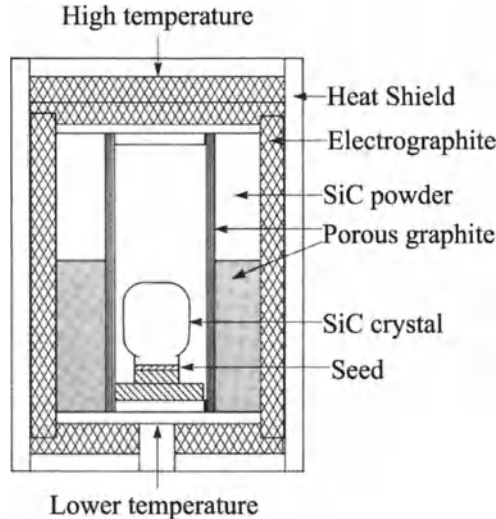


Fig. 1.22. Crucible for growing SiC monocrystals by the sublimation method ([57], reprinted with permission from the Institution of Electrical Engineers)

the concentration of donors equal to $1 \times 10^{16} / \text{cm}^3$ in maximum purity crystals. With nitrogen doping, the maximum donor concentration was as high as $2 \times 10^{19} / \text{cm}^3$. The donor concentration was found to decrease when the growth rate increased and this relationship is of potential value for increasing the purity of the grown boules [56].

Growth of bulk crystals with a diameter more than 25 mm (1 inch) and length of several centimeters was demonstrated in 1993 for both 6H and 4H polytypes [46]. Both n-doped and p-doped crystals were demonstrated using an RF-heated graphite furnace shown in Fig. 1.22. A porous graphite cylinder is placed at the center of the graphite crucible. An interesting feature of this design is the placement of seed at the bottom of the crucible. The space between the crucible wall and the porous graphite is filled with the SiC source material in the form of a powder. The temperature of the seed was between 2150 and 2350 °C and the axial temperature gradient was $\sim 20 \text{ }^\circ\text{C/cm}$.

1.6.2 Intermediate Stage Development

One of the earliest references, in the open literature, to commercially produced SiC (25 mm diameter) by CREE Research Inc., using the modified Lely method, was made in an article in 1991 [58]. In this reference, the key figures of merit were provided for SiC based high power and frequency devices, indicating the advantages of SiC over Si and GaAs based devices, thus heralding a new era in the fabrication of practical devices based on SiC. In this reference, Barrett et al. provided a fairly detailed description of the crystal growth system design for obtaining SiC bulk crystals and wafers for device fabrication.

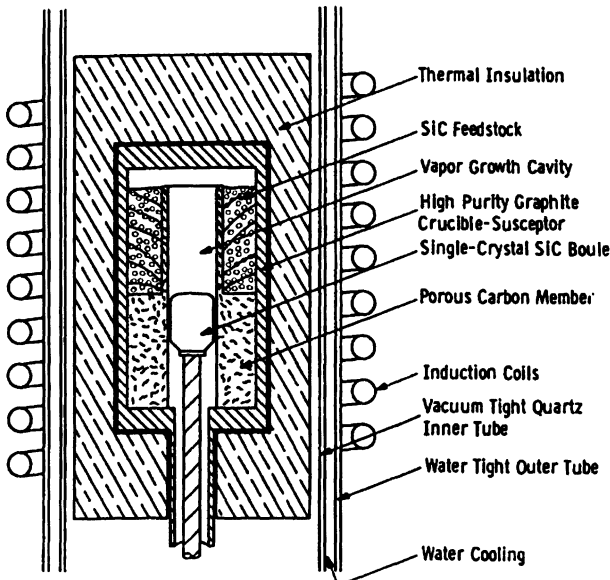


Fig. 1.23. Schematic illustration of sublimation vapor transport growth cavity ([58], reprinted with permission from Elsevier)

Figure 1.23 shows the schematic of the sublimation vapor transport system used for SiC bulk growth. A quartz-wall induction heated system was adopted using purified graphite and carbon parts within the hot crystal growth zone. A degassable rigid carbon foam was used as thermal insulation to provide a clean environment. The enclosing vessel consists of concentric 170 mm OD and 150 mm ID quartz tubes sealed with vacuum-tight integrity using stainless steel end flanges (plates) using double O-ring seals on ground flat ends of the quartz tubes. Cooling water was circulated into the bottom-end flange, between the concentric quartz tubes, and out the top flange. A liquid nitrogen trapped 4-inch oil diffusion pump maintained a vacuum of 2×10^{-7} Torr at room temperature after bakeout, and $\sim 5 \times 10^{-6}$ Torr at 2000 °C. Access into the tube for purposes of loading and unloading was provided through an 8-inch top flange. Additionally, the top and bottom plates provided for windows (for temperature monitoring using an optical pyrometer), probes, and mechanical devices for moving the seed and source [58]. The graphite crucible also serves as a susceptor. Heating of the source and seed containing crucible was provided by a 9-turn induction coil, 8-inch high, and 7.5 inch ID rigidly held by insulating members to an insulating coil holder attached to an xyz stage. The above feature permits the coil to be moved in any direction for adjustment of thermal gradients within the hot zone. The temperature difference between the source and the seed was controlled by axial positioning of the induction heating coil energized by a 10 kHz generator. The low-frequency induction system has the advantage of not coupling to the rigid graphite foam used for

thermal insulation, eliminating the difficult thermal shielding problems characteristic of RF induction-heated systems. The quartz-wall containment vessel provides a passive ultra-clean environment for the growth of high-purity crystals. In a typical growth sequence, prior to initiating growth by PVT, a high temperature ($> 800^{\circ}\text{C}$) vacuum degas step ($> 10^{-5}$ Torr) was used to reduce the background nitrogen contamination, and the temperature was stabilized at the growth value in high-purity argon to achieve optimum ΔT between the source and seed.

The basic arrangement of the growth cavity was similar to that presented in Fig. 1.22. The SiC source or feedstock was located in the hottest zone, which was typically 2100–2400 °C depending on the process and polytype desired. The seed was positioned several centimeters away in the colder region of the cavity. Growth occurred at pressures less than 20 Torr with a temperature gradient of 20–35 °C/cm between the source and seed. A Lely grown platelet measuring 5 × 8 mm, used as seed, resulted in a boule 33 mm in diameter and 18 mm in length. Single crystal areas measuring 20 × 25 mm, of 6H polytype were produced. The initial data showed the growth rate to be unaffected by seed orientation – C- or Si-face.

In 1993, Barrett et al. reported the growth of large 60 mm diameter 6H-SiC boules using the PVT process [44]. A boule was grown using a 25 mm wafer seed in a 40 mm diameter growth cavity at system pressure of 20 Torr and $\Delta T \cong 100^{\circ}\text{C}$. Single crystal 40 mm 6H boules were grown at an average growth rate of 0.9 mm/h over a 58 hour period. Scale-up to 60 mm diameter boules was achieved using larger seeds and a larger growth cavity. Wafers were fabricated using diamond sawing and polishing techniques. The density of micropipes was in the range of 100–1000/cm². The chemical purity of the as-grown crystals was assessed by spark source mass spectroscopy, which is sensitive to impurities in the ppma range. B, F, Al, Cl, Ca, Ti, Cu, and Zr were detected at concentrations in excess of the system detection limits. B and Al are known shallow acceptors. Crystals grown from a prepurified SiC source exhibited a resistivity in the $10^5 \Omega \text{ cm}$ range. Although the compensation mechanism responsible for the near semi-insulating behavior was reported to be unknown [44], based on more recent studies the compensation is believed to be due to the vanadium impurity.

4H-SiC wafers, 1.1875 inch (~ 30 mm) in diameter, 250 μm thick fabricated using the modified Lely method were commercially available from CREE Research Inc. in 1993 [59].

1.6.3 Recent Developments and Current Status of SiC Wafers

CREE Research Inc. is a pioneer in the commercial production of both 6H- and 4H-SiC wafers for device applications. Using the PVT technique, the company has steadily increased both the diameter and the quality of SiC wafers [32], releasing 50 mm diameter wafers for sales in 1998 and 75 mm diameter wafers for sales in 2002. Monocrystal boules, 100 mm in diameter, were

demonstrated in 1999. Research at CREE has steadily reduced micropipe density, demonstrating in year 1999, micropipe-free material of 25 mm diameter and densities as low as $1.1/\text{cm}^2$ for an entire 50 mm 4H wafer, for the best R&D wafers [32]. For comparison, the micropipe density (MPD) for the R&D best wafer was $\sim 200/\text{cm}^2$ in year 1993. In production 4H-SiC wafers, the MPD decreased steadily from July 1997 to March 1999: from ~ 60 to less than $10/\text{cm}^2$ for 35 mm wafers and ~ 90 to slightly greater than $10/\text{cm}^2$ for 50 mm 4H-SiC wafers. Currently, CREE is offering commercial 50 mm wafers with $\leq 5/\text{cm}^2$ and $\leq 15/\text{cm}^2$ for 75 mm wafers. Under non-optimized growth conditions, low angle grain boundaries are present especially at the periphery of a boule. In SiC wafers, the above defects extend down from the wafer surface, not necessarily passing through the entire wafer thickness. The low angle grain boundary linear defects generally follow crystallographic planes over its length. With advances in growth technology, these defects are drastically reduced.

An overview of the state of art, up to year 2001 of SiC bulk sublimation growth, is presented in [33]. Industrial production of 75 mm 6H and 4H wafers for external sales became available in the fall of 1999 and crack-free fully single crystal 100 mm 4H and 6H wafers were also demonstrated in Fall 1999 [33]. The R&D best 75 mm wafers exhibited an average micropipe density of $\sim 20/\text{cm}^2$ in Fall 1999.

Although CREE Research is by far the dominant commercial provider of SiC wafers, other providers include Dow Corning Corp. [www.dowcorning.com], II-VI, Inc. [www.ii-vi.com], Bandgap Technologies, Inc. [www.bandgap.com], Okmetic AB [www.okmetic.com], SICrystal [www.sicrystal.de], and Nippon Steel Corporation [www.nsc.co.jp].

Achievements in the bulk growth of large size SiC crystals by Nippon Steel Corp. are reviewed in [60] and in the accompanying chapter in this book authored by Ohtani *et al.*

Generally, the quality of the grown crystal, in terms of defect density, improves if the impurities in the growth reactor are decreased. Hence, selection of the graphite/carbon components is of great importance in order to reduce impurities in the growing boule. The graphite components can be purified to below parts per million weight (ppm wt) range; but this process is expensive and adds to the cost of the resulting wafers. Reduction of B and S is especially difficult. Generally, the SiC source is formulated using high purity Si and C sources. The level of any background impurity in the commercial undoped wafers is reported to be less than $\sim 0.1 \text{ ppm}$, including nitrogen [32].

1.6.4 Bulk Crystal Growth of Semi-Insulating SiC

Semi-insulating SiC (SI-SiC) substrates are essential for the fabrication of high frequency and microwave power devices including SiC MESFETs and GaN/AlGaN high electron mobility transistors (HEMTs). There are two distinct methods available to achieve SI properties in SiC: (i) by incorporating

specific impurities into the material that introduces deep energy levels within the bandgap; this method is called extrinsic doping and (ii) by incorporating intrinsic defects into the growing high purity SiC boule to introduce the deep levels. In both cases, the deep levels compensate the shallow dopants (nitrogen and boron) to pin the Fermi level near the middle of the bandgap. In the first generation commercial SI-SiC, vanadium (V) was used for compensating the shallow dopants [61]. In this technique, seeded sublimation process was used that involved doping of the SiC source material with vanadium to pin the Fermi-level preferentially at the V donor level [62]. Studies suggest that the RF power densities of SiC MESFETs in V doped SI-SiC substrates are much lower than expected and this is attributed to the presence of deep level elemental V impurities which causes carrier trapping and backscattering in devices [62]. Other issues related to V-doped SI-SiC include poor yield of the wafers from a given boule and non-uniform electrical properties within a wafer area [63]. When vanadium is added as a solid source to the SiC starting material, it will deplete during growth at a higher rate than SiC due to the higher partial pressure of V [63]. Consequently, in the initial stage of growth, vanadium incorporation exceeds the solubility limit leading to precipitation in the growing boule and hence, severe degradation in the quality of the grown crystal. In the late stages of growth, the V concentration in the crystal may even fall below ($N_D - N_A$), the effective concentration of the shallow impurities. Hence, with increasing growth time, the crystal resistivity can fall drastically as nitrogen becomes the dominant impurity (under compensation) and the SI behavior changes to n-type conduction. A method to avoid depletion of V in the source is presented in reference [63]. The presence of V is also known to degrade the thermal conductivity of SiC, which is detrimental for high power device applications.

Two distinct types of vanadium-free high purity SI-SiC substrates, one grown by the conventional sublimation (PVT) method referred to as HPSI, and the second by high temperature chemical vapor deposition (HTCVD), are now commercially available. In both cases, intrinsic defects are believed to be responsible for the SI properties. Two and three inch (50 mm and 75 mm) 4H-SI-SiC wafers produced using a high purity PVT process are commercially available. Please see reference [62] for additional details.

In the HTCVD technique, purified silane and ethylene are used as gas precursors (source material) [64]. Diluted in a carrier gas, the above precursors are continuously fed into an open heating zone, at > 2000 °C, where nucleation of Si and C containing clusters takes place in the gas phase. Above this hot zone where nucleation of Si and C clusters takes place, the axial temperature distribution is similar to that in a PVT system. In this region, further sublimation (dissociation) of the clusters into vapor species occur which are then crystallized on to a 50 mm diameter 4H-SiC seed surface which is maintained at a lower temperature. The above growth process can be seen as gas fed sublimation [64]. A lower concentration of shallow impurities introduced by the growth system (compared to PVT) will require a smaller concentration of deep levels needed for compensation to produce the SI material. Hence, high

system purity is an essential part of producing SI-SiC without the addition of an extrinsic dopant such as vanadium. In the SI crystals produced by the HTCVD process, the concentrations of the reported average residual impurities per cm^{-3} are: N (7.5×10^{15}), B (1.2×10^{15}), and Al (6.6×10^{13}), all close to the measurement limit.

Control of the Fermi level in SI-SiC requires clear knowledge of the impurities and defects that are involved in the compensation process. Electron paramagnetic resonance (EPR) is a powerful characterization technique employed for the identification of defects responsible for different electrical activation energies in SI-SiC and for the identification of defects introduced by different crystal growth and process conditions. The role of different impurities and defects, the compensation processes, and the total concentration of impurities and intrinsic defects needed for controlling the Fermi level in HTCVD and HPSI SiC materials are discussed and compared in [61].

A further advantage of the HTCVD process is that the resulting SI-substrates exhibit a much lower micropipe density compared to the PVT grown material [64]. The increased performance of devices fabricated on the HTCVD SI-SiC substrates further allows one to conclude that the reduction or elimination of vanadium and the reduction of the concentration of residual shallow impurities (nitrogen and boron) is essential for reducing the carrier trapping effects in SiC high power MESFETs [64].

Finally, it is to be noted that the HTCVD bulk growth process can also be used for the growth of n-doped SiC.

1.6.5 SiC Bulk Crystal Growth with p-Type Doping

The most common application of SiC at the present time is for the commercial production of gallium nitride (GaN) based blue light emitting diodes. Silicon Carbide Schottky diodes are also commercially available. For both the above applications, n-type doped SiC substrates are used. In order to produce n-doped SiC, as noted earlier in this section, the source material used for bulk growth is either industrial-grade SiC abrasive powder or specially prepared material synthesized using high purity silicon and carbon. The n-type doping is achieved by controlling the amount of nitrogen added to the inert gas in the growth reactor, which is the most commonly used n-type dopant in SiC. However, p-type doped SiC wafers are required for the manufacture of a variety of high power electronic devices.

Aluminum, being a shallow acceptor in SiC, is the most commonly used impurity to produce p-type SiC. Normally Al doping of SiC is carried out by adding the Al dopant to the SiC powder source material. Addition of Al directly to the SiC powder source material has a major drawback. The partial pressure of the Al species at the high growth temperatures ($\geq 2200^\circ\text{C}$) is significantly higher than that of the silicon and carbon gas species [65, 66]. As a result, depletion of Al in the source material is observed, with crystal growth time, leading to a strong decrease of dopant incorporation along the

length of the boule. A further consequence of the higher evaporation rate of Al at the beginning of growth is the generation of defects and the nucleation of misoriented grains in the growing boule. Hence, the non-uniform sublimation of Al from the source over the long boule growth period results in non-uniform doping concentration along the length of the grown boule and further, leads to high defect generation. It is therefore essential to maintain a constant supply of Al over an extended period.

The development of a modified physical vapor transport (M-PVT) growth set up for improved p-type doping of SiC boules was demonstrated [66]. To improve the Al supply into the growth reactor, an additional gas line was installed, as shown in Fig. 1.24 which provides a continuous flux of Al atoms from an external reservoir. The system shown in Fig. 1.24 is essentially a conventional PVT set up which was modified by adding a pipe running through the lower part of the furnace, penetrating through the thermal insulation jacket, crucible wall, and the source volume, into the growth cell. This arrangement enabled the supply of an external gas flux directly to the crystal growth surface. The set up was inductively heated to temperatures above 2000 °C. The pressure inside the growth cell was adjusted by the argon gas flux outside the growth reactor shown in Fig. 1.24 and by an inert or doping gas flux through the additional inner gas line (M-PVT). It is important to reduce the additional gas flux to values comparable to or less than the total PVT sublimation flux from the SiC powder source. Two concepts were considered for the supply of Al atoms to the growth surface: (i) supply a mixture of carrier gas (e.g., Ar) and Trimethylaluminum (TMAI); the latter gas is

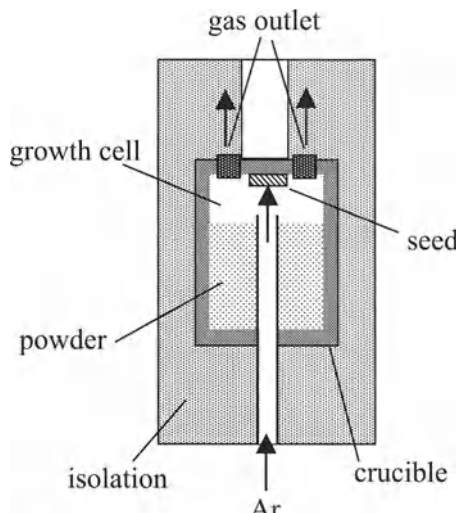


Fig. 1.24. Setup for growth by M-PVT process ([66], reprinted with permission from Elsevier)

a commonly used p-dopant in chemical vapor deposition (CVD) film growth of SiC, (ii) supply a carrier gas which transports the Al dopant atoms from an external aluminum reservoir. Using the above approaches, the amount of Al transported to the growth front is controlled by the carrier gas flux. The reservoir approach (the second one) is superior considering safety issues and the absence of hydrogen (a byproduct of TMAl) carried into the growth cell. Using the above M-PVT system n-doped (nitrogen), nominally undoped, and p-doped 6H and 4H-SiC boules 35 and 40 mm in diameter were grown. The crystal quality was comparable to that grown by a conventional PVT system with micropipe density less than $100/\text{cm}^2$. In the grown crystals, a significant reduction of graphite inclusions (carbon clusters) was achieved, an outcome attributed to movement of carbon particles, from the SiC source, away from the crystallization surface by the gas flowing through the inner gas line. Further, the M-PVT system enabled nitrogen (in the case of n-doping) to be supplied directly to the growth surface giving rise to an efficient use of the provided doping gas, an advantage over conventional systems [66]. Figure 1.25 shows the axial distribution of carrier (hole) density for different wafers cut along the length of the boules grown from a conventional system (open squares) and that grown using the M-PVT system (solid squares). In the case of the conventional system with an Al containing SiC source charge, the hole concentration decreased exponentially over crystal length by more than one order of magnitude. Using the M-PVT system, the decrease with length was linear, and a factor of 0.5 reduction over the boule length was observed. In the latter case, the reduction in carrier concentration was not due to depletion of the

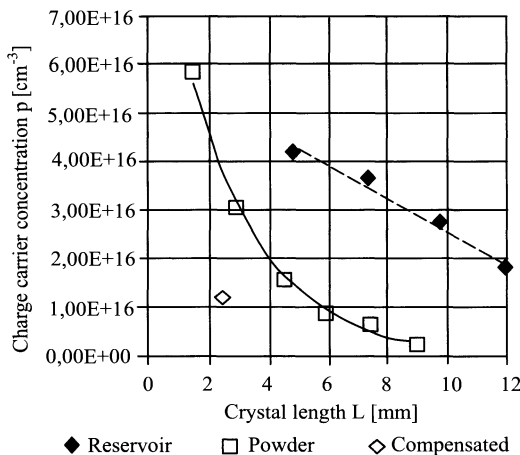


Fig. 1.25. Axial charge carrier distribution in 4H-SiC crystals grown on the C face with aluminum in the powder (*open squares*) ([67], reprinted with permission from Elsevier) and with external source (*solid symbols*) ([66], reprinted with permission from Elsevier)

Al source but due to changing temperature conditions during the long growth period. The crystal grown using the M-PVT system also exhibited superior quality in terms of mis-oriented regions. The crystals exhibited improved axial Al doping homogeneity: for 4H, $2 \times 10^{16} < p < 4 \times 10^{16} / \text{cm}^3$; for 6H, $8 \times 10^{16} < p < 1.2 \times 10^{17} / \text{cm}^3$. The doping uniformity across the area of a given wafer also showed significant improvement.

1.7 Evaluation and Characterization of SiC Wafers

From a SiC user point of view, the manufactured wafers must be evaluated or qualified to confirm crystal quality and material characteristics as per specifications provided by the manufacturer or required by the user including polytype, carrier type and density, and the density of different types of defects. Hence, the wafer must undergo testing using various characterization tools depending on the objective, which can be broadly divided into three groups: (a) material evaluation, (b) defect characterization by non-destructive methods, and (c) defect characterization by destructive methods.

1.7.1 Material Evaluation

X-ray rocking curves, obtained using a high resolution X-ray diffractometer (HRXRD), are used for evaluating crystal quality. Here, the principle is based on elastic scattering of X-ray radiation from a periodic array of atoms or atom groups forming the crystal lattice. The intensity of the diffracted X-ray beam in arbitrary units is plotted versus the angular position of the wafer with respect to the incident beam [68]. The full width half maximum (FWHM) of the rocking curve is the parameter used for evaluating crystal quality. A FWHM of ~ 15 arcsec. indicates good crystalline quality of the wafer.

HRXRD is valuable for observing the effects of strain and domain misorientation (mosaicity) in the crystal. Mosaicity causes broadening and asymmetry in the rocking curves. In the case of strongly misoriented domains, multiple peaks appear. Sample bending also broadens the rocking curves [69].

Raman spectroscopy is a vibrational spectroscopic technique, which is widely used for nondestructive SiC characterization. For example, polytype analysis of the SiC wafers can be accomplished using Raman technique. During Raman spectroscopy measurements, the sample is illuminated by the monochromatic light (laser) and the spectrum of the scattered light is analyzed. Due to the interaction of the incident light with the phonons, the scattered light has a small fraction of photons with a frequency slightly different from the laser frequency. A plot of the scattered light intensity versus frequency shift from the laser frequency (typically expressed in terms of wave number shift) produces the Raman spectrum. Each SiC polytype has its own characteristic Raman spectrum, which allows distinguishing between SiC polytypes. Polytype determination can also be made using the methods

of X-ray diffraction (XRD) or low temperature photoluminescence (LTPL) spectroscopy.

The carrier type (n- or p-type) and carrier density are most simply evaluated using the capacitance-voltage (C - V) characterization method. A depletion layer is formed on the wafer surface by the placement of a metal contact. For non-destructive C - V measurements, a mercury Schottky contact is formed. The capacitance of the depletion layer is measured as a function of the applied reverse bias voltage, V . A typical C - V curve obtained for a n-type SiC wafer is shown in Fig. 1.26. The type of conductivity can be determined by the polarity of the C - V profile. From the $1/C^2$ versus V characteristic, the effective carrier concentration ($N_d - N_a$) versus depth from the wafer surface (i.e., the doping profile) can be obtained for intentionally or unintentionally doped wafers. For a uniformly doped wafer the $1/C^2$ versus V plot is a straight line with a slope proportional to the difference between donor and acceptor concentrations as shown in Fig. 1.26.

Scanning C - V systems are available that can provide the carrier concentration profile across the area of an entire wafer. The wafer can be evaluated for crystal purity, specifically for the presence of unintentionally doped nitrogen (a donor) and for non-metallic impurities (B, Al, V, Ti, etc.), using low temperature photoluminescence (LTPL) spectroscopy. It is also a sensitive technique for identification of energy levels in the bandgap due to the presence of defects. The technique is based on measuring photons arising from radiative recombination processes in the material. A fine beam of laser light, focused on the wafer surface, is absorbed by the material under evaluation. Electrons and holes are excited across the material bandgap and become bound (localized) at an energy center corresponding to an impurity or defect where they recombine, resulting in a PL spectrum (PL intensity versus wavelength of the emitted light). The characteristic lines of the PL spectrum are used to identify the specific impurity or defect energy level (center). A review of this topic can be found in [70].

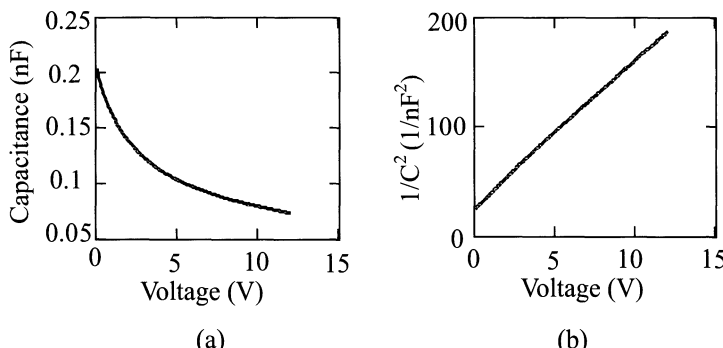


Fig. 1.26. Capacitance–Voltage and $1/C^2$ versus Voltage characteristics for a commercial n-type 6H-SiC wafer doped with nitrogen to about $2 \times 10^{17} \text{ cm}^{-3}$

1.7.2 Defect Characterization

In SiC substrates, generally the most common structural and crystallographic defects are micropipes, planar defects, inclusions, screw and edge dislocations, stacking faults, grain boundaries, etc. [50, 71–76]. The screw dislocations, running approximately along the [0001] growth axis, can be further divided into hollow-core and closed-core screw dislocations. The Burgers vectors of closed core screw dislocations are $1c$ or $2c$ for 4H SiC and $1c$ for 6H SiC (c is the lattice constant along [0001] growth axis, $c = 10 \text{ \AA}$ for 4H and $c = 15 \text{ \AA}$ for 6H). Screw dislocations with Burgers vector larger than the above values in the corresponding polytypes (4H, 6H) usually have hollow cores.

In most common c -axis cut SiC wafers, the edge dislocations with dislocation lines parallel to the basal plane are referred to as basal plane dislocations, while the defects propagating through the wafer are referred to as threading or extended defects, which include micropipes, screw dislocations, threading edge dislocations, and grain boundaries. These threading defects, especially micropipes and screw dislocations, are of particular interest to the SiC field because they are known to penetrate active device layers and degrade device performance [77, 78]. Hence, identification and delineation of the above defects on a wafer scale, mapped using non-destructive techniques, is essential to improving the quality of bulk crystals and epitaxial films (via rapid feedback to crystal growers), to establish device/defect correlations, and as a tool for device development research. Generally, characterization of defects in SiC single crystal wafers have been established by X-ray topography, optical microscopy, chemical etching, AFM, SEM, TEM, and Polarized Light Microscopy (PLM). Among these techniques, each has its own strength and most of them are used in a complementary manner to obtain detailed information on various defects present in the SiC wafer.

X-ray topography, a technique based on Bragg diffraction [69], provides information on the spatial distribution of the crystallographic defects throughout the wafer volume. The technique is sensitive to the strain associated with lattice distortions and defects in the crystal. Both SEM and AFM are capable of revealing structural morphology of defects in detail, such as micropipes, basal plane dislocations, stacking faults, low-angle grain boundaries, as-grown surface features, and surface morphologic defects on epitaxial films; however, closed core dislocations such as threading edge or screw dislocations are difficult to reveal. Detailed examination of the quality of a SiC wafer is obscured by the presence of a high density of defects [69] and hence, the X-ray topography methods are best used in the study of low defect density crystals. TEM investigations can provide valuable fundamental information, including atomic-level defect structure, however it is time-consuming, expensive, and destructive due to the necessary special requirement for sample preparation.

Compared to X-rays from classical sources, synchrotron white (polychromatic) beam radiation has the advantages of high intensity, low divergence, and wide continuous spectrum up to gamma-ray energies [69]. These advan-

tages are utilized in Synchrotron White Beam Topography (SWBXT). With its high strain sensitivity and suitable spatial resolution, SWBXT has played a strong role in the progress of SiC growth by providing valuable understanding of the nature of screw dislocations, the origin of micropipes, and other defects. Amongst the various SWBXT defect imaging modes, back-reflection topography is apparently the most efficient method for imaging screw dislocations in the commonly (0001)-oriented SiC wafers. As shown in Fig. 1.27, the hollow-core and closed-core screw dislocations are clearly revealed as circular white spots surrounded by black rings in the back-reflection SWBXT. Micropipes are imaged as large white spots (circular or elliptical, Fig. 1.27) depending on their orientation. While the synchrotron white beam technique is powerful in its ability to detect and identify defects and non-destructive in nature, its application is constrained because of the very limited availability of this rather specialized equipment facility [68].

Polarized light microscopy is an old and well established technique used for delineating residual strain around dislocations and other defects using a pair of crossed polarizers. Using the principle of polarized light microscopy, a fully automated instrumentation has been developed to delineate and map defects on a wafer scale. This instrument, called the “PLM automated scanning system” (PASS) has demonstrated its ability to fully characterize a 50 mm diameter wafer in ~ 20 minutes, making possible routine, yet detailed characterization of SiC wafers with and without an epitaxial layer on the sub-

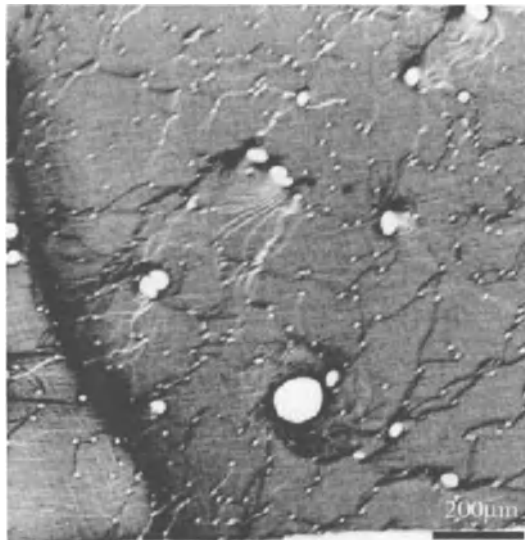


Fig. 1.27. SWBXT back-reflection image recorded from a 6H-SiC (0001) wafer thinned to approximately 30 μm . The circular images (*black rings surrounding white circles*) correspond to screw dislocations. Sample-to-film distance $D_{\text{sf}} = 10 \text{ cm}$ ([73], reprinted with permission from the author and IOP Publishing Ltd)

strate [75, 76, 79]. While polarized light microscopy has been used in the past by researchers to detect defects (especially micropipes) at specific localized regions of a wafer [33, 80, 81], Ma et al. have successfully implemented PASS for the identification and mapping, by category, of the various defects in SiC wafers [75, 76, 79]. In addition to micropipes, stressed striations, inclusions, dislocations, and grain boundaries (dislocation walls) can be visualized. The most important feature is that the characterizations based on the PLM technique are rapid, non-destructive and low cost.

Figure 1.28 shows the image patterns corresponding to different defects in a high-quality commercial 6H SiC wafer. The micropipe is usually highlighted as a butterfly shape (Fig. 1.28a), with a size bigger than that of the wave-shaped dislocations (Fig. 1.28b and c). The wave-shaped features delineated by PLM were verified to be screw dislocations by comparing the images with those obtained by SWBXT [79]. Likewise, the butterfly-shaped features were identified to be micropipes. Dark and bright regions demarcated along a straight line are observed at different locations even in good quality wafers. Such brightness-striated regions are called stress striations. The difference between a dislocation wall or grain boundary (Fig. 1.28d) and stressed striation (Fig. 1.28e) is that the former has a dislocation stress pattern along a straight line. These two types of line defects: dislocation walls (Fig. 1.28d) and stress striations (Fig. 1.28e), were concluded to be grain boundary-related defects.

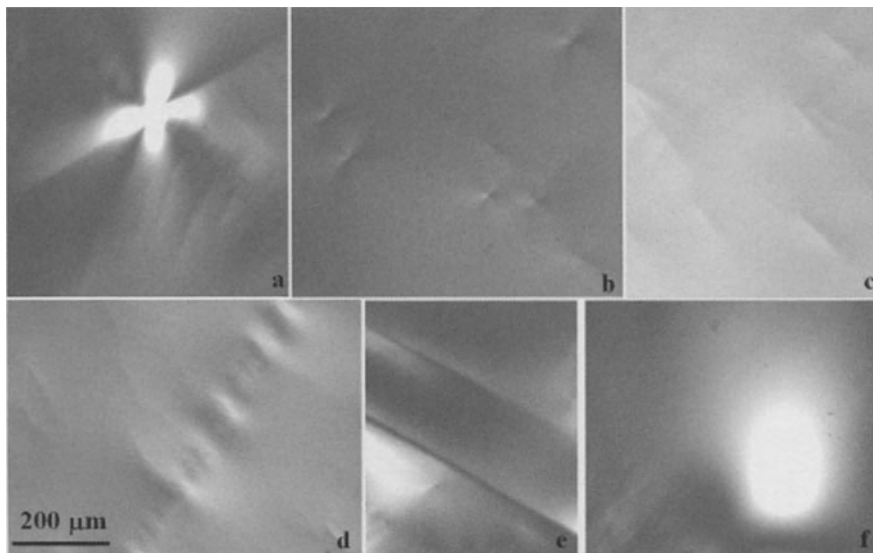


Fig. 1.28. Typical PLM defect patterns observed in a 6H-SiC (0001) wafer: (a) micropipes; (b) closed-core screw dislocations, parallel to the *c*-axis; (c) closed-core screw dislocations, slightly off *c*-axis; (d) dislocation wall; (e) stress striation; (f) highly stressed zone

While a rapid and non-destructive means of evaluating material quality, in terms of micropipes and other defects is presently not available especially for use on a routine and inexpensive basis, PASS has been demonstrated to meet the above objectives, providing a wafer scale map of micropipes and elementary screw dislocations. Further, this imaging system can simultaneously delineate micropipes, screw dislocations, and grain boundaries, the primary threading defects deleterious to device performance.

All of the techniques discussed so far, aside from TEM, offer SiC material and defect characterization in a non-destructive manner.

1.7.3 Evaluation of Crystalline Quality by Chemical Etching: Destructive Method

Chemical etching allows delineation of both nano- and micro-scale defects present in SiC wafers. The delineation of the defects is due to the creation of etch pits (selective etching) or hillocks around defects and in some cases due to the difference in the contrast between the defected area and bulk material. The main defects in SiC that can be delineated by chemical etching are micropipes, planar defects, sub-grain boundaries, dislocations and stacking faults.

The first, most comprehensive study on chemical etching of SiC was done by Faust [82,83]. He studied a large number of oxygen containing salts used in molten state to reveal the dislocation structure in both hexagonal and cubic SiC.

It was shown that the etch pits are hexagonal in shape, in accordance with the crystallographic symmetry of the plane being etched. It is accepted that one etch pit corresponds to one dislocation and thus allows the estimation of dislocation density.

The most common etchant for SiC used in the past two decades is Potassium Hydroxide (KOH). Even though etching occurs at temperatures greater than 450 °C, this etchant has the advantage of selectively etching SiC without leaving the reaction products on the surface. Moreover, suitable etching rates can be obtained using KOH. Below is presented a brief description of various SiC defects and their delineation by KOH.

Micropipes. Micropipes are hollow tubes penetrating the SiC crystal along the *c*-direction and in most cases represent super-screw dislocations with a very large Burgers vector [84]. They can be revealed by KOH etching as shown in Fig. 1.29.

Planar Defects. Hexagonal voids, also called tubelike cavities [29], planar macro-defects [17] or planars (used here), are revealed as hexagonal prism shaped empty spaces with typical sizes up to several hundreds μm in width, and length (thickness) along the *c*-axis from 5 to 25 μm [52]. The base of the planars is usually parallel to the (0001) plane when the SiC crystal is sliced perpendicular to the *c*-axis; some of the planars can be “open”, i.e. exposed to the surface. Very often planar defects can be observed on as-lapped

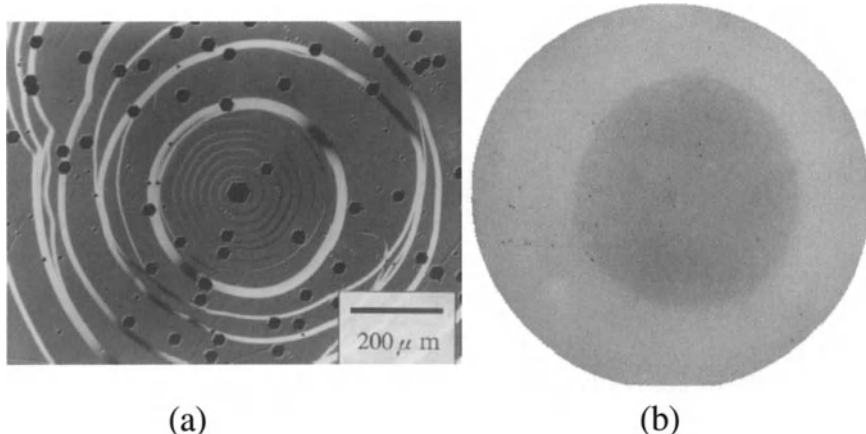


Fig. 1.29. Micropipes as seen on KOH-etched SiC surface: (a) Nomarski image of growing (crown) surface ([85], reprinted with permission from Elsevier) and (b) 50 mm KOH-etched 4H-SiC wafer with a micropipe density of 1.1 cm^{-2} (micropipes show up as black dots on the image) ([32], reprinted with permission from Elsevier)

(Fig. 1.30a) and as-polished surfaces by optical microscopy. KOH etching allows observation of fine crystallographic structure inside and outside of the planar (Fig. 1.30b). This is very important in the case of verifying the nature of other growth defects, the presence of which can be initiated from the planar defects.

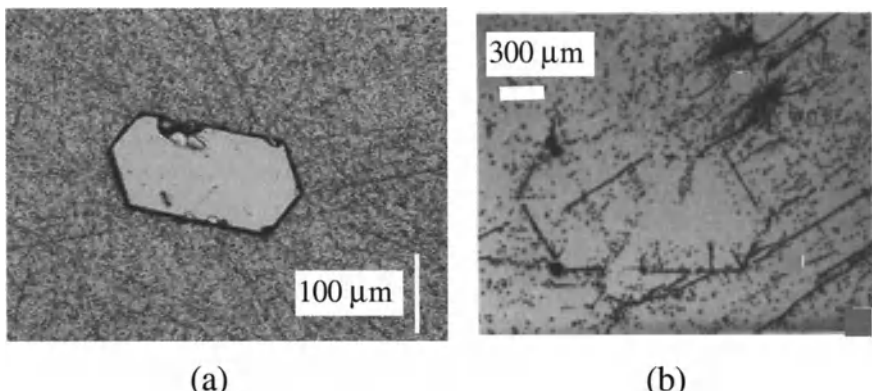


Fig. 1.30. Planar defects as seen on (a) a lapped SiC surface [76] and (b) an etched 6H-SiC wafer from a boule grown on the Si face ([52], reprinted with permission from the authors and the American Institute of Physics)

Grain Boundaries. Grain boundaries and sub-grain boundaries are areas between different polytypes or slightly misoriented crystalline blocks of the same polytype. In both cases, the presence of a boundary results in the generation of edge dislocations that can be delineated using KOH etching. Grain boundaries are usually observed at the crystal edges and are generated due to the release of stress, which is higher at the edges of the growing crystal. Grain and sub-grain boundaries appear on etched surfaces as line of etch pits (Fig. 1.31) and can be easily distinguished from scratch marks.

Dislocations. Dislocations are of major interest for SiC-based electronics since they represent electrically active defects that may significantly limit device performance. Therefore, the evaluation of dislocation density and their origin is very important for feedback in crystal growth as well as for device fabrication. Thus far, the dislocation density in SiC remains significantly higher ($\geq 10^4 \text{ cm}^{-2}$) than for Si or GaAs. The most common technique used for dislocation delineation in SiC is KOH etching.

Molten KOH attacks SiC preferentially and therefore creates etch pits on the surface. It is to be noted that the Carbon face does not exhibit etch pits in molten KOH and therefore the Si-terminated face is used for defect characterization by KOH etching. There are a number of studies providing KOH etching regimes to reveal dislocations. However, the most systematic works were done by research groups in Linköping University [88–90] and Nippon Steel Corporation [91]. It was shown that KOH etching clearly reveals dislocations and associated with them defects such as micropipes (Fig. 1.32).

Molten KOH etching allows delineation of dislocations associated with crystal growth (Fig. 1.33a) as well as those associated with the glide system in SiC (sea-shell pits in Fig. 1.33b represent basal plane dislocations).

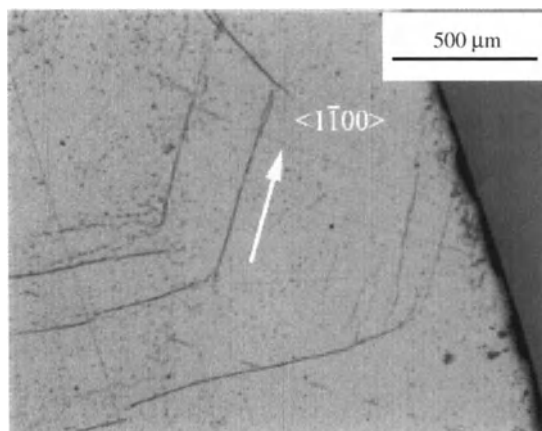


Fig. 1.31. Etch pit features on the 6H-SiC (0001) Si surface revealed by KOH selective etching. The subgrain boundaries are polygonized into $\langle 1\bar{1}00 \rangle$ directions ([87], reprinted with permission from Elsevier)

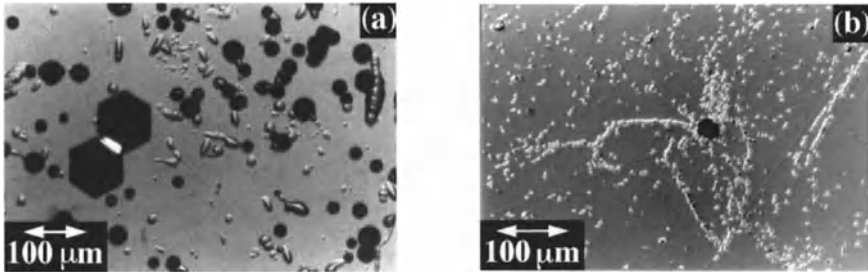


Fig. 1.32. Defect appearance on the Si face of SiC after etching in molten KOH: (a) a general view, (b) a micropipe surrounded by dislocations ([89], reprinted with permission from author)

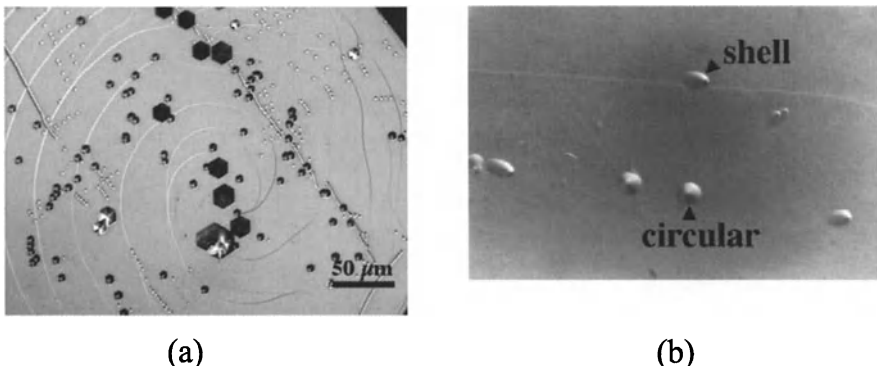


Fig. 1.33. (a) A 6H-SiC as-grown surface after etching with molten KOH, and (b) circular and shell-like etch pits ([89], reprinted with permission from author)

Alternate orientation wafers such as axial cuts ($11\bar{2}0$) (*a*-face) and prism cuts ($1\bar{1}00$) (*p*-face) offer new possibilities for the fabrication of SiC based electronic and opto-electronic devices. As noted before, *p*- and *a*-face wafers are attractive for device fabrication because of their low micropipe density, polytype homogeneity, higher growth rates, etc. [45, 92, 93]. The majority of existing SiC electronic devices are fabricated on the Si-terminated face of SiC. However, etch pit patterns delineating defects on the C-face of SiC are invaluable for crystal growers since C-terminated wafers can be potentially used as seed surfaces for bulk growth. Therefore, it was important to develop a simple method for preferential etching of SiC that can evaluate defects on all the significant crystal faces and planes. For this purpose, the interaction between KOH vapor and the SiC surfaces was investigated with the specific objective of delineating various crystallographic defects [94].

Etch pits associated with dislocations were observed in all crystallographic planes including $(0001)\text{C}$, $(11\bar{2}0)$, and $(1\bar{1}00)$ planes (Fig. 1.34).

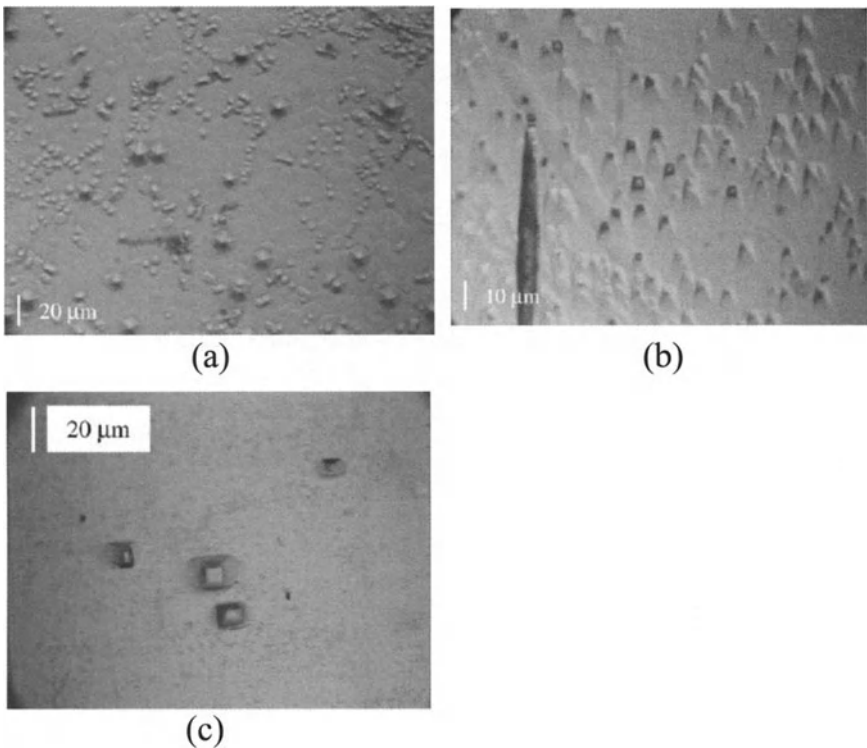


Fig. 1.34. Etch pits on (a) $(000\bar{1})\text{C}$, (b) $(11\bar{2}0)$, and (c) $(1\bar{1}00)$ planes of SiC after KOH vapor etching at 1000°C for 5 min

KOH vapor etching also has advantages of producing characteristic shape etch pits in accordance to the plane of symmetry and it is very useful for etching large diameter wafers without requiring large crucibles (to contain KOH).

Stacking Faults. When SiC crystal is grown perpendicular to the *c*-axis, spiral growth is prevented and therefore micropipe density is significantly reduced or eliminated. However, a very high density of stacking faults is observed. Stacking faults lying in the basal plane appear as linear etch pits produced by molten KOH extending along $\langle 11\bar{2}0 \rangle$ directions on the $(1\bar{1}00)$ surface (Fig. 1.35).

It is thus clear that KOH etching of SiC is a very powerful method that allows delineation of major growth and crystallographic defects and the determination of the density of different defects. In spite of being a destructive method, it is widely used by researchers and wafer manufacturers because of its ease of use, low cost, ready availability, and rapid turn around time.

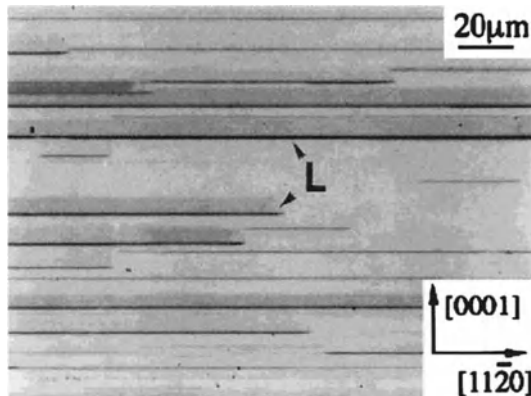


Fig. 1.35. Nomarski micrograph of the etched $(1\bar{1}00)$ surface for the $(1\bar{1}00)$ -grown crystal ([45], reprinted with permission from Wiley and Sons)

1.8 Market and Application Needs and Future Prospects

Silicon Carbide, because of its unmatched physical and electronic properties, including high critical electric breakdown field strength, high electron saturation velocity, high thermal conductivity (higher than copper), chemical inertness, and resistance to radiation environments is an attractive semiconductor material for device applications capable of operation at high temperatures, high power levels, and high frequencies. In spite of these intrinsic advantages, advances in material quality and cost must be achieved before devices can be manufactured with a competitive cost advantage.

From the time the modified Lely method of bulk growth was reported in 1978 by Tairov and Tsvetkov, significant progress has been made in understanding the science of the sublimation growth process and in the development of technology for the growth of good quality large diameter SiC boules. Further, there has been a concurrent development of the technologies of slicing large diameter boules into wafers (up to 100 mm) and that of lapping and polishing SiC surfaces to produce epitaxy ready wafers. In the last five to six years, the commercial development of 50 mm (2 inch) SiC wafers has enabled the volume production of nitride based, high brightness blue and green light emitting diodes (LEDs) fabricated on SiC substrates. The commercial availability of 4H- and 6H-substrates of good quality and also the ability to deposit good quality epitaxial films of different thicknesses of controlled doping concentration (both n- and p-type doping) has enabled the demonstration of many types of device breakthroughs in laboratories around the world [32]. The state of art SiC devices (as of 2002) include microwave MESFETs with power densities of 4.6 W/mm at 3.5 GHz and a total CW power of 80 W at 3.1 GHz from a single chip, 19 kV P-i-N diodes on epitaxial film, thyristors conducting 12 A at 6.5 V with 2600 V blocking voltage, and GaN/AlGaN high electron mobility transistors on semi-insulating SiC substrates with a power

density of 11.4 W/mm at 10 GHz [2]. 4H-SiC offers great potential for many types of high current power-electronic devices. The high micropipe density in commercial grade SiC wafers and the high cost of low micropipe density ($< 10/\text{cm}^2$) wafers has been a main barrier for the commercialization of a variety of SiC high current power devices with high device yields. Reduction of micropipe density will enable the commercial development of large area power devices that can conduct large currents.

Schottky diodes up to 6×6 mm, strategically located on a wafer to avoid micropipes, were successfully fabricated in 2001 with a blocking voltage of ~ 600 volts; 1200 volts is currently available [33]. High device yields under realistic production conditions is essential for device production on an industrial scale. Device yield calculations were made for non-strategically placed large area Schottky diodes on 4H 50 mm wafers and compared with fabricated devices. For a forward current density of 150 A/cm^2 , assuming a micropipe density of $10/\text{cm}^2$, the yield of 3.5 mm diameter devices was $\sim 40\%$ which decreased to $\sim 25\%$ for 4.5 mm diameter devices. The yields from fabricated devices actually exceeded calculated yields, due to an observed clustering of micropipes.

Production of large diameter (≥ 100 mm) wafers is essential for reducing the production cost of SiC devices through economies of scale and the use of existing Si or GaAS device fabrication lines. In this respect there is optimism since 75 mm diameter 4H and 6H wafers are commercially available and single crystal wafers of 100 mm diameter have been demonstrated [33]. Generally, the quality of the SiC wafer degrades as the crystal diameter increases. However, it is essential to improve material quality in order to take advantage of the many superlative intrinsic properties of the SiC material and to realize its full potential as a high power and high temperature electronic material. In addition to micropipes as the major obstacle in the production of high performance SiC devices, SiC device commercialization is also hampered by the presence of low-angle grain boundaries (subgrain boundaries), which prevents the implementation of large-area ($\geq 1 \text{ cm}^2$) SiC devices [60]. Recent technological advances have made it possible to reduce these defects. It has been shown that the presence of both micropipes and low-angle grain boundaries present in the SiC substrate propagate or thread through the grown epitaxial films and become “killer” defects if they intersect active regions where devices are fabricated. The high cost of commercial SiC wafers is still a major barrier for many university laboratories to enter research in the field of this very promising material, and undoubtedly for device fabrication on a commercial scale, since the cost of the best quality material is prohibitively expensive. Hence, the main challenges for the future is the commercial availability of large diameter (≥ 100 mm) wafers with ultra low micropipe density or zero micropipes and zero mosaicity (low angle grain boundaries), and equally important, a significant reduction in the cost of wafers.

High voltage P-i-N diodes are a very important power electronic device of significant practical interest. A key parameter of bipolar (P-N) diodes is

the forward voltage drop. In order to reduce the forward voltage drop the on-state resistance must be as low as possible. In addition, the voltage drop must be stable throughout the operating time of the device. The main obstacle to the commercialization of SiC high power P-N and P-i-N diodes, for a variety of applications, is the so called “forward voltage drop degradation” or “voltage drift” with time; here the value of the voltage drop increases or creeps with time. This phenomenon was observed in P-N diodes formed by both ion implantation and epitaxial growth [95]. The initiation of diode degradation is attributed to the generation and movement of structural defects, stacking faults, in the active region of the diode [96]. The stacking faults may thus prevent the realization of any long-term reliable SiC bipolar devices. Such has been the concern over this issue that research groups from around the world have focused their efforts to identify methods to reduce or eliminate these faults. However, at the present time it is not clear that the problem of P-i-N forward voltage degradation, which is attributed to the generation and movement of stacking faults, arises from the stacking faults in the SiC substrate itself (i.e., a bulk crystal quality issue) or as a result of processing steps that are a part of the device fabrication. Hence, the role of stacking faults in the SiC substrate need to be thoroughly investigated for the development of high voltage SiC P-i-N power diodes for commercial and other specific applications.

Generally, p-doped SiC material has received much less attention than its n-type counterpart, both by researchers and wafer manufacturers. The most common current application of SiC is for the production of GaN based green and blue LEDs. Many high power electronic devices will require p-type doped substrates. In addition to the requirements of increasing crystal (wafer) diameter and improving crystal quality (low defect density, especially micropipes and low angle boundaries), it is important to increase the doping concentration of the p-type material to produce hole concentration close to $10^{19} / \text{cm}^3$, and to improve the uniformity of doping concentration over the entire wafer area.

Semi-insulating SiC material with resistivity greater than $10^5 \Omega \text{ cm}$, wafer diameter 50 mm (2 inches) is commercially available. The high-resistivity material is produced in one of two ways: (i) by the incorporation (doping) of deep level impurities (e.g., vanadium) to provide compensation of the existing donors and acceptors or (ii) by “deep purification” where bulk crystal growth takes place under extremely clean conditions of the source, graphite parts (crucible and thermal insulation), carrier gas, etc. and in this case, intrinsic point defects are responsible for compensation, resulting in semi-insulating SiC. There are advantages to producing semi-insulating SiC by the latter approach. It is to be noted the 50 mm diameter commercial semi-insulating material currently available is prohibitively expensive. The high wafer cost is clearly indicative of a very low yield of good quality wafers derived from a given boule. Hence, production of large diameter (100 mm) semi-insulating wafers of high quality (low micropipe density and mosaicity) at low costs represents the greatest need and currently, its absence is the main barrier for the commercialization of high-power microwave devices.

Silicon Carbide wafers fabricated in alternate orientations, especially the [1 $\bar{1}00$] and [11 $\bar{2}0$] directions offer many opportunities for device fabrication, to wit, absence of micropipes and screw dislocations, no polytype-inclusion defects, enhanced channel mobility, etc. However, the mechanism of growth in these materials is not well understood. A primary challenge for crystal growers is to establish growth processes that will substantially reduce the stacking fault density in crystals grown perpendicular to *c*-directions. The implications of stacking faults in terms of device characteristics need to be investigated. The existence of new defects, hitherto not known need to be determined and their influence on device characteristics need to be fully investigated before the potential of these materials (alternate SiC orientations) can be evaluated. Again, issues related to size, quality, and cost need to be addressed, similar to *c*-axis grown wafers.

The primary focus of silicon carbide single crystal bulk growth has been for its application as an electronic material for device applications. Striking similarities exist between SiC and bulk crystalline diamond in optical properties, thermal conductivity, mechanical hardness, and density. This similarity has led to the use of SiC as a rather novel gemstone material, also called moissanite [32]. Very similar to diamond, it exhibits broad transparency in the visible spectrum, optical brilliance, and refractive index that shows similar wavelength dependence over the visible spectrum. Further, while diamond is unstable in oxidizing environments, moissanite is very stable and also resistant to chemical and abrasive attack [32]. The crystal is colorless and can be fabricated from large single crystal boules grown by the PVT method, thus enabling the production of large “carat” gemstones. It can be faceted to produce jewelry caliber crystals nearly indistinguishable from cut diamonds. Further, SiC crystals can be selectively doped to produce different color moissanite gemstone crystals. Since the requirements for gemstone material is stringent in terms of crystal quality (very low defect density), the application of SiC as a gemstone material has provided added impetus to produce very high quality large size single crystal boules, a requirement identical to that demanded by the high power electronic device market. It is noted that the market for cubic zirconia requires the material to be produced at a very high volume of 440 tons per year [32]. Hence, the semiconductor industry is expected to benefit greatly from the requirements and demand put on improving the quality of bulk SiC crystals for the gemstone market.

Acknowledgements

This work was supported in part from ONR, Grant No.N0000140210667. I would like to thank Dr.C. Wood of ONR, my colleagues: Drs. R. Bondokov, D. Cherednichenko, Y. Gao, X. Ma, P. Muzykov, and I. Khlebnikov, as well as S. Maximenko and Z. Zehong for their contributions to this project. I also thank Ms. J. Morris for her invaluable assistance in the preparation of this manuscript.

References

1. R.J. Trew, J. Yan, and P.M. Mock, "The Potential of Diamond and SiC Electronic Devices for Microwave and Millimeter-Wave Power Applications", Proc. IEEE **79**, 598–620 (1991).
2. A.R. Powell and L.B. Rowland, "SiC materials—Progress, status and potential roadblocks", Proc. IEEE **90**(6), 942–955 (2002).
3. J.L. Hudgins, "Wide and Narrow Bandgap Semiconductors for Power Electronics: A New Valuation", J. Elect. Mat. **32**(6), 471 (2003).
4. T.P. Chow and R. Tyagi, "Wide Bandgap Compound Semiconductors for Superior High Voltage Unipolar Power Devices", IEEE Trans. ED **41**, 1481 (1994).
5. M. Bhatnagar and B.J. Baliga, "Comparison of 6H-SiC, 3C-SiC, and Si for Power Devices", IEEE Trans. ED **40**, 645 (1993).
6. B.J. Baliga, "Power semiconductor device figure of merit for high-frequency applications", IEEE EDL **10**, 455 (1989).
7. R.C. Clarke and J.W. Palmour, "SiC Microwave Power Technologies", Proc IEEE **90**(6), 987–992 (2002).
8. W.F. Knippenberg, "Growth Phenomena in Silicon Carbide", Philips Res. Reports **18**, 161–274 (1963).
9. J.A. Lely, "Silizium carbide von Art und Menge der eingebeunten verunreinigungen", Ber. Dtsch. Keram. Ges. (Germany) **32**, 229 (1955).
10. Y.M. Tairov and V.F. Tsvetkov, "Investigation of Growth Processes of Ingots of Silicon Carbide Single Crystals", J. Cryst. Growth **43**, 209 (1978).
11. P.T.B. Schaffer, "Problems in Silicon Carbide Device Development", Mat. Res. Bull. pp. S13–S23 (1969).
12. W.F. Knippenberg and G. Verspui, Philips Res. Reports **21**, 113 (1966).
13. R.C. Marshall, "Growth of Silicon Carbide from Solution", Mat. Res. Bull. pp. S73–S84 (1969).
14. Y.M. Tairov, "Growth of Bulk SiC", Mat. Sci. Eng. B **29**, 83–89 (1995).
15. J. Smiltens, "The Growth of SiC Crystals from Vapor by the Bridgman-Stockbarger Method", Mat. Res. Bull. S85–S96 (1969).
16. M. Syväjärvi, *High Growth Rate Epitaxy of SiC: growth processes and structural quality* PhD Dissertation Linköping University, Linköping, Sweden 1999.
17. S. Nishino, T. Higashino, T. Tanaka, and J. Saraie, "Growth mechanism and defects in SiC prepared by sublimation method", J. Crystal Growth **147**, 339 (1995).
18. F.C. Frank, "The influence of dislocations on crystal growth", Disc. Faraday Soc. **5**, 48 (1949).
19. W.T. Read, *Dislocations in crystals*, McGraw-Hill, New York 1953.
20. W.J. Yang and P. Pirouz, In: *Presented at Int. Conf. on Amorphous and Crystalline Silicon Carbide 1991* (October 1991).
21. R. Yakimova, M. Syväjärvi, T. Iakimov, H. Jacobsson, A. Kakanakova-Georgieva, P. Råback, and E. Janzén, "Growth of silicon carbide: process-related defects", Appl. Surf. Sci. **184**, 27–36 (2001).
22. V.D. Heydemann, G.S. Rohrer, E.K. Sanchez, and M. Skowronski, "The structural evolution of seed surfaces during the initial stages of physical vapor transport SiC growth", Mater. Sci. Forum **264–268**, 37 (1998).

23. V.D. Heydemann, E.K. Sanchez, G.S. Rohrer, and M. Skowronski, "The structural evolution of Lely seeds during the initial stages of SiC sublimation growth", in *Power Semiconductor Materials and Devices*, ed. by S. Pearton, F. Ren, R. Shul, S. Tenconi, and E. Wolfgang, Mater. Res. Soc. Proc. **483**, Pittsburgh (1998), 295–301.
24. D. Hofmann, E. Schmitt, M. Bickermann, M. Kölbl, P.J. Wellmann, and A. Winacker, "Analysis on defect generation during the SiC bulk growth process", Mater. Sci. Eng. B **61–62**, 48–53 (1999).
25. R. Madar, M. Anikin, K. Chourou, M. Labeau, M. Pons, E. Blanquet, J.M. Dedulle, C. Bernard, S. Milita, and J. Baruchel, "Defects formation in sublimation grown 6H-SiC single crystal boules", Diamond Relat. Mater. **6**, 1249 (1997).
26. A.R. Verma and P. Krishna, *Polymorphism and Polytypism in Crystals* John Wiley & Sons, Inc., New York 1966.
27. W. van Haeringen, P.A. Bobbert, and W.H. Backes, "On the Band Gap Variation in SiC Polytypes", Phys. Stat. Sol. (b) **202**, 63–79 (1997).
28. R. Yakimova, T. Iakimov, M. Syväjärvi, H. Jacobsson, P. Råback, A. Vehanen, and E. Janzén, "Polytype Stability and Defect Reduction in 4H-SiC Crystals Grown Via Sublimation Technique", Proc. MRS Spring Meeting, April 5–9, San Francisco (1999).
29. R. Stein and P. Lanig, "Control of polytype formation by surface energy effects during the growth of SiC monocrystals by the sublimation method", J. Cryst. Growth **131**, 71 (1993).
30. V.D. Heydemann, N. Schulze, D.L. Barrett, and G. Pensl, "Growth of 6H and 4H silicon carbide single crystals by the modified Lely process utilizing a dual-seed crystal method", Appl. Phys. Lett. **69**, 3728 (1996).
31. G. Augustine, McD. Hobgood, V. Balakrishna, G. Dunne, and R.H. Hopkins, "Physical vapor transport growth and properties of SiC monocrystals of 4H polytype", Phys. Stat. Sol. (b) **202**, 137 (1997).
32. S.G. Müller, R.C. Glass, H.M. Hobgood, V.F. Tsvetkov, M. Brady, D. Henshall, J.R. Jenny, D. Malta, and C.H. Carter Jr., "The status of SiC bulk growth from an industrial point of view", J. Cryst. Growth **211**, 325–332 (2000).
33. S.G. Müller, R.C. Glass, H.M. Hobgood, V.F. Tsvetkov, M. Brady, D. Henshall, D. Malta, R. Singh, J. Palmour, and C.H. Carter Jr., "Progress in the industrial production of SiC substrates for semiconductor devices", Mat. Sci. Eng. B **80**, 327–331 (2001).
34. M. Pons, E. Blanquet, J.M. Dedulle, I. Garcon, R. Madar and C. Bernard, "Thermodynamic heat transfer and mass transport modeling of the sublimation growth of silicon carbide crystals", J. Electrochem. Soc. **143**(11) 3727 (1996).
35. Q.S. Chen, H. Zhang, and V. Prasad, "Heat transfer and kinetics of bulk growth of silicon carbide", J. Cryst. Growth **230**, 239 (2001).
36. H.J. Rost, D. Siche, J. Dolle, W. Eiserbeck, T. Muller, D. Schultz, G. Wagner, and J. Woolweber, "Influence of different growth parameters and related conditions on 6H-SiC crystals grown by the modified Lely method", Mater. Sci. Eng. B **61–62**, 68 (1999).
37. B.F. Yudin and B.G. Borisov, Refractories **7–8**, 499, **8** 44 (1967).
38. S.K. Lilov and I.Y. Yanchev, "Peculiarities of silicon carbide crystal growth under the diffusion mechanism of vapour transfer", Adv. Mat. Optics Elect. **1**, 203 (1992).

39. S.K. Lilov, V.F. Tsvetkov, and B.F. Yudin, *Izv. LETI* **167**, 63 (1975).
40. D.I. Cherednichenko, Y.I. Khlebnikov, R.V. Drachev, I.I. Khlebnikov, and T.S. Sudarshan, "Influence of crystal thickness on the SiC PVT growth rate," *Mater. Sci. Forum*, **389–393**, 95–98 (2002).
41. R.V. Drachev, D.I. Cherednichenko, I.I. Khlebnikov, M. Parker, and T.S. Sudarshan, "Graphitization of the seeding surface during the heating stage of SiC PVT bulk growth" *ECS CRM* Linkoping, Sweden, Sept. 2002.
42. D.I. Cherednichenko, R.V. Drachev, I.I. Khlebnikov, X. Deng, and T.S. Sudarshan, "Thermal stress as the major factor of defect generation in SiC during PVT growth", *MRS Boston*, MA, (2002).
43. R. Yakimova and E. Janzén, "Current status and advances in the growth of SiC", *Diamond Relat. Mater.* **9**, 432–438 (2000).
44. D.L. Barrett, J.P. McHugh, H.M. Hobgood, R.H. Hopkins, P.G. McMullin, R.C. Clarke, and W.J. Choyke, "Growth of large SiC single crystals", *J. Cryst. Growth* **128**, 358–362 (1993).
45. J. Takahashi and N. Ohtani, "Modified-Lely SiC crystals grown in [1 $\bar{1}$ 00] and [11 $\bar{2}$ 0] directions", *Phys. Stat. Sol. (b)* **202**, 163 (1997).
46. R.A. Stein, "Formation of macrodefects in SiC", *Physica B*, **185**, 211–216 (1993).
47. J.W. Yang, "SiC: problems in crystal growth and polytypic transformation", PhD Thesis, Case Western Reserve University (1993).
48. R.C. Glass, D. Henshall, V.F. Tsvetkov, and C.H. Carter Jr., "SiC Seeded Crystal Growth", *Phys. Stat. Sol. (b)* **202**, 149 (1997).
49. M. Tuominen, R. Yakimova, A. Vehanen, and E. Janzén, "Defect origin and development in sublimation grown SiC boules", *Mater. Sci. Eng. B* **57**, 228–233 (1999).
50. M. Dudley, S. Wang, W. Huang, C.H. Carter, Jr., V.F. Tsvetkov, and C. Fazi, "White-beam synchrotron topographic studies of defects in 6H-SiC single crystals", *J. Phys. D* **28**, A63 (1995).
51. I. Khlebnikov, V.P. Madangulari, M.A. Khan, and T.S. Sudarshan, "Thick Film SiC Epitaxy For 'Filling Up' Micropipes", *Mater. Sci. Forum* **264–268**, 167–170 (1998).
52. T.A. Khur, E.K. Sanchez, M. Skowronski, W.M. Vetter, and M. Dudley, "Hexagonal voids and the formation of micropipes during SiC sublimation growth", *J. Appl. Phys.* **89**, 4625, (2001).
53. Y. Khlebnikov, "Investigation of the Growth Processes and Defect Formation in Epitaxial Layers and Bulk Crystals of Silicon Carbide," PhD Thesis, University of South Carolina (2002).
54. I. Khlebnikov, D. Cheredinchenko, Y. Khlebnikov, and T.S. Sudarshan "Initial Stage of Crystallization in the Growth of Silicon Carbide on Substrates with Micropipes", *Mater. Sci. Forum* **338–342**, 59–62 (2000).
55. Y.M. Tairov and V.F. Tsvetkov, in: *First European Conference on Crystal Growth*, Abstract Book, p. 188 (1976).
56. Y.M. Tairov and V.F. Tsvetkov, "General principles of growing large-size single crystals of various silicon carbide polytypes", *J. Cryst. Growth* **52**, 146–150 (1981).
57. S. Nishino, "Bulk growth of SiC", in: *Properties of Silicon Carbide*, ed. G. Harris, INSPEC, the Institution of Electrical Engineers, United Kingdom, 1995.

58. D.L. Barrett, R.G. Seidensticker, W. Gaida, R.H. Hopkins, and W.J. Choyke, “SiC boule growth by sublimation vapor transport”, *J. Cryst. Growth* **109**, 17–23 (1991).
59. M. Tuominen, R. Yakimova, R.C. Glass, T. Tuomi and E. Janzén, “Crystalline imperfections in 4H SiC grown with a seeded Lely method”, *J. Cryst. Growth* **144**, 267–276 (1994).
60. N. Ohtani, T. Fujimoto, M. Katsuno, T. Aigo, and H. Yashiro, “Growth of large high-quality SiC single crystals”, *J. Cryst. Growth* **237–239**, 1180–1186 (2002).
61. N.T. Son, B. Magnusson, Z. Zolnai, A. Ellison, and E. Janzén, “Defects in semi-insulating SiC substrates”, *Mater. Sci. For.* **433–436**, 45–50 (2003).
62. S.G. Müller, M.F. Brady, W.H. Brixius, R.C. Glass, McD. Hobgood, J.R. Jenny, R.T. Leonard, D.P. Malta, A.R. Powell, V.F. Tsvetkov, S.T. Allen, J.W. Palmour, and C.H. Carter, Jr., “Sublimation-grown semi-insulating SiC for high frequency devices”, *Mater. Sci. For.* **433–436**, 39–44 (2003).
63. M. Bickermann, D. Hofmann, T.L. Straubinger, R. Weingärtner, and A. Winnacker, “Preparation of semi-insulating silicon carbide by vanadium doping during PVT bulk crystal growth”, *Mater. Sci. For.* **433–436**, 51–54 (2003).
64. A. Ellison, B. Magnusson, N.T. Son, L. Storasta, and E. Janzén, “HTCVD grown semi-insulating SiC substrates”, *Mater. Sci. For.* **433–436**, 33–38 (2003).
65. V.P. Rastegaev, D.D. Avrov, S.A. Reshanov, and A.O. Lebedev “Features of SiC single-crystals grown in vacuum using the LETI method”, *Mater. Sci. Eng. B*, **61–62**, 77–81 (1999).
66. T.L. Straubinger, M. Bickermann, R. Weingärtner, P.J. Wellmann, and A. Winnacker, “Aluminum p-type doping of silicon carbide crystals using a modified physical vapor transport growth method”, *J. Cryst. Growth* **240**, 117–123 (2002).
67. P.J. Wellmann, S. Bushevoy, and R. Weingärtner, “Evaluation of n-type doping of 4H-SiC and n-/p-type doping of 6H-SiC using absorption measurements”, *Mater. Sci. Eng. B* **80**, 352 (2001).
68. R.C. Glass, L.O. Kjellberg, V.F. Tsvetkov, J.E. Sundgren, and E. Janzén, “Structural macro-defects in 6H-SiC wafers”, *J. Cryst. Growth* **132**, 504–512 (1993).
69. M. Tuominen, E. Prieur, R. Yakimova, R.C. Glass, T. Tuomi and E. Janzén “Defect analysis in Lely-grown 6H SiC”, *J. Cryst. Growth* **165**, 233–244 (1996).
70. R.P. Devaty and W.J. Choyke, “Optical Characterization of Silicon Carbide Polytypes”, *Phys. Stat. Sol. (a)* **162**, 5–38 (1997).
71. X.R. Huang, M. Dudley, W.M. Vetter, W. Huang, S. Wang, and C.H. Carter, Jr., “Direct evidence of micropipe-related pure superscrew dislocations in SiC”, *Appl. Phys. Lett.* **74**, 353 (1999).
72. M. Dudley, W. Huang, S. Wang, J.A. Powell, P. Neudeck, and C. Fazi, “White-beam synchrotron topographic analysis of multi-polytype SiC device configurations”, *J. Phys. D* **28**, A56 (1995).
73. M. Dudley, X.R. Huang, and W. Vetter, “Contribution of X-ray topography and high-resolution diffraction to the study of defects in SiC”, *J. Phys. D*, **36**, A30 (2003).
74. K. Byrappa and T. Ohachi, *Crystal Growth Technology*, William Andrew publishing, New York, 2002.
75. X.Y. Ma, M. Parker, and T.S. Sudarshan, “Nondestructive defect delineation in SiC wafers based on an optical stress technique”, *App. Phys. Lett.* **80**, 3298 (2002).

76. X.Y. Ma, M. Parker, Y.F. Ma, T. Kubota, and T.S. Sudarshan, "Non-destructive SiC wafer evaluation based on an optical stress technique", ECSCRM 2002, Linköping, Sweden (2002).
77. P.G. Neudeck, W. Huang, and M. Dudley, "Study of bulk and elementary screw dislocation assisted reverse breakdown in low-voltage (< 250 V) 4H-SiC p+n junction diodes – Part 1: DC properties", IEEE Trans. Electron Dev. **46**, 478 (1999).
78. P.G. Neudeck and J.A. Powell, "Performance limiting micropipe defects in silicon carbide wafers," IEEE Electron Dev. Lett. **15**, 63–65 (1994).
79. X.Y. Ma, T.S. Sudarshan, M. Dudley, and W. Vetter, "Extended SiC defects: polarized light microscopy and SWBXT ratification", Jap. Appl. Phys. Lett. **42**, L1077–L1079 (2003).
80. T. Kato, H. Ohsato, and T. Okuda, "Origin of the internal stress around the micropipe of 6H-SiC single crystal", Mater. Sci. Forum **338–342**, 449 (2000).
81. E. Kalinina, A.S. Zubrilov, N.I. Kuznetsov, I.P. Nikitina, A.S. Tregubova, M.P. Shcheglov, and V.Ya. Bratus, "Structural, electrical and optical properties of bulk 4H and 6H p-type SiC", Mater. Sci. Forum **338–342**, 497 (2000).
82. J.W. Faust, Jr., The etching of silicon carbide, in "Silicon Carbide a High Temperature Semiconductor" Proc. of the Conference on Silicon Carbide Boston MA April 2–3, 1959, Eds. J.R. O'Connor and J. Smiltens, Pergamon Press, 1960.
83. J.W. Faust, Y. Tung, and H.M. Liaw, *A Study of Etch Pits on Pure Polytypes of SiC, in Silicon Carbide – 1973*, Eds. R.C. Marshall, J.W. Faust, C.E. Ryan, University of South Carolina Press, Columbia, SC 1973.
84. J. Heindl, H.P. Strunk, V.D. Heydemann, and G. Pensl, "Micropipes: Hollow Tubes in Silicon Carbide", Phys. Stat. Sol. (a) **162**, 251 (1997).
85. N. Sugiyama, A. Okamoto, K. Okumura, T. Tani, and N. Kamiya "Step structures and dislocations of SiC single crystals grown by modified Lely method", J. Cryst. Growth **191**, 84–91 (1998).
86. Author's unpublished material.
87. M. Katsuno, N. Ohtani, T. Aigo, T. Fujimoto, H. Tsuge, H. Yashiro, M. Kanaya, "Structural properties of subgrain boundaries in bulk SiC crystals", J. Cryst. Growth **216**, 256–262 (2000).
88. R. Yakimova, A.L. Hylen, M. Tuominen, M. Syväjärvi, and E. Janzén, "Preferential etching of SiC crystals", Diamond Relat. Mater. **6**, 1456–1458 (1997).
89. M. Syväjärvi, R. Yakimova, A.L. Hylen, and E. Janzén, "Anisotropy of dissolution and defect revealing on SiC surfaces", J. Phys. Cond. Matter **11**, 10041–10046 (1999).
90. M. Syväjärvi, R. Yakimova, and E. Janzén, "Anisotropic etching of SiC", J. Electrochem. Soc. **147**, 3519–3522 (2000).
91. M. Katsuno, N. Ohtani, J. Takahashi, T. Fujimoto, H. Yashiro, and M. Kanaya, "Mechanism of molten KOH etching of SiC single crystals: comparative study with thermal oxidation", Jap. J. Appl. Phys. Part 1, **38**, 4661 (1999).
92. J. Takahashi, N. Ohtani, and M. Kanaya, "Structural defects in α -SiC single crystals grown by the modified-Lely method", J. Cryst. Growth **167**, 596–606 (1996).
93. J. Takahashi, N. Ohtani, M. Katsuno, and S. Shinoyama, "Sublimation growth of 6H- and 4H-SiC single crystals in the [1100] and [1120] directions", J. Cryst. Growth **181**, 229–240 (1997).

94. R.T. Bondokov, I.I. Khlebnikov, T. Lashkov, E. Tupitsyn, G. Stratiy, Y. Khlebnikov, and T.S. Sudarshan “A Method for defect delineation in silicon carbide using potassium hydroxide vapor”, Jap. J. Appl. Phys. **41**(12) 7312–7316 (2002).
95. H. Lendenmann, F. Dahlquist, N. Johansson, R. Söderholm, P.A. Nilsson, J.P. Bergman, and P. Skytt, “Long term operation of 4.5 kV PiN and 2.5 kV JBS diodes”, Mater. Sci. Forum **353–356**, 727–730 (2001).
96. J.P. Bergman, H. Lendenmann, P.A. Nilsson, U. Lindefelt, and P. Skytt “Crystal defects as source of anomalous forward voltage increase of 4H-SiC diodes”, Mater. Sci. Forum **353–356**, 299 (2001).

Fundamental Properties of SiC: Crystal Structure, Bonding Energy, Band Structure, and Lattice Vibrations

J. Dong and A.-B. Chen

As a result of intensive research in the past decade, SiC has matured as a semiconductor for electronic-device applications. The knowledge of the fundamental materials properties for SiC is also as mature as that for other semiconductors. This is particularly true for the three most common polytypes 3C, 4H, and 6H. This chapter attempts to summarize the current status of the crystal structure, bonding energy, band structure, and lattice vibrations for the four polytypes 3C, 2H, 4H, and 6H of SiC. We evaluate these properties with our theoretical tools and make an effort to compare different polytypes. We then conclude by separating the well-established results from those that remain uncertain. Such an emphasis not only provides an updated source for these fundamental properties but may also encourage further refinement of these results.

2.1 Introduction

The purpose of this review is to provide an updated summary of the following fundamental properties of SiC: crystal structure, bonding energy, band structure near the gap, and lattice vibration. We limit ourselves to the four simplest polytypes, i.e. the simplest hexagonal polytype 2H, and the three common polytypes 3C, 4H, and 6H used in device applications. A rather comprehensive review of these properties for SiC prior to 1997 is available in two special volumes devoted to SiC [1, 2]. Our chapter will include a condensed summary of these results plus new findings. We will combine the available experimental and theoretical results to assess the status of these properties. We have also independently calculated these properties and made systematic comparisons among different polytypes to enhance our evaluation.

The theoretical tool that we used is the self-consistent density functional theory (DFT) in the local density approximation (LDA) and/or in the general gradient approximation (GGA). Extensive *ab initio* theoretical studies have been performed to understand the structural and energetic properties of

SiC in the past decade [3–8]. Despite that different band structure techniques have been used to implement the *ab initio* calculations, recent calculations have provided consistent converged results, in terms of structural parameters, order of relative energy of various polytypes, band structures, and phonon dispersion. Most of our calculations presented here are performed using the Vienna *ab initio* Simulation Package (VASP) [9, 10], which adopts the plane-wave (PW) basis and ultra-soft pseudo-potentials (USPP) [11–13] in its implementation of DFT. Such PW-DFT calculations have a long history, and the method has been extensively tested on a wide variety of systems with success [14].

For the crystal structures, both the experimental and theoretical results show that all hexagonal polytypes studied are only slightly deviated from the ideal tetrahedral structures. LDA calculated lattice parameters are shown to be accurate to 1%. We have also extracted the relative bonding energies and phonon free energies among the four polytypes from our calculations to address the polytype stability. However, the very small relative energies (of order of meV per atom) are probably comparable to the uncertainty of the calculation. This makes it difficult to make an affirmative evaluation of the thermodynamic stability.

Our band structure discussion will focus on the states near the band gaps. The combined experimental and theoretical results are used to pin down the values for the band gap for all the four polytypes, the locations of the conduction band minima for the 3C, 2H and 4H polytypes, and most of the conduction electron effective masses. Uncertainty still remains for some specific polytype-dependent conduction band details, such as the exact location of the conduction band minimum and barrier height at M in 6H, the small energy separation between the two conduction band minima at M for 4H. For the valence band edge, calculations have converged for the spin-orbit splitting, crystal-field splitting, and the hole effective masses. However, experimental verification of these results is still sketchy.

We have carried out complete phonon dispersion calculations for the four polytypes. These results are in excellent agreements with available experimental [15–17] and previous *ab initio* calculations [18–20]. As a result, we now have rather complete information for the lattice vibration in SiC, not only for the phonon modes at high symmetry points in the Brillouin zone but also for the dispersions.

We will devote the next three sections to the discussion of crystal structure and bonding energy, electronic structure, and lattice vibration respectively. The last section contains a summary.

2.2 Crystal Structure and Bonding Energy

A huge number of polytypes of SiC have been reported [21]. Each polytype is a crystal with a different one-dimensional stacking sequence [22]. An in-

depth description of the crystallography of these polytypes is available in many references, for example [6] and [7]. Here we only describe the terms to be used in this chapter. A simple way to view different polytypes of SiC is to use a Silicon-Carbon bilayer as the building “unit”. Within each bilayer, the Carbon atoms are arranged in a two-dimensional hexagonal close-packed pattern and Silicon atoms are directly on top of the Carbon atoms. The three-dimensional lattices are then built by stacking the bilayers along their normal direction. As shown in Fig. 21 of [23], for a given bilayer (say bilayer-**A**), the next bilayer on top can be either bilayer-**B** or bilayer-**C**. The only difference between **B** and **C** is a 60° rotation. Different polytypes of SiC can then be described in terms of different repeated bilayer stacking sequences. 2H has the simplest repeated **AB** sequence. 3C has the **ABC** repeated sequence. The repeated sequence in 4H is **ABAC**, and that for 6H is **ABCACB**.

All SiC polytypes have almost identical nearest neighbor bonding; each Carbon atom is bonded nearly tetrahedrally to four Silicon atoms and vice versa. In the 2H polytype, each bilayer (say **A**) is sandwiched by two neighboring bilayers of the same type (say **B**). In the 3C polytype, **A** is sandwiched by two different bilayers **B** and **C**. The atom sites with the same local environment as those in the 2H polytype are labeled as the hexagonal-sites (H-sites), whereas those similar to the 3C crystal are labeled as the cubic-sites (K-sites). For example, 4H has as many H-sites as the K-sites, while 6H has twice as many K-sites as the H-sites. Based on this analysis, a hexagonality parameter h of a SiC polytype can be defined as: $h = N_H/(N_H + N_K)$, where N_H and N_K are the numbers of hexagonal and cubic sites respectively. The values of h are 0, $1/3$, $1/2$, and 1 for 3C, 6H, 4H, and 2H SiC respectively.

The crystal structures of all polytypes can be easily described in terms of the stacking of the hexagonal layers. The hexagonal lattice is defined by two lattice constants a and c , where a is the distance between two neighboring atoms in the same hexagonal plane and c is the shortest repeated distance along the stacking direction (also referred to as the axial direction). Within the unit cell, all non-equivalent atomic layers can be completely defined by specifying the spacing d_i from the bottom layer. Conventionally these spacing are expressed in terms of the internal parameters (ratios) $u_i \equiv nd_i/c$, where n is the number of the bilayers per unit cell. For the purpose of comparison, the cubic lattice of 3C is sometimes expressed using an equivalent 3H hexagonal setting, with $a_{3H} = a_{3C}/\sqrt{2}$ and $c_{3H} = \sqrt{3}a_{3C}$, where a_{3C} is the lattice constant of the cubic 3C polytype. The 3C lattice is an “ideal” lattice because its crystal symmetry enforces uniform bond lengths and exact tetrahedral bond angles. An ideal hexagonal polytype has the $c/(na)$ ratio of $r_0 = \sqrt{2/3} = 0.8165$ and the ideal internal parameters $u_1 = 0.375$, $u_2 = 0.5$, and $u_3 = 0.875$. Table 2.1 contains a summary of the experimental and our calculated crystal structural parameters for the four polytypes considered.

Table 2.1. Experimental structural parameters of 3C-, 6H-, 4H-, and 2H-SiC polytypes and the present LDA results. The 3C polytype is treated as the ideal 3H hexagonal structure. Experimental data with superscripts a, b, c, and d are cited from [24], [25], [26], and [27], respectively. $r_0 = \sqrt{2}/3$ is the ideal ratio

Polytype		3C	6H	4H	2H
Hexagonality		$h = 0$	$h = 1/3$	$h = 1/2$	$h = 1$
a (Å)	LDA	3.0553	3.0534	3.0526	3.0505
	EXPT	3.0819 ^a	3.081 ^b	3.073 ^c	3.076 ^d
c/n (Å)	LDA	2.4946	2.4972	2.4984	2.5035
	EXPT	2.5164	2.5195 ^b	2.5133 ^c	2.524 ^d
$r = c/na$	LDA	$1.0000r_0$	$1.0017r_0$	$1.0024r_0$	$1.0051r_0$
	EXPT	$1.0000r_0$	$1.0015r_0$	$1.0016r_0$	$1.0050r_0$
$u_i = nd_i/c$	LDA	–	$u_{C1} = 0.$	$u_{Si1} = 0.$	$u_{Si} = 0.$
			$u_{C2} = 0.3762$	$u_{C1} = 0.3748$	$u_C = 0.3742$
			$u_{C3} = 0.5003$	$u_{Si2} = 0.5008$	
			$u_{Si1} = 0.8753$	$u_{C2} = 0.8762$	
			$u_{Si2} = 0.9997$		
			$u_{Si3} = 1.3747$		
EXPT	–		$u_{Si1} = 0.^b$	$u_{Si1} = 0.^c$	$u_{Si} = 0.000^d$
			$u_{C1} = 0.3750^b$	$u_{C1} = 0.374^c$	$u_C = 0.375^d$
			$u_{Si2} = 0.500^b$	$u_{Si2} = 0.500^c$	
			$u_{C2} = 0.8756^b$	$u_{C2} = 0.874^c$	
			$u_{Si3} = 1.000^b$		
			$u_{C3} = 1.3755^b$		

Converged LDA calculations can accurately predict the crystal structures. The 1% error in the structure parameters for SiC shown in Table 2.1 is typical for the LDA calculations [3–8]. Both experiment [24–27] and theory show that, despite very small differences (less than 0.2%) in the lattice constants of the four SiC polytypes, there is a clear correlation between the lattice constants and hexagonality h : the lattice constant a decreases slightly with the increase of h , while c slightly increases. Consequently, the $r = c/na$ ratio increases by about 0.5% in the 2H ($h = 1$) from the ideal value of $r_0 = \sqrt{2}/3$ in the 3C ($h = 0$). Also shown in Table 2.1, the hexagonal planes for the non-ideal polytypes are shifted only slightly along c -axis from their “ideal” positions. The standard deviation of shifting is as small as $1\text{--}3 \times 10^{-3}$ Å.

Next, we discuss the bonding energy. We calculate the bonding energy E_0 , which is the total energy of the bulk SiC, subtracting the sum of atomic energy of the constituent atoms. Therefore, our calculated $-E_0$ minus the small zero-point lattice vibrational energy is the cohesive energy of the bulk solid. Listed in Table 2.2 are the cohesive energies cited in [28] and our calculated $-E_0$ per pair of atoms for 3C SiC, and Si and C solids in their ground state diamond structures. Both LDA and GGA calculations significantly overestimate the cohesive energy. This DFT overestimation of the cohesive energy becomes significant when the electronic charge distribution in the bonded system (solid

Table 2.2. Experimental and theoretical cohesive energies (eV per pair of atoms)

	EXPT	LDA	GGA
Si	9.28	11.90	10.83
C	14.72	20.32	18.39
SiC	12.58	16.68	15.11

Table 2.3. Heat of formation for 3C-SiC – theory versus experiment

	EXPT	LDA	GGA
ΔH_f (eV/SiC)	0.68	0.57	0.50

in this case) is distinctly different from that in the atoms. The GGA is shown to be better than LDA in this respect. Using the cohesive energy of bulk Si, C, and SiC, we can calculate the heat of formation of SiC defined by: Si(bulk) + C(bulk) \Rightarrow SiC(bulk) + ΔH_f . As shown in Table 2.3, both LDA and GGA yielded the ΔH_f values comparable to the experimental value of 0.68 eV per SiC pair [28].

Although relative large errors are found in the *absolute* energy in LDA and GGA, the calculated *relative* energy between two polytypes ought to have much higher accuracy, since the local charge distributions in the two systems are very close. Based on this assumption, many LDA calculations of cohesive energies in SiC have been performed. A statistical model, with its parameters fitted from the total energy calculations, has also been proposed to predict stability conditions of various SiC polytypes [3, 7, 8]. After the fully structural relaxation, the energy differences are found to be extremely small (less than 10 meV per SiC pair) among the four SiC polytypes studied. Previous studies have shown that different implementation of the calculations, for example, adopting different basis sets, pseudopotentials, or exchange-correlation functionals, might predict slight different energy differences in the SiC-polytypes [3–8]. In Fig. 2.1, the relative energies to the 3C SiC from the present calculation are plotted as function of hexagonality. Whether such small energy differences among different polytypes of SiC are within the error bars of the calculation is still debatable. Nevertheless, the plot in Fig. 2.1 is intended to show the trend and for future reference. Although the energies vary, depending on whether theoretical or experimental lattice constants are used, or whether LDA or GGA approximation is adopted, the 2H SiC is always found to have highest bonding energy. Furthermore, the energy *versus* h curves always concave downward in our calculations. This seems to be consistent with the easiness in growth of 4H and 6H polytypes as compared to the other polytypes.

In addition to static bonding energy, the temperature dependent free energy due to lattice vibration should also be considered in term of thermodynamic stability at finite temperature. However, understanding of phonon free

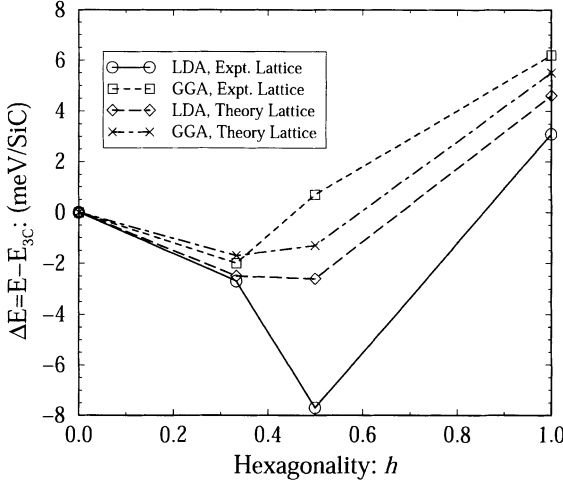


Fig. 2.1. LDA-calculated total energy differences per pair of SiC relative to the 3C polytype, $\Delta E = E_0 - E_0^{3C}$

energy of SiC is very limited. We recently evaluated free energy of four SiC polytypes C based the statistical quasi-harmonic theory:

$$F_{\text{phonon}}(V, T) = k_B T \int_0^\infty \left[\frac{\hbar \omega(V)}{2k_B T} + \ln \left(1 - e^{-\hbar \omega(V)/k_B T} \right) \right] D(\omega) d\omega, \quad (2.1)$$

where F , ω , $D(\omega)$ are Helmholtz free energy of lattice vibration, phonon frequency, and phonon density of states (DOS) respectively. An accurate determination of phonon dispersion of SiC polytypes is the necessary first step in this calculation. Below we will present the results of phonon DOS and free energy, and delay the discussion of phonon calculation to Sect. 2.4.

Figure 2.2 shows our recently calculated phonon DOS of the four SiC polytypes studied. Phonon frequency is plotted here in term of wave-number cm^{-1} . Phonon DOS in these polytypes are almost identical in the low frequency acoustic region (below 250 cm^{-1}), while only minor differences appear at medium frequency regions (between 300 cm^{-1} to 600 cm^{-1}). The most significant differences are in the high frequency LO region, where hexagonal polytypes have much large dispersions than the 3C-SiC. These *ab initio* LDA results are in qualitative agreement with the previous studies of Hofmann et al., who calculated full BZ phonon dispersion of SiC polytypes using an empirical bonded charge model (BCM) [29]. However, small differences in phonon DOS might be important for accurately calculating the differences of Helmholtz free energy of phonons in various SiC polytypes. In Fig. 2.3, we plot the relative Helmholtz free energies of the three hexagonal polytypes relative to 3C SiC. Our results suggest that 6H-SiC becomes more thermodynamically stable at high-temperature, while 4H-SiC becomes less stable at high-temperature. Note that our calculated ordering $F^{6H} < F^{3C} < F^{2H} < F^{4H}$ in the four poly-

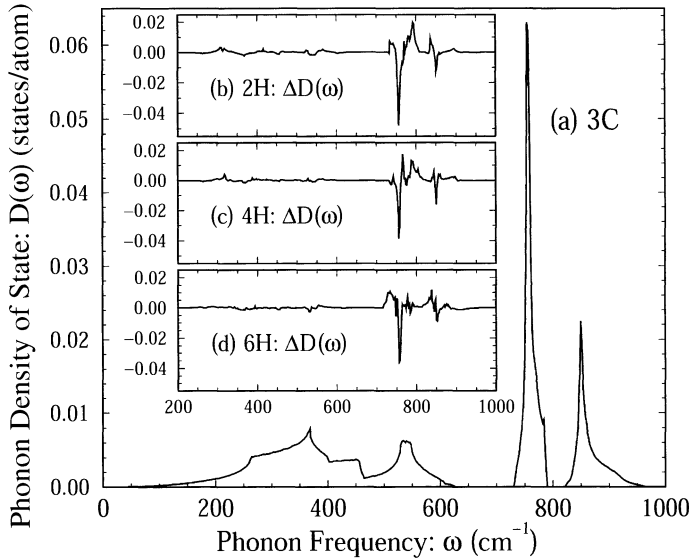


Fig. 2.2. LDA-calculated phonon density of states $D(\omega)$ of 3C-SiC and the difference $\Delta D(\omega)$ relative to 3C for 2H-, 4H-, and 6H-SiC. The frequency is in units of wavenumber (cm^{-1})

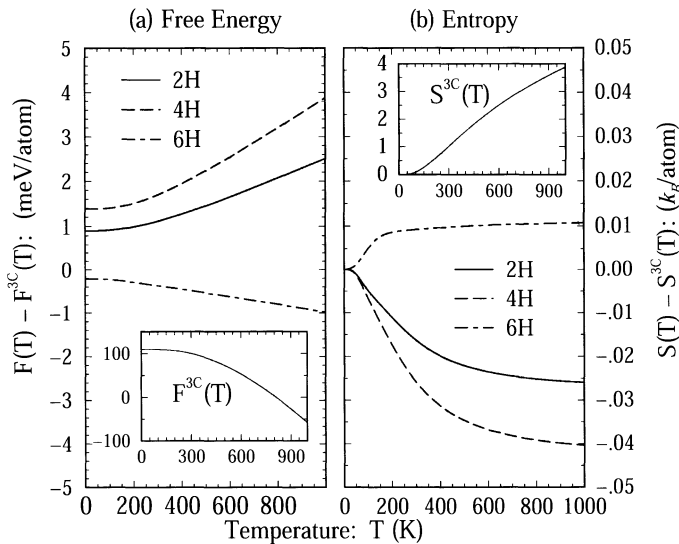


Fig. 2.3. Theoretical Helmholtz free-energy difference between the hexagonal and 3C polytypes, $\Delta F(T) = F(T) - F^{3C}(T)$, at their zero-temperature equilibrium volume

types differs from previous empirical results [7, 29]. However, our results seem to be consistent with the observed 2H-to-3C [30] and 2H-to-6H [31] polytype transition at high-temperatures.

Since the differences in phonon Helmholtz free energies shown in Fig. 2.3 are of the same order of the differences among static bonding energies shown in Fig. 2.1, phonon contribution should be included for modeling the thermodynamic stability of SiC at high temperatures. However, we caution not to take the above results too affirmatively, because these small energy differences (of order of 1–10 meV per SiC pair) are envably prone to both errors in the numerical calculation and in the accuracy of the LDA theory.

2.3 Electronic Band Structure

We will focus on the parts of the band structures that are most relevant to device applications, namely the bands near band gap. As a result of combined experimental and theoretical studies, the current understanding of the band structures for SiC is as good as that for other semiconductors. This is quite remarkable, considering the large variation of the conduction bands among different polytypes. To facilitate the discussion, Fig. 2.4 shows the first Brillouin zones for the cubic and hexagonal structures. Figure 2.5a–d respectively show the band structures of the 2H, 4H, 6H, and 3C SiC resulted from our LDA calculation described in Sect. 2.1.

Let us start with the band gaps. All available calculations show that the tops of the valence bands for all the four polytypes of SiC considered here are at the center of the Brillouin zone (the Γ -point), while the minima of the conduction bands are located off center. In other words, these semiconductors have *indirect* band gaps. The values for the band gaps: 3.33 eV for 2H, 3.25 eV for 4H, 3.023 eV for 6H, and 2.416 eV for 3C SiC, were experimentally

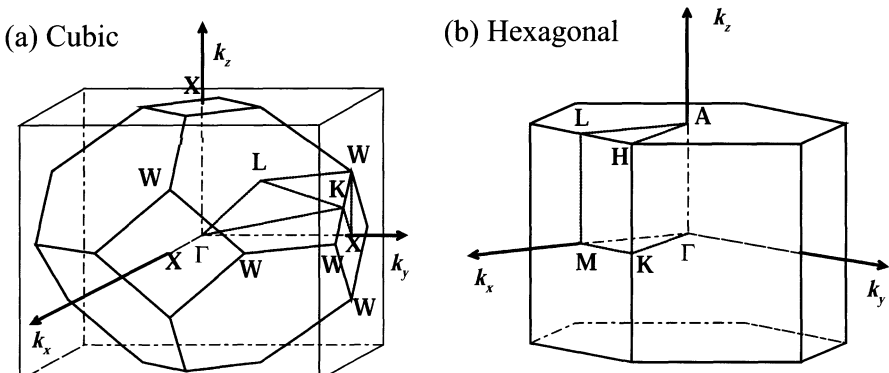


Fig. 2.4. First Brillouin zone of (a) cubic and (b) hexagonal lattice

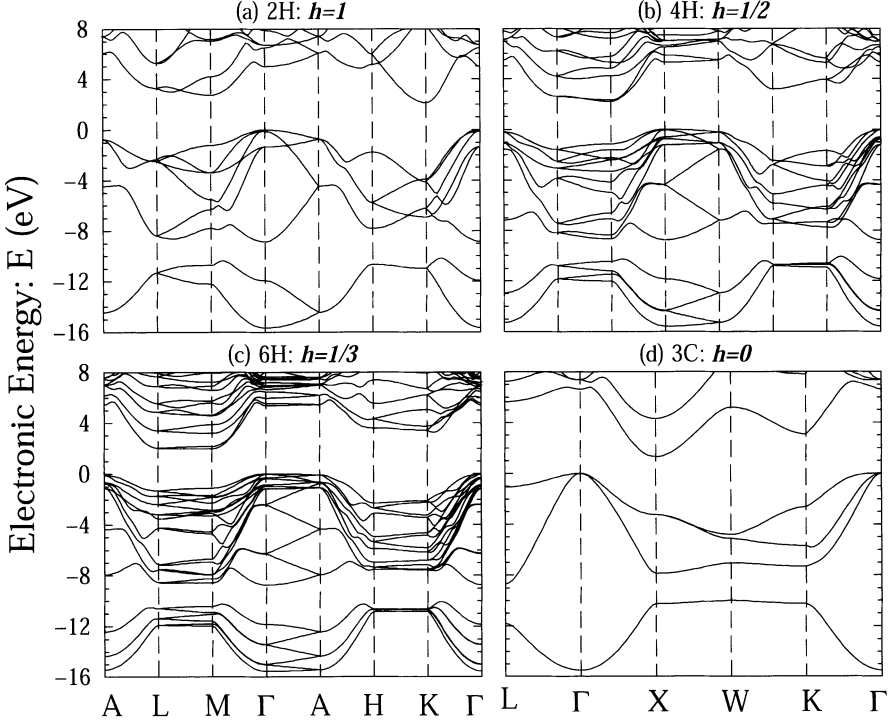


Fig. 2.5. Band structures of (a) 2H-, (b) 4H-, (c) 6H-, and (d) 3C-SiC

determined long time ago [32–34], but still remain the best-accepted values to date. A recent soft X-ray spectroscopy experiment has confirmed these values to within its energy resolution (0.1 eV) [35]. The currently accepted locations of the conduction band minima are 3C at X -point, 2H at K -point, 4H at M -point, and between M - and L -point for 6H SiC. Although it is difficult to measure these minima directly, these assignments are consistent with the band models used to interpret relevant experimental results.

It is well known that LDA calculations [4–7, 36, 37] consistently underestimate the band gaps in semiconductors and insulators. For SiC, our LDA calculated band gaps are 2.13 eV, 2.19 eV, 1.98 eV, and 1.30 eV for 2H, 4H, 6H, and 3C respectively. Despite approximately 1 eV underestimation, these calculations have yielded approximately the correct ordering of the band gaps among different polytypes and the locations of the conduction band minima. To illustrate this point, Fig. 2.6 shows an enlarged plot of our LDA band for the 6H SiC near the conduction band minimum along the ML line. The band is very flat and the minimum is between M and L and is about 40% from M -point along the ML line. Note that the energy barrier (located at M -point) separating the mania is only 3–4 meV. Our calculated energy barrier height is comparable to the results of 10 meV and 5 meV from previous

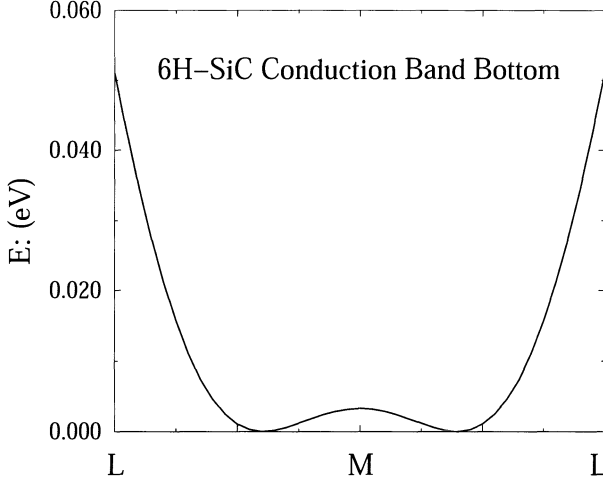


Fig. 2.6. Conduction bands near the minimum along $L\text{--}M$ direction in 6H-SiC

LDA calculations [6, 36]. Inclusion of the quasi-particle self energy in LDA band structures [38] have improved the band gaps, but has not helped pin down the location of the conduction band minimum for 6H SiC. For example, a quasi-particle study showed that the self-energy correction tends to push the minimum toward the M -point [38]. It is useful to pin down the actual location of this minimum and the value of the barrier height, because this band structure governs the donor energy levels and the electrical and transport properties of 6H SiC.

Another interesting point to note is the existence of a second conduction band minimum at M in 4H SiC. As shown in Fig. 2.7 from our LDA calculation, the second band is only 130 meV higher than the lowest band. This value is close to the 110 and 130 meV found from other calculations [6, 37]. A ballistic electron emission microscopy (BEEM) experiment [39] has resolved this energy separation to be (140 ± 15) meV. However, a recent BEEM experiment [40] failed to resolve this second minimum. If these two bands are indeed so close as those shown in Fig. 2.7, both bands have to be included in the shallow donor energy calculations [41]. They also are important in the high field transport.

The conduction band structures as a function of the wave vector \vec{k}_i along a specified direction i near a minimum \vec{k}_{\min} can be approximated by a quadratic form

$$E(\vec{k}_i) = E_0 + \frac{\hbar^2}{2m_e} \frac{(\vec{k}_i - \vec{k}_{\min})^2}{m_i}, \quad (2.2)$$

where E_0 is the band energy at the minimum \vec{k}_{\min} , m_e is the free-electron mass, and m_i is the effective mass ratio along that direction. The effective

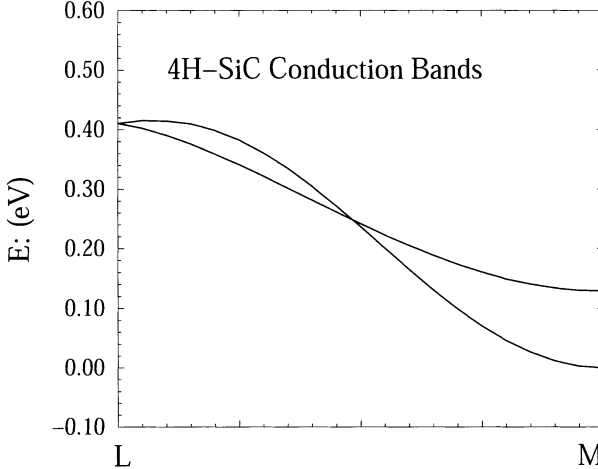


Fig. 2.7. Conduction bands near the minimum at M -point in 4H-SiC

masses at the conduction band minima have also been well studied. Experimentally, the cyclotron resonance (CR) and particularly the optically detected CR (ODCR) measurements [42–44] have pinned down the values and the anisotropy of the conduction masses for 3C and 4H SiC. The ODCR experiment [45, 46] has also been performed for the 6H SiC to deduce an average effective mass in the plane perpendicular to the c -axis. The LDA band structures have shown to be able to predict the conduction-band masses not only in SiC [6, 36, 37, 47] but also in other semiconductor [48]. Table 2.4 summarizes the most updated experimental and theoretical values for the conduction-band masses in SiC masses. To compare with experiment, the effective masses based on the band structures have to be corrected to include polaron mass enhancement and the effect of doping [49]. In view of the results in Table 2.4, the only relatively large uncertainty is the heavy mass along ML and the mass

Table 2.4. Important conduction band edge structures for SiC. The band gaps are the experimental values. The values inside the parentheses for the electron effective masses are the experimental data, and the other values are our LDA results. The superscripts a , b , c , d , e , and f refer to [32], [33], [34], [42], [44], and [46], respectively. For 3C, m_1 , m_2 , and m_3 are the electron masses along the XU , XW , and $X\Gamma$ directions, respectively. For 2H, the three masses are along the $K\Gamma$, KM , and KH directions. For 4H and 6H, the three masses are along directions parallel to $M\Gamma$, MK , and ML , respectively

Polytype	E_g (eV)	Location	m_1	m_2	m_3
3C	1.302(2.417 ^a)	X	0.22(0.25 ^d)	0.22(0.25 ^d)	0.64(0.67 ^d)
2H	2.129(3.30 ^b)	K	0.42	0.42	0.25
4H	2.194(3.25 ^c)	M	0.53(0.58 ^e)	0.27(0.31 ^e)	0.30(0.33 ^e)
6H	1.980(3.023 ^c)	$U(M \rightarrow L)$	0.71	0.24	1.95(2.0 ^f)

anisotropy along $\mathbf{M}\mathbf{K}$ and $\Gamma\mathbf{M}$ for 6H-SiC. Good experimental measurement for the 2H polytype is also needed to make the electron effective-mass results complete for the four simple polytypes of SiC considered.

Finally we examine the band structure near the top of the valence bands. Figure 2.8 shows the enlarged top valence bands from our LDA calculations. The top is at Γ -point. The spin-orbit coupling introduces a small splitting Δ_{so} between top two bands. The lowest band is separated from the top by a crystal-field splitting Δ_{cf} . Each of the three energies at Γ is doubly degenerate for the hexagonal 2H, 4H and 6H SiC. For 3C SiC, Δ_{cf} is zero, so the top of the valence band is four-fold degenerate. Several LDA calculations have been used to study the detailed valence band structures near the top [6,36,37]. These band structures can also be reasonably described using the $\vec{k} \cdot \vec{p}$ Hamiltonians. The parameters for the $\vec{k} \cdot \vec{p}$ Hamiltonians for the four polytypes of SiC have been derived [6,47] based on the calculated LDA bands. Our calculated values of Δ_{so} for the three hexagonal polytypes (listed in Table 2.5) are very close to 8.5 meV, similar to those obtained in [37] and the 7.7 meV for 6H-SiC derived from experiment [50]. However, the corresponding Δ_{so} for 3C SiC should be about 1.5 times larger as confirmed from our calculated value of 14.5 meV. This value is very close to the 14.4 meV calculated in [51], yet it is considerably larger than the 8 meV used in [6] and [47] and the 10 meV experimental value [32]. The crystal field splitting Δ_{cf} is found to be a very good linear function of the hexagonality h , starting from $\Delta_{cf} = 0$ at $h = 0$ (3C) to a value of $\Delta_{cf} = 132$ meV at $h = 1$ (2H) [6]. This result was based on LDA calculations performed at the theoretical lattice constants. These values are similar to our calculated results shown in Table 2.5. It would be interesting to confirm this result experimentally. A recent study [37] shows that while

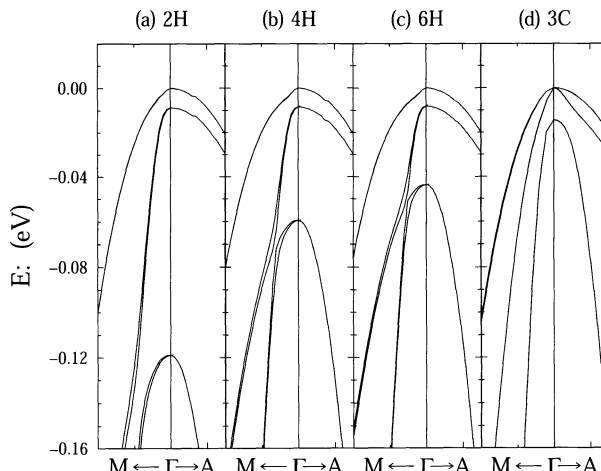


Fig. 2.8. Enlarged plots of the valence band tops to show the spin-orbit and crystal-field splitting

Table 2.5. Important valence band edge structures based on our LDA calculations. Hole masses along the $\Gamma\mathbf{A}$, $\Gamma\mathbf{M}$, and $\Gamma\mathbf{K}$ directions in the hexagonal BZ are listed here. The subscripts 1, 2, and 3 describe the ordering of the bands shown in Fig. 2.8; the subscript 1 stands for the state at the top of the valence band for all the SiC polytypes, while the subscripts 2 and 3 stand for different bands in cubic 3C-SiC and hexagonal 2H-, 4H-, and 6H-SiC. For 3C, bands 2 and 3 are the light-hole band and the spin-orbit band, respectively. For the hexagonal polytypes, bands 2 and 3 are the spin-orbit split band and the crystal-field split band, respectively

	Δ_{so}	Δ_{cf}	$\Gamma\mathbf{A}$			$\Gamma\mathbf{M}$			$\Gamma\mathbf{K}$		
	(meV)	(meV)	m_1	m_2	m_3	m_1	m_2	m_3	m_1	m_2	m_3
3C	14.5	0	1.62	0.29	0.47	1.35	0.28	0.54	2.54	0.26	0.44
2H	8.7	119	1.64	1.58	0.20	0.64	0.52	1.47	0.62	0.51	1.37
4H	8.5	59.5	1.58	1.32	0.21	0.86	0.55	1.13	0.95	0.52	1.30
6H	8.2	43.6	1.77	1.35	0.20	1.07	0.39	1.71	1.24	0.34	2.76

Δ_{so} is relatively insensitive to slightly different lattice parameters used in the LDA calculations, the crystal-field splitting can vary substantially.

With a sign change in (2.2), the curvatures of the bands at the Γ -point are the hole effective masses. The LDA calculations for the hole effective masses for SiC have converged. Table 2.5 show a set of the effective masses for \vec{k} along $\Gamma\mathbf{A}$, $\Gamma\mathbf{M}$, and $\Gamma\mathbf{K}$ direction based on our LDA calculation, which are similar the previous calculations [6, 37]. Persson and Lindefelt [37] also showed that these masses were not sensitive to the slightly different lattice parameters used in their LDA calculations. Unfortunately, while LDA bands have generated *electron* effective masses in good agreement with experiment, no good agreements have yet been established for the *hole* masses. This is true not only for SiC but also for other semiconductors [48]. More accurate determination of the hole masses is needed before good progress can be made for calculating acceptor energy levels and hole transport properties in SiC.

2.4 Lattice Vibration

It is comforting to note that the status is good for the phonon spectra of the four polytypes of SiC to be discussed in this section. On one hand, currently we have a theoretical tool that can calculate the phonon frequencies and eigen modes accurately. On the other hand, there are experimental tools, such as Raman spectroscopy, infrared absorption, low temperature photo luminescent experiment, and inelastic X-ray and neutron scattering experiments. These experimental techniques not only can probe the modes at high symmetry points in the Brillouin zone, but also have recently probed the whole dispersion. Below we will first briefly review the theoretical methods for calculating phonon frequencies. We will then summarize both the experimental and theoretical results and comment on special features.

Lattice vibration calculation requires the knowledge of the dynamic matrix \mathbf{D} , whose matrix elements are the second order energy derivatives with respect to the atomic positions. In principle, LDA is a reliable *ab initio* theory for studying lattice dynamics of a crystal, because it can accurately treat the energy variation due to small atomic displacements. The major stumbling block in such approach is the computational load, which increases very rapidly with of the size of systems. The load is far surpassing that required in the structural and band structure calculation. For phonon modes with their wave vector at a high symmetry point in the Brillouin zone, density functional perturbation theory (DFPT) with in the framework of linear response theory [52] or real-space frozen phonon methods [53] using small supercells can be used to construct dynamic matrix \mathbf{D} for that particular \mathbf{k} -point. For either theoretical approaches, the computational loads increase very rapidly for the low symmetry \mathbf{k} -points. Despite this difficulty, LDA calculations of phonon dispersions of simple 3C and 2H polytypes have been reported for nearly a decade [18]. Phonon modes at certain high-symmetry \mathbf{k} -points for 4H and 6H SiC were also calculated in recent years [16, 17, 19]. However, *ab initio* calculations of *full* phonon dispersion of 4H, 6H, and other more complex polytypes are still limited.

Empirical approaches have been adopted to predict phonon dispersion of 4H and 6H SiC [29]. The parameters of these empirical models were obtained by fitting experimental data of Γ -point and/or first-principles phonon results of smaller 3C and 2H polytypes. Recently, a fitting approach referred as the local-coupling transfer procedure is proposed to construct force constants of 4H SiC polytypes [17] based on the force constants of 2H and 3C polytype directly calculated with LDA method [18]. The reported results were in good agreement with experimental data of 4H SiC, as well as previous empirical calculations. It is not yet clear whether these semi-empirical models are capable of capturing all the important polytype-dependent differences. In this sense, it is necessary to adopt *ab initio* methods to accurately describe lattice dynamics in various SiC polytypes.

We recently carried a detailed study of phonon band-structures of 3C, 2H, 4H, and 6H SiC using an *ab initio* real-space super-cell force-constant (SC-FC) method. This approach is efficient and accurate to directly predict *full phonon dispersion*. In this method, the most important source of numerical errors is related to the truncation of real space force constant matrices, and such errors can be in principle reduced by calculating force-constant matrix for a larger super-cell model to increase the real space range before it is truncated. Usually, the TA-branches are most sensitive to truncation errors, and results of TA branches have to be carefully checked to ensure reasonable convergence. For ionic solids, such as SiC, Born effective charges (BEC) Z^* are induced due to lattice vibration, and the macroscopic electrostatic interaction of Z^* in turn alter the frequencies of certain longitude phonon modes and causes the LO-TO splitting. Although periodic super-cell calculation is incapable to directly calculate Z^* and dielectric constants, an algorithm proposed by Kunc

and Martin is used to correct the LO-TO splitting based on inter-planar force constants [54]. We find this correction is able to predict the LO-TO splitting in various ionic-crystals. Using this method, we have calculated the detailed phonon band-structures of the four SiC polytypes considered here. The full dispersions of the four studied polytypes are shown in Fig. 2.9. These phonon dispersions were used to calculate the phonon densities of states shown in Fig. 2.2 for the discussion of phonon contribution to the free energy (Fig. 2.3). As will be shown in the following more detailed analysis, our results are in excellent agreement with available experimental [15–17] and theoretical DFPT results [18, 19].

Tables 2.6, 2.7, 2.8, and 2.9 list the phonon modes at the Γ -point (BZ center) from our calculations for the four polytypes studied. For comparison, we also list the experimental results from Raman [55–59] and infrared [60, 61]

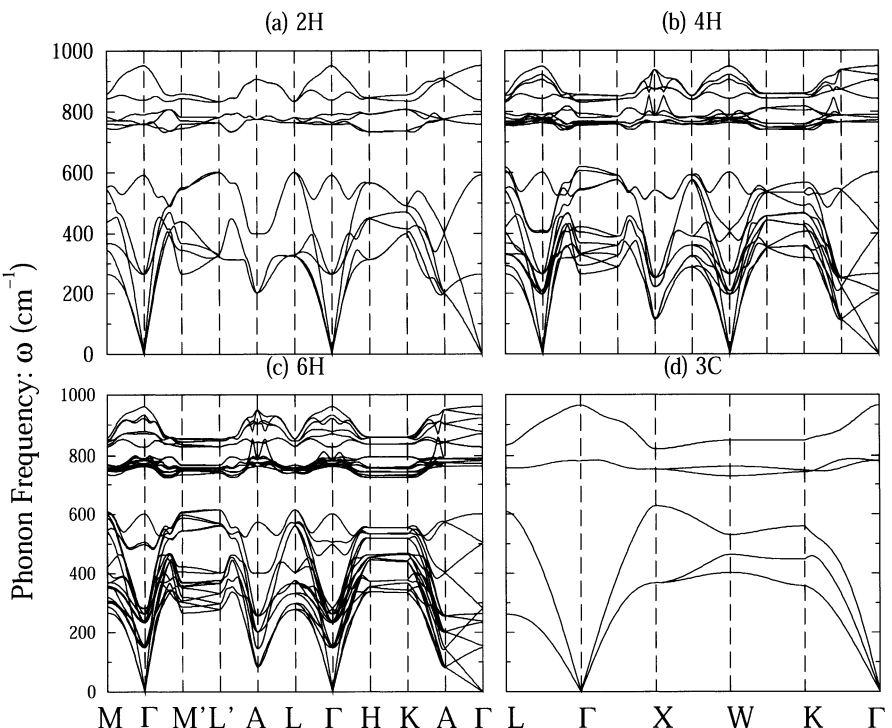


Fig. 2.9. Full phonon dispersion of (a) 2H-, (b) 4H-, (c) 6H-, and (d) 3C-SiC

Table 2.6. Γ -point phonon modes of 3C-SiC. The irreducible representation of the 3C optic phonons at the Γ -point is $2T_2$, where the T_2 modes are both Raman and infrared active. Experimental data are taken from [58]

Mode	LDA (cm^{-1})	Expt. (cm^{-1})	Mode	LDA (cm^{-1})	Expt. (cm^{-1})
$T_2(\text{TO})$	783	796	$T_2(\text{LO})$	964	972

Table 2.7. Γ -point phonon modes of 2H-SiC. The irreducible representation of the 2H optic phonons at the Γ -point is $A_1+2B_1+E_1+2E_2$, where the A_1 , E_1 , and E_2 modes are Raman active and the A_1 and E_1 modes are infrared active. The A_1 -LO frequency is due to the LO-TO splitting for ordinary rays and the E_1 -LO frequency is due to LO-TO splitting for extraordinary rays. Experimental data are taken from [58]

Mode	LDA (cm^{-1})	Expt. (cm^{-1})	Mode	LDA (cm^{-1})	Expt. (cm^{-1})
E_2	263	264	$E_1(\text{TO})$	789	799
B_1	592	—	B_1	838	—
E_2	757	764	$E_1(\text{LO})$	951	—
$A_1(\text{TO})$	759	—	$A_1(\text{LO})$	950	968

Table 2.8. Γ -point phonon modes of 4H-SiC. The irreducible representation of the 4H optic phonons at the Γ -point is $3A_1+4B_1+3E_1+2E_2$. Experimental data are taken from [58]

Mode	LDA (cm^{-1})	Expt. (cm^{-1})	Mode	LDA (cm^{-1})	Expt. (cm^{-1})
E_2	197	196	$A_1(\text{TO})$	772	—
E_2	205	204	E_2	779	—
E_1	264	266	E_1	788	796
B_1	399	—	A_1	836	838
B_1	407	—	B_1	905	—
A_1	600	610	B_1	913	—
$E_1(\text{TO})$	763	—	$E_1(\text{LO})$	948	—
E_2	771	776	$A_1(\text{LO})$	948	964

Table 2.9. Γ -point phonon modes of 6H-SiC. The irreducible representation of the 6H optic phonons at the Γ -point is $5A_1+6B_1+5E_1+6E_2$. Experimental data are taken from [58]

Mode	LDA (cm^{-1})	Expt. (cm^{-1})	Mode	LDA (cm^{-1})	Expt. (cm^{-1})
E_2	149	145	E_1	772	—
E_2	153	150	$A_1(\text{TO})$	776	—
E_1	234	236	E_2	781	789
E_1	240	241	E_2	782	—
E_2	264	266	$E_1(\text{TO})$	787	797
B_1	282	—	B_1	836	—
B_1	284	—	A_1	878	—
A_1	500	504	A_1	883	889
A_1	507	514	B_1	930	—
B_1	603	—	B_1	938	—
E_2	762	767	$E_1(\text{LO})$	960	—
E_1	765	—	$A_1(\text{LO})$	960	965

studies. Note the excellent theory-experiment agreement, i.e. with percentage errors of less than 3%, is typical for *ab initio* LDA calculations [18, 19].

In contrast to the rich experimental data of phonons at the zone center, very limited experimental data are known for phonons at other \mathbf{k} -points within the BZ. However, the non-zone-center phonons are needed to interpret the low temperature photo luminescent (LTPL) data [62, 63]. This technique involves electron excitation from the valence top (the Γ -point) to the conduction minimal (e.g. M -point in 4H) with assist from phonons. In 4H SiC, only phonons from M -points involved in this process due to conservation of total momentum. Based on this theory, Choyke et al. further proposed [62] to probe the location of conduction minimal in 6H-SiC (also see discussion in Sect. 2.3) by the measured LTPL data in 6H-SiC and the LDA calculated phonon frequencies. We plot the theoretical phonon dispersion along L-M direction in 4H and 6H in Fig. 2.10, along with the LTPL frequencies (indicated with the horizontal dash lines). Only the acoustic branches are shown for simplicity. It is clear that in either polytypes, the LTPL data are much better fitted with M -point phonons than the L -point phonons. These results are consistent with the LDA band-structure calculations. However, it is obvious that the small intrinsic uncertainty of LDA phonon calculation makes it difficult to “pin down” the exact location of the conduction band minimal in 6H SiC.

Due to technical limitation, the general phonon dispersion was not well determined in experiment until very recent years. The exception is the dispersion along the stacking direction, which is the ΓL direction in the cubic crystal or the ΓA direction in the hexagonal crystals. Because structures of SiC polytypes only differ in their axial stacking order, it has been postulated

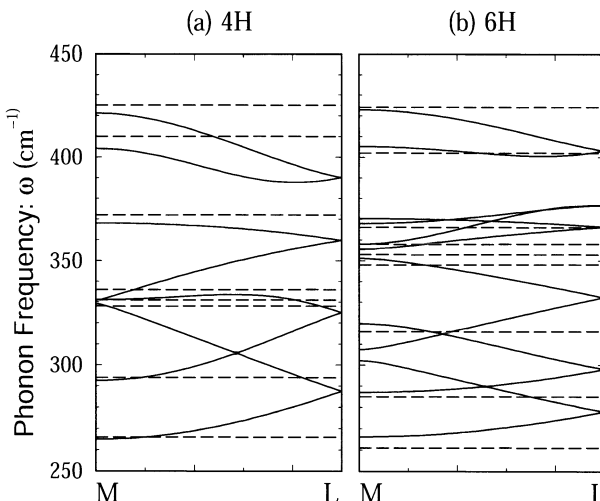


Fig. 2.10. LTPL data compared with our calculated phonon energies along the $L\text{-}M$

that all the SiC polytypes have very close dispersion relation along the stacking direction [64]. If this is true, one can folding the phonon dispersion of 3C-SiC along ΓL to predict the Γ -point phonon frequencies of 3C, 2H, 4H, 6H, and 15R observed in optical spectroscopy experiments [56]. To verify this point, plotted in Fig. 2.11 are our theoretical phonon axial dispersions of 3C, 2H, 4H, and 6H SiC. All the dispersion is plotted within the 1st-BZ of 3C. Two straight dash lines in the figure indicate the elastic limits at the long wavelength. Consistent with the previous postulation, our LDA calculation shows that the four polytypes have a nearly identical dispersion along the axial direction, except some very minor splitting (usually less than 1%) at the k -points corresponding to the zone boundaries of larger hexagonal crystals. The results are also in close agreement with experimental data, which are illustrated with discrete symbols in Fig. 2.11.

Experimental detecting phonon dispersion other than the axial stacking direction is a very challenging task, and the breakthroughs were made only in recent years [15–17]. 3C-SiC is currently most well characterized polytype. Serrano et al have successfully measured the phonon dispersion in 3C-SiC along three important high-symmetry directions using the inelastic X-ray scattering (IXS) technique [16]. As shown in Fig. 2.12 the experimental data (circle symbols) are in excellent agreement with our theoretical dispersion (solid lines).

Using the similar IXS technique, Serrano et al. recently reported the phonon dispersion in 4H SiC, along the axial [0001] direction (also referred as ΓA direction, and this direction is comparable to the ΓL [111] direction in the cubic 3C-SiC) and basal ΓM and $\Gamma-K-M'$ directions [17]. In Fig. 2.13, the experimental results are shown along with our calculated full dispersion curves. Except for the highest frequency data, all the other data points seem

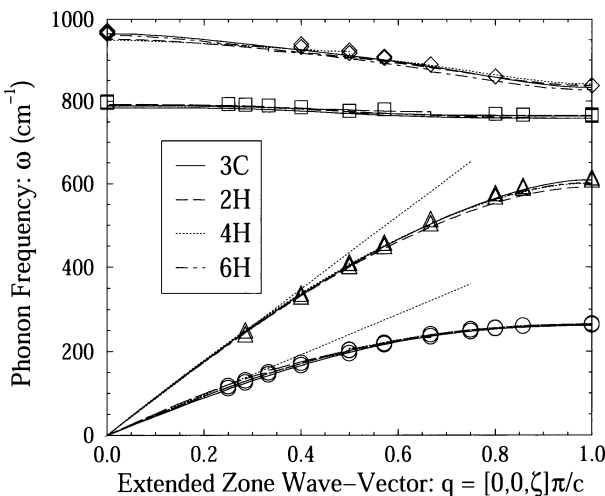


Fig. 2.11. Back-folded phonon dispersions along the axial direction

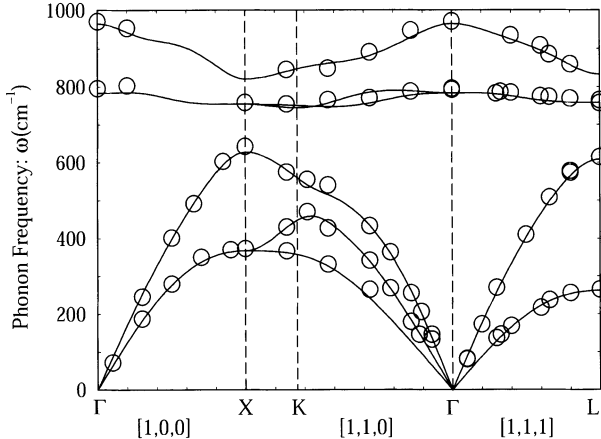


Fig. 2.12. Calculated phonon dispersion in 3C-SiC (*solid lines*) and the experimental measurements (*circles*)

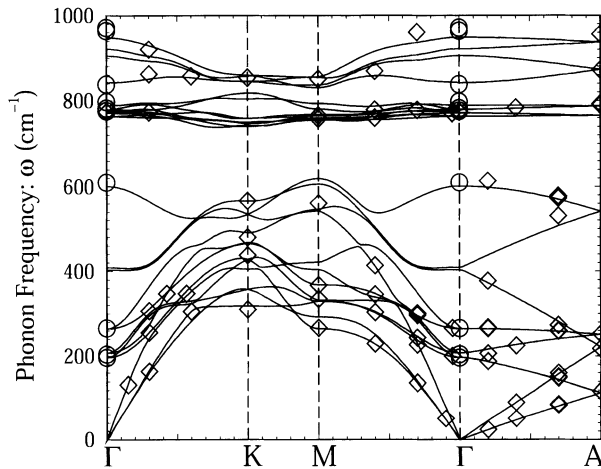


Fig. 2.13. Calculated phonon dispersion in 4H-SiC (*solid lines*) and the experimental measurements (*symbols*)

to coincide with the calculated curve. Due to technical difficulty, only a portion of phonon branches along the two basal directions have been successfully determined. More experimental data are needed to have a more detailed comparison between theory and experiment.

Phonon dispersion of 6H-SiC was recently studied by Dorner et al. using inelastic neutron scattering [15]. As shown in Fig. 2.14, most phonon branches along $\Gamma\mathbf{L}$ direction and 14 out of 36 branches basal along $\Gamma\mathbf{M}$ direction were successfully measured. The measured $\Gamma\mathbf{A}$ dispersion is consistent with previous Raman and infrared experiments based on the zone-folding approximation. With no *ab initio* phonon dispersion of 6H to compare, Dorner et al. com-

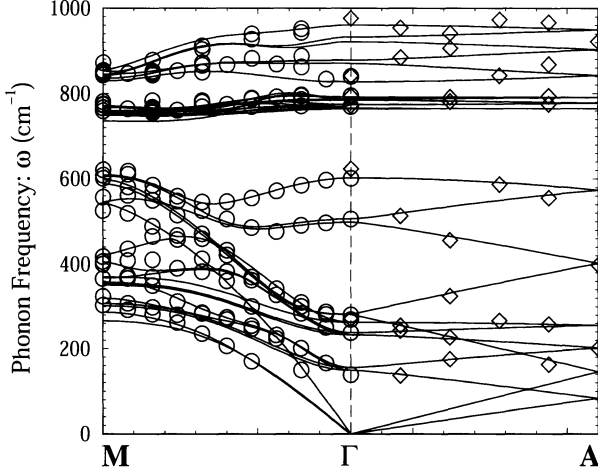


Fig. 2.14. Calculated phonon dispersion in 6H-SiC (*solid lines*) and the experimental measurements (*symbols*)

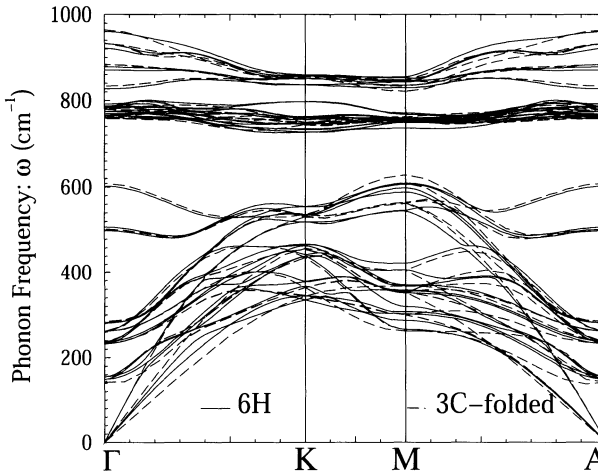


Fig. 2.15. Comparison of the dispersion of 6H (*solid lines*) and the back-folded dispersion of 3C (*dashed lines*)

pared their experimental data by back-folding 3C-SiC dispersion [15]. They found good agreement for k -points close to the zone-center (Γ -point). However, the discrepancy becomes much larger when the k -points approaching the zone boundary (M -point). Apparently, the structure differences in stacking sequences have larger effects on the part of the Brillouin zone. The experimental observation is now confirmed by our calculation. As shown in Fig. 2.14, both the optic and acoustic branches detected in experiment match well with theoretical dispersion. We further directly compare the 6H-dispersion and back-folded 3C dispersion with the in BZ of 6H, and the results are plotted

in Fig. 2.15 with solid and dash lines respectively. As observed in experiment, most differences are found around the zone boundaries of 6H BZ, which can be simply related to the symmetry based “flattening” effect at BZ boundary. However, for certain branches, such at the lowest LA braches along Γ -K direction, relative large difference between two dispersions are found even near zone center.

2.5 Conclusion

In this chapter, we have summarized our current understanding of the crystal structure and bonding energy, the electron band structures near the band gaps, and the phonon spectra for the four simplest types of SiC. While the overall understanding of these properties is as good as that for other semiconductors, there remain several uncertain issues, for example, the bonding energies governing the stability of different polytypes, the detailed conduction band structures around the conduction band minima of 4H- and 6H-SiC, and the hole masses in general. These quantities may be difficult to pin down directly using the available theoretical or experimental tools. However, as more studies and applications using these properties become available, particularly studies of the growth, transport, and electrical properties, links may be found to improve our understanding. We have also shown that the complete phonon spectra can be calculated accurately using the state-of-the-art *ab initio* theory. Good experimental phonon data are available for the whole dispersions for the simple 3C polytype, and parts of the spectra for the more complicated 4H and 6H polytypes. More complete experimental dispersions for the 4H and 6H polytypes are still desired.

Acknowledgments

J.D. would like to acknowledge useful discussions with J.R. Williams, C.C. Tin, and M. Bozack and the financial support from the Alabama Space Grant Consortium and NASA (Contract number UAHSUB 2001-172E). A.B.C. would like to acknowledge the support of J T Walter Professorship.

References

1. *Fundamental Questions and Applications of SiC (Part I)*, ed. W.J. Choyke, H. Matsunami, and G. Pensl, Phys. Stat. Sol. (b) **202**, 1–642 (1997).
2. *Fundamental Questions and Applications of SiC (Part II)*, ed. W.J. Choyke, H. Matsunami, and G. Pensl, Phys. Stat. Sol. (a) **162**, 1–512 (1997).
3. C. Cheng, V. Heine, and I.L. Jones, “Silicon carbide polytypes as equilibrium structures”, J. Phys.: Condens. Matt. **2**, 5097–5113 (1990).

4. C.H. Park, B.-H. Cheong, K.-H. Lee, and K.J. Chang, “Structural and electronic properties of cubic, 2H, 4H, and 6H SiC”, Phys. Rev. **B 49**, 4485–4493 (1994).
5. P. Kackel, B. Wenzien, and F. Bechstedt, “Influence of atomic relaxations on the structural properties of SiC polytypes from *ab initio* calculations”, Phys. Rev. **B 50**, 17037–17046 (1994).
6. S. Limpijumnong, W.R.L. Lambrecht, S.N. Rashkeev, and B. Segall, “Electronic band structure of SiC polytypes. A discussion of theory and experiment”, Phys. Stat. Sol. (b) **202**, 5–33 (1997).
7. F. Bechstedt, P. Kackell, A. Zywietsz, K. Karch, B. Adolph, K. Tenelsen, and J. Furthmuller, “Polytypism and Properties of Silicon Carbide”, Phys. Stat. Sol. (b) **202**, 35–62 (1997).
8. S. Limpijumnong and W.R.L. Lambrecht, “Total energy differences between SiC polytypes revisited”, Phys. Rev. **B 57**, 12017–12022 (1998).
9. G. Kresse and J. Hafner, “*Ab initio* molecular dynamics for liquid metals”, Phys. Rev. **B 47**, 558–561 (1993).
10. G. Kresse, J. Furthmuller, “Efficiency of *ab-initio* total energy calculations for metals and semiconductors using a plane-wave basis set”, Comput. Mater. Science **6**, 15–50 (1996).
11. D. Vanderbilt, “Soft self-consistent pseudopotentials in a generalized eigenvalue formalism”, Phys. Rev. **B 41**, 7892–7895 (1990).
12. K. Laasonen, R. Car, C. Lee, and D. Vanderbilt, “Implementation of ultrasoft pseudopotentials in *ab initio* molecular dynamics”, Phys. Rev. **B 43**, 6796–6799 (1991).
13. G. Kresse and J. Hafner, “Norm-conserving and ultrasoft pseudopotentials for first-row and transition elements”, J. Phys.: Condensed Matter **6**, 8245–8257 (1994).
14. J. Dong, O.F. Sankey, and G. Kern, “Theoretical study of the vibrational modes and their pressure dependence in the pure clathrate-II silicon framework”, Phys. Rev. **B 60**, 950–958 (1999); J. Dong, J.K. Tomfohr, and O.F. Sankey, “Rigid intertetrahedron angular interaction of nonmolecular carbon dioxide solids”, Phys. Rev. **B 61**, 5967–5971 (2000); J. Dong, O.F. Sankey, S.K. Deb, G. Wolf, and P.F. McMillan, “Theoretical study of β -Ge₃N₄ and its high-pressure spinel γ -phase”, Phys. Rev. **B 61**, 11979–11992 (2000).
15. B. Dorner, H. Schober, A. Wonhas, M. Schmitt, and D. Strauch, “The phonon dispersion in 6H-SiC investigated by inelastic neutron scattering”, Eur. Phys. J. **B 5**, 839–846 (1998).
16. J. Serrano, J. Strempfer, M. Cardona, M. Schwoerer-Bohning, H. Requardt, M. Lorenzen, B. Stojetz, P. Pavone, and W.J. Choyke, “Determination of the phonon dispersion of zinc blende (3C) silicon carbide by inelastic X-ray scattering”, Appl. Phys. Lett. **80**, 4360–4362 (2002).
17. J. Serrano, J. Strempfer, M. Cardona, M. Schwoerer-Bohning, H. Requardt, M. Lorenzen, B. Stojetz, P. Pavone, and W.J. Choyke, “Lattice dynamics of 4H-SiC by inelastic X-ray scattering”, Mater. Sci. Forum **433-436**, 257–260 (2003).
18. K. Karch, P. Pavone, W. Windl, O. Schutt, and D. Strauch, “*Ab initio* calculation of structural and lattice-dynamical properties of silicon carbide”, Phys. Rev. **B 50**, 17054–17063 (1994).

19. G. Wellenhofer, K. Karch, P. Pavone, U. Rossler, and D. Strauch, "Ionicity of SiC polytypes", in *Proc. Silicon Carbide and Related Materials 1995 Conf.*, Inst. Phys. Conf. Ser. **142**, Chap. 2, 301 (1996).
20. K. Karch and F. Bechstedt, Phys. Rev. Lett. **77**, 1660 (1996).
21. N.W. Jepps and T.F. Page, "Polytypic transformations in silicon carbide", in *Progress in Crystal Growth and Characterization (Cryst. Growth Charact. Polytype Struct.)* **7**, 259–307, 1983).
22. A.R. Verma and P. Krishna, *Polymorphism and Polytypism in Crystals*, Wiley, New York (1966).
23. C. Kittel, *Introduction to Solid State Physics*, 7th Edition, John Wiley & Sons, New York (1996), P18, Fig. 21.
24. O. Madelung (ed.), *Semiconductors – basic data*, Springer, Berlin (1996).
25. A.H. Gomes de Mesquita, "Refinement of the crystal structure of SiC type 6H", Acta. Cryst. **23**, 610–617 (1967).
26. N.W. Thibault, "Morphological and strucrural crystallography and optical properties of Silicon Carbide", Z. fuer Krist. **63**, 1–18 (1926).
27. R.F. Adamsky and K.M. Merz, "Synthesis and crystallography of the wurtzite form of silicon carbide", Z. fuer Krist. **111**, 350–361 (1959).
28. See Table 7–3 and footnotes by W.A. Harrison in *Electronic Structure and Properties of Solids*, Dover Pub., Inc, New York (1989), p. 176.
29. M. Hofmann, A. Zywicki, K. Karch, and F. Bechstedt, "Lattice dynamics of SiC polytypes within the bond-charge model", Phys. Rev. B **50**, 13401–13411 (1994).
30. P. Krishna, R.C. Marshall, and C.E. Ryan, "Discovery of a 2H-3C solid state transformation in silicon carbide single crystals", J. Cryst. Growth **8**, 129–131 (1971)
31. P. Krishna and R.C. Marshall, "Direct transformation from the 2H to the 6H structure in single-crystal silicon carbide", J. Cryst. Growth **11**, 147–150 (1971).
32. R.G. Humphreys, D. Bimberg, and W.J. Choyke, "Wavelength modulated absorption in silicon carbide", Solid State Commun. **39**, 163–167 (1981).
33. L. Patrick, D.R. Hamilton, and W.J. Choyke, "Growth, luminescence, selection rules, and lattice sums of SiC with wurtzite structure", Phys. Rev. **143**, 526–536 (1966).
34. W.J. Choyke, D.R. Hamilton, and L. Patrick, "Optical properties of cubic SiC: luminescence of nitrogen-exciton complexes, and interband absorption", Phys. Rev. **133**, A1163–A1166 (1964).
35. J. Lüning, S. Eisbitt, J.-E. Rubensson, C. Allmers, and W. Eberhardt, "Electronic structure of silicon carbide polytypes studied by soft X-ray spectroscopy", Phys. Rev. B **59**, 10573–10582 (1999).
36. C. Persson and U. Lindefelt, "Detailed band structure for 3C-, 2H-, 4H-, 6H-SiC, and Si around the fundamental band gap", Phys. Rev. B **54**, 10257–10260 (1996).
37. C. Persson and U. Lindefelt, "Dependence of energy gaps and effective masses on atomic positions in hexagonal SiC", J. Appl. Phys. **86**, 5036 (1999).
38. B. Wenzien, P. Käckell, and F. Bescstedt, "Quasiparticle band structure of silicon carbide polytypes", Phys. Rev. B **52**, 10897–10905 (1995).
39. B. Kaczer, H.-J. Im, J.P. Pelz, J. Chen, and W.J. Choyke, "Direct observation of conduction-band structure of 4H- and 6H-SiC using ballistic electron emission microscopy", Phys. Rev. B **57**, 4027–4032 (1998).

40. I. Shalish, L.B. Altufeder, and V. Narayananamurti, “Observations of conduction-band structure of 4H- and 6H-SiC”, Phys. Rev. B **65**, 073104 (2002).
41. A.-B. Chen and P. Srichaikul, “Shallow Donor Levels and the Conduction Band Edge Structures in Polytypes of SiC”, Phys. Stat. Solidi (b) **202**, 81–106 (1997).
42. J. Kono, S. Takeyama, H. Yokoi, N. Miura, M. Yamanaka, M. Shinohara, and K. Ikoma, “High-field cyclotron resonance and impurity transition in *n*-type and *p*-type 3C-SiC at magnetic fields up to 175 T”, Phys. Rev. B **48**, 10909–10916 (1993).
43. W.M. Chen, N.T. Son, E. Janzén, D.M. Hofmann, and B.K. Meyer, “Effective masses in SiC determined by cyclotron resonance experiments”, Phys. Stat. Solidi (a) **162**, 79–93 (1997).
44. D. Volm, B.K. Meyer, D.M. Hofmann, W.M. Chen, N.T. Son, C. Persson, U. Linddefelt, O. Kordina, E. Sörman, A.O. Konstantinov, B. Monemar, and E. Janzén, “Determination of the electron effective-mass tensor in 4H SiC”, Phys. Rev. B **53**, 15409–15412 (1996).
45. B.K. Meyer, D.M. Hofmann, D. Volm, W.M. Chen, N.T. Son, and E. Janzén, “Optically detected cyclotron resonance investigations on 4H and 6H SiC: Band-structure and transport properties”, Phys. Rev. B **61**, 4844–4849 (2000).
46. N.T. Son, O. Kordina, A.O. Konstantinov, W.M. Chen, E. Soerman, B. Monemar, and E. Janzen, “Electron effective masses and mobilities in high-purity 6H-SiC chemical vapor deposition layers”, Appl. Phys. Lett. **65**, 3209–3211 (1994).
47. G. Wellenhofer and U. Rössler, “Global band structure and near-band-edge states”, Phys. Stat. Solidi (b) **202**, 107–123 (1997).
48. V. Fiorentini, “Semiconductor band structures at zero pressure”, Phys. Rev. B **46**, 2086–2091 (1992).
49. C. Persson, U. Linddefelt, and B.E. Sernelius, “Doping-induced effects on the band structure in *n*-type 3C-, 2H-, 4H-, 6H-SiC, and Si”, Phys. Rev. B **60**, 16479–16493 (1999).
50. F. Engelbrecht, J. Zeman, G. Wellenhofer, C. Peppermuller, R. Helbig, M. Martinez, and U. Rossler, “Hydrostatic-pressure coefficient of the indirect gap and fine structure of the valence band of 6H-SiC”, Phys. Rev. B **56**, 7348–7355 (1997).
51. M. Willatzen, M. Cardona, and N.E. Christensen, “Relativistic electronic structure, effective masses, and inversion-asymmetry effects of cubic silicon carbide (3C-SiC)”, Phys. Rev. B **51**, 13150 (1995).
52. P. Giannozzi, S. de Gironcoli, P. Pavone, and S. Baroni, “*Ab initio* calculation of phonon dispersions in semiconductors”, Phys. Rev. B **43**, 7231–7242 (1991).
53. J. Ihm, M.T. Yin, and M.L. Cohen, “Quantum mechanical force calculations in solids: The phonon spectrum of Si”, Solid State Commun. **37**, 491–494 (1981).
54. K. Kunc and R.M. Martin, “*Ab initio* force constants of GaAs: a new approach to calculation of phonons and dielectric properties”, Phys. Rev. Lett. **48**, 406–109 (1982).
55. D.W. Feldman, J.H. Parker, W.J. Choyke, and L. Patrick, “Raman scattering in 6H SiC”, Phys. Rev. **170**, 698–704 (1968).
56. D.W. Feldman, J.H. Parker, W.J. Choyke, and L. Patrick, “Phonon dispersion curves by raman scattering in SiC, polytypes 3C, 4H, 6H, 15R, and 21R”, Phys. Rev. **173**, 787–793 (1968).
57. C.C. Tin, R. Hu, J. Liu, Y. Vohra, and Z.C. Feng, “Raman microprobe spectroscopy of low-pressure – grown 4H-SiC epilayers”, J. Cryst. Growth **158**, 509–513 (1996).

58. S. Nakashima and H. Harima, "Raman investigation of SiC polytypes", *Phys. Status Solidi (a)* **162**, 39–64 (1997).
59. F. Widulle, T. Ruf, O. Buresch, A. Debernardi, and M. Cardona, "Raman study of isotope effects and phonon eigenvectors in SiC", *Phys. Rev. Lett.* **82**, 3089–3092 (1999).
60. L. Patrick, "Infrared absorption in SiC polytypes", *Phys. Rev.* **167**, 809–813 (1968).
61. C.Q. Chen, R. Helbig, F. Engelbrecht, and J. Zeman, "Infrared absorption spectra of 4H silicon carbide", *Appl. Phys. A* **72**, 717–720 (2001).
62. W.J. Choyke, R.P. Devaty, L.L. Clemen, M.F. MacMillan, M. Yoganathan, and G. Pensl, *Inst. Phys. Conf. Ser.* **142**, 257 (1996).
63. I.G. Ivanov, U. Lindefelt, A. Henry, O. Kordina, C. Hallin, M. Aroyo, T. Egilsson, and E. Janzen, "Phonon replicas at the M point in 4H-SiC: A theoretical and experimental study", *Phys. Rev. B* **58**, 13634–13647 (1998).
64. C.H. Hodges, "Theory of phonon dispersion curves in silicon carbide polytypes", *Phys. Rev.* **187**, 994–999 (1969).

Sublimation Growth of SiC Single Crystals

N. Ohtani, T. Fujimoto, M. Katsuno, and H. Yashiro

The technological potential of silicon carbide (SiC) single crystals for high-power, high-temperature, and high-frequency electronic devices has been recognized for several decades; however, such applications have been greatly hindered by problems related to bulk crystal growth. SiC bulk crystal growth technology has recently achieved drastic improvement and enabled the growth of large high-quality single crystals. This chapter overviews the recent achievements in SiC bulk crystal growth aimed at producing high-quality large-diameter crystals, highlighting the improvement of the crystal diameter enlargement process and the reduction of crystallographic defects in SiC crystals.

3.1 Introduction

Materials have always played a key role in the history of technology evolution. One of the most illustrative examples is perhaps given by the introduction of semiconductor materials into electrical engineering, providing the foundation for modern electronics technology.

Silicon is today, and will be the dominant material in the semiconductor industry; silicon is a material with properties suited to a wide range of applications. Silicon is abundant, and large high-quality single crystals can be produced at an economical cost. This prominent material may be termed a first generation of semiconductor materials in the evolution of semiconductor technology. A second generation of semiconductor materials was developed in the 1960's. They are III-V compound materials, such as GaAs and InP, at present used mainly in microwave systems and most optoelectronic components. In the early 1980's, a third generation of semiconductor materials emerged: wide band gap materials, such as silicon carbide (SiC) and gallium nitride (GaN).

The technological potential of SiC for electronic applications stems from an outstanding combination of physical and electronic properties. The large band gap (roughly three times that of Si) enables device operation at an increased temperature (600 °C for transistors) and low leakage currents. SiC

can withstand high electric fields before breakdown, ten times greater than Si, and also high current densities. The large electron saturation velocity enables SiC to generate high power at high frequencies. SiC has excellent thermal conductivity, larger than copper at room temperature, which makes it suitable for high power operation. The strong chemical stability of SiC is a prominent advantage for sensors intended to operate in severe environments, for example in aerospace and automotive industries.

The superior material properties of SiC have long been recognized, and SiC research was intensively pursued in the United States and Europe during the 1960's and 70's. However, around 1973, many research institutes halted research when they failed to grow SiC in large single crystals [1]. In 1978, Tairov and colleagues made a major step in the development of SiC, with the use of a seeded sublimation growth technique, the so-called "modified-Lely method," for SiC bulk crystal growth [2], and this breakthrough led to the possibility of growing large single crystalline SiC.

In the last decade, SiC bulk crystal growth technology has achieved significant progress and enabled the growth of large high-quality SiC crystals. The availability of large diameter SiC single crystal substrates has resulted in the rapid progress in SiC thin film epitaxy and device fabrication, and the application of SiC to electronic and optoelectronic semiconductor devices is fast reaching its real potential.

The potential of SiC to outperform and replace silicon for many applications has already been demonstrated by several device prototypes. These include *pin* rectifiers with a blocking voltage of 19 kV [3], Schottky barrier diodes with a breakdown voltage higher than 5 kV, UMOSFETs with a blocking voltage of 1.4 kV at a specific on-resistance of $15.7 \text{ m}\Omega\text{cm}^2$ and with a figure of merit of 125 MW/cm^2 [4], thyristors which operate to 500°C and microwave MESFETs with a frequency of about 40 GHz and high power density of 5.2 W/mm and 63% power added efficiency (PAE) at 3.5 GHz [5]. The low lattice mismatch between SiC and GaN also makes SiC an excellent substrate for the growth of III-nitrides structure, used in the volume fabrication of blue LEDs [6]. With a hardness almost equivalent to diamond, SiC crystals are also being used as gemstones in jewellery.

This chapter reviews the current status of SiC bulk crystal growth technology and discusses the important technological advances in the sublimation growth of SiC single crystals. A key issue for the implementation of SiC based devices is further improvements in SiC bulk crystal growth technology, leading to the development of SiC crystals of large diameter and increased length with well defined crystalline and electrical properties.

SiC bulk crystals are almost always produced by a sublimation growth process, where SiC source powder sublimes and is recrystallized on a slightly cooled seed crystal at uncommonly high temperatures ($> 2000^\circ\text{C}$). The growth is generally conducted on an SiC platelet or wafer with a {0001} face, resulting in a crystal growth direction parallel to the $\langle 0001 \rangle$ *c*-axis. The extremely high process temperature of SiC bulk crystal growth gives rise to

increased difficulty in growing high-quality crystals as the crystal diameter increases, and the successful development of the diameter enlargement process has been a key topic for the SiC bulk crystal growth technology.

One of the major problems with SiC bulk crystals grown along the *c*-axis is the so-called “micropipes,” which are small pinhole defects that penetrate the entire crystal and cause critical flaws in SiC devices. Over the past several years, a significant reduction in micropipe density has been achieved and SiC substrates with a micropipe density of less than a few tens per square centimeters have been commercially available. However, micropipes are still a major obstacle to the widespread use of SiC devices, and thus, understanding of the origin of micropipes is of the utmost importance to extend the successful application of SiC technology. Furthermore, the investigation of structural defects other than micropipes is at an even earlier stage and thus, little is known about the causes and formation mechanisms of these defects. Particularly, low angle grain boundaries (subgrain boundaries) are commonly observed crystallographic defects in bulk SiC crystals. They are fully replicated from the substrates into the device epitaxial layers by the thin film growth process and consequently, have a major impact on the performance of SiC devices made on them. Sections 3.2–3.6 of this chapter review the recent development of SiC bulk crystal growth technology in the $\langle 0001 \rangle$ *c*-axis direction, devoting much attention to the improvement of the crystal diameter enlargement process and crystallographic defect reduction of SiC crystals.

Section 3.7 of this chapter concentrates on the sublimation growth of bulk SiC crystals perpendicular to the $\langle 0001 \rangle$ *c*-axis. Many aspects are different between the growth parallel and that perpendicular to the $\langle 0001 \rangle$ *c*-axis. It is well known that the growth parallel to the *c*-axis involves two basic problems. Firstly, SiC polytypes tend to mix during growth; and secondly, the crystals contain micropipe defects. In contrast to the *c*-axis growth, the polytypic structure of crystals grown perpendicular to the *c*-axis perfectly succeeds to that of the seed, and thus, polytype mixing never occurs during growth, and more importantly, the growth prevents micropipe formation. However, the growth tends to yield a large number of basal plane stacking faults in SiC crystals, and it was found that the density of the stacking faults strongly depends on the crystal growth direction and polytype. Based on these results, we discuss the defect formation process during the $[1\bar{1}00]$ and the $[11\bar{2}0]$ growth and try to provide a possible method to circumvent this problem.

3.2 Polytypism of SiC

The polytypic nature of SiC, i.e., that the crystal structure exhibits a number of different one-dimensional ordering sequences without any variation in stoichiometry, has been known for many years. Polytypism in SiC can be represented by various periodic hexagonal Si-C double layer structures along the *c*-axis. Figure 3.1 shows commonly observed polytypes in the sublima-

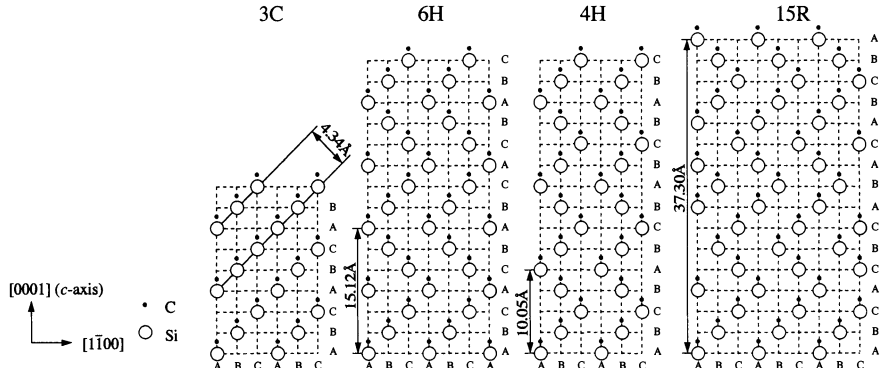


Fig. 3.1. Stacking sequences of Si–C double layers forming different polytypes (seen from [1120] (after [7], reproduced with permission from Springer-Verlag)

tion bulk growth, where large and small circles represent Si and C atoms, respectively [7]. The structure (3C, 6H, 4H and 15R) of SiC is represented by a figure indicating the number of (double) layers in the unit cell, followed by a letter recording the symmetry of the cell (C: cubic, H: hexagonal, R: rhombohedral). Another way of representing the polytypes is by the “ABC” notation. The order or sequence of the hexagonal double layers in the stack, either the (0001) basal plane of hexagonal structure or the (111) plane of cubic structure, is referred to by fixing one layer as an A layer and all other layers with atoms in positions identical thereto as A layers also. Layers of atoms in other positions in the stack are referred to as B, C layers. For example, 3C is represented as ABC by this notation, 6H as ABCBAC and 4H as ABCB. The lone cubic polytype (3C-SiC) is denoted by β -SiC, while the hexagonal and rhombohedral polytypes are collectively referred to as α -SiC. More than 250 different polytypes of SiC have been reported, and many physical and electronic properties of SiC vary depending on the polytype (e.g. bandgap energy [8]).

Owing to its high figures of merit for device applications (e.g. large band gap, high electron saturation drift velocity and mobility), the 4H polytype has gained much attention in recent years. 6H substrates are, however, used in the volume production of blue LEDs as substrate material for GaN heteroepitaxy. Experimentally, establishing crystal growth conditions for 4H-SiC has been more difficult than for 6H-SiC. A well-known result obtained by Knippenberg based on the annealing investigations of 3C polycrystalline rods grown from the vapor phase and the statistical polytype occurrence in a Lely furnace [9] indicates that the 4H polytype is an equilibrium phase in a lower and narrower temperature range than 6H. The 15R polytype is stable at an intermediate temperature of ~ 2450 °C whereas the 3C polytype is here described as metastable over all temperatures (Fig. 3.2).

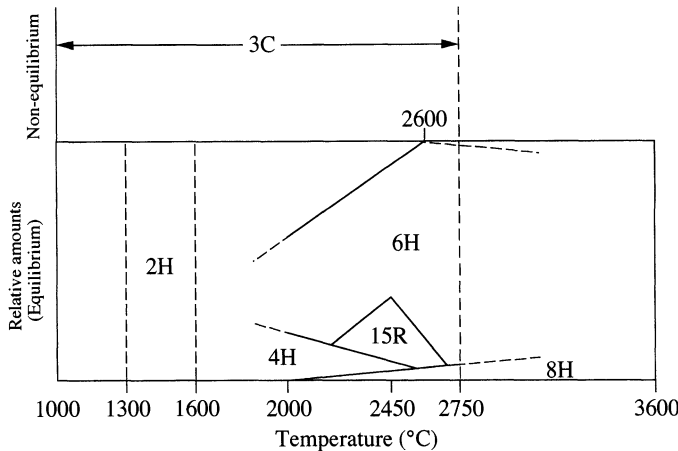


Fig. 3.2. Relation between structure and the temperature at which each polytype occurs. The relative amounts of the different hexagonal and rhombohedral structures of SiC are shown (after [9], reproduced with permission from Philips Research Laboratories)

A large body of literature already exists on the theories for the cause of SiC polytypism [10–12]. However, many aspects of the polytype formation during SiC bulk crystal growth remain unclear. The formation of various SiC polytypes has been discussed from the perspectives of thermodynamics [10, 11] and kinetics [10, 12] of SiC crystal growth. The occurrence of the short-periodic polytypes of SiC (e.g. 3C, 6H, 4H and 15R-SiC) is mainly affected by thermodynamics such as the formation enthalpy of SiC polytypes and the vapor phase composition, while the long-periodic structures of SiC are assumed to be stabilized by growth kinetics such as spiral growth due to screw dislocations [12].

Under crystal growth conditions, where the growth rates are of the order of mm/hour, the relative influence of thermodynamic and kinetic effects on the polytype stability may not be obvious [13]. It should, however, be noted that a temperature dependence of the 4H *versus* 6H polytype occurrence similar to the one observed by Knippenberg has been reported in sublimation growth [14]. As reported by several groups [15, 16], the gas phase stoichiometry also plays an important role in SiC crystal growth. Higher C/Si ratios favor the formation of the 4H polytype. This has been related to a higher relative concentration of Si versus C vacancies in the structures with increased hexagonality [15]. The addition of some impurities (e.g. Sc [17], Ce [18]) in the powder also favors 4H-SiC formation. They are characterized by a low solubility ($\sim 10^{16} \text{ cm}^{-3}$) in SiC and assumed to work as a “surfactant,” which changes the surface energetics of the nuclei. By contrast, N [19], which also stabilizes the 4H polytype, is highly incorporated in SiC crystals ($> 10^{20} \text{ cm}^{-3}$). A number of nitrogen impurities injected into the growth zone contribute to

Table 3.1. Polytype formation on seed crystals of different polytypes and surface polarity

Polytype	Seed Face Polarity	Grown Crystal Polype
6H	(0001)C	4H, 6H
	(0001)Si	6H (15R is often mixed)
4H	(0001)C	4H (dominant)
	(0001)Si	6H (15R is often mixed)

a relative enrichment of the growing surface with carbon and stabilize more hexagonal polytypes, i.e. 4H-SiC.

As first discussed by Stein *et al.* [20], the surface polarity affects the polytype formation. Table 3.1 summarizes the seed surface polarity effect on the polytype formation during sublimation growth of SiC [21]. The 6H, 4H and 15R polytypes occur on the (0001)C surface, while the 6H and 15R polytypes are grown on the (0001)Si surface, regardless of the polytype of the seed crystal. The 4H polytype does not occur on the (0001)Si surface even when a seed crystal of the 4H polytype is used. In contrast, the 4H polytype is preferentially grown on a 4H-SiC(0001)C seed crystal [19], and thus, the use of a 4H-SiC(0001)C seed crystal gives a great advantage for obtaining a single polytypic 4H-SiC crystal. These surface polarity effects were explained by the sp^2 hybridized bonds on the C-terminated (0001)C surface [22], or as more recently reported, by an interplay between the surface energy difference ((0001)Si *versus* (0001)C) and the difference in formation enthalpy of the 4H and 6H polytypes [20].

3.3 Sublimation Growth of SiC

Most bulk semiconductor single crystals, such as Si and GaAs, are grown from melt, i.e. by the Czochralski method. In contrast, the growth of bulk single crystals from the vapor phase is a less common practice in the semiconductor industry. For materials with no congruent melting temperature or at least one component having too high a vapor pressure at the melting point, vapor phase growth methods have to be employed. SiC belongs to this category of materials, since it decomposes into a Si-rich liquid phase with a carbon solid phase [23].

SiC was synthesized in a laboratory for the first time in the last decade of the 19th century. Acheson realized the technical importance of this hard and stable compound for grinding and cutting uses. Acheson's method for producing an abrasive, employing a reaction mixture of silica and carbon at more than 2500 °C, is still used in an essentially unaltered form. The original sublimation process of SiC growth was developed in 1955 by Lely. This was the first step in the preparation of pure SiC crystals, which enabled their semi-

conductor properties to be investigated. The starting materials here are SiC crystallites or even Si and C, which are heated to 2500–2700 °C and sublimed on the walls of the growth cavity. Several electronic devices were fabricated and their performances were demonstrated using these Lely crystals. However, difficulties in obtaining larger crystals and controlling the polytype of grown crystals prevented further development of SiC technology for the Lely platelets.

Currently, SiC bulk single crystals are almost always produced by the modified-Lely (seeded sublimation) growth method. The use of a seed crystal provides better control over the nucleation process, while the argon growth ambience can control the diffusion process of Si-C gas species. The growth scheme of the method is as follows. The gas species, mainly Si, SiC₂ and Si₂C [24], sublimated from a solid powder source condense epitaxially on a seed crystal maintained at a lower temperature. The material transport and, hence, the growth rate are mainly determined by the growth temperature, temperature gradient from the source to the seed crystal and pressure inside the crucible. A schematic diagram of the sublimation growth system in our laboratory is shown in Fig. 3.3. The seed wafer is mounted to directly face the source SiC powder in a graphite crucible. The crucible is covered with heat insulators made of graphite felt. Heating is performed by RF induction. The crucible assembly is placed asymmetrically to the RF coil to produce an adjustable negative temperature gradient of 10 to 25 °C/cm. The temperature profile inside the crucible is measured by a pyrometer through small holes in the top and bottom covering insulators. During heating, an argon overpressure of about 600 Torr is maintained to avoid crystallization at lower temperatures,

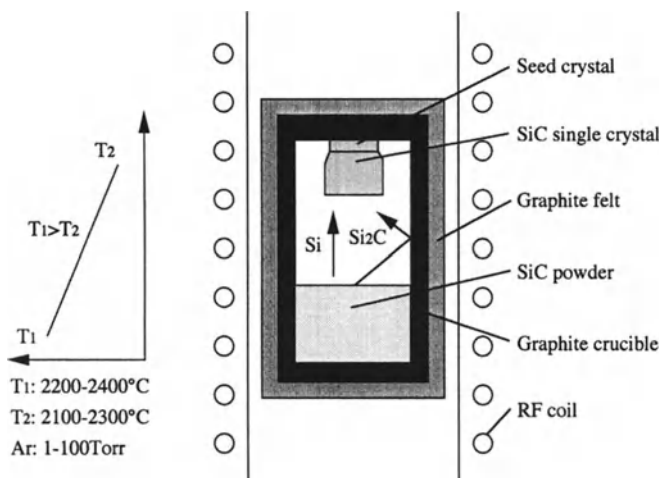


Fig. 3.3. Schematic diagram of SiC sublimation growth system used in our laboratory

which would lead to undesired polytype formation. When the growth temperature of 2200–2400 °C is reached, the argon pressure is lowered to 1–40 Torr to initiate crystal growth. Many of the problems in SiC bulk crystal growth derive from this uncommonly high growth temperature.

3.4 Crystal Diameter Enlargement

The seeded sublimation growth process developed by Tairov and Tsvetkov paved the way to growing large SiC single crystals. After their pioneering work, many research laboratories performed research in the sublimation growth field. In 1983, Ziegler *et al.* [25] reported a 20 mm in diameter, 24 mm long 6H-SiC crystal grown by the seeded sublimation growth method, and they demonstrated fabrication of blue SiC LEDs with a high quantum efficiency. Following the work of Ziegler *et al.*, several research groups in Europe, Japan and the USA have developed large diameter SiC crystal growth technology. In Japan, Koga *et al.* succeeded in growing 6H-SiC crystals with diameters of up to 30 mm in 1985 [26], and in 1994, Nippon Steel Corporation succeeded in growing a 40 mm in diameter 6H-SiC crystal [27] and a two-inch SiC crystal of the 4H polytype in 1996 [28], and has recently demonstrated growth of four-inch diameter SiC crystals [29]. In 1989, Cree Research Inc., USA first commercially released 6H- and 4H-SiC wafers of one-inch diameter, and they have recently brought three-inch diameter SiC substrates to the market [30].

Increasing the wafer diameter is crucial for reducing the cost of SiC devices through economies of scale and the use of Si or GaAs device fabrication lines. In this respect, much effort has been made over the last decade, leading to the recent fabrication of fully single crystal wafers with a diameter of up to 100 mm [29, 31]. The crystal quality, however, is generally largely degraded as the crystal diameter increases. This is due to the lack of an established methodology for expanding the single crystal area without degrading crystal quality. The difficulty in growing high-quality crystals rapidly increases as the crystal diameter increases, and various technological problems have become apparent in the diameter enlargement process.

To avoid these problems, a high degree of control of both the transient and continuous thermal profiles during growth is required. However, experimental optimization of such growth parameters usually takes much effort and is time-consuming. Consequently, the results of numerical simulation of the temperature profiles inside the crucible are utilized, taking into account the heat transfer through conductive and radiative mechanisms, and then the results are combined with compiled experimental database to determine the key growth parameters for SiC crystal growth. This approach allowed us to achieve successful diameter enlargement of up to 10 mm during a single growth run without degrading crystal quality (Fig. 3.4), where the enlarged portion of grown crystal contains very few micropipes [29]. Figure 3.5 shows four-inch diameter 6H-SiC substrate fabricated in our laboratories. In the course of this

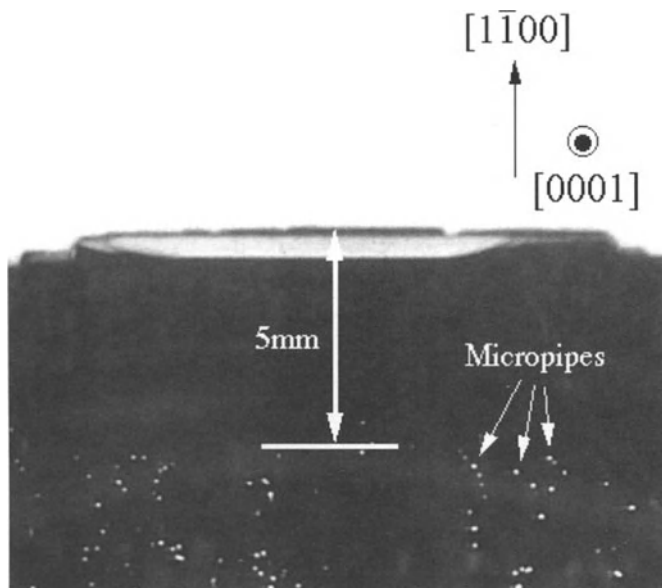


Fig. 3.4. Example of successful diameter enlargement of a SiC crystal: the photo shows a top view of the as-grown surface of a diameter-enlarged crystal, where a 10 mm enlargement in diameter was achieved during a single growth run. The white dots on the as-grown crystal surface represent micropipes under strong light illumination (after [29], reproduced with permission from Trans Tech Publishing)

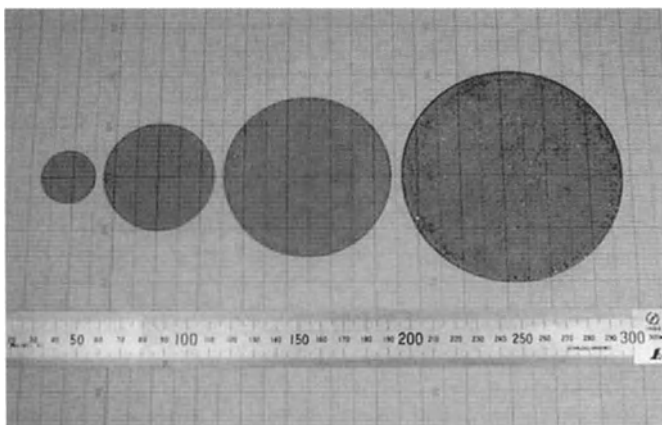


Fig. 3.5. Four-inch diameter 6H-SiC substrate fabricated in our laboratories, together with smaller-diameter (1, 2, and 3 inches) 6H-SiC substrates

development, increased attention was paid to crucible design and optimization of the thermal profile in the growth cavity to avoid undesirable polycrystallite nucleation and minimize thermoelastic stresses.

3.5 Reduction of Micropipe Defects

The advance of SiC bulk crystal growth technology has enabled the growth of large single polytypic SiC single crystals. With the availability of large high-quality substrates, SiC device research has accelerated. However, defects such as micropipes (hollow tubes) [32,33], voids [34], subgrain boundaries [35] and dislocation networks [36] exist in the SiC crystals grown by the seeded sublimation growth method. Among these, micropipes, which penetrate the entire crystal along the growth direction as hollow tubes, are defects of the most serious concern since they are replicated into the device epitaxial layers and become a critical defect for SiC power devices [37]. Figure 3.6 shows a transmission optical micrograph of an SiC wafer longitudinally sliced along the $\langle 0001 \rangle$ growth direction, where the “micropipe” defects lying approximately parallel to the c -axis are visible.

Synchrotron white beam X-ray topographic (SWBXT) studies provide evidence that micropipes are large Burgers vector screw dislocations [36]. The magnitude of the Burgers vector of micropipes in 6H-SiC crystals is 2–7 times the unit c lattice parameter (15.12 Å), while no discernible hollow cores are detected for the elementary c screw dislocations [36]. Dislocations with such a large Burgers vector are energetically favored to have open cores, as predicted by Frank in 1951 [38].

Figure 3.7 shows an atomic force microscope (AFM) image of the $(0001)\text{Si}$ surface of 6H-SiC, where a spiral step ending at a micropipe is visible. The almost archimedean circular spiral step is characterized by a large step height

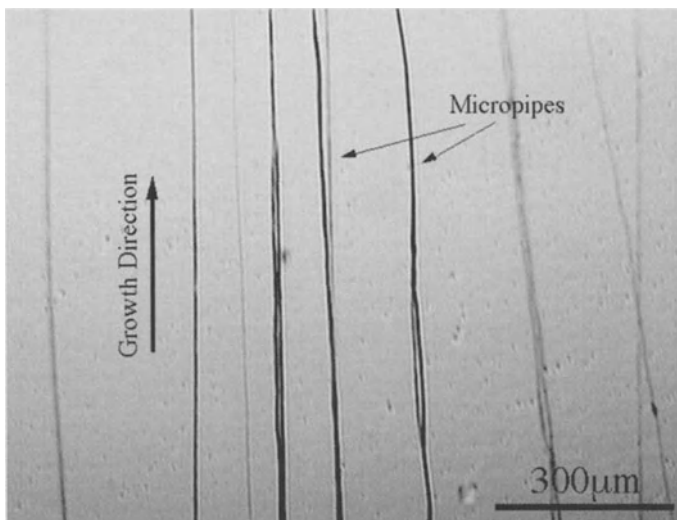


Fig. 3.6. Transmission optical micrograph of SiC wafer longitudinally sliced along the $\langle 0001 \rangle$ c -axis growth direction, showing “micropipes” lying approximately parallel to the c -axis

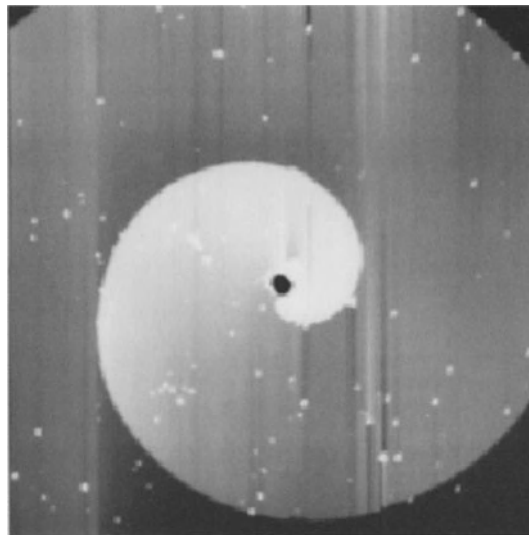


Fig. 3.7. AFM image of a growth spiral due to a micropipe on the 6H-SiC(0001)Si surface. The scan size was $40 \mu\text{m} \times 40 \mu\text{m}$, and the step height was 13.5 nm, which is nine times the c lattice parameter of 6H-SiC (after [46], reproduced with permission from Elsevier)

(13.5 nm corresponding to nine times the unit c lattice parameter of 6H-SiC) due to the large Burgers vector of the micropipe.

Seeded sublimation grown SiC crystals contain micropipe defects of typically $10^2\text{--}10^3 \text{ cm}^{-2}$ [39]. The existence of hollow core dislocations in SiC crystals has long been recognized, and several empirically determined characteristics have been reported. The micropipe formation has been related to the purity of the starting SiC source material [32], and the generation and propagation of micropipes are also sensitive to specific seeding techniques employed and to growth parameters, such as pressure and temperature [39]. Micropipes appear to originate in the vicinity of the seed wafer, lie generally along the growth direction and are often associated with subgrain boundaries [39].

Several possible causes for the formation of micropipes exist, and are categorized into three groups: (1) thermodynamic, (2) kinetic and (3) technological causes [40]. For example, the thermodynamic causes include thermo-elastic stress due to non-uniform heating, while the kinetic causes are related to the nucleation process and growth surface morphology. In all these cases, one must also consider the technological aspects, such as the seed surface preparation and contamination of the growth system. An example of the causes for micropipe formation is illustrated in Fig. 3.8. The figure shows an optical micrograph of a 6H-SiC crystal vertically sliced along the $\langle 0001 \rangle$ c -axis growth direction, where polytype instabilities (15R-SiC polytype inclusions) cause micropipes. They are visible as vertical line defects in the micrograph, and

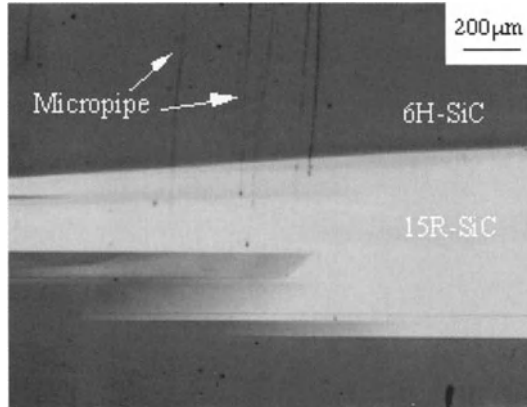


Fig. 3.8. Longitudinally sliced 6H-SiC crystal along the growth direction, showing a multitude of micropipes emerging at the polytype boundaries between 6H and 15R (after [46], reproduced with permission from Elsevier)

a multitude of micropipes emerge slightly above the non-basal plane interfaces between the 6H and 15R polytypes.

An important aspect of micropipes is that while they are forming during growth, simultaneous processes also occur which reduce their concentration, such as dissociation, coalescence, recombination and transformation [41]. These processes are largely controlled by growth kinetics rather than equilibrium thermodynamics, and many of them are believed to be surface-mediated processes [42]. In principle, a dislocation with a Burgers vector $\mathbf{b} = n\mathbf{c}$ (\mathbf{c} smallest translation vector) is energetically unfavorable compared to the distribution of n elementary dislocations with a Burgers vector \mathbf{c} . The fact that micropipes appear stable and propagate in the crystal implies that a large kinetic energy barrier exists to nucleate a dislocation in SiC crystals adjacent to micropipe [43].

To date, several models have been proposed to elucidate the formation mechanism of micropipes. They are classified into two groups: one is mechanisms that generate depressions or voids at the growing surface, which subsequently or almost simultaneously attract dislocations to stabilize voids (hollow cores) during growth, and the other is mechanisms that lead to an extremely large Burgers vector and the hollow core is a consequence of the energy reduction according to Frank.

Giocondi *et al.* [44] proposed a surface depression model, which tried to explain an accumulation of unit c screw dislocations *via* the formation of a surface depression surrounded by a macrostep at the growing surface. Macrosteps, which are very often observed on the SiC{0001} surface, sweep up screw dislocations during growth by shifting their emergence points in the direction of motion. Once the macrostep stops at an obstacle, e.g. secondary phase precipitate, it bows around the obstacle, reunifies and moves further as a reformed

complete macrostep. Consequently, the obstacle is surrounded by a macrostep forming a depression, into which the screw dislocations have been collected.

On the other hand, a mechanism that leads to a dislocation with an extremely large Burgers vector was elucidated by Pirouz [45]. He pointed out that the twist-type misorientation existing in SiC crystals plays a major role in the micropipe formation. Seeded sublimation-grown SiC crystals have a mosaic structure, with all the domains having a strong [0001] texture. The boundaries among these domains may have both the tilt and twist nature of misorientation, and a small twist misorientation between the adjacent domains is accommodated by arrays of screw dislocations lying on the boundary plane. Pirouz considered a triple junction of such twist-type low angle grain boundaries, and that at the triple junction, there will be a screw dislocation with $\mathbf{b} = 3\mathbf{c}$ when all the twist boundaries are in the same sense. Since the magnitude of the Burgers vector of the $\mathbf{b} = 3\mathbf{c}$ screw dislocation exceeds the critical value (2–3 nm) for the dislocation core to be empty, this junction dislocation will become a hollow core dislocation (micropipe). This relatively small micropipe will further attract unit c screw dislocations, by the image force mechanism [45], to become a larger diameter micropipe.

Ohtani *et al.* has recently proposed a surface step model for the micropipe formation in SiC crystals, taking into account several important aspects experimentally observed for micropipe formation [46]. Micropipes are very often observed at the foreign polytype and secondary phase inclusions during growth, where high density unit c screw dislocations are introduced and the spiral steps emanating from them are very closely located and interact with each other. The model assumes that the strong repulsive interaction between these steps [47] coalesces the underlying unit c screw dislocations through the energetic bunching of the spiral steps.

For simplicity, two unit c screw dislocations with the same sign Burgers vector are considered (the discussions below can be extended to include the cases that involve more than two screw dislocations). Each screw dislocation provides a spiral step of unit cell height as denoted by A and B in Fig. 3.9a. If the dislocations are placed very close together, the spiral steps are intermixed and arranged alternately, as schematically illustrated in Fig. 3.9a. In this step system, steps A and B interact *via* the strong repulsive force between them, and this repulsive interaction induces the energetic bunching of steps A and B .

In general, the coalescence of steps, i.e. step bunching, costs more energy than an equivalent height of a distribution of isolated steps. However, when the steps are located close to each other (Fig. 3.9b), this energy is outweighed by the decrease in step repulsive energy since the coalescence of steps A and B increases the average separation between the steps (Fig. 3.9c).

The energetic bunching of spiral steps drives the coalescence of the two adjacent screw dislocations at their centers, giving rise to a screw dislocation with a Burgers vector $\mathbf{b} = 2\mathbf{c}$. It should be noted that the coalescence of dislocations only occurs *via* the crystal growth process, and thus, the parts of

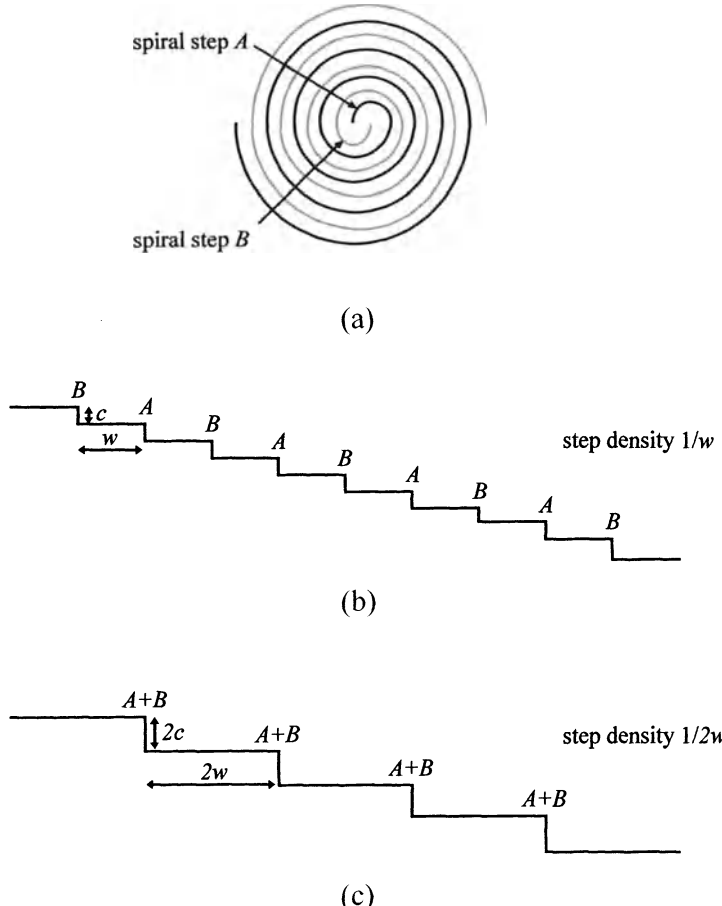


Fig. 3.9. Schematic diagrams of (a) the intermixed growth spirals from two adjacent screw dislocations with Burgers vector of the same sign, and a step train comprising alternately arranged steps *A* and *B* (b) before and (c) after energetic step bunching (after [46], reproduced with permission from Elsevier)

the screw dislocations already existing in the crystal before the spiral steps are bunched are not coalesced.

It is obvious that the coalescence of dislocations occurs at the cost of bulk elastic energy. In terms of energetics, the energy gain by the coalescence of spiral steps needs to overcome the energy cost due to the elastic strains to form a screw dislocation with twice the size of Burgers vector $\mathbf{b} = 2\mathbf{c}$ (super screw dislocation). This condition is satisfied at the initial stage of coalescence, since the coalesced length of dislocations is small; the coalescence is limited to a near surface region. When the growth proceeds and the coalesced length of dislocations becomes larger, the energy cost due to the elastic strains tends to be greater than the energy gain due to the reduced step repulsive energy. At

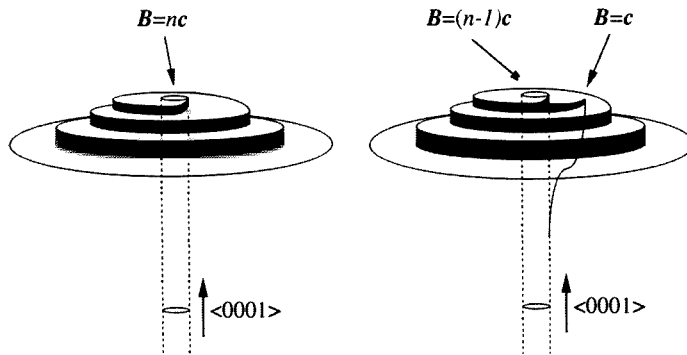


Fig. 3.10. Schematic drawing of micropipe dissociation process, where a micropipe is dissociated into a micropipe with a slightly smaller Burgers vector plus one unit c screw dislocation

this stage, however, the core substance is evaporated, releasing the large elastic strains at the core, and this hollow core formation further stabilizes the super screw dislocation (micropipe) and kinetically prevents it from dissociating.

As discussed above, a large kinetic energy barrier exists to micropipes being dissociated; however, it was importantly suggested that this kinetic barrier can be reduced by optimizing the growth conditions, and micropipes are dissociated [48]. For example, a micropipe can be dissociated into a micropipe

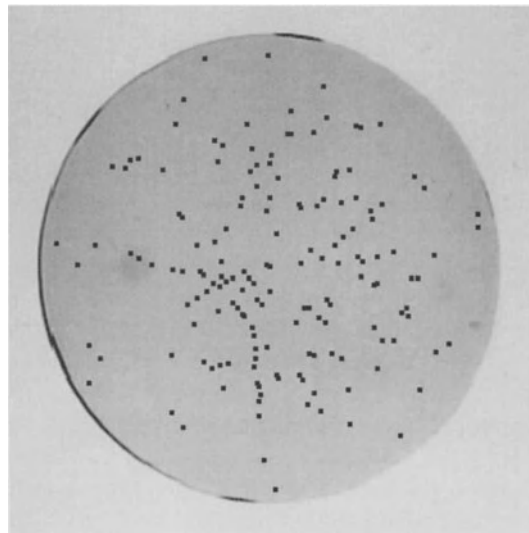


Fig. 3.11. Digitized image of a KOH-etched two-inch 6H-SiC wafer. The *black dots* correspond to micropipe defects. The micropipe density has been reduced to 8 cm^{-2} after several growth runs under optimized growth conditions

with a slightly smaller Burgers vector *plus* one unit *c* screw dislocation as schematically shown in Fig. 3.10. It is worth noting here that this dissociation process only occurs during growth [46]. By optimizing the growth conditions, continuous reduction in micropipe density has been made over the past few years, and recently, micropipe density has been successfully reduced to less than ten micropipes per square centimeter for two-inch 6H-SiC substrates (Fig. 3.11).

3.6 Improved Mosaicity of Bulk SiC Crystals

As described in the previous section, a significant reduction in micropipe density has been successfully demonstrated by several groups [29, 49]. However, while the micropipe density is decreasing, SiC device commercialization is still largely limited by the presence of crystallographic defects other than micropipes. In particular, low angle grain boundaries (subgrain boundaries) are another critical defect for the implementation of large-size ($> 1 \text{ cm}^2$) SiC devices.

Subgrain boundaries are commonly observed in seeded sublimation grown bulk SiC single crystals produced to date. The crystals typically contain slightly misoriented subgrains bordered by regions of high dislocation density. These subgrains are fully replicated into the device epitaxial layers by a thin film growth process, and consequently, the subgrain structure of the substrate has a major impact on the performance of SiC devices made on it [50]. The domain (mosaic) structure in SiC single crystal wafers was first reported by Glass *et al.* [35]. They examined commercially available 6H-SiC substrates by high-resolution X-ray diffractometry and reciprocal space mapping, and the results indicated a presence of domain structure in SiC crystals, with varying domain densities. The X-ray diffraction curves obtained from the substrates showed multiple peaks distributed over several hundred arcseconds, while a single diffraction peak with a full width at half maximum (FWHM) of 15 arcsec was obtained for Lely platelets grown *via* the non-seeded sublimation process. They ascribed this difference to a lower growth temperature and higher degree of supersaturation in the seeded sublimation growth process than in the non-seeded sublimation (Lely) growth process; these growth conditions are expected to increase the nucleation density on the growing surface. Following the work by Glass *et al.* [35], Tuominen *et al.* [51] conducted a series of X-ray rocking curve measurements for commercial 4H-SiC substrates by varying the beam spot size for a constant 0004 reflection and changing the order of reflection at a constant beam spot size. They obtained very similar results to those for 6H-SiC substrates reported by Glass *et al.*

Ellison *et al.* [52] studied the relationship between the warpage and mosaic structure of SiC substrates. They found that the warpage of SiC substrates results from a convolution of the surface preparation and intrinsic properties inherited from the bulk growth process. A high defect content present in the

substrates easily enables them to deform plastically (crystal bending). The warpage of SiC wafers severely hampers the full wafer processing of micron or sub-micron optical lithography patterning, and the final quality of SiC epilayers is also expected to be influenced by the crystal bending of the underlying substrates.

Several causes and mechanisms of the misoriented subgrain formation in seeded sublimation grown SiC crystals have been proposed and discussed. Glass *et al.* [35] found that the micropipe density was approximately consistent with the number of multiple peaks or the broadening magnitude of X-ray rocking curves (over several hundred arcseconds), and thus, suggested the possibility that micropipes are the main cause of the mosaicity in seeded sublimation grown bulk SiC crystals. More recently, Pirouz [45] discussed the dislocation systems lying on a prism plane, e.g., $\{11\bar{2}0\}$ or $\{1\bar{1}00\}$ plane. $\{11\bar{2}0\}$ and $\{1\bar{1}00\}$ have never been reported as a slip plane in hexagonal SiC polytypes, even though the subgrain boundaries commonly observed in seeded sublimation grown SiC crystals lie in the $\{11\bar{2}0\}$ plane, which implies that the dislocations comprising the subgrain boundaries are not introduced by thermal stress after growth, and that they are grown-in type dislocations and rather introduced during growth by the growth process itself. Pirouz [45] and Glass *et al.* [13] claimed that the strong $[0001]$ texture in seeded sublimation grown SiC crystals originates in a spiral growth mechanism. The interaction between two growth spirals can be assumed to result in low angle grain boundaries due to twist misorientation between the two growth spirals.

Recently, Katsuno *et al.* revealed that micropipes and unit *c* closed-core screw dislocations only slightly affect the shape of the X-ray rocking curves [53]. The rocking curves obtained from regions that contained micropipes (density $\sim 200 - 600 \text{ cm}^{-2}$) and/or unit-*c* closed core screw dislocations (density $\sim 2 \times 10^4 \text{ cm}^{-2}$) showed a relatively narrow single diffraction peak with an FWHM of 13–27 arcsec. The width of the rocking curves slightly increased with the increase of micropipe density. However, even for crystal areas with a micropipe density of 600 cm^{-2} , the width remained less than 30 arcsec and the rocking curves did not show multiple peaks. These results preclude the possibility of micropipes being the cause of the strong (0001) mosaicity present in SiC bulk crystals.

Katsuno *et al.* [54] found that seeded sublimation grown SiC crystals have a strong $[0001]$ texture around etch pit rows due to edge dislocation walls aligned along $\langle 1\bar{1}00 \rangle$ directions. Figure 3.12 shows the 0006 X-ray rocking curves obtained from a region that accommodates two parallel etch pit rows (coupled subgrain boundaries) with the incident plane (a) parallel and (b) perpendicular to the etch pit rows. The rocking curve with the incident plane parallel to the boundaries shows a narrow single diffraction peak (Fig. 3.12a), while the one with the incident plane perpendicular to the boundaries shows a much broader peak (40–80 arcsec), often splitting into multiple peaks as shown in Fig. 3.12b. Based on these results, Katsuno *et al.* concluded that the tilting of the (0001) lattice plane has a rotation axis parallel to both the

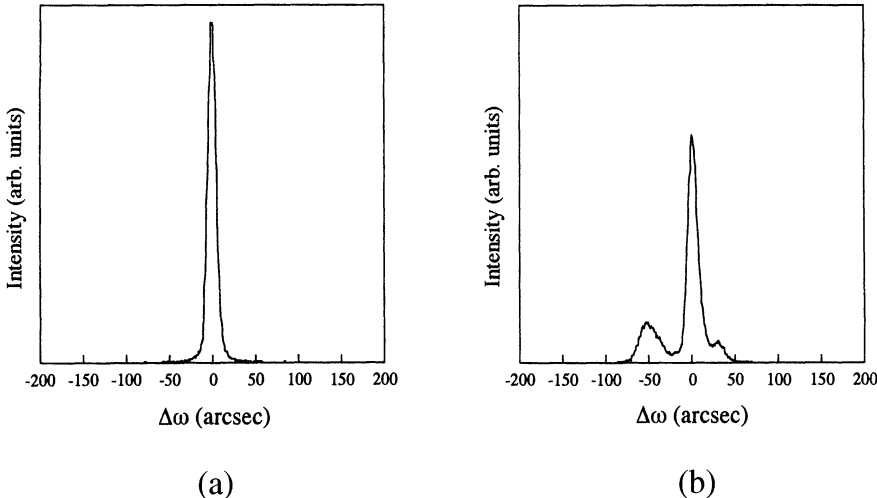


Fig. 3.12. 0006 X-ray rocking curves obtained from two parallel etch pit rows with the incidence plane (a) parallel and (b) perpendicular to the etch pit rows (after [54], reproduced with permission from Elsevier)

boundary plane and the (0001) basal plane, which is quite contradictory to the twist misorientation model due to the growth spiral interaction by Glass *et al.* [13] and Pirouz [45]; the twist misorientation causes the tilting of the (0001) basal plane with a rotation axis perpendicular to the boundary plane.

Katsuno *et al.* have attributed the tilting of the (0001) basal plane to the inclination of the boundary dislocations from the *c*-axis [54]. The polygonization of edge dislocations along $\langle 1\bar{1}00 \rangle$ directions requires glide and climb motions of the dislocations. The glide and climb of dislocations are temperature-activated processes [55], and thus, they most probably occur during growth. In the course of these motions, the edge dislocations predominantly lie along the *c*-axis but often jog toward $\langle 1\bar{1}00 \rangle$ directions due to the climb motion. These jogs are assumed to virtually bend the edge dislocations at the grain boundary from the *c*-axis and bring about a tilting of the (0001) basal plane around it; recently, such a jog structure of boundary dislocations was observed by Hong *et al.* using transmission electron microscopy (TEM) [56].

One of the major causes of the subgrain formation in seeded sublimation grown SiC crystals is the inclusion of foreign polytypes during growth [57]. Figure 3.13 shows the evolution of mosaicity in SiC crystal during growth after polytype instabilities at the near seed regions. The $(11\bar{2}0)$ X-ray rocking curve with the incident plane perpendicular to the growth direction becomes broader and splits into multiple peaks as the scan moves further from the foreign polytype inclusion along the growth direction. The polytypic inclusion would result in stresses due to the differences in the lattice constant and the coefficient of thermal expansion between different polytypes. During growth,

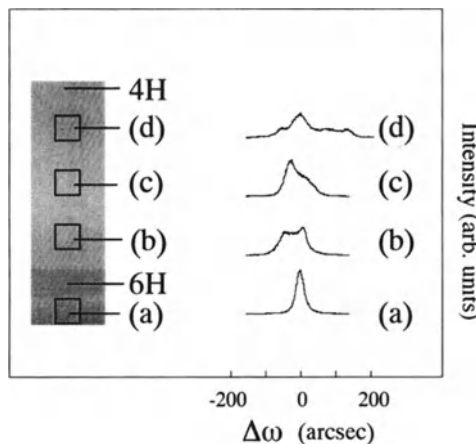


Fig. 3.13. Evolution of the crystal mosaicity during crystal growth in the $[000\bar{1}]$ direction after polytype instabilities have occurred. The $11\bar{2}0$ X-ray rocking curves with the incidence plane perpendicular to the growth direction were acquired at points along the growth direction (a) before polytype instabilities occurred, (b) 1 mm, (c) 3 mm, and (d) 5 mm from a foreign-polytype inclusion. The inset figure is an optical photo of a polytype-mixed 4H-SiC crystal (after [57], reproduced with permission from Trans Tech Publishing)

the stresses are released by the introduction of dislocations, which are further activated to glide and climb in the crystals to minimize their total strain energy by aligning themselves along $\langle 1\bar{1}00 \rangle$, forming subgrain boundaries.

An important aspect of the subgrain boundaries is that they are not uniformly distributed, and most often occur at the peripheral regions of the

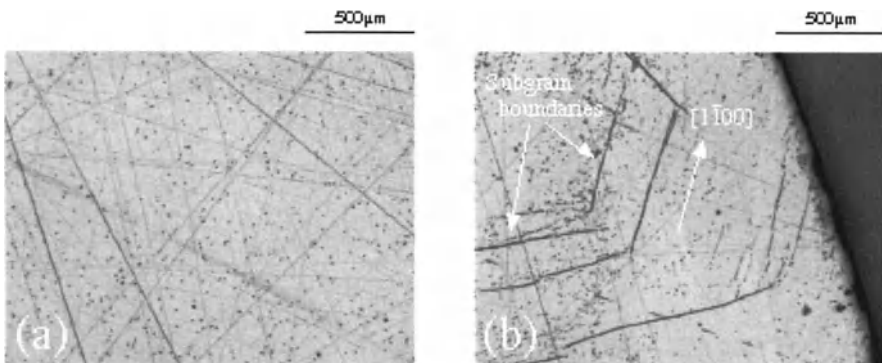


Fig. 3.14. Etch pit features on the $(0001)\text{Si}$ surface of a 6H-SiC wafer: (a) the central and (b) the peripheral regions. The central region appears free of subgrain boundaries, while the peripheral region contains polygonized subgrain boundaries

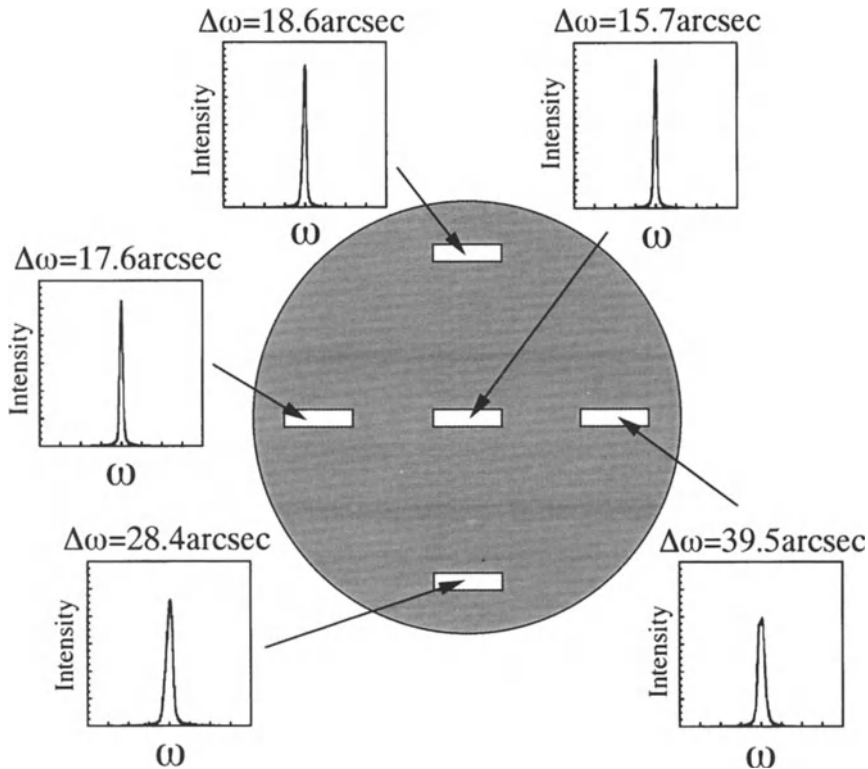


Fig. 3.15. Two-inch 4H-SiC substrate with a low mosaicity. The rocking curves obtained across the entire wafer show a single diffraction peak as narrow as a few ten arcseconds (spot size 2 mm × 8 mm)

crystal [54, 58]. Figure 3.14 shows the etched (0001)Si surfaces of the central and peripheral regions of a 6H-SiC wafer. As seen in the figure, the central region of the wafer appears free of subgrain boundaries, while the peripheral region often contains polygonized subgrain boundaries.

Powell *et al.* [59] analyzed SiC wafers fabricated in their laboratory by crossed polarizer imaging and found that the wafers had three distinct regions: i) the central region free of contrast, ii) the cross-hatched region (contrasts due to localized strain fields at subgrain boundaries) surrounding the central area and iii) the wafer rind, composed of polycrystalline SiC. They claimed that, to expand the central region of a better crystallinity, a high degree of control of both the transient and continuous thermal profiles is required. To achieve this, they employed a numerical modeling of the heat dissipation and flow in the growth reactor, and developed an optimal design and growth process for the single crystal area expansion. Hofmann *et al.* also pointed out the critical role of the numerical growth process analysis [60]. After adjustment of heat-

ing distribution and modification of the thermal insulation, they successfully achieved the reduction of stress variations due to subgrain boundaries.

We have also continued to optimize the crucible design and growth process to minimize the undesirable temperature gradients existing in SiC crystals during growth, with the aid of the numerical simulation of temperature profile inside the crucible. An example of this effort is shown in Fig. 3.15. The figure shows a series of X-ray rocking curves (X-ray spot size: 2 mm \times 8 mm) obtained from a two-inch 4H-SiC wafer with improved crystalline quality. As seen in the figure, all the rocking curves acquired across the entire wafer show a single diffraction peak as narrow as a few tens of arcseconds, indicating that the wafer possesses a low mosaicity.

3.7 SiC Bulk Crystal Growth in Directions Perpendicular to the *c*-Axis

A new degree of freedom in the sublimation growth of bulk SiC crystals is the growth of crystals in directions perpendicular to the *c*-axis, i.e. [1 $\bar{1}$ 00] and [11 $\bar{2}$ 0]. Recently, a drastic improvement in the channel mobility of SiC MOSFETs has been demonstrated on the (11 $\bar{2}$ 0) surface [61, 62]. SiC MOSFETs on the (11 $\bar{2}$ 0) surface showed a drastically-enhanced channel mobility compared to that of the conventional MOSFETs fabricated on the (0001) surface. Some additional advantageous characteristics have also emerged for thin film epitaxy [63] and ion implantation [64] for the SiC(11 $\bar{2}$ 0) surface, and these outstanding achievements have naturally spurred interest in bulk crystal growth in the [11 $\bar{2}$ 0] direction. The bulk crystal growth in this direction is essential for the fabrication of SiC(11 $\bar{2}$ 0) substrates with a large diameter and reasonable uniformity of doping concentration.

Figure 3.16 shows a schematic figure of crystal orientation of hexagonal SiC. In general, for SiC sublimation growth, SiC platelets or wafers with {0001} faces have been used as the seed crystal, resulting in a crystal growth direction along the <0001> *c*-axis. However, this involves two basic problems. Firstly, SiC polytypes tend to mix during growth; and secondly, the crystals contain a number of micropipes.

One approach to grow SiC crystals free of micropipes is to grow crystals in directions perpendicular to the *c*-axis. Takahashi *et al.* has proposed SiC crystal growth in the [1 $\bar{1}$ 00] and the [11 $\bar{2}$ 0] directions and proved that micropipes can be eliminated in SiC crystals grown in these growth directions [65, 66], which are naturally favored in the Acheson and Lely growth processes [9].

Figure 3.17 shows optical micrographs of {0001} wafers fabricated from (a) [000 $\bar{1}$] and (b) [1 $\bar{1}$ 00] grown crystals. The micrographs were taken under crossed polarizers and the interference contrasts in the figure reveal the strains accommodated in the wafers by a photoelastic effect. It is clear from the figure that there exist large strains associated with micropipes in the [000 $\bar{1}$] grown crystal (Fig. 3.17a) [65]. On the other hand, no interference contrasts due to

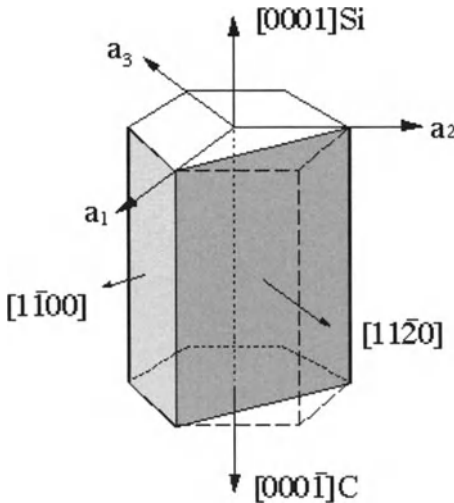


Fig. 3.16. Schematic illustration of crystal orientation of hexagonal SiC

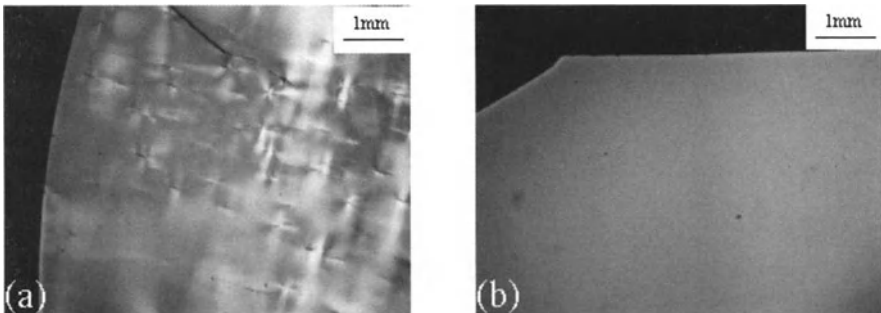


Fig. 3.17. Polarizing-microscope images of $\{0001\}$ wafers sliced from SiC crystals grown in (a) the $[000\bar{1}]$ and (b) the $[1\bar{1}00]$ direction. The strain fields associated with micropipes are visible for the $[000\bar{1}]$ -grown crystal, while no such contrast is detected for the $[1\bar{1}00]$ -grown crystal

micropipes are observed for the $[1\bar{1}00]$ grown crystal (Fig. 3.17b), indicating that micropipes are fully eradicated from the crystal.

Another advantage of polytype control for the growth in the $[1\bar{1}00]$ and the $[11\bar{2}0]$ directions has also been experimentally demonstrated [65]. Figure 3.18 shows the luminescence at 77 K under ultra-violet irradiation from an SiC crystal grown in the $[1\bar{1}00]$ direction on a seed crystal of mixed polytypes. Due to the different band structures of polytypes, each polytype shows a specific luminescence color: reddish purple for 6H, yellowish green for 4H and orange for 15R. As seen in the figure, the polytypic structure of the grown crystal perfectly succeeds to that of the seed crystal in the $[1\bar{1}00]$ growth: 6H always grows on the 6H part of the seed, and 4H always grows on the 4H part of

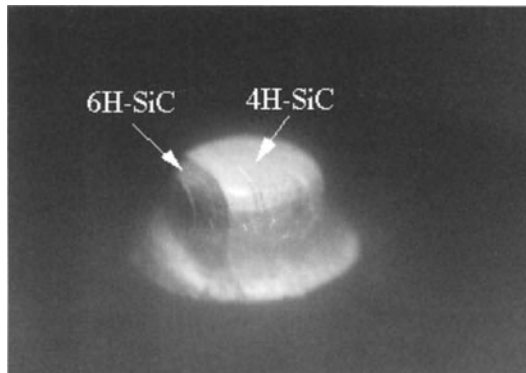


Fig. 3.18. Luminescence at 77 K under ultra-violet irradiation from a SiC crystal grown in the $[1\bar{1}00]$ direction on a seed crystal of mixed polytypes (after [33], reproduced with permission from Elsevier)

the seed crystal. The polytypic structure of the seed crystal is also perfectly inherited in the $[11\bar{2}0]$ growth, independently of the growth conditions such as the growth temperature and the Ar pressure. These results are reasonably understood from the fact that the information on the stacking sequence of atomic layers appears on the $(1\bar{1}00)$ and the $(11\bar{2}0)$ surfaces.

As seen in Fig. 3.17, micropipe formation is fully suppressed by the growth perpendicular to the *c*-axis. At the same time, however, the growth brings about another problem, which is the stacking fault formation during growth [67]. Figure 3.19 shows a Nomarski micrograph of the etched surface of a $(1\bar{1}00)$ wafer prepared from a 6H $[1\bar{1}00]$ grown crystal, where linear etch pits (*L*) along $\langle 11\bar{2}0 \rangle$ are observed. By a direct comparison with X-ray topographs, it was concluded that the etch pits are caused by the stacking faults in the basal plane [67]. They are scarcely observed in $\langle 0001 \rangle$ grown crystals, which are used as the seed crystal for the $[1\bar{1}00]$ and the $[11\bar{2}0]$ growth, thus implying that the stacking faults are introduced during growth.

Figure 3.20 shows (a) a high-resolution transmission electron microscope (HRTEM) image of a stacking fault structure in a 6H-SiC $[1\bar{1}00]$ grown crystal and (b) a corresponding schematic stacking sequence of Si-C bilayers along the *c*-axis. In Fig. 3.20a, the dot images correspond to Si-C pairs and the alternate bright and dark bands correspond to the *ACB:ABC* stacking sequence; each comprises three Si-C double layers. A slightly thicker dark band, indicated by an arrow, can be seen in the middle of the figure. The band consists of four Si-C double layers and the local stacking sequence is *ACB:ACA:BCB*, which represents an extrinsic type stacking fault. HRTEM observations over a reasonable number of specimens revealed that most of the stacking faults are produced by an excess or lack of single Si-C double layer.

Figure 3.21 shows micrographs of the etched surface of the $(10\bar{1}0)$ wafer 60° inclined from the $[1\bar{1}00]$ growth direction prepared from a 6H $[1\bar{1}00]$ grown

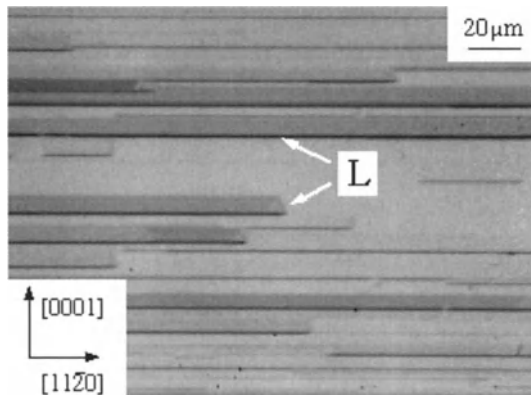


Fig. 3.19. Nomarski micrograph of the etched (1̄100) surface of a [1̄100] grown crystal

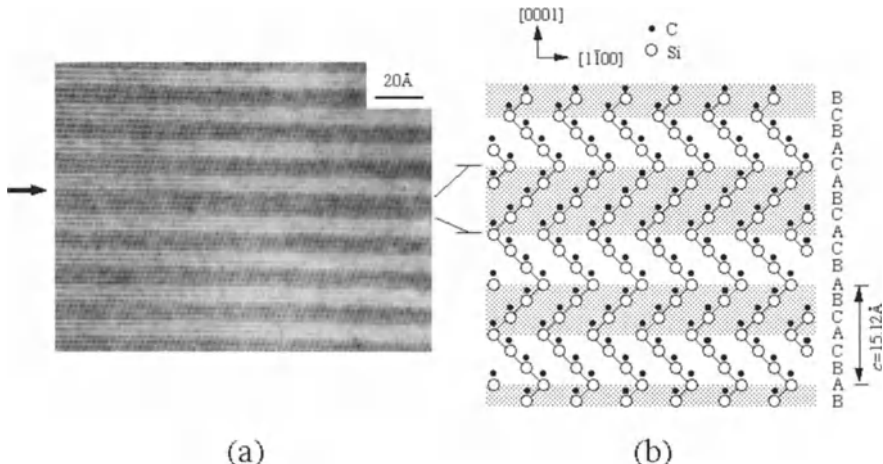


Fig. 3.20. (a) HRTEM micrograph of a stacking fault in a 6H [1̄100] grown crystal, and (b) a corresponding schematic stacking sequence of Si-C bilayers along the *c*-axis

crystal: each micrograph corresponds to (a) the top and (b) the middle parts of the crystal, and (c) the interface region between the seed and the grown crystals. The stacking faults appear as linear etch pits extending along the growth direction. As seen in the figure, the etch pit density increases as the growth proceeds. Once the stacking faults are generated, they proceed to grow and are not terminated. Stacking faults are scarcely observed in the seed crystal, and there are also very few stacking faults introduced at the interface between the seed and the grown crystals (Fig. 3.21c), implying that the stacking fault formation occurs throughout the entire growth process rather than at the initial stage.

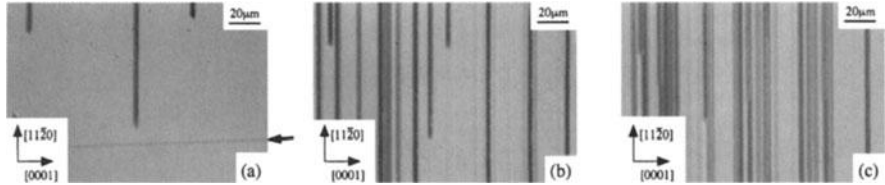


Fig. 3.21. Etched surfaces of $(10\bar{1}0)$ wafers sliced from 6H $[1\bar{1}00]$ grown crystal: the etched surfaces correspond to (a) the interface region between the seed and the grown crystal, and (b) the middle and (c) the top part of the crystal. The interface is indicated by an arrow

Stacking fault formation strongly depends on the crystal growth direction and grown polytype [67]. Table 3.2 summarizes the densities of stacking faults for the $[1\bar{1}00]$, $[1\bar{1}\bar{2}0]$ and $[000\bar{1}]$ grown crystals of the 6H and 4H polytypes. In particular, the 6H $[1\bar{1}00]$ grown crystal contains a large number of stacking faults, whose density is at least 10 times higher than that for the 6H $[11\bar{2}0]$ grown crystal and 10^3 times higher than that for the 6H $[000\bar{1}]$ grown crystal. By contrast, for 4H-SiC, the $[1\bar{1}00]$ and $[1\bar{1}\bar{2}0]$ grown crystals have similar densities of stacking faults, though both still contain a higher density of stacking faults than the 4H $[000\bar{1}]$ grown crystal.

Based on all these results, Takahashi *et al.* ascribed a major cause for the stacking fault formation to the SiC growth kinetics on the $(1\bar{1}00)$ surface [55]. Figure 3.22 illustrates the configuration of Si and C atoms of the 6H $(1\bar{1}00)$ surface seen from the $[1\bar{1}\bar{2}0]$ direction. The 6H $(1\bar{1}00)$ surface is assumed to comprise $(1\bar{1}02)$ and $(1\bar{1}0\bar{2})$ microfacets of three Si-C double layers, which are alternately arranged in the $\langle 0001 \rangle$ direction. As seen in the figure, the $(1\bar{1}02)$ and $(1\bar{1}0\bar{2})$ microfacets have identical bond configurations to $(000\bar{1})\text{C}$ and $(0001)\text{Si}$, respectively. The assumption of the $(1\bar{1}02)$ and $(1\bar{1}0\bar{2})$ microfacetting of the $(1\bar{1}00)$ surface is supported by TEM observations of the zigzag structure of stacking faults in the $(1\bar{1}00)$ prismatic plane [68].

When the nucleation occurs on the microfacet, there are two possible bonding configurations *S* (staggered) and *E* (eclipsed), as depicted in Fig. 3.22. The two configurations have a small energy difference [11], and thus, while configuration *S* is the most favorable in terms of bulk total energy, *E* is also kinetically established during growth. Stacking faults are caused by this

Table 3.2. Densities of stacking faults for 6H- and 4H-SiC crystals grown in various directions

Growth direction	Stacking fault density (cm^{-1})	
	6H	4H
$[1\bar{1}00]$	$\geq 10^4$	$10^2 - 10^3$
$[1\bar{1}\bar{2}0]$	$10^2 - 10^3$	$10^2 - 10^3$
$[000\bar{1}]$	≥ 10	≥ 10

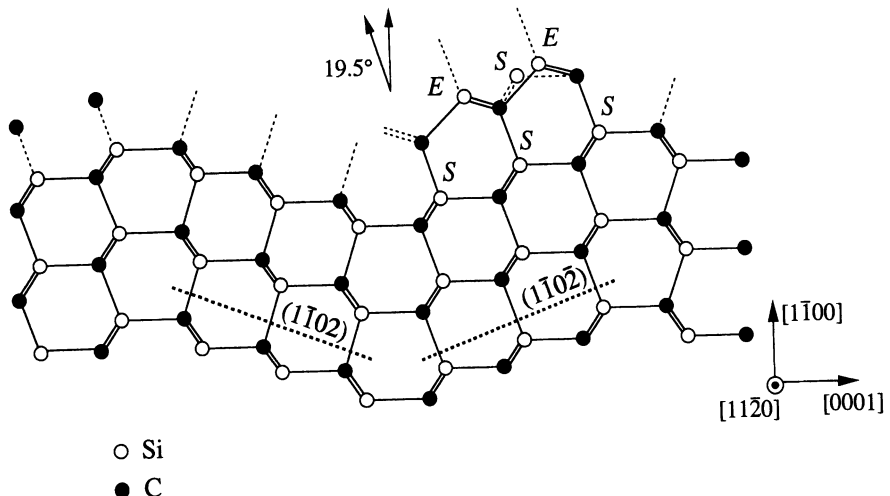


Fig. 3.22. Atomistic surface model of 6H (1100)

kinetically-induced misarrangement of surface adatoms. When a bilayer island with configuration E nucleates on the microfacet, it brings about regions of disregistry at the microfacet boundaries. Stacking fault formation may relax this disregistry and relieve the associated large localized strains at the boundaries.

The difference between 6H (1100) and 4H (1100) is the width of microfacets, narrower microfacets on 4H (1100). This causes a large difference in the nucleation behavior of surface adatoms, i.e., they more frequently nucleate at the microfacet boundaries. When a bilayer island nucleates over the microfacet boundary, the bond configuration is uniquely determined, and regions of disregistry do not occur.

The above surface kinetics model well accounts for the observed dependence of stacking fault density on the growth direction and the polytype of grown crystals; 4H-SiC crystals grown on the (1120) surface exhibit the lowest stacking fault density. Stacking fault density, however, is still high compared to the crystals grown on the (0001) surface. A similar mechanism to that on the (1100) surface is assumed also to govern the stacking fault formation on the (1120) growing surface, where occurrences result from the formation of the (1010) and (0110) facets on the (1120) growing surface. The (1010) and (0110) facets are likely to be kinetically induced on the (1120) growing surface since they are singular surfaces closest to (1120) (30° inclined from (1120)) and have a lower surface energy compared to (1120). On these (1010) and (0110) facets, stacking fault formation occurs in the same manner as on the (1100) surface. Therefore, to further reduce the stacking fault density in SiC crystals grown on the (1120) surface, establishing a more kinetically-controlled process is required at the (1120) crystal growth front.

Recently, it was found that an introduction of the off-angle at the $(1\bar{1}\bar{2}0)$ crystal growth surface would be a successful strategy to prevent stacking fault formation [69]. The effect of the off-angle growth on the stacking fault formation is illustrated in Fig. 3.23. Figure 3.23a shows the etched $(1\bar{1}00)$ surface of wafers vertically sliced along the growth direction from 4H-SiC crystals grown on a well-oriented $(1\bar{1}\bar{2}0)$ seed crystal, where the observed linear etch pits extending along the growth direction correspond to the stacking faults in the basal plane. As shown, a number of stacking faults were introduced during growth on a well-oriented $(1\bar{1}\bar{2}0)$ seed crystal. The stacking fault density, which was estimated at the near top growth surface region, was $100\text{--}150\text{ cm}^{-1}$.

The result for the growth on an off-oriented $(1\bar{1}\bar{2}0)$ seed crystal is shown in Fig. 3.23b. The direction and the degree of off-orientation were $[0001]\text{Si}$ and 10° degrees from the $(1\bar{1}\bar{2}0)$ surface, respectively. The growth conditions were the same as in Fig. 3.23a except for the off-orientation of seed crystal. As seen in the figure, very few stacking faults were detected for the growth on a 10° off-oriented $(1\bar{1}\bar{2}0)$ seed crystal.

The dependence of stacking fault density on the degree of off-orientation is summarized in Fig. 3.24, where the stacking fault density is plotted against the degree of off-orientation toward $[0001]\text{Si}$. As seen in the figure, the stacking fault density rapidly decreases as the off-orientation is increased. Though the average stacking fault density for the crystal grown on a 10° off-oriented seed

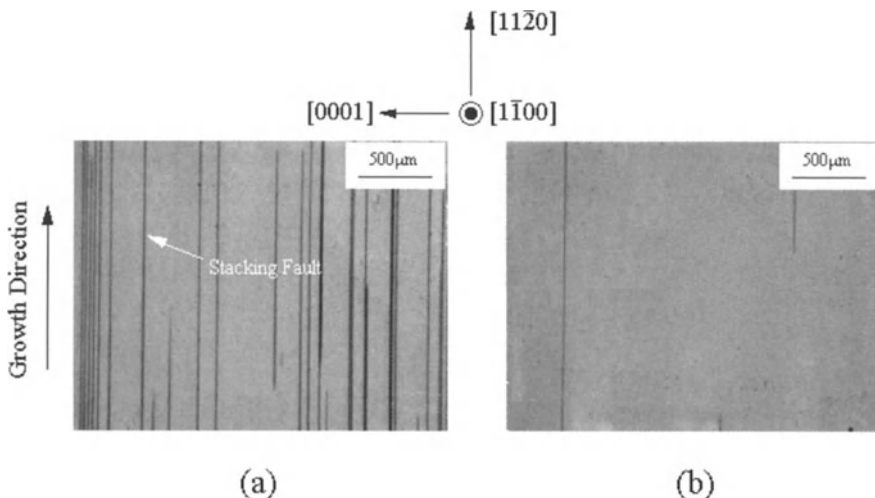


Fig. 3.23. Etched $(1\bar{1}00)$ surfaces of wafers sliced vertically along the growth direction from 4H-SiC crystals grown in the $[1\bar{1}\bar{2}0]$ direction on (a) a well-oriented seed crystal and (b) a seed crystal off-oriented by 10° toward the $[0001]\text{Si}$ direction. The observed linear etch pits extending along the growth direction correspond to stacking faults in the basal plane

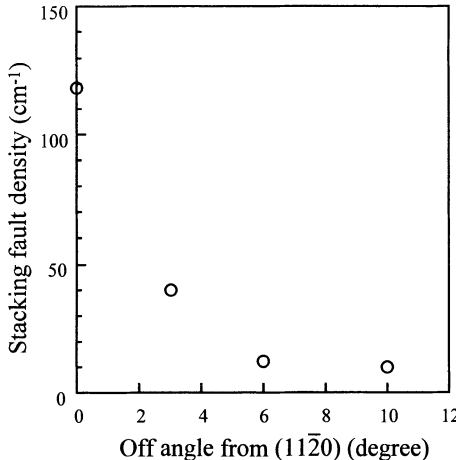


Fig. 3.24. Dependence of stacking fault density on the degree of off-orientation toward [0001]Si from the (11̄20) seed crystal surface

crystal was 10 cm^{-1} , significant portions of the grown crystal were free of stacking faults.

There are three possible directions for the off-orientation from the (11̄20) surface, i.e. [0001]Si, [000̄1]C and [1̄100]. 4H-SiC crystals were also grown on a (11̄20) seed crystal off-oriented toward [000̄1]C and [1̄100] and the growth on an off-oriented (11̄20) seed crystal toward [000̄1]C similarly resulted in the reduction of stacking fault density, while no such reduction was observed for the growth on an off-oriented (11̄20) seed crystal toward [1̄100]; the stacking fault density rather increased when the seed crystal was off-oriented toward [1̄100]. The introduction of the off-orientation of seed crystal toward $\langle 0001 \rangle$ is assumed to prevent the (10̄10) and (01̄10) facet formation through modification of the surface growth kinetics and suppress the stacking fault formation. The fact that off-orientation toward [1̄100] increased the stacking fault density lends support to this assumption.

3.8 Summary

The recent advance of SiC bulk crystal growth technology has given a great advantage to SiC-based semiconductor devices. SiC single crystals with a diameter of four inches can be grown by the seeded sublimation growth method. Considerable progress has been made in the polytype control and defect reduction of SiC crystals, and high-quality single-polytype SiC wafers are now available for device fabrication. Nevertheless, many aspects of the crystal quality and size are still being further improved. A better understanding of the crystal growth process and the defect formation mechanism is indispensable for producing SiC crystals with increased diameter and higher crystallographic

perfection. Efforts to address these problems are already under way, and more highly advanced SiC electronic and optoelectronic devices will become commercially available within the not too distant future.

Acknowledgments

This work was partly conducted under the management of the R&D Association for Future Electron Devices (FED) as part of the Ministry of Economy, Trade and Industry (METI) New Sunshine (NSS) program (R&D of Ultra-Low-Loss Power Device Technologies) supported by the New Energy and Industrial Technology Development Organization (NEDO).

References

1. *Silicon Carbide 1973, Proceedings of the 3rd Int. Conf. Silicon Carbide, Miami, Florida*, University of South Carolina Press, Columbia, South Carolina, 1973.
2. Yu.M. Tairov and V.F. Tsvetkov, "Investigation of growth processes of ingots of silicon carbide single crystals," *J. Cryst. Growth* **43**, 209–212 (1978).
3. Y. Sugawara, D. Takayama, K. Asano, R. Singh, J.W. Palmour and T. Hayashi, "12–19 kV 4H-SiC pin diodes with low power loss," in *Proceedings of 2001 International Symposium on Power Semiconductor Devices & ICs*, pp. 27–30, Osaka, Japan, 2001.
4. J. Tan, J.A. Cooper, Jr. and M.R. Melloch, "High-voltage accumulation-layer UMOSFET's in 4H-SiC," *IEEE Electron Device Lett.* **19**, 487–489 (1998).
5. R.A. Sadler, S.T. Allen, W.L. Pribble, T.S. Alcorn, J.J. Sumakeris and J.W. Palmour, "SiC MESFET hybrid amplifier with 30-W output power at 10 GHz," in *Proc. IEEE/Cornell Conf. IEEE Cat. No. 00CH37122*, 173–177, 2000.
6. V. Härle, N. Hiller, S. Kugler, B. Hahn and N. Stath, "Industrial aspects of GaN/SiC blue light emitting diodes in Europe," *Mater. Sci. Eng. B* **61–62**, 310–313 (1999).
7. Y.M. Tairov and V.A. Vodakov, "Group IV materials (mainly SiC)," in *Electroluminescence*, edited by J.I. Pankove, 31–58, Springer-Verlag, Berlin, 1977.
8. Ch. Gaberstroh, R. Helbig and R.A. Stein, "Some new features of the photoluminescence of SiC(6H), SiC(4H) and SiC(15R)," *J. Appl. Phys.* **76**, 509–513 (1994).
9. W.F. Knippenberg, "Growth phenomena in silicon carbide," *Philips Res. Reports* **18**, 161–274 (1963).
10. G.R. Fisher and P. Barnes, "Towards a unified view of polytypism in silicon carbide," *Phil. Mag. B* **61**, 217–236 (1990).
11. V. Heine, C. Cheng and R.J. Needs, "The preference of silicon carbide for growth in the metastable cubic form," *J. Am. Ceram. Soc.* **74**, 2630–2633 (1991).
12. F.C. Frank, "The growth of carborundum: dislocations and polytypism," *Phil. Mag.* **42**, 1014–1021 (1951).
13. R.C. Glass, D. Henshall, V.F. Tsvetkov and C.H. Carter, Jr., "SiC seeded crystal growth," *phys. stat. sol. (b)* **202**, 149–162 (1997).

14. G. Augustine, H. McD. Hobgood, V. Balakrishna, G. Dunne and R.H. Hopkins, "Physical vapor transport growth and properties of SiC monocrystals of 4H polytype," *phys. stat. sol. (b)* **202**, 137–148 (1997).
15. Y.M. Tairov and V.F. Tsvetkov, "Progress in controlling the growth of polytypic crystals," *Prog. Cryst. Growth Characterization* **4**, 111–162 (1982).
16. A. Ellison, "Silicon carbide growth by high temperature CVD techniques," Ph.D. dissertation, 183–188, Linköping University, 1999.
17. Yu.A. Vodakov, E.N. Mokhov, A.D. Roenkov and M.M. Anikin, "Effect of impurities on the polymorphism of silicon carbide," *Sov. Tech. Phys. Lett.* **5**, 147–148 (1979).
18. A. Ito, T. Kimoto and H. Matsunami, "High-quality 4H-SiC homoepitaxial layers grown by step-controlled epitaxy," *Appl. Phys. Lett.* **65**, 1400–1402 (1994).
19. M. Katsuno, N. Ohtani, J. Takahashi, H. Yashiro, M. Kanaya and S. Shinoyama, "Polytype and resistivity control of α -SiC by in-situ nitrogen doping during sublimation growth," in *Abstracts of the International Workshop on Hard Electronics*, p. 5, Tsukuba, Japan, 1997.
20. R.A. Stein, P. Lanig and S. Leibenzeder, "Influence of surface energy on the growth of 6H- and 4H-SiC polytypes by sublimation," *Mater. Sci. Eng. B* **11**, 69–71 (1992).
21. J. Takahashi, N. Ohtani and M. Kanaya, "Influence of the seed face polarity on the sublimation growth of α -SiC," *Jpn. J. Appl. Phys.* **34**, 4694–4698 (1995).
22. Yu.A. Vodakov, E.N. Mokhov, A.D. Roenkov and D.T. Saidbekov, "Effect of crystallographic orientation on the polytype stabilization and transformation of silicon carbide," *phys. stat. sol. (a)* **51**, 209–215 (1979).
23. R.I. Scace and G.A. Slack, "Solubility of carbon in silicon and germanium," *J. Chem. Phys.* **30**, 1551–1555 (1959).
24. J. Drowart, G.De. Maria and M.G. Inghram, "Thermodynamic study of SiC utilizing a mass spectrometer," *J. Chem. Phys.* **29**, 1015–1021 (1958).
25. G. Ziegler, P. Lanig, D. Theis and C. Weyrich, "Single crystal growth of SiC substrate material for blue light emitting diodes," *IEEE Trans. Electron Devices ED-30*, 277–281 (1983).
26. K. Koga, T. Nakata and T. Niina, "Single crystal growth of 6H-SiC by a vacuum sublimation method," in *Extended Abstracts of the 17th Conf. Solid State Devices and Materials*, Tokyo, 249–252, Japan Society of Applied Physics, Tokyo, Japan, 1985.
27. J. Takahashi, M. Kanaya and N. Ohtani, "Growth of large SiC single crystals," in *Extended Abstracts (The 41st Spring Meeting, 1994); The Japan Society of Applied Physics and Related Societies*, 30p-ZX-2, The Japan Society of Applied Physics, Japan, 1994 (in Japanese).
28. N. Ohtani, M. Katsuno, J. Takahashi, H. Yashiro and M. Kanaya, "Present status and future outlook of SiC crystal growth," in *Abstracts Book of the 5th National Conference on Silicon Carbide and Related Materials*, p. 13, Kyoto, Japan, 1996 (in Japanese).
29. N. Ohtani, T. Fujimoto, M. Katsuno, T. Aigo and H. Yashiro, "Growth and defect reduction of bulk SiC crystals," *Mater. Sci. Forum* **389–393**, 29–34 (2002).
30. Cree Inc., <http://www.cree.com>.
31. D. Hobgood, M. Brady, W. Brixius, G. Fechko, R. Glass, D. Henshall, J. Jenny, R. Leonard, D. Malta, St.G. Müller, V. Tsvetkov and C.H. Carter, Jr., "Status of large diameter SiC crystal growth for electronic and optical applications," *Mater. Sci. Forum* **338–342**, 3–8 (2000).

32. K. Koga, Y. Fujikawa, Y. Ueda and T. Yamaguchi, "Growth and characterization of 6H-SiC bulk crystals by the sublimation method," in *Amorphous and Crystalline Silicon Carbide IV*, Springer Proceedings in Physics, Vol. 71, edited by C.Y. Yang, M.M. Rahman and G.L. Harris, pp. 96–100, Springer-Verlag, Berlin, 1992.
33. J. Takahashi, M. Kanaya and Y. Fujiwara, "Sublimation growth of SiC single crystalline ingots on faces perpendicular to the (0001) basal plane," *J. Cryst. Growth* **135**, 61–70 (1994).
34. R.A. Stein, "Formation of macrodefects in SiC," *Physica B* **185**, 211–216 (1993).
35. R.C. Glass, L.O. Kjellberg, V.F. Tsvetkov, J.E. Sundgren and E. Janzén, "Structural macro-defects in 6H-SiC wafers," *J. Cryst. Growth* **132**, 504–512 (1993).
36. M. Dudley, S. Wang, W. Huang, C.H. Carter, Jr., V.F. Tsvetkov and C. Fazi, "White-beam synchrotron topographic studies of defects in 6H-SiC single crystals," *J. Phys. D: Appl. Phys.* **28**, A63–A68 (1995).
37. P.G. Neudeck and J.A. Powell, "Performance-limiting micropipe defects in silicon carbide wafers," *IEEE Electron Device Lett.* **15**, 63–65 (1994).
38. F.C. Frank, "Capillary equilibria of dislocated crystals," *Acta. Cryst.* **4**, 497–501 (1951).
39. H.M. Hobgood, D.L. Barrett, J.P. McHugh, R.C. Clarke, S. Sriram, A.A. Burk, J. Greggi, C.D. Brandt, R.H. Hopkins and W.J. Choyke, "Large diameter 6H-SiC for microwave device applications," *J. Cryst. Growth* **137**, 181–186 (1993).
40. V.F. Tsvetkov, S.T. Allen, H.S. Kong and C.H. Carter, Jr., "Recent progress in SiC crystal growth," *Inst. Phys. Conf. Ser.* **142**, 17–22 (1996).
41. N. Ohtani, J. Takahashi, M. Katsuno, H. Yashiro and M. Kanaya, "Defect formation during sublimation bulk crystal growth of silicon carbide," *Mater. Res. Soc. Symp. Proc.* **510**, 37–45 (1998).
42. N. Ohtani, M. Katsuno, T. Aigo, T. Fujimoto, H. Tsuge, H. Yashiro and M. Kanaya, "Step bunching behaviour on the {0001} surface of hexagonal SiC," *J. Cryst. Growth* **210**, 613–622 (2000).
43. J. Takahashi, N. Ohtani and M. Kanaya, "Structural defects in α -SiC single crystals grown by the modified-Lely method," *J. Cryst. Growth* **167**, 596–606 (1996).
44. J. Giocondi, G.S. Rohrer, M. Skowronski, V. Balakrishna, G. Augustine, H.M. Hobgood and R.H. Hopkins, "An atomic force microscopy study of super-dislocation/micropipe complexes on the 6H-SiC(0001) growth surface," *J. Cryst. Growth* **181**, 351–362 (1997).
45. P. Pirouz, "On micropipes and nanopipes in SiC and GaN," *Phil. Mag. A* **78**, 727–736 (1998).
46. N. Ohtani, M. Katsuno, T. Fujimoto, T. Aigo and H. Yashiro, "Surface step model for micropipe formation in SiC," *J. Cryst. Growth* **226**, 254–260 (2001).
47. N. Ohtani, M. Katsuno, J. Takahashi, H. Yashiro and M. Kanaya, "Evolution of macrosteps on 6H-SiC(0001): Impurity-induced morphological instability of step trains," *Phys. Rev. B* **59**, 4592–4595 (1999).
48. N. Ohtani, J. Takahashi, M. Katsuno, H. Yashiro and M. Kanaya, "Development of large single-crystal SiC substrates," *Electron. and Commun. in Japan Part 2* **81**, 8–19 (1998).
49. St.G. Müller, M.F. Brady, W.H. Brixius, G. Fechko, R.C. Glass, D. Henshall, H.McD. Hobgood, J.R. Jenny, R. Leonard, D. Malta, A. Powell, V.F. Tsvetkov,

- S. Allen, J. Palmour and C.H. Carter, Jr., "High quality SiC substrates for semiconductor devices: from research to industrial production," Mater. Sci. Forum **389–393**, 23–28 (2002).
50. J.P. Bergman, G. Pozina, C. Hallin and E. Janzén, "Carrier lifetime in 4H-SiC, studied by different optical techniques," in *Abstracts of International Conference on Silicon Carbide and Related Materials 1999*, No. 398, North Carolina, USA, 1999.
 51. M. Tuominen, R. Yakimova, R.C. Glass, T. Tuomi and E. Janzén, "Crystalline imperfections in 4H SiC grown with a seeded Lely method," J. Cryst. Growth **144**, 267–276 (1994).
 52. A. Ellison, H. Radamson, M. Tuominen, S. Milita, C. Hallin, A. Henry, O. Kordina, T. Tuomi, R. Yakimova, R. Madar and E. Janzén, "Wafer warpage, crystal bending and interface properties of 4H-SiC epi-wafers," Diamond Relat. Mater. **6**, 1369–1373 (1997).
 53. M. Katsuno, N. Ohtani, T. Aigo, H. Yashiro and M. Kanaya, "Investigation of low angle grain boundaries in modified-Lely SiC crystals by high resolution X-ray diffractometry," Mater. Sci. Forum **338–342**, 493–496 (2000).
 54. M. Katsuno, N. Ohtani, T. Aigo, T. Fujimoto, H. Tsuge, H. Yashiro and M. Kanaya, "Structural properties of subgrain boundaries in bulk SiC crystals," J. Cryst. Growth **216**, 256–262 (2000).
 55. K. Maeda, K. Suzuki, S. Fujita, M. Ichihara and S. Hyodo, "Defects in plastically deformed 6H SiC single crystals studied by transmission electron microscopy," Phil. Mag. A **57**, 573–592 (1988).
 56. M.H. Hong and P. Pirouz: to be published in J. Electron. Mater.
 57. M. Katsuno, N. Ohtani, T. Fujimoto, T. Aigo and H. Yashiro, "Evolution of crystal mosaicity during physical vapor transport growth of SiC," Mater. Sci. Forum **389–393**, 55–58 (2002).
 58. H. Yamaguchi, S. Nishizawa, W. Bang, K. Fukuda, S. Yoshida, K. Arai and Y. Takano, "Reflection and transmission X-ray topographic study of a SiC crystal and epitaxial wafer," Mater. Sci. Eng. B **61–62**, 221–224 (1999).
 59. A.R. Powell, S. Wang, G. Fechko and G.R. Brandes, "Sublimation growth of 50-mm diameter SiC wafers," Mater. Sci. Forum **264–268**, 13–16 (1998).
 60. D. Hofmann, R. Eckstein, M. Kölbl, Y. Makarov, St.G. Müller, E. Schmitt, A. Winnacker, R. Rupp, R. Stein and J. Völk, "SiC-bulk growth by physical-vapor transport and its global modelling," J. Cryst. Growth **174**, 669–674 (1997).
 61. H. Yano, T. Hirao, T. Kimoto, H. Matsunami, K. Asano and Y. Sugawara, "Anisotropy of inversion channel mobility in 4H- and 6H-SiC MOPSFETs on (11̄20) face," Mater. Sci. Forum **338–342**, 1105–1108 (2000).
 62. J. Senzaki, K. Fukuda, K. Kojima, S. Harada, R. Kosugi, S. Suzuki, T. Suzuki and K. Arai, "Significant improvement of inversion channel mobility in 4H-SiC MOSFET on (11̄20) face using hydrogen post-oxidation annealing," Mater. Sci. Forum **389–393**, 1061–1064 (2002).
 63. Z.Y. Chen, T. Kimoto and H. Matsunami, "Specular surface morphology of 4H-SiC epilayers grown on (11̄20) face," Jpn. J. Appl. Phys. Part 2 **38**, L1375–L1378 (1999).
 64. M. Satoh, "Annealing of implanted layers in (1100) and (11̄20) oriented SiC," Mater. Sci. Forum **389–393**, 773–778 (2002).

65. J. Takahashi, M. Kanaya and T. Hoshino, "Sublimation growth and characterization of SiC single crystalline ingots on faces perpendicular to the (0001) basal plane," *Inst. Phys. Conf. Ser.* **137**, 13–16 (1994).
66. J. Takahashi and N. Ohtani, "Modified-Lely SiC crystals grown in the [1 $\bar{1}$ 00] and [11 $\bar{2}$ 0] directions," *phys. stat. sol. (b)* **202**, 163–175 (1997).
67. J. Takahashi, N. Ohtani, M. Katsuno and S. Shinoyama, "Sublimation growth of 6H- and 4H-SiC single crystals in the [1 $\bar{1}$ 00] and [11 $\bar{2}$ 0] directions," *J. Cryst. Growth* **181**, 229–240 (1997).
68. I. Lhermitte-Sebire, J. Vicens, J.L. Chermant, M. Levalois and E. Paumier, "Transmission electron microscopy and high-resolution electron microscopy studies of structural defects induced in 6H α -SiC single crystals irradiated by swift Xe ions," *Phil. Mag. A* **69**, 237–253 (1994).
69. N. Ohtani, M. Katsuno and T. Fujimoto, "Reduction of stacking fault density during SiC bulk crystal growth in the [11 $\bar{2}$ 0] direction," *Jpn. J. Appl. Phys.* **42**, 277–279 (2003).

Crystal Growth of Silicon Carbide: Evaluation and Modeling

E. Pernot, M. Pons, and R. Madar

Silicon carbide ingots were grown by a sublimation method, also called the modified Lely method. The modeling and simulation of heat and mass transfer during the growth of single crystals and the characterization tools used, mainly X-ray imaging, polarized light microscopy, and Raman spectroscopy imaging, are described in this paper. These are powerful tools for a better understanding of the process and for its optimization.

The influence of pressure and geometry on the crystal shape, the growth rate, and the enlargement process was investigated. X-ray topography on as-grown ingots showed the influence of seed characteristics such as seed polarity or structural quality on the stabilization of the polytype and on defect propagation. The occurrence of macrodefects and microdefects was related to the thermal field by using thermodynamic modeling. Finally, the stress and the densities of structural defects in the wafer were evaluated by X-ray topography, birefringence imaging, and Raman spectroscopy. The relations between the stress, the distribution of defects, and the thermal gradient in the crucible have been quantified by simplified thermoelastic considerations.

4.1 Introduction

Wide-bandgap semiconductors are considered to be the materials of the future in the field of electronics. The specific properties of semiconductors such as diamond, silicon carbide, gallium nitride, and aluminum nitride make them likely candidates for the fabrication of electronic devices that perform better than silicon at high temperatures, high frequencies, and high power. SiC was one of the first semiconductor materials discovered, and is by far the most developed of the wide-bandgap materials. Although the semiconducting properties of SiC have been known for a long time, numerous technological obstacles have hindered any rapid electronic developments based on silicon carbide. Until recently [1–3], the lack of suitable SiC crystal growth processes was the key factor preventing the commercialization of SiC devices. Growth

of bulk single crystals is complex for two main reasons. The first one concerns the stability of the material. SiC does not melt under a reasonable pressure; rather, it sublimes incongruently, at temperatures greater than 2000 K. The techniques of growth from the melt used on a large scale for the fabrication of silicon and GaAs are consequently not applicable. The second reason comes from the multiplicity of polytypes; about 175 are known. Each of them has different electronic characteristics and can grow under apparently identical conditions. Only the 6H and 4H polytypes are now commercially available. In this paper, our recent results concerning SiC bulk growth technology are summarized from an academic viewpoint. The originality of our results lies in an integrated research program taking into account fabrication, process modeling, and characterization. Step by step, virtual modeling was used to separate the intricate mixture of phenomena leading to bulk growth. Some quantification of macroscopic problems and some guidelines have resulted and will be presented. Different characterization techniques were used to visualize the nature of the polytypes, stress, and structural defects such as dislocations or subgrain boundaries. These methods, X-ray topography, birefringence imaging, and Raman spectroscopic imaging, will be presented and the results discussed.

The aim of this paper is to quantify some of the relations between growth conditions, defect formation, and ingot shapes.

4.2 History of Crystal Growth

Classical single-crystal growth techniques such as the Czochralski or Bridgman technique cannot be considered for the growth of silicon carbide crystals. In fact, under atmospheric pressure, SiC does not exist in the liquid state. It will, however, sublime under atmospheric pressure above 2000 K. This is why the majority of growth techniques are based on the physical vapor transport of SiC. Tentative attempts at the growth of SiC have been made by dissolving silicon and carbon in baths of scandium, terbium, or praseodymium silicides. However, the low solubility of carbon in these alloys and the contamination induced by the metals in the bath make this process complex. Hence most of the research efforts across the world are concentrating on growth by physical vapor transport, for which the basic technique is the sublimation of powdered SiC, transport in the gaseous state of the products formed by sublimation, and lastly condensation and crystallization.

In 1955 Lely proposed a method that enabled one to process very pure and good-quality silicon carbide crystals, which opened the door to the development of microelectronics based on SiC. The Lely method of growth is the following. A hollow, porous cylinder of SiC is placed inside a graphite crucible. The crucible is then heated to 2700 K and placed in an atmosphere of argon. The graphite cylinder is then heated on the sides resistively. The upper and lower parts of the graphite crucible are designed to dissipate some

of the heat through radiation. A temperature gradient is therefore established between the heart of the crucible and its outside: the temperature on the interior surface of the SiC cylinder is lower than that of the walls of the graphite. The gases produced through the sublimation of SiC pass through the porous cylinder to condense on the colder inner wall. The best crystals in terms of size and crystal defects are obtained at very low temperature gradients (lower than 5 K/cm). The crystals obtained by Lely's method are wafers of hexagonal form and are mostly of 6H-SiC type.

The crystalline quality of the crystals is very good, as the growth occurs with no constraints from the seeds spontaneously formed. The crystals have a low density of dislocations ($\sim 100 / \text{cm}^2$), and the misorientation is about 10 arcsec. The main inconvenience of the Lely process is that the single crystals are limited to a maximum size of just over 1 cm². It is difficult to use SiC substrates with a hexagonal and irregular form and of only 1 cm² in industry. Therefore a new technique for single-crystal growth was needed in order to produce SiC substrates of larger size but still keeping the good crystalline quality.

In 1978, Tairov and Tsvetkov introduced a modification of Lely's method of crystal growth [4]. In order to control of the polytype of the crystals produced by spontaneous nucleation on the graphite walls, they introduced a SiC single-crystal seed into the growth cavity. Physical vapor transport is driven by the temperature gradient between the powdered source and the surface of the seed (Fig. 4.1).

The powder is placed in the lower half of a graphite crucible, and the single-crystal seed is stuck on the graphite lid with carbonized sugar or graphite glue. In our experimental setup (Fig. 4.2), SiC powder is also loaded onto the periphery of the crucible as a thin-walled cylinder, as in the Lely method [5].

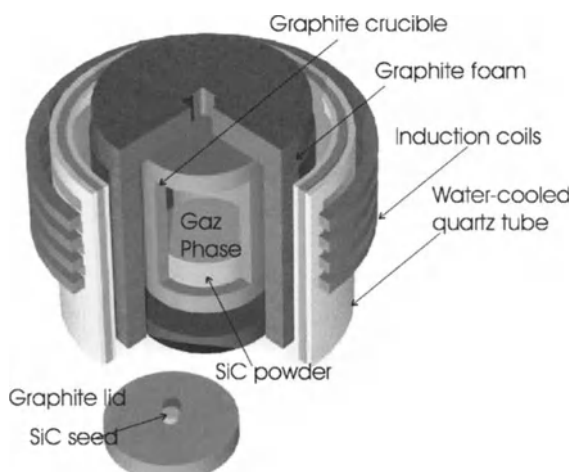


Fig. 4.1. The modified-Lely-method crucible for the fabrication of SiC single crystals

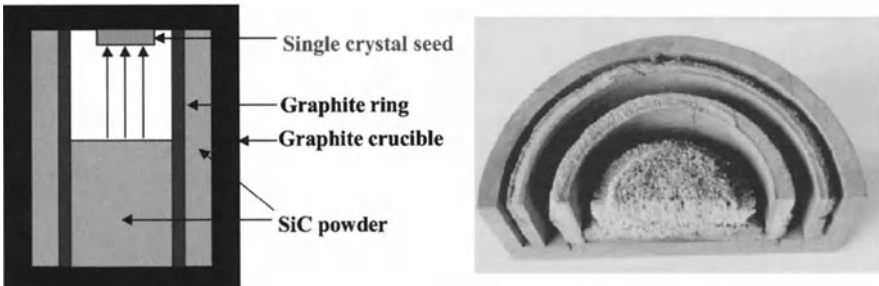


Fig. 4.2. (a) Schematic representation of the crucible, and (b) view of half of the bottom of the crucible after an experiment

This allows us to reduce the influence of Si leakage and its reaction with the graphite walls. The main interest of this growth method is that it allows one to obtain several circular single-crystalline slices from the same ingot, as in the case of silicon crystal growth.

The viability of this growth technique for obtaining SiC single-crystal substrates of large diameter has been proved by several different laboratories. In 1999, CREE presented the first SiC wafers of 100 mm diameter at the Raleigh international conference in the USA [2]. Concurrently with the progress made in enlarging the substrate size, the reduction of the micropipe density is also striking. The improvement in the quality of crystals makes the production of power devices that need an active surface area of around 1 cm^2 without micropipes possible.

The next section presents tools for the modeling and simulation of the growth procedure. They provide additional methods for completing our knowledge about the formation of the defects and for linking the materials science with process parameters such as crucible geometry, temperature field, and pressure in the reactor.

4.3 Modeling and Simulation of the Growth Procedure

4.3.1 Introduction

It is obvious that improvement in SiC growth technology is occurring through extensive experimentation. However, the advances made in process modeling and in the various tools for numerical simulation [6–23] prove the effectiveness of modeling and simulation for the understanding of problems [7,13,22,24–27] and the design of equipment [14,28–30]. This effort was initially motivated by the need for a better knowledge of the local temperature range in the cavity. The modeling and simulation allow one to acquire the thermal history of the growth, and this information completes ongoing experimental efforts.

The heat transfer phenomena include conduction, convection, radiation, heating through induction, and the latent heat of sublimation and condensation at the gas–solid interface. It was recently demonstrated that minor modifications in the reactive cavity were part of the many causes of the creation of defects during growth. Furthermore, a precise knowledge of the thermo-physical properties of the component materials of the reactor as well as of the powder, monocrystalline and polycrystalline forms of SiC is essential for obtaining realistic results [30, 31].

The modeling and simulation of heat transfer are not sufficient to determine the rate of growth and the shape of the crystal. Mass transfer models must therefore be coupled to the preceding phenomena as well as to thermodynamic and kinetic databases.

We are primarily interested in SiC ingots grown by the modified Lely method with graphite walls of the reactive cavity. Other, similar procedures are also in use. These use tantalum walls or a short distance between the powder and the seed (sandwich sublimation method) [32, 33].

First of all, the different models and the database sets will be described. They will be applied to the standard configuration in order to visualize the different macroscopic fields. Secondly, the influence of geometric modifications on the thermal history of the cavity will be discussed. The first series of simulations were carried out at the beginning of growth. The growth of ingots 8 to 10 mm in size provokes geometric modifications that are not insignificant in view of the dimensions of the reaction cavity (15 to 20 mm). The modifications of the local thermal field in the cavity will then be presented as a function of the stage of crystal growth.

4.3.2 Modeling and Databases

For two-dimensional axisymmetric geometry, a software package has been built from commercial and in-house software packages. The current knowledge of thermal, electrical, and chemical databases has also been inserted.

Thermodynamic Modeling

The thermodynamic calculations were carried out by minimization of the total free energy of the Si–C–Ar system in the temperature range 2300–3000 K. A self-consistent set of data was generated for the gaseous molecules from a literature review, measurements, and heat capacity and entropy calculations using recent results on molecular structures, vibrational frequencies, and electronic spectra. Nine gaseous species in addition to argon (Si_1 , Si_2 , Si_3 , C_1 , C_2 , C_3 , SiC , Si_2C , and SiC_2) and three condensed phases (SiC , Si , and C graphite) were considered [8]. The parameters introduced in the calculations were the temperature, the crucible volume, and the initial quantities of argon and solid silicon carbide in the source.

Gas and Surface Chemistry

A comprehensive capability to simulate multistep gas and surface chemistry must be available. Large sets of multistep reactions or thermodynamic equilibria must be handled in the code. The surface chemistry is treated by considering a complete reaction–diffusion balance at the surface to obtain the surface concentrations of species. The heat release from the gas/surface reactions are included in the model.

The use of local thermodynamic equilibrium (LTE) assumes an infinite length scale or timescale. We have checked that mass transport computations linked with LTE can give the trends in the crystal shape and in the influence of pressure, but they give too high an absolute growth rate. High-temperature spectrometry (2000–2300 K) was used to evaluate sublimation coefficients (Table 4.1). It is clear that the chemical system does not reach thermodynamic equilibrium. One order of magnitude has been measured between the equilibrium partial pressure and the measured pressure (Fig. 4.3). These data have now to be included in the previous models to compute the growth rates and crystal shapes.

Table 4.1. Measured values of the evaporation coefficient as compared with literature data [13, 22]

Mixture	Gas species	Evaporation coefficient
SiC + C powder	Si ₁ (g)	0.052
Norton HP100F	Si ₂ C(g)	0.060
	SiC ₂ (g)	0.080
SiC + TaC + C (powder)	Si ₁ (g)	0.077
	Si ₂ C(g)	0.079
	SiC ₂ (g)	0.010
	Si ₂ (g)	0.010

Induction Heating and Temperature Distribution

Electromagnetodynamics must be coupled with heat transfer, especially radiative heat transfer within the growth cavity. In our code, the radiation model is tightly coupled to the fluid transport, conjugate heat transfer, and chemistry models to ensure energy conservation.

These calculations make use of the materials database, which includes the electrical and thermal conductivities of the crucible and insulation materials, the material properties of the source and the boule, the gas species present and the associated reactivity data, the induction frequency, and the current density. The current database has been partially validated by external and indirect measurements.

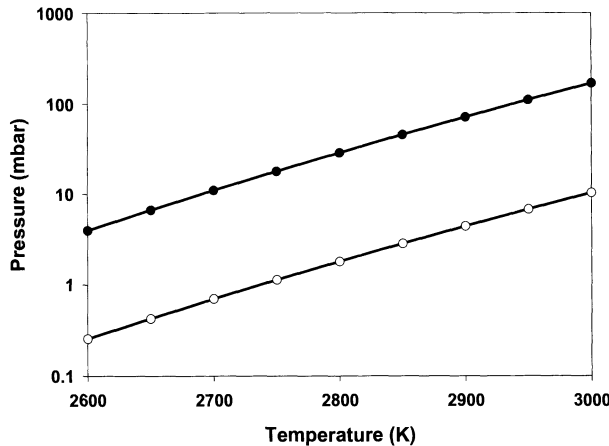


Fig. 4.3. Total pressure of reactive gas species over solid SiC as a function of temperature with (○) and without (●) taking evaporation coefficients into account

Multicomponent Fluid Transport

The fluid transport model is based on the low-pressure kinetic theory of gases. Transport coefficients such as viscosity, conductivity, specific heat, diffusivity, and thermodiffusion coefficients are calculated as local functions of temperature, pressure, and composition. The Stefan–Maxwell formulation for diffusive transport ensures complete mass conservation of all species in the system. The transport database is interactive with the calculations and is obtained from the kinetic theory of gases.

For the modified Lely method with a graphite crucible, within the range of experimental parameters investigated, we have verified that the natural convective transport of heat and of chemical species can be neglected when compared with diffusive transport and heat conduction and radiation.

4.3.3 Selected Results for Heat Transfer

A General Overview of the Simulation Results

A generic representation of the different macroscopic fields is presented in Fig. 4.4. Contours of the magnetic vector potential for a five-turn coil and a frequency of 120 kHz are shown in Fig. 4.4a. A large amount of energy is absorbed by the susceptor (Fig. 4.4b) within a thin skin depth. A temperature field is established inside the reactor (Fig. 4.4c). In our experiments, a thermal gradient of less than 80 K cm^{-1} is typical (see zoom in Fig. 4.4d).

The value of the growth rate is determined by the growth temperature, the total pressure in the system, the temperature difference between the surfaces of the source and seed, and the seed–source distance. It is important to note, at this stage, that the challenge is to control small temperature differences

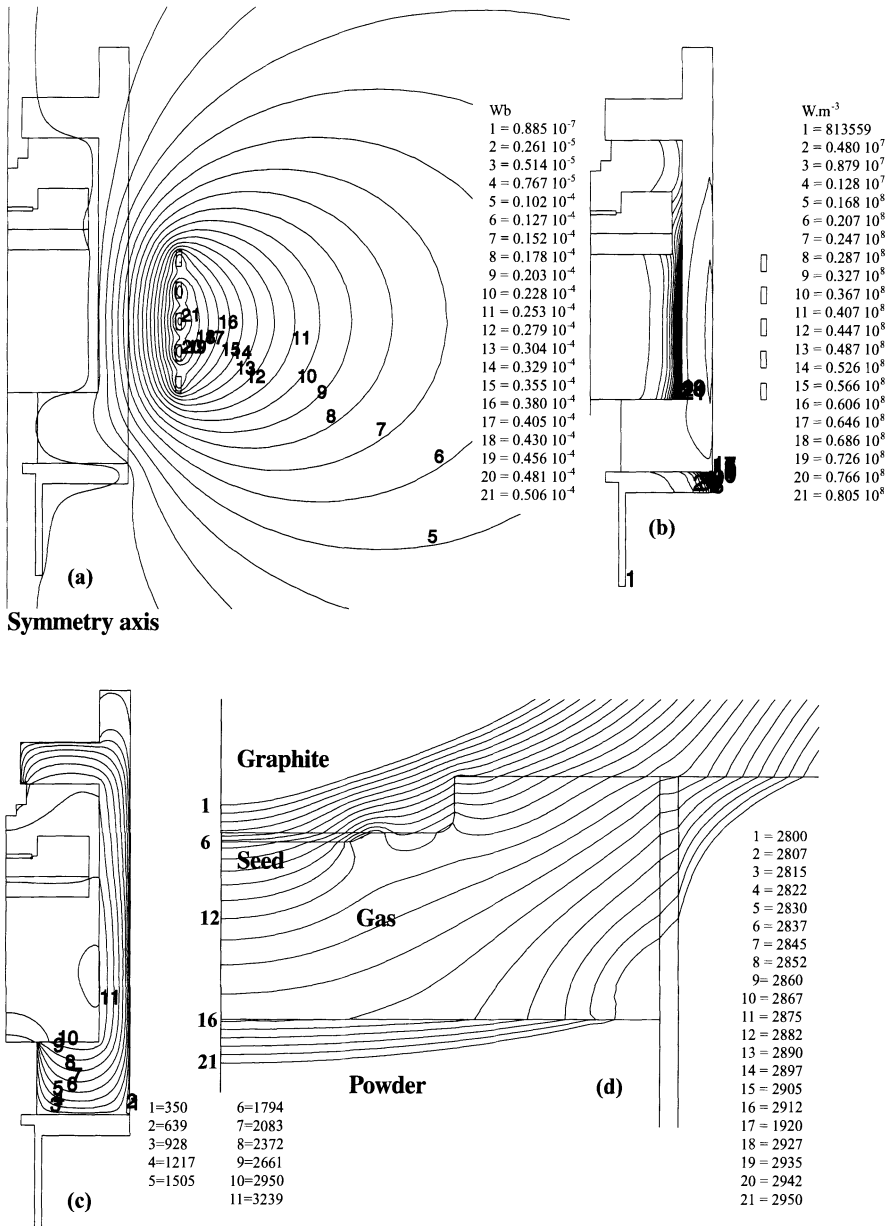


Fig. 4.4. Sectional view of the right part of the axisymmetric reactor; (a) potential vector, (b) Joule losses, (c) temperature field, (d) temperature field in the cavity ($f = 120$ kHz)

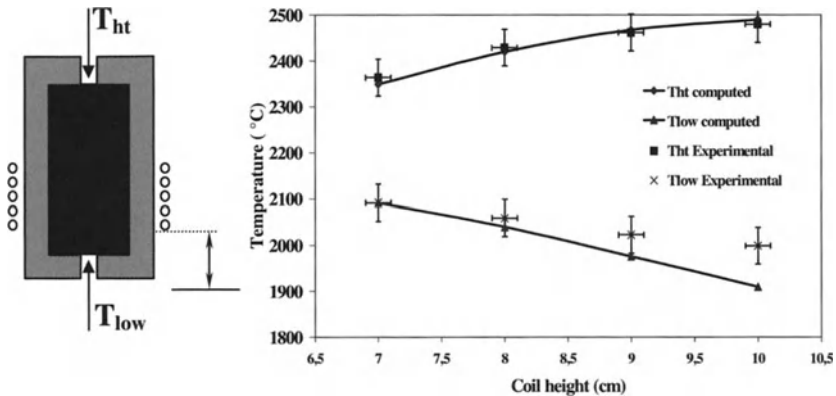


Fig. 4.5. Comparison of experimental and computed results as a function of coil position

(less than 100 K) in the gas cavity, as compared with the total temperature difference (about 2500 K).

This kind of simulation was validated by changing the frequency, current, and coil position (Fig. 4.5). The electromagnetic numerical tool seems able to give guidelines for a better control of the temperature field in the cavity.

Heat Transfer: Influence of the Diameter of the Pyrometric Holes

The next example deals with the ability of the simulation tools to predict the influence of any modification of the crucible design on the thermal field

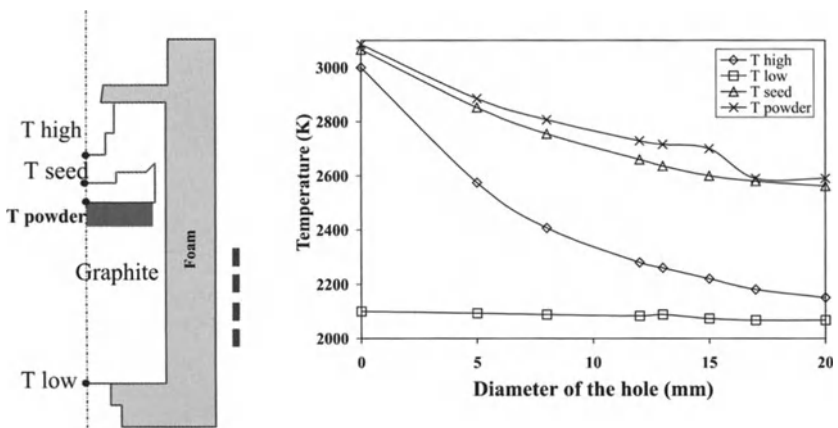


Fig. 4.6. Influence of the diameter of the hole used for pyrometric measurements on the calculated temperature of different parts of the reactor along the symmetry axis

inside the reaction chamber. We shall discuss one example, the influence of modification of the size of the hole in the graphite lid (Fig. 4.6). A simulation of the variation of the axial temperature as a function of the diameter of the hole at the back of the seed crystal is also shown. The thermal gradient can be strongly increased by increasing the diameter of the hole. We shall discuss later what the implications of such modifications are.

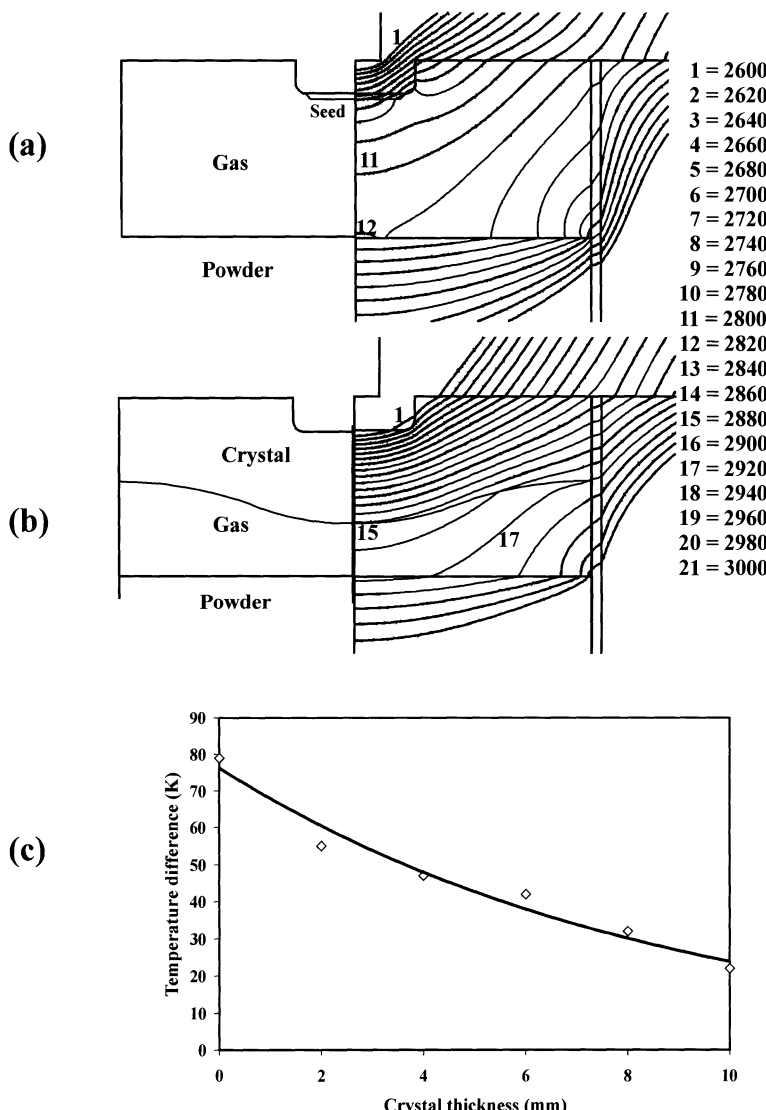


Fig. 4.7. Influence of the crystal thickness on the thermal field and on the axial temperature difference in the cavity

Heat Transfer: Influence of the Growing Crystal

Many simulations have been performed at the beginning of the growth process. Nevertheless, it is also important to simulate the evolution of the temperature field as the growth proceeds. In fact, during the growth process, the distance between the crystal and the powder varies. The shape of the reaction chamber is modified and one must take into account the variation of the electrical and thermal conductivities of the SiC powder due to its sintering. An example of the evolution of the thermal field inside the reaction chamber as the crystal grows is given in Fig. 4.7. When the length of the boule increases, the radiative transfer inside the crucible leads to lower values of the axial and radial temperature differences. An exact knowledge of this evolution is of importance for further discussions about the modeling of the crystal shape, the stress pattern, and the defect, dislocation, and micropipe densities.

Heat Transfer and the Scaling Up of the Reactor

It is possible to propose a design for the scaling up of the reactor described above. The size of the pedestal supporting the seed was changed from 30 to 50 mm and all dimensions of the different parts of the reactor were increased. It is possible, by changing the frequency, to obtain a temperature distribution in the cavity of the scaled-up reactor (right of Fig. 4.8) similar to that of the

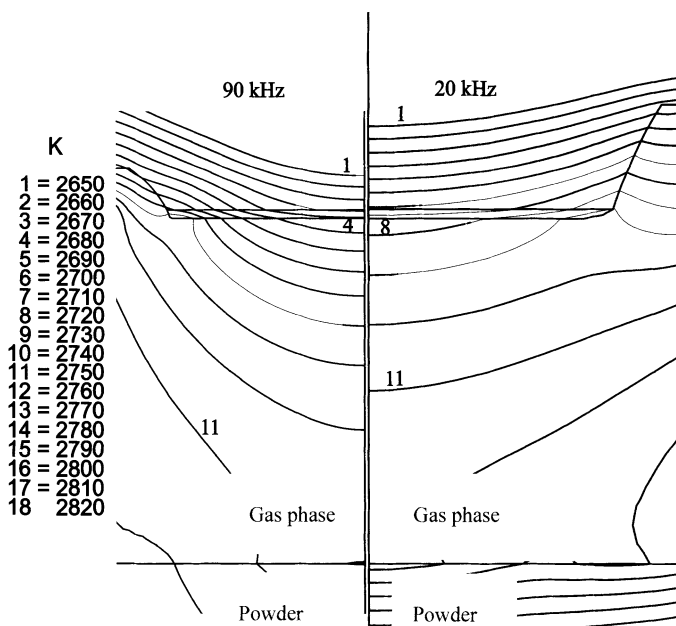


Fig. 4.8. Influence of heating frequency on the scaled-up reactor

standard reactor (left of Fig. 4.8). This kind of quantification does not give all the keys to success but may allow one to minimize design problems.

4.4 Crystal Evaluation Methods

To improve the crystalline quality of SiC wafers grown by the modified Lely method, it is necessary to identify the defects and to evaluate their density. For that purpose, several additional methods were used.

The polytype identification was generally performed by X-ray diffraction, Raman spectroscopy, and photoluminescence at low temperature. The crystal defect densities and distributions were assessed by X-ray diffraction imaging, also known as X-ray topography, polarized-light microscopy, and optical microscopy on samples chemically etched in molten KOH at 500 °C for 15 min in order to distinguish between screw and edge dislocations, hollow defects such as macrodefects or micropipes [34, 35], low-angle boundaries between grains, and inclusions. The following sections described polarized-light microscopy, X-ray diffraction imaging, and Raman spectroscopy imaging.

4.4.1 Optical Microscopy

The Polarized-Light Technique

Wafers cut from the as-grown ingot were characterized by optical microscopy using white light. Transmission micrographs were recorded using a polarizing microscope with a crossed analyzer. This technique allows one to reveal strains accompanying micropipes and grain boundaries via the photoelastic effect, and polytype inclusions with different refractive-index values.

The Rotating-Polarizer Technique

This recent characterization method is both a quantitative and a qualitative optical imaging technique to study the stress in a transparent, birefringent material [36, 37]. The phenomenon of optical linear birefringence is a result of anisotropy within a sample, leading to a variation of the refractive index n as a function of the polarization of the incoming light. This variation can be represented by an ellipsoid, called the indicatrix, which is described by three principal refractive indices. For any general direction of the light, an elliptical cross section of the indicatrix is observed, the anisotropy then being given by the difference in length of the axes of the ellipse. Figure 4.9 shows such an elliptical section, where the refractive indices are n_1 and n_2 , and the slow direction (largest refractive indices) is oriented at an angle φ from the horizontal. The difference in the refractive index $\Delta n = n_1 - n_2$ implies that two different polarizations will emerge from the sample, with a phase difference $\delta = \Delta n L 2\pi/\lambda$, where L is the sample thickness and λ is the wavelength

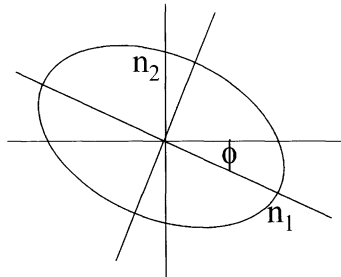


Fig. 4.9. The optical indicatrix: φ is the angle between the slow vibration direction of the light and the horizontal direction

of the light involved. In our case λ is equal to 580 nm. Thus, a beam of linearly polarized light will, in general, when passing through a birefringent sample, become elliptically polarized with a phase difference δ . In addition, the amplitude difference depends on the inclination angle φ between the incoming electric field and the axes of the ellipse.

The birefringence imaging system consists of a polarizing microscope fitted with a computer-controlled rotating polarizer and a circular analyzer. The formula describing the intensity passing through this system is $I = (I_0/2)[1 + \sin[2(\alpha - \varphi)] \sin \delta]$, where α is the orientation of the polarizer and I_0 is the incident light intensity. The values of the transmittance I , the phase difference δ (or the retardation $|\sin \delta|$), and the orientation φ can be obtained by varying the angle α . A CCD camera is used to record these three quantities for each pixel, and false-color or gray-scale images are then reconstructed to display them.

4.4.2 X-Ray Diffraction Imaging (Also Called Topography)

In white-beam synchrotron diffraction imaging [38, 39], the most commonly used topographic technique in this paper, the sample is just placed into the beam without any need for exact adjustment. Many lattice planes will find the reflection condition and form a Laue pattern, so that several topographs can be recorded simultaneously within one exposure on the film; see Fig. 4.10. In the samples investigated, it is easy to identify the contrast coming from dislocations, inclusions and misorientations. A fundamental advantage of this technique as compared with the monochromatic technique is that the very strongly deformed regions of the crystal are fully imaged with the white beam, generating more or less strongly distorted topographs.

The experiments were performed using synchrotron radiation at the ID19 and BM5 beam lines at the European Synchrotron Radiation Facility (Grenoble, France). The topographs in white-beam mode were recorded as Laue patterns on Kodak Industrex SR films with a typical exposure time between 0.1 s and 30 s and a crystal-to-film distance between 20 cm and 40 cm. The spatial resolution is about 5 μm .

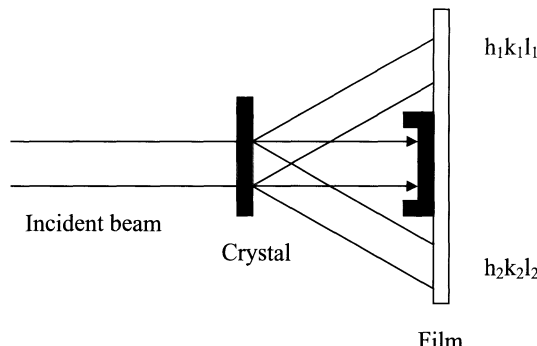


Fig. 4.10. Schematic representation of the experimental setup for white-beam synchrotron topography in transmission mode

Investigation of Ingots

The section technique of diffraction topography allows the visualization of deformations and misorientations within a “virtual” slice of a single crystal by restricting the incident beam width in one direction using a slit. The experimental setup is schematically drawn in Fig. 4.11a. In the case of very bulky samples (thicknesses of a few cm), this is a simple way to avoid the projection of a huge crystal volume onto a two-dimensional detector. This “virtual” projection is primarily useful if the crystalline quality of the sample investigated is not very high, as in the case of SiC, unlike industrial Si crystals.

Section topographs recorded at different positions of the incident beam on the sample, together with the use of four distinct geometries, schematically depicted in Fig. 4.11, allow the determination of the three-dimensional shape of defects inside the ingot. In the case of 4H-SiC, owing to the 8° off-axis orientation of the seed, the growth is not symmetric, and it is useful to record topographs with four positions with respect to the axis of growth.

The “horizontal” sections were performed with the main axis of a cylindrical ingot vertical and the *c*-axis (perpendicular to the facet visible on the top of each ingot) pointed upwards and to the left with respect to the incident beam direction; see Fig. 4.11a and 4.11b, respectively. Accordingly, the horizontal sections correspond to areas of the ingot formed approximately at the same moment of crystal growth.

The “vertical” sections were carried out with the main axis of the ingot lying along the incident beam direction and with the *c*-axis pointed upwards and to the left with respect to the beam direction; see Fig. 4.11c and 4.11d, respectively. The vertical sections allow one to visualize the seed–crystal interface and the propagation of a given defect during crystal growth. To study growth from on-axis seeds, as in the case of 6H-SiC, only one horizontal geometry and one of the vertical geometries were used, the facet being at the center of the ingot.

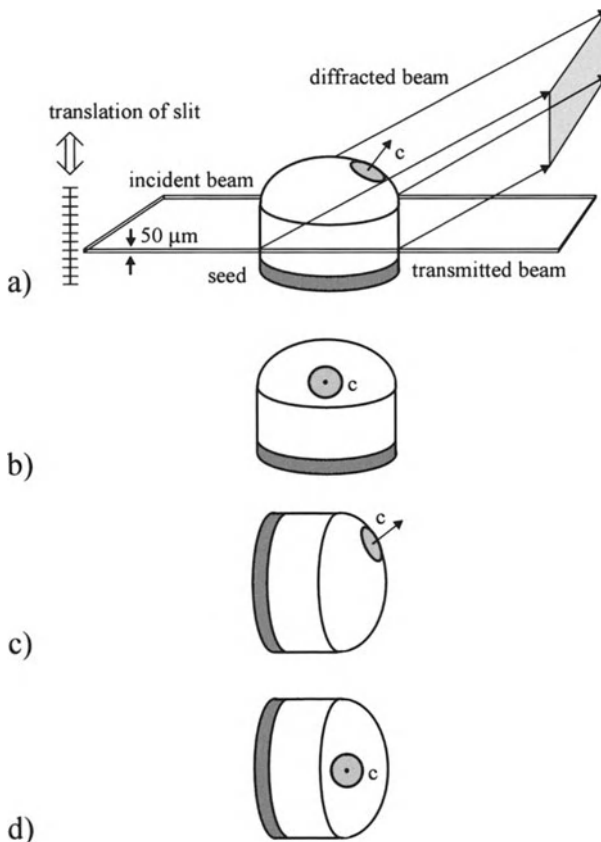


Fig. 4.11. Experimental arrangement for section topography on an off-axis ingot with the possibility of modifying the incident beam position on the sample by displacement of the slit. Four geometries of an ingot with respect to the facet perpendicular to the *c*-axis are presented: (a) and (b) horizontal sections, and (c) and (d) vertical sections

Investigation of Wafers

Two topographic techniques were used to investigate the structural defects in the wafers. White-beam projection topography in transmission shows the defects inside the bulk of the sample. In contrast, white-beam back-reflection topography has the advantage of investigating only a reduced thickness near to the surface of the crystal. In our case this thickness is about 20 μm. It is a very useful technique for studying an epilayer, for example.

Screw and edge dislocations induce some contrast in both kind of topographic images. When $\mathbf{b} \cdot \mathbf{g} = 0$, where \mathbf{b} is the Burgers vector of the dislocation and \mathbf{g} is the diffraction vector, the contrast associated with the dislocation is minimal. When the face of the wafer is approximately perpendicular to the *c*-

axis, the dislocations with their Burgers vector parallel to the c -axis, i.e. screw dislocations with $\mathbf{b} \parallel \mathbf{c}$ and basal-plane edge dislocations, are studied more easily by white-beam back-reflection topography because the recorded reflections are often 000ℓ ones. In contrast, in the case of transmission topography, the reflective crystallographic planes are often almost parallel to the prismatic planes of the hexagonal structure of 4H and 6H-SiC. Hence, the diffraction vector is almost perpendicular to the c -axis. The dislocations studied by this method are, rather, those which have their Burgers vector perpendicular to the c -axis, for example edge dislocations parallel to the c -axis.

4.4.3 Raman Spectroscopy Imaging

Raman spectroscopy is a characterization method sensitive to the stress in a crystal, and also to the doping and charge carrier mobility in silicon carbide. Raman microprobe imaging was performed at room temperature. Raman spectra were recorded using a Dilor XY multichannel spectrometer and a CCD detector. Measurements were carried out in the backscattering geometry from the (0001) face of the sample using the 514.5 nm line from an argon ion laser for excitation. The incident laser power was 10 mW at the surface of the sample. The light was focused to a spot 2.5 μm in diameter, with a penetration depth of 20 μm . Calibration of each Raman spectrum was performed using plasma lines of the laser.

4.4.4 Some Conclusions

These characterization tools allow the investigation of defect propagation during ingot growth and allow one to evaluate the structural quality of ingots and wafers. In the next sections, numerous characterizations and some examples of simulations will be set out, with the objective of understanding the complex relationship that exists between the parameters of the process, the shape of the crystal, and the occurrence of defects. Numerous questions and conflicts must be resolved and quantified: what is the influence of the Si/C ratio, the role of thermal gradients at the surfaces, the role of pressure, and the importance of thermal stress compared with stresses that arise from growth or from misorientation? Recent experimental results will complete this presentation to verify, validate, and compare the trends predicted by the modeling.

4.5 Results of Modeling and Characterization

4.5.1 Introduction

In view of the increasing importance of silicon carbide in electronic device applications, it may seem quite surprising that a good understanding of the nature of the structural defects and their formation during the crystal growth of

this material has not been achieved. This situation results in part from the fact that the material itself is quite complex, crystallizing into several modifications known as polytypes, whose c parameters vary with the stacking sequence [40]. More than 175 different polytypes have already been reported, the 3C, 4H, 6H, and 15R polytypes being the most familiar. The nature of the lattice defects has already been studied, and these defects have been categorized as surface strain, internal strain centers, long-range elastic deformations, dislocations, inclusions, and hollow defects – micropipes and macrodefects [41–46].

In this section, we describe the use of modeling to understand the influence of the pressure and of the geometry of the crucible on the growth rate and the crystal shape. The ingots were evaluated by optical microscopy and synchrotron diffraction imaging. Thus, the influence of the seed polarity, the enlargement, the evolution of the polycrystal around the single crystal, and the propagation of defects were studied. Finally, the macrodefects, the microdefects, and the general stress were identified and evaluated by X-ray topography, birefringence imaging, Raman spectroscopic imaging, and etching. The relations between these structural defects and the growth conditions were analyzed using macroscopic modeling.

4.5.2 Multicomponent Mass Transport and Crystal Growth Rate

Evaluation of Mass Transfer

A mass transfer analysis linked with previously measured evaporation coefficients allows computation of the fluxes of carbon- and silicon-containing gaseous species and of the subsequent growth rate and shape of the crystal. Careful attention must be paid to the deposited flux, as the geometry evolves owing to the crystal growth. The calculated temperature field at different growth times showed that the temperature gradient decreases and, subsequently, the growth rate decreases. Only results for the Crystal shapes in the first hour of the reaction (about 1 mm of growth) are presented, for better clarity.

The calculations were performed for a fixed geometry for the growth cavity and a fixed temperature profile. Only the value for the total pressure was varied, by adding an appropriate amount of argon. The growth rate is determined by the total carbon flux normal to the surface [10]. This carbon flux is drawn for an axially symmetric configuration in Fig. 4.12. On the left side of the schematic drawing, the total pressure in the chamber is 13 mbar, and on the right side it has been adjusted to 4 mbar. The carbon flux profile for the higher pressure is almost flat at the early stages of the single-crystal growth. Almost all the arrows are normal to the surface. The growth rate is around 0.6 mm/h, which is observed experimentally. The profile changes for the lower growth pressure. It is much more convex, especially close to the edge of the seed surface, where the flux is directed at a 45° angle relative to the seed surface. The growth rate is three to four times higher. This behavior

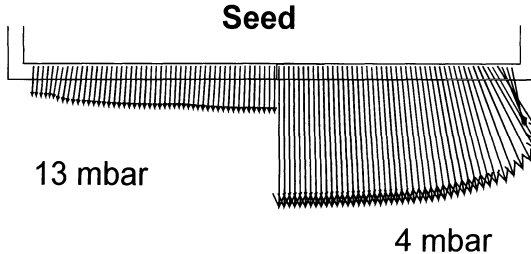


Fig. 4.12. Carbon flux on the surface of a 35 mm seed for two different total pressures at the beginning of the growth: *left side* 13 mbar, *right side* 4 mbar. The normal component of the arrows is identical to the shape of the growing crystal

of an increased growth rate and a convex growth profile has been confirmed experimentally. Because the crucible geometry and the temperature profile are identical in the two cases, the transport of the reactive species towards the seed surface is the origin of this different behavior. It is difficult to generalize this information, which is valid for our reactor configuration. However, the main trend for standard configurations of the sublimation method is that when the argon pressure is low, the growth rate increases and the shape tends to be convex.

Geometry Modification and Crystal Shape

Some years ago, with seeds of size 20 mm, two different configurations of the cavity were studied [10], a standard configuration (Fig. 4.13a) and a configuration with a flat screen acting as a radiation shield (Fig. 4.13b). It could be advantageous for the growth of SiC crystals to prevent the formation of SiC deposits on the crucible around the seed. To achieve this, it is necessary to establish a temperature field on the surface of the crucible which is everywhere higher than the temperature of the surface of the growing crystal. This provides material transport predominantly to the seed. A flat screen allows crystal growth while avoiding poly-SiC growth. Mass transport modeling shows that no deposition occurs on the screen. The crystal grows with free boundaries. But, after an initial enlargement, the ingot diameter progressively decreases. The screen becomes too far from the growing interface to ensure the same conditions as in the first few hours. This geometry allows growth without poly-SiC but is inadequate for ensuring long-lasting enlargement, owing to changes in the thermal and flux fields during growth.

4.5.3 Ingot Evaluation

For a given growth rate of a single-crystal ingot, grown in the standard configuration of the Fig. 4.13a, the crystal quality and the occurrence of defects are mainly functions of three parameters of the growth process: the seed characteristics, the thermal field, and the pressure inside the growth chamber.

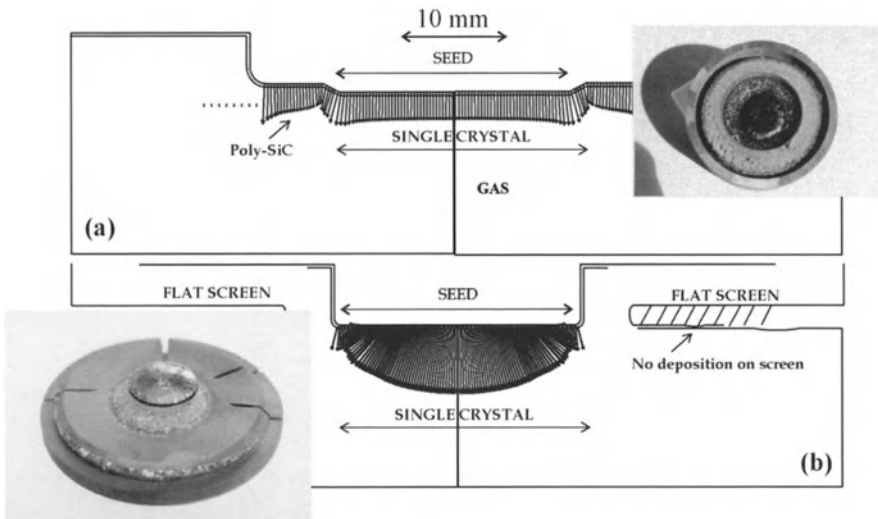


Fig. 4.13. Initial growth flux for (a) a standard configuration and (b) a configuration with a flat screen inserted in the cavity

To improve the quality of the wafers, it is of prime importance to identify the mechanisms of formation of the different defects and to understand the relation between their occurrence and the experimental parameters of the growth process.

This part is mainly devoted to the determination of the influence of the seed characteristics on the occurrence of defects in the as-grown ingot. Polytype identification, studies of morphology and structural perfection, and defect analysis were performed using mainly optical microscopy and X-ray white-beam synchrotron topography.

Surface Polarity and Polytype

It has already been reported that 4H-SiC and 6H-SiC ingots can be preferentially grown by the modified Lely method on the C face of a 4H-SiC seed crystal and on both the C and the Si faces of a 6H-SiC seed crystal, respectively. Polytype conversions occur when the face polarity is not respected. A 4H-SiC ingot grown from a Si face often changes to the 6H polytype, while the 6H or 15R-SiC polytype can be grown on the C face of a 6H-SiC seed [47, 48].

Milita et al. [49] have reported analyses by white-beam vertical-section topography of a 6H-SiC ingot grown on the Si face of a Lely seed. The interface between the seed and the grown crystal was observed. Figure 4.14 shows the result of a similar experiment performed on an ingot grown on the C face of a Lely seed. The seed diffracted at the top of the topograph and the as-grown ingot surface diffracted at the bottom. In this case, in contrast to what was observed by Milita et al. [49], the seed/grown-crystal interface is highly

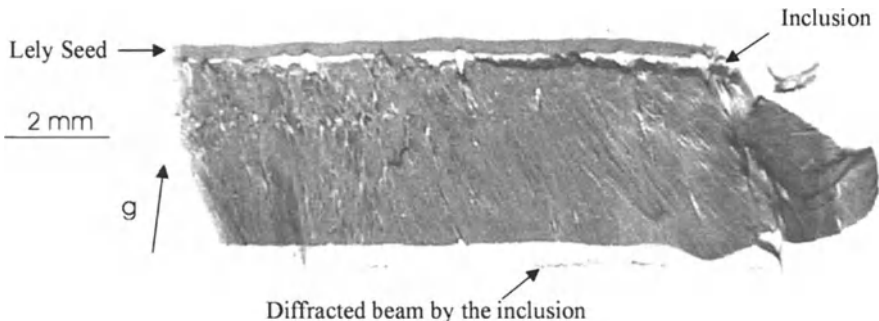


Fig. 4.14. Vertical section of a 6H-SiC ingot. The C face of a Lely crystal was used to grow this ingot

perturbed. Moreover, after a study of the whole film in order to observe other reflections, it appears that there is a small inclusion at the interface. Indeed, at the bottom of the topograph of Fig. 4.14, a small line, corresponding to the beam diffracted by this inclusion, is visible. It has already been observed that 6H/15R-SiC conversion often occurs when the growth takes place on the C face of a 6H seed. This is also probably the case here. A small 15R-SiC inclusion was grown on the seed and returned to 6H-SiC after less than 1 mm of growth. The low crystalline quality of this 6H-SiC ingot must also be noticed.

This observation confirms that the growth of the 6H polytype is difficult if the growth occurs on the C face of a seed. But the fact that the main part of the grown ingot is 6H-SiC means that for our experimental conditions, pressure and temperature, the 6H polytype is the thermodynamically stable structure.

Enlargement Process

In the simplest experimental configuration, the growth starts simultaneously on the SiC seed, the pedestal part not covered by the seed, and the remaining surface of the lid. At first, on the latter two graphite surfaces, the SiC deposit is essentially polycrystalline. Hence, the achievement of a cylindrical single-crystal boule needs enlargement of the original single-crystal surface of the grown material at the expense of adjacent polycrystalline small islands.

This enlargement process has been studied by white-beam synchrotron topography. Here we shall just give some indications of the main information obtained to date. The investigation of a SiC boule by horizontal- and vertical-section topography reveals that the enlargement process results from a progressive alignment of domains that are adjacent to the seed and initially misoriented by a continuous deformation of the boundary zones during growth. A complete description and analysis of the results obtained so far by this technique has been published elsewhere, together with a comparison with the work already published on this subject [27, 49, 50].



Fig. 4.15. Vertical section (D-geometry) of a 4H-SiC ingot showing the enlargement of the crystal during the growth. The seed is at the top

Figure 4.15 shows a vertical-section topograph of a 4H-SiC ingot. A better quality in the center of the boule (lighter region) can be noticed. The darker regions are, essentially, observable at the edge of the boule and at the beginning of the growth. The central part of the crystal under the seed keeps the good structural quality of the seed, whereas the enlarged part originating from the alignment of the polycrystal is more stressed.

Heat transfer modeling provides a good understanding of this enlargement phenomenon on the basis of the radial gradient over the growth surface. Owing to this radial gradient, the ingot diameter increases with the increase in length if the growth of polycrystalline SiC on the graphite lid follows the ingot growth. An increase in the radial gradient increases the lateral growth rate.

Growth of the Polycrystal and Cracks

The propagation of defects and the evolution of the polycrystalline part around the single-crystal ingot have been investigated by polarized-light microscopy. Figure 4.16 shows optical micrographs of three 4H-SiC slices cut from the same ingot close to the seed, at the middle of the ingot, and close to the as-grown surface. The design of the growth chamber was such that there was no enlargement of the ingot. Its size was 20 mm diameter \times 7 mm.

Some polycrystal has grown around the main crystal. Near the seed, the grain size is very small. Probably because of their particular orientation, some grains grow from the seed level to the top of the ingot. It has been shown [49, 50] that some crystallites in the polycrystal have a common axis

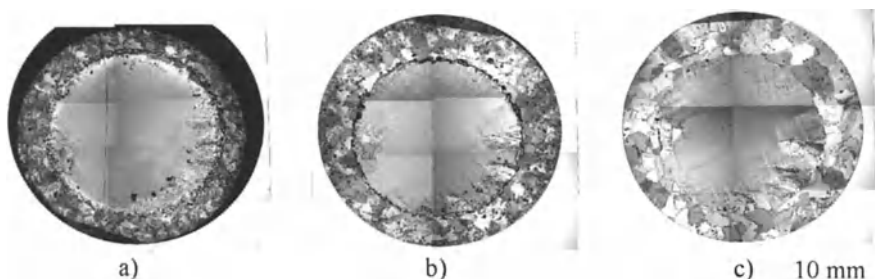


Fig. 4.16. Polarized-light microscopy of three wafers from the same ingot: (a) near the seed, (b) in the middle of the ingot, and (c) near the as grown surface

and an orientation similar to that of the main crystal. In the case of an enlargement process, these crystallites form subgrains which gradually join the main crystal.

The seed used for this growth includes some crystallites and cracks at its periphery. During the growth, these defects partially disappear in the first few millimeters of growth. But some other large cracks occur in the upper part of the ingot. Most of these cracks are located in the zone opposite to the facet which is perpendicular to the inclined *c*-axis, showing the asymmetry of the growth.

Defect Propagation

Figure 4.17a and 4.17b shows optical transmission micrographs, recorded using a polarizing microscope with a crossed analyzer, of an 8° off-axis seed wafer and of a wafer cut from the middle of the 4H-SiC ingot grown from this seed, respectively. The good-quality seed wafer includes a few micropipes and cracks, mainly located at its right side; see Fig. 4.17a. The wafer cut from the middle of the newly grown crystal indicates clearly the enlargement of the lateral size of the ingot with respect to that of the seed. The enlargement is mainly produced by the reorientation of the crystallites of the polycrystals growing around the main crystal and their incorporation into it. The quality of this new, enlarged crystal is not very good; a number of micropipes and cracks can be observed at the wafer periphery, while its central part is nearly defect-free. The small black spots present on the micrographs correspond to carbon particles deposited during the growth. An inclusion of another polytype formed during crystal growth is located in the lower right corner of

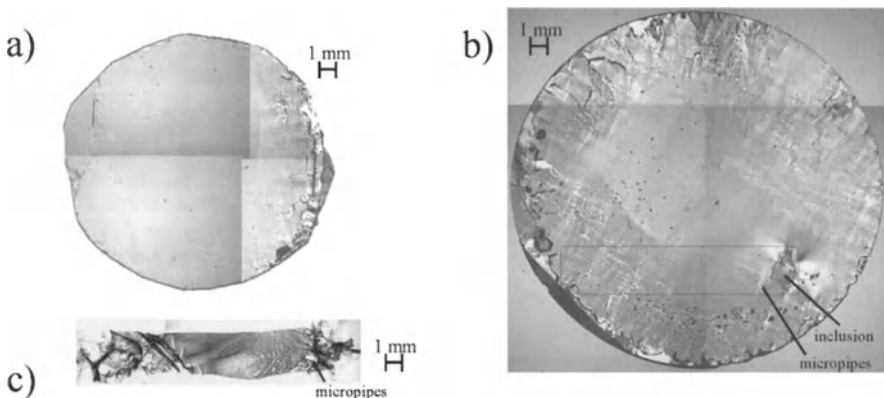


Fig. 4.17. Optical transmission micrographs recorded using a polarizing microscope with a crossed analyzer, of (a) a seed wafer and (b) a wafer cut from the middle of the grown ingot. (c) Projection topograph in reflection of the wafer area marked by the rectangle in (b), 000ℓ reflection, $2\theta \sim 150^\circ$

Fig. 4.17b. Figure 4.17c is a projection topograph in reflection of the wafer area marked by the rectangle in Fig. 4.17b. Various defects can be detected, such as micropipes (white spots) [45, 51, 52], diagonal cracks on the left, and distortions associated with the inclusion on the right-hand side of the image. Such investigations, using both optical transmission microscopy and projection topography techniques, are possible only after slicing of the ingot and consecutive polishing of wafer surfaces.

However, much useful information can be obtained without any preparation of as-grown ingots using the section topography technique. Figure 4.18 presents a set of section topographs of the ingot grown from the seed shown in Fig. 4.17a, recorded using the four different geometries described in Fig. 4.11. The horizontal and vertical sections, Figs. 4.18a,b and Figs. 4.18c,d, respectively, correspond approximately to the central part of the ingot. For the sake of simplicity, the sections recorded at various heights of the incident beam on the ingot are not presented. Owing to the geometrical projection onto the film, the horizontal sections have an elliptical shape, although the cross section of the sample and the incident beam are circular. The presence of the polycrystal surrounding the main crystal leads to deformation of the ellipse and produces additional contrast at the periphery of the ingot.

The sample volume diffracting to create the image of Fig. 4.18a corresponds roughly to the wafer shown in Fig. 4.17b. There is an inclusion in the lower right part of the topograph, apparently the same one as in Fig. 4.18. A number of micropipes appear, mainly at the lower left part of the image; however, the central part of the ingot remains nearly defect-free. The facet, i.e. the natural surface perpendicular to the *c*-axis, observed as a light elliptical feature in the upper left region of the section, corresponds to a part of the

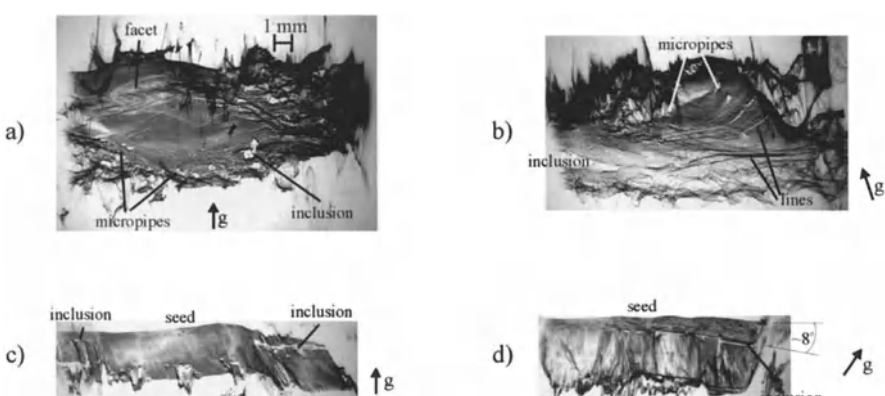


Fig. 4.18. (a)–(d) Section topographs of the ingot grown from the seed wafer of Fig. 4.17a recorded for the four different experimental geometries represented in Fig. 4.11a–d, respectively. The inclusion marked in the optical micrograph of Fig. 4.17b is indicated also in (a). The vector *g* is the projection of the diffraction vector on the film

crystal with elevated crystalline quality. Defects similar to these inclusions and micropipes are revealed in Fig. 4.18b, which is a horizontal-section topograph recorded with the ingot turned by 90° around its vertical axis with respect to the position of the crystal in Fig. 4.18a. The sections of Fig. 4.18a,b both correspond to 000ℓ reflections. However, an additional feature is observed in Fig. 4.18b: the lines nearly perpendicular to the projection of the diffraction vector \mathbf{g} . The lines are curved if the crystal matrix is deformed; they can show either white or black contrast and their density is higher when closer to the seed. The corresponding distortion of the 000ℓ reflecting planes is schematically drawn in Fig. 4.19 for the four geometries used. The lines can be observed only if the projections of the c -axis and the diffraction vector on the film are approximately perpendicular; see Fig. 4.18b and Fig. 4.19b.

The vertical-section topographs recorded with the incident beam parallel to the main, vertical axis of the cylindrical ingot allow us to follow the crystal growth from the seed to its natural top surface. The seed-crystal interface is hardly visible in both vertical sections of Fig. 4.18c,d, indicating a smooth start of the crystal growth. The vertical sections recorded with the projections of the c -axis and the diffraction vector nearly parallel (or perpendicular) (see Fig. 4.18c (or Fig. 4.18d)) show a crystal with good (or poor, respectively) crystalline quality, at least in its central part. Two inclusions of other polytypes, 6H-SiC or 15R-SiC, near to the seed can be observed in Fig. 4.18, one at the right side of the image, corresponding to the periphery of the ingot, while the second inclusion, in the left part of the image, is located closer to the central part of the crystal. The section in Fig. 4.18d was recorded approximately at the level of the SiC inclusion at the left of Fig. 4.18c. Figure 4.18d indicates

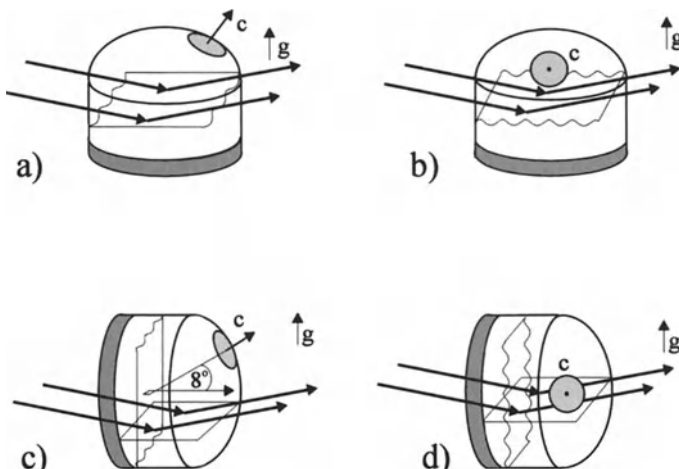


Fig. 4.19. (a)–(d) Schematic drawings of the observed distortion of the reflecting planes with respect to the c -axis direction for the four geometrical set-ups used, as represented in Fig. 4.11a–d, respectively

that this inclusion starts to grow from one side of the ingot and propagates at an angle of 8° with respect to the horizontal axis of the ingot until it reaches the other side of the ingot. The inclusion provokes a number of planar defects that grow parallel to the vertical axis of the ingot up to the natural crystal surface. These planar defects are the origin of the observation of the lines in Fig. 4.18b. A systematic investigation of several 4H-SiC ingots indicates that these 6H inclusions at 8° occasionally appear and are generally reversible. The defects generated often affect only a part of the crystal; however, they deteriorate its crystalline quality considerably. This polytype switching originates from the 8° off-axis orientation of the seed. If some instability appears at the beginning of the growth process, a 6H-SiC or 15R-SiC single-crystal grain can be created outside the seed. In the case where this grain is located at the right extremity of the seed and has the same orientation as the 4H main crystal, it starts to grow, and progressively covers part of the 4H crystal. If, during further crystal growth, the process parameters such as pressure and temperature are favorable to the growth of the 4H polytype, a conversion back to 4H-SiC appears. However, this reconversion provokes the appearance of distortions in the newly grown crystal, such as grain boundaries.

4.5.4 Wafer Evaluation

Relations Between Defects and Macroscopic Modeling

Now we shall address the complex domain of defect formation and localization from a macroscopic point of view.

Macrodefects and micropipes are classified as hollow defects. Macrodefects are large vertical holes with horizontal enlargement at their end. They may start at the holder–seed interface and penetrate deep into the growing crystal. The formation of these defects has been explained by secondary local sublimation of the seed and of the growing ingot and not as a result of instabilities at the growth interface. High temperatures and large temperature gradients between the seed and the graphite holder lead to local sublimation at the back surface of the seed at the beginning of growth, and then to macrodefect formation. These macrodefects can be eliminated by using a specific design of the seed–holder attachment which determines the local gradient at the interface between the seed and the holder. They can also be partly eliminated by increasing the radial thermal gradient. Their growth angle increases and they are blocked at the single-crystal–polycrystal interface. They can also be eliminated by reducing the growth temperature or by changing the composition of the powder, and so the composition of the gas phase.

Macrodefects. Since macrodefect formation involves back-surface sublimation from the seed, both the temperature and the temperature gradient are important key parameters in controlling the occurrence of macrodefects in SiC boules. Some years ago, with seeds of size 20 mm, we investigated various crucible designs, growth chamber geometries, and seed attachment techniques in

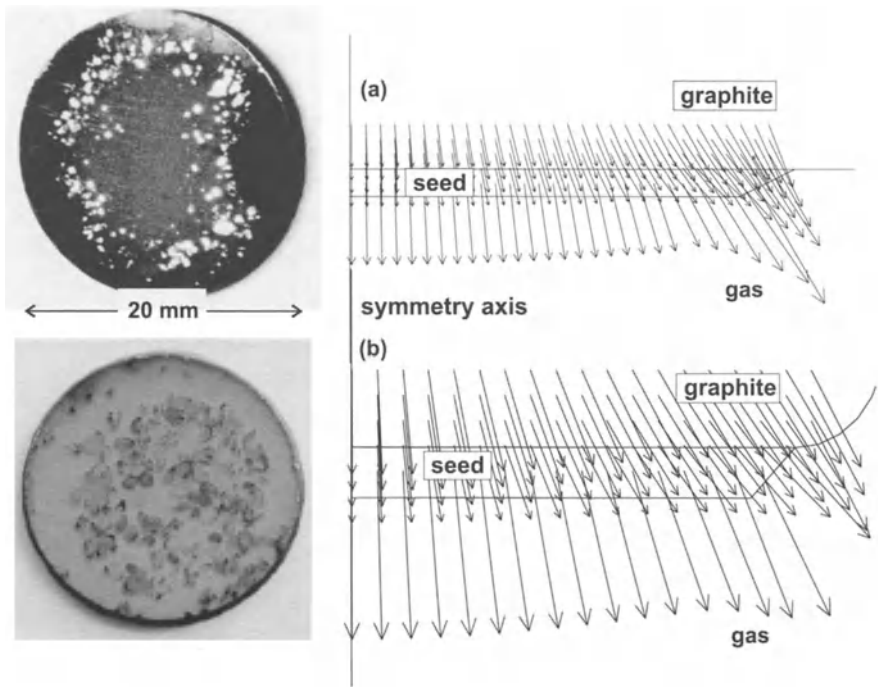


Fig. 4.20. Influence of the thermal gradient near the seed on the appearance of macrodefects, and cross section of the boule, (a) before and (b) after increasing thermal gradients

relation to the macrodefect distribution. Figure 4.20 shows the temperature gradient profile and the corresponding SiC wafers for two different configurations. There is a strong correlation between the temperature gradient at the back of the seed and the macrodefect distribution. In case (a), the maximum concentration of macrodefects is reached where the temperature gradient is maximum, at the periphery of the seed. In case (b), the temperature gradient is higher at the graphite–seed interface. Here, macrodefects are observed in the totality of the wafer. Even if the occurrence of macrodefects involves complex phenomena, local thermal-gradient fields and their absolute values give some guidelines about their distribution. Careful control of the temperature gradient at the back surface of the seed allows the fabrication of macrodefect-free boules.

Microdefects. A major problem in the growth of SiC is the presence of other defects, called pinholes or micropipes. The origin of the formation processes of micropipes in SiC is complex. Most of the explanations are based on Frank's theory, which proposes that a micropipe is the hollow core of a screw dislocation with a large Burgers vector (several times the unit cell), with the diameter of the core directly related to the magnitude of the Burgers vector. Generally,

in our experiments, a higher concentration of micropipes has been observed in the regions of lower growth rate, indicating the importance of the crystal shape. There is no doubt that the enlargement of the crystal is the main cause of the high stress level in the periphery region, as shown by our recent results using synchrotron radiation and polarized-light optical microscopy.

The macroscopic approach is able to qualitatively contribute to explaining some of the phenomena leading to the appearance of certain types of defects and their spatial distribution. The remaining problem is to evaluate the relative importance of technological problems and mechanical, transport, and physico-chemical phenomena and so to propose a microscopic model linking macroscopic data, particularly local fields, to defect initiation on the nanometric scale.

It is now well known that micropipes can originate from seed defects. But generally, no other defects are observed at the seed-holder interface. In the final crystal, second phases of different morphology and size (1 to 10 μm) are detected. Carbon inclusions and liquid silicon droplets lead to the generation of micropipes. A thermodynamic equilibrium calculation reveals the possibility of obtaining silicon droplets during the process (Fig. 4.21). In the example presented, the powder is at 2900 K and the composition of the gas phase above the powder is calculated for the SiC-C system. For a temperature difference of about 300 K between the powder and the seed, it is possible to shift the system toward the SiC + Si system. These values are not engineering values, because of the departure of the system from equilibrium. As we shall see later, a small variation of the axial temperature difference leads to the appearance of silicon. One can conclude that this phenomenon is a physico-chemical one.

According to Hofmann et al. [7, 53], there are conflicts; for example, (i) avoiding both carbon and silicon inclusions, and (ii) achieving a high growth rate and defect-free boules. Previous modeling results have shown that a high temperature gradient in the crucible ($30\text{--}50\text{ Kcm}^{-1}$) seems necessary

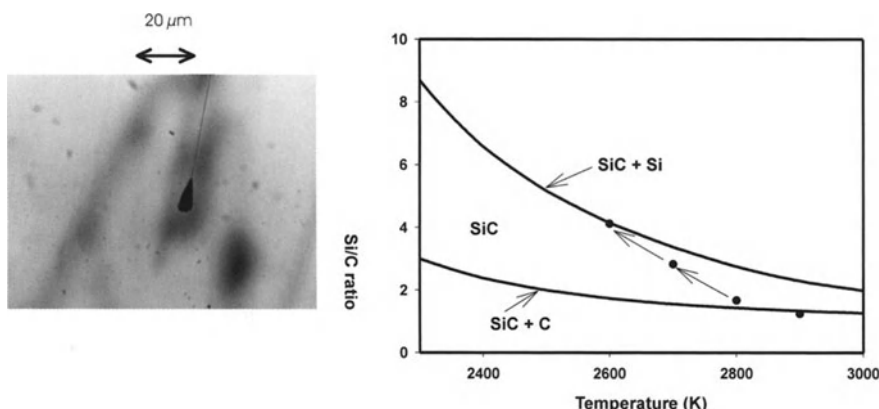


Fig. 4.21. Thermodynamic modeling of the appearance of silicon droplets

to achieve growth conditions with reasonable growth rates ($> 0.5 \text{ mm h}^{-1}$). However, low temperature gradients are necessary to reduce the thermal stress in the crystal and to reach a low dislocation density.

The question is, how to find a reasonably large experimental window which allows one to manage these conflicts. Simulation is a powerful tool for exploring and quantifying the impact of small change in design. The following examples will demonstrate the impact of the evolution of experimental parameters. The relations between the results of materials science and process modeling are still difficult to quantify and generalize. The relations which will be presented are mainly the results of our extensive experimental work.

Increase of the Temperature Difference in the Cavity. The simulation shows that an increase of the diameter of the pyrometric hole leads to an increase of the axial and radial temperature differences of 20%. The mass transport simulation shows that the Si/C ratio in the gas phase near the growing interface increases. The result is the occurrence of a second phase containing silicon due to an increase of the axial temperature difference and a drastic change in the shape of the graphitization area of the final source powder due to an increase in the radial temperature difference.

Heat Transfer and a Problem of Materials Science [27]. The combination of experiment and calculations shows that the material characteristics are sensitive to small parameter variations, and that they can be deteriorated by minor variations compared with the working temperatures.

A graphite foam is always used around the crucible to ensure good thermal insulation. Some experiments have been conducted with two different thicknesses of insulating foam. The other parameters for the two sets of experiments were kept the same. Processes carried out with a reduced foam thickness (a reduction of about 30% compared with the stabilized process) have led to crystals displaying the following characteristics: the single crystal initially grows as the 4H polytype and then switches to the 6H polytype. A vertical slice of such a crystal is presented in Fig. 4.22.

By only increasing the insulating-material thickness by about 40%, the 4H polytype was stabilized again. The effect of the insulating-material thickness has been simulated. The results are presented in Fig. 4.23. When the thickness is increased by about 40%, the heat transfer simulation predicts a decrease of the radial temperature difference along the seed (25 mm in diameter) by

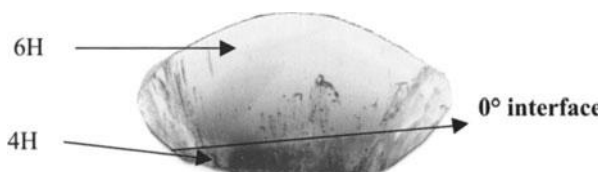


Fig. 4.22. Vertical slice of a single crystal displaying 4H to 6H polytype switching

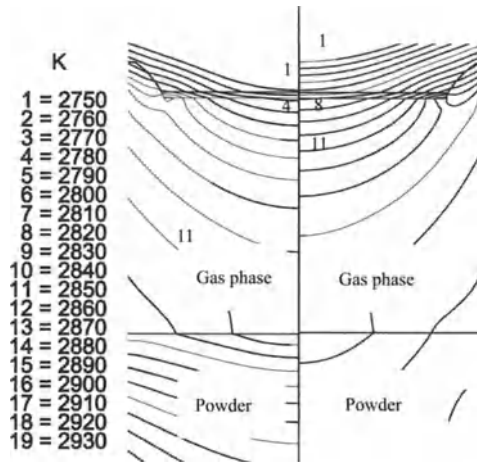


Fig. 4.23. Influence of the foam thickness on heat transfer [27]

about 30%. This difference drops from 60 K with poor insulation to 40 K in the case where the thickness is increased by 40%. These results indicate that a small increase of the radial temperature difference (in comparison with the working temperature) is sufficient to change the growth mode and strongly deteriorate the material.

Density of Dislocations and Micropipes

It must be kept in mind that chemical etching in molten KOH is the best method for the determination of the density of dislocations intersecting the surface [54, 55]. Figure 4.24 shows two optical micrographs of a chemically etched wafer. According to the classification in the literature, these micrographs correspond to large, medium, and hexagonal pits appearing on the (000ℓ) Si-side face after etching. Each of these pits has six sidewalls, corresponding to the traces of the $[1100]$ planes intersecting the surface, and a pointed bottom.

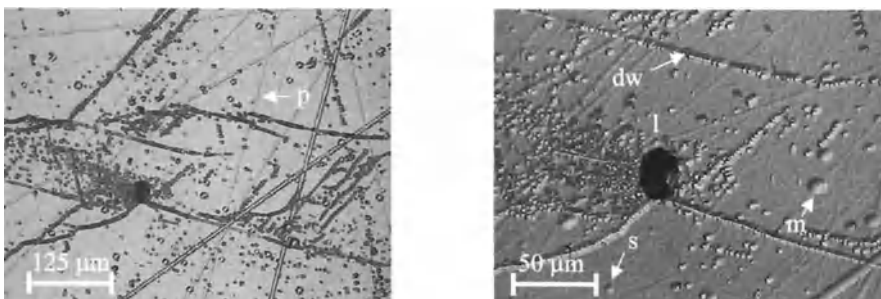


Fig. 4.24. 4H-SiC wafer chemically etched in molten KOH

The medium etch pits correspond to $\langle 000\ell \rangle$ screw dislocations with a unit c Burgers vector, while the small pits correspond to $(1/3) [11\bar{2}0]$ type edge dislocations. It was often observed that the small pits were aligned along $\langle 1\bar{1}00 \rangle$, indicating the existence of low-tilt-angle boundaries in the crystal.

The large hexagonal etch pits correspond to micropipes. These defects are hollow tubes, which generally run along the c -axis through the entire crystal boule and arise from screw dislocations with large Burgers vectors $b \geq 2c$.

4.5.5 Evaluation of Stress Patterns

This part of this paper is devoted to the global characterization of stress by optical microscopy, X-ray diffraction imaging, and Raman spectroscopic imaging. Stress analysis can be performed by all of these techniques; however, the physical phenomena involved in the creation of a recorded image are different.

The interest of these three methods in comparison with chemical etching is that they are not destructive techniques. They also give some information about the density of dislocations and micropipes.

Figure 4.25 presents a 000ℓ reflection X-ray topograph. The diffraction vector is parallel to the c -axis. So it is easy to observe screw dislocations along this axis. Contrast appearing as white circles is associated with the strain field around dislocations, or around micropipes for the large features. Except in a small region at the center of the wafer, the dislocation density is homogeneous and less than 10^5 cm^{-2} . Most of the micropipes are localized in a 25 mm^2 region.

The results of a diffraction imaging experiment on a part of an average-quality crystal are presented on Fig. 4.26. The slice has an average structural quality. Some contrast associated with subgrains and micropipes is visible. The rectangle indicates a highly-deformed area. About ten micropipes and

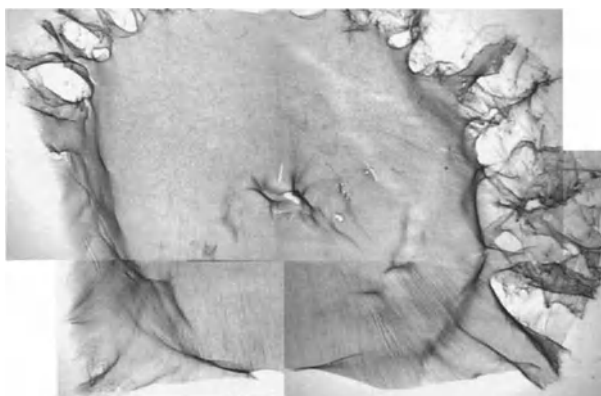


Fig. 4.25. X-ray reflection topography of a 35 mm 4H-SiC wafer. 000ℓ reflection

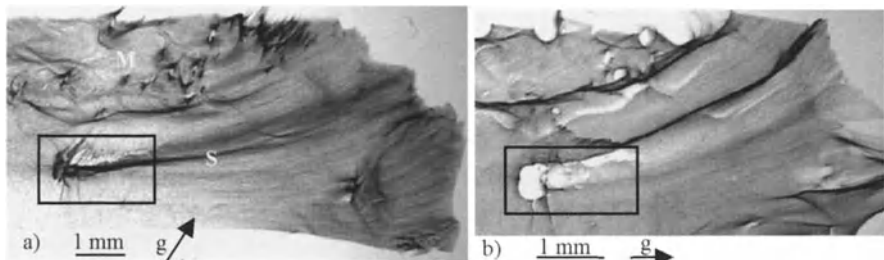


Fig. 4.26. X-ray topography: (a) in transmission, $d = 20\text{ cm}$; (b) in reflection, $d = 40\text{ cm}$. The rectangle indicates approximately the area studied by Raman spectroscopy and birefringence imaging. The letters S and M denote a subgrain boundary and a micropipe, respectively

a high dislocation density were observed in this region by classical optical measurement and etching in molten KOH.

Birefringence Imaging

4H-SiC is an optically birefringent material. Defects in SiC crystals produce local stresses that modify the orientation and the form of the optical indicatrix. Figure 4.27a shows an orientation image of the region of the crystal defined by the rectangle in Fig. 4.26.

The background of the retardation image (Fig. 4.27b) is homogeneous. This means that the indicatrix and consequently the stress are homogeneous in this area of the crystal. The orientation and the retardation are modified considerably only in the part of the image where the micropipes are located. The features marked DW in Fig. 4.27a probably correspond to some dislocation walls. A complex contrast induced by micropipes, denoted by M, can be distinguished.

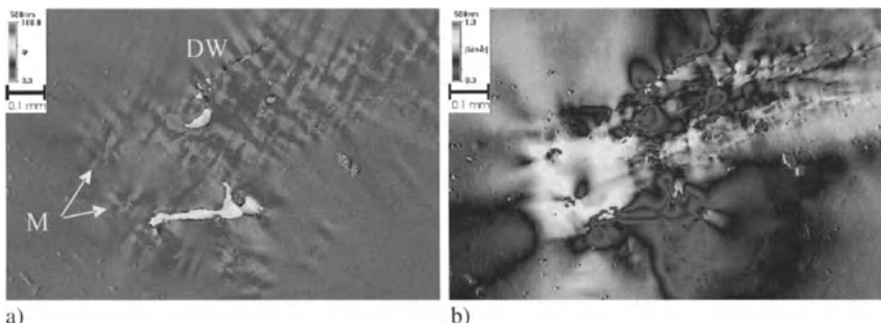


Fig. 4.27. Birefringence images: (a) orientation φ ; (b) retardation $|\sin \delta|$. Area $1.2 \times 0.8\text{ mm}^2$

Raman Imaging

Figure 4.28 shows some Raman spectra and images recorded in the same region as that observed by X-ray topography and birefringence imaging. Spectra were recorded for each $1\text{ }\mu\text{m}$ on a $70 \times 70\text{ }\mu\text{m}^2$ area covering several large micropipes, $\sim 10\text{ }\mu\text{m}$ in diameter. Micro-Raman spectroscopy is a technique sensitive to the stress and doping in SiC. It is also a powerful tool for detecting inclusions in the crystals. Micro-Raman imaging, applied to our sample, provides these three kinds of information. Some graphite has been detected inside the micropipes. Moreover, some Raman lines, for example the 776 cm^{-1} TO mode shown in Fig. 4.28b, are shifted toward higher values. But the shift is constant in the area observed, even close to the micropipes. This indicates a homogeneous stress in this part of the crystal. Finally, the LO phonon-plasmon coupling mode at 964.5 cm^{-1} is shifted and its shape changes close to the micropipes, as can be seen in Fig. 4.28b. This effect is produced by a modification of the electronic properties of the material. The carrier concentration has been evaluated as 10^{18} cm^{-3} and $7 \times 10^{17}\text{ cm}^{-3}$ in the bulk and close to the defects, respectively. This suggests a high density of trapping centers in the vicinity of micropipes [56, 57].

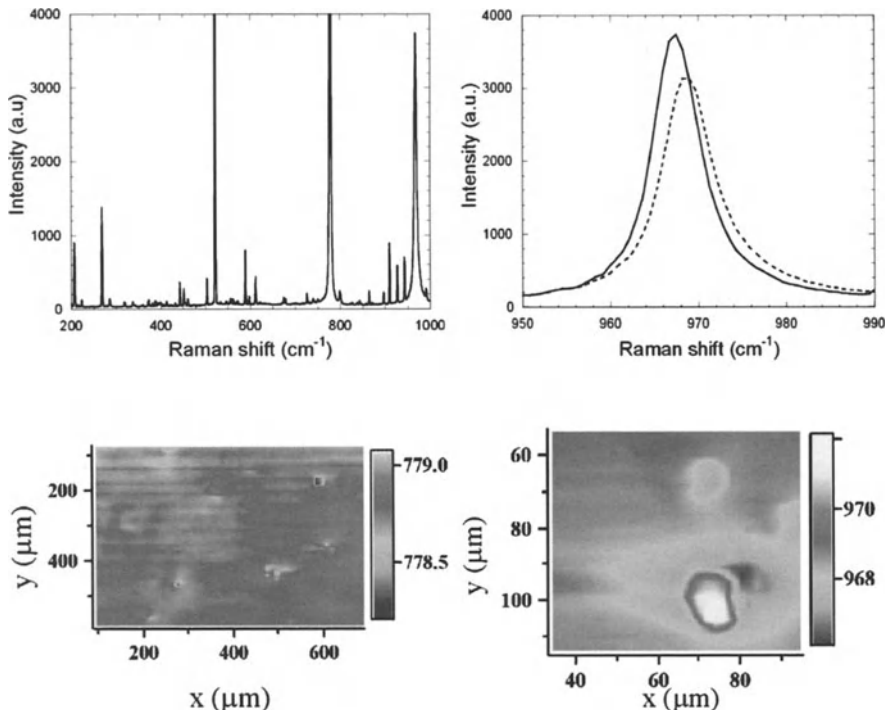


Fig. 4.28. (a) 776 cm^{-1} TO mode image; (b) LO phonon–plasmon coupling mode around a micropipe

Model Development

The present development of the simulation tools is now focused on the prediction of dislocation formation [21, 26, 53]. Thermoelastic stresses are considered to be one of the major reasons for the formation of crystalline defects (dislocations and micropipes). Not all of the necessary thermoelasticity and plasticity data are available to implement the model of dislocation generation and multiplication that is already used for silicon. Experiments and analysis of measurements have to be done in the future.

In our experiments, the attachment of the initial seed and of the subsequent boule is only rigid near the symmetry axis, owing to evaporation of the graphite glue. The von Mises stress field is presented in Fig. 4.29. The stress field (Fig. 4.29a) may be used, as a first approximation, like a picture of a virtual plastic zone. The magnitude of the shear stress can be also an indication of the start of plastic deformation if it exceeds the critical resolved stress [21, 26]. The profile has a W shape with two maxima, at the center and at the periphery. Characterization of the density of stress by synchrotron radiation (Fig. 4.29b) was performed on the whole boule and on various wafers sliced from it. This reveals the same position of the dark zones in all the wafers, in the center and at the periphery. These results have been confirmed by KOH etching. These first results show that a careful control of the shape of the boule is needed to control the temperature gradient and the subsequent stress field.

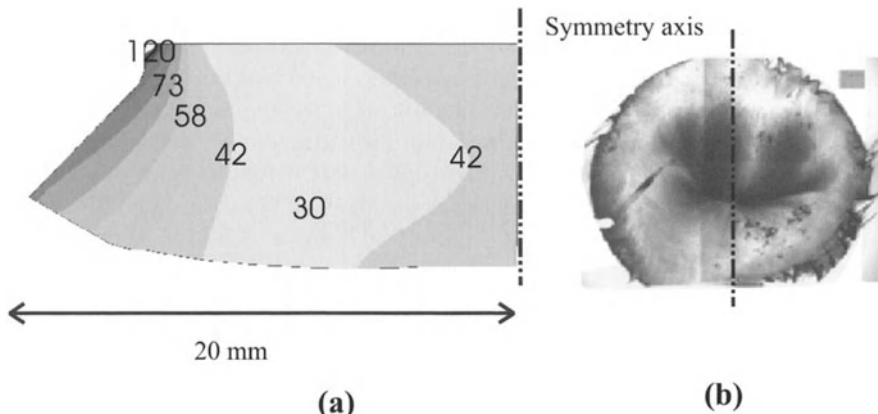


Fig. 4.29. (a) Von Mises stress (MPa) in the whole crystal. (b) Synchrotron image of a slice

4.6 Conclusions

Further understanding of PVT growth can be obtained by the joint use of numerical modeling and characterization methods. The numerical modeling tools must be ready to solve known problems and must also be evolutionary to solve the problems that will arise in the near future. We have developed, by a succession of patches, a numerical tool able to compute the known phenomena. The databases associated with it and their validation make the numerical modeling sufficiently mature to help with the optimization of SiC growth conditions. A lot of problems have been visualized. The roles of minor geometric modifications and minor temperature variations have been displayed. A great effort has to be made in the acquisition of material data for future predictions of microscopic-defect generation and of in situ visualization of growth.

The propagation of the defects occurring during the growth of 4H-SiC crystals has been investigated using the X-ray section topography technique in transmission mode. Thanks to the high flux and high energy of the X-ray beams available at the ESRF, together with the large beam size, a very simple setup could be to study the whole volume of ingots with a diameter of up to 50 mm.

The general stress and the densities of structural defects were evaluated by techniques such as X-ray topography, birefringence, Raman spectrometry, and KOH etching. The last method is the most used and the best for evaluating the density of structural defects intersecting the surface, but it is a destructive technique. X-ray topography is very sensitive to the strain field. It is impossible to separate the contrast associated with an individual micropipe. Difficulties in the interpretation of a topograph arise from the high density of defects in a crystal with an average structural quality. When using birefringence imaging with a good magnification, it is possible to distinguish individual defects such as micropipes and dislocation walls even in regions of low structural quality. Raman spectroscopy revealed the presence of graphite within micropipes and a lower carrier concentration close to them. However, surprisingly, no variations of the stress have been detected, although X-ray topography and birefringence imaging indicated the presence of highly deformed regions. Some initial relations between the distribution of the defects, the stress in the wafer, and the thermal gradient in the crucible have been quantified using simplified thermoelastic considerations.

The characterization methods and the modeling tools are complementary for understanding the formation of structural defects, their propagation, and the shape of ingots grown by the sublimation method. The characterization methods were used to evaluate the structural quality of the SiC ingots and wafers, and the simulation tools were used to give some indications about the mechanisms of growth. Some relations between all these pieces of information and the working parameters were proposed.

References

1. V. Tsvetkov, R. Glass, D. Henshall, D. Asbury, and C.H. Carter Jr., “SiC boule growth”, Mater. Sci. Forum **264–268**, 3–8 (1998).
2. D. Hobgood, M. Brady, W. Brixius, G. Fechko, R. Glass, D. Hensall, J. Jeny, R. Leonard, D. Malta, S.G. Müller, V. Tsvetkov, and C. Carter, “Status of large diameter SiC crystal growth for electronic and optical applications”, Mater. Sci. Forum **338–342**, 3–8 (2000).
3. S.G. Müller, R.C. Glass, H.M. Hobgood, V.F. Tsvetkov, M. Brady, D. Henshall, J.R. Jenny, D. Malta, and C.H. Carter Jr., “The status of SiC bulk growth from an industrial point of view”, J. Cryst. Growth **211**, 325–332 (2000).
4. Yu.M. Tairov, and V.F. Tsvetkov, “Investigation of growth processes of ingots of silicon carbide single crystals”, J. Cryst. Growth **43**, 208–212 (1978).
5. M. Anikin, O. Chaix, E. Pernot, B. Pelissier, M. Pons, A. Pisch, C. Bernard, P. Grosse, C. Faure, Y. Grange, G. Basset, C. Moulin, and R. Madar, “Progress in SiC bulk growth”, Mater. Sci. Forum **338–342**, 13–16 (2000).
6. D. Hofmann, M. Heinze, A. Winnacker, F. Durst, L. Kadinski, P. Kaufmann, Y. Makarov, and M. Schäfer, “On the sublimation growth of SiC bulk crystals: development of a numerical process model”, J. Cryst. Growth **146**, 214–219 (1995).
7. D. Hofmann, E. Schmitt, M. Bickermann, M. Kolbl, P.J. Welmann, and A. Winnacker, “Analysis on defect generation during the SiC bulk growth process”, Mater. Sci. Eng. B **61–62**, 48–53 (1999).
8. M. Pons, E. Blanquet, J.M. Dedulle, I. Garcon, R. Madar, and C. Bernard, “Thermodynamic heat transfer and mass transport modeling of the sublimation growth of silicon carbide crystals”, J. Electrochem. Soc. **143**, 3727–3736 (1996).
9. M. Pons, M. Anikin, J.M. Dedulle, R. Madar, K. Chourou, E. Blanquet, and C. Bernard, “Macroscopic modelling of silicon carbide sublimation: toward a microscopic modelling of defect formation”, Surf. Coat. Technol. **94–95**, 279–284 (1997).
10. M. Pons, M. Anikin, K. Chourou, J.M. Dedulle, R. Madar, E. Blanquet, A. Pisch, C. Bernard, P. Grosse, C. Faure, G. Basset, and Y. Grange, “State of the art in the modelling of SiC sublimation growth”, Mater. Sci. Eng. B **61–62**, 18–28 (1999).
11. P. Raback, R. Nieminen, R. Yakimova, M. Tuominen, and E. Janzen, “A coupled finite element model for the sublimation growth of SiC”, Mater. Sci. Forum **264–268**, 65–68 (1998).
12. S.Y. Karpov, Yu.N. Makarov, and M.S. Ram, “Simulation of sublimation growth of SiC single crystals”, Phys. Stat. Sol. (b) **202**, 201–220 (1997).
13. A. Pisch, E. Blanquet, M. Pons, C. Bernard, M. Anikin, J.M. Dedulle, and R. Madar, “Modelling of SiC sublimation growth process: influence of experimental parameters on crystal shape”, J. Phys. IV Fr. **9**, 213–219 (1999).
14. K. Chourou, M. Anikin, J.M. Bluet, J.M. Dedulle, R. Madar, M. Pons, E. Blanquet, C. Bernard, P. Grosse, C. Faure, G. Basset, and Y. Grange, “Modelling of SiC sublimation growth process: analyses of macrodefects formation”, Mater. Sci. Eng. B **61–62**, 82–85 (1999).
15. M. Selder, L. Kadinski, F. Durst, T. Straubinger, D. Hofmann, and O. Wellmann, “Global numerical simulation of heat and mass transfer during SiC bulk crystal PVT growth”, Mater. Sci. Forum **338–342**, 31–34 (2000); M. Selder,

- L. Kadinski, Yu. Makarov, F. Durst, P. Wellmann, T. Straubinger, D. Hofmann, S. Karpov, and M. Ramm, "Global numerical simulation of heat and mass transfer for SiC bulk crystal growth by PVT", *J. Cryst. Growth* **211**, 333–338 (2000).
16. S. Nishizawa, Y. Kitou, W. Bahng, N. Oyanagi, M. Khan, and K. Arai, "Shape of SiC bulk single crystal grown by sublimation", *Mater. Sci. Forum* **338–342**, 99–102 (2000).
 17. R.H. Ma, Q.S. Chen, H. Zhang, V. Prasad, C.M. Balkas, and N.K. Yushin, "Modeling of silicon carbide crystal growth by physical vapor transport method", *J. Cryst. Growth* **211**, 352–359 (2000).
 18. Q.S. Chen, H. Zhang, and V. Prasad, "Heat transfer and kinetics of bulk growth of silicon carbide", *J. Cryst. Growth* **230**, 239–246 (2001).
 19. P.J. Wellmann, M. Bickermann, D. Hofmann, L. Kadinski, M. Selder, T.L. Straubinger, and A. Winnaker, "In situ visualization and analysis of silicon carbide physical vapor transport growth using digital X-ray imaging", *J. Cryst. Growth* **216**, 263–272 (2000).
 20. P.J. Wellmann, D. Hofmann, L. Kadinski, M. Selder, T.L. Straubinger, and A. Winnaker, "Impact of source material on silicon carbide vapor transport growth process", *J. Cryst. Growth* **225**, 312–316 (2001).
 21. M. Selder, L. Kadinski, F. Durst, and D. Hofmann, "Global modeling of the SiC sublimation growth process: prediction of thermoelastic stress and control of growth conditions", *J. Cryst. Growth* **226**, 501–510 (2001).
 22. A. Pisch, A.M. Feraria, C. Chatillon, E. Blanquet, M. Pons, C. Bernard, M. Anikin, and R. Madar, "Evaporation behavior of SiC powder for single crystal growth: an experimental study on thermodynamics and kinetics", *Mater. Sci. Forum* **338–342**, 91–94 (2000).
 23. C. Raffy, L. Magaud, E. Blanquet, M. Pons, and A. Pasturel, "Ab initio study of silicon carbide: bulk and surface structures", *Mater. Sci. Forum* **353–356**, 11–14 (2001).
 24. N. Oyanagi, S. Nishizawa, T. Kato, H. Yamaguchi, and K. Arai, "SiC single crystal growth rate measurement by in-situ observation using the transmission X-ray technique", *Mater. Sci. Forum* **338–342**, 75–78 (2000).
 25. D.D. Avrov, A.S. Bakin, S.I. Dorozhkin, V.P. Rastegaev, and Yu.M. Tairov, "The analysis of mass transfer in system beta-SiC-alpha-SiC under silicon carbide sublimation growth", *J. Cryst. Growth* **198–199**, 1011–1014 (1999).
 26. I.A. Zhmakin, A.V. Kulik, S.Yu. Karpov, S.E. Demina, M.S. Ramm, and Yu.N. Makarov, "Evolution of thermoelastic strain and dislocation density during sublimation growth of silicon carbide", *Diamond Relat. Mater.* **9**, 446–451 (2000).
 27. C. Moulin, M. Pons, A. Pisch, P. Grosse, C. Faure, G. Basset, A. Passero, T. Billon, B. Pelissier, M. Anikin, P. Pernot, and R. Madar, "SiC single crystal growth by sublimation: experimental and numerical results", *Mater. Sci. Forum* **353–356**, 7–10 (2001).
 28. M.V. Bogdanov, A.O. Galyukov, S.Yu. Karpov, A.V. Kulik, S.K. Kochuguev, D.Kh. Ofengeim, A.V. Tsiryulnikov, M.S. Ramm, A.I. Zhmakin, and Yu.N. Makarov, "Virtual reactor as a new tool for modeling and optimization of SiC bulk crystal growth", *J. Cryst. Growth* **225**, 307–300 (2001).
 29. Yu.E. Egorov, A.O. Galyukov, S.G. Gurevich, Yu.N. Makarov, E.N. Mokhov, M.G. Ramm, M.S. Ramm, A.D. Roenkov, A.S. Segal, Yu.A. Vodakov,

- A.N. Vorob'ev and A.I. Zhmakin, "Modeling analysis of temperature field and species transport inside the system for sublimation growth in tantalum container", Mater. Sci. Forum **264–268**, 61–64 (1998).
30. S.G. Müller, R. Eckstein, J. Fricke, D. Hofmann, R. Hofmann, R. Horn, H. Mehling, and O. Nilsson, "Experimental and theoretical analysis of the high temperature thermal conductivity of monocrystalline SiC", Mater. Sci. Forum **264–268**, 623–626 (1998).
 31. S.G. Müller, J. Fricke, D. Hofmann, R. Horn, O. Nilsson, and B. Rexer, "Experimental and theoretical analysis of the thermal conductivity of SiC powder as a source material for SiC bulk growth", Mater. Sci. Forum **338–342**, 43–46 (2000).
 32. A.S. Segal, A.N. Vorob'ev, S.Yu. Karpov, E.N. Mokhov, M.G. Ramm, M.S. Ramm, A.D. Roenkov, Yu.A. Vodakov, and Yu.N. Makarov, "Growth of silicon carbide by sublimation sandwich method in the atmosphere of inert gas", J. Cryst. Growth **208**, 431–441 (2000).
 33. Yu.A. Vodakov, A.D. Roenkov, M.G. Ramm, E.N. Mokhov, and Yu.N. Makarov, "Use of Ta-container for sublimation growth and doping of SiC bulk crystals and epitaxial layers", Phys. Stat. Sol. (b) **202**, 177–200 (1997).
 34. F.C. Frank, "Capillary equilibria of dislocated crystals", Acta Crystallogr. **4**, 497–501 (1951).
 35. J. Heindl, H.P. Strunk, V.D. Heydemann, and G. Pensl, "Micropipes: hollow tubes in silicon carbide", Phys. Stat. Sol. (a) **162**, 251–262 (1997).
 36. A.M. Glazer, J.G. Lewis, and W. Kaminsky "An automatic optical imaging system for birefringent media", Proc. R. Soc. Lond. Ser. A **452**, 2751–2765 (1996).
 37. M. Geday, J. Kreisel, A.M. Glazer, and K. Roleder, "Birefringence imaging of phase transitions: application to $\text{Na}_{0.5}\text{Bi}_{0.5}\text{TiO}_3$ ", J. Appl. Crystallogr. **33**(2), Part 3, 909–914 (2000).
 38. J. Baruchel, Y. Epelboin, J. Gastaldi, J. Hartwig, J. Kulda, P. Rejmankova, M. Schlenker, and F. Zontone, "First topographic results at the European Synchrotron Radiation Facility", Phys. Stat. Sol. (a) **141**, 59–69 (1994).
 39. A. Authier, S. Lagomarsino, and B.K. Tanner, *X-Ray and Neutron Dynamical Diffraction: Theory and Applications*, NATO ASI Series (1996).
 40. G.R. Fisher, and P. Barnes, "Towards a unified view of polytypism in silicon carbide" Phil. Mag. B **61**(2), 217–236 (1990).
 41. J. Takahashi, M. Kanaya, and Y. Fujiwara, "Sublimation growth of SiC single crystalline ingots on faces perpendicular to the (0001) basal plane", J. Cryst. Growth **135**, 61–70 (1994).
 42. I. Sunagawa, K. Narita, P. Bennema, and B. Van Der Hoek, "Observation and interpretation of eccentric growth spirals", J. Cryst. Growth **42**, 121–126 (1977).
 43. P. Bennema, "Spiral growth and surface roughening: developments since Burton, Cabrera and Frank", J. Cryst. Growth **69**, 182–197 (1984).
 44. A.N. Pilyankevich, and V.F. Britun, "Motion of partial dislocation in silicon carbide", Phys. Stat. Sol. (a) **82**, 449–457 (1984).
 45. P. Krishna, S.S. Jiang, and A.R. Lang, "An optical and X-ray topographic study of giant screw dislocations in silicon carbide", J. Cryst. Growth **71**, 41–56 (1985).
 46. R.C. Glass, L.O. Kjellberg, K.F. Tsvetkov, J.E. Sundgren, and E. Janzen, "Structural macro-defects in 6H-SiC wafers", J. Cryst. Growth **132**, 504–512 (1993).

47. N. Schulze, D.L. Barrett, G. Pensl, S. Rohmfeld, and M. Hundhausen, "Near-thermal equilibrium growth of SiC by physical vapor transport", Mater. Sci. Eng. B **61–62**, 44–47 (1999).
48. K. Chourou, M. Anikin, J.M. Bluet, V. Lauer, G. Na0.5Bi0.5TiO3Guillot, J. Camaressel, S. Juillaguet, O. Chaix, M. Pons, and R. Madar, "Experimental investigation of 4H-SiC bulk crystal growth", Mater. Sci. Forum **264–268**, 17–20 (1998).
49. S. Milita, R. Madar, J. Baruchel, and A. Mazuelas, "X-ray section topographic investigation of the growth process of SiC crystals", Mater. Sci. Forum **264–268**, 29–32 (1998).
50. R. Madar, M. Anikin, K. Chourou, M. Labeau, M. Pons, E. Blanquet, J.M. Dedulle, C. Bernard, S. Milita, and J. Baruchel, "Defects formation in sublimation grown 6H-SiC single crystal boules", Diamond Relat. Mater. **6**, 1249–1261 (1997).
51. X.R. Huang, M. Dudley, W.M. Vetter, W. Huang, S. Wang, and C.H. Carter, "Direct evidence of micropipe-related pure superscrew dislocations in SiC", Appl. Phys. Lett. **74**, 353–355 (1999).
52. M. Dudley, and X. Huang, "Characterisation of SiC using synchrotron white beam X-ray topography", Mater. Sci. Forum **338–342**, 431–436 (2000).
53. D. Hofmann, M. Bickermann, D. Ebbling, B. Epelbaum, L. Kadinski, M. Selder, T. Straubinger, R. Weingaertner, P. Welmann, and A. Winnaker, "SiC crystal growth from the vapor and liquid phase", Mater. Res. Soc. Symp. Proc. **640**, 1–14 (2001).
54. J. Takahashi, N. Ohtani, and M. Kanaya, "Structural defects in alpha-SiC single crystals grown by the modified-Lely method", J. Cryst. Growth **167**, 596–606 (1996).
55. J. Takahashi, and N. Ohtani, "Modified-Lely SiC crystals grown in [1100] and [1120] directions, sublimation growth of 6H- and 4H-SiC single crystals in the [1100] and [1120] directions", Phys. Stat. Sol. (b) **202**, 163–175 (1997).
56. H. Harima, S.I. Nakashima, and T. Uemura, "Raman scattering from anisotropic LO-phonon–plasmon-coupled mode in n-type 4H- and 6H-SiC", J. Appl. Phys. **78**, 1996–2005 (1995).
57. H. Harima, T. Hosoda, and S. Nakashima, "Raman imaging characterization of electric properties of SiC near a micropipe", Mater. Sci. Forum **338–342**, 603–606 (2000).

Lattice Dynamics of Defects and Thermal Properties of 3C-SiC

D.N. Talwar

Using a realistic theoretical scheme, a comprehensive study of the lattice dynamics of defects in 3C-SiC and of the thermal properties of that material is presented. For the perfect compound, the data on lattice constants, elastic constants, and high-symmetry phonon modes have allowed us to optimize the parameters of the lattice-dynamical model to obtain accurate values of the phonon dispersions, the one-phonon density of states, the mode Grüneisen parameters $\gamma(\vec{q})$, the specific heat $C_v(T)$, and the thermal expansion coefficient $\alpha(T)$ within the quasi-harmonic approximation. Despite a small softening of the TA modes in 3C-SiC, the variation of $\alpha(T)$ with temperature is seen to be much like that of $C_v(T)$, and unlike silicon and most other tetrahedrally coordinated materials, it exhibits no negative values at lower temperatures. The lattice-dynamical behavior of isolated and complex defect centers in 3C-SiC is studied in the framework of a Green's function technique. Theoretical results obtained for the characteristic vibrational modes of some prototypical centers are analyzed, compared, and discussed in relation to experimental results and first-principles calculations.

5.1 Introduction

Research on silicon carbide (SiC) in recent years has led to significant advances in the development of optoelectronic and microelectronic devices [1–3]. The large bonding energy of Si-C makes SiC highly resistant to radiation and chemical attack ensuring the stability of high-frequency, high-temperature, and high-power devices [4–9]. Silicon carbide is an interesting semiconductor for basic research not only due to its special position among the popular wide-bandgap III-nitrides (GaN and AlN) but also because of its superior electrical, mechanical and thermal properties over many other binary compounds [10–12]. Apparently, the material has a substantial advantage over several compound semiconductors because it can be oxidized to form on its surface a stable layer of insulating SiO_2 . It is also a good substrate for the

epitaxial growth of GaN, which opens the possibility of fabrication of electroluminescent devices emitting blue light. Its disadvantage, for some applications, lies in its indirect energy band gap.

5.1.1 Polymorphic Forms of SiC

Silicon carbide is the only group IV-compound that forms stable, long-range complex-ordered structures (polytypes) [13–16]. These ordered-structures differ by the stacking sequence of Si and C double layers. Although more than 200 SiC polymorphic forms are known to exist, only a few of these are found to have practical significance [1–3]. Essentially, all polytypes can be divided into three groups: (i) cubic (3C) – with crystal structure similar to one of sphalerite or zinc-blende (space group $T_d^2\{F\bar{4}3m\}$), (ii) hexagonal (2H) – with the wurtzite crystal structure (space group $C_{6V}^4\{P6_3mc\}$), and (iii) rhombohedral (space group $C_{3V}^5\{R3m\}$) – which includes all other known polytypes. It has been suggested that all polymorphs of the third group may be considered as a natural superlattice in which the atomic layers with cubic and hexagonal symmetry follow in a certain alteration.

5.1.2 Issues Related to Defects and Polytypism

Before a wider use of SiC polytypes is made in producing electronic devices, a series of technological problems related primarily to the control of doping (with suitable donors and acceptors) and polytypism [17–20] have to be solved.

One of the most important issues in semiconductor device processing is to understand the properties of point defects because their presence can strongly alter the material's electronic characteristics. The perfect wide band gap SiC is basically an insulator up to high temperatures. Introduction of selectively chosen defects can create states relatively close to the conduction and valence band edges allowing excitation of electrons (donor) or holes (acceptor) into the bands. This way a majority of *n*- or *p*-type carriers can be achieved and the conductivity is proportional to the concentration of dopants. The shallower the dopant states are, the lower is the temperature, allowing the full dopant concentration to become active. This simple picture is valid only if the lattice imperfections other than the dopants are disregarded. In reality, however, one has to take into account the inevitable intrinsic defects of the crystal and the impurities which enter the material during processing. Therefore, a detailed knowledge about the electronic structure of the crystal and how it is affected by the chosen dopants and/or the intrinsic defects and impurities is crucial. Unfortunately, despite numerous experimental efforts [27–30] made in recent years using electron paramagnetic resonance (EPR), Hall measurements, Photoluminescence (PL) and deep level transient spectroscopy (DLTS), there is still much controversy and mystery surrounding the identification of intrinsic and doped defects in SiC which produce nonstoichiometry and deep localized

levels. An alternative way to characterize defects in semiconductors is to investigate their structural and dynamical behavior by vibrational spectroscopy.

The second major concern in device processing has been the control of polytypism during growth because the electronic [17–20] and vibrational properties of different ordered structures [21–25] are significantly different. As the crystal field experienced by the same “chemical” impurity incorporated in different inequivalent sites in SiC can be different [26] one expects significant spectroscopic changes depending upon the site it occupies. Understanding these differences has been and still is a challenge for both experimentalists [27–34] and theorists [17–19, 35–37].

Another obstacle to the ongoing research and development efforts in SiC for applications is the lack of substrates which are both lattice and thermally matched [38]. At present only the 3C-SiC form has been grown epitaxially on Si (100) substrates [39–43]. The cubic SiC exhibits the simplest structure different from other polytypes and is the most suitable to investigate the nature of defects. This has stimulated considerable interest for studying the optical, structural and electrical properties [27–34] of defects in 3C-SiC/Si films by using X-ray, DLTS, Hall measurements, PL, infrared (IR) and Raman spectroscopy [44–48].

5.1.3 Structural and Dynamical Properties of 3C-SiC

In recent years, attempts have been to understand the mechanism of the polytype growth by using X-ray diffraction (XRD) [42], high resolution transmission electron microscopy (HRTEM) [43] and optical (IR and Raman) spectroscopy [44–47]. Raman scattering has the capability of characterizing the electronic properties [48] of the material as well as detecting the coupled modes of LO-phonon and plasma oscillations of free carriers [49]. Some studies have gone even deeper into the high-pressure behavior of SiC and reported the effects of atomic relaxation on its lattice vibrations. From the critical-point analysis of the pressure dependent Raman spectra [50–55], one can obtain information about the variation of acoustical and optical phonons and hence the mode-Grüneisen parameters at high-symmetry points in the Brillouin zone. Several thermodynamic quantities [56–59], the lattice and elastic properties [60–64] (e.g., the lattice constant, the bulk modulus B , and its pressure derivative B') along with the Born's transverse effective charge e_T^* [54, 65] have been reported experimentally in an extended pressure range. Although, Raman scattering can be used to identify the substitutional impurities or structural defects, only very few studies have been reported in the SiC system [44–46].

More recently, the measurements of phonon dispersions in 3C-SiC have been achieved by inelastic X-ray [66] scattering (IXS). This information is significant because phonons can influence the behavior of carriers in devices through electron-phonon interaction and help investigate important material properties such as phonon-assisted photoemission, defect vibrations, thermal

expansion, phonon conductivity, etc. Experiments involving direct detection of the propagating phonons have also provided an excellent method for studying the electron-phonon interactions which is significant for understanding the operation of electronic devices. Due to different sound velocities, the contribution to heat pulse signals from the individual phonon modes may be resolved and by observing the variation of heat pulse signals with temperature or phonon frequency, a great deal of information on phonon scattering can be obtained. Quite recently, the phonon imaging [67] techniques have been used to study phonon emission in multi-quantum well structures, non radiative processes in ternary alloys and phonon drag in bulk semiconductors. These methods can provide effective means of observing the effects of defects and interfaces, as both can scatter phonons.

Despite plethora of experimental results accumulated over the years [27–35], the accurate evaluation of electronic levels of impurities, annealing behavior, and/or the vibrational properties of defects in 3C-SiC have not yet been fully understood theoretically. Earlier, Bechstedt et al. [18] used *ab initio* methods and reported the structural effects of polytypes on the optical properties of SiC by focussing their attention on the effects of atomic structures, layered combinations of polytypes and surface equilibrium structures, etc. More recently Gali et al. [36] have studied the structural, electronic and vibrational properties of carbon clusters, H-carbon (silicon) vacancy ($V_{C(Si)} + nH$) complexes in SiC by using *ab initio* supercell-density-functional calculations. The purpose of the present paper is to review the recent developments on the vibrational behavior and report our results on the lattice dynamics, thermal and pressure dependent properties of 3C-SiC with special emphasis on impurity vibrations. We strongly believe that theoretical analysis of the electrical and vibrational data based on realistic defect models with expected symmetries can be very fruitful in identifying the nature of impurities in SiC. By using realistic lattice dynamical schemes, and carefully analysing the optical experiments (infrared and Raman scattering) one can obtain the strength of interatomic forces in the perfect SiC as well as valuable information about the nature and site selectivity of intrinsic and doped defects. To extract the knowledge of interatomic forces under compression and to relate it to the charge-transfer effects and structural instabilities, the Raman data has provided a very good testing ground for studying the lattice dynamics, mechanical as well as thermal properties [51–54]. As the knowledge of thermal expansion coefficient $\alpha(T)$ over an extended temperature range is critical for predicting the residual stress distribution in 3C-SiC/Si-based devices, we report our results of the mode-Grüneisen parameters, thermal expansion coefficient and specific heat in 3C-SiC. Since the cubic SiC is regarded as an intermediate between silicon and diamond in its mechanical and electronic properties, the lattice dynamical results of 3C-SiC are compared and discussed with the existing experimental [59] data as well as with those of silicon [68] and diamond [69, 70].

The paper is outlined as follows: After a brief description of the theoretical methods used for impurity identification and characterization (see Sect. 5.2), we present in Sects. 5.2.1 and 5.2.2 a simple account of the atomic and geometrical configurations [4] of various types of point defects in semiconductors and emphasize the significance of lattice relaxation and distortion (see Sect. 5.2.3). This is preceded by a section on the lattice dynamical schemes (see Sect. 5.3) used to treat the vibrational properties of host semiconductors. Although a short comment is made on the status of the *ab initio* phonon methods, our prime motive here is to stress on the ease and usefulness of the phenomenological schemes. In the frame work of a Green's function theory for impurity vibrations the choice of a rigid-ion-model (RIM) is presented in Sects. 5.3.1 and 5.3.2. In the quasi-harmonic approximation, we outlined a methodology (see Sect. 5.3.3) for extracting the pressure dependent phonon and thermodynamical properties. The practicality of the Green's function theory (see Sect. 5.4) for analysing the lattice vibrations of defects in semiconductors and extracting relevant information about the impurity-host bonding is presented in Sects. 5.4.1 and 5.4.2. The perturbation models for the isolated and complex defects are given in Sect. 5.4.3. Numerical calculations are performed for the dynamical properties of perfect/imperfect 3C-SiC in Sect. 5.5. Theoretical results of the lattice dynamics, mode Grüneisen parameters and thermal expansion coefficients (see Sects. 5.5.1 and 5.5.2) are compared and discussed with the available experimental data. In Sect. 5.5.3 we have studied the dynamical properties of both isolated and complex defects in 3C-SiC. The results are compared analyzed, and discussed with the existing experimental and *ab initio* calculations. Finally, the summary of conclusions are drawn in Sect. 5.6.

5.2 Theoretical Background

Two equally reliable theoretical methods have been used in recent years to study the dynamical properties of defects in semiconductors: (a) A microscopic analysis based on local-density-functional approach – with the use of ionic pseudopotentials, it has now become possible to perform parameter free (first principles) calculations of phonon energies of perfect [18, 36] and/or imperfect systems. (b) A macroscopic analysis [71] based on the general treatment of lattice dynamics in terms of interatomic forces – with the use of Green's function methods for the perfect/imperfect lattice, the displacement response to the sinusoidal driving forces may be estimated. For perfect systems, the former type of calculations start with the atomic and electronic structures obtained within the density functional theory and local density approximation. For isoelectronic defect vibrations, the microscopic calculations require heavy computation and presumably they are much more cumbersome for charged defects. Except for a few attempts made in recent years to understand the optical data of SiC polytypes [18], the information about the lattice

dynamics of defects [36] especially the nature of ‘impurity-host bonding’ for donors or acceptors is rather sparse.

An alternative to the parameter free calculations is the more elegant Green’s function technique [71]. Its advantage over the first principles methods is that it allows the coupling of the vibrations of the defect to the bulk crystal, and one can visualize which types of vibrational modes remain localized around the defect. In the Green’s function theory: (i) the lattice dynamics of the perfect lattice must be known in details by means of phonon models, (ii) the models describing the vibrations of impurities on the basis of the perfect lattice vibrations must be constructed, and (iii) the comparison of the model calculation with “spectroscopic” (infrared and Raman) measurements determines a “force-constant ratio” for the impurity host lattice coupling, and the systematics of this parameter permits a discussion of impurity properties.

Although, the methodology of the Green’s function technique is documented in several review articles [71], monographs and books [72, 73], it may be of value to some readers to have a brief and simple account of the atomic and geometrical configurations of point defects, lattice relaxation and what is actually involved in the lattice dynamical calculations before proceeding to emphasize on different defect structures. The discussion presented here is thus very brief for the purpose only of establishing the notations to be used throughout the paper.

5.2.1 Atomic Configuration of Defects

The type of isolated “point defects” (intrinsic or extrinsic) in crystals is generally defined by its “chemical” nature and “geometrical” configuration. The notion of isolated point defects implies that the perturbation of the lattice remain localized, i.e., it involves an atomic site and few neighbors. The associated electronic perturbation can, however, extend to larger distances and be, at the limit, delocalized. Schematic representation of some of the important “intrinsic” (vacancy, self-interstitial, antisite) and “extrinsic” (substitutional, interstitial) point defects in semiconductors is shown in Fig. 5.1A. Complex centers are formed by the association of two or more intrinsic and/or extrinsic defects (see: Fig. 5.1B). A vacancy close to a self-interstitial forms a Frenkel pair; two vacancies on neighboring lattice sites form a divacancy, etc. Unlike elemental semiconductors, the lattice sites for intrinsic and extrinsic (substitutional, interstitial) defects in SiC are not equivalent as they differ in their environment and lattice neighbors. If the defect concentration increases such that there is an overlap of the perturbation caused by individual defects, they can not be regarded as isolated point defects; “defect ordering” or alloy formation can occur. We have not included one-dimensional (dislocation), two-surfaces, grain boundaries) or three-dimensional (voids and cavities) defects in this review.

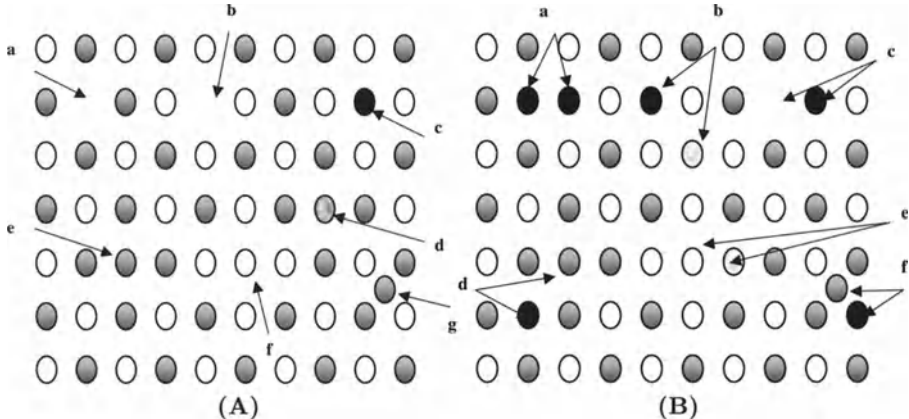


Fig. 5.1. (A) Schematic representation of simple isolated point defects in cubic SiC: (a) C vacancy, V_C ; (b) Si vacancy, V_{Si} ; (c) substitutional impurity on Si site, I_{Si} ; (d) substitutional impurity on C site, I_C ; (e) Si substituted on C site (antisite), Si_C ; (f) C substituted Si site (antisite), C_{Si} ; (g) Si self-interstitial. (B) Schematic representation of complex defects in cubic SiC: (a) nearest-neighbor (NN) pair ($I_C - I'_{Si}$) defect; (b) second-nearest-neighbor (2NN) pair ($I_{Si} - I'_{Si}$) defect; (c) NN vacancy–substitutional pair ($V_C - I'_{Si}$) defect; (d) 2NN antisite–substitutional pair ($Si_C - I_C$) defect; (e) NN antisite–substitutional pair ($C_{Si} - I_C$) defect; (f) Si self-interstitial–substitutional pair ($Si_{int} - I_C$) defect

5.2.2 Geometrical Configuration of Defects

a) The vacancy

To create an isolated vacancy in diamond/zinc blende type solids one has to remove an atom by breaking its four bonds (see Fig. 5.2a). The broken or dangling bonds can lead to new bonding depending upon the charge state of the vacancy, i.e., on the number of electrons which occupy these dangling bonds (see Fig. 5.2b,c). The neighboring atoms of the vacancy can have small displacements either inward or outward to preserve the local symmetry (relaxation) or alter it (distortion). The amplitude of these displacements as well as the new symmetry of the defect depend upon the types of bonding. In 3C-SiC an isolated Si vacancy in its negative charge state V_{Si}^- has a T_d symmetry, while the positively charged carbon vacancy V_C^+ is found to be in the D_{2d} configuration [31]. Another important case of a possible distortion is the “split-vacancy” (saddle point) configuration in which one neighbor of the vacancy is displaced half way between its original position and the center of the vacancy (see Fig. 3a). In a divacancy (see Fig. 5.3b) the type of bonding that dangling bonds form also depends upon their electronic occupancy. In Fig. 5.3c, the configuration of a “split-divacancy” is displayed.

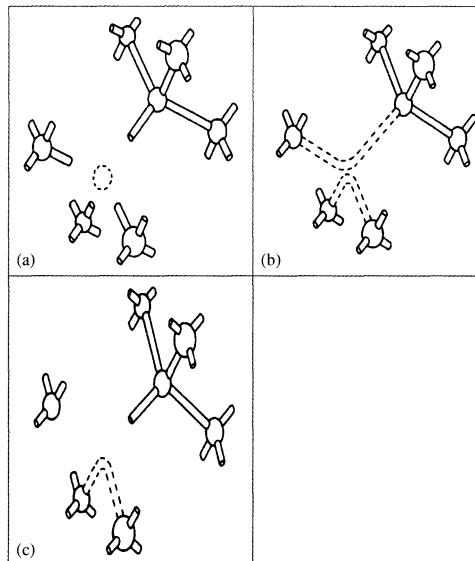


Fig. 5.2. Two-dimensional schematic representation [4] of a vacancy in the diamond structure. To create a vacancy, four bonds that connect an atom to its NN are to be broken (a). For the neutral vacancy V^0 , there is one electron per dangling bond, which can form two new bonds, leading to local distortion (b). If there is a missing electron (positive vacancy V^+), one of these new bonds will be weakened, resulting in a different distortion (c)

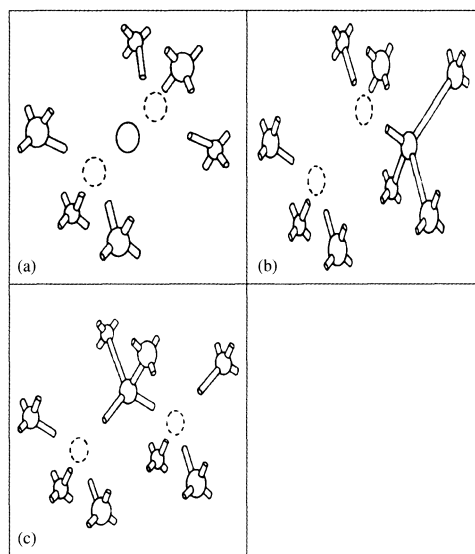


Fig. 5.3. Two-dimensional schematic representation [4] of a split-vacancy configuration in the diamond structure (a); divacancy configuration (b); and split-divacancy configuration (c)

b) The interstitials

In semiconductors, mobile interstitials and vacancies play a pivotal role in the annealing kinetics and mass transport. There exists two configurations of highest symmetry for an interstitial in diamond lattice – the hexagonal and tetrahedral (see Fig. 5.4a,b). In zinc-blende lattice one can consider the center of fcc conventional unit cell as the tetrahedral interstitial site (Fig. 5.4c). In this configuration an interstitial can have two possibilities (i) either surrounded by a cation or (ii) by anion neighbors. Another site of high symmetry for an interstitial corresponds to the “bond-centered” configuration in which the interstitial sits at the center of the bond (Fig. 5.4d). A possible distortion of the bond-centered case leads to “split” interstitial configuration in which the interstitial atom and one of its neighbors are displaced in such a way that they form a dumbbell centered on the original substitutional site of this neighbor. The split-interstitial can have different configurations depending upon the orientation of the dumbbell (see Fig. 5.5a–c). In 3C-SiC the singly charged and neutral carbon $\langle 100 \rangle$ split-interstitial are suggested as microscopic models [37] for the T5 and EI3 centers, respectively [33].

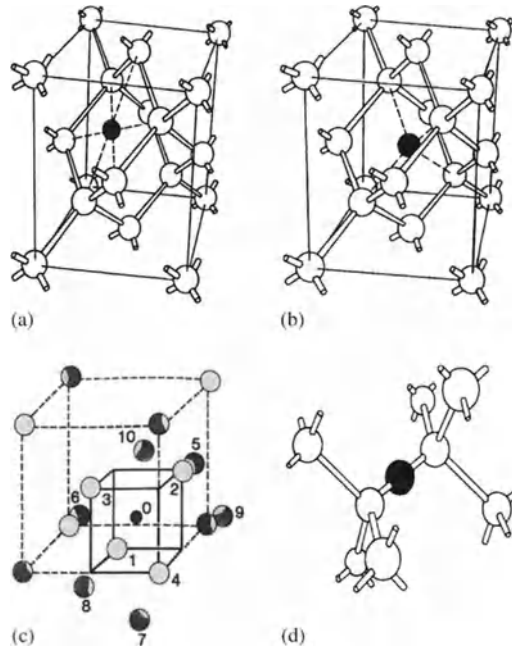


Fig. 5.4. Interstitial sites of highest symmetry [4] in the diamond/zinc-blende structure. The hexagonal interstitial configuration in the diamond structure (a); the tetrahedral interstitial configuration in the diamond structure (b); the tetrahedral interstitial configuration in the zinc-blende structure (c); and the bond-centered interstitial configuration in the diamond structure (d)

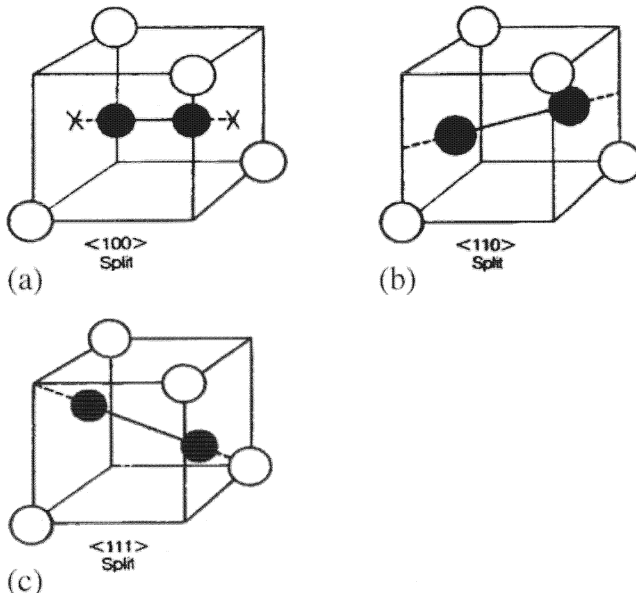


Fig. 5.5. Split-interstitial configuration in the diamond structure [4] in various orientations: $\langle 100 \rangle$ split (a); $\langle 110 \rangle$ split (b); and $\langle 111 \rangle$ split (c)

c) The complex defects

An isolated substitutional defect on C or Si site in 3C-SiC can interact with other intrinsic as well as extrinsic point defects giving rise to complex defect centers (see Fig. 5.6). The ideal nearest neighbor pair defect can be assumed to have an impurity atom (say phosphorous) substituting for Si (P_{Si}) site 2 and another impurity atom (say vacancy) occupying the C (V_C) site 1. The point-group symmetry of this defect center is C_{3v} with the axis along the 1–2 bond (see Fig. 5.6a). Another defect with orthorhombic symmetry can be considered assuming an impurity atom substituting for the C site 1 and a second impurity atom occupying the nearest C site 6 (say) in the [100] direction. The point-group symmetry is C_{2v} (see Fig. 5.6b) if the two impurity atoms are similar otherwise it is C_s .

Vacancies attached to off center substitutional defects in semiconductors can form complex centers. For instance, in Si the mobile vacancy when trapped by an oxygen atom present in the Czochralski material forms a V-O complex (A-center: see Fig. 5.6c) or if it is attached to Al dopant it forms V-Al complex (E-center). In 3C-SiC, the relaxed structure of P_{Si} - V_C can reconstruct from C_{3v} to a lower C_{1h} symmetry.

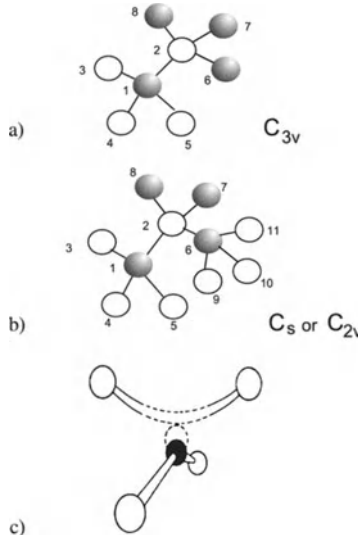


Fig. 5.6. Impurity perturbation models for the vibrations of one, two, and three defects in the zinc-blende structure. (a) An isolated defect I_C (I_{Si}) if located at site 1 (2) bound to NN Si (C) atoms at 2 (1), 3 (6), 4 (7), and 5 (8) will have T_d symmetry, and the NN pair defect with impurity atoms occupying the Si (2) and C (1) sites ($I_{Si}-I_C$) will have C_{3v} symmetry. (b) The most extended case of three substitutional defects occupying sites 1, 2, and 6 (see text). A 2NN pair with an impurity on the C site (1) and another impurity on an NN C site (6). The pair will have C_s symmetry if the impurities at sites 1 and 6 are different; if the impurities at sites 1 and 6 are the same the symmetry will be C_{2v} . (c) The A-center configuration (vacancy + oxygen complex) in the diamond structure. The oxygen atom is slightly displaced off the substitutional position

5.2.3 Lattice Relaxation and Distortion

The introduction of point defects generally induces displacements of the host lattice atoms that surround it. The atoms involved are first nearest neighbors, second nearest neighbors, etc., depending upon the range of the perturbation induced by the defect. If the symmetry of the lattice is conserved, the displacements of the neighboring atoms are said to result in a relaxation and if the symmetry is lowered, the induced displacements of the neighboring atoms are said to result in a distortion. The amplitudes as well as the type of displacements the lattice atoms undergo are obtained theoretically by minimizing the total energy of the system, lattice plus defect, versus the positions of the various atoms involved in the relaxation or distortion.

There exist two tractable approaches for studying the lattice relaxation or distortion around simple defects in semiconductors (i) self-consistent pseudopotential methods [18, 36] and, (ii) macroscopic theories [74]. With a few exception, the former method is still regarded as too intricate to be applied to

a great variety of impurity-host systems. A semi-empirical method outlined in Sect. 5.4.3 can be used for studying the lattice relaxation around substitutional impurity atoms and its effect on the vibrational properties of simple defects in 3C-SiC.

5.3 Lattice Dynamical Models

The problem of studying the vibrational properties of defects in semiconductors demands lattice dynamics of the perfect lattice from a reliable phenomenological model. We are not intended to give a comprehensive treatment on the subject because the description of phonon models is not the main theme of this paper. A number of excellent reviews and books have treated the subject extensively [75, 76]. Although we made a short comment on the status of *ab initio* calculations, our prime motive is to emphasize, within the Green's function theory, the usefulness of phenomenological phonon models.

a) Phenomenological methods

As the electric field plays an important role in the lattice dynamics of compound semiconductors, it is justified to neglect those models which only consider forces of the short-range. The models of interest, therefore, are those which assume the ions and/or electrons to be charged and polarizable, besides assuming short-range forces describing the covalent parts of the interaction. The most notable schemes in this category are the shell-model, deformation dipole model, bond-charge model, rigid-ion-model (RIM) etc. [75, 76]. The simplest among these is the RIM in which the charges $\pm Ze$ are assigned to ions giving rise to the Coulomb forces, besides the short-range potentials. We have chosen a second-neighbor RIM [77–79] not only because it represents the phonons of the host crystal very well but also due to its conceptual simplicity the model has an added advantage in accurately defining the impurity perturbations.

b) Ab initio methods

Contrary to the phenomenological schemes, *ab initio* methods do not assume any form for the interactions of the atoms in the system and tries to calculate every thing from first-principles quantum mechanical quantities. It seems natural that phonons can be calculated once the electronic band structure of the lattice is known with good accuracy. The practical answer to such a proposal is, however, extremely complicated. First, it is necessary to have a good handle on the electronic structure of perfect lattices without vibrations. Second, a formalism permitting calculation of phonon properties from the band structure must be found.

There exist number of different *ab initio* approaches with respective advantage and disadvantages. The so called “frozen-phonon” technique was the

first *ab initio* method considered to find the phonon displacement patterns and energies at high symmetry points of the Brillouin zone. For phonon energies at arbitrary points in the Brillouin zone, the displacement pattern required a large unit cell and calculations became prohibitively complex. Nowadays, the standard tool for calculating electronic and lattice properties is the density-functional theory within the so called local density approximation and pseudopotentials [18, 36]. Despite the involved complexity, the method has been used successfully to extract information such as lattice constant, the cohesive energy, the lattice and defect structures, etc.

5.3.1 The Second-Neighbor Rigid-Ion Model

In the harmonic approximation, the invariance of potential energy with respect to rigid-body translations, rotations, and symmetry operations of the crystal lattice results in only two nearest neighbor force constants (A, B) required to treat the lattice dynamics of diamond- or zinc-blende-type crystals. Calculations by Grimm et al. [80] based on this 2-parameter force model failed to describe the measured phonon dispersion curves for GaAs, suggesting the need of an elaborate force model involving interactions with more distant neighbors. The RIM of Kunc [75] considered short-range interactions up to second-nearest-neighbors and included the long-range Coulomb effects. Our choice of this model will help facilitate comparison of the results in 3C-SiC with the analogous ones obtained earlier in other compound semiconductors [77].

The quantities of interest in the second-neighbor RIM are the force constant $\vec{\phi}^{sC} (\equiv \vec{\phi}^s + \vec{\phi}^C)$ and dynamical $\vec{D}^{sC} (\equiv \vec{D}^s + \vec{D}^C)$ matrices, respectively. Due to tetrahedral symmetry of the zinc-blende lattice, the off-diagonal Cartesian blocks of the short-range force constant matrix $\vec{\phi}^s$ between nearest-neighbors is shown to have the form [75]

$$\langle l\kappa | \phi^s | l\kappa' \rangle = \begin{pmatrix} A & B & B \\ B & A & B \\ B & B & A \end{pmatrix}, \quad (5.1)$$

while the force constant matrices between the second-nearest-neighbors can be written as:

$$\langle l\kappa | \phi^s | l\kappa' \rangle = \begin{pmatrix} C_\kappa & D_\kappa & \pm E_\kappa \\ D_\kappa & C_\kappa & \pm E_\kappa \\ \mp E_\kappa & \mp E_\kappa & F_\kappa \end{pmatrix}; \quad \text{with } \kappa = 1, 2. \quad (5.2)$$

Here, l labels the basic unit cells and κ represents the atoms within each unit cell.

For the long-range Coulomb ϕ^C force constant matrix elements, another parameter Z (the effective charge) is chosen thus giving rise to a total of 11 parameters. In this generalized 11-parameter RIM, the atomic displacements \mathbf{u} of each j -th mode are considered to have a sinusoidal spatial dependence

allowing a unique wave vector \vec{q} to be associated with each mode frequency $\omega_j(\vec{q})$:

$$u_\alpha(l\kappa|\vec{q}j) = (M_\kappa)^{-1/2} e_\alpha(\kappa|\vec{q}j) \exp i[\vec{q}\vec{x}(l\kappa) - \omega_j(\vec{q})t] ; \quad \text{with } \alpha = x, y, z . \quad (5.3)$$

The components of eigenvectors $e_\alpha(\kappa|\vec{q}j)$ for each mode frequency $\omega_j(\vec{q})$ satisfy the familiar orthogonality

$$\sum_{\alpha\kappa} e_\alpha^*(\kappa|\vec{q}j) e_\alpha(\kappa|\vec{q}j') = \delta_{jj'} , \quad (5.4)$$

and closure relations

$$\sum_j e_\alpha^*(\kappa'|\vec{q}j) e_\beta(\kappa|\vec{q}j) = \delta_{\alpha\beta} \delta_{\kappa\kappa'} . \quad (5.5)$$

The lattice vibrations in the harmonic approximation are obtained by solving the equation of motion

$$\omega_j^2(q) e_\alpha(\kappa|\vec{q}j) = \sum_{\kappa'\beta} D_{\alpha\beta}^{sC}(\kappa\kappa'|\vec{q}) e_\beta(\kappa'|\vec{q}j) , \quad (5.6)$$

with

$$D_{\alpha\beta}^{sC}(\kappa\kappa'|\vec{q}) = D_{\alpha\beta}^s(\kappa\kappa'|\vec{q}) - \frac{Z_\kappa Z_{\kappa'} e^2}{(M_\kappa M_{\kappa'})^{1/2}} D_{\alpha\beta}^C(\kappa\kappa'|\vec{q}) . \quad (5.7)$$

The elements of the dynamical matrices \vec{D}^s and \vec{D}^C describing the general short-range and long-range Coulomb interactions are reported elsewhere [75]. In zinc-blende type crystals, the primitive unit cell contains two atoms, which produces an eigenvalue problem of dimension (6×6) . The values of the wave vector \vec{q} are restricted to lie within the first Brillouin zone of the fcc lattice. Hence \vec{q} assumes the form

$$|\vec{q}| = \frac{\pi}{a_o}(q_1, q_2, q_3) , \quad -1 \leq q_1, q_2, q_3 \leq 1 , \quad (5.8a)$$

with

$$|q_1 + q_2 + q_3| \leq \frac{3}{2} . \quad (5.8b)$$

The triples (q_1, q_2, q_3) are distributed with uniform density throughout the volume of the Brillouin zone. Once the RIM parameters are optimized (see Sect. 5.3.2) the eigenvalue equation (5.6) is solved numerically for each \vec{q} -vector in the Brillouin-zone to obtain the phonons [eigen frequency $\omega_j(\vec{q})$ and the eigenvector $e_\alpha(\kappa|\vec{q}j)$] of the normal modes. By plotting $\omega_j(\vec{q})$ versus \vec{q} displays the phonon dispersion curves. Besides the phonon modes, many

physical quantities (e.g., the heat capacity $C_v(T)$, Grüneisen parameters $\gamma_j(\vec{q})$, thermal expansion coefficient $\alpha(T)$, etc.) of the perfect solid may be calculated *á posteriori* to be compared (see Sect. 5.5.2) with the experimental data. It is to be noted that the phonons of the host crystals are needed to obtain the elements of the Green's function matrix (see Sect. 5.4) for the calculations of defect vibrations.

Table 5.1. Relevant data for 3C-SiC for optimizing the eleven rigid-ion-model parameters at ambient pressure and 22.5 GPa pressure. The values of the phonons at critical points (in wavenumbers), the elastic constants (in 10^{11} dyn/cm 2) and their pressure derivatives, the bulk modulus B (in GPa) and its pressure derivative, and the lattice constants (in Å) are taken from the existing experimental or theoretical data

Relevant data used in the lattice dynamics of 3C-SiC		
Phonon mode	Frequency (cm $^{-1}$) at 1 atm	Frequency (cm $^{-1}$) at 22.5 GPa
LO(Γ)	971 ^a	1066 ^g
TO(Γ)	796, 793 ^a	872
LO(X)	830 ^a	
TO(X)	759, 763 ^a	
LA(X)	640, 644 ^a	
TA(X)	373 ^a	
LO(L)		
TO(L)	766, 758 ^a	
LA(L)	615 ^a	
TA(L)	265 ^a	
Elastic constants	10^{11} dyn/cm 2	
C_{11}	39.0 ^b	
C_{12}	14.2 ^b	
C_{44}	25.6 ^b	
C'_{11}	4.33	
C'_{12}	4.19	
C_{44}'	0.8	
Bulk modulus (GPa)		
B_o	225 ^c , 248 ^d , 252 ^e	
B'_o	4.0	
Lattice constant (Å)	1 atm	22.5 GPa
a_o	4.3596 ^f	4.2484

References: a) [66]; b) [26], Feldman et al. (1968); c) [63]; d) [61]; e) [64]; f) [62]; g) (Estimated from the Raman data) [54]

5.3.2 The Phonon-Model Parameters

With the availability of elastic constants, lattice parameter and experimentally determined phonon energies for 3C-SiC (see Table 5.1), the RIM parameters are optimized by means of a least-squares method. The values of the final set of parameters represent the strength of the model potentials and yield the phonon frequencies in the entire \vec{q} -space. While the least-squares procedure seems to be straightforward, questions nevertheless arise as to the uniqueness and the physical interpretation of the model parameters. Clear trends obtained in the model parameters of the host semiconductors [75] along with the simple physical understanding of bonding situation for charged defects [71] have given us confidence in the choice of a RIM for studying the dynamical properties of perfect/imperfect 3C-SiC.

5.3.3 Pressure Dependent and Thermo-Dynamical Properties

The pressure and thermo-dynamical properties in solids are generally treated in the framework of anharmonic models, where the second order coefficients in the potential energy are volume dependent [53]. To a first-order approximation, these properties can be studied within the quasi-harmonic theory by treating phonons as harmonic but with assumed volume- and pressure-dependent frequencies. In this approximation, the lattice vibrational entropy S_{lat} is expressed as the sum of contributions from $\omega_j(\vec{q})$ [78] obtained within the RIM scheme

$$S_{\text{lat}} = \sum S_j = \sum S \left(\frac{\hbar\omega_j(\vec{q})}{k_B T} \right) , \quad (5.9)$$

where T is the temperature and k_B is the Boltzmann constant. The entropy function $S(x)$ for the harmonic oscillator is defined as:

$$S(x) = k_B [\{x / \exp(x) - 1\} - \ln \{1 - \exp(-x)\}] . \quad (5.10)$$

From 5.9, it follows that

$$\begin{aligned} \left(\frac{\partial S_j}{\partial \ln V} \right)_T &= \left(\frac{d \ln \omega_j(\vec{q})}{d \ln V} \right) \left(\frac{\partial S_j}{\partial \ln \omega_j(\vec{q})} \right)_T \\ &= - \left(\frac{d \ln \omega_j(\vec{q})}{d \ln V} \right) \left(\frac{\partial S_j}{\partial \ln T} \right)_V = \gamma_j(\vec{q}) C_j(\vec{q}) , \end{aligned} \quad (5.11)$$

where

$$\gamma_j(\vec{q}) = - \frac{d \ln \omega_j(\vec{q})}{d \ln V} = \frac{d \ln \omega_j(\vec{q})}{d P} \frac{d P}{d \ln V} = \frac{B_o}{\omega_j(\vec{q})} \left(\frac{\partial \omega_j(\vec{q})}{\partial P} \right) , \quad (5.12)$$

and $C_j(\vec{q})$ is the contribution of a single harmonic oscillator $\omega_j(\vec{q})$ to the specific heat C_V

$$C_j(\vec{q}) = Nk_B x^2 \frac{\exp(x)}{[\exp(x) - 1]^2}, \quad (5.13)$$

with

$$C_V = \sum_j \left(\frac{\partial S_j}{\partial \ln T} \right)_V = \sum_j C_j(\vec{q}). \quad (5.14)$$

By using (5.12–5.14), one can define the average Grüneisen constant $\bar{\gamma}$

$$\bar{\gamma} = \frac{\sum_j \gamma_j(\vec{q}) C_j(\vec{q})}{\sum_j C_j(\vec{q})} = \frac{\Omega \alpha}{\chi_T C_V}. \quad (5.15)$$

The terms $B_o (= 1/\chi_T)$, Ω , P , χ_T and α in (5.12–5.15) are respectively, the isothermal bulk modulus, crystal volume, pressure, isothermal compressibility and thermal expansion coefficient. If the mode-Grüneisen parameters are known for all the phonon branches $\omega_j(\vec{q})$ throughout the Brillouin zone, then the thermal expansion coefficient $\alpha(T)$ can be calculated using

$$\alpha(T) = \frac{1}{\Omega} \int k_B x^2 \frac{\exp(x)}{[\exp(x) - 1]^2} \left(\frac{\partial \omega}{\partial P} \right) g(\omega) d\omega, \quad (5.16)$$

where $g(\omega)$ is the density of phonon states i.e., the number of phonons lying within the fraction of frequencies between the range of ω and $\omega + d\omega$

$$g(\omega) = \frac{\Omega}{(2\pi)^3} \sum_j \int_{BZ} \delta [\omega - \omega_j(\vec{q})] d^3 q. \quad (5.17)$$

It has also become customary to convert the specific heat values (5.14) into a more slowly varying Debye temperature data $\theta_D(T)$.

5.4 The Green's Function Method

As mentioned before, the Green's function theory is a powerful mathematical tool for studying the dynamical properties of simple defects in solids. Unlike perfect crystal, where the equations of motion (5.6) have a small dimension tractable by numerical methods, the normal modes are solutions of a very large dimensional system of equations when the translational symmetry is broken by impurities or disorder. The Green's function method is practical for the numerical work in analysing the lattice vibrations of defects and extracting relevant information about the impurity-host bonding. In fact, this formalism can also be applied to host crystals, thus unifying the treatment of both perfect and imperfect materials.

5.4.1 The Lattice Green's Function

The lattice dynamics of a perfect crystal can be expressed in the Green's-function notation by

$$\left(\vec{M} \omega^2 - \vec{\phi}^{sC} \right) \vec{G}(\omega) = \vec{I}, \quad (5.18)$$

where $\vec{G}(\omega)$ is the lattice Green's-function matrix. The eigen frequencies of the perfect crystal can be easily found by solving the equation

$$\det \left(\omega^2 \vec{I} - \vec{D}^{sC} \right) = \det \vec{G}^{-1}(\omega) / \det \vec{M}, \quad (5.19)$$

where $\vec{D}^{sC} = \vec{M}^{-1/2} \vec{\phi}^{sC} \vec{M}^{-1/2}$ is the dynamical matrix used in the secular equation for studying the phonon dispersions of the host materials (see Sect. 5.3.1). The component form of the host-lattice Green's-function matrix is defined as

$$\begin{aligned} G_{\alpha\beta}(l\kappa; l'\kappa' : \omega) &= \frac{1}{N(M_\kappa M_{\kappa'})^{1/2}} \\ &\times \sum_{\vec{q}j} \frac{e_\alpha(\kappa|\vec{q}j)e_\beta^*(\kappa'|\vec{q}j)}{\omega^2 - \omega_j^2(\vec{q})} \exp \{i\vec{q}[\vec{x}(l\kappa) - \vec{x}(l'\kappa')]\}, \end{aligned} \quad (5.20)$$

where N denotes the number of wavevectors, $\vec{x}(l\kappa)$ is the equilibrium position vector of the atom $l\kappa$, and $e_\alpha(\kappa|\vec{q}j)$ are the components of the eigenvectors (see Sect. 5.3.1).

5.4.2 The Impurity Green's Function

Here we describe the Green's function method applicable to one impurity atom substituting for one atom in the host lattice. Interstitials and other impurities, adding degrees of freedom to the lattice, can be treated analogously. Given the knowledge of \vec{G} the Green's-function matrix of the imperfect lattice [71] \vec{U} with a substitutional defect can be defined as

$$\left[\left(\vec{M} + \Delta \vec{M} \right) \omega^2 - \left(\vec{\phi}^{sC} + \Delta \vec{\phi}^{sC} \right) \right] \vec{U}(\omega) = \vec{I}, \quad (5.21a)$$

or, equivalently,

$$\left(\vec{I} + \vec{G} \vec{P} \right) \vec{U}(\omega) = \vec{G}, \quad (5.21b)$$

with the perturbation matrix

$$\vec{P} = -\Delta \vec{M} \omega^2 + \Delta \vec{\phi}^{sC}. \quad (5.21c)$$

Here, $\Delta\tilde{M}$ and $\Delta\tilde{\phi}^{sC} [= \Delta\tilde{\phi}^s + \Delta\tilde{\phi}^C]$ are the mass-change and force-constant-change matrices. It is worth pointing out that we do not consider perturbations in the Coulomb interactions [i.e., $\Delta\tilde{\phi}^C = 0$] since their long range would render the Green's function method intractable.

As $\Delta\tilde{M}$ and $\Delta\tilde{\phi}^s$ matrices are usually non-zero only in the vicinity of the impurity atom, we only need to solve the small sub-block of (5.21b) corresponding to the non-zero elements of the perturbation matrix \tilde{P} . In this subspace, the frequencies of localized and gap modes caused by substitutional impurity can be easily obtained by solving

$$\det |\tilde{I} + \tilde{G}\tilde{P}| = 0 . \quad (5.22)$$

If the crystal contains a finite concentration of defects with different masses and interactions, the changes in the coupling parameters $\Delta\tilde{\phi}^{si}$ of the individual defects can be superimposed in the first-order approximation neglecting the overlap effects. Thus, the total perturbation (5.21c) can be expressed in terms of \tilde{P}^i 's for the individual defects as

$$\tilde{P}(\omega^2) = \sum_i \tilde{P}^i(\omega^2) = \sum_i (-\Delta\tilde{M}^i \omega^2 + \Delta\tilde{\phi}^{si}) . \quad (5.23)$$

The Green's function of the perturbed crystal is then given by

$$\tilde{U} = \tilde{G} - c \sum_i \tilde{G}\tilde{X}^i U , \quad (5.24)$$

with

$$\tilde{X}^i = \tilde{T}^i \left(\tilde{I} - c\tilde{G}\tilde{T}^i \right)^{-1} = \tilde{P}^i \left[\tilde{I} + (1 - c)\tilde{G}\tilde{P}^i \right]^{-1} , \quad (5.25)$$

and

$$\tilde{T}^i = \tilde{P}^i \left(\tilde{I} + \tilde{G}\tilde{P}^i \right)^{-1} . \quad (5.26)$$

Here, the term c in (5.24,5.25) represents the defect concentration. Since the macroscopic properties of the imperfect solid do not depend on the exact position of all impurities but upon the defect type and on the average impurity concentration c , in writing (5.24,5.25) we have performed a statistical average over all configurations containing the same type of defects. Once again, it is worth mentioning that the resonance denominator contained in the inverse of $(\tilde{I} + \tilde{G}\tilde{P}^i)^{-1}$ is of central importance for investigating the impurity modes.

5.4.3 Impurity Perturbation

In any defect calculation, the most important problem has been to give an adequate representation of the impurity perturbation. The matrix \tilde{P}

$[-\Delta \tilde{M} \omega^2 + \Delta \tilde{\phi}^{sC}]$ required to explain the observed dynamical behavior of defects demands an accurate description of the short-range, long-range (Coulomb) interactions, lattice relaxation etc. To the best of our knowledge there does not exist any unified theory where all these factors are properly included in defining the \tilde{P} matrix. In the RIM, however, one can avoid some of these factors and construct reasonably well the \tilde{P} matrix [71] by using the scaling properties and trends found in the force constant matrix elements of the host-crystals [75].

Substitutional Defects

The simplest crystal defect considered here is an isolated substitutional impurity (T_d symmetry: see Fig. 5.6a) replacing either the C atom ($\kappa = 1$) or the Si atom ($\kappa = 2$) in 3C-SiC lattice. Both the atomic mass and the NN force constants (A, B) in the RIM framework are assumed to be changed to (A', B') or (A'', B'') and the changes are described by the parameters

$$\varepsilon_1 = (M_1 - M_1^I) / M_1 , \quad (5.27a)$$

$$t \equiv (A - A') / A = (B - B') / B = 1 - a , \quad (5.27b)$$

or

$$\varepsilon_2 = (M_2 - M_2^I) / M_2 , \quad (5.27c)$$

$$u \equiv (A - A'') / A = (B - B'') / B = 1 - b , \quad (5.27d)$$

when the impurity M_1^I or M_2^I occupies the C- or the Si-site, respectively. To make the problem tractable we have neglected the changes in long-range Coulomb potentials. In an effort to save the computer time, the 15-dimensional \tilde{P} and \tilde{G} matrices for an isolated defect may be block-diagonalized by using the symmetry coordinates which transform according to the irreducible representations Γ of the T_d point group as

$$\Gamma_{T_d} = A_1 \oplus E \oplus F_1 \oplus 3F_2 . \quad (5.28)$$

Since the impurity vibrates only in the F_2 representation, the force constant changes for isolated defects are generally obtained by fitting the existing optical data on impurity modes by solving the equation $\{\det |\tilde{I} + \tilde{G}_{F2}\tilde{P}_{F2}| = 0\}$. In the absence of optical data, however, the force constant variations can be calculated from the lattice relaxation (see Sect. 5.4.3) around the impurity atoms by using the semi-empirical bond orbital model (BOM) [74]. This method is found reasonable for studying the dynamical properties of isolated defects, especially in 3C-SiC, where the estimation of force variations is not feasible due to the sparse data on defect vibrations. Before considering perturbation models to treat the vibrational properties of more complex defects, it is important to make a few comments on the choice of (5.27b) or (5.27d).

- (i) For very light substitutional impurities producing local vibrational modes, it may be assumed that they alone vibrate in the lattice with all the host atoms “frozen” in their equilibrium sites. Under such conditions, the recoil force f_r due to short-range interactions on the substituted atom for a small displacement along one of the [100], [010], and [001] directions (the equivalent directions of the impurity vibrations in the F_2 -mode) depends upon the force constants appearing on the diagonals of the coupling matrices between nearest-neighbors (A) and second nearest-neighbors (F_κ and C_κ). Considering the only change to be in $A(A \rightarrow aA)$, the recoil force can be written as

$$f_r = 4(aA + F_\kappa + 2C_\kappa) , \quad (5.29)$$

where $\kappa(= 1, 2)$ denotes, respectively, the substitutional atom number in the unit cell. The local mode frequency can be calculated approximately by using the expression $\omega_l [= 2\pi(f_r/M_\kappa)^{1/2}]$, and comparison with the complete Green’s-function method suggest that the frequencies obtained from the empirical relation are not far off. This supports our assumption that the vibrational energy is mainly centered on the light impurities in the local vibrational mode.

- (ii) It can be noted that the force constant B , a non-diagonal term of the coupling matrix between nearest-neighbors is not involved in the empirical calculation of local modes (using (5.29)). In the Green’s-function method, however, our hypothesis that B varies in the same way as A (i.e., $aA = aB$) will hardly affect the calculated high frequency impurity modes. Again, by imposing the condition $aA = aB$, the perturbation matrix \vec{P} satisfies the rotational invariance requirement, which is explicitly invariant with respect to translations and crystal symmetry operations. Convinced by the above arguments, we believe that the vibrational properties of more complex centers can be understood in terms of simple perturbation models.

Complex Defect Centers

The perturbation model of a single isolated defect can be extended to nearest-neighbor (NN) pair (with C_{3v} symmetry, see Fig. 5.6a) and second nearest-neighbor (2NN) complex centers (with C_s and C_{2v} symmetry, see Fig. 5.6b). The NN pair-defect (C_{3v} -symmetry) consists of an atom of mass defect $\varepsilon_1 = (M_1 - M_1^I)/M_1$ at C site 1 and another atom of mass defect $\varepsilon_2 = (M_2 - M_2^I)/M_2$ occupying the NN Si atom at site 2. This causes an increase in the size of \vec{P} and \vec{G} matrices to (24×24) requiring a minimum of two force variation parameters t and u . The vector spaces formed by the displacement of the impurity molecule and its NN transform according to the irreducible representations Γ of the C_{3v} point group

$$\Gamma_{C_{3v}} = 6A_1 \oplus 2A_2 \oplus 8E . \quad (5.30)$$

Again, in the C_{3v} symmetry, the impurity center does not move in the A_2 representation and only A_1 and E types of modes are optically active.

If a complex is formed with three impurity atoms (see Fig. 5.6b) occupying the C site 1, NN Si site 2, and another on 2NN C site (say 6), we need an additional parameter v . Following (5.27a–d), the mass change and force constant change parameter of an impurity on the C site 6 can be defined as

$$\varepsilon_6 = (M_6 - M_6^I) / M_6 , \quad (5.31a)$$

and

$$v \equiv (A - A''') / A = (B - B''') / B = 1 - c . \quad (5.31b)$$

To make the perturbation models more appropriate, we considered direct interactions in between the impurities by two additional parameters Γ_{12} and Γ_{26} . The force variations are given by

$$F_{12} = 1 - ab + \Gamma_{12} = u + t - ut + \Gamma_{12} , \quad (5.32a)$$

and

$$F_{26} = 1 - bc + \Gamma_{26} = u + v - uv + \Gamma_{26} . \quad (5.32b)$$

The term F_{12} (F_{26}) < 0 (or > 0) corresponds to the stiffening (or softening) in the bonds 1–2 (or 2–6), respectively. Although no explicit consideration of the Coulomb interactions between the charged impurities occupying the sites 1, 2, and 6 has been made, their effects causing changes in the electronic charge densities and hence the variation of forces in the 1–2 and 2–6 bonds are indirectly contained in the F_{12} and F_{26} parameters. The 2NN pair defect [e.g., $I_{C(1)}\text{-Si-}I_{C(6)}$] with impurity atoms at C sites 1, and 6 in the [100] direction can have orthorhombic symmetry (C_s) if $\varepsilon_1 \neq \varepsilon_6$ otherwise, the point group symmetry will be C_{2v} if $\varepsilon_1 = \varepsilon_6$. If the force constant changes are confined in the NN approximation, the size of the defect space will increase to 33×33 and the vector spaces formed by the displacements of the impurity and its NN may transform according to the following irreducible representations

$$\Gamma_{C_{2v}} = 10A_1 \oplus 6A_2 \oplus 8B_1 \oplus 9B_2 , \quad (5.33a)$$

and

$$\Gamma_{C_s} = 19A_1 \oplus 14A_2 . \quad (5.33b)$$

The impurity complex with C_{2v} point-group symmetry give rise to A_1 , B_1 and B_2 types of vibrations, whereas in the C_s -symmetry both A_1 and A_2 types of modes are optically allowed.

Interstitial Defect Centers

Unlike the substitutional defects, the isolated interstitials in 3C-SiC do not necessarily occupy the tetrahedral sites and might find themselves to be more stable in a less symmetric positions. In the Green's function approach, however, we assume the interstitial site to be tetrahedral. This assumption will help us exploit the symmetry properties of the defect environment to make the vibrational problem tractable. The present choice of an interstitial site preserving the cubic symmetry is supported, at least, for the case of Li atoms in Si and CdTe [79]. To treat the vibrational properties of an interstitial [I_{int}] impurity in a 3C-SiC lattice, we assume the center of the face-centered cubic (fcc) conventional unit cell to be the defect site. The vacancy or any other charge compensating impurity if present in the crystal is sufficiently far away from the I_{int} to prevent distortion of the tetrahedral symmetry. Again, the perturbation is assumed limited to the interstitial interacting with its NN Si (or C) atoms. In defining the impurity vibration by a single dimensionless parameter τ (or v) the I_{int} -host couplings (α, β) are assumed proportional to (A, B) if the interstitial has the Si (or C) NN in the 3C-SiC lattice. Similar to the case of a NN pair defect, the impurity modes of an I_{int} paired with a NN substitutional defect can be treated [79] by τ (v), u (t) and ϕ_{12} depending upon the situation when I_{int} is surrounded by a substitutional defect occupying the Si or C site, respectively.

Lattice Distortion

A semi-empirical method of Harrison [74] is used to study the lattice relaxation around impurity atoms and its effect on the dynamical properties in 3C-SiC. In terms of the Hartee-Fock atomic term values, this method provides simple analytical expressions for the change in impurity-host and host-host bond energies and suggests a computationally efficient and reasonable way to estimate the bond-length distortions. In the notation of Harrison, the gain in the impurity-host bond energy per bond connected with a distortion Δd ($\Delta d > 0$ outwards and $\Delta d < 0$ inwards) can be calculated as

$$\Delta E_b = \Delta E_b^1 + \Delta E_b^2 , \quad (5.34)$$

where ΔE_b^1 and ΔE_b^2 are the changes in the energy of the bonds caused by distortion in the NN and the second nearest-neighbor (2NN) atom positions respectively. The local distortion is calculated by taking $\frac{\partial \Delta E_b}{\partial \Delta d} = 0$.

5.5 Numerical Computations and Results

A novel optimization procedure was used to determine the RIM parameters (see Table 5.2) which accurately predicted both the eigen-displacements [45]

Table 5.2. Optimized set of rigid-ion-model parameters (10^5 dyn/cm) for the lattice dynamics of 3C-SiC in the notation of [75], at pressures of 1 atm and 22.5 GPa

Model parameters	1 atm	22.5 GPa
A	-0.91723	-1.1944
B	-0.445	-0.6
C_1	-0.0405	-0.0685
C_2	-0.159	-0.143
D_1	0.0644	0.01792
D_2	-0.33088	-0.3247
E_1	0.062	-0.016
E_2	0.1085	0.03
F_1	-0.041	-0.078
F_2	0.288	0.427
Z	1.053	1.1536

and eigenvalues [66] of 3C-SiC at ambient pressure. The model parameters at 22.5 GPa (or 225 kbar) were optimized by using the critical-point phonon energies from the high pressure Raman data [54] as an input and considering the known pressure-dependent elastic [C_{ij}] and lattice constant [a] values as constraint (see Table 5.1). The optimization process followed closely the procedures developed earlier [81] in which similar methodology was applied for treating the pressure-dependent phonon properties of II-VI and III-V compound semiconductors.

The volume ratio (V/V_o) [or the lattice constant ratio (a/a_o)] in 3C-SiC was calculated at 22.5 GPa from the experimental values known for the bulk modulus (B_o) and its pressure derivative (B'_o) [60–64] by using the well known Murnaghan's equation of state [82]

$$\frac{V}{V_o} = \left[1 + P \frac{B'_o}{B_o} \right]^{-1/B'_o}, \quad (5.35)$$

valid for pressures up to several hundred kbar (see Fig. 5.7).

In order to assess the significance of the two sets of optimized RIM parameters (see Table 5.2) and to treat the phonon properties of 3C-SiC at any desired pressure P , we used a linear interpolation scheme

$$\text{par}_i(P) = \text{par}_i(\text{ambient}) + P \frac{\partial \text{par}_i}{\partial P}, \quad (5.36)$$

where par_i ($i = 1, 11$) are the eleven RIM parameters.

5.5.1 Dynamical Properties of Perfect 3C-SiC

The results of phonon dispersions along high-symmetry directions and the corresponding one-phonon density of states [both at 1 atm pressure (solid lines)

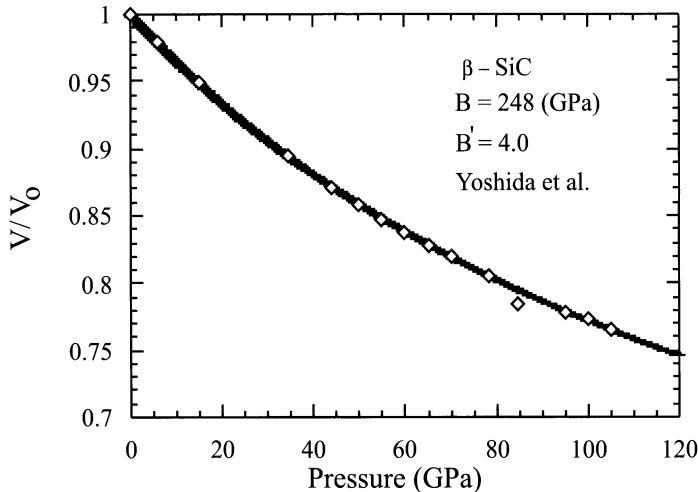


Fig. 5.7. Calculated variation of the volume ratio (using (5.35)) as a function of pressure for cubic SiC. The diamonds represent the data of Yoshida et al. [61]

and 22.5 GPa (dotted lines)] are displayed in Figs. 5.8a and 5.8b, respectively. Clearly, the density of phonon states show a wide gap ($620\text{--}765\text{ cm}^{-1}$) between the acoustical and optical branches (see Fig. 5.8b) and the results of $\omega_j(\vec{q})$ at ambient pressure (see Fig. 5.8a) compare favorably with the recent inelastic X-ray scattering [61] and Raman data [26]. Our values of eigen-displacements and phonon frequencies at critical-points in the Brillouin zone are found in good agreement with those of the local-density functional [18] and valence-overlap shell-model [21] calculations.

Like most other elemental and compound semiconductors we find that the increase of pressure in 3C-SiC causes an increase in its short-range interatomic forces (see Table 5.2). This increase in the force constants is responsible for the increase in the longitudinal and transverse optical (LO, TO), and longitudinal acoustic (LA) modes throughout the Brillouin zone (see Fig. 5.8a). Unlike other zinc-blende type materials where the effective charge (Z) decreases with pressure our calculations in 3C-SiC, however, suggest an increase in the Z value with P (see Table 5.2). This increase in Z corroborates the increase of LO-TO splitting with P observed by Raman scattering spectroscopy [54]. We attribute this relationship of the variation of LO-TO splitting with Z to the charge transfer from Si to C by compression. Although most zinc-blende materials become less ionic under pressure [83], it is noted that 3C-SiC is an exception and becomes more ionic with compression.

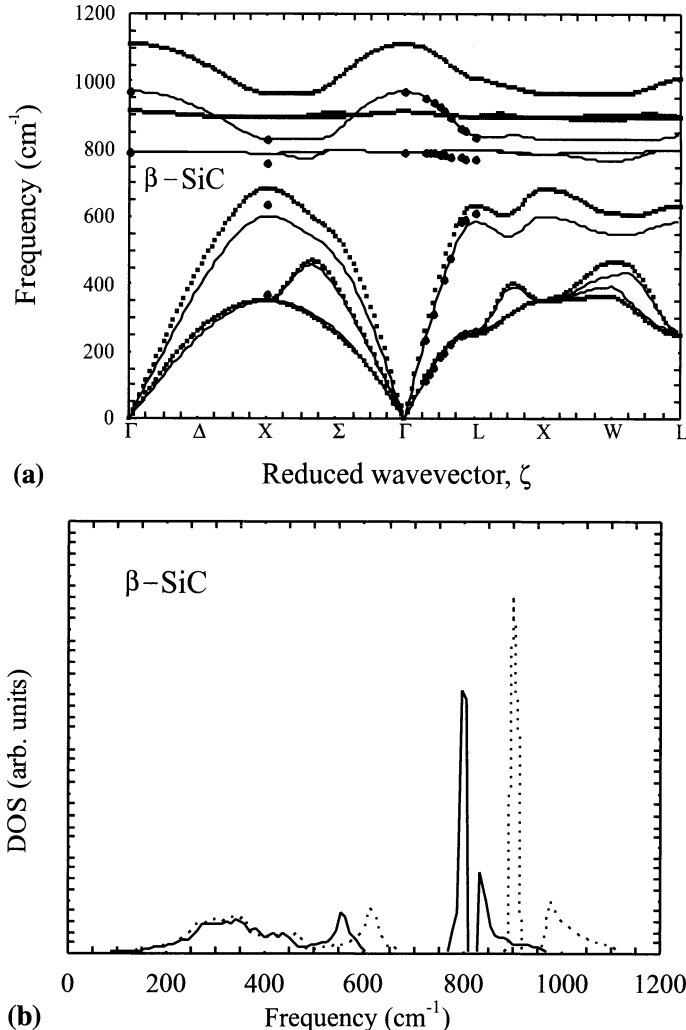


Fig. 5.8. (a) Rigid-ion-model calculations for the phonon dispersions along high-symmetry directions for 3C-SiC based on the set of parameters of Table 5.2. The *solid curves* show the calculations at ambient pressure, whereas the *dotted lines* show the calculations at 22.5 GPa. The *filled diamonds* represent the data from [54]. (b) Rigid-ion-model calculations for the one-phonon density of states for 3C-SiC based on the set of parameters of Table 5.2. The *solid curves* show the calculations at ambient pressure, whereas the *dotted lines* show the calculations at 22.5 GPa

5.5.2 Debye Temperature, Mode Grüneisen Parameters and Thermal Expansion

By incorporating the phonon energies at ambient and high pressure, we have also calculated thermodynamical properties (e.g., specific heat and Debye temperature) for 3C-SiC. In Fig. 5.9 the results of our calculated Debye temperature are displayed for 3C-SiC both at ambient and high (22.5 GPa) pressure. The RIM results for the specific heat $C_v(T)$ as a function of T shown in Fig. 5.10 are compared with the existing experimental $C_p(T)$ data [62]. Theoretical values for the pressure variation of phonon energies ($\partial\omega_j(\vec{q})/\partial P$) at each wave-vector \vec{q} in the Brillouin zone are used to compute the mode Grüneisen parameters $\gamma_j(\vec{q})$ along high symmetry directions (see Fig. 5.11). The mode Grüneisen parameters are found predominantly positive with the exception of the small part of the lowest branches, corresponding to the transverse acoustic modes, around the X point. This behavior of $\gamma_j(\vec{q})$ in 3C-SiC is identical to that of diamond, for which all mode Grüneisen parameters are found positive, and is in sharp contrast to that of silicon for which almost all of the TA branches of $\gamma_j(\vec{q})$ are strongly negative. Once again, our results for the mode Grüneisen parameters are in good agreement with the *ab initio* calculations [24].

Finally, the Grüneisen constant $\bar{\gamma}$ (see Fig. 5.12) and the temperature dependence of the linear thermal expansion coefficient $\alpha(T)$ (see Fig. 5.13) are derived following (5.15,5.16). It can be noted that at the high temperature regime as all the phonon modes are excited the thermal expansion coefficient tends to saturate at a constant value (see Fig. 5.13). Although our theoretical results of $\alpha(T)$ in 3C-SiC compare very well with the experimental data

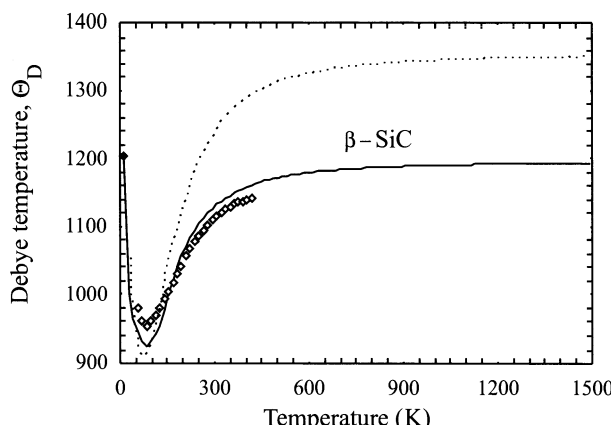


Fig. 5.9. Rigid-ion-model results for the Debye temperature versus T for 3C-SiC using the set of parameters of Table 5.2. The *solid* and *dotted* lines represent the results at ambient pressure and 22.5 GPa, respectively. The *open diamonds* represent the experimental data

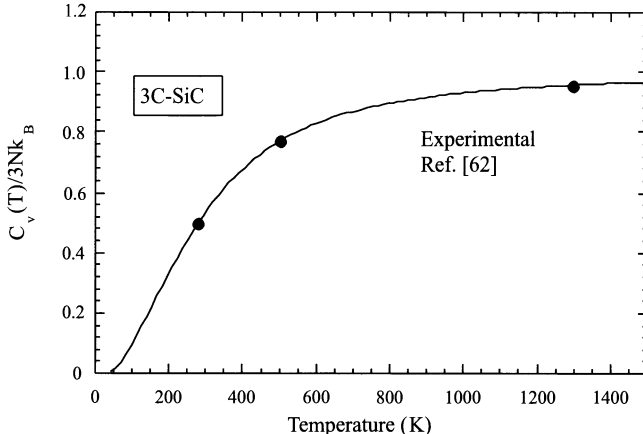


Fig. 5.10. RIM calculation of the specific heat at constant volume $C_v(T)$ of 3C-SiC as a function of T . The *filled circles* denote the experimental data $C_P(T)$ from [62]

of Li and Bradt [59], however, we note that the variation of linear thermal expansion with T exhibits a behavior much like that of the specific heat (see Fig. 5.10) and unlike silicon and most other III-V and II-VI compounds it does not attain negative values at lower temperatures. This behavior can be understood (see Sect. 5.6) qualitatively from the materials' bonding mechanisms and elastic properties. The values of $\alpha(T)$ at selected temperatures are reported in Table 5.3.

Table 5.3. Experimental and recommended values of the linear thermal expansion coefficient a for silicon, diamond, and cubic silicon carbide

System	Experimental	Recommended ^e	Lattice dynamical ^f
Silicon	$-0.60 \times 10^{-6} \text{ K}^{-1}$ at 70 K ^a	$-0.41 \times 10^{-6} \text{ K}^{-1}$ at 100 K	
	$-0.46 \times 10^{-6} \text{ K}^{-1}$ at 85 K ^b	$4.5 \times 10^{-6} \text{ K}^{-1}$ at 1600 K	
Diamond	$\sim -0.1 \times 10^{-6} \text{ K}^{-1}$ at 60 K ^c	$\sim 0.0 \times 10^{-6} \text{ K}^{-1}$ at 100 K	
		$5.9 \times 10^{-6} \text{ K}^{-1}$ at 1600 K	
Cubic SiC	$3.50 \times 10^{-6} \text{ K}^{-1}$ at 300 K ^d	$0.27 \times 10^{-6} \text{ K}^{-1}$ at 100 K	$0.26 \times 10^{-6} \text{ K}^{-1}$ at 100 K
		$2.77 \times 10^{-6} \text{ K}^{-1}$ at 300 K	$2.47 \times 10^{-6} \text{ K}^{-1}$ at 300 K
		$5.64 \times 10^{-6} \text{ K}^{-1}$ at 1600 K	$5.16 \times 10^{-6} \text{ K}^{-1}$ at 1600 K

References: a) Shah and Straumanis, [68]; b) White, [68]; c) [69]; d) [59]; e) [70]; f) Our calculations

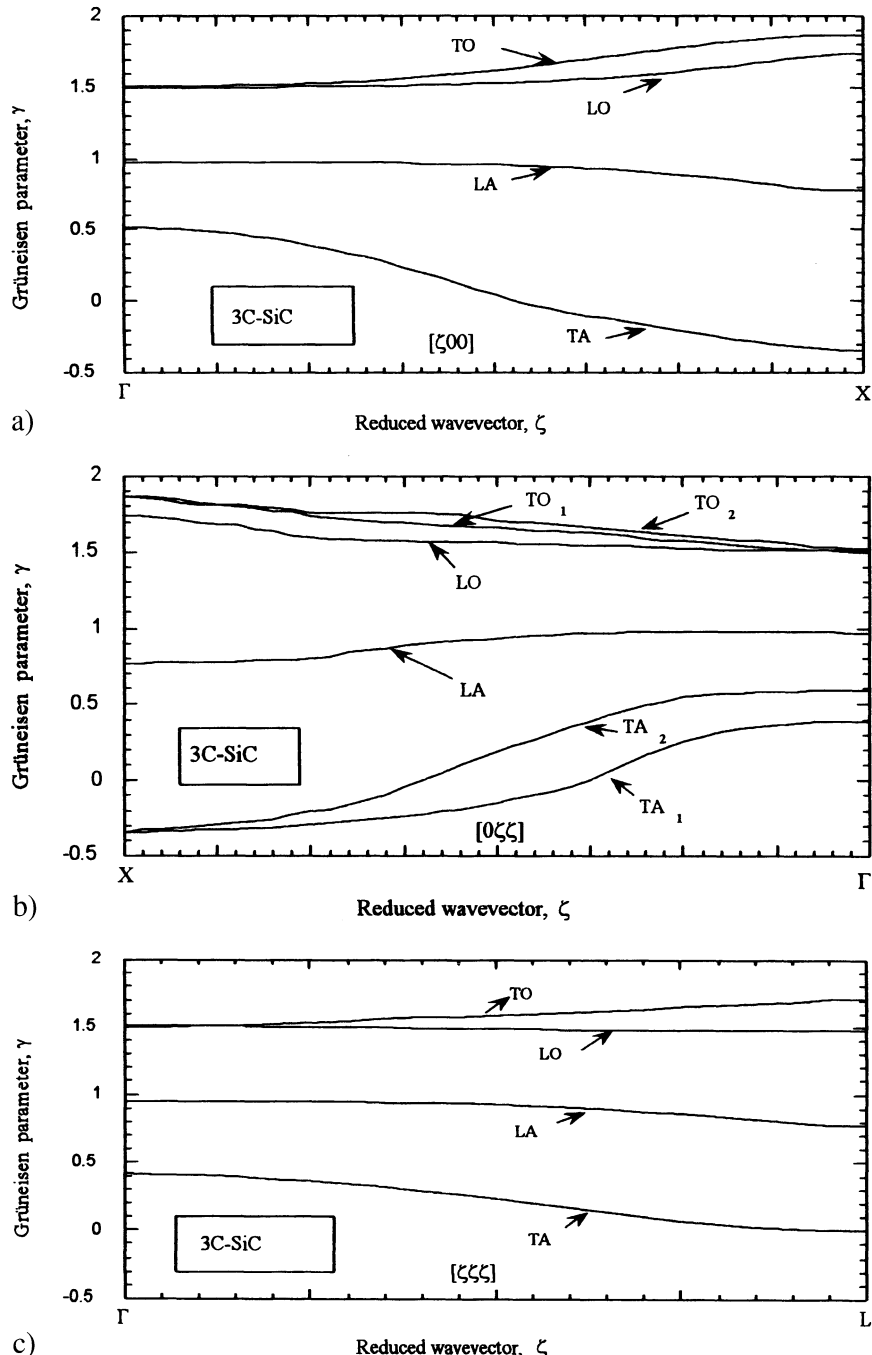


Fig. 5.11. RIM calculations of the mode Grüneisen dispersions $\gamma_j(\vec{q})$ for 3C-SiC along high-symmetry directions $[\zeta 00]$ (a), $[0\zeta\zeta]$ (b), and $[\zeta\zeta\zeta]$ (c), using the set of parameters of Table 5.2

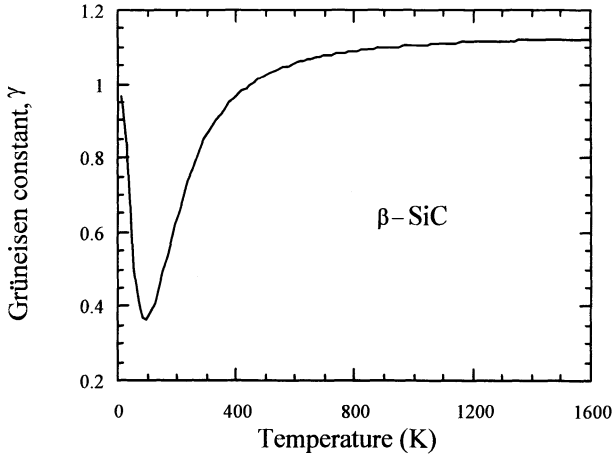


Fig. 5.12. Rigid-ion-model calculations for the Grüneisen constant γ versus T for 3C-SiC using the set of parameters of Table 5.2

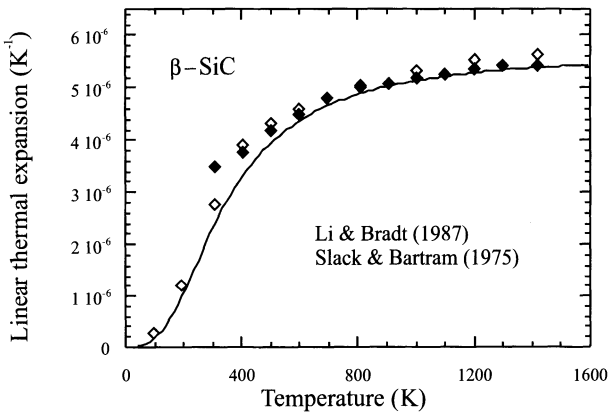


Fig. 5.13. Rigid-ion model calculations for $\alpha(T)$ versus T for 3C-SiC using the parameters of Table 5.2. The results are compared with the existing experimental and accepted data

5.5.3 Dynamical Properties of Defects in 3C-SiC

The study of LVMs in semiconductors has provided us valuable information about the site selectivity and chemical nature of light impurities. In 3C-SiC, however, except for H-related modes [36], the vibrational data for other intrinsic or extrinsic defects is rather sparse. In the frame work of Green's function theory, we have predicted the possibility of LVMs for isolated light impurities on C and Si-sites in 3C-SiC and analyzed the phonon modes of various defect structures (e.g., $B_{Si}-N_C$; $C_{Si}-N_C$; $C_{Si}-SiC$ C-H; $B_{Si}-H$; $Al_{Si}-H$ complexes; clusters of carbon interstitials C_i etc.).

Isolated Single Substitutional Defect

In zinc-blende type materials, the light substitutional impurity vibrates in the triply degenerate F_2 mode causing high frequency infrared and Raman active LVMs [84]. The heavier impurity with appropriate “impurity-host interactions” can give rise to A_1 , E , and F_2 type “quasi-localized” modes which are Raman active. By analyzing nearly 80 cases of LVMs due to isolated defects in 15 elemental and compound semiconductors we have intuitively established [71] valuable trends in the force-constant variation relating them to the redistribution of electron charge density in the impurity-host bonding. We hope that these trends in the bonding mechanism will help us establish the role of intrinsic and extrinsic defects in 3C-SiC.

In the Green’s function theory we calculated the impurity modes as a function of u (or t) by solving (5.22) in the A_1 , E , F_1 , and F_2 irreducible representations. For heavy impurity atoms (e.g., N, O, Si, etc.) on C-sites in 3C-SiC besides “quasi-localized” modes we find F_2 -type gap modes emerging from the minimum of the optical band. The light impurities (e.g., Li, B, Be, N, etc.) on Si-sites on the other hand provide both high frequency LVMs as well as gap-modes emerging from the top of the acoustical branch (see Figs. 5.14, 5.15). We discuss the following cases.

a) The Nitrogen Donor

Nitrogen present in all SiC polymorphs from crystal growth is the only relevant shallow donor available for the production of electronic devices [28]. It is somewhat surprising, however, that until recently not much is known about its microscopic and/or electronic structure. At this time we are still not aware of any direct experimental evidence supporting the site selectivity of nitrogen

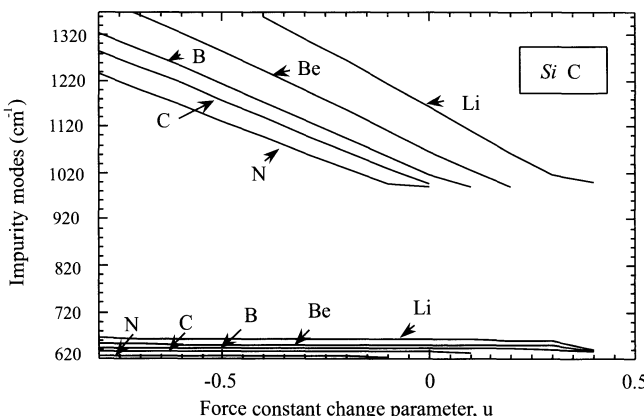


Fig. 5.14. Green’s function calculations of the impurity (localized and gap) modes as a function of the force constant change parameter u for impurities occupying the Si site in 3C-SiC

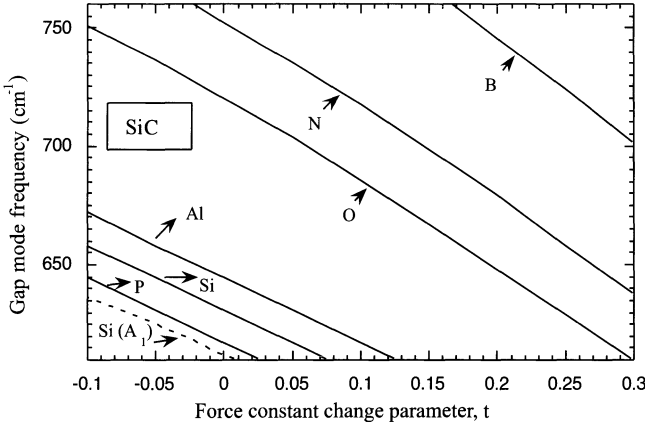


Fig. 5.15. Green's function calculations of the gap modes as a function of the force constant change parameter t for impurities occupying the C site in 3C-SiC

on Si-site (N_{Si}) in 3C-SiC. The ionization energies (40–54 meV) estimated from the electrical measurements [28, 85, 86], however, strongly favor the N impurity to occupy the C-site (N_C). Also, there has been some controversy as if nitrogen is the only residual donor (N_C) in 3C-SiC or if there is a second donor level due to a structural defect [87].

The local structure due to isolated N_C donor in 3C-SiC is obtained using BOM (see Sect. 5.4.3). Constraints similar to those suggested by Harrison [74] are imposed in relating the lattice relaxation to the variation in the radial force constant between the Si-N bond. Green's function calculations for the dynamical behavior of N_C predict in addition to the “in band” modes a gap mode emerging from the bottom of the optical bands (see Fig. 5.15) which attain a value 638 cm^{-1} with softening in the force constant parameter u (~ 0.3). On the other hand, the N_{Si} impurity (with appropriate softening in the force constant) provides a gap-mode ($\sim 620\text{ cm}^{-1}$) as well as a local-mode ($\sim 985\text{ cm}^{-1}$) near the maximum phonon frequency of 3C-SiC.

b) Phosphorous Donors

Like nitrogen, phosphorous is another relatively shallow donor in SiC. It can be introduced during chemical vapor deposition (CVD) growth, by ion implantation, diffusion, and neutron transmutation of Si [88, 89]. At present, there is no consistent picture of whether P acts as an isolated defect or participates with intrinsic defects (vacancy) to form complexes. Based on its covalent radius, it is expected that P substitute preferentially on the silicon sublattice to form P_{Si} [90] and/or $P_{Si}-V_C$ complex center. From the BOM calculations the relaxation of NN C-atoms for P_{Si} in 3C-SiC is found different from the relaxation of NN Si-atoms for N_C case. The changes in the C-P and Si-N bond lengths are believed to arise from the difference in atomic sizes of the impurity-host atoms. Since the P-impurity is heavier than the Si-atom, we

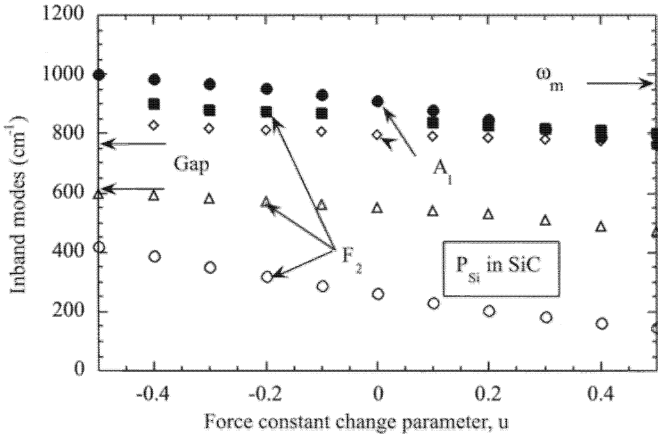


Fig. 5.16. Green's function calculations of in-band modes as a function of force constant change parameter u for phosphorous impurity occupying the Si site (P_{Si}) in 3C-SiC

find no solution for the gap-mode with a reasonable value of u . However, softening in the C-P bond predicts, similar to the case of P_{Si} in Si-lattice, the possibilities of low lying inband modes (see Fig. 5.16).

c) Al and B Acceptors

Among the p -type dopants, aluminum is generally believed to occupy the silicon site (Al_{Si}) producing a shallow acceptor level (0.19–0.25 eV above E_v) in different polytypes [28]. Boron, on the other hand, is suggested to occupy silicon (B_{Si}) as well as carbon (B_C) sites with preference for the Si-site. From IR absorption, capacitance and DLTS measurements several ionization energies have been determined for B-related defects in SiC with an unusually large number of levels in 6H-SiC [28]. Although no conclusive proof has been presented it is suggested, however, that an off-center boron substituting for Si atom (B_{Si}) and boron occupying C atom (B_C) [or B_C related complex] are respectively responsible for the shallow and the deep acceptors [91–93]. By using electron spin resonance (ESR) [94] and electron nuclear double resonance (ENDOR) [95] experiments the deep acceptor in 6H-SiC has been identified as a NN pair B_{Si} – V_C with axial symmetry parallel to the crystal c -axis. In 3C-SiC boron produces a deep acceptor center B_C with energy level at $E_v + 0.735$ eV [96].

In the mass-defect-approximation (MDA) our study for B_{Si} provides a triply degenerate LVM (~ 1010 cm $^{-1}$) as well as a gap mode ~ 620 cm $^{-1}$ (see Fig. 5.14). However, the softening in u pushes down the local mode (~ 990 cm $^{-1}$) close to the maximum phonon frequency of 3C-SiC. The Al_{Si} on the other hand, resembles an impurity for which there is no significant mass change but the ‘impurity-host bonding’ is modified. By considering an

appropriate variation in the ‘impurity-host bonding’, it is feasible that Al_{Si} acceptor may give rise to inband modes similar to P_{Si} .

Dynamical Properties of Pair and Complex Defects in 3C-SiC

Intrinsic point defects (viz., vacancy, self interstitial, antisite) inevitably occur in SiC. Incorporated either during growth or induced by processing (e.g., ion-implantation, dry etching and electron irradiation) they can influence the electronic quality of the material. In addition, the mobile intrinsic defects play a pivotal role in the annealing kinetics and mass transport [97, 98]. Shallow (n - or p -type) dopants which govern the conductivity type in semiconductors can also form complexes with intrinsic defects. Recent theoretical studies have indicated that Si_i and V_C are the most abundant mobile defects in p -type and intrinsic materials [36]. The latter defects also dominate under n -type conditions. In n -type material, V_{Si} which lead over Si_i , play a special role. Although, the behavior of isolated Si_i and C_i in 3C-SiC has been investigated theoretically [36] no experimental fingerprint has yet been found.

Hydrogen is another very common impurity, introduced both by wet and dry etching among other methods and can have profound influence on the material characteristics and device processing. In III-V compounds [99], the passivation of shallow and deep defects by hydrogen is well documented and one expects similar effect in SiC as well [100–103]. At present the most intriguing problem is to understand the role of H in SiC – how it interacts with intrinsic as well as doped defects – the nature of complexes responsible for the passivation mechanism. Since H -complexes are expected to cause high-frequency LVMs, theoretical modeling will be valuable in providing information about the site selectivity and energetics in the formation of stable defect structures. We discuss the following cases.

The NN Pair Defects in 3C-SiC

A prototypical D_I defect center in SiC responsible for the sharp emission lines in the low temperature photoluminescence (LTPL) is well known for decades [104]. Its fingerprint is an efficient PL at a photon energy 0.35–0.45 eV below the excitonic gap and is seen in all polytypes after different kinds of irradiation. The D_I is observed in as-grown material after quenching from growth temperature as well as in epitaxial layers grown by CVD or MBE methods [105, 106]. The sharp L_i emission lines are followed by characteristic phonon assisted structures around 83 meV in the phonon band gap. These facts suggests that D_I center has an intrinsic nature and is formed by vacancies, antisites and/or interstitials introduced by the damage. Several models have been proposed for the D_I center including a divacancy; carbon divacancy; $\text{V}_{\text{Si}}-\text{N}_C$ complex, etc. Using Green’s function theory we have calculated the impurity modes for several NN pair defects of C_{3v} symmetry in 3C-SiC. Theoretical results are evaluated for $\text{V}_{\text{Si}}-\text{N}_C$; $\text{Si}_C-\text{C}_{\text{Si}}$ pairs to best support the observed vibrational features for the D_I center.

The point group symmetry of the NN pair defect is C_{3v} with the axis along the bond joining the two impurities (see Fig. 5.6a). For very light impurity atoms four local vibrational modes are expected [two because of their movement along the line of joining, $\omega_1(A_1^+)$ \longleftrightarrow and $\omega_4(A_1^-)$ $\rightarrow\leftarrow$, and two as a result of movement perpendicular to it, $\omega_2(E^+)$ $\uparrow\downarrow$ and $\omega_3(E^-)$ $\uparrow\uparrow$] generally with $\omega_1 > \omega_2 > \omega_3 > \omega_4$. However, if one of the pair atoms is relatively heavier only two vibrational modes can be observed experimentally. For the case of a NN pair defect, the block diagonal Green's function and perturbation matrices in different irreducible representations are obtained using the symmetry coordinates and the details have been reported elsewhere [71].

- (i) $B_{Si}-N_C$ NN Pair. As an example (see Fig. 5.17) we have displayed our Green's function results of LVMs in the MDA for B_{Si} paired with different impurities on the NN C-site in 3C-SiC. The perusal of Fig. 5.17 reveals that even the lightest impurity atom on C-site paired with B_{Si} can provide only three impurity modes [$\omega_1(A_1^+)$, $\omega_2(E^+)$, and $\omega_3(E^-)$] above the maximum phonon frequency while the fourth one $\omega_4(A_1^-)$ falls into the phonon continuum. As expected for $\epsilon_1 = 0$, we obtain $\omega_1(A_1^+) = \omega_2(E^+)$ the triply degenerate local mode frequency of an isolated B_{Si} . We also noted that the change in force constant between the bond joining the pair (not shown here) affects only the impurity modes related with the movement of atoms along their line of joining, while the modes related with the movement of atoms perpendicular to it remain almost unchanged. All vibrational modes, on the other hand, are found affected by the variation of impurity host parameters (t , u and F_{12}). By including appropriate force constant changes in the $B_{Si}-N_C$ pair (for example), our theory predicts two impurity modes near $\sim 979\text{ cm}^{-1}$ $\omega_1(A_1^+)$ and 982 cm^{-1} $\omega_2(E^+)$ and a gap mode at $\sim 631\text{ cm}^{-1}$ (E) along with an A_1 band mode ($\sim 610\text{ cm}^{-1}$) falling into the phonon continuum.

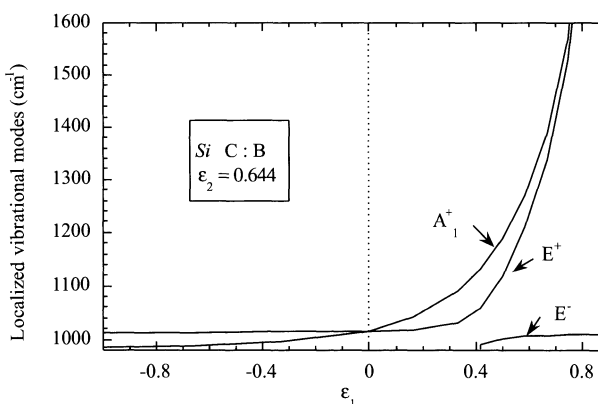


Fig. 5.17. Calculated LVMs in the MDA for $B_{Si}-I_C$ pair in 3C-SiC (see text)

- (ii) N_C-Al_{Si} and N_C-C_{Si} NN Pairs. In the MDA and using Green's function theory, we have also studied the vibrational modes of N_C paired with impurities on the NN Si-sites in 3C-SiC. As mentioned before (see Sect. 5.5.3) the isolated N_C defect can provide a triply degenerate F_2 mode in the phonon gap. If paired with a second impurity on Si-site I_{Si} the degeneracy at the N_C and I_{Si} sites will be lifted providing non degenerate A_1 and doubly degenerate E -modes, respectively. In addition to the split in the gap mode of N_C we expect the split in the I_{Si} local mode for very light impurities on Si-site ($\varepsilon_2 > 0.58$). In the N_C-I_{Si} pair while the gap mode frequencies remained almost unchanged, the local modes vary monotonically with ε_2 and merge into the phonon continuum for $\varepsilon_2 < 0.58$. For N_C-Al_{Si} pair in 3C-SiC, however, the N_C gap mode shifts to a lower value $\sim 620\text{ cm}^{-1}$ due to the combined effects of ε_2 ($= 0.04$ for Al_{Si}) and weaker interaction between the Al–N bond. In the case of N_C-C_{Si} pair with ε_2 ($= 0.57$ for C_{Si}) although local modes lie close to ω_m [$\sim 986\text{ cm}^{-1}$ (A_1), 980 cm^{-1} (E)] the stronger interaction between the N–C bond cause splitting in the gap mode of N_C [$\sim 643\text{ cm}^{-1}$ (A_1), 639 cm^{-1} (E)]. This analysis reveals that for the NN pair defects in 3C-SiC the number of localized and gap modes strongly depend upon the mass defect parameters as well as on the strength between the “impurity-impurity” bonding. Based on these results we believe that the possibility of observing impurity modes for N_C-Al_{Si} and N_C-V_{Si} pairs by optical (IR and Raman) spectroscopy diminishes significantly in 3C-SiC.
- (iii) Si_C-C_{Si} NN Pair. In the Green's function theory, the calculated LVM of an isolated C_{Si} (T_d symmetry) defect ($\sim 1000\text{ cm}^{-1}$) falls close to the maximum phonon frequency ω_m of 3C-SiC, while the isolated Si_C antisite defect (T_d symmetry) provides two impurity modes in the phonon gap: a triply degenerate F_2 mode ($\sim 648\text{ cm}^{-1}$) and a non degenerate A_1 mode ($\sim 622\text{ cm}^{-1}$) (see Fig. 5.15). The pairing of antisite defects Si_C-C_{Si} lifts the degeneracies of the F_2 modes. With appropriate stiffening between the impurity bond the F_2 gap mode splits up into two modes $\sim 651\text{ cm}^{-1}$ (A_1) and $\sim 647\text{ cm}^{-1}$ (E). These results compare favorably with the impurity modes of the D_I center.

Dynamical Behavior of Carbon-Interstitials and Their Aggregates

Ion-implantation causes damage in crystals which creates intrinsic defects. In SiC, the migration of carbon interstitials (C_i) forming aggregates, seems quite feasible at high temperature ($> 1500^\circ\text{C}$) used for annealing after ion-implantation. One Raman [107] and several PL [108, 109] centers with replica due to LVMs above the phonon continuum indicated that C–C bonds were indeed created during ion-implantation or electron irradiation. In electron irradiated 6H-SiC, the participation of carbon atoms was unambiguously proven based on shift of LVMs upon isotopic substitution. The D_{II} PL center [108], observed first in 3C-SiC, is most likely also C-related, based on the LVMs

detected above the phonon continuum. Again, the D_{II} center can be created only by high energy ion-implantation both in n - and p -type SiC and since its creation does not depend on the species of ions but only the energy of the ions, it is thought that D_{II} originates from an intrinsic defect. Despite the evidence for aggregation of C_i in SiC the knowledge about the behavior of C-clusters is rather limited and often contradictory [110, 111].

Dynamics of H-Related Complexes in 3C-SiC

In III-V compounds, the passivation of shallow acceptors resulting from the pairing with atomic hydrogen is well known [99]. Rapidly diffusing hydrogen atoms, present in the positive charge state (H^+) can be trapped by the negatively charged acceptor impurities (a^-) to form electrically inactive " $H^+ - a^-$ " pairs. High frequency LVMs observed for the paired H (D) atom by IR and Raman spectroscopy helped investigate the stability of defect structures and energetics of complexes through model calculations [99]. In III-V compounds a simple coupled oscillator model [112] (see Fig. 5.18) provided not only a good physical picture for the center but also reasonable agreement with the experimental frequencies of various modes by the choice of appropriate (different) force constants for the longitudinal and transverse displacements of the atoms relative to the pair axis.

In SiC, on the other hand, the only evidence known for decades for the existence of H-related defects was the low temperature PL center [113]. The PL bands arose as phonon replica due to local modes in 6H- and 4H-SiC after H^+ implantation in p -type material. These bands were interpreted as C–H stretch modes due to hydrogen in silicon vacancies at different inequivalent

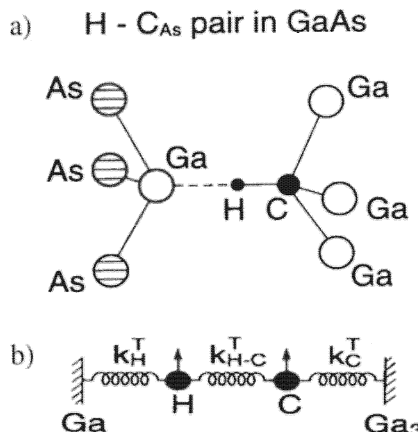


Fig. 5.18. The H–C_{As} pair in GaAs, showing the H atom in the bond-centered position, only weakly coupled to the neighboring Ga atoms (a). The pair is modeled as an H atom and a C atom coupled together by force constants k_{H-C} , k_H and k_C connecting the individual masses to rigid walls (b)

Table 5.4. Localized vibrational modes for hydrogen-related defects in 3C-SiC [116]. The frequencies (cm^{-1}) were calculated in the quasi-harmonic approximation. Columns H-H, H-D, and D-D indicate the number of H atoms substituted by D

Defect	Mode	H-H	H-D	D-D
$(\text{H})^+$	stretching	2747		
$(\text{H})^-$	stretching	1268		
$(\text{H}_2)^o$	stretching	3452		
$(\text{V}_{\text{Si}}+\text{H})^o$	stretching	2961	2170	
$(\text{V}_{\text{Si}}+2\text{H})^o$	symmetric	3051	3014	2229
	asymmetric	2999	2206	2200
$(\text{V}_C+\text{H})^o$	asymmetric	1570		
	symmetric	991		
$(\text{V}_C+\text{H})^+$	asymmetric	1770		
	symmetric	1189		
$(\text{V}_C+2\text{H})^o$	symmetric	1332	1177	952
	asymmetric	976	975	730
	asymmetric	976	797	730
$(\text{V}_C+2\text{H})^+$	asymmetric	1279		
	asymmetric	1271		
	symmetric	1000		
$(\text{B}_{\text{Si}}+\text{H})^o$	stretching	3114		
$(\text{Al}_{\text{Si}}+\text{H})^o$	stretching	2908		

sites. More recently [114] with improved method of crystal growth, ion implantation and spectroscopy the PL spectra is revisited in 6H-SiC. It is found that the lines due to C–H (C–D) modes appear only in slightly *p*-type but not in *n*- or heavily *p*-type materials. New phonon bands are detected besides the known lines which were associated with the overtone modes of the C–H (C–D) stretch frequencies. Similar to III-V compounds, it is likely that the mobile hydrogen (H^+) atoms in SiC are captured by ionized acceptors (a^-) to form electrically inactive “ $\text{H}^+ - a^-$ ” pairs. Despite a strong evidence of complex formation with hydrogen passivating acceptors (B and Al) ($\sim 90\%$) and donors (N) ($\sim 75\%$) in SiC, no fingerprints of LVMs are found by IR [115] or Raman spectroscopy although predictions for the stretching modes of $\text{B}_{\text{Si}}-\text{H}$, $\text{Al}_{\text{Si}}-\text{H}$ complexes have been made recently [116] (see Table 5.4) by using *ab initio* calculations.

5.6 Summary and Conclusion

By using a second-neighbor RIM, we have calculated the phonon dispersion curves of 3C-SiC for several high-symmetry directions, the density of one-phonon states, the specific heat, the and Debye temperatures at ambient (1 atm) and high (22.5 GPa) pressure. Our lattice-dynamical results are found to be (see Fig. 5.8a) in good agreement with recent inelastic X-ray scattering [66], Raman [54], and *ab initio* [24] data. The role played by carbon rather

than silicon atoms in the lattice dynamics of 3C-SiC is clearly reflected, as its phonon dispersions are found to be closer to diamond than to silicon. The flatness of the transverse acoustic modes near the Brillouin zone boundaries, a typical behavior in most tetrahedral semiconductors, is absent in 3C-SiC. In contrast to the materials with the diamond structure, the LO and TO modes in 3C-SiC split up at the Γ point owing to its polar character. Again, the weak dispersion of the phonon branches in the optical range causes a small gap and sharp peaks in the one-phonon density of states (see Fig. 5.8b) – a feature which is uncommon in most other tetrahedral compounds.

In the quasi-harmonic approximation, we used the calculated phonons and Grüneisen parameters $\gamma_j(\vec{q})$ to compute the temperature dependence of the Grüneisen constant $\bar{\gamma}$ and the linear thermal expansion coefficient $\alpha(T)$. Unlike the case for Si and most other compound semiconductors, the dispersions of the mode Grüneisen parameters $\gamma_j(\vec{q})$ in 3C-SiC along high-symmetry directions are predominantly positive, with the exception of a small part of the lowest branches, corresponding to the TA modes, around the Γ and L points in the Brillouin zone. This behavior is similar to that of diamond, for which the $\gamma_j(\vec{q})$ are found to be positive [117], but different from that of Si, where strong negative values are found for almost the entire TA branches. It has been argued that the TA mode softening is indicative of the weakening of the noncentral forces of long-range origin needed to stabilize the tetrahedral lattice against a short-wavelength shear distortion. Therefore, it is conjectured that the softening of zone-boundary TA phonons is likely to be a driving mechanism for the pressure-induced phase transition that is ubiquitous in the diamond/zinc-blende materials [118]. An empirical relation between the negative Grüneisen parameters of the TA(X) phonons and the pressure-induced transition was first suggested by Weinstein [119]. Since anisotropic strain plays an important role in high-pressure phase transitions [120], it is useful to measure the pressure dependence of the sound velocities (or elastic constants) in 3C-SiC (using Brillouin scattering in diamond anvil cells) and relate them to $\gamma_j(\vec{q})$ to validate Weinstein's relation.

The unusual trends in the temperature variation of $\alpha(T)$ in 3C-SiC can be understood qualitatively in terms of the critical balance between the central and noncentral elastic forces associated with the stretching and bending of bonds. For the shear-type TA(L) mode, the angular forces tend to make it stiffer under pressure, whereas the central elastic forces act in the opposite way. As a consequence, the signs of the mode Grüneisen parameters of the zone-boundary TA phonons and thus of $\alpha(T)$ at low T are positive for diamond, for which the angular forces are dominant, but negative for Si (see Table 5.3). Compared with other zinc-blende semiconductors, the compensation between central and noncentral forces in 3C-SiC is such that it exhibits much smaller mode softening, and hence smaller pressure coefficients for the TA modes. These effects are a consequence of the strong directional covalent bonding found both in carbon-based materials such as SiC and in solids containing elements in the same row as carbon (viz., BP and the III–Ns) [121]. Although

there are no experimental data at low temperatures available for $\alpha(T)$ for 3C-SiC, our results agree very well with the existing recommended values [70]. At low temperatures the negative values of $\alpha(T)$, if they existed, would have been extremely small. The lattice-dynamical calculations reported here should serve as a basis for residual-stress estimations in multilayer 3C-SiC/Si devices and for other theoretical studies.

We have performed comprehensive Green's function calculations in the framework of an RIM and predicted the possibilities of LVMs due to several isolated and complex defect centers in 3C-SiC. Our results in the MDA, for light isolated defects on Si sites (e.g., Be_{Si} , B_{Si} , and C_{Si}) and for heavy defects on C sites (e.g., N_C , O_C , and Si_C), provided localized and gap modes, respectively. From the correlation of the force variation with bond covalency [71], while stiffening in the bond strength is expected for antisite defects (C_{Si} , Si_C), softening is found for B_{Si} and Al_{Si} acceptors and P_{Si} and N_C donors in 3C – SiC. As compared with the strength of an Si–N bond of a single donor (N_C), we found much more softening in the Si–O bond when the double donor oxygen was substituted on a C site (O_C). A similar trend of weakening in the impurity–host bonding (Be–C) for the double acceptor Be_{Si} is found compared with the bonding (B–C) of the single acceptor B_{Si} .

By including the appropriate force constant variations in the Green's function theory, our calculation predicted the local modes for B_{Si} ($\sim 990 \text{ cm}^{-1}$, $\sim 620 \text{ cm}^{-1}$), C_{Si} ($\sim 1000 \text{ cm}^{-1}$, 620 cm^{-1}), and N_{Si} ($\sim 985 \text{ cm}^{-1}$, $\sim 620 \text{ cm}^{-1}$), and gap modes for N_C ($\sim 638 \text{ cm}^{-1}$, F_2) and Si_C ($\sim 648 \text{ cm}^{-1}$, F_2 ; $\sim 622 \text{ cm}^{-1}$, A_1). In 3C-SiC, while O_C is energetically more stable [36] than O_{Si} and O_i , the weakening in the Si–O bond, however, pushes its gap mode into the acoustic phonon region. Although the calculated LVMs are infrared and Raman active, most of them fall close to the phonon continuum of 3C-SiC. This could be the prime reason why no such vibrations have been detected. Again, despite the relatively high frequency, the C-antisite (C_{Si} ($\sim 1000 \text{ cm}^{-1}$)) local mode is not [122] observed experimentally, because the center is both electrically and optically inactive.

To the best of our knowledge, there exist no vibrational studies of N-defects in 3C-SiC. However, low-temperature Raman measurements [44, 123] on N-doped 6H-SiC with different carrier concentrations have revealed three sharp electronic transitions near ~ 13.0 , 60.3 , and 62.6 meV. These lines of E_2 symmetry, confirmed by polarization measurements, were assigned to the $1s(A_1)$ and $1s(E)$ valley–orbit transitions at the three (one hexagonal and two cubic) inequivalent N-donor sites. A fourth line observed near ~ 78.8 meV was interpreted as the vibrational mode in the phonon gap region [44, 123]. Although the absorption study by Helbig et al. [124] did find a line near ~ 78 meV in 6H-SiC, those authors assigned it to the gap mode of N_{Si} . As the structural differences between 6H- and 3C-SiC occur first at the third neighbors, our calculation for the N_C gap mode ($\sim 638 \text{ cm}^{-1}$) agrees well with the ~ 79 meV ($\sim 630 \text{ cm}^{-1}$) line observed by both IR and Raman spectroscopy.

Like the case for P_{Si} in 3C-SiC, we have predicted some distinct impurity-induced phonon features for substitutional Ge (Ge_{Si}) near $\sim 105\text{ cm}^{-1}$ (A_1), $\sim 235\text{ cm}^{-1}$, and 490 cm^{-1} (F_2). The low-energy $\sim 105\text{ cm}^{-1}$ “breathing mode” is Raman active, where the heavier Ge impurity remains stationary in the 3C-SiC lattice while the neighboring C atoms move radially towards it. As the mode falls in a phonon region where the density of states is low (see Fig. 5.8b), we expect it to be observed by Raman scattering. The incorporation of substitutional Ge into 3C-SiC alloys has recently been studied by using molecular dynamics simulations within a valence force field model [125]. The main impurity-induced feature near $\sim 240\text{ cm}^{-1}$, which decays on moving toward the zinc-blende GeC compound, is in agreement with our calculations.

The appearance of the prototypical D_I center in irradiated as well as in as-grown SiC materials suggests its intrinsic character. Although several models (divacancy, C-divacancy, $V_{Si}-N_C$, etc.) have been proposed, most of them are based on the electronic structure of native point defects [106]. By combining experimental and theoretical studies Gali, et al. [36] have recently shown that the properties of an antisite pair ($C_{Si}-SiC$) can produce both the measured one-electron-level position and the local vibrational modes of the D_I center consistent with other experimental findings [104–106]. The authors of [36] also provided theoretical values of the hyperfine constants of the antisite pair in its paramagnetic state as a means to validate the model. In corroboration with the findings of Gali et al. [36], our Green’s function calculations for the gap modes ($\sim 651\text{ cm}^{-1}$ (A_1) and $\sim 647\text{ cm}^{-1}$ (E)) of an antisite pair compare fairly well with the experimental data of 669 and 661 cm^{-1} for D_I in 3C-SiC.

Quite recently, first-principles calculations have been carried out to establish the stable configurations of hydrogen complexes with dopants which passivate shallow acceptors (B and Al) and donors (N) in 3C-SiC [36]. Similar approaches have been extended to understand the structural and electronic properties of isolated vacancies (V_C and V_{Si}), interstitials (C_i and S_i), and clusters of carbon interstitials [36, 110], to establish the microstructure of the D_{II} center. The calculated local vibrational modes and hyperfine parameters were used to facilitate the spectroscopic identification of several complexes. Although two different C-split interstitial-based models have been proposed for the D_{II} center [36, 110], no fingerprints of the LVMs have been found by IR or Raman spectroscopy for the B–H; Al–H and N–H complexes. Further investigations are very much needed to address some of these and related issues.

Acknowledgments

The author wishes to thank Drs. Z. C. Feng (Georgia Tech/National Taiwan University), David Look (Wright State University), Manual Cardona (Max-Planck Institut, Stuttgart), W. J. Choyke (University of Pittsburgh)

for valuable discussions on the subject matter and to Dr. A. Gali and Professor Peter Deák (Budapest University) for providing some of their recent publications. This research was supported in part by the Cottrell College Science Award (Research Corporation) CC4600 and by the National Science Foundation Grant ECS-9906077.

References

1. "Process Technology for Silicon Carbide Devices" edited by C.-M. Zetterling, IEE Publishing, London, 2003.
2. S.I. Vlaskina, 'Silicon carbide LED', Semiconductor Physics, Quantum Electronics & Optoelectronics. **5**, 71, 2002.
3. "Silicon Carbide: A Review of Fundamental Questions and Applications to Current Device Technology", edited by W.J. Choyke, Hiroyuki, Matsunami, and G. Pensl, Akademie Verlag GmbH, Berlin, 1997; 'Properties of Silicon Carbide', edited by G.L. Harris, IEE Publishing, London, 1995.
4. "Point Defects in Semiconductors I – Theoretical Aspects" by M. Lanoo and J. Bourgoin, Springer-Verlag, Berlin, Heidelberg, New York, 1981.
5. 'Silicon Carbide and Related Materials' Proceedings of the Sixth International Conference, Kyoto, Japan, 18–21 September 1995 edited by S. Nakashima, H. Matsunami, S. Yoshida, H. Harima, Institute of Physics Conf. Series **142**, 1996.
6. P.G. Neudeck, 'Progress towards high temperature, high power SiC devices', Institute of Physics Conf. Series **141**, 1994.
7. S. Onda, R. Kumar, and K. Hara, '*SiC Integrated MOSFETs*' in Ref. [2] pp. 369–388.
8. M. Bhatnagar and B.J. Baliga, IEEE Trans. Electron Devices **40**, 645 (1993).
9. B.J. Baliga, Proc. IEEE **82**, 1112 (1994).
10. H. Morkoç, S. Strite, G.B. Gao, M.E. Lin, B. Sverdlov, and M. Burns, J. Appl. Phys. **76**, 1363 (1994).
11. J.T. Torvic, M. Leksono, J.I. Pankove, B.V. Zeghbroeck, H.M. Ng and T.D. Moustakas, "Electrical characterization of GaN/SiC n-p heterojunction diodes" Appl. Phys. Lett. **72**, 1371 (1998).
12. 'Properties of Advanced Semiconductor Materials-GaN, AlN, InN, BN, SiC, SiGe', edited by M.E. Levinshtein, S.L. Rumyantsev and M.S. Shur, John Wiley (Europe), 2001.
13. A.P. Verma and P. Krishna, "Polymorphism and Polytypism in Crystals", Wiley: New York, 1966; P. Krishna, "Crystal Growth and Characterization of Polytype structures", Pergamon Press, Oxford 1983.
14. R.S. Ramsdell, Am. Mineral (USA) **32**, 64 (1947).
15. H. Jagodzinski, Acta Crystallogr. (Denmark) **2**, 201 (1949).
16. G.R. Zhadanov, C. R. Acad. Sci. (France) **48**, 39 (1945).
17. W.R.L. Lambrecht, S. Limpijumnon, S.N. Rashkeev, and B. Segall "Band structure interpretation of the optical transitions between low-lying conduction bands in n-type doped SiC polytypes", in Proceeding of the 7th International Conference on Silicon Carbide, III-Nitrides and Related Materials, edited by G. Pensl, H. Morkoc, B. Monemar, and E. Janzen, (Trans Tech Publication, Stockholm, 1997), pp.271–274. W.R.L. Lambrecht, S. Limpijumnon,

- S.N. Rashkeev, and B. Segall, "Electronic band structure of SiC polytypes: a discussion of theory and experiment", *Phys. Stat. Sol. (b)* **202**, 5 (1997); S. Limpijumnong and W.R.L. Lambrecht, "Total energy differences between SiC polytypes revisited", *Phys. Rev. B* **57**, 12017 (1998); S. Limpijumnong, W.R.L. Lambrecht, S.N. Rashkeev, and B. Segall, "Theory of the optical absorption bands in the 1–3 eV range in n-type Silicon Carbide polytypes", *Phys. Rev. B* **59**, 012890 (1999).
18. F. Bechstedt, P. Käckell, A. Zywietsz, K. Karch, B. Adolph, K. Tenelsen, and J. Furthmüller, "Polytypism and properties of silicon carbide", *Phys. Stat. Sol. (b)* **202**, 35 (1997).
 19. Z. Jiang, X. Xu, H. Wu, F. Zhang, and Z. Jin, "Ab initio calculation of SiC polytypes", *Solid State Commun.* **123**, 263 (2002).
 20. W.R.L. Lambrecht, S. Limpijumnong, and B. Segall, "Theory of Below Gap Absorption Bands in n-Type SiC Polytypes; Or, How SiC Got Its Colors", in *Silicon Carbide and Related Materials-1999*, ed. by C.H. Carter, Jr., R.P. Devaty, and G.S. Rohrer, *Mater. Sci. Forum* **338–342**, 545 (2000).
 21. C. Cheng, K. Kunc, and V. Heine, *Phys. Rev. B* **39**, 5892 (1989).
 22. M. Hofmann, A. Zywietsz, K. Karch, and F. Bechstedt, "Lattice dynamics of SiC polytypes within the bond-charge model", *Phys. Rev. B* **50**, 13401–11, (1994); K. Karch, P. Pavone, W. Windl, O. Schütt, and D. Strauch, "Ab initio calculation of structural and lattice dynamical properties of silicon carbide", *Phys. Rev. B* **50**, 17054 (1994).
 23. W. Windl, K. Karch, P. Pavone, O. Schütt, D. Strauch, W.H. Weber, K.C. Hass, and L. Rimai, "Second-order Raman spectra of SiC: experimental and theoretical results from *ab initio* calculations", *Phys. Rev. B* **49**, 8764 (1994).
 24. K. Karch, P. Pavone, W. Windl, D. Strauch, and F. Bechstedt, "Ab-initio calculation of structural, lattice-dynamical, and thermal properties of cubic silicon carbide", *Int. J. Quantum Chem.* **56**, 801 (1995).
 25. K. Karch, G. Wellenhofer, P. Pavone, U. Rössler, and D. Strauch, "Structural and electronic properties of SiC polytypes", in *The Physics of Semiconductors*, edited by D. J. Lockwood, World Scientific: Singapore, 401–404 (1995).
 26. W.J. Choyke and L. Patrick, *Phys. Rev.* **127**, 1868 (1962); W.J. Choyke, D.R. Hamilton, and L. Patrick, *Phys. Rev.* **133**, A1163 (1964); D.W. Feldman, J.H. Parker, Jr., W.J. Choyke, and L. Patrick, *Phys. Rev.* **173**, 787 (1968).
 27. J.P. Bergman, O. Kordina, and E. Janzen, "Time resolved spectroscopy of defects in SiC", *Phys. Stat. Sol. (a)* **162**, 65 (1997).
 28. S. Greulich-Weber, "EPR and ENDOR investigations of shallow impurities in SiC polytypes", *Phys. Stat. Sol. (a)* **162**, 95 (1997).
 29. J. Baur, M. Kunzer, and J. Schneider, "Transition metals in SiC polytypes as studied by magnetic resonance techniques", *Phys. Stat. Sol. (a)* **162**, 153 (1997).
 30. T. Dalibor, G. Pensl, H. Matsunami, T. Kimoto, W.J. Choyke, A. Schöner, and N. Nordell, "Deep defect centers in silicon carbide monitored by deep level transient spectroscopy", *Phys. Stat. Sol. (a)* **162**, 199 (1997).
 31. H. Itoh, A. Kawasuso, T. Oshima, M. Yoshikawa, I. Nashiyama, S. Tanigawa, S. Misawa, H. Okumura, and S. Yoshida, "Intrinsic defects in cubic silicon carbide", *Phys. Stat. Sol. (a)* **162**, 173 (1997).
 32. X.D. Chen, C.C. Ling, S. Fung, C.D. Beling, M. Gong, T. Henkel, H. Tanoue, and N. Kobayashi, "Beryllium implantation induced deep level defects in p-type

- 6H silicon carbide”, J. Appl. Phys. **93**, 3117 (2003); C.C. Ling, C.D. Beling, and S. Fung, “Isochronal annealing studies of n-type 6H-SiC with the use of positron lifetime spectroscopy”, Phys. Rev. B **62**, 8016 (2000).
33. S.Yu. Davydov, A.A. Lebedev, O.V. Posrednik, Yu.M. Tairov, “Role of silicon vacancies in formation of Schottky barriers at Ag and Au contacts to 3C- and 6H-SiC”, Semiconductors **36**, 652–654 (2002).
 34. V.V. Zelenin, D.V. Davydov, M.L. Korogodskii, and A.A. Lebedev, “The effect of hydrogen etching on the electrical properties of autoepitaxial silicon carbide layers”, Tech. Phys. Lett. **28**, 382–384 (2002); D.V. Davydov, A.A. Lebedev, V.V. Kozlovski, N.S. Savkina, and A.M. Strel’chuk “DLTS study of defects in 6H- and 4H-SiC created by proton irradiation”, Physica B **308–310**, 641–644 (2002).
 35. F. Gao, E. Bylaska, W. Weber, and L. Corrales, “Native defect properties in beta-SiC: ab initio pseudopotential and empirical potential calculations”, Nucl. Instrum. Methods B **180**, 286 (2001); F. Gao, E. Bylaska, W. Weber, and L. Corrales, “Ab initio and empirical potential studies of defect properties in 3C-SiC”, Phys. Rev. B **64**, 245208 (2001).
 36. A. Gali, P. Deák, E. Rauls, N.T. Son, I.G. Ivanov, F.H.C. Carlsson, E. Janzén, and W.J. Choyke, “The correlation between the anti-site pair and the D₁ center in SiC”, Phys. Rev. B **67**, 155203/1–5 (2003); P. Deák, A. Gali, and B. Aradi, “Hydrogen in SiC” in “Recent advances in SiC Research”, eds. W.J. Choyke, H. Matsunami, and G. Pensl, Springer: Berlin 2003; A. Gali, D. Heringer, P. Deák, Z. Hajnal, Th. Frauenheim, R.P. Devaty, and W.J. Choyke, “Isolated oxygen defects in 3C- and 4H-SiC: a theoretical study”, Phys. Rev. B **66**, 125208–1, (2002); A. Gali, B. Aradi, D. Heringer, W.J. Choyke, R.P. Devaty, and S. Bai, Appl. Phys. Lett. **80**, 237 (2002); B. Aradi, A. Gali, P. Deák, J.E. Lowther, N.T. Son, E. Janzén, and W.J. Choyke, Phys. Rev. B **63**, 245202 (2001); A. Gali, B. Aradi, P. Deák, W.J. Choyke, and N.T. Son, Phys. Rev. Lett. **84**, 4926 (2000); N.T. Son, W.M. Chen, J.L. Lindström, B. Monemar, and E. Janzén, Mater. Sci. Eng. B **61/62**, 202 (1999).
 37. T.T. Petrenko, T.L. Petrenko, and V.Ya. Bratus, “The carbon ⟨100⟩ split interstitial in SiC” J. Phys. Cond. Matter **14**, 12433 (2002).
 38. F.R. Chien, S.R. Nutt, J.M. Carulli Jr., N. Buchan, C.P. Beetz Jr., and W.S. Yan, “Heteroepitaxial growth of β-SiC films on TiC substrates: interface structure and defects”, J. Mat. Res. **9**, 2086 (1996).
 39. M.I. Chaudhry and Robert L. Wright, “Epitaxial growth of β-SiC on Si by low temperature chemical vapor deposition, J. Mat. Res. **5**, 1595 (1996).
 40. K.C. Kim, H.W. Shim, E. Suh, H.J. Lee, and K.S. Nahm, “Growth of high quality 3C-SiC on a Si(111) substrate by chemical vapor deposition”, J. Korean Phys. Soc. **32**, 588 (1998).
 41. Y. Irokawa, N. Yamada, M. Kodama, and T. Kachi, “Growth of 3C-SiC layers on silicon substrates with a novel stress relaxation”, MRS Proc. Vol. **680 E**, edited by T.E. Kazior, P. Parikh, C. Nguyen, E.T. Yu, 2001.
 42. W. Bahng and H.J. Kim, “Heteroepitaxial growth of β-SiC thin films on Si(100) substrate using bis-trimethylsilylmethane”, Appl. Phys. Lett. **69**, 4053 (1996).
 43. T. Hatayama, T. Fuyuki, and H. Matsunami, “Gas source molecular beam epitaxial growth of 3C-SiC on Si with heterointerface modification by a Si-C-Ge ternary system”, Mater. Sci. Forum **264–268**, 235 (1998).
 44. S. Nakashima and H. Harima, “Raman investigations of SiC polytypes”, Phys. Stat. Sol. (a) **162**, 39 (1997) and references there in.

45. B. Herzog, S. Rohmfeld, R. Püsche, M. Hundhausen, L. Ley, K. Semmelroth, and G. Pensl, "Experimental determination of the phonon-eigenvectors of silicon carbide by raman spectroscopy", *Mater. Sci. Forum* **389–393**, 625 (2002).
46. S. Rohmfeld, M. Hundhausen, L. Ley, C.A. Zorman, and M. Mehregany, "Quantitative evaluation of biaxial strain in epitaxial 3C-SiC layers on Si(100) substrates by Raman spectroscopy", *J. Appl. Phys.* **91**, 1113 (2002).
47. N. Sieber, T. Stark, Th. Seyller, L. Ley, C.A. Zorman, and M. Mehregany, "The origin of the split Si-H stretch mode on hydrogenated 6H-SiC(0001): Titration of crystal truncation", *Appl. Phys. Lett.* **80**, 4726 (2002).
48. M. Cardona (Ed.) *Light Scattering in Solids I*, Springer Verlag, Berlin/Heidelberg/New York 1983.
49. R. Hillenbrand, T. Taubner, and F. Keilmann, "Phonon enhanced light-matter interaction at the nanometer scale", *Nature* **418**, 159 (2002).
50. C. Ulrich, A. Debernardi, E. Anastassakis, K. Syassen, and M. Cardona, "Raman linewidths of phonons in Si, Ge and SiC under pressure", *Phys. Stat. Sol. (b)* **211**, 293 (1999).
51. A.R. Goni, and K. Syassen "Optical properties of semiconductors under pressure (review)" in *Semiconductors and Semimetals Vol. 54*, ed. by T. Suski and W. Paul (Academic, New York 1998), 247.
52. A. Debernardi, C. Ulrich, K. Syassen, and M. Cardona "Raman linewidths of optical phonons in 3C-SiC under pressure: first-principles calculations and experimental results" *Phys. Rev. B* **59**, 6774 (1999).
53. A Jayaraman, "Diamond anvil cell and high-pressure physical investigations", *Rev. Mod. Phys.* **55**, 65 (1983); B.A. Weinstein and R. Zallen, in *Light Scattering in Solids*, edited by M. Cardona and G. Güntherodt, Springer-Berlin, 1984.
54. D. Olego and M. Cardona, *Phys. Rev. B* **25**, 1151 (1982); D. Olego, M. Cardona, and P. Vogl, *Phys. Rev. B* **25**, 3878 (1982); F. Widulle, T. Ruf, O. Buresch, A. Debernardi, and M. Cardona, *Phys. Rev. Lett.* **82**, 3089 (1999).
55. J. Liu and Y.K. Vohra, *Phys. Rev. Lett.* **72**, 4105 (1994).
56. C.C. Chiu, S.B. Desu, and Z.J. Chen, "Local equilibrium phase diagrams: SiC deposition in a hot wall LPCVD reactor", *J. Mater. Res.* **9**, 2066 (1996).
57. L.J. Porter, J. Li, and S. Yip, "Atomistic modeling of finite temperature properties of crystalline β -SiC: lattice vibrations, heat capacities and thermal expansion", *J. Nucl. Mater.* **246**, 53 (1997).
58. K. Karch, P. Pavone, A.P. Mayer, F. Bechstedt, and D. Strauch, "First-principles study of thermal properties of 3C-SiC", *Physica B* **219 & 220**, 448 (1996).
59. Z. Li and R.C. Bradt, "Thermal Expansion and Elastic Anisotropies of SiC as Related to Polytype Structure", Silicon Carbide Symposium 1987.
60. W. Li and T. Wang, "Elasticity, stability, and ideal strength of β -SiC in plane-wave-based ab initio calculations", *Phys. Rev. B* **59**, 3993 (1999).
61. K. Strössner, M. Cardona, and W.J. Choyke, "High pressure X-ray investigations on 3C-SiC", *Solid State Commun.* **63**, 113 (1987); M. Yoshida, A. Ono-dera, M. Ueno, K. Takemura, and O. Shimomura, *Phys. Rev. B* **48**, 10587 (1993).
62. Numerical Data and Functional Relationships in Science and Technology, edited by O. Madelung, Landolt-Bornstein, New Series Group III, Vol. 17, Pt. a (Springer, Berlin, 1982), 49.

63. R.D. Carnahan, *J. Am. Ceram. Soc.* **51**, 223 (1968).
64. See Appendix II of Silicon Carbide 1973 (Edited by R.C. Marshall, J.W. Faust, and C.E. Ryan) (University of South Carolina Press, City 1974).
65. A.R. Gõni, H. Siegle, K. Syassen, C. Thomsen, and J.-M. Wagner, *Phys. Rev. B* **64**, 035205-1 (2001).
66. J. Serrano, J. Strempfer, M. Cardona, M. Schwoerer-Böhning, H. Requardt, M. Lorenzen, B. Stojetzs, P. Pavone, and W.J. Choyke, "Determination of the phonon dispersion of zinc-blende (3C) silicon carbide by inelastic X-ray scattering", *Appl. Phys. Lett.* **80**, 4360 (2002).
67. N.M. Stanton, A.J. Kent, and D. Lehmann, "Phonon transport in 6H-SiC", *Semicon. Sci. Technol.* **18** L4-L7 (2003).
68. J.S. Shah and M.E. Straumanis, *Solid State Commun.* **10**, 159 (1972); G.K. White, *J. Phys. D* **6**, 2070 (1973).
69. S.I. Novakova, *Sov. Phys. Solid State* **2**, 1464 (1961).
70. G.A. Slack and S.F. Bartram, *J. Appl. Phys.* **46**, 89 (1975).
71. D.N. Talwar, "Site selectivity of defects in III-V compounds by local mode spectroscopy and model calculations", edited by Di Bartolo and Chen, World Scientific 2001, p. 487.
72. A.M. Stoneham, "Theory of Defects in Solids", Clarendon, Oxford 1975; M. Jaros, *Adv. Phys.* **29**, 409 (1980).
73. W.G. Spitzer, "Festkörperprobleme XI", edited by O Madelung, Pergamon, New York 1971, pp. 1-44; A.A. Maradudin, E.W. Montroll, C.H. Weiss, and I.P. Ipatova, in "Solid State Physics", 2nd Edition, edited by F. Seitz, D. Turnbull, and H. Ehrenreich, Academic, New York 1971.
74. W.A. Harrison, "Electronic Structure and the Properties of Solids", Freeman, San Francisco, 1980; An-Ban Chen and Arden Sher, "Semiconductor Alloys – Physics and Material Properties", Plenum, New York, 1995; D.N. Talwar, K.S. Suh, and C.S. Ting, *Philos. Mag. B* **54**, 93 (1986).
75. K. Kunc, *Ann. Phys. (Paris)* **8**, 319 (1973-74); K. Kunc, M. Balkanski, and M.A. Nusimovici, *Phys. Rev. B* **12**, 4346 (1975); *Phys. Stat. Solidi B* **71**, 341 (1975).
76. H. Bilz and W. Kress, "Phonon Dispersion Relations in Insulators", Springer Series in Solid State Sciences, Vol. 10 (Springer Berlin 1979); O.H. Nielsen and W. Weber, *Comput. Phys. Comm.* **18**, 101 (1979); *J. Phys. C* **13**, 2449 (1980).
77. D.N. Talwar, M. Vandevyver, K.K. Bajaj, and W.M. Theis, "Gallium-isotope fine structure of impurity modes due to defect complexes in GaAs", *Phys. Rev. B* **33**, 8525 (1986).
78. D.N. Talwar, "Pressure dependent phonon properties of cubic group III nitrides", in the Proceedings of Tenth International Conference on High Pressure Semiconductor Physics (HPSP-X), Guildford 2002, edited by B. Murdin, *Phys. Stat. Solidi b* **235**, 254 (2003).
79. D.N. Talwar, M. Vandevyver, and K.K. Bajaj, "Theory of impurity vibrations due to isolated interstitials and interstitial-substitutional pair defects in semiconductors", *Phys. Rev. B* **36**, 1715 (1987).
80. A. Grimm, A.A. Maradudin, I.P. Ipatova, and A.V. Subashiev, *J. Phys. Chem. Solids* **33**, 775 (1972).
81. D.N. Talwar and M. Vandevyver, "Pressure-dependent phonon properties of III-V compound semiconductors", *Phys. Rev. B* **41**, 12129 (1990).
82. F.D. Murnaghan, *Proc. Nat. Acad. Sci. (USA)* **30**, 244 (1944).

83. T.H.K. Barron, J.G. Collins, and G.K. White, *Adv. Phys.* **29**, 609 (1980).
84. Throughout this paper we have adopted the common, but not universal, terminology of describing a mode with a frequency above the host lattice cut-off as a localized vibrational mode (LVM) and a mode with a frequency lying between the bands in the phonon spectrum of the host crystal as a gap mode. The term localized mode is taken to mean either type of mode.
85. B. Segall, S.A. Alterovitz, E.J. Haugland, and L.G. Matus, *J. Appl. Phys.* **74**, 584 (1986).
86. W.J. Moore, *J. Appl. Phys.* **74**, 1805 (1993); W.J. Moore, J.A. Freitas, Yu.M. Altaiskii, V.L. Zuev, and L.M. Ivanova, "Donor excitation spectra in 3C-SiC", *Inst. Phys. Conf. Ser.* No. 137, edited by M.G. Spencer, R.P. Devaty, J.A. Edmond, M. Asif Khan, R. Kaplan, and M. Rahman 1994, p. 181.
87. W.E. Carlos, "Impurities and structural defects in SiC determined by ESR" in *Properties of Silicon Carbide*, edited by G.L. Harris, IEE, INSPEC No. **13**, 42 (1995).
88. A.I. Veinger, A.G. Zabrodskii, G.A. Lomakina, and E.N. Mokhov, *Fiz. Tverd. Tela* **28**, 1659 (1986) (*Sov. Phys. Solid State* **28**, 917 (1986)).
89. S. Greulich-Weber, M. Feege, J.-M. Speath, E.N. Kalabukhova, S.N. Lukhin, and E.N. Mokhov, *Solid State Commun.* **93**, 393 (1995).
90. T. Troffer, C. Peppermüller, G. Pensl, K. Rottner, and A. Schöner, *J. Appl. Phys.* **80**, 3739 (1996).
91. M.M. Anikin, A.A. Lebedev, A.L. Syrkin, and A.V. Suvorov, *Sov. Phys. Semicond.* **19**, 69 (1985).
92. W. Sutrop, G. Pensl, and P. Lanig, *Appl. Phys. A* **51**, 231 (1990).
93. V.S. Ballandovich and E.N. Mokhov, *Semiconductors* **29**, 187 (1995).
94. P.G. Baranov and E.N. Mokhov, *Semicon. Sci. Technol.* **11**, 489 (1996).
95. A. Duijn-Arnold, T. Ikoma, O.G. Poluektov, P.G. Baranov, E.N. Mokhov, and J. Schmidt, *Phys. Rev. B* **57**, 1607 (1998).
96. H. Kuwabara and S. Yamada, *Phys. Stat. Solidi A* **30**, 739 (1975).
97. M. Laube, G. Pensl, and H. Itoh, "Suppressed diffusion of implanted boron in 4H-SiC", *Appl. Phys. Lett.* **74**, 2292 (1999).
98. H. Bracht, N.A. Stolwijk, M. Laube, and G. Pensl, "Diffusion of boron in silicon carbide: evidence for the kick-out mechanism", *Appl. Phys. Lett.* **77**, 3188 (2000).
99. "Hydrogen in Semiconductors", *Semiconductors and Semimetals*, edited by J.I. Pankove and N.M. Johnson Vol. 34 (Academic Press, New York, 1991).
100. D.J. Larkin, *Phys. Stat. Solidi B* **202**, 305 (1997).
101. G.J. Gerardi, E.H. Pointdexter, and D.J. Keeble, *Appl. Spectrosc.* **50**, 1428 (1996).
102. M.S. Janson, A. Hallén, M.K. Linnarson, and B.G. Svensson, *Mater. Sci. Forum* **353**, 427 (2001).
103. N. Achtziger, J. Grillenberger, W. Witthuhn, M.K. Linnarsson, M. Janson, and B.G. Svensson, *Appl. Phys. Lett.* **73**, 945 (1998).
104. W.J. Choyke and L. Patrick, *Phys. Rev. B* **4**, 1843 (1971); W.J. Choyke, in "The Physics and Chemistry of Carbides, Nitrides and Borides", NATO ASI Series, Vol. 185, edited by R. Freer (Kluwer Academic, Dordrecht, 1990), p. 563; J. Schneider and K. Maier, *Physica* **B185**, 199 (1993).
105. K. Nishino, T. Kimoto, and H. Matsunami, *Jpn. J. Appl. Phys.* **34**, L1110 (1995).

106. A. Fissel, W. Richter, J. Furthmüller, and F. Bechstedt, *Appl. Phys. Lett.* **78**, 2512 (2001).
107. L.A. Rahn, P.J. Colwell, and W.J. Choyke, *Bull. Am. Phys. Soc.* **21**, 408 (1976).
108. L. Patrick and W.J. Choyke, *J. Phys. Chem. Solids* **34**, 565 (1973).
109. G.A. Evans, J.W. Steeds, L. Ley, M. Hundhausen, N. Schulze, and G. Pensl, *Phys. Rev. B* **66**, 035204 (2002).
110. A. Mattausch, M. Bockstedte, and O. Pankratov, *Mater. Sci. Forum* **389–393**, 481 (2002).
111. A. Gali, N.T. Son, P. Deák, and E. Janzén, *Mater. Sci. Forum* **389–393**, 477 (2002).
112. B.R. Davidson, R.C. Newman, T.J. Bullough, and T.B. Joyce, *Phys. Rev. B* **48**, 17106 (1993).
113. W.J. Choyke and L. Patrick, *Phys. Rev. Lett.* **29**, 355 (1972); *Phys. Rev. B* **9**, 3214 (1974).
114. W.J. Choyke, R.P. Devaty, S. Bai, A. Gali, P. Deák, and G. Pensl, *Mater. Sci. Forum* **389**, 585 (2001).
115. B. Clerjaud, F. Gendron, C. Porte, W. Wilkening, *Solid State Commun.* **93**, 463 (1995).
116. P. Deák, A. Gali, and B. Aradi (private communication)
117. P. Pavone, K. Karch, O. Schütt, W. Windl, D. Strauch, P. Giannozzi, and S. Baroni, *Phys. Rev. B* **48**, 3156 (1993).
118. W. Weber, *Phys. Rev. Lett.* **33**, 371 (1974).
119. B.A. Weinstein, *Solid State Commun.* **24**, 595 (1977).
120. S. Limpijumpong and W.R.L. Lambrecht, *Phys. Rev. Lett.* **86**, 91 (2001); *Phys. Rev. B* **63**, 104103 (2001).
121. D.N. Talwar, *Appl. Phys. Lett.* **80**, 1553 (2002).
122. L. Torpo, S. Pöykkö, and T.P. Nieminen, *Phys. Rev. B* **57**, 6243 (1998).
123. P.J. Colwell and M.V. Klein, *Phys. Rev. B* **6**, 498 (1972).
124. R. Helbig, C. Haberstroh, and T. Lauterbach, Extended Abstract # 477, Electrochemical Society Fall 1989 Meeting, Hollywood, Florida.
125. G. Katulka, C. Guedj, J. Kolodzey, R.G. Wilson, C. Swann, M.W. Tsao, and J. Rabolt, “Electrical and optical properties of Ge-implanted 4H-SiC”, *Appl. Phys. Lett.* **74**, 540 (1999); C. Guedz and J. Kolodzey, “Substitutional Ge in 3C-SiC”, *App. Phys. Lett.* **74**, 691 (1999).

Optical and Interdisciplinary Analysis of Cubic SiC Grown on Si by Chemical Vapor Deposition

Z.C. Feng

A comprehensive review of the materials analysis of cubic silicon carbide films grown on Si substrates by chemical vapor deposition is presented. Results from various materials analysis techniques, including low-temperature photoluminescence, Raman scattering, optical reflectance and transmission, Fourier transform infrared spectroscopy, X-ray diffraction, electron microscopy, and theoretical analysis, are shown. Analyses by X-ray photoelectron spectroscopy, secondary-ion mass spectrometry, Rutherford backscattering, ion channeling, and other techniques are introduced. This chapter briefly reviews the results and achievements of the author and his collaborators in the past two decades. Interesting problems, further developments, and directions to be explored are discussed. This review shows the necessity for an interdisciplinary analysis of modern materials.

6.1 Introduction

Cubic silicon carbide (3C-SiC) is a promising material for electronic and optical devices working at high temperature, in a high radiation flux, and in other severe environments. It possesses special properties, such as a large energy gap (2.2 eV at room temperature), a high electric breakdown field, a high saturation drift velocity, a moderately high electron mobility, chemical inertness, and temperature stability [1, 2]. In the early years, cubic SiC crystals of high quality were obtained by the Lely method [3]. The size of the crystals grown by this technique is too small to be used in industry. 3C-SiC has a lattice constant of 4.359 Å at room temperature (RT) [4], which is lower than that of Si, 5.430 Å at RT [2]. This large lattice difference of about 20% and an 8% mismatch in the thermal expansion coefficients between the two materials hindered the exploration of how to grow epitaxial 3C-SiC layers on Si wafers. The lack of suitable epitaxial substrate materials and other difficulties cooled down the enthusiasm for SiC for a long time.

However, this situation has been changed owing to the achievement of the successful growth of large-size 3C-SiC films on Si wafers by way of chemical vapor deposition (CVD) from the NASA Lewis group in 1983 [5]. Since then, strong interest has been rekindled, and a great deal of effort and progress has been made [1, 2, 5–8]. This interest is also due to another factor, i.e. the realization and commercialization of hexagonal silicon carbide wafers, mainly 6H- and 4H-SiC wafers; the research on and applications of SiC and related materials/devices have been greatly developed in the last two decades.

Although the current development and device applications of SiC are focused more on 6H- and 4H-SiC materials, the 3C-SiC/Si system is still very attractive for the following reasons. (i) The high cost of and difficulty in obtaining large areas of 6H-/4H-SiC materials limit their wide commercial use. One way to overcome these limits is to use 3C-SiC films on Si substrates. It is possible to obtain larger-area SiC wafers on Si at low cost. (ii) 3C-SiC has been shown to provide an excellent microwave device with high-temperature ($\sim 400^{\circ}\text{C}$) operation and a high output power density of 67 kW/cm^2 , which is about 30 times larger than that of devices made from GaAs [9]. (iii) There is a small difference of lattice constants and thermal expansion coefficients between SiC and GaN, and therefore SiC can serve as a promising substrate for the epitaxial growth of cubic [10] and hexagonal [11] GaN, cubic InGaN [12], and InGaN/GaN multiple quantum wells [13]. (iv) 3C-SiC is possibly a convenient intermediate-layer material for GaN epitaxy, for example, in silicon-on-insulator (SOI) structures [14]. (v) It is also attractive to realize combined devices that use Si and wide-bandgap SiC and GaN with the help of the well-established Si-based integrated technology.

Therefore, great efforts have continually been made in relation to the heteroepitaxy and applications of 3C-SiC/Si materials and structures/devices in recent years. These include the traditional chemical vapor deposition (CVD) of 3C-SiC/Si by Powell et al. [15], Nishino et al. [16], and Tin et al. [17]. Improvements were achieved by using off-axis Si substrates [18, 19]. Explorations were made of various growth methods and technologies, including reactive-ion-beam deposition [20], gas source molecular-beam epitaxy (GSMBE) [21], and MBE [22]. CVD from silacylobutane [23], reactive magnetron sputtering [24], electron cyclotron resonance CVD [25, 26], pyrolysis of polyimide Languir–Blodgett films [27], low-pressure organometallic CVD using dimethylsilisopropylsilane [28], rapid thermal CVD [29], thermal decomposition of methyltrichlorosilane [30], LT-CVD using methylsilane [31] and flash lamp annealing [32], T-programmed organometallic CVD [33], supersonic-jet epitaxy [34], DC magnetron sputtering [35], selective epitaxy on patterned Si [36], solid-source MBE [37], CVD on undulant Si [38, 39], epitaxial lateral overgrowth (ELO) [40], and so on have also been used. Also, nanocrystalline cubic SiC was formed by laser-assisted CVD [41] and hydrogen-reactive magnetron sputtering [42]. Single-crystal 3C-SiC nanowhiskers on Si were grown via an atomic-hydrogen-assisted vapor–liquid–solid (VLS) growth mechanism [43].

This chapter reviews the materials analysis of CVD-grown cubic SiC films grown on Si, which has been performed mainly by the author and his collaborators. The author has been involved and engaged in the materials characterization and analysis of these CVD-grown 3C-SiC/Si since 1983. Interdisciplinary techniques were employed, including X-ray diffraction (XRD), low-temperature (LT) photoluminescence (PL), Raman scattering, Fourier transform infrared (FTIR) spectroscopy, optical reflectance and transmission, X-ray photoelectron spectroscopy (XPS), secondary-ion mass spectroscopy (SIMS), Rutherford backscattering spectroscopy (RBS), and ion channeling. The major concerns in this chapter are the optical and structural properties of 3C-SiC/Si materials. In the next section, on experimental details, the techniques CVD growth and materials analysis of 3C-SiC on Si are briefly introduced.

In Sect. 6.3, the general materials characterization of cubic SiC is presented, by way of XRD, PL, Raman, an UV–Vis and FTIR spectroscopy; this belongs to the primary materials analysis of and studies on 3C-SiC. More advanced materials analyses are presented in the subsequent parts of this review. In Sect. 6.4, surface science and nuclear-physics analyses, including XPS, SIMS, RBS, and ion channeling, are described. The stress and strain are important in the 3C-SiC/Si system and exert great influence on the material properties. In Sect. 6.5, some theoretical aspects of layer stress and strain in 3C-SiC/Si are set out, and a series of theoretical formulas related to the axial-stress-induced Raman phonon shift and energy bandgap variations are presented. Advanced material analyses based upon Raman and PL are given in next two sections, including the application of theories described in Sect. 6.5. Infrared reflectance spectroscopic analysis of 3C-SiC/Si is described in Sect. 6.8. In Sect. 6.9, additional issues are introduced, including combined UV-excitation PL and Raman spectroscopy on 3C-SiC/Si, the successful epitaxial lateral overgrowth of 3C-SiC on Si, the recent achievement of large-area (6") and thick (200 μm) 3C-SiC grown on undulant Si(001) substrates, and an excellent review volume on the materials characterization of SiC. Some concluding remarks are given, finally. It should be emphasized that much of the work reviewed and presented in this chapter, including many results and data plots reported for the first time, was performed not only by the author but also by collaborators. Special acknowledgments are given to Prof. W.J. Choyke, Dr. J.A. Powell, and Profs. C.C. Tin, J. Williams, A.T.S. Wee, J. Lin, I. Ferguson, and C.C. Yang. They are indeed also the cocontributors and coauthors of this review chapter. Without them, this review could never have been written.

6.2 Experiment

6.2.1 Sample Growth

The experimental samples involved in this review were prepared by chemical vapor deposition. The experimental details of the growth of the materials can

be found in [2,7,15,17]. This CVD procedure produces an initial SiC layer from a carbonization layer, which was produced by way of an initial temperature ramp of the Si substrate in the presence of a hydrocarbon [15, 17]. This thin (\sim several hundreds of angstroms) SiC mixed alloy layer served as buffer for subsequent CVD growth of SiC. It has been shown that the first 1–3 μm layer contains a high density of dislocations, stacking faults, microcracks and other defects [7]. After a certain thickness ($> 10 \mu\text{m}$) of CVD film growth, high-quality single-crystal cubic SiC films on Si with a size larger than 1" dimension were obtained [3, 7]. The 3C-SiC films were found to be single-crystal with a (100) surface, provided that (100) Si wafers were used as the substrates.

6.2.2 Materials Analysis Techniques

Various characterization and analysis techniques were employed in this study. X-ray diffraction measurements were made using a Philips machine [44]. The LT PL system included an LT dewar with the sample immersed in pumped liquid He at $< 2 \text{ K}$, a He–Cd laser and a filtered Hg lamp for UV excitation, a SPEX-1400 spectrometer for signal light dispersion, a photomultiplier for detection, a lock-in amplifier, and related electronics and a computer for signal amplification and processing [7]. Raman scattering was measured in a near-backscattering geometry, with excitation by an Ar ion laser, and using a triple-spectrometer-optical multichannel analyzer system [45]. FTIR spectra were measured by a Perkin Elmer 2000 FTIR spectrometer [44]. Optical reflectance and transmission spectra were obtained using a Hitachi 3410 spectrometer. XPS measurements were made with a VG ESCALAB MkII spectrometer using a Mg K α X-ray source, and SIMS was performed in a VG SIMSLAB, which was connected to the XPS chamber [46]. RBS experiments were done using 2 MeV He $^+$ ions from 3 MeV Dynamitron accelerator with light-ion channeling capability [47].

6.2.3 Absorption Coefficients

3C-SiC has an energy gap of approximately 2.4 eV at LT below 10 K [48] and about 2.2 eV at RT, and there is a large change in the absorption coefficient α and the penetration depth $d_p = 1/\alpha$ from below the bandgap to the deep ultraviolet wavelength region [7]. These data, taken at RT, are presented in Fig. 6.1. The absorption data at LT (2 K) can be obtained by a small shift of about 25 meV towards higher energy from the RT values [7]. From the figure, we can find the penetration depth d_p of 3C-SiC at RT to be 83 μm at 2.6 eV (4767 Å), 48 μm at 2.7 eV (4591 Å), 5 μm at 3.4 eV (3650 Å), and $\sim 1.5 \mu\text{m}$ at 3.8 eV (3250 Å). Therefore, if ones use an Ar ion laser with lines at 4880 and 4579 Å, only weak absorption and weak luminescence from 3C-SiC can be obtained. If a UV excitation from an Ar $^+$ laser 3651 Å or He–Cd laser 3250 Å line is employed, more absorption in the 3C-SiC and a stronger PL signal can

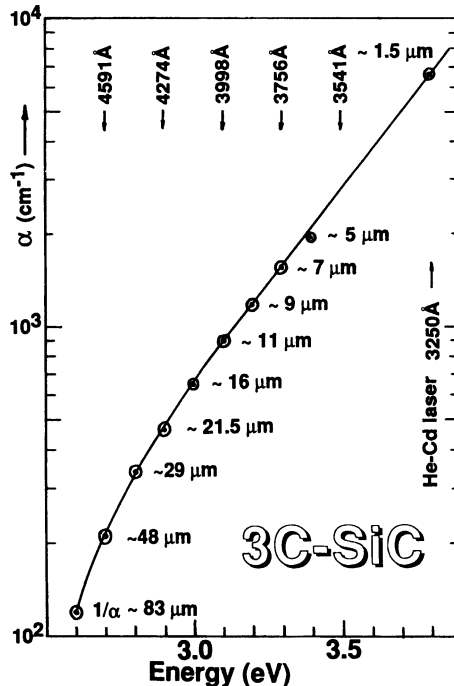


Fig. 6.1. Absorption coefficient α and penetration depth $d_p = 1/\alpha$, of cubic SiC at 300 K (from Choyke et al. [7], reprinted with permission of the American Institute of Physics)

be obtained. These two lasers and also a filtered high-pressure Hg lamp [7] or Xe lamp are good excitation light sources for pumping 3C-SiC beyond the bandgap for PL measurements.

6.3 General Materials Characterization of 3C-SiC

6.3.1 X-ray Diffraction

X-ray diffraction has been used to identify the polycrystalline or single-crystal nature of CVD 3C-SiC films. A $2\theta-\omega$ scan for 3C-SiC/Si(100) with a film thickness of 3 μm , shown in Fig. 6.2, exhibits only $(h00)$ (where h is even) patterns. The strongest peak, at 69.12° , is the Si (400) diffraction from the Si substrate. The peak at 41.39° is from the 3C-SiC (200) diffraction, and the peak at 89.95° is the high-order 3C-SiC (400) pattern. These are characteristic of single-crystal cubic SiC with a (100) orientation. The width of the XRD pattern is characteristic of the crystalline perfection [44]. With an increase of the film growth time, i.e. the film thickness, the widths of the XRD peaks decrease [44].

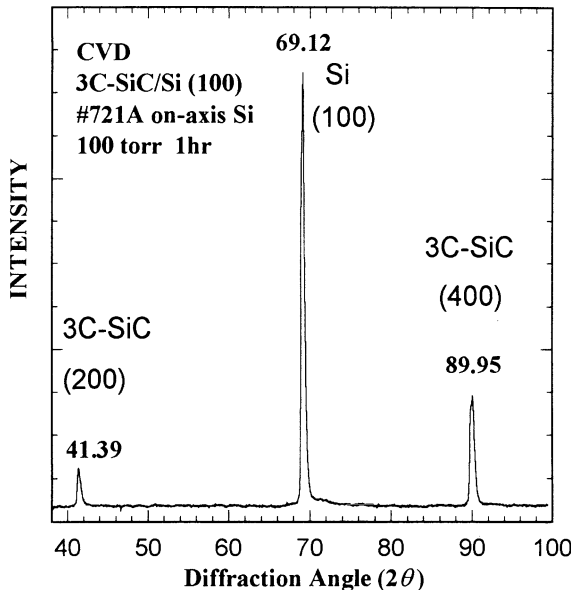


Fig. 6.2. X-ray diffraction θ - 2θ scan of 3C-SiC/Si(100) (3 μm thick) (from Feng et al. [44], reprinted with permission of the Materials Research Society)

6.3.2 Photoluminescence

Shim et al. [49] have reported that, as an indirect-gap material, 3C-SiC/Si does not exhibit any luminescence at room temperature, but when the excitation comes from the interface side of a free 3C-SiC film with the Si substrate etched away, a broad PL band centered around 2.4 eV and a weak peak at 3.0 eV can be observed. The origin of these luminescence emissions is speculated to be due to either the recombination center associated with the OH group or some localized states such as a CH band near the interface [49].

Low-temperature photoluminescence can be a more sensitive and nondestructive technique for the characterization of SiC materials. A great deal of information about the energy-band structure, impurities, structural defects, stress, and strain may be obtained from LT PL measurements [7].

Figure 6.3 shows 2K PL spectra for three CVD 3C-SiC/Si(100) samples with SiC film thickness d of 3.2, 4, and 11 μm . The thinnest film showed a dominant 1.90 eV PL band, i.e. the so-called G band, plus a weak D_I band at 1.972 eV and weak emissions near 2.15 eV, all of which are defect-related features in 3C-SiC [7]. As the film becomes thicker, exciton lines appear in the wavelength range of 5200–5500 Å. When the film is thicker than 10 μm , a non-zero-phonon line, labeled “O”, appears, the nature of which is due to an exciton bound to neutral nitrogen donors [7]. Its first-order phonon replicas, labeled TA(X), LA(X), TO(X), and LO(X) [7,48], appear sharp. Their second-

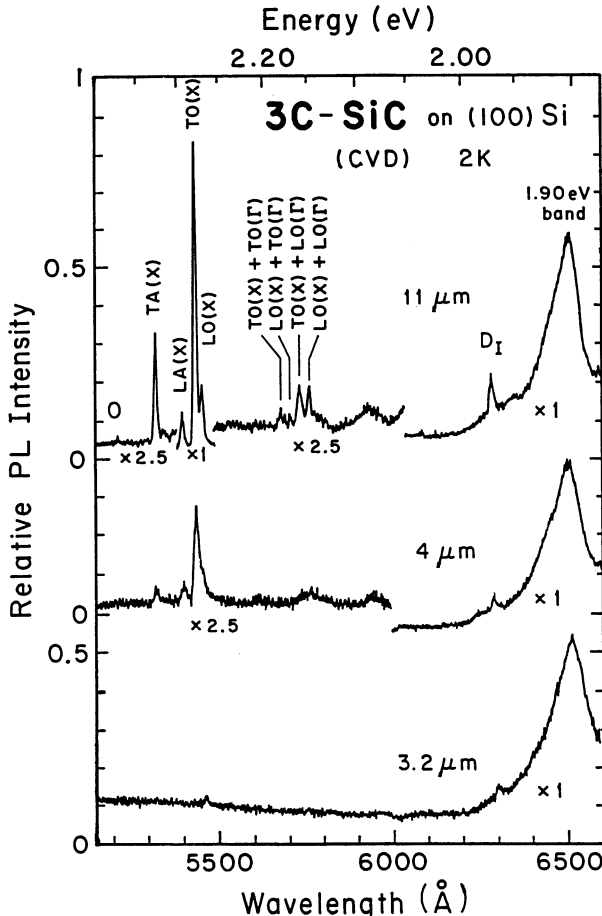


Fig. 6.3. 2K photoluminescence spectra of three CVD 3C-SiC/Si(100) samples with $d = 3.2, 4$ and $11 \mu\text{m}$

order combinations can be also observed. The observation of exciton lines is characteristic of the good quality of the experimental samples.

Figure 6.4 shows a 2K PL bound-exciton (BE) spectrum including momentum-conserving phonon replicas up to third order, from an excellent-quality 3C-SiC free film with the Si substrate removed. This spectrum exhibits a nitrogen-bound-exciton (N-BE) zero-phonon line N_0 at 2.3779 eV, and one-, two-, and three-phonon replicas, labeled in the figure [7]. Another B-series BE zero-phonon line, B_0 , at 2.3691 eV, and its first-order phonon replica, B-TA(X), B-LA(X), and B-LO(X), are also seen and marked in Fig. 6.4. These B-series lines are displaced by 8.8 meV to lower energy from the corresponding N-series lines [7]. The BE lines in Fig. 6.4 have a full width at half maximum (FWHM) of less than 2 meV, which is very similar to that of high-purity bulk

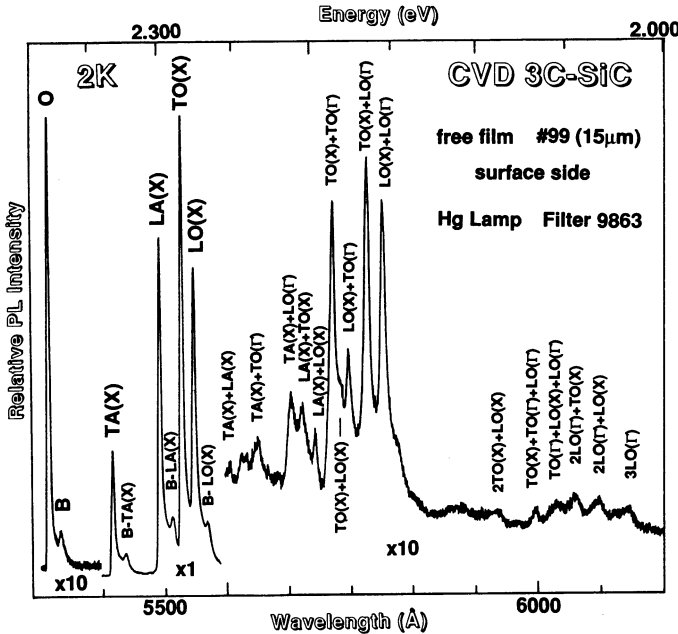


Fig. 6.4. A 2K PL spectrum from a high-quality CVD-grown 3C-SiC free film with $d = 16 \mu\text{m}$ and the Si substrate removed (from Choyke et al. [7], reprinted with permission of the American Institute of Physics)

single-crystal 3C-SiC [48, 50, 51]. Further discussion of these BE emissions in 3C-SiC will be given in Sect. 6.7 of this review chapter.

6.3.3 Raman Scattering

Figure 6.5 shows Raman spectra for the three 3C-SiC/Si(100) samples with LT PL results shown in Fig. 6.3. We see, as $d(\text{SiC})$ increases from $4 \mu\text{m}$ to $11 \mu\text{m}$, that the intensities of the 3C-SiC longitudinal optical (LO) and transverse optical (TO) phonon modes increase with respect to those of the Si substrate. For the poor-quality sample with $d(\text{SiC}) = 3.2 \mu\text{m}$, the allowed LO mode is weaker than the forbidden TO mode. Also, some extra features exist, corresponding to other polytypes of SiC or defects. After removal of the Si substrate, the LO and TO lines will shift their position a little. These Raman line shifts can be used to determine the stress and strain inside the 3C-SiC films [52]. We have studied the variations of the Raman spectra with film thickness and other growth conditions [2, 44, 47, 52]. The relationship between the Raman features and film quality has been established and is discussed in Sect. 6.5.

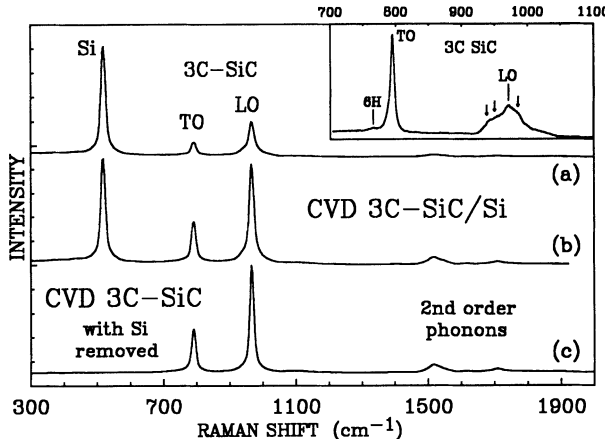


Fig. 6.5. Raman spectra of three CVD 3C-SiC samples grown on (100) Si with a film thickness of 3.2 μm (top right corner), (a) 4 μm , (b) 11 μm , and (c) 11 μm with the Si substrate removed

6.3.4 UV–Vis Optical Spectroscopy

The optical reflectance (OR) over the UV–visible–near-infrared range (190 nm – 2.5 μm) has been measured for CVD samples. Figure 6.6a exhibits an OR spectrum for a CVD 3C-SiC(100) sample with a growth time of 30 minutes. Sharp interference fringes (IFs) appear. When we convert the x -axis into units of energy, eV, these IFs become spread out with an almost constant interval over the range 0.5–5.0 eV, as shown in Fig. 6.6b. These are characteristic of the film flatness and uniformity. The film thickness is given by [53]

$$d = \frac{1}{2} \times \frac{\Delta m \lambda_2 \lambda_2}{\lambda_1 [n^2(\lambda_2) - \sin^2 \theta]^{1/2} - \lambda_2 [n_2(\lambda_1) - \sin^2 \theta]^{1/2}}, \quad (6.1)$$

where θ is the angle with respect to the surface normal, λ_1 and λ_2 are the wavelengths at two maxima or minima of the interference fringes, Δm is the number of fringes, and $n(\lambda_1)$ and $n(\lambda_2)$ are the refractive indices at the corresponding wavelengths, respectively. Under the simplified condition of $\theta = 0$, $\Delta m = 1$, and $n(\lambda_1) = n(\lambda_2) = n$, the film thickness can be roughly estimated from the IFs, using a simple formula:

$$d = (1/2n)/\Delta\nu,$$

where n is the refractive index and $\Delta\nu$ is the interval between two adjacent maxima or minima in units of wavenumbers (cm^{-1}). This thickness is 1.15 μm for the film measured in Fig. 6.6.

6.3.5 Infrared Transmission and Reflectance

Fourier transform infrared spectroscopy was used to study the initial growth of 3C-SiC films. Figure 6.7A shows FTIR transmission spectra for four CVD 3C-

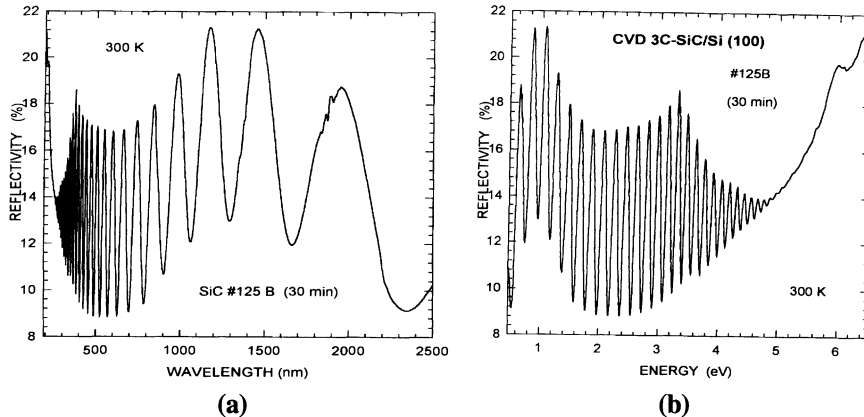


Fig. 6.6. Optical reflectance of a CVD 3C-SiC/Si sample, with x -axis units in (a) nm and (b) eV

SiC/Si(100) samples with different growth times or different film thicknesses. For a very thin film, with a growth time τ of only 2 minutes, a transmission band near 800 cm^{-1} in Fig. 6.7A indicates the initial stage of the formation of a SiC-like crystal but not true 3C-SiC yet. As τ increases to 30 minutes, a deep, flat band between 770 and 920 cm^{-1} appears in Fig. 6.7A, with the two edges corresponding to the TO and LO phonon frequencies. This characterizes the complete formation of 3C-SiC. As τ increases to 1 or 2 hours, i.e. with the film thickness increased to 3 or 6 μm , respectively, this reststrahlen band

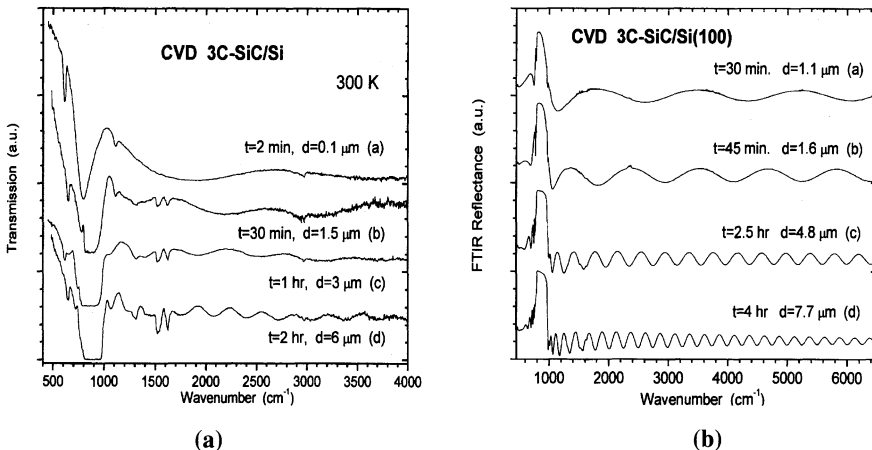


Fig. 6.7. Fourier transform infrared spectra of (a) transmission from four CVD 3C-SiC/Si(100) samples with film thicknesses of 0.1, 1.5, 3, and 6 μm , and (b) reflectance from four CVD 3C-SiC/Si(100) samples with film thicknesses of 1.1, 1.6, 4.8 and 7.7 μm

becomes even more broad and flat, indicating the improvement of the cubic crystalline perfection of the 3C-SiC layers grown on the Si substrate.

FTIR reflectance spectroscopy has been employed for the materials evaluation of CVD-grown 3C-SiC films on substrates of Si [54–56] and silicon on sapphire (SOS) [57]. Figure 6.7B shows FTIR reflectance spectra from another set of four CVD 3C-SiC/Si(100) samples, with different growth times and film thicknesses of 1.1, 1.6, 4.8, and 7.7 μm . Theoretical simulation can be applied to the 3C-SiC/Si system to give more information about the material properties [55, 56].

6.4 Surface Science and Nuclear-Physics Analysis

6.4.1 X-Ray Photoelectron Spectroscopy

For electronic-device applications of SiC, an understanding of the characteristics of the surface exposed to air is important. Wee et al. [46] have employed the surface science technique of X-ray photoelectron spectroscopy to investigate the surface states of CVD-grown 3C-SiC films. XPS showed that the surface of CVD 3C-SiC consists of Si oxides (SiO_2 and SiO_x , where $x < 2$), unreacted CH, and unreacted elemental Si, the amount of which decreases with increasing growth time. The elemental Si and CH species on the surface of 3C-SiC films are caused by the un-reacted source materials SiH_4 and C_3H_8 or their reaction intermediates during the CVD growth. Their relative surface concentrations probably depend on the gas shutdown procedure [46].

Figure 6.8 shows X-ray photoelectron spectroscopy (XPS) of a CVD 3C-SiC/Si(100) sample with a growth time of 3 hours. On changing the photoelectron takeoff angle from 75° to 20° , it was found that the intensity of the CH/SiC ratio in the C 1s peak increases by $\sim 100\%$, while the $(\text{SiO}_2 + \text{SiO}_x)/\text{SiC}$ ratio in the Si 2p peak increases by only $\sim 50\%$. This indicates that the CH species predominates on the surface, with the SiO_2 and SiO_x layer underneath it.

Chemical etching was performed to remove any unreacted Si, CH, and Si oxides. Figure 6.9 shows XPS wide scans of a CVD 3C-SiC/Si(100) sample with a growth time of 4 hours, before and after chemical etching [46]. The O 1s and C 1s peaks are clearly reduced relative to the Si peaks after etching, indicating that the etching is efficient in removing the Si oxides, and to a lesser extent, the CH layer from the 3C-SiC film surface.

It was concluded from these XPS studies that an unreacted elemental Si layer exists atop the stoichiometric SiC film, followed by an overlayer consisting of a mixture of Si oxides and a carbonaceous CH species. This overlayer probably has a passivation effect that minimizes oxidation of the SiC in the atmosphere [46].

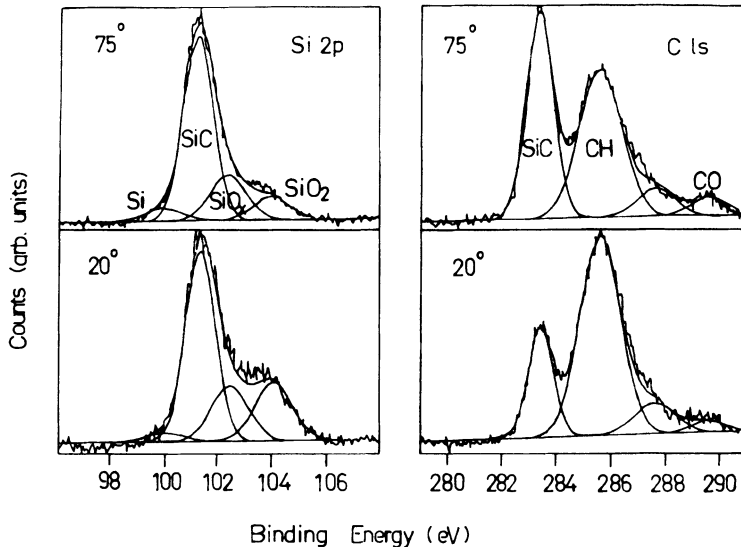


Fig. 6.8. X-ray photoelectron spectroscopy of a CVD 3C-SiC/Si(100) sample with a growth time of 3 hours: *left*, Si 2p; *right*, C 1s, with takeoff angles of 20° and 75° (from Wee et al. [46], reprinted with permission of Elsevier)

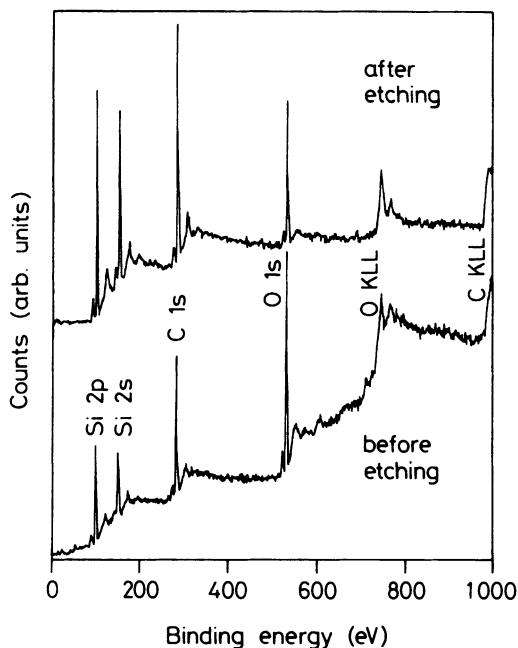


Fig. 6.9. XPS wide scan of a CVD 3C-SiC/Si(100) sample with a growth time of 4 hours, before and after chemical etching (from Wee et al. [46], reprinted with permission of Elsevier)

6.4.2 Secondary-Ion Mass Spectrometry

Secondary-ion mass spectrometry is a powerful technique for studying the interface properties of materials in an epitaxial structure. Positive SIMS depth profiling has been performed to investigate the compositional variations of CVD-grown 3C-SiC films with sputter time, and hence depth. A typical profile of a CVD 3C-SiC/Si(100) sample with a film growth time of 15 minutes is shown in Fig. 6.10A. The SiC/Si interface between the film and substrate is clearly shown in this depth profile, as can be judged by the sharp decrease in the SiC^+ and C^+ signals. Positive SIMS mass spectra were detected for this sample in different regions, as shown in Fig. 6.10B, including the sample surface and the SiC and Si regions. It is observed that there is an increase in N^+ on going deeper inside the sample. This is attributed to the diffusion of nitrogen from the growth chamber ambient during high-temperature SiC growth [46].

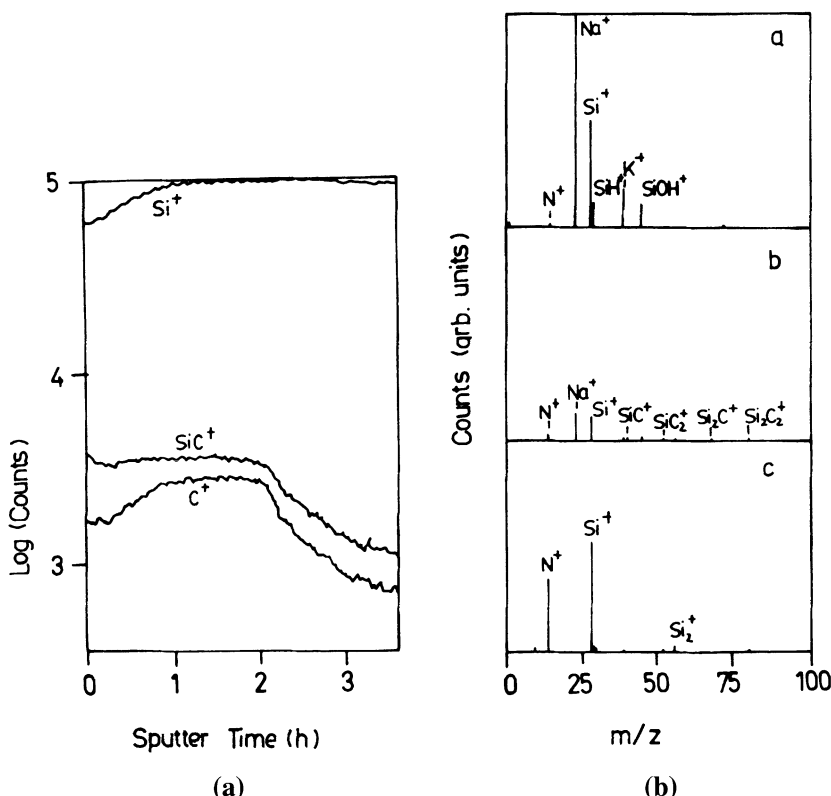


Fig. 6.10. Positive SIMS data: (a) depth profile of a CVD 3C-SiC/Si(100) sample with a film growth time of 15 minutes; (b) mass spectra of (a) sample surface, (b) SiC region, and (c) Si region of a CVD 3C-SiC/Si(100) sample with a film growth time of 15 minutes (from Wee et al. [46], reprinted with permission of Elsevier)

6.4.3 Rutherford Backscattering

Rutherford backscattering (RBS) is a powerful nuclear-physics technique for semiconductor materials investigation, and it has been used in combination with Raman spectroscopy to analyze CVD-grown 3C-SiC/Si by Feng et al. [47]. Figure 6.11A shows RBS data and RUMP simulations for three CVD-grown 3C-SiC/Si(100) samples with different film growth times of (a) $\tau = 2$ min, (b) $\tau = 30$ min, and (c) $\tau = 3$ hrs. The solid lines in the figure are the RUMP [58] simulations of the experimental data. From these simulations,

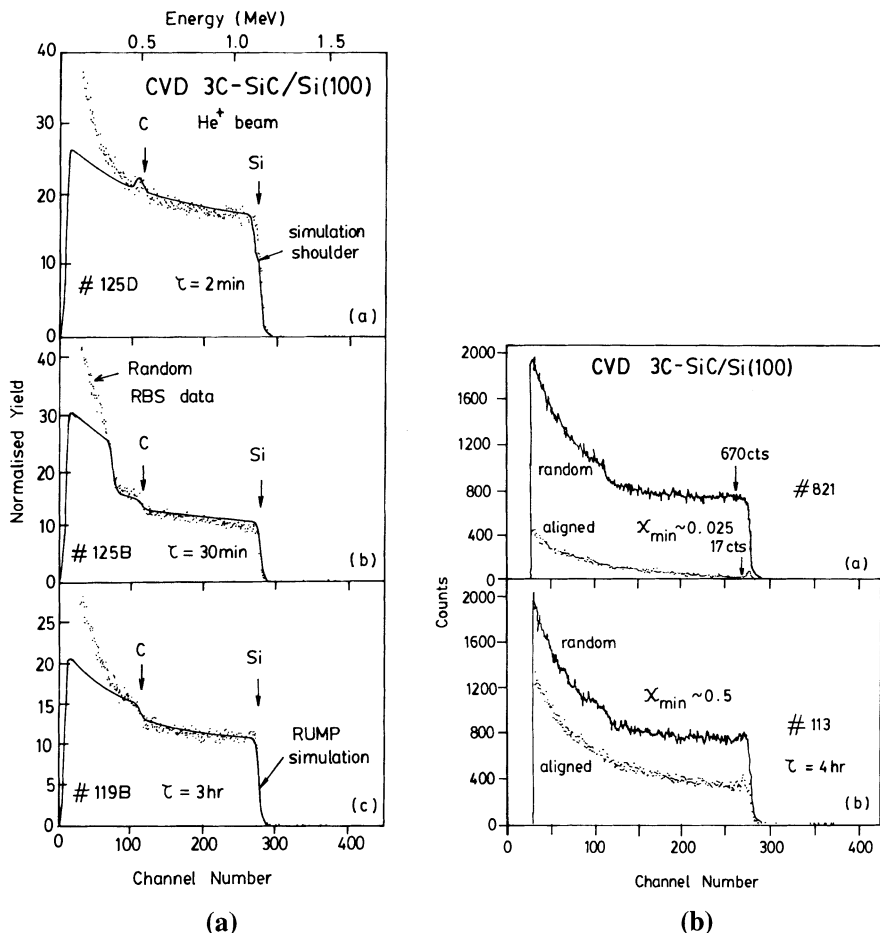


Fig. 6.11. (a) Rutherford backscattering data and RUMP simulations for three CVD-grown 3C-SiC/Si(100) samples with different film growth times of (a) $\tau = 2$ min, (b) $\tau = 30$ min, and (c) $\tau = 3$ hrs (from Feng et al. [47], reprinted with permission of Elsevier); (b) comparative random RBS and channeling (aligned) spectra for two CVD 3C-SiC/Si(100) samples with different χ_{\min} , indicating different crystalline quality

the thickness of the thin film can be determined accurately. For example, the thinnest film in Fig. 6.11Aa is 600 Å thick, and the one in Fig. 6.11Ab is 1.05 µm thick. Also, the Si:C ratios in the 3C-SiC films are found to be a stoichiometric 1:1 for these samples.

6.4.4 Ion Channeling

The single-crystallinity of CVD 3C-SiC films can be determined from ion channeling measurements [47]. Figure 6.11B shows comparative random RBS and channeling (aligned) spectra for two CVD 3C-SiC/Si(100) samples. In (a), a very low χ_{\min} value of ~ 0.025 was obtained, indicating a high crystalline perfection of this film. In contrast, in (b), a high χ_{\min} value of ~ 0.5 was obtained, indicating a poor crystalline quality of this sample. These results correspond to those obtained that from Raman and other measurements [47].

Combined characterizations by way of various optical, structural, surface science, and nuclear-physics techniques have helped us to improve the materials growth and device fabrication greatly in past years, and have deepened our understanding of CVD-grown 3C-SiC and of the related physical mechanisms [2, 7, 44, 46, 47, 52, 56].

6.5 Theoretical Aspects of Layer Stress and Strain in 3C-SiC/Si

6.5.1 Generalized Axial Stress and Strain

Stress Tensor

Epitaxial growth of thin-layer films on a thick substrate may lead to the introduction of layer stresses and strains owing to differences in lattice constants and thermal expansion coefficients between the substrate and the film. The component of the stress in the layer in the direction perpendicular to the surface of the substrate is expected to be different from that parallel to the surface of the substrate. The components of the stress and strain in the parallel plane can be regarded as isotropic. A generalized axial stress can be defined by the stress tensor

$$\sigma = \begin{vmatrix} X & 0 & 0 \\ 0 & X & 0 \\ 0 & 0 & Z \end{vmatrix}, \quad (6.2)$$

which is symmetric about the z -axis and is sometimes called simply an axial stress. It has equal stress components in the $x-y$ plane and a different z -component, and zero off-diagonal elements, i.e. no shear stress components. When X or $Z < 0$ we have a compressive stress and when X or $Z > 0$ we

have a tensile stress. The axial (z -axis symmetry) stress can be decomposed into a hydrostatic pressure and a uniaxial stress along the z -axis as follows:

$$\sigma = \begin{vmatrix} X & 0 & 0 \\ 0 & X & 0 \\ 0 & 0 & Z \end{vmatrix} = \begin{vmatrix} X & 0 & 0 \\ 0 & X & 0 \\ 0 & 0 & X \end{vmatrix} + \begin{vmatrix} 0 & 0 & 0 \\ 0 & 0 & 0 \\ 0 & 0 & P \end{vmatrix}, \quad (6.3)$$

where $Z = X + P$. There are three important special cases. The hydrostatic case has zero uniaxial stress ($P = 0$), the uniaxial case has no hydrostatic component ($X = 0$), and the so-called biaxial stress [59] case has equal and opposite magnitudes of the hydrostatic and uniaxial components ($X = -P$). The stress tensors for these three cases are expressed by σ_H , σ_U , and σ_B , respectively;

$$\sigma_H = \begin{vmatrix} X & 0 & 0 \\ 0 & X & 0 \\ 0 & 0 & X \end{vmatrix}, \quad \sigma_U = \begin{vmatrix} 0 & 0 & 0 \\ 0 & 0 & 0 \\ 0 & 0 & P \end{vmatrix}, \quad \text{and} \quad \sigma_B = \begin{vmatrix} X & 0 & 0 \\ 0 & X & 0 \\ 0 & 0 & 0 \end{vmatrix}. \quad (6.4)$$

Strain Tensor

The strain tensor for a generalized axial stress and a cubic solid may be obtained from Hooke's law [60]:

$$\varepsilon = \begin{vmatrix} (S_{11} + 2S_{12})X + S_{12}P & 0 & 0 \\ 0 & (S_{11} + 2S_{12})X + S_{12}P & 0 \\ 0 & 0 & (S_{11} + 2S_{12})X + S_{11}P \end{vmatrix}, \quad (6.5)$$

or

$$\begin{aligned} \varepsilon_{xy} &= \varepsilon_{xz} = \varepsilon_{yz} = 0, \\ \varepsilon_{zz} &= (S_{11} + 2S_{12})X + S_{11}P = \varepsilon_{\perp}, \\ \varepsilon_{xx} &= \varepsilon_{yy} = (S_{11} + 2S_{12})X + S_{12}P = \varepsilon_{\parallel}, \end{aligned} \quad (6.6)$$

where ε_{\parallel} is called the in-plane strain and ε_{\perp} is the normal strain. Correspondingly, the strain tensors and the components for the three special cases are given by

$$\begin{aligned} \varepsilon_H &= \begin{vmatrix} (S_{11}+2S_{12})X & 0 & 0 \\ 0 & (S_{11}+2S_{12})X & 0 \\ 0 & 0 & (S_{11}+2S_{12})X \end{vmatrix}, \\ \varepsilon_U &= \begin{vmatrix} S_{12}P & 0 & 0 \\ 0 & S_{12}P & 0 \\ 0 & 0 & S_{11}P \end{vmatrix}, \end{aligned}$$

and

$$\varepsilon_B = \begin{vmatrix} (S_{11}+S_{12})X & 0 & 0 \\ 0 & (S_{11}+S_{12})X & 0 \\ 0 & 0 & 2S_{12}X \end{vmatrix}. \quad (6.7)$$

Conversion Between S_{ij} and C_{ij}

In (6.5)–(6.7), the S_{ij} are the elastic compliances, from which the elastic stiffnesses can be obtained by means of the following relations [60]:

$$\begin{aligned} C_{11} &= (S_{11} + S_{12}) / [(S_{11} - S_{12})(S_{11} + 2S_{12})] , \\ C_{12} &= -S_{12} / [(S_{11} - S_{12})(S_{11} + 2S_{12})] , \\ C_{44} &= 1/S_{44} . \end{aligned} \quad (6.8)$$

The inverse transformation from C_{ij} to S_{ij} may be obtained by exchanging C_{ij} with S_{ij} in (6.8).

Poisson Ratio

The negative of the ratio of the strains perpendicular and parallel to the stress axis is defined as the Poisson ratio ν [61]:

$$\begin{aligned} \nu &= -\varepsilon_{xx}/\varepsilon_{zz} = -\varepsilon_{yy}/\varepsilon_{zz} \\ &= -[(S_{11} + 2S_{12})X + S_{12}P] / [(S_{11} + 2S_{12})X + S_{11}P] \\ &= [\nu_S P - (1 - 2\nu_S)X] / [P + (1 - 2\nu_S)X] , \end{aligned} \quad (6.9)$$

where

$$\nu_S = -S_{12}/S_{11} . \quad (6.10)$$

The Poisson ratio can be easily obtained for three special stress cases:

(i) for a hydrostatic pressure,

$$\nu_H = -1 ; \quad (6.11)$$

(ii) for a uniaxial stress along the z -axis,

$$\nu_U = \nu_S = -\varepsilon_{xx}/\varepsilon_{zz} = -\varepsilon_{yy}/\varepsilon_{zz} = -S_{12}/S_{11} = C_{12}/(C_{11} + C_{12}) ; \quad (6.12)$$

(iii) for a biaxial stress in the x – y plane,

$$\begin{aligned} \nu_B &= -\varepsilon_{xx}/\varepsilon_{zz} = -\varepsilon_{yy}/\varepsilon_{zz} = -(S_{11} + S_{12})/2S_{12} \\ &= C_{11}/2C_{12} = (1 - \nu_S)/2\nu_S . \end{aligned} \quad (6.13)$$

The Poisson ratio given in (6.9) for a generalized axial stress depends on the stress components and is not a constant. However, for our three special cases, we have constant Poisson ratios. In addition, the Poisson ratios for biaxial and generalized axial stresses can be expressed by means of the Poisson ratio for a uniaxial stress.

Volume Dilation

The ratio of the difference between the original and strained volumes ΔV to the original unstrained volume V is defined as the volume dilation

$$\Xi = -\Delta V/V \approx -(\varepsilon_{xx} + \varepsilon_{yy} + \varepsilon_{zz}) . \quad (6.14)$$

For a general axial stress, we have

$$\Xi = -(S_{11} + 2S_{12})(3X + P) . \quad (6.15)$$

The volume dilation and other components, for our three special cases, are shown in Table 1 of [52]. Our formulation given above may be clearer and more transparent to the reader.

6.5.2 Axial-Stress-Induced Raman Shifts

Secular Equation

In a cubic crystal with strains, the Raman optical-phonon frequencies may be obtained from the secular equation [52, 62]

$$\begin{vmatrix} p\varepsilon_{xx} + q(\varepsilon_{yy} + \varepsilon_{zz}) - \lambda & 2r\varepsilon_{xy} & 2r\varepsilon_{xz} \\ 2r\varepsilon_{xy} & p\varepsilon_{yy} + q(\varepsilon_{xx} + \varepsilon_{zz}) - \lambda & 2r\varepsilon_{yz} \\ 2r\varepsilon_{xz} & 2r\varepsilon_{yz} & p\varepsilon_{zz} + q(\varepsilon_{xx} + \varepsilon_{yy}) - \lambda \end{vmatrix} = 0 , \quad (6.16)$$

with

$$\omega \approx \omega_0 + \lambda/2\omega_0 , \quad (6.17)$$

where λ is the eigenvalue of the secular equation (6.16), and ω and ω_0 are the Raman frequencies with and without strain, respectively. In (6.16), p , q , and r are optical-mode constants related to the effective spring constants of the interatomic forces in the crystal in units of s^{-2} [52, 62]. The units of both ω and ω_0 are s^{-1} . For an axial stress with strains (6.6) of ε_{ij} ($i \neq j$) = 0 and $\varepsilon_{xx} = \varepsilon_{yy}$, from (6.16) and (6.17) we have the phonon frequencies

$$\begin{aligned} \omega_1 &= \omega_2 = \omega_0 + [(p + q)\varepsilon_{xx} + q\varepsilon_{zz}] / 2\omega_0 , \\ \omega_3 &= \omega_0 + [p\varepsilon_{zz} + 2q\varepsilon_{xx}] / 2\omega_0 . \end{aligned} \quad (6.18)$$

It is well known that in the absence of an external stress, the first-order Raman spectrum of a diamond-type material exhibits a single peak, which corresponds to the $q \approx 0$, T-symmetry, triply degenerate optical phonons ($\Gamma_{25'}$), while in a zinc blende material one has two peaks, corresponding to the $q \approx 0$ A-symmetry (singly degenerate) LO and E-symmetry (doubly degenerate) TO phonons [52, 62]. This splitting is due to the long-range Coulomb forces [63] and reflects the polar character of the crystal and the lack of inversion symmetry [52, 63]. It can also be a measure of the effective charge and the degree of ionicity [64].

Raman Optical-Phonon Frequencies from Axial Strains

In order to use (6.18) for a zinc blende crystal, we put the superscripts TO and LO on the ω_0 term; for a diamond-type crystal, $\omega_0^{\text{TO}} = \omega_0^{\text{LO}}$. Furthermore, we rewrite (6.18) with axial strains (6.6) as

$$\begin{aligned}\omega^{\text{TO}} &= \omega_0^{\text{TO}} + \Delta\omega_{\text{H}}^* - \frac{1}{3}\Delta\omega_{\text{S}}^*, \\ \omega^{\text{LO}} &= \omega_0^{\text{LO}} + \Delta\omega_{\text{H}}^* + \frac{2}{3}\Delta\omega_{\text{S}}^*,\end{aligned}\quad (6.19)$$

where

$$\begin{aligned}\Delta\omega_{\text{H}}^* &= (p + 2q)(S_{11} + 2S_{12})(3X + P)/6\omega_0, \\ \Delta\omega_{\text{S}}^* &= (p - q)(S_{11} - S_{12})P/2\omega_0.\end{aligned}\quad (6.20)$$

Equations (6.19) and (6.20) show the linear relations of ω^{TO} and ω^{LO} with respect to the hydrostatic-pressure and uniaxial-stress components. $\Delta\omega_{\text{S}}^*$ represents the splitting of LO and TO phonons due to the uniaxial-stress component, while $\Delta\omega_{\text{H}}^*$ represents the shift of the center of mass of the LO and TO phonons due to the hydrostatic and uniaxial components, which is equal to the trace of the stress matrix in (6.3), $\text{Trace}(\sigma) = (3X + P)$. Hydrostatic pressure does not contribute to the phonon splitting.

Raman Stress Coefficients η_{S} and η_{H}

In the expressions of (6.16–6.20), the Raman frequencies are in units of s^{-1} . Experimentally, one likes to use wavenumbers, cm^{-1} , as the unit of Raman frequency. For clarity, let us understand that lower-case ω is in units of s^{-1} and capital Ω is in units of cm^{-1} , where $\omega = 2\pi c\Omega$. For convenience, in practice, we introduce additional parameters and coefficients.

Now, the TO and LO Raman frequencies of (6.19) can be expressed as:

$$\begin{aligned}\Omega^{\text{TO}} &= \Omega_0^{\text{TO}} + \Delta\Omega_{\text{H}}^* - \frac{1}{3}\Delta\Omega_{\text{S}}^* = \Omega_0^{\text{TO}} - \eta_{\text{H}}(3X + P) - \frac{1}{3}\eta_{\text{S}}P, \\ \Omega^{\text{LO}} &= \Omega_0^{\text{LO}} + \Delta\Omega_{\text{H}}^* + \frac{2}{3}\Delta\Omega_{\text{S}}^* = \Omega_0^{\text{LO}} - \eta_{\text{H}}(3X + P) + \frac{2}{3}\eta_{\text{S}}P,\end{aligned}\quad (6.21)$$

where

$$\Delta\Omega_{\text{H}}^* = -\eta_{\text{H}}(3X + P), \quad \Delta\Omega_{\text{S}}^* = \eta_{\text{S}}P, \quad (6.22)$$

and

$$\begin{aligned}\eta_{\text{H}} &= -(p + 2q)(S_{11} + 2S_{12})\Omega_0/6\omega_0^2 = \gamma_0(S_{11} + 2S_{12})\Omega_0, \\ \eta_{\text{S}} &= -(p - q)(S_{11} - S_{12})\Omega_0/2\omega_0^2 = \gamma_{\text{S}}(S_{11} - S_{12})\Omega_0.\end{aligned}\quad (6.23)$$

In (6.21)–(6.23), η_{H} is called the Raman hydrostatic stress coefficient and η_{S} the Raman uniaxial stress coefficient [52].

Mode Grüneisen Parameter

In (6.23),

$$\gamma_0 = -(p + 2q)/6\omega_0^2 \quad (6.24)$$

is the mode Grüneisen parameter for hydrostatic pressure [52, 62, 65], and

$$\gamma_S = (p - q)/2\omega_0^2 \quad (6.25)$$

is another mode parameter defined by us [52] for a uniaxial stress. Both of these parameters are dimensionless.

General Raman Stress Coefficients η

In (6.22), $\Delta\Omega_H^*$ is the Raman shift of the center of mass and $\Delta\Omega_S^*$ is the additional splitting of the LO and TO phonons. They are determined by two stress coefficients, η_S and η_H in (6.23). We now introduce a general Raman stress coefficient η , which is the slope of the Raman shifts with respect to the applied stresses, i.e.

$$\eta = \frac{d\Omega}{d(-X_i)}, \quad (6.26)$$

where Ω is in units of cm^{-1} , and X_i in dyn/cm^2 , Pa ($1 \text{ Pa} = 10 \text{ dyn}/\text{cm}^2$), or GPa (10^9 Pa). In (6.26), X_i corresponds to some specific stress component, and η is positive for compressive stress and negative for tensile stress. The Raman frequencies and Raman stress coefficients for different kinds of applied stresses, such as hydrostatic, uniaxial, and biaxial stresses, may be obtained from (6.15–6.20), and the results are shown in Table 6.1. The Raman stress coefficients for different stress cases and the TO and LO Raman shifts are expressed in terms of two coefficients, η_H and η_S . We also find from Table 6.1 that the Raman stress coefficients for hydrostatic pressure consist of only η_H and are equal to each other. Consequently, if we determine η_H from hydrostatic-pressure measurements, we may use it to help us calculate the stress and strain for the uniaxial and biaxial cases.

LO–TO Phonon Splitting

The difference between the LO and TO phonons is obtained from (6.21):

$$\Delta\Omega = \Omega^{\text{LO}} - \Omega^{\text{TO}} = (\Omega_0^{\text{LO}} - \Omega_0^{\text{TO}}) + \eta_S P. \quad (6.27)$$

Equation (6.27) shows that $\Delta\Omega$ varies only with the uniaxial-stress component, i.e. that the existing splitting of LO and TO phonons in a zinc blende crystal is not changed by the hydrostatic component. By way of measurement

Table 6.1. Generalized stress and strain, Raman stress parameters, and bandgap variations

Feature	General axial σ_{ij} ($i \neq j$) = 0	Hydrostatic $P = 0$	Uniaxial $X = 0$	Biaxial $P = -X$
Stress tensor	$\begin{matrix} X & 0 & 0 \\ 0 & X & 0 \\ 0 & 0 & X+P \end{matrix}$	$\begin{matrix} X & 0 & 0 \\ 0 & X & 0 \\ 0 & 0 & X \end{matrix}$	$\begin{matrix} 0 & 0 & 0 \\ 0 & 0 & 0 \\ 0 & 0 & P \end{matrix}$	$\begin{matrix} X & 0 & 0 \\ 0 & X & 0 \\ 0 & 0 & 0 \end{matrix}$
Strains:				
$\varepsilon_{xy} = \varepsilon_{xz} = \varepsilon_{yz}$	0	0	0	0
$\varepsilon_{xx} = \varepsilon_{yy}$	$(S_{11} + 2S_{12})X + S_{12}P$	$(S_{11} + 2S_{12})X$	$S_{12}P$	$(S_{11} + S_{12})X$
ε_{zz}	$(S_{11} + 2S_{12})X + S_{11}P$	$(S_{11} + 2S_{12})X$	$S_{11}P$	$2S_{12}X$
Poisson ratio	$\nu = -\varepsilon_{xx}/\varepsilon_{zz}$	$\nu_H = -1$	$\nu_S = -S_{12}/S_{11}$ $= C_{12}/(C_{11} + C_{12})$	$\nu_B = -(S_{11} + S_{12})/2S_{12}$ $= C_{11}/2C_{12}$ $= (1 - \nu_S)/2\nu_S$
Volume dilation	$-(S_{11} + 2S_{12})(3X + P)$	$-3(S_{11} + 2S_{12})X$	$-(S_{11} + 2S_{12})P$	$-2(S_{11} + 2S_{12})X$
Raman modes:				
Ω_{TO}	$\Omega_0^{\text{TO}} + \Delta\Omega_{\text{H}}^* - \Delta\Omega_{\text{S}}^*/3$	$\Omega_0^{\text{TO}} - 3\eta_{\text{H}}X$	$\Omega_0^{\text{TO}} - (\eta_{\text{H}} + \eta_{\text{S}}/3)P$	$\Omega_0^{\text{TO}} - (2\eta_{\text{H}} - \eta_{\text{S}}/3)X$
Ω_{LO}	$\Omega_0^{\text{LO}} + \Delta\Omega_{\text{H}}^* + 2\Delta\Omega_{\text{S}}^*/3$	$\Omega_0^{\text{LO}} - 3\eta_{\text{H}}X$	$\Omega_0^{\text{LO}} - (\eta_{\text{H}} - 2\eta_{\text{S}}/3)P$	$\Omega_0^{\text{LO}} - 2(\eta_{\text{H}} + \eta_{\text{S}}/3)X$
η_{TO}	$3\eta_{\text{H}}$	$3\eta_{\text{H}}$	$\eta_{\text{H}} + \eta_{\text{S}}/3$	$2\eta_{\text{H}} + \eta_{\text{S}}/3$
η_{LO}	$3\eta_{\text{H}}$	$\eta_{\text{H}} - 2\eta_{\text{S}}/3$		$2\eta_{\text{H}} + 2\eta_{\text{S}}/3$
	$\{\eta_{\text{H}} = \gamma_0(S_{11} + 2S_{12})\Omega_0\}$ $\{\eta_{\text{S}} = \gamma_0(S_{11} - S_{12})\Omega_0\}$			
Energy bands:				
δE_s	$2bP(S_{11} - S_{12})$ $= 2bP/(C_{11} - C_{12})$	0	$2bP(S_{11} - S_{12})$ $= 2bP/(C_{11} - C_{12})$	$-2bX(S_{11} - S_{12})$ $= -2bX/(C_{11} - C_{12})$
δE_h	$a(3X + P)(S_{11} + 2S_{12})$ $= a(3X + P)/(C_{11} + 2C_{12})$	$3aX(S_{11} + 2S_{12})$ $= 3aX/(C_{11} + 2C_{12})$	$aP(S_{11} + 2S_{12})$ $= aP/(C_{11} + 2C_{12})$	$2aX(S_{11} + 2S_{12})$ $= 2aX/(C_{11} + 2C_{12})$
ΔE_g	$\delta E_h \pm \delta E_s/2$	δE_h	$\Delta E_g(hh) = \delta(E_c - E_{\text{v}1})$ $= \delta E_h - \delta E_s/2$	$\Delta E_g(hh) = \delta(E_c - E_{\text{v}2})$ $= \delta E_h + \delta E_s/2$
	$\Delta E_g(lh) = \delta(E_c - E_{\text{v}1})$ $= \delta E_h + \delta E_s/2$		$\Delta E_g(lh) = \delta(E_c - E_{\text{v}2})$ $= \delta E_h - \delta E_s/2$	

of the LO and TO splitting with and without stress, we may obtain the additional shift given by (6.27). By use of this method, we have determined the stresses in CVD SiC films on Si, which were discussed in detail in [52].

From Table 6.1 and the above analyses, we can obtain a clearer appreciation of the physical meanings of η_H and η_S . The coefficient of the Raman shift of the optical phonons for hydrostatic pressure is $3\eta_H$, and that of the Raman splitting between LO and TO phonons for a uniaxial stress component is η_S .

6.5.3 Axial-Strain-Induced Energy Gap Variations

Strain Hamiltonian

The layer strain and stress have important effects on the energy bands, which are described by the strain-orbit Hamiltonian and some deformation potential coefficients ([7] and references therein). For a valence band with p-like states and $\Gamma_{25'}$ symmetry (diamond) or Γ_{15} symmetry (zinc blende) near $\mathbf{k} = 0$, i.e. the Brillouin zone (BZ) center or Γ point, the Hamiltonian is given by [7, 66]

$$H_\varepsilon = -a(\varepsilon_{xx} + \varepsilon_{yy} + \varepsilon_{zz}) - 3b \left[\left(L_x^2 - \frac{1}{3}L^2 \right) \varepsilon_{xx} + \text{c.p.} \right] - \frac{\sqrt{3}}{6}d(\{L_x L_y\} \varepsilon_{xx} + \text{c.p.}), \quad (6.28)$$

where ε_{ij} ($i, j = x, y, z$) denotes the components of the strain tensor, L_i is the angular-momentum operator, $(\{L_x L_y\} = (1/2)(L_x L_y + L_y L_x))$, “c.p.” means the cyclic permutation of x, y , and z , a is the hydrostatic-pressure deformation potential, and b and d are the uniaxial deformation potentials appropriate to strains of tetragonal and rhombohedral symmetry, respectively. The values of a , b , and d are negative, as a tensile strain and stress are defined to be positive, and thus a , b , and d are positive as a compressive strain and stress are applied. In this study of cubic SiC, we are dealing with indirect transitions related to the bottom of the conduction band at the X point and the top of the valence band at the Γ point. Therefore, the deformation potentials a , b , and d given here are those of the valence band at the Γ point with respect to the bottom of the conduction band at the X point.

Axial-Strain Hamiltonian

Applying (6.28) to the case of a thin-layer film on a thick substrate, such as 3C-SiC epitaxially grown on Si, i.e. the case of generalized axial stress and strain with the ε_{ij} of (6.4), we have

$$H_\varepsilon = -\delta E_h - \frac{3}{2}\delta E_s \left[L_z - \frac{1}{3}L^2 \right], \quad (6.29)$$

where

$$\begin{aligned}\delta E_s &= 2b(S_{11} - S_{12})P, \\ \delta E_h &= a(S_{11} + 2S_{12})(3X + P),\end{aligned}\quad (6.30)$$

or, for stiffnesses instead of compliances,

$$\begin{aligned}\delta E_s &= 2bP/(C_{11} - C_{12}), \\ \delta E_h &= a(3X + P)/(C_{11} + 2C_{12}).\end{aligned}\quad (6.31)$$

Equation (6.29) is written in the same form as used by Pollak and Cardona in [66] for the case of uniaxial stress, while δE_s and δE_h in our expressions of (6.30) and (6.31) are different from those in [66].

Energy Band Splitting

It has been shown [66, 67] that with a spin-orbit splitting $\Delta_0 \gg \delta E_s$, the energy differences between the conduction and valence bands at $\mathbf{k} = 0$ are given by

$$\begin{aligned}\Delta(E_c - E_{v1}) &= -\frac{1}{3}\Delta_0 + \delta E_h - \frac{1}{2}\delta E_s, \\ \Delta(E_c - E_{v2}) &= -\frac{1}{3}\Delta_0 + \delta E_h + \frac{1}{2}\delta E_s, \\ \Delta(E_c - E_{v3}) &= +\frac{2}{3}\Delta_0 + \delta E_h.\end{aligned}\quad (6.32)$$

We note that δE_s , the splitting between the heavy-hole (v_1) and light-hole (v_2) bands, depends only on the uniaxial component P , and not on the hydrostatic component X . The heteroepitaxial growth or deposition of a thin film on a thick substrate, in most cases, can be regarded as possessing a biaxial stress distribution inside the thin film with a uniaxial stress component $P = -X$. Therefore, a tensile biaxial stress has the same effect on δE_s as a compressive uniaxial stress, and a compressive biaxial stress has the same effects as a tensile uniaxial stress. For a compressive uniaxial stress component or a tensile biaxial stress with $P < 0$, and $\delta E_s > 0$ because $b < 0$ and $(S_{11} - S_{12}) > 0$, we have the heavy-hole band higher than the light-hole band, and the change of the energy gap is

$$\Delta E_g = \delta E_h - \frac{1}{2}\delta E_s. \quad (6.33)$$

For a tensile uniaxial stress component or a compressive biaxial stress with $P > 0$ and $\delta E_s < 0$, we have the light-hole band higher than the heavy-hole band, and the change of the energy gap is

$$\Delta E_g = \delta E_h + \frac{1}{2}\delta E_s. \quad (6.34)$$

We have summarized the detailed expressions for the energy gap changes in Table 6.1. More details of the changes due to various stress situations in terms of stress or strain, using S_{ij} or C_{ij} , and a schematic demonstration can be found in [7].

6.6 Raman Analysis of the 3C-SiC/Si Structure

6.6.1 Evaluation of Raman Stress Coefficients and Elastic Constants of 3C-SiC

In [52], the values of the Raman hydrostatic stress coefficients of 3C-SiC have been obtained, by way of analyzing the Raman measurement data obtained under hydrostatic pressure by Olego and Cardona [65], to be

$$\eta_H^{\text{TO}} = 1.29 \text{ cm}^{-1}/\text{GPa} \quad \text{and} \quad \eta_H^{\text{LO}} = 1.58 \text{ cm}^{-1}/\text{GPa}, \quad (6.35)$$

where $1 \text{ GPa} = 10^{10} \text{ dyn/cm}^2$.

The mode Grüneisen parameter is, from the same hydrostatic-pressure Raman measurements [52, 65], $\gamma_0 = 1.56 \pm 0.01$. From these values, ones can calculate via (6.23) that $S_{11} + 2S_{12} = (1.05 \pm 0.01) \times 10^{-3}/\text{GPa}$. Using this value of $(S_{11} + 2S_{12})$, the authors of [52] examined the published data on the elastic stiffness or compliance of cubic SiC in the literature [68–71], listed in Table 6.2, and recommended one set of data [69] for practical use.

Recently, Debernardi et al. [72] have performed a new combined experimental and first-principles theoretical study of the Raman optical phonons in 3C-SiC under pressure. The mode Grüneisen parameter is expressed as

$$\gamma_0 = -\frac{\partial \ln \omega}{\partial \ln V} = \frac{B_0}{\omega_0} \frac{\partial \omega}{\partial P}, \quad (6.36)$$

where V is the volume, P is the pressure, and B_0 is the bulk modulus. In [65], an average $B_0 = 321.9 \text{ GPa}$ for Si and C was used for 3C-SiC. The authors of [72] have employed an up-to-date value of $B_0 = 227 \text{ GPa}$ for 3C-SiC and made a correction to the results of [65], yielding

$$\gamma_0 = 1.10. \quad (6.37)$$

Table 6.2. 3C-SiC elastic constants and related parameters

C_{11}	C_{12}	C_{44}	S_{11}	S_{12}	S_{44}	$S_{11}+2S_{12}$	ν_S	Ref.	Error of $S_{11}+2S_{12}$ from $1.49 \times 10^{-3}/\text{GPa}$
$(\times 10^{12} \text{ dyn/cm}^2)$					$(\times 10^{-13} \text{ dyn/cm}^2)$				
3.523	1.404	2.329	3.67	-1.05	4.294	1.58	0.29	[68]	6.0%
5.4	1.8	2.5	2.22	-0.56	4.0	1.11	0.25	[69]	-25.5%
3.489	1.384	2.082	3.70	-1.05	4.803	1.60	0.28	[70]	7.4%
3.71	1.69	1.76	3.77	-1.18	5.68	1.41	0.31	[71]	-5.4%

Correspondingly, we have the corrected value of

$$S_{11} + 2S_{12} = 1.49 \times 10^{-3} / \text{GPa} \quad (6.38)$$

for cubic SiC, which can be used to reexamine the 3C-SiC elastic parameters in Table 6.2. This shows that the elastic parameters used in [68] lead to a positive error of only 6% in comparison with the value in (6.38) and that the value in [70] has a negative error of -5.4% , both of which are reasonably reliable within $\pm 10\%$.

The calculated elastic compliance constants given by Tolpygo [68],

$$S_{11} = 3.67 \times 10^{-3} / \text{GPa} \quad \text{and} \quad S_{12} = -1.05 \times 10^{-3} / \text{GPa}, \quad (6.39)$$

have been used in another recent work [73]. Rohmfeld et al. [73], considering the case of nonzero components of the uniaxial stress and strain in the normal direction of the film, have recently performed an accurate measurement of the biaxial stress and strain by using a pressure sensor and tuning the biaxial strain via applying a differential nitrogen pressure, on two 3C-SiC membranes (1.5 and 1.8 μm thick), and obtained the Raman stress coefficients of 3C-SiC as

$$\eta_H^{\text{TO}} = 1.38 \text{ cm}^{-1} / \text{GPa} \quad \text{and} \quad \eta_H^{\text{LO}} = 1.64 \text{ cm}^{-1} / \text{GPa}, \quad (6.40)$$

$$\eta_S^{\text{TO}} = -0.56 \pm 0.16 \text{ cm}^{-1} / \text{GPa} \quad \text{and} \quad \eta_S^{\text{LO}} = 1.31 \pm 0.13 \text{ cm}^{-1} / \text{GPa}. \quad (6.41)$$

In the above calculation, the authors of [73] used the values of the calculated Raman hydrostatic stress coefficients [71] and the calculated elastic compliance constants given by Tolpygo [68] (listed in (6.40)), which is consistent with our judgment given above.

6.6.2 Raman Determination of Stress and Strain in 3C-SiC/Si

To study the effects of biaxial stress and strain in CVD 3C-SiC films, we etched 3C-SiC/Si samples so as to remove a square window in the central portion of the Si substrate, with an HF/HNO₃ 1:1 etch solution and a wax mask (see Fig. 1 in [52]). In this way, we can measure two regions of a sample, i.e. the unetched 3C-SiC/Si region and the Si-etched 3C-SiC window region, by use of a micrometer screw movement, with the measurements of the two regions being made under the same conditions. Figure 6.12 shows such comparative backscattering Raman spectra of a CVD 3C-SiC/Si sample. In the perfect backscattering geometry, only the LO(Γ) phonon is allowed and the TO(Γ) phonon is forbidden. About 2 cm^{-1} Raman shift difference between the two regions of the 3C-SiC film with and without the Si substrate can be clearly seen.

In order to use our theoretical formulas given in Sect. 6.5.2 to calculate the stress and strain in the 3C-SiC layer, we have to obtain the TO(Γ) and

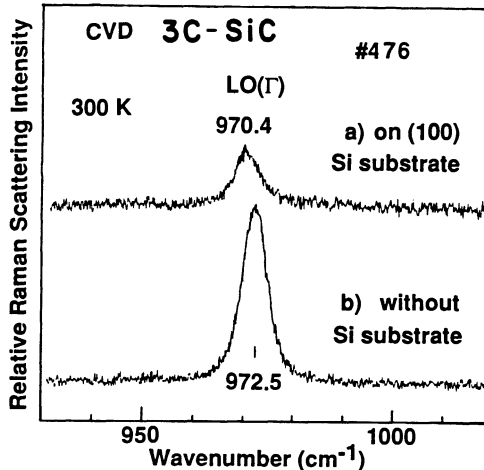


Fig. 6.12. Comparative backscattering Raman spectra of a CVD 3C-SiC/Si sample with the incident laser beam normal to the surface, (a) on 3C-SiC/Si region, and (b) on 3C-SiC film region with the Si substrate removed (from Feng et al. [52], reprinted with permission of the American Institute of Physics)

LO(Γ) phonon lines at one and the same time. We arranged for the incident laser excitation beam to be deviated from the direction normal to the sample surface by an angle, for example 26° in [52]. In this arrangement, a near but not true backscattering geometry is obtained, and both the allowed LO(Γ) phonon and the forbidden TO(Γ) phonon are obtained.

A series of CVD-grown 3C-SiC/Si(100) samples with SiC film thicknesses from 600 \AA to $17\text{ }\mu\text{m}$ have been measured by Raman spectra [2], and the stresses and strains in the films of thickness $4\text{--}17\text{ }\mu\text{m}$ were calculated [52]. The stresses in the 3C-SiC film are in the order of 10^9 dyn/cm^2 or one-tenth of a GPa and the strains are $0.1\text{--}0.2\%$, despite of the high lattice mismatch of $\sim 20\%$ between bulk 3C-SiC and Si.

Similar results have been obtained by other researchers. Mukaida et al. [74] have performed Raman scattering measurements on CVD-grown 3C-SiC/Si and estimated the internal stress in 3C-SiC on Si to be $5.4 \times 10^9\text{ dyn/cm}^2$ for a $5\text{ }\mu\text{m}$ thick film. Rohmfeld et al. [73] have obtained a built-in tensile strain of $0.1\text{--}0.4\%$ from their 3C-SiC films on Si. Furthermore, they have tuned the biaxial strain in two 3C-SiC membranes, 1.5 and $1.8\text{ }\mu\text{m}$ thick, with the help of their sensitive apparatus that applies a differential nitrogen pressure, and obtained the Raman strain relationships

$$\Omega^{\text{TO}} = (795.9 \pm 0.1) - (1125 + 20)\Delta a_{\parallel}/a_0(\text{cm}^{-1}), \quad (6.42)$$

$$\Omega^{\text{LO}} = (974.1 \pm 0.1) - (1585 + 32)\Delta a_{\parallel}/a_0(\text{cm}^{-1}). \quad (6.43)$$

Zhu et al. [75] performed a Raman study on residual strains in thin 3C-SiC epitaxial layers grown on Si(001), with film thickness in the range of 0.1–1.2 μm.

Hagiwara et al. [76] have applied the same set of equations [52] and also considered the case of nonzero uniaxial strain and stress in the direction perpendicular to the film, assuming $\eta_H = \eta_S$. In this way, they have $X \approx -Z$, i.e. the biaxial tension in the $x-y$ plane induces a compression of the same magnitude in the z -direction, which is different from the situation in [52], which assumes $Z = 0$. They used a 2.2 μm thick, CVD-grown single-crystal 3C-SiC sample on a 6-inch (100) Si substrate and reactive ion etching (RIE) to prepare a series of $1 \times 1 \text{ cm}^2$ 3C-SiC/Si samples having different SiC thicknesses (0.44, 0.54, 0.75, 1.30, and 2.20 μm). The values of the stress and strain determined as a function of the distance from the interface show a maximum at the interface, decrease rapidly between 0 and 0.7 μm, and become constant between 0.7 and 2.2 μm. This provides clear evidence for the relaxation of stress and strain in the first 0.7 μm of growth of a 3C-SiC film on Si. Furthermore, by taking account of the TEM observations, which showed a high concentration of Si antisite line defects created at the SiC/Si interface, it was suggested that these Si antisite line defects are responsible for releasing the stress in 3C-SiC/Si.

Bluet et al. [77] have performed a Raman investigation of stress relaxation at the 3C-SiC/Si interface, for films with thicknesses ranging between 2 and 20 μm from different sources. The strain is relaxed for sufficiently thick ($> 3 \mu\text{m}$) layers of 3C-SiC on Si, while relaxation is never achieved in the Si substrate. In the case of 3C-SiC grown on silicon on insulator (SOI), a very good strain relaxation is found in both the SiC layer and SOI substrate.

6.6.3 Active Raman Studies of 3C-SiC/Si

In the past two decades, in particular recently, Raman scattering spectroscopy has been actively applied in the investigation of 3C-SiC materials and structures. We shall introduce some more work in this field besides what we have referred to in previous sections.

Okumura et al. [78] have employed Raman scattering to distinguish and identify the heteroepitaxy of 3C-SiC films on 6H-SiC substrates. Harima et al. [79] have conducted a characterization of 3C-SiC epitaxial layers on TiC(111) by Raman scattering. TiC has a rock-salt-type cubic structure and is chemically stable at high temperatures. It gives a very small lattice mismatch with 3C-SiC of only 0.7% at RT and 0.2% at 1400–1500 °C. Through precise Raman measurements on 3C-SiC/TiC(111) with different layer thicknesses of 0.3–4 μm, Harima et al. have shown, for layers thicker than 1 μm, that the 3C-SiC(111) planes have an in-plane compressive strain of 0.24%, and a tensile strain of 0.10% in the normal direction. It is interesting to see that, in spite of the much better lattice match of 3C-SiC with TiC than with

Si, the observed residual in-plane stress for 3C-SiC on TiC(111) is larger than that for 3C-SiC on Si(111) [79].

Falkovsky, Bluet, and Camassel [80] have performed a combined experimental and theoretical study of the strain-fluctuation effect and strain relaxation at the 3C-SiC/Si interface. A model of phonon interaction with strain fluctuations is proposed to account for the asymmetric Raman line form. A theory of the inhomogeneous shift and broadening of optical phonons has been developed. The Raman scattering cross section was calculated, including both disorder and the spatial dependence of the average strain on the distance from the interface. It was shown that two regimes, of short- and long-range disorder, with different line shapes, can be observed [80].

Rohmfeld, Hundhausen, and Ley [81] have performed temperature-dependent Raman measurements (up to 1700 K) on polycrystalline 3C-SiC free-standing films which were grown on Si, and studied the influence of stacking faults or disorder. To explain the observed phonon line broadening, they have simulated 3C-SiC with randomly distributed stacking faults in the (111) direction, and calculated its Raman spectrum in the framework of a bond polarizability model. Owing to the disorder in the bond polarizability, phonon models with wave vectors away from the center of the BZ become accessible to Raman scattering. The standard phonon confinement model is also considered. Although the TO line broadening could be accounted for in both models, the stacking-fault model is more successful in accounting for the density-of-states feature.

Bezerra et al. [82] have calculated the Raman spectra of 3C-SiC/Si superlattices (SLs), using a linear-chain description associated with the bond polarizability model. It was found that the optical-modes region of the spectrum is severely affected by the existence of the interfacial transition regions. New peaks appear in between those related to the Si quasi-confined and 3C-SiC confined modes. The effects of atomic displacements and localization or delocalization of the vibrations are much stronger than those observed for other systems such as GaAs/AlAs, Si/Ge, and AlN/GaN SLs [82].

Lysenko, Barbier, and Champagnon [83] have studied the stress relaxation effect in a porous 3C-SiC/Si heterostructure by micro-Raman spectroscopy. The porous heterostructure was obtained by an anodization procedure in an HF acid solution used for fabrication of porous Si. 3C-SiC layers with an initial biaxial stress of ~ 0.4 GPa were observed to be completely relaxed after formation of a porous network in the 3C-SiC/Si heterostructure. The relaxation is caused by pore propagation down to the 3C-SiC/Si interface.

6.6.4 Raman Mode Intensity Variation of 3C-SiC with and Without Si Substrate

In [2], some interesting enhancements of Si and 3C-SiC Raman signals are reported. The Si 522 cm^{-1} phonon obtained from a Si wafer is enhanced in intensity by a factor of 2–3 by a CVD overlayer of cubic SiC. Furthermore, the

3C-SiC LO(Γ) phonon obtained from SiC/Si samples is enhanced by a factor of 2 or 3 following the removal of the Si substrate. In addition, the strict selection rules are no longer obeyed in this case. The enhancement of the Si signal is possibly due to the electric-field-induced inelastic scattering from the SiC/Si heterojunction. The enhancement of the 3C-SiC signal can be explained by the multiple reflection in free 3C-SiC films. Our theoretical analysis shows that if the cross section for forward scattering is about one order of magnitude larger than that for backscattering, this enhancement will appear. The forward scattering may have different selection rules from the backscattering and may lead to the appearance of the forbidden TO(Γ) phonon and the depolarization of the 3C-SiC Raman phonons in a free SiC film.

Raman Selection Rule for 3C-SiC/Si

Figure 6.13A shows Raman spectra (RT) of a 17 μm CVD 3C-SiC film on (100) Si in the backscattering geometry. Two bands near 522 cm^{-1} and 971 cm^{-1} with the same parallel-polarization behavior are recorded. The former characterizes the optical Raman phonon of the Si single crystal, and the latter

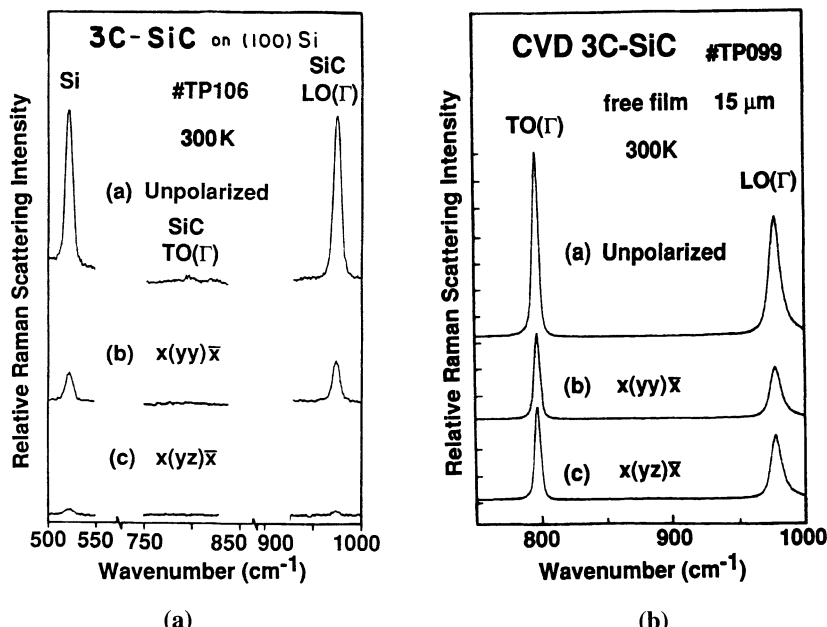


Fig. 6.13. Raman spectra in the backscattering geometry obtained with (a) no polarization arrangements, and (b) parallel and (c) perpendicular polarization arrangements, for (a) a 17 μm CVD 3C-SiC film on (100) Si, and (b) a 15 μm free film (from Feng et al. [2], reprinted with permission of the American Institute of Physics)

corresponds to the LO phonon at the Γ point with $\mathbf{q} = 0$ for a single crystal of cubic SiC, shifted by $1\text{--}2\text{ cm}^{-1}$ to lower energy [52]. In Si, with the diamond structure, having O_h symmetry, the LO and TO modes are triply degenerate at the center of the Brillouin zone because of nonionicity, with the optical phonons polarized in the same direction as the incident polarized beam in the backscattering geometry. In cubic SiC, with the zinc blende structure with T_d symmetry, the polarization behavior produces a long-range Coulomb force owing to the ionicity and splits the LO and TO modes at $\mathbf{q} = 0$. The doubly degenerate TO phonons at the Γ point are forbidden and the singly degenerate LO phonon at the Γ point is allowed, with the same polarization behavior as the incident polarization [52,84]. It is seen in Fig. 6.13A that the above selection rules are obeyed, and therefore the CVD deposited SiC film has the same crystal orientation as the (100) Si substrate.

Selection Rule Broken

Upon removal of the Si substrate, the above selection rule can be broken, leading to quite different Raman scattering spectra. Figure 6.13B shows the Raman spectra of a $15\text{ }\mu\text{m}$ thick free film of CVD 3C-SiC. The forbidden 3C-SiC TO(Γ) phonon appears near 796 cm^{-1} , and is even stronger than the allowed LO(Γ) mode. Both the LO(Γ) and the TO(Γ) line are depolarized.

This exception can be briefly explained. The refractive index of 3C-SiC is about 2.7 near 5000 \AA [65], yielding a reflectivity with respect to air of 21%. Light in the thin free film of 3C-SiC, in contrast to the situation when there is a Si substrate, can now undergo substantial reflection (multiple reflection) from the rear. The reflected component leads to forward scattering and, according to Richter's analysis [84], the TO(Γ) mode is now permitted.

Enhancements of Si and SiC Raman Signals

From our Raman measurements, we have also observed some interesting enhancement phenomena of the SiC and Si phonon intensities. In Fig. 6.12, one finds that the SiC LO(Γ) phonon measured in the etched window region is nearly three times stronger than that in the unetched region. For the free-film measurements as in Fig. 6.13B, we found similar results, i.e. the SiC Raman phonons from the SiC free film without the Si substrate are much stronger than those from the SiC/Si system. A careful comparison of Raman measurements with different incident laser powers, shown in Fig. 9 of [2], shows that the intensity of the Si 522 cm^{-1} Raman phonon with a CVD 3C-SiC film on top of the Si is about three times stronger than that for the Si wafer, and that the intensity of the 3C-SiC LO(Γ) phonon for the etched window region is about two times stronger than that for the SiC/Si unetched region. When we change the incident light power level from 10 to 300 mW, the results stay the same. This experiment was repeated on ten different samples, always with nearly identical intensity ratios.

Multiple Reflections and Forward Scattering

In order to give a satisfactory explanation of the intensity enhancement of the Raman signals of the 3C-SiC free film with respect to those of the 3C-SiC film on the Si substrate, we shall analyze the reflection processes at the SiC/air and SiC/Si interfaces, as well as the multiple reflection in the free SiC film and the SiC film on a Si substrate; see Fig. 6.14A. The refractive indices for Si and 3C-SiC at 5145 Å are $n_{\text{Si}} = 4.2$ and $n_{\text{3C-SiC}} = 2.7$ [85], respectively. The reflectance of the interface between media 1 and 2 is

$$R = (n_2 - n_1)^2 / (n_2 + n_1)^2 . \quad (6.44)$$

We have, for the SiC/air interface,

$$R = (n_{\text{SiC}} - 1)^2 / (n_{\text{SiC}} + 1)^2 = 0.21 ,$$

and for the SiC/Si interface,

$$R = (n_{\text{SiC}} - n_{\text{Si}})^2 / (n_{\text{SiC}} + n_{\text{Si}})^2 = 0.047 . \quad (6.45)$$

In Fig. 6.14A, the odd-numbered lines inside the SiC film cause backscattering, while even-numbered lines cause forward scattering. The intensities of line 1 in both cases are same, but the others will not be same. Therefore, we

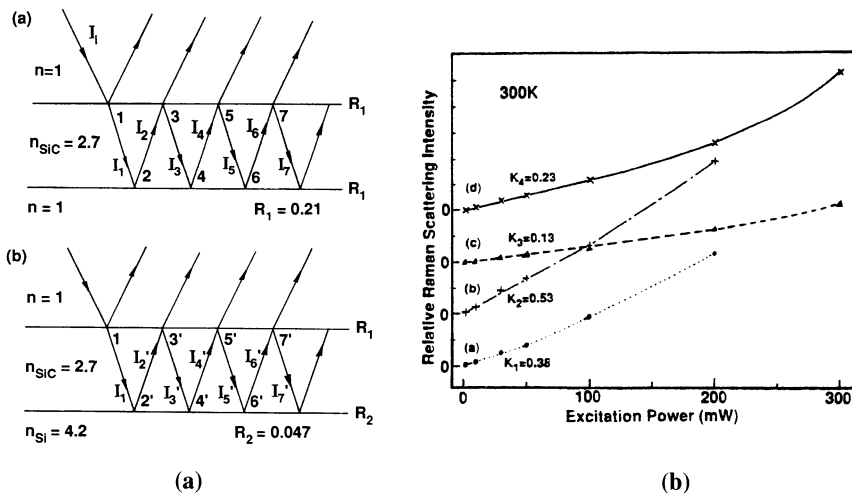


Fig. 6.14. (a) Multiple reflections from (a) free SiC film and (b) air/SiC/Si system. (b) Relationship between Raman line intensity and excitation power for (a) Si 522 cm^{-1} line from a Si wafer, (b) Si 522 cm^{-1} line from 3C-SiC/Si, (c) 3C-SiC LO(Γ) line from 3C-SiC/Si, and (d) 3C-SiC LO(Γ) line from a 3C-SiC film with the Si substrate removed (from Feng et al. [2], reprinted with permission of the American Institute of Physics)

put a prime on the numbers and intensities for the other lines in (b). The intensity for backscattering in (a) is

$$\begin{aligned} I_B(\text{SiC}) &= I_1 + I_3 + I_5 + \dots = I_1(1 + R_1^2 + R_1^4 + \dots) \\ &= I_1/(1 - R_1^2) = 1.046I_1, \end{aligned} \quad (6.46)$$

and for forward scattering we have

$$\begin{aligned} I_F(\text{SiC}) &= I_2 + I_4 + I_6 + \dots = I_1(R_1 + R_1^3 + R_1^5 + \dots) \\ &= I_1R_1/(1 - R_1^2) = 0.22I_1. \end{aligned} \quad (6.47)$$

For SiC on Si in case (b), the intensity for backscattering is

$$\begin{aligned} I_B(\text{SiC/Si}) &= I_1 + I'_3 + I'_5 + \dots = I_1(1 + R_1R_2 + R_1^2R_2^2 + \dots) \\ &= I_1/(1 - R_1R_2) = 1.010I_1, \end{aligned} \quad (6.48)$$

and for forward scattering we have

$$\begin{aligned} I_F(\text{SiC/Si}) &= I'_2 + I'_4 + I'_6 + \dots = I_1(1 + R_1R_2 + R_1^2R_2^2 + \dots) \\ &= I_1R_2/(1 - R_1^2) = 0.047I_1. \end{aligned} \quad (6.49)$$

As pointed by W. Richter [84], the cross sections for back and forward scattering might be different. They are denoted by $S_{\alpha\beta}^0$ for forward scattering and by $S_{\alpha\beta}^{180}$ for backscattering in Richter's notation. The scattered light intensity for the free 3C-SiC film will be proportional to

$$I_S(\text{SiC}) = 1.046I_1S_{\alpha\beta}^{180} + 0.220I_1S_{\alpha\beta}^0, \quad (6.50)$$

and for SiC/Si,

$$I_S(\text{SiC/Si}) = 1.010I_1S_{\alpha\beta}^{180} + 0.047I_1S_{\alpha\beta}^0. \quad (6.51)$$

The intensity ratio of the scattered light for these two situations is

$$\begin{aligned} K_S &= I_S(\text{SiC})/I_S(\text{SiC/Si}) \\ &= (1.046I_1S_{\alpha\beta}^{180} + 0.220I_1S_{\alpha\beta}^0) / (1.010I_1S_{\alpha\beta}^{180} + 0.047I_1S_{\alpha\beta}^0). \end{aligned} \quad (6.52)$$

We find from (6.51), that if $S_{\alpha\beta}^0 = S_{\alpha\beta}^{180}$, $K_S = 1.2$, and that if $S_{\alpha\beta}^0 + 8S_{\alpha\beta}^{180}$, $K_S = 2.0$. This means that if the cross sections for both forward scattering and backscattering are the same, we have a 20% enhancement, but if the cross section for forward scattering is more than eight times larger than that for backscattering, we shall have an enhancement by more than a factor of two. This is a possible mechanism for the 3C-SiC Raman signal enhancement on removal of the Si substrate. However, we have no independent theoretical estimate of the Raman cross sections in the forward and backward scattering geometries.

In addition, the scattered light itself also undergoes multiple reflections, and this results in an enhancement of the intensity. A factor of $1/(1 - R_1^2)$, or 1.046, should be added to (6.46) and (6.47) for the case of a free SiC film. Another factor of $1/(1 - R_1 R_2)$, or 1.010, should be incorporated into (6.48) and (6.49) for the case of SiC/Si. Thus, the ratio K_S in (6.52) should be multiplied by a factor of $1.046/1.010 = 1.036$, i.e. enhanced further by an additional 4%. This does not affect our analysis substantially.

6.6.5 Raman Cross Section of 3C-SiC

The Variation of Raman Signal Strength with Excitation Intensity

Figure 6.14B gives the relative Raman line intensity I_R versus the incident light power I_i , which was obtained from Fig. 9 in [2]. We observe a nearly linear relation between I_R and I_i below a certain value (200 mW here) of the incident power for all four curves, i.e.

$$I_{\text{Raman}} \propto I_{\text{incident power}} \quad \text{or} \quad I_R \propto I_i . \quad (6.53)$$

The coefficients are designated as K_i ($i = 1 - 4$), where

$$\begin{aligned} K_1 &= K_1(522 \text{ cm}^{-1} \text{ Si wafer}) = 0.38 , \\ K_2 &= K_2(522 \text{ cm}^{-1} \text{ SiC/Si}) = 0.53 , \\ K_3 &= K_3(970 \text{ cm}^{-1} \text{ SiC/Si}) = 0.13 , \\ K_4 &= K_4(972 \text{ cm}^{-1} \text{ SiC window}) = 0.23 . \end{aligned} \quad (6.54)$$

We find that K_1 for the Si phonon from the Si wafer and K_2 for the Si phonon from the SiC/Si sample are similar, and that K_3 for the 3C-SiC LO phonon from SiC/Si and K_4 from the 3C-SiC film without Si are similar too, i.e.

$$\begin{aligned} K_1 &\approx K_2 \approx K_{\text{Si}} = 0.45 \pm 0.08 , \\ K_3 &\approx K_4 \approx K_{\text{3C-SiC LO}} = 0.18 \pm 0.05 , \end{aligned} \quad (6.55)$$

and

$$K_{\text{Si}} > K_{\text{3C-SiC LO}} . \quad (6.56)$$

The fact that K_2 is slightly larger than K_1 may be due to the enhancement effects of the Si phonon from a SiC/Si heterojunction. K_4 is also slightly larger than K_3 , which may come from the enhancement of the SiC phonon on removal of the Si substrate. But it is still possible to group K_1 and K_2 together into K_{Si} , and to group K_3 and K_4 together into $K_{\text{3C-SiC LO}}$ as in (6.55). We believe that K_{Si} and $K_{\text{3C-SiC LO}}$ should be representative of the material properties of Si and 3C-SiC, respectively.

A Simple Experimental Determination of the Raman Cross Section

The classical [86] and quantum [88] theories of Raman scattering in solids indicate that the Raman-scattered light intensity is proportional to the incident light intensity and the square of the Raman cross section. From Brüesch [88], we have

$$I_R \propto (\omega_L - \omega_S)^4 (S_{\alpha\beta})^2 I_i \sim (\omega_R)^4 (S_{\alpha\beta})^2 I_i , \quad (6.57)$$

where $S_{\alpha\beta}$ is the Raman scattering cross section with the polarization of the incident light in the direction α and the polarization of the detected scattered light in the direction β , and ω_L , ω_S , and $\omega_R = \omega_L - \omega_S$ are the frequencies of the incident, scattered, and Raman phonon, respectively. We may use this relation to estimate the unknown Raman cross section of 3C-SiC. Considering K_{Si} and $K_{3C-SiC\ LO}$ as well as (6.57), we have

$$\begin{aligned} K_{Si}/K_{3C-SiC\ LO} &= [\omega_R(Si)]^4 [S_{\alpha\beta}(Si)]^2 [\omega_R(3C-SiC\ LO)]^{-4} \\ &\times [S_{\alpha\beta}(3C-SiC\ LO)]^{-2} \end{aligned} \quad (6.58)$$

and

$$\begin{aligned} S_{\alpha\beta}(3C-SiC\ LO) &= S_{\alpha\beta}(Si) [\omega_R(Si)]^2 (K_{3C-SiC\ LO})^{1/2} \\ &\times [\omega_R(3C-SiC\ LO)]^{-2} (K_{Si})^{-1/2} . \end{aligned} \quad (6.59)$$

We use $S_{\alpha\beta}(Si) = 500 \times 10^8 \text{ cm}^{-1} \text{ ster}^{-1}$ from [2, 89], and $\omega_L = 19\ 435 \text{ cm}^{-1}$ (514.5 nm), $\omega_S(Si) = 522 \text{ cm}^{-1}$, $\omega_S(3C-SiC\ LO) = 972 \text{ cm}^{-1}$, $\omega_R(Si) = 18\ 913 \text{ cm}^{-1}$, and $\omega_R(3C-SiC\ LO) = 18\ 463 \text{ cm}^{-1}$, from our Raman measurements. From curves (b) and (c) in Fig. 6.14B or (6.54), we have $K_{Si}/K_{3C-SiC\ LO} \sim 4.1$. From (6.57), we get $S_{\alpha\beta}(3C-SiC\ LO) \sim 259 \times 10^{-8} \text{ cm}^{-1} \text{ ster}^{-1}$. By use of curves (a) and (d) in Fig. 6.14B or (6.54), we have $K_{Si}/K_{3C-SiC\ LO} \sim 1.6$ and $S_{\alpha\beta}(3C-SiC\ LO) \sim 415 \times 10^8 \text{ cm}^{-1} \text{ ster}^{-1}$. We then take an average

$$S_{\alpha\beta}(3C-SiC\ LO) \sim (340 \pm 80) \times 10^{-8} \text{ cm}^{-1} \text{ ster}^{-1} . \quad (6.60)$$

Because the cross section for Si is $500 \times 10^{-8} \text{ cm}^{-1} \text{ ster}^{-1}$ [89] and was measured at $1.06 \mu\text{m}$ by a YAG laser, which is close to the energy gap of Si and near the resonance, the above $S_{\alpha\beta}$ value for 3C-SiC may in fact be higher. A measure of $S_{\alpha\beta}(Si)$ at a wavelength equally remote from a resonance would give a better comparison. We might then get a more precise value of $S_{\alpha\beta}(3C-SiC\ LO)$.

6.6.6 Raman Defect Modes

In many CVD-grown 3C-SiC/Si samples, we have observed some extra modes besides the ordinary Raman phonon modes. Figure 6.15 shows an example,

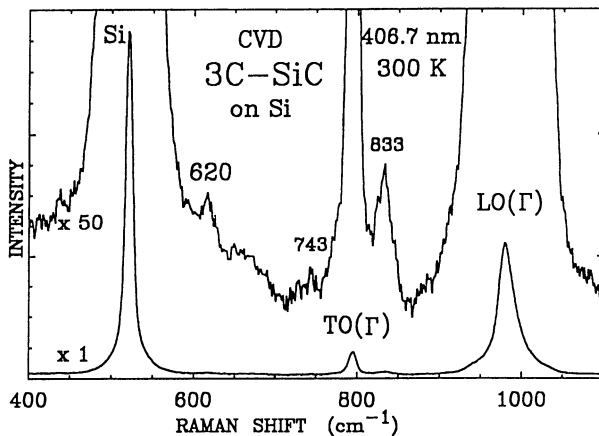


Fig. 6.15. Raman scattering from a CVD 3C-SiC/Si(100) sample excited by the 406.7 nm line from a Kr⁺ laser at 300 K. In the curve magnified 50 times, weak modes at 620, 743, and 833 cm⁻¹ are clearly observed

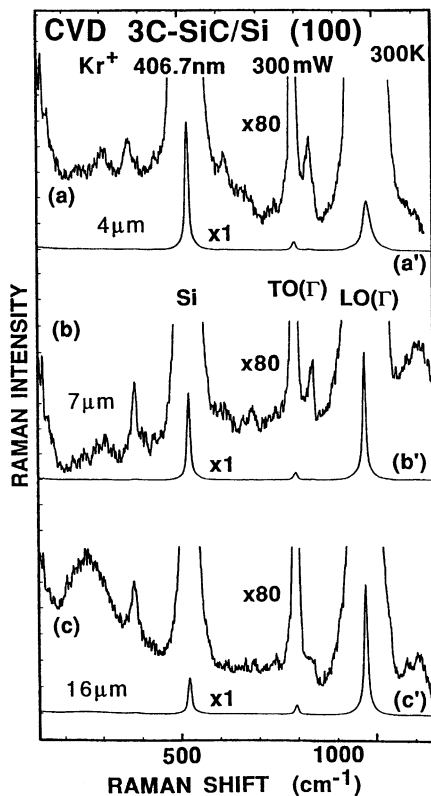


Fig. 6.16. Raman spectra from three CVD 3C-SiC/Si(100) samples

Raman scattering from a CVD 3C-SiC/Si(100) sample excited by the 406.7 nm line from a Kr⁺ laser at 300 K. In the curve magnified 50 times, weak modes at 620, 743, and 833 cm⁻¹ are clearly observed. Figure 6.16 exhibits Raman spectra from three CVD 3C-SiC/Si(100) samples, with different thicknesses of 4, 7, and 16 μm . In (a), for the thinnest film, modes at 620 and 833 cm⁻¹ are observed. In (b), for a 7 μm 3C-SiC/Si film, besides the 620 cm⁻¹ mode, a mode at ~ 680 cm⁻¹ is seen. However, for the thickest film, the features at 620, 680, and 833 cm⁻¹ are not so obvious. Therefore, it is reasonable to correlate these modes with the defects near the 3C-SiC/Si interface region, where a high density of structural defects exists.

To understand the nature or origin of the observed Raman defect modes described above, we have conducted a combined experimental and theoretical exploration [90, 93]. By incorporating Raman scattering data of phonons at critical points in the BZ, Talwar et al. [93] have constructed a phenomenological lattice-dynamical model for perfect 3C-SiC, and used a Green's function theory to treat the vibrations of both intrinsic and radiation-induced defects. In the early 1970s, Patrick and Choyke [94] reported the so-called D_I and D_{II} vibration spectra in LT PL of ion-implanted/annealed 3C-SiC. The luminescent centers D_I and D_{II} are intrinsic and are formed from Si or C vacancies or interstitials. It has been suggested that D_I is a divacancy and D_{II} is a carbon di-interstitial. These centers also produce two gap modes, with phonon energies of 83.9 and 89.0 meV (or 677 and 718 cm⁻¹), located between the LA mode (76.7 meV) and TO phonon (95.7 meV) [94]. Our comprehensive calculations have reexamined the divacancy model for the D_I center, and concluded that the doublet observed near ~ 83 meV in PL experiments can best be explained by gap modes of a nearest-neighbor “antisite pair” defect of C_{3v} symmetry. Our calculations have revealed a gap mode at 625 cm⁻¹ due to an isolated nitrogen defect in SiC, which is suggested to be responsible for the defect mode observed at 620 cm⁻¹ in our Raman measurements. It can be considered that the features at ~ 680 cm⁻¹ in Fig. 6.16b could be due to the D_I vibration gap mode. A further theoretical description can be found in Chap. 5 in this book.

6.6.7 Second-Order Raman Scattering of 3C-SiC

The second order Raman scattering gives an insight into the lattice-dynamical properties and ultimately information about the strength and range of interatomic forces [95]. Figure 6.17 shows a second-order Raman spectrum from a CVD 3C-SiC free film (16 μm), which is similar to the spectrum first reported by Choyke in 1977 [96]. Figure 6.18 shows the polarization behavior of the first- and second-order Raman spectra from this 3C-SiC film.

Owing to momentum conservation, the first-order Raman modes can only be observed at the center of the BZ (Γ point) for perfect zinc blende cubic SiC. The requirement of a net zero wavevector for two phonon states leads to observable phonon overtones and combinations from the Γ , X, and L symmetry points. The zone center TO and LO phonon frequencies (at Γ) have been

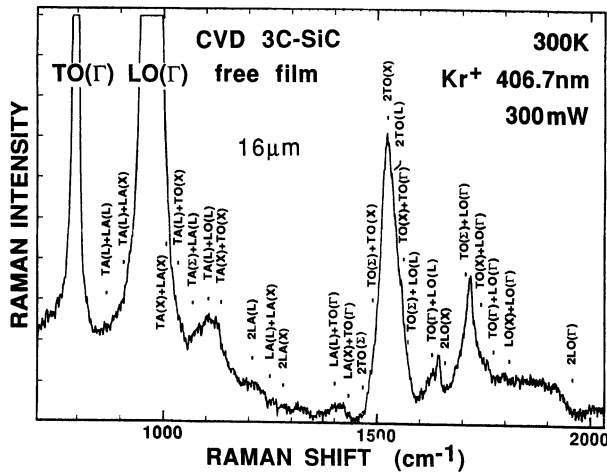


Fig. 6.17. Second-order Raman spectrum from a CVD 3C-SiC free film

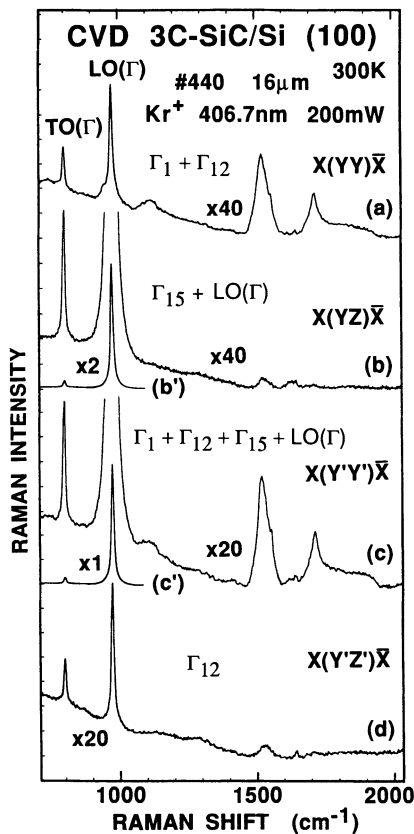


Fig. 6.18. Polarization behavior of the first- and second-order Raman spectra from a 3C-SiC film

determined from Raman measurements for bulk [65, 87] and film [2, 52, 72–77] 3C-SiC. The frequencies for the TO and LO phonons at L were known from the phonon dispersion curves along the (111) direction deduced from phonon data for different SiC polytypes [97]. The TO(X) and LO(X) values were obtained from PL measurements on 3C-SiC, which has an indirect gap and conduction minima at X [7, 48, 51]. With these data, one can obtain all possible combinations of Raman phonon modes below 2000 cm⁻¹. Our experimental Raman features at 1121, 1239, 1312, 1402, 1520, 1624, 1714, 1856, and 1896 cm⁻¹ are assigned to two-phonon Raman scattering, as shown in Fig. 6.17. The strongest second-order Raman phonon mode, located at 1520 cm⁻¹, is assigned to 2TO(X). The second strongest two-phonon feature, at 1714 cm⁻¹, is close to TO(X)+LO(Γ). The intensities of the second-order Raman features are more than one order of magnitude weaker than those of the first-order phonons.

Theoretical calculations of the phonon density of states for SiC have been done by several groups [93, 95, 98, 99]. In [93, 98, 99], densities of states for SiC up to 1000 cm⁻¹ have been presented. Windl et al. [95] have calculated, using *ab initio* phonon eigensolutions and phenomenological polarizability coefficients, the theoretical Raman spectra up to 2000 cm⁻¹, including the first- and second-order features, and made a comparison with experimental results.

6.7 Penetrative Luminescence Analysis

6.7.1 Effects of a Tensile Biaxial Stress on Bound-Exciton Transitions

Shifts of N-BE Lines

The lattice constant of 3C-SiC at RT is 4.359 Å and is smaller than that of Si (5.430 Å at RT). The thermal expansion coefficient of 3C-SiC is slightly larger than that of Si [92]. Consequently, when an epitaxial 3C-SiC film is grown on a Si substrate by CVD, we have a tensile biaxial stress inside the SiC film. Our Raman scattering studies [2, 52] have shown that this tensile biaxial stress shifts the optical phonons of 3C-SiC to lower energies. According to the analyses in Sect. 6.5 and [7], it also splits the $\mathbf{k} = 0$ (Γ point) degenerate valence band, puts the heavy-hole band on top, and narrows the energy bandgap as shown in Fig. 1-(6) of [7]. The bandgap change due to a tensile biaxial stress is calculated, from Table 6.1 or (6.33) and (6.30) with $P = -X$, by the formula

$$\Delta E_g = \delta E_h - (1/2)\delta E_s = X [2a(S_{11} + 2S_{12}) + b(S_{11} - S_{12})] . \quad (6.61)$$

Because $a < 0$, $b < 0$, and $X > 0$ for a tensile stress, we have $\Delta E_g < 0$. Our PL measurements in Fig. 6.19 confirm this conclusion. The N-BE line and phonon replicas from 3C-SiC on Si shift to longer wavelengths, i.e. lower energies, in comparison with 3C-SiC free films in the figure. Because

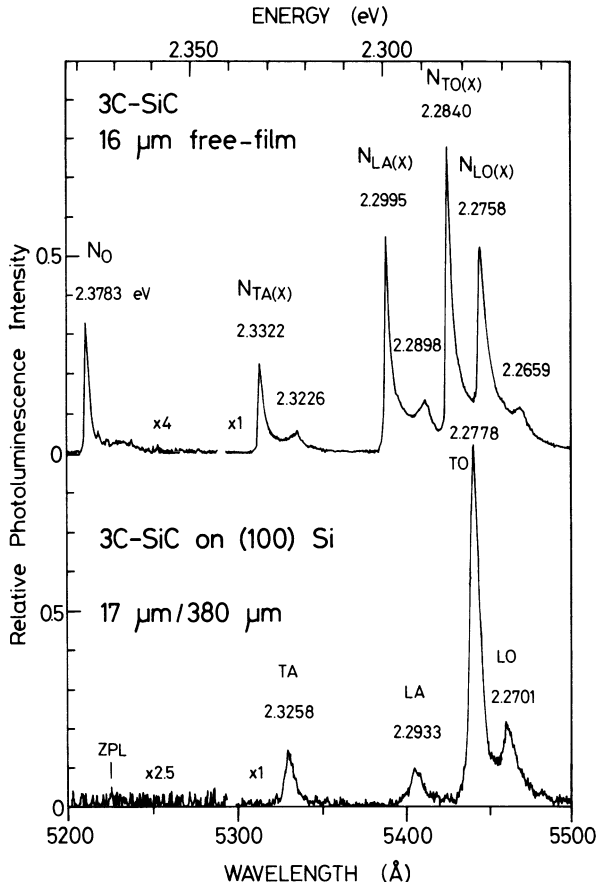


Fig. 6.19. Comparative 2K PL spectra for nitrogen-bound-exciton (N-BE) peaks from a $16\text{ }\mu\text{m}$ 3C-SiC free film and $17\text{ }\mu\text{m}$ 3C-SiC film on Si

the 3C-SiC deformation potentials at $\mathbf{k} = 0$ for the top of the valence band relative to the bottom of the conduction band at the X point of the Brillouin zone are not available, we cannot use (6.61) to calculate the stress inside the 3C-SiC film on Si. However, we have an estimate of the value of the stress X from our Raman measurements and we observe line shifts presumably related to the bandgap shift ΔE_g obtained from the PL measurement. This enables us to make a rough estimate of the range of the deformation potentials in 3C-SiC.

Layer Stress and Deformation Potentials

Let us consider the lower sample in Fig. 6.19, a $17\text{ }\mu\text{m}$ thick 3C-SiC film on Si. The Raman measurements in [52] give an average stress inside the film of $X = 0.61\text{ GPa}$. As a consequence of the analysis in Sect. 6.6.1, a preference

has developed for the use of the compliances of 3C-SiC in (6.39), i.e. $S_{11} = 3.67 \times 10^{-3}$ /GPa and $S_{12} = -1.05 \times 10^{-3}$ /GPa, and we have

$$\begin{aligned} S_{11} + 2S_{12} &= 1.57 \times 10^{-3} \text{ GPa ,} \\ S_{11} - S_{12} &= 4.72 \times 10^{-3} \text{ GPa .} \end{aligned} \quad (6.62)$$

With these values, and $\Delta E_g = -6.2$ meV and $X = 0.61$ GPa for this sample, we have from (6.61)

$$3.1a + 4.7b \sim -10 \text{ eV ,}$$

or approximately,

$$3a + 5b \sim -10 \text{ eV , i.e. } 0.6a + b \sim -2 \text{ eV ,} \quad (6.63)$$

where the deformation potentials a and b are in units of eV. Equations (6.62–6.63) should replace (11–12) in [7].

In [7], we have measured LT PL spectra from a series of CVD 3C-SiC/Si samples with film thicknesses in the range of 4–25 μm . The N-BE TO(X) peak was found to shift down linearly with the film thickness. Consequently, we obtained the rate of decrease of the energy gap with the film thickness, $\delta E_g/\delta d_{\text{SiC}}$, which was of the order of 0.1 meV/ μm , and the rate of change of the axial tensile stress in the film with d_{SiC} , $\delta X/\delta d_{\text{SiC}}$, which was 0.01–0.02 GPa/ μm .

Influence of Spin-Orbit Splitting on the Energy Gap Shift

In the previous discussions in Sect. 6.5.3, there is a requirement for $\delta E_S \ll \Delta_0$, i.e. the spin-orbit splitting should be much larger than the splitting of the heavy- and light-hole bands due to the stress. The spin-orbit splittings of Si, cubic SiC, and the uniaxial polytypes of SiC are 44, 10 and 7 meV, respectively [69]. For the case of Si, the requirement $\delta E_S \ll \Delta_0$ is easily satisfied. But for CVD cubic SiC on Si, we observe shifts of the bound-exciton line from 4 meV to 7 meV due to the removal of the Si substrate [7]. The condition $\delta E_S \ll \Delta_0$ may not be satisfied. We shall give a discussion of the effect of a small spin-orbit splitting on the energy band shifts here.

From the strain-orbit Hamiltonian (6.29), Pollak and Cardona [66] have obtained the changes of the energy band differences between the conduction band and the heavy- and light-hole valence bands at $\mathbf{k} = 0$ without the limitation of $\delta E_S \ll \Delta_0$:

$$\Delta(E_c - E_{v1}) = \frac{1}{6}\Delta_0 + \delta E_h - \frac{1}{4}\delta E_S - \frac{1}{2} \left[\Delta_0^2 + \Delta_0 \delta E_S + \frac{9}{4} (\delta E_S)^2 \right]^{1/2} \quad (6.64)$$

and

$$\Delta(E_c - E_{v2}) = -\frac{1}{2}\Delta_0 + \delta E_h + \frac{1}{2}\delta E . \quad (6.65)$$

From (6.65), the position of the light-hole band, v2, is not affected by the relation between δE_S and Δ_0 . In the case of uniaxial tension and biaxial compression, the light-hole band, which lies above the heavy-hole band, determines the bandgap that is not affected by a small spin-orbit splitting. In contrast, the position of the heavy-hole band, v2, with respect to the bottom of the conduction band is changed, according to (6.64). For $\delta E_S < \Delta_0$, keeping first- and second-order terms, we have

$$\Delta E_g = \Delta E_g(\text{hh}) = \delta(E_c - E_{v1}) = \delta E_h - \frac{1}{2}\delta E_S - \frac{1}{2}(\delta E_S)^2/\Delta_0 + \dots . \quad (6.66)$$

The first and second terms in (6.66) are the energy-gap change in (6.33) under the limitation of a large spin-orbit splitting. The third term in (6.66) represents an additional energy shift ΔE_g^* , which appears for a small spin-orbit splitting as

$$\Delta E_g^* = -\frac{1}{2}(\delta E_S)^2/\Delta_0 , \quad (6.67)$$

which further decreases the energy bandgap.

For $\delta E_S > \Delta_0$, we have from (6.64)

$$\begin{aligned} \Delta E_g = \Delta E_g(\text{hh}) &= \delta(E_c - E_{v1}) \\ &= \delta E_h - \frac{1}{2}\delta E_S - \frac{1}{2}\delta E_S - \frac{4}{27}(\Delta_0)^2/\delta E_S + \dots . \end{aligned} \quad (6.68)$$

Another additional shift of ΔE_g^{**} appears in (6.68) in comparison with (6.33),

$$\Delta E_g^{**} = -\frac{1}{2}\delta E_S - \frac{4}{27}(\Delta_0)^2/\delta E_S , \quad (6.69)$$

which makes the energy bandgap decrease for $\delta E_S > 0$ and increase for $\delta E_S < 0$. For the case of CVD 3C-SiC/Si, we have a tensile biaxial stress and $\delta E_S > 0$ in the SiC film. The energy bandgap becomes smaller owing to the tensile biaxial stress under the approximation of a large spin-orbit splitting. From (6.64)–(6.69), we find that under the condition of a small spin-orbit splitting, a further decrease of ΔE_g^* is given in (6.67) for the case of $\delta E_S < \Delta_0$ and a decrease of ΔE_g^{**} is given in (6.69) for the case of $\delta E_S > \Delta_0$. Indeed, supposing that the maximum value of δE_S for CVD cubic SiC is 7 meV, we have a further reduction of the energy bandgap of

$$\Delta E_g^* = -\frac{1}{2}(\delta E_S)^2/\Delta_0 \sim 2.5 \text{ meV} . \quad (6.70)$$

This represents a *maximum* error of 30%. Our qualitative analyses given above are unchanged by this correction.

Effects on the BE Line Intensities

An interesting phenomenon related to the effects of biaxial stress on the relative intensities of N-BE lines can be observed. For CVD 3C-SiC free films relieved of the biaxial stress due to the Si substrate, such as those shown in Figs. 6.4 and 6.19, the N-BE zero-phonon N_0 line is clearly visible and its intensity is one-tenth of that of the strongest TO line. The other one-phonon lines, TA, LA, and LO, have intensities of about 28%, 74%, and 67% of the TO line intensity, respectively (see also Table 6 in [7]). However, for CVD samples with Si substrates, the N_0 lines are usually very weak (sometimes unobservable), and the LA and LO lines become much weaker than the TO line. It seems that the N-BE zero- and longitudinal-phonon replica lines are severely depressed by the biaxial stress due to the deposition of SiC on Si.

Certain trends are apparent:

1. The N_0 zero-phonon line is attenuated more than other lines with respect to the free film.
2. A shift towards lower energy is caused by the biaxial stress.
3. The intensity of the LA mode appears to be affected most by the biaxial stress, with the LO mode second and the TA mode third. The TO mode is hardly affected.

We believe that the intensity changes for the N_0 zero phonon line because this line is from a direct transition without phonon participation. The effect of the biaxial stress on the band structure at $\mathbf{k} = 0$ could influence the matrix elements for this transition, while for the transitions of the phonon replica lines, which should obey momentum conservation, the reduction in intensity with respect to the free film may have its origin in a reduced density of phonon states at the zone boundary. Further detailed theoretical work is needed to give a satisfactory explanation of this interesting phenomenon.

6.7.2 Crystallinity Dependent Luminescence Characteristics and Defect Bands

The LT PL investigation of CVD 3C-SiC/Si samples with film thicknesses ranging from 600 Å to 17 μm has shown the following features [7]:

1. A broad band at ~ 2.15 eV, which dominates the spectrum of the thinnest sample (600 Å), but becomes less important for thicker films.
2. A strong, broad band, named G, around 1.90–1.92 eV, is apparent in the 2000 Å film and appears for almost all of the samples.
3. As the film thickness increases beyond 3 μm, we can see the appearance of the D_I center no-phonon line at 1.972 eV.
4. With increase of the film thickness, the N-BE line structure is developed, accompanied by the virtual disappearance of the 2.15 eV band.

TEM and Defect W-band at 2.15 eV

TEM studies of CVD-grown 3C-SiC on (100) Si have shown that near the SiC/Si interface (within 2–3 μm), there exists a high density of defects and that the defect density decreases rapidly over a distance of 3–4 μm from the interface [100, 101]. The main structural defects are misfit dislocations, stacking faults, twins, and microcracks [10, 92, 100, 101]. High-resolution TEM showed also a high density of low-angle grain boundaries and interfacial voids, depending on the growth conditions, such as the growth pressure and the Si/C ratio associated with the precursor [102]. Our PL results are consistent with these TEM observations. The PL spectra of samples with d_{SiC} less than 3 μm show very weak BE emission, and the dominant emission is a 2.15 eV band and the G band near 1.90–1.92 eV [7]. The broad band near 2.15 eV is reminiscent of the W band seen in plastically deformed 6H-SiC near 2.7–2.8 eV [103]. To emphasize the similarity to the 6H SiC 2.7–2.8 eV feature, we refer to the 2.15 eV band as a W band also. It dominates the spectrum of the thinnest sample, with $d_{\text{SiC}} = 600 \text{ \AA}$, and gradually becomes less important with increase of film thickness.

When d_{SiC} is larger than 4 μm, the W band is much weaker than the two phonon replicas of N-BE [7]. It is reasonable to assume that the W band near 2.15 eV has a similar origin to the W band in 6H-SiC [103] and is therefore due to heavy deformation in the near-interface region. For $d_{\text{SiC}} > 3 \mu\text{m}$, the W band appears occasionally in a few samples [7], which may mean that these samples have a thicker deformation region. For most of the samples with $d_{\text{SiC}} > 4 \mu\text{m}$, the region beyond the transition region has been shown [2, 52] to possess a relatively small amount of strain, on the order of 0.1–0.2%. Therefore, the W band, which we presume to be related to deformation, is too weak to be seen beyond the transition region.

Intensity Ratio ρ – a Figure of Merit of Film Quality

It is seen (from Fig. 6.3 and [7]) that the strong, broad band G, around 1.90–1.92 eV, appears for almost all of the CVD 3C-SiC/Si samples. The D_I zero-phonon line at 1.972 eV, which has been attributed to a divacancy-related center, appears at a film thickness of at least 3.2 μm. The D_I line and G band both sharpen as we go from 4 to 11 μm. We find an interesting variation of the relative intensities between the N-BE line and G band, such that with an increase of d_{SiC} , the N-BE luminescence increases greatly relative to the G band and their intensity ratio seems to approach a constant value. In line with common practice for other semiconductors [104], one may take the ratio ρ between the intensities of the G band and the N-BE TO(X) replica as a figure of merit for CVD 3C-SiC films. The ρ values have been shown to decrease rapidly with increasing film thickness in the first few microns and become stable at a low value of about 0.1 for film thicknesses larger than 10 μm [7]. With an increase of d_{SiC} and a decrease of the excitation depth, the ρ values

decrease, indicating a decrease of the density of defects away from the SiC/Si interface.

Itoh et al. [105] have grown 3C-SiC films epitaxially on crystalline Si(100) substrates at 1400 °C by means of CVD with an improved growth procedure. The 3C-SiC films, with thicknesses of about 30 μm, showed n-type low electron densities of $\sim 10^{16} \text{ cm}^{-3}$ and Hall mobilities of $\sim 500 \text{ cm}^2/\text{Vs}$ at RT. A quite small value of $\rho = 0.005$ was obtained, indicating the excellent quality of these single-crystal 3C-SiC films [105].

Spectral Comparison of Luminescence from 3C-SiC Films with and Without Si Substrate

In order to study further the structural differences between the surface and interface regions, as well as the effect of stress, we performed 2K PL measurements, as shown in Fig. 6.20, on the same piece of CVD 3C-SiC film, (a) with the Si substrate underneath, and on the free film with the substrate removed, excited (b) from the surface side and (c) from the interface side. The 3250 Å line from a He–Cd laser was employed, which penetrated only about 1.5 μm into cubic SiC. The interface region and surface region, under tensile stress (with the Si substrate) and without stress (substrate removed), can be better probed by this means. The PL from the interface side in (c) showed the defect features of D_I, G, G₁, and G₂ bands more strongly than in the other two cases, plus a very broad background spreading from 6000 Å to beyond 8000 Å with its center near 7000 Å.

It is seen that the G₁ and G₂ bands in (a) for 3C-SiC with the Si substrate are much weaker than the G band. This might imply that the tensile stress depresses these bands.

D_I Line at 1.972 eV

The behavior of the D_I line at 1.972 eV shows some interesting features. It was found [7] that the D_I line does not appear in thinner film samples with d_{SiC} less than 3 μm, and sharpens when d_{SiC} increases beyond 4 μm in our case. This means that the appearance and sharpness are also, to some extent, an indication of sample perfection. The D_I line was reported in ion-implanted and electron-irradiated Lely-grown 3C-SiC [103], and in electron-irradiated [105], ion-implanted [106,107], and as-grown [7,108,109] CVD 3C-SiC films. The ion implantation and electron irradiation produce Frenkel pairs and may subsequently form impurity–vacancy complexes, which in turn may be responsible for the recombination radiation from the D_I centers. In the CVD samples which we have examined, the interface region contains a large number of dislocations and other extended defects, and these line defects appear to dominate the observed spectra. For thick films with $d_{\text{SiC}} > 10 \mu\text{m}$, the number of dislocations and extended defects near the surface is considerably reduced and recombination due to point defect complexes appears to become more

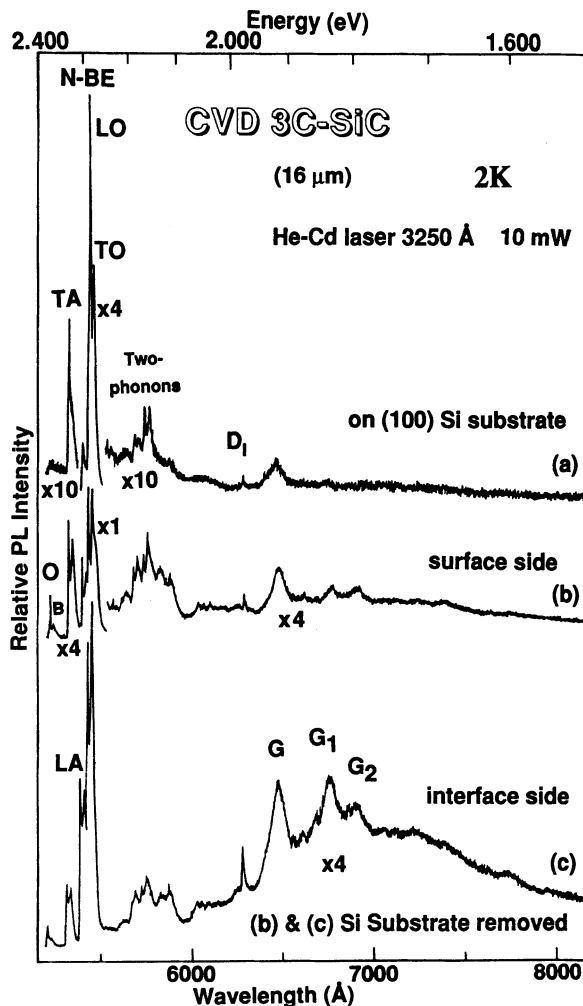


Fig. 6.20. 2K photoluminescence spectra of a CVD 3C-SiC/Si(100) sample, $d_{\text{SiC}} = 16 \mu\text{m}$; (a) film on substrate and with excitation, (b) from the surface side of the free film and (c) from the interface side of the free film. The Si substrate was removed for (b) and (c)

prominent. Another feature of the D_1 line should be pointed out. In Fig. 6.20, we compare three PL spectra from the same sample with a d_{SiC} of $16 \mu\text{m}$. When the Si substrate is removed, i.e. there is a release of the SiC/Si tensile biaxial stress, the D_1 line does not shift by more than 0.5 meV for either side of the free film. This is to be compared with the large shifts of $4\text{--}8 \text{ meV}$ that occur upon removal of the tensile stress for the N-BE lines. All of the D_1 line positions which we have measured for 3C-SiC with and without Si substrates, including measurements from both sides of the free films, yield D_1 line posi-

tions that are almost identical. These observations imply that the D_I center is not affected in the same manner by external and internal stresses as the bound-exciton lines. A deep center such as D_I is made up of wavefunctions from many bands, and thus there may be an averaging of the band shifts due to stress and thus a small net shift.

Our work has reached the following conclusions on the D_I center. The D_I band associated with a point defect complex shows only a very slight change in wavelength when the Si substrate is removed. For thick films (16 μm), its position is unchanged, whether the free SiC film is irradiated from the front or the back. This result has been duplicated on numerous samples. It appears that this deep center ($\sim 0.5 \text{ eV}$) is little affected by the internal stresses in the SiC film. This result is consistent with the fact that the wavefunction for a deep level is made up of contributions from many bands in the crystal and is likely to be insensitive to energy shifts of the conduction band at X and the valence band at Γ .

Dislocation- and Extended-Defect-Related G Band

Choyke and Patrick [106] have reported the 1.84–1.98 eV PL spectra of ion-implanted and annealed bulk samples of cubic SiC. They suggested that the observed 66.5 meV sideband is a resonant mode shifted to lower energy from the normal LA phonon replica [106]. This 66.5 meV mode is located at 1.907 eV, roughly the same position as our G band. Our PL measurements for CVD 3C-SiC/Si have revealed a broad band G near 1.90–1.92 eV and additional structure from 1.90 eV to 1.50 eV, seen in Fig. 6.20. Although the phonon sidebands of the D_I line are located within this region, we believe that the G band and the G₁ and G₂ bands, as well as the broad background, are not related to the D_I center. We have evidence relating them to dislocations and other extended defects. The following experimental facts support this suggestion.

1. The D_I line, associated with point-like defects such as a divacancy, is not seen in CVD SiC near the interface layer. The G band, on the other hand, is seen in layers close to the interface.
2. The D_I lines from different samples have almost the same energy position (1.972 eV), with an error of less than 0.3–0.5 meV, whilst the peak positions of the G band are very different from sample to sample, with a shift of up to 10–20 meV. G₁ and G₂ are almost always seen at a constant distance from the G band. Figure 6.21 shows such an example, where the D_I lines of two samples are located at the same position (1.9723 eV) but the two G bands are displaced by ~ 7 meV. If we shift the energy scale for these two samples and align the two G bands then we also find coincidence for the G₁ and G₂ bands. It is possible that G₁ and G₂ are in some way involved with the longitudinal LA(X) and LO(Γ) phonons. But for such a very deep center, there is no a priori reason to require such momentum conservation.

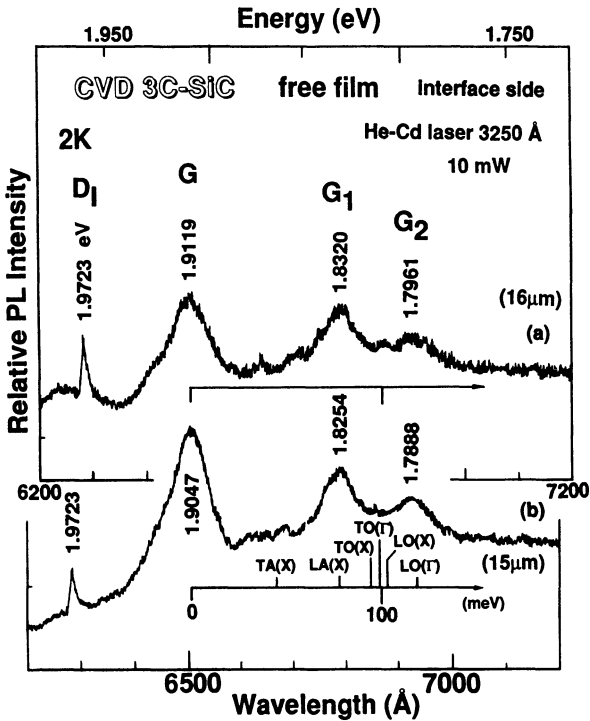


Fig. 6.21. A comparison of the D_1 , G , G_1 , and G_2 bands from two CVD 3C-SiC free films (from Choyke et al. [7], reprinted with permission of the American Institute of Physics)

3. In Fig. 6.20, we have a comparison of the PL spectra from 3C-SiC on (100) Si and both sides of a CVD 3C-SiC free film. The top (surface) side, which was excited with 3250 \AA light ($1/\alpha = 1.5 \mu\text{m}$), shows sharp, strong N-BE lines and relatively weak D_1 , G , G_1 , and G_2 lines and bands. The bottom (interface) side shows PL emission from $\sim 1.5 \mu\text{m}$ from the SiC/Si interface. This emission consists of much weaker N-BE lines and relatively stronger D_1 , G , G_1 , and G_2 bands, indicating a much larger density of line defects in this region. This is consistent with cross-sectional TEM observations on such films [10, 100, 101]. The broad background, which may also be related to the line defects, extends down to at least 1.50 eV as seen in Fig. 6.20.
4. When we measure PL spectra with an Hg lamp and a He-Cd laser as excitation sources, the deep excitation shows a higher ρ value than does the shallow excitation [7]. This reflects the fact that the density of defects decreases with an increase of the distance from the interface.

These results indicate that the D_1 and G -series bands have different origins. The G -series bands seem to be correlated with extended-defect damage originating at the SiC/Si interface. The density of the line defects decreases

as we move away from the interface transition region. It seems likely that the PL emission between 1.5 and 1.9 eV is a superposition of lines and bands from the D_I series and G series, i.e. a mixture of point and line defects.

6.7.3 Photoluminescence Excitation, Time-Resolved, and Infrared Transmission Studies

Freitas, Bishop, and collaborators have conducted a series of detailed studies, by way of photoluminescence, photoluminescence excitation (PLE), time-resolved PL, and other techniques, on CVD-grown 3C-SiC/Si and related materials [107–113].

In [107], they carried out LT PL studies on CVD-grown 3C-SiC ion-implanted with B, Al, and P. The D1 and D2 defect PL bands and effects of high-temperature annealing were studied. Freitas et al. observed that the intensity of the D1 and D2 defect PL bands in 3C-SiC films was increased substantially by ion implantation. Annealing both the as-grown and the ion-implanted films causes an increase in the intensities of the D1 and D2 PL bands up to about 600 °C, above which the D2 zero-phonon PL intensity is sharply reduced, suggesting a possible lattice recovery which quenches this defect PL band. The intensity of the D1 PL band remains roughly constant for annealing temperatures up to 1600 °C and even 1800 °C [107].

Freitas et al.'s measurements of the temperature (T) dependence of N-Al donor–acceptor pair PL spectra in 3C-SiC films demonstrate [108] that the thermal activation energy for the nitrogen donors is equivalent to the 54 meV binding energy for nitrogen determined from the spectral energies of the sharp-line close-pair spectra, and that the 15–20 meV donor which dominates the electrical properties of n-type films is not isolated, substitutional nitrogen. These authors also observed weak shoulders on the low-energy side of the zero-phonon line (ZPL) and the phonon replicas, similar to the B-series lines that we observed in Figs. 6.4 and 6.19. They studied further the relative strengths of the N-BE spectrum and these low-energy shoulders as a function of the C/Si source gas ratio, and showed that for low C/Si ratios the intensity of the shoulders (i.e. the B-series lines) is greatly enhanced. This suggested that the recombination centers giving rise to these B-series PL transitions might be associated directly or indirectly with nonstoichiometric defects such as Si interstitials or C vacancies [108].

Freitas and Bishop [109] have performed an investigation of the dependence of the PL on the excitation power and T for several lightly Al-doped and undoped CVD 3C-SiC films, using the G-bands which we have described [7]. These authors revealed the G band to be present in every CVD 3C-SiC film which they studied, and that the G band intensity increased with decreasing C/Si source gas ratio, which varied from 1.2 to 2.4. This G band was observed weakly in the high-power spectra, but the low-power spectra can be dominated by the G-series bands, i.e. the G-ZPL and its phonon replicas. The low-power spectra of some of Freitas and Bishop's samples can be resolved

into a free-to-bound (FB) transition at 1.932 eV and a distant-pair band about 20 meV lower in energy. Their detailed power- and temperature-dependent PL measurements [109, 112] confirmed the deep-donor–acceptor pair PL characteristics of the G band, involving a deep acceptor with a binding energy of $E_A = 470$ meV.

The pervasive character of this deep acceptor suggests that it is at least partially responsible for the high compensation observed in undoped 3C-SiC films. Although these observations are consistent with an association of the G band with a native defect such as a nonstoichiometric defect, the facts could be explained equally well in terms of a background acceptor impurity whose incorporation is influenced by film stoichiometry. Furthermore, as pointed out by Freitas and Bishop [109], it is well known that impurities are gettered by the strains associated with extended defects such as dislocations.

In addition, time-resolved PL measurements [41, 111] revealed that all of the PL features in the near-band-edge spectra in 3C-SiC have lifetimes in the ~ 400 ns range expected for donor-bound excitons (in indirect-bandgap semiconductors) whose lifetime is limited by Auger recombination processes. Excitons bound at isoelectronic defects (e.g. Si on a C site) are expected to have much longer decay times (~ 10 μ s) [112].

Bishop and Freitas [110, 112] have identified that the residual donor in 3C-SiC with a binding energy of 54 meV is an isolated N impurity substituted on a C site. The shoulders below the N-BE sharp lines, i.e. the B-series lines, which are well separated in Figs. 6.4 and 6.19 and in [7], may arise from recombination centers which occur in very high concentrations or in strained environments in inhomogeneities in the SiC films.

The PLE measurements of Bishop and Freitas have provided further support for the above assignments [113]. For undoped and n-type 3C-SiC, plots of the integrated PL intensity (1.5–2.4 eV) as a function of the wavelength of the exciting light are in good agreement with optical absorption spectra reported for bulk 3C-SiC. The observed shape of the absorption edge is characteristic of phonon-assisted indirect transitions, and spectral features attributable to LA and TA phonons are discernible. Therefore, PLE spectra provide a faithful representation of the indirect optical absorption edge. The PLE spectra of the Al-doped samples exhibit extrinsic absorption attributed to photoneutralization of compensation shallow donors. The extrinsic PLE spectra of the Al-doped samples contain peaks corresponding to the ZPLs of the donor BE PL bands observed in undoped films, and onsets corresponding to the thresholds for photoneutralization of the 54 meV N-donors and of the 15–20 meV donors of unknown origin [113].

Later on, Moore et al. [114] measured infrared transmission spectra of high-quality vapor-grown 3C-SiC in the region of 1s–2p donor excitation transitions, which reveal three sequences of donor transitions. Two of these sequences, a broad sequence and a sharp one, occur when the sample is held near 4.2 K. The broad sequence is assigned to transitions arising from the 1s(A) ground state of nitrogen. On warming, a second broad sequence, assigned to

transitions from the $1s(E)$ ground state of nitrogen, is observed. The measured separation of these sequences, the $1s(A)-1s(E)$ valley–orbit splitting, is 8.34 meV. Excellent correspondence with theory is found for a nitrogen binding energy of 54.2 meV, consistent with other optical determinations of the nitrogen donor binding energy, and a static dielectric constant of 9.8. The sharp sequence, which is similar to sharp sequences found in very pure germanium, is attributed to a unidentified second donor whose excitation transitions are not broadened by grown-in local strain, e.g. an impurity free of chemical shift.

Furthermore, Moore et al. [115] have studied infrared transmission as a function of temperature and applied magnetic field, PL in the two-electron satellite region, and Zeeman spectra. Accurate positions for excited states of nitrogen on carbon sites have been determined, which are in agreement with effective-mass theory. PL for the two-electron satellites gives the nitrogen $2s$ state binding energy. Two other donors are observed with low concentrations: an effective-mass donor at 47.7 meV and a very shallow donor with a binding energy of 34 meV. Zeeman splitting measurements provide the values of the $2p_{\pm}$ excited states. It is suggested that the very shallow donor has a repulsive core (negative chemical shift) and inverted ordering, with the $1s(A_1)$ ground state above the $1s(E)$ ground state [115].

6.7.4 Bound Electronic States of Isolated Single and Paired Native Defects

Native Defects and DLTS Results

As discussed in previous parts of this section, PL measurements on CVD-grown 3C-SiC have revealed luminescence transitions related to deep centers, which might be due to native defects. As reported, CVD-grown SiC is Si-rich. Also, a small deviation ($\sim 0.1\%$) from stoichiometry may result in native defects (e.g. vacancies, self-interstitials, or antisites) with concentrations as high as 10^{19} cm^{-3} [116]. Since vacancies are mobile and migrate in the material, they can be trapped by intentionally doped defects and/or other native (say, antisite) impurities to form complexes. Such “impurity–vacancy” complexes can produce shallow or deep defect states. The deep-level states produced have a deleterious effect on the lifetime of minority carriers and exert important effects on the performance of optoelectronic devices.

The deep-level states can be identified or characterized by way of PL, deep-level transient spectroscopy (DLTS), optical and IR absorption, Raman scattering, electron spin resonance (ESR), etc. For example, a few DLTS studies on CVD-grown 3C-SiC/Si have been performed [117–119]. Nagesh et al. [117] reported a deep center with an ionization energy of 0.49 eV. Zhou et al. [118] reported two deep impurity states at $E_c - 0.34$ eV and $E_c - 0.68$ eV. Zekentes et al. [119] detected three defect centers located at about $E_c - 0.32$ eV, $E_c - 0.52$ eV, and $E_c - 0.56$ eV.

Tight-Binding Calculation in the Framework of the Green's Function

In order to give a proper theoretical analysis or interpretation for the PL and DLTS data, Talwar and Feng [116] have studied theoretically the bound electronic states of isolated single and paired native defects in cubic SiC. The band structure of 3C-SiC has been calculated, on the basis of a tight-binding theory in the Green's function framework for the electronic energy states of sp^3 -bonded native, substitutional (isolated), and pair defects occupying either Si and/or C sites. A second-neighbor tight-binding scheme was developed to provide an accurate set of model parameters. Local distortions around impurity atoms are estimated in terms of a simple, but first-principles, bond-orbit model. To account for the off-diagonal elements in the perturbation matrix, the effects of lattice relaxations are systematically included. The calculation also leads to theoretical information about the bound electronic states of several isolated and complex defects.

Our Green's function calculation suggests that the energies of the bound states (t_2 symmetry) of silicon and carbon vacancies are near $E_v + 0.54$ eV and $E_c - 0.75$ eV, respectively. This indicates that the Si vacancy in 3C-SiC, V_{Si} , behaves as an acceptor and the C vacancy in 3C-SiC, V_C , behaves as a donor.

The calculation and theoretical analysis [116] have shown that for the antisite defects $Si_{C\!}\!\!_{\cdot}$ and $C_{Si\!}\!\!_{\cdot}$ in 3C-SiC, there are no corresponding bound-state levels that exist in the forbidden bandgap, unlike the case of III-V compounds. Furthermore, for “ $Si_{C\!}\!\!_{\cdot}$ – $C_{Si\!}\!\!_{\cdot}$ ” antisite pairs in 3C-SiC, no impurity-induced bound states in the forbidden gap are found. However, for nearest-neighbour divacancy ($V_{Si\!}\!\!_{\cdot}$ – V_C) and antisite–vacancy pair ($C_{Si\!}\!\!_{\cdot}$ – V_C , $Si_{C\!}\!\!_{\cdot}$ – $V_{Si\!}\!\!_{\cdot}$) defects of C_{3v} symmetry, our calculations suggest the possibility of localized impurity states that could be detected in the gap. More details can be seen in Chap. 5 in this book.

Other Theoretical Calculations

Other researchers have also contributed to the theoretical calculation of the energy structure of native defects in 3C-SiC. Wang et al. [120] have performed an *ab initio* pseudopotential calculation of the formation energies, abundances, and electronic structure of native defects in cubic SiC. Their results showed that the dominant defect is determined by the stoichiometry (Si-rich or C-rich) and the doping state of the 3C-SiC material. For Si-rich cubic SiC, the $Si_{C\!}\!\!_{\cdot}$ antisite is the dominant defect in n-type material, while the C vacancy, which is a double donor, dominates in p-type materials. In C-rich SiC, the dominant defect is the electrically inactive $C_{Si\!}\!\!_{\cdot}$, regardless of the position of the Fermi level. The authors of [111] suggested that a slightly C-rich cubic SiC is more suitable for p-type doping and electronic applications using 3C-SiC.

Lu et al. [121] have adopted a linear muffin-tin method in the tight-binding representation to study the electronic structures of the native defects in cubic SiC by the Green's function approach. They obtained the result that the antisites do not have electronic states in the bandgap, while Si and C vacancies induce split-off states at $E_v + 0.45$ eV and $E_v + 1.67$ eV, respectively.

Ishida et al. [91] have recently proposed a model to explain antiphase domain (APD) annihilation mechanism in CVD 3C-SiC on Si. It is found that the growth on C face S site prevents the antiphase boundary (APB) propagation to the $\langle 111 \rangle$ direction and the number of layers to annihilate APDs increases with the increase of secondary nucleation rate.

Interpretation of PL and DLTS Data on Native Defect Centers

The above theoretical investigations help us interpret better the PL and DLTS data related to native defect centers in 3C-SiC. As mentioned before, a D_I PL emission line at 1.972 eV is observed from most CVD-grown 3C-SiC (Figs. 6.3, 6.20, and 6.21). This so-called D_I center was first observed in He-ion-implanted and/or fast-electron-bombarded cubic SiC [106], and its origin was first speculated to be related to either an “impurity–vacancy complex” or some form of divacancy [103]. Suleimanov et al. [122] studied the polarization behavior of the D_I luminescence spectrum, which identified the center to have local C_{3v} symmetry and confirmed the model of the D_I center to be an “impurity–vacancy complex”.

Taking the values of E_g (= 2.417 eV) and $E(D_I)$ (= 1.972 eV) for 3C-SiC, one finds a difference of 0.445 eV for the transition between the conduction band X-minimum and the D_I center. This value of 0.445 eV for D_I compares reasonably well with our theoretical result for the V_{Si}–Si_C (0.44 eV) center and is not far from that for the V_{Si}–V_C (0.48 eV) divacancy [116]. Our study [116] also confirms the point-group symmetry of the D_I center to be C_{3v} . This center involves either a nearest-neighbor “divacancy” or a “vacancy–antisite complex”, most likely a V_{Si}–Si_C complex. The D_I band at 1.972 eV in Figs. 6.3 and 6.21 possesses a line width of ~ 5 meV. This, we believe, might be due to a combination of transitions involving both the vacancy–antisite V_{Si}–Si_C complex and the divacancy center, with the former providing the major contribution to the 1.972 eV band with a 5 meV width.

The G-band located near 1.91 eV has been proved to have an origin different from that of the D_I center [7] and possibly involves a deep acceptor ($E_A = 470$ meV) [109, 112]. We notice that the DLTS measurement has revealed an electron trap with an activation energy of 0.49 eV [117]. Moreover, using a realistic lattice-dynamical model for both the perfect and the imperfect 3C-SiC, we are now studying the vibronic sidebands in the D_I spectrum. Our preliminary calculations have suggested that the main strength of the D_I vibrational spectrum lies in the acoustic phonon branch, with a general shift towards lower energies from the normal lattice modes [116]. These results lead us to suggest that the G-band luminescence might involve mainly the V_{Si}–V_C

(0.48 eV) divacancy and other complex centers. Because of the large width of the G-emissions and strong phonon sidebands, more divacancy and complex centers with pairs at different distances could be involved.

Sharp 1.913 eV PL Line from Electron-Irradiated 3C-SiC

Itoh et al. [105] have used PL to study defects produced by 1 MeV electron irradiation in CVD 3C-SiC/Si. As mentioned in Sect. 6.7.2, the LT PL showed a very small intensity ratio ($I_{\text{G-band}}/I_{\text{N-BE-TO}}$) of $\rho = 0.05\%$, indicating the excellent quality of the CVD-grown 3C-SiC films. For 3C-SiC/Si irradiated by 1 MeV electrons, a dominant PL line appeared at 1.913 eV with an FWHM of ~ 2.5 meV at 4 K. In addition, a radiation-induced D₁ (1.973 eV) line and several sharp lines at 1.964, 1.959, 1.955, and 1.954 eV were found at 4 K. These are presumably caused by simple point defects introduced primarily by electron irradiation, because large aggregates of defects are less likely to exhibit such sharp PL lines.

The 1.913 eV PL line was found to disappear in annealing stages at ~ 100 and 700 °C. This feature and its fraction annealed at each annealing stage were in good agreement with the results obtained for the T1 electron spin resonance (ESR) center, which is attributed to isolated vacancies at Si sublattice sites [123]. Taking account of the bandgap of 3C-SiC ($E_g = 2.417$ eV) and the assumption that the 1.913 eV line is due to a transition between the bottom of the conduction band and an electronic level of V_{Si}, a defect level of V_{Si} at 0.50 eV above the top of the valence band, i.e. $E_v + 0.50$ eV, is obtained. This value is quite close to our theoretical value for V_{Si}, $E_v + 0.54$ eV. These and further analyses lead the authors of [105] to conclude that the 1.913 eV sharp PL line obtained from irradiated 3C-SiC epilayers arises from Si vacancies in 3C-SiC.

6.8 Infrared Reflectance Spectroscopy Analysis

Among various advanced materials characterization techniques for 3C-SiC materials and structures, Fourier transform infrared spectroscopy is a non-destructive, convenient, and useful tool. It has been used for the analysis of the 3C-SiC material system [124–128]. Feng et al. [128] have recently presented a combined investigation by theory and experiment of the infrared properties of 3C-SiC films grown on Si by chemical vapor deposition. Some observed phenomena, for example, the interference fringe damping behavior, have been interpreted on the basis of new theoretical simulations.

6.8.1 Basic Theoretical Model

In order to understand better the IR features of the 3C-SiC/Si system, we performed extensive theoretical simulations of IR reflectance spectra of 3C-SiC/Si

under various film conditions, including variable film thickness, damping level, doping carrier concentration, and surface roughness. A basic theoretical model was used for the lattice dielectric function $\varepsilon(\omega)$ with the form [124, 129]

$$\begin{aligned}\varepsilon(\omega) &= (n + ik)^2 \\ &= \varepsilon_\infty \left\{ 1 + (\omega_{\text{LO}}^2 - \omega_{\text{TO}}^2)/(\omega_{\text{LO}}^2 - \omega^2 - i\gamma_{\text{TO}}\omega) - \omega_p^2/[\omega(\omega + i\gamma_p)] \right\},\end{aligned}\quad (6.71)$$

where n is the refractive index, k is the extinction coefficient, ω is the infrared frequency, ε_∞ is the high-frequency dielectric constant, ω_{TO} and ω_{LO} are the transverse and longitudinal optic-phonon frequencies, respectively, γ_{TO} is the phonon damping constant, $\omega_p^2 = 4\pi Ne^2/m^*\varepsilon_\infty$ defines the plasma frequency due to free carriers of density N and effective mass m^* , and γ_p is the plasma damping constant.

On the basis of (6.71), IR reflectance spectra of 3C-SiC/Si were calculated, as shown in Fig. 6.22A, for different film thickness and including bulk SiC. For a very thin ($0.05\text{ }\mu\text{m}$) SiC film, the IR reflectance only exhibits a peak near ω_{TO} . As the film thickness increases, the peak rises and broadens. When the films reach several micrometers in thickness, they present a well-developed

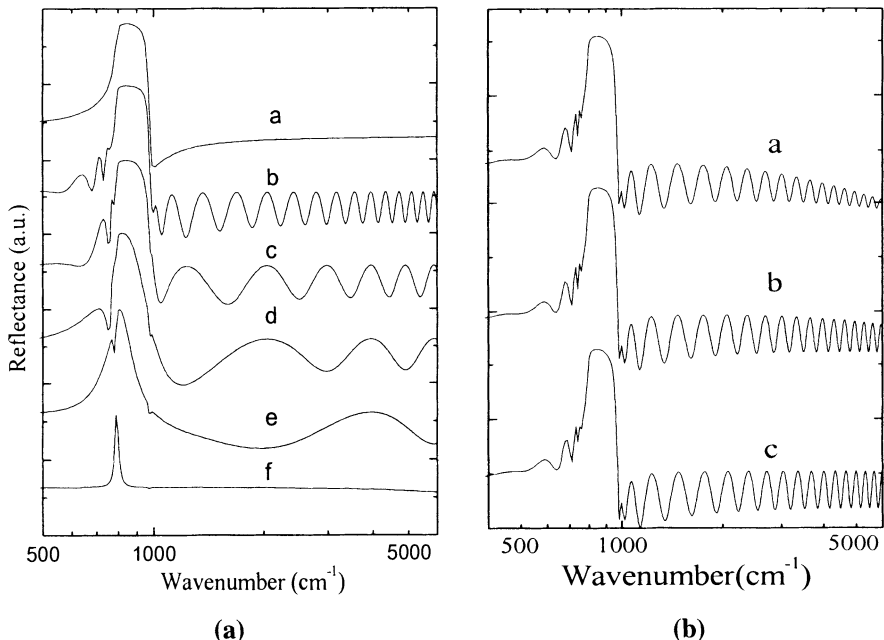


Fig. 6.22. (a) Calculated IR spectra of 3C-SiC on Si for different film thicknesses: (a) bulk SiC, (b) $5\text{ }\mu\text{m}$, (c) $2\text{ }\mu\text{m}$, (d) $1\text{ }\mu\text{m}$, (e) $0.5\text{ }\mu\text{m}$, and (f) $0.05\text{ }\mu\text{m}$. (b) Calculated IR spectra for different surface conditions of δ : (a) $0.15\text{ }\mu\text{m}$, (b) $0.08\text{ }\mu\text{m}$, and (c) 0 (with a film thickness of $6.0\text{ }\mu\text{m}$) (from Feng et al. [128], reprinted with permission of Springer-Verlag)

reststrahlen band. The reflectance has a peak close to that of bulk SiC but with a skewed edge at the high-frequency side. Fabry–Perot (F–P) interference fringes are observed in the transparent region. This simple model can describe the results well for many 3C-SiC/Si samples. For example, the four curves in Fig. 6.7B can be fitted well using (6.71) (the fit is not shown here).

6.8.2 Effect of Surface Roughness

However, our practice has shown that sometimes the above simple model expressed by (6.71) is not able to describe all the experimental IR spectra. For example, some samples show IR spectra with an F–P fringe damping at frequencies in the high-energy region, as shown in Fig. 6.23 (solid line for experiment).

We have considered theoretically two possible effects causing this experimental phenomenon, i.e. surface roughness and an interfacial transition layer. First, surface roughness can lead to a loss of reflectance with increase of incident light frequency, and the contrast of interference fringes becomes smaller, i.e. a damping behavior occurs. This behavior can be described by [130]:

$$R = R_0 \exp [-16(\pi\delta/\lambda)^2], \quad (6.72)$$

where R_0 is the ideal reflectance and δ is the film surface roughness in μm . Figure. 6.22B shows the theoretical variation of the IR spectrum when surface roughness is taken into account.

Further, we have performed a theoretical simulation with a model with an interfacial transition layer between the SiC and the Si, which could also lead to the spectral damping of the F–P fringes (the results of this model are

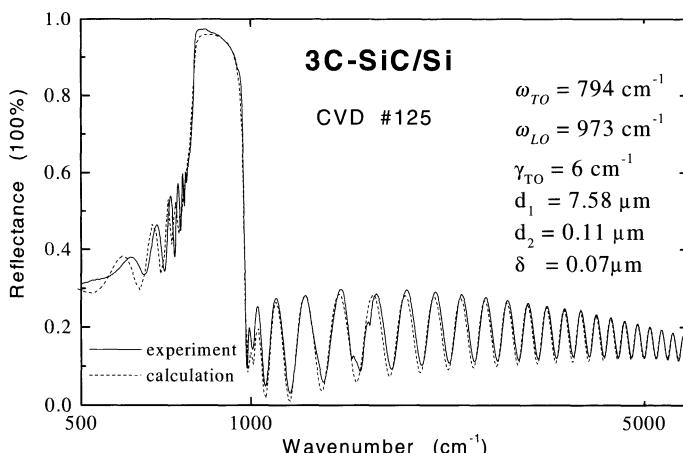


Fig. 6.23. IR reflectance spectrum of 3C-SiC on Si and the theoretical fitting (from Feng et al. [128], reprinted with permission of Springer-Verlag)

not shown here). The thickness of this transition layer is about 50–100 nm in the samples studied. Its variation exerts obvious influences on the IR spectra such as the degree of damping and the contrast of interference fringes. But the central line of the damped F-P fringes stays at the same level, which is different from the damping behavior in Fig. 6.22B, where a large surface roughness causes the F-P fringe damping to bend down with increasing frequency.

6.8.3 Damping of Interference Fringes

In practical cases, these two effects should be considered together to obtain the best fits to the experimental IR spectra. Figure 6.23 shows such an example. As can be seen, an excellent fit is obtained by considering a 0.11 μm thick interfacial transition layer between the Si substrate and a rough surface with a roughness of 0.11 μm , on a 7.38 μm thick cubic SiC layer.

We have extensively examined more than fifty CVD-grown samples. This kind of damping does not occur in high-quality 3C-SiC/Si samples. Therefore, the F-P fringe damping is assumed to reveal structural features of the sample as described above. The samples characterized by the FTIR reflectance spectra shown in Fig. 6.7B possess no F-P fringe damping, and indeed have a good quality of the 3C-SiC/Si interface and of the surface. Therefore, our work shows that IR spectroscopy can be a useful tool to reveal the structural features of 3C-SiC/Si and other material systems.

6.9 Additional Issues

6.9.1 Combined PL–Raman Spectroscopy under UV Excitation

It was reported previously, as mentioned in Sect. 6.3.2, that 3C-SiC/Si does not exhibit any luminescence at room temperature [49]. In contrast to this indication, recently we have realized the detection of RT PL from 3C-SiC/Si, as shown in Fig. 6.24. The luminiscence was measured using a sensitive UV (325 nm) Raman–PL microscope system. Figure 6.24a shows a scan in the energy range 2.0–3.75 eV. The PL band at 2.3 eV is from the cubic SiC, and is representative of PL emission across the indirect bandgap. Near the right end of the figure, a sharp line near 3.7 eV and a weak feature at ~ 3.62 eV are observed, which are due to Raman scattering. In Fig. 6.24b, this part of the spectrum is replotted on the scale of Raman shift (cm^{-1}) for the x -axis. This plot clearly exhibit the 3C-SiC LO(Γ) phonon mode near 980 cm^{-1} (with an FWHM of 14 cm^{-1}) and second-order Raman scattering features in the 1500 – 1800 cm^{-1} region.

Shim et al. [49], when they applied the excitation from the interface side of the free 3C-SiC film, observed a strong RT PL peak centered around 2.4 eV. From their data (Fig. 1 in [49]), this band has a very broad value of the

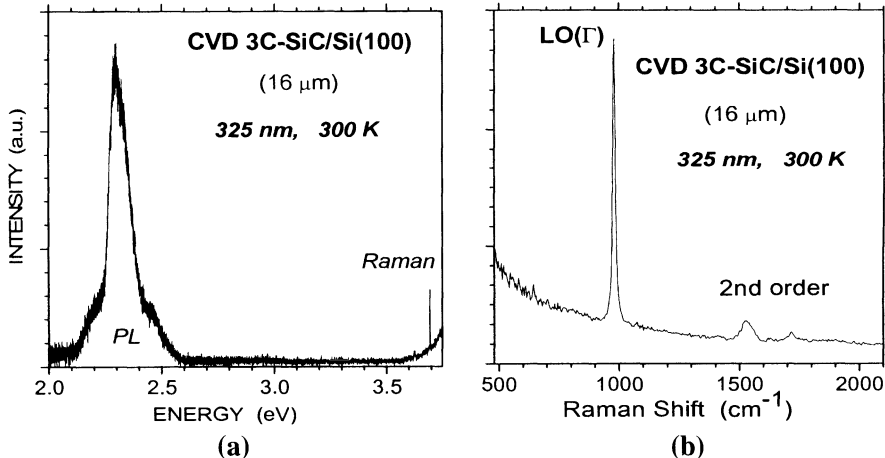


Fig. 6.24. Combined PL and Raman spectra, under UV (325 nm) excitation, from a 16 μm thick CVD 3C-SiC/Si(100) sample: (a) PL and Raman together, with the x -axis labeled in eV, and (b) Raman alone, with the x -axis labeled in cm^{-1}

FWHM, near 0.7 eV. In contrast, our 2.3 eV PL band in Fig. 6.24a from 3C-SiC with a Si substrate has an FWHM of about 0.11 eV, very much (~ 6 times) narrower than Shim et al.'s result. This indicates a much better 3C-SiC film quality in our CVD 3C-SiC/Si samples. Also, the Raman scattering signals are usually much weaker than the PL emissions in such samples. However, Fig. 6.24a shows the combined PL-Raman spectrum in the same run, with the Raman mode peak intensity on the same scale as the PL peak intensity. This provides additional evidence for the high crystalline quality of the 3C-SiC/Si sample studied here.

Therefore, we may conclude that RT PL emissions from an indirect 3C-SiC film grown on Si can be detected from high-quality crystalline 3C-SiC by the use of a sensitive measurement system. Similarly, for the case of 6H-SiC, Feng et al. [131] have recently performed a combined UV Raman and PL study on n-type 6H-SiC bulk wafers – another type of indirect-bandgap SiC material. This work has in turn provided a good and convenient way for the characterization of CVD growth of 3C-SiC on Si.

6.9.2 Large-Diameter Thick 3C-SiC Epitaxially Grown on Si

Nagasawa et al. [38, 39] have recently reported the successful growth of large-diameter (6 inches), thick (200 μm) 3C-SiC layers on (001) Si substrates. 3C-SiC has a great advantage for large-area, low-cost fabrication, among SiC polytypes, because it is the only one that can be grown heteroepitaxially on Si substrates. However, device applications of 3C-SiC grown on Si have lagged very much behind those of hexagonal 6H- and 4H-SiC. This is mainly due to the problem of a high density of defects, in particular a large number

of planar defects such as antiphase boundaries (APBs) and twin boundaries (TBs), generated at the interface between the 3C-SiC and Si, where a near 20% lattice mismatch exists. Nagasawa et al. [38, 39] have developed a novel technique to eliminate planar defects in the 3C-SiC epitaxial layer by growing on an “undulant Si” substrate. This substrate has a “wavy” surface, consisting of a Si(001) base with the countered slopes oriented in the [110] and [$\bar{1}\bar{1}0$] directions. During the initial 3C-SiC growth, step flow epitaxy occurred on the surface slopes of the substrate, reducing the number of APBs. The twinning domains in the 3C-SiC formed a triangular-shaped plate, with its flat faces (coherent TBs) oriented parallel to the (111) or ($\bar{1}\bar{1}1$) planes, forming steps on the surface. Thus, as the 3C-SiC film thickness increased, TBs were combined, leading to a decrease of the density of TBs.

As described in [38, 39], the “undulant Si” was prepared from “just Si” (well-oriented Si(001)), which was scraped with diamond slurry in the [$\bar{1}\bar{1}0$] direction, followed by oxidation and removal. A cold-wall-type, low-pressure CVD system was employed for 3C-SiC epitaxial growth on the “undulant Si”. After 5 hours of growth, about 200 μm thickness of 3C-SiC film was achieved, with a remarkable reduction of both APBs and TBs at the upper surface of the 200 μm thick 3C-SiC layer. After removal of the Si substrate, a thick 3C-SiC free film was obtained.

Optical and electrical characterization have been conducted on some of these free-standing thick (200 μm) 3C-SiC films grown on undulant 6 inch Si substrates by way of LT PL and Hall measurements [132]. The films had a free-electron concentration near $2 \times 10^{16} \text{ cm}^{-3}$ and showed a clear difference in the electron mobility before and after removal of the highly defective region near the 3C-SiC/Si interface. The LT PL spectra showed sharp features corresponding to the nitrogen bound-exciton (N-BE) zero-phonon line and multiphonon replicas, and also Al-BE as well as D_I and D_{II} lines. PL due to free-exciton (FE) recombination, which is a good measure of the crystalline quality of a sample, has been observed at 30 K in as-grown 3C-SiC/Si.

6.9.3 Epitaxial Lateral Overgrowth of 3C-SiC on Si

Jacob et al. and Nishino et al. [36, 40] have recently succeeded in the epitaxial lateral overgrowth of 3C-SiC on patterned Si (001) and (111) substrates. This is another good approach for decreasing the high density of defects near the SiC/Si interface, which has so far limited the development of 3C-SiC/Si. The ELO technology has been employed earlier to grow low-interface-defect-density films in the GaN/sapphire system [133]. Now it has been applied to the 3C-SiC/Si system. The substrates used were patterned Si substrates prepared by depositing a SiO₂ layer as a mask, followed by conventional lithography. The windows were of different shapes with edges oriented mostly along the $\langle 110 \rangle$ directions. Nishino et al. [40] employed hexachlorodisilane (HCDS) and propane (C₃H₈) to achieve low-temperature (1250 °C) ELO, which is an important factor in keeping the SiO₂ mask stable during the deposition. At

$T > 1250^{\circ}\text{C}$, the oxide mask is damaged owing to a reaction between SiO_2 and Si, resulting in the formation of gaseous SiO . This leads to bulging and the SiO_2 mask peeling off. It is expected that this ELO technique might open another way to achieving high-quality 3C-SiC/Si.

6.9.4 Excellent Reviews of Materials Characterization of SiC

Now that we are close to the end of this chapter, in which the optical and structural properties of CVD-grown 3C-SiC/Si have been reviewed, the author would like to recommend readers who need to obtain further information about optical and structural characterization and investigation to refer two excellent set of reviews edited by Choyke, Matsunami, and Pensl [134]. The section “Characterization of SiC” contains various chapters, grouped via characterization techniques, about the different SiC polytypes; the emphasis is mostly on 6H- and 4H-SiC, although the 15R, 3C, and other polytypes are also involved in some of the content.

6.10 Conclusion

This chapter has revied the materials analysis of CVD-grown cubic SiC films grown on Si, including X-ray diffraction, low-temperature photoluminescence, Raman scattering, Fourier transform infrared spectroscopy, optical reflectance and transmission, X-ray photoelectron spectroscopy, secondary-ion mass spectroscopy, Rutherford backscattering spectroscopy, and ion channeling. The major concerns in this chapter were the optical and structural properties of 3C-SiC/Si materials. General materials characterization of cubic SiC has been presented, by way of XRD, and PL, Raman, UV-Vis, and FTIR spectroscopy; this belongs to the primary materials analysis of 3C-SiC and is essential for a quick feedback to the characterization of grown materials. More advanced or detailed materials analyses using surface science and nuclear-physics techniques, including XPS, SIMS, RBS, and ion channeling, and advanced or detailed Raman and PL analyses, have been described. The stress and strain are important in the 3C-SiC/Si system and exert great influence on the material properties. Some theoretical aspects of layer stress and strain in 3C-SiC/Si have been set out, and a series of theoretical formulas related to the axial-stress-induced Raman phonon shift and energy bandgap variations have been presented and applied to the case of 3C-SiC/Si. Infrared reflectance spectroscopic analysis of 3C-SiC/Si has been described. Some additional issues have been introduced, including combined UV-excitation PL and Raman spectroscopy on 3C-SiC/Si, the recent achievement of large-area (6”), thick (200 μm) 3C-SiC grown on undulant Si(001) substrates, and the epitaxial lateral overgrowth of 3C-SiC/Si, as well as an excellent review volume useful in this field.

This report has briefly reviewed the results and achievements of the author and his collaborators in the past two decades. Some related results from other contributors have also been introduced. Interesting and unsolved problems, and directions for future exploration have been discussed. The characterization and analysis methods should also be useful for other SiC polytypes and other semiconductor materials, in particular, wide-gap materials. This review also provides evidence that interdisciplinary analysis is necessary for modern materials analysis.

Acknowledgments

With great pleasure, the author would like to acknowledge many professors, other scientists, colleagues, collaborators, and students for their support and help in this field: W.J. Choyke, J.A. Powell, A.J. Mascarenhas, D.N. Talwar, C.C. Tin, J. Williams, R. Hu, A.T.S. Wee, J. Lin, W.Y. Chang, S.J. Chua, I. Ferguson, and C. C. Yang.

References

1. J.A. Powell, P. Pirouz, and W.J. Choyke, "Growth and characterization of silicon carbide polytypes for electronic applications", in *Semiconductor Interfaces, Microstructures and Devices: Properties and Applications*, ed. Z.C. Feng, Institute of Physics Publishing, Bristol, pp. 257–293 (1993).
2. Z.C. Feng, A.J. Mascarenhas, W.J. Choyke, and J.A. Powell, "Raman scattering studies for chemical vapor deposited 3C-SiC films on (100) Si", *J. Appl. Phys.* **64**, 3176–3186 (1988).
3. J. Lely, *Ber. Dtsch. Keram. Ges.* **32**, 229 (1951).
4. J. Schlichting, G. Czack, and P. Kuhn, *Gmelin Handbook of Inorganic Chemistry*, 8th ed., *Si Supplement*, Vol. B2, Springer, New York p. 17/126, (1984).
5. S. Nishino, J.A. Powell, and H.A. Will, "Production on large-scale single-crystal wafers of cubic SiC for semiconductor devices", *Appl. Phys. Lett.* **42**, 460–462 (1983).
6. J.W. Palmour, H.S. Kong, and R.F. Davis, "Characterization of device parameters in high-temperature metal-oxide-semiconductor field-effect transistor in β -SiC thin films", *J. Appl. Phys.* **64**, 2168–2177 (1988).
7. W.J. Choyke, Z.C. Feng, and J.A. Powell, "Low temperature photoluminescence studies of CVD grown cubic SiC on Si", *J. Appl. Phys.* **64**, 3163–3175 (1988).
8. R.F. Davis, G. Kelner, M. Shur, J.W. Palmour, and J.A. Edmond, "The film deposition and microelectronic and optoelectronic device fabrication and characterization in monocrystalline alpha and beta silicon carbide", *Proc. IEEE* **79**, 677–701 (1991).
9. V.A. Kubanov and C.Y. Fong, "Doping in cubic silicon-carbide", *Appl. Phys. Lett.* **75**, 88–90 (1999).
10. X.H. Zheng, B. Qu, Y.T. Wang, Z.Z. Dai, J.Y. Han, H. Yang, and J.W. Liang, "Comprehensive analysis of microtwins in the 3C-SiC films on Si(100) substrates", *J. Cryst. Growth* **233**, 40–44 (2001).

11. C.I. Park, J.H. Kang, K.C. Kim, K.S. Nahm, E.-K. Suh, and K.Y. Lim, "Metal-organic chemical vapor deposition growth of GaN thin film on 3C-SiC/Si(111) substrate using various buffer layers", *Thin Solid Films* **401**, 60–66 (2001).
12. S.F. Chichibu, M. Sugiyama, T. Kuroda, A. Tackeuchi, T. Sota, S.P. DenBaars, S. Nakamura, Y. Ishida, and H. Okumura, "Band gap bowing and exciton localization in strained cubic $In_xGa_{1-x}N$ films grown on 3C-SiC (001) by rf molecular-beam epitaxy", *Appl. Phys. Lett.* **79**, 3600–3602 (2001).
13. T. Kitamura, S.-H. Cho, Y. Ishida, X.-Q. Shen, H. Nakanishi, S.F. Chichibu, and H. Okumura, "Growth and characterization of cubic InGaN/GaN multiple quantum wells on 3C-SiC by RF-MBE", *Proc. International Workshop on Nitride Semiconductors, IPAP Conf. Series 1*, pp. 93–96 (2000); S.F. Chichibu, T. Onuma, T. Aoyama, K. Nakajima, P. Ahmet, T. Chikymow, T. Sota, S.P. DenBaars, S. Nakamura, T. Kitamura, Y. Ishida, and H. Okumura, "Recombination dynamics of localized excitons in cubic $In_xGa_{1-x}N/GaN$ multiple quantum wells grown by radio frequency molecular-beam epitaxy on 3C-SiC substrate", *J. Vac. Sci. Technol. B* **21**, 1856–1862 (2003).
14. A.J. Steckl, J. Devrajan, C. Tran, and R.A. Stall, "SiC rapid thermal carbonization of the (111)Si semiconductor-on-insulator structure and subsequent metalorganic chemical vapor deposition of GaN", *Appl. Phys. Lett.* **69**, 2264–2266 (1996).
15. J.A. Powell, L.G. Matus, and M.A. KuczmarSKI, "Growth and characterization of cubic SiC single-crystal films on Si", *J. Electrochem. Soc.* **134**, 1558–1565 (1987).
16. S. Nishino, H. Suhara, H. Ono, and H. Matsunami, "Epitaxy growth and electrical characterization of cubic SiC on silicon", *J. Appl. Phys.* **61**, 4889–4893 (1987).
17. C.C. Tin, R. Hu, R.L. Coston, and J. Park, "Reduction of etch pits in heteroepitaxial growth of 3C-SiC on silicon", *J. Cryst. Growth* **148**, 116–124 (1995).
18. J.A. Powell, L.G. Matus, M.A. KuczmarSKI, C.M. Chorey, T.T. Cheng, and P. Pirouz, "Improved β -SiC heteroepitaxial films using off-axis Si substrates", *Appl. Phys. Lett.* **51**, 823–825 (1987).
19. H.S. Kong, Y.C. Wang, J.T. Glass, and R.F. Davis, "The effect of off-axis Si (100) substrates on the defect structure and electrical properties of β -SiC thin films", *J. Mater. Res.* **3**, 521–530 (1988).
20. H. Yamada, "Low-temperature 3C-SiC heteroepitaxial film grown on Si by reactive-ion-beam deposition", *J. Appl. Phys.* **65**, 2084–2089 (1989).
21. T. Yoshinobu, H. Mitsui, Y. Tarui, T. Fuyuki, and H. Matsunami, "Heteroepitaxial growth of single crystalline 3C-SiC on Si substrates by gas source molecular beam epitaxy", *J. Appl. Phys.* **72**, 2006–2013 (1992).
22. M. Kitabatake, M. Deguchi, and T. Hirao, "Simulation and experiments of SiC heteroepitaxial growth on Si(001) surface", *J. Appl. Phys.* **74**, 4438–4445 (1993).
23. A.J. Steckl, C. Yuan, J.P. Li, and M.J. Loboda, "Growth of crystalline 3C-SiC on Si at reduced temperature by chemical vapor deposition from silacyclobutane", *Appl. Phys. Lett.* **63**, 3347–3349 (1993).
24. Q. Wahab, M.R. Sardela, Jr., L. Hultman, A. Henry, M. Willander, E. Janzén and J.-E. Sundgren, "Growth of high-quality 3C-SiC epitaxial films on off-axis Si(001) substrates at 850 °C by reactive magnetron sputtering", *Appl. Phys. Lett.* **65**, 725–727 (1994).

25. C.-C. Liu, C. Lee, K.-L. Cheng, H.-C. Cheng, and T.-R. Yew, "Effect of SiH₄/CH₄ flow ratio on the growth of β -SiC on Si by electron cyclotron resonance chemical vapor deposition at 500 °C", *Appl. Phys. Lett.* **66**, 168–170 (1995).
26. P. Mandracchi, A. Chiodoni, G. Cicero, S. Ferrero, F. Giorgis, C.F. Pirri, G. Barucca, P. Musumeci, and R. Reitano, "Heteroepitaxy of 3C-SiC by electron cyclotron resonance-CVD technique", *Appl. Surf. Sci.* **184**, 43–49 (2001).
27. B. Yang, W. Cai, P. He, Y. Sheng, B. Jin, Y. Ruan, K. Hu, Y. Huang, and G. Zhou, "Growth of β -SiC film by pyrolysis of polyimide Langmuir–Blodgett films on silicon", *J. Appl. Phys.* **77**, 6733–6735 (1995).
28. J.-H. Boo, K.-S. Yu, M. Lee, and Y. Kim, "Deposition of cubic SiC films on silicon using dimethylisopropylsilane", *Appl. Phys. Lett.* **66**, 3486–3488 (1995).
29. J.D. Hwang, Y.K. Fang, K.H. Wu, and D.N. Yaung, "Visible electroluminescence from a novel β -SiC/p-Si *n*–*p* heterojunction diode prepared by rapid thermal chemical vapor deposition", *Appl. Phys. Lett.* **67**, 1736–1738 (1995).
30. A.J. Steckl, J. Devrajan, S. Tlali, H.E. Jackson, C. Tran, S.N. Gorin, and L.M. Ivanova, "Characterization of 3C-SiC crystals grown by thermal deposition of methyltrichlorosilane", *Appl. Phys. Lett.* **69**, 3824–3826 (1996).
31. C.W. Liu and J.C. Sturm, "Low temperature chemical vapor deposition growth of β -SiC on (100) Si using methylsilane and device characteristics", *J. Appl. Phys.* **82**, 4558–4565 (1997).
32. D. Panknin, J. Stoemenos, M. Eickhoff, V. Heera, M. Voelskow, and W. Skorupa, "The beneficial role of flash lamp annealing on the epitaxial growth of the 3C-SiC on Si", *Appl. Surf. Sci.* **184**, 377–382 (2001).
33. J. Hofmann and S. Veprek, "Pseudomorphic growth of ultra thin cubic 3C-SiC films on Si(100) by temperature programmed organometallic chemical vapor deposition", *J. Appl. Phys.* **85**, 2652–2657 (1999).
34. C. Long, S.A. Ustin, and W. Ho, "Structural defects in 3C-SiC grown on Si by supersonic jet epitaxy", *J. Appl. Phys.* **86**, 2509–2515 (1999).
35. Y.M. Lei, Y.H. Yu, L.L. Cheng, B. Sundaraval, E.Z. Luo, C.X. Ren, S.C. Zou, S.P. Wong, D.H. Chen, and I.H. Wilson, "Investigation and modeling of the infrared optical properties of direct current sputtered SiC films on silicon", *J. Appl. Phys.* **88**, 3053–3058 (2000).
36. C. Jacob, M.-H. Hong, J. Chung, P. Pirouz, and S. Nishino, "Selective epitaxial growth of silicon carbide on patterned silicon substrates using hexachlorodisilane and propane", *Mater. Sci. Forum* **338–342**, 249–252 (2000).
37. A. Fissel, W. Richter, J. Furthmüller, and F. Bechstedt, "On the nature of the D₁ defect center in SiC: a photoluminescence study of layers grown by solid-source molecular-beam epitaxy", *Appl. Phys. Lett.* **78**, 2512–2514 (2001).
38. H. Nagasawa, T. Kawahara, and K. Yagi, "Hetero-epitaxial growth and characterization of 3C-SiC on large-diameter Si(001) substrates", *Mater. Sci. Forum* **389–393**, 319–322 (2002).
39. H. Nagasawa, K. Yagi, and T. Kawahara, "3C-SiC hetero-epitaxial growth on undulant Si(001) substrates", *J. Cryst. Growth* **237–239**, 1244–1249 (2002).
40. S. Nishino, C. Jacob, Y. Okui, S. Ohshima, and Y. Masuda, "Lateral overgrowth of 3C-SiC on patterned Si(111) substrates", *J. Cryst. Growth* **237–239**, 1250–1253 (2002).
41. Y. Kamlag, A. Goossens, I. Colbeck, and J. Schoonman, "Laser CVD of cubic SiC nanocrystals", *Appl. Surf. Sci.* **184**, 118–122 (2001).

42. S. Kerdiles, R. Madelon, and R. Rizk, "Spectroscopic ellipsometry analysis of nanocrystalline silicon carbide obtained at low temperature", *Appl. Surf. Sci.* **184**, 150–155 (2001).
43. Y. Zhang, M. Nishitani-Gamo, C. Xiao, and T. Ando, "Synthesis of 3C-SiC nanowhiskers and emission of visible photoluminescence", *J. Appl. Phys.* **91**, 6066–6068 (2002).
44. Z.C. Feng, C.C. Tin, K.T. Yue, R. Hu, J. Williams, S.C. Liew, Y.G. Foo, S.K.L. Choo, W.E. Ng, and S.H. Tang, "Combined structural and optical assessment of CVD grown 3C-SiC/Si", *Mater. Res. Soc. Symp. Proc. Vol. 339, Diamond, Silicon Carbide and Nitride Wide-Bandgap Semiconductors*, eds. C.H. Carter, Jr., S. Nakamura, G. Gildenblat, and R.J. Nemanich, Materials Research Society, Pittsburgh, pp. 417–422 (1994).
45. Z.C. Feng, S. Perkowitz, D.K. Kinnel, R.L. Whitney, and D.N. Talwar, "Compositional dependence of optical phonon frequencies in $\text{Al}_x\text{Ga}_{1-x}\text{As}$ ", *Phys. Rev. B* **47**, 13466–13470 (1993).
46. A.T.S. Wee, Z.C. Feng, H.H. Hgn, K.L. Tan, C.C. Tin, R. Wu, and R. Coston, "Surface chemical states on 3C-SiC/Si epilayers", *Appl. Surf. Sci.* **81**, 377–385 (1994).
47. Z.C. Feng, C.C. Tin, R. Hu, and J. Williams, "Raman and Rutherford backscattering analyses of cubic SiC thin films grown on Si by vertical chemical vapor deposition", *Thin Solid Films* **266**, 1–7 (1995).
48. W.J. Choyke, D.R. Hamilton, and L. Patrick, "Optical properties of cubic SiC: luminescence of nitrogen-exciton complex, and interband absorption", *Phys. Rev.* **133**, A1163–A1166 (1964).
49. H.W. Shim, K.C. Kim, Y.H. Seo, K.S. Nahm, E.-K. Suh, H.J. Lee, and Y.G. Hwang, "Anomalous photoluminescence from 3C-SiC grown on Si(111) by rapid thermal chemical vapor deposition", *Appl. Phys. Lett.* **70**, 1757–1759 (1997).
50. R.L. Hartman and P.J. Dean, "Magneto-optical properties and recombination rate of the green luminescence in cubic SiC", *Phys. Rev. B* **2**, 951–959 (1970).
51. P.J. Dean, W.J. Choyke, and L. Patrick, "The location and shape of the conduction band minima in cubic silicon carbide", *J. Lumin.* **15**, 299–314 (1977).
52. Z.C. Feng, W.J. Choyke, and J.A. Powell, "Raman determination of layer stresses and strains for heterostructures and its application to the cubic 3C-SiC/Si system", *J. Appl. Phys.* **64**, 6827–6835 (1988).
53. K. Li, A.T.S. Wee, J. Lin, K.L. Tan, L. Zhou, S.F.Y. Li, Z.C. Feng, H.C. Chou, S. Kamra, and A. Rohatgi, "A microstructural study on the surface and interface of CdTe/CdS solar cells", *J. Mater. Sci. E* **8**, 125–132 (1997).
54. A. Addamiano and P.H. Klein, "Chemically-formed buffer layers for growth of cubic silicon carbide on silicon single crystals", *J. Cryst. Growth* **70**, 291–294 (1984).
55. R.T. Holm, P.H. Klein, and P.E.R. Nordquist, Jr., "Infrared reflectance evaluation of chemically vapor deposited β -SiC films grown on Si substrates", *J. Appl. Phys.* **60**, 1479–1485 (1986).
56. Z.C. Feng, W.Y. Chang, S.J. Chua, J. Lin, and C.C. Tin, "Infrared optical investigation of 3C-SiC on Si", in *Proceedings of the 25th International Conference on the Physics of Semiconductors*, pp. 1559–1560, eds. N. Miura and T. Ando, Springer Proceedings in Physics Vol. 87, Springer, Berlin (2001).

57. J.C. Pazik, G. Kelner, and N. Bottka, "Epitaxial growth of β -SiC on silicon-on-sapphire substrates by chemical vapor deposition", *Appl. Phys. Lett.* **58**, 1419–1421 (1991).
58. L.R. Doolittle, *Nucl. Instrum. Methods B* **9**, 344 (1985).
59. T.W. Nee, T.L. Cole, A.K. Green, M.E. Hills, C.K. Lowe-Ma, and V. Rehn, in *Modern Optical Characterization Techniques for Semiconductors and Semiconductor Devices*, eds. O.J. Glembocki, F.H. Pollak, and J.J. Song, Proc. SPIE, Vol. 794, p. 142 (1987).
60. J.E. Nye, *Physical Properties of Crystals*, Oxford University Press, Oxford, Chapter VIII (1957).
61. S.G. Lekhnitskii, *Theory of Elasticity of an Anisotropic Elastic Body*, Translated by P. Fern, Holden-Day, Inc., San Francisco, p. 13 (1963).
62. F. Cerdeira, C.J. Buchenauer, F.H. Pollak, and M. Cardona, "Stress-induced shifts of first-order Raman frequencies of diamond- and zinc-blende-type semiconductors", *Phys. Rev. B* **5**, 580–593 (1972).
63. R. Loudon, "Theory of the first-order Raman effect in crystals", *Proc. R. Soc. Lond. A* **275**, 218–232 (1963); "The Raman effect in crystals", *Adv. Phys.* **13**, 423–482, p. 461 (1964).
64. F.H. Pollak and R. Tsu, in *Spectroscopic Characterization Techniques for Semiconductor Technology*, eds. F.H. Pollak and R.S. Bauer, Proc. SPIE, Vol. 452, p. 26 (1983).
65. D. Olego and M. Cardona, "Pressure dependence of Raman phonons of Ge and 3C-SiC", *Phys. Rev. B* **25**, 1151–1160 (1982); D. Olego, M. Cardona, and P. Vogl, "Pressure dependence of the optical phonons and transverse effective charge in 3C-SiC", *Phys. Rev. B* **25**, 3878–3888 (1982).
66. F.H. Pollak and M. Cardona, "Piezo-electroreflectance in Ge, GaAs, and Si", *Phys. Rev.* **172**, 816–837 (1968).
67. H.D. Liu and Z.C. Feng, "The stresses and photoelastic effects in stripe geometry GaAs–GaAlAs DH lasers with masked and selective thermal oxidation (MSTO) structure", *IEEE J. Quantum Electron.* **QE-19**, 1016–1020 (1983).
68. K.B. Tolpygo, *Sov. Phys. Solid State* **2**, 2367 (1960).
69. G.A. Slack, *J. Appl. Phys.* **35**, 3460 (1964).
70. M. Miura, H. Murata, Y. Shiro, and K. Lishi, *J. Phys. Chem. Solids* **42**, 931 (1981).
71. D.H. Lee and J.D. Joannopoulos, *Phys. Rev. Lett.* **48**, 1846 (1982).
72. A. Debernardi, C. Ulrich, K. Syassen, and M. Cardona, "Raman linewidths of optical phonons in 3C-SiC under pressure: first-principles calculations and experimental results", *Phys. Rev. B* **59**, 6774–6783 (1999).
73. S. Rohmfeld, M. Hundhausen, L. Ley, C.A. Zorman, and M. Mehregany, "Raman spectroscopy on biaxially strained epitaxial layers of 3C-SiC on Si", *Mater. Sci. Forum* **338–342**, 595–598 (2000); "Quantitative evaluation of biaxial strain in epitaxial 3C-SiC layers on Si(100) substrates by Raman spectroscopy", *J. Appl. Phys.* **91**, 1113–1117 (2002).
74. H. Mukaida, H. Okumura, J.H. Lee, H. Daimon, E. Sakuma, S. Misawa, K.E. Endo, and S. Yoshida, "Raman scattering of SiC: estimation of the internal stress in 3C-SiC on Si", *J. Appl. Phys.* **62**, 254–257 (1987).
75. J. Zhu, S. Liu, and J. Liang, "Raman study on residual strains in thin 3C-SiC epitaxial layers grown on Si(001)", *Thin Solid Films* **368**, 307–311 (2000).

76. C. Hagiwara, K.M. Itoh, J. Muto, H. Nagasawa, K. Yagi, H. Harima, K. Mizoguchi, and S. Nakashima, "Raman determination of stresses and strains in 3C-SiC films grown on 6-inch Si substrates", Mater. Sci. Forum **264–268**, 669–672 (1998).
77. J.M. Bluet, L.A. Falkovsky, N. Planes, and J. Camassel, "Raman investigation of stress relaxation at the 3C-SiC/Si interface", Mater. Sci. Forum **264–268**, 395–398 (1998).
78. H. Okumura, E. Sakuma, J.H. Lee, H. Mukaida, S. Misawa, K.E. Endo, and Y. Yoshida, "Raman scattering of SiC: application to the identification of heteroepitaxy of SiC polytypes", J. Appl. Phys. **61**, 1134–1136 (1987).
79. H. Harima, S. Nakashima, J.M. Carulli, C.P. Beetz, and W.S. Yoo, "Characterization of 3C-SiC epitaxial layers on TiC(111) by Raman scattering", Jpn. J. Appl. Phys. **36**, Part 1, 5525–5531 (1997).
80. L.A. Falkovsky, J.M. Bluet, and J. Camassel, "Strain-fluctuation effect on Raman spectra", Phys. Rev. B **55**, R14697–14700 (1997); "Strain relaxation at the 3C-SiC/Si interface: Raman scattering experiments", Phys. Rev. B **57**, 11283–11294 (1998).
81. S. Rohmfeld, M. Hundhausen, and L. Ley, "Raman scattering in polycrystalline 3C-SiC: influence of stacking faults", Phys. Rev. B **58**, 9858–9862 (1998); "Influence of stacking disorder on the Raman spectrum of 3C-SiC", Phys. Stat. Sol. (b) **215**, 115–119 (1999).
82. E.F. Bezerra, V.N. Freire, A.G.S. Filho, J.M. Filho, V. Lemos, Y. Ikoma, F. Watanabe, and T. Motooka, "Strong interface-induced changes on the numerical calculated Raman scattering in Si/3C-SiC superlattices", Appl. Phys. Lett. **77**, 4316–4318 (2000).
83. V. Lysenko, D. Barbier, and B. Champagnon, "Stress relaxation effect in porous 3C-SiC/Si heterostructure by micro-Raman spectroscopy", Appl. Phys. Lett. **79**, 2366–2368 (2001).
84. W. Richter, "Resonant Raman scattering in semiconductors", in *Solid-State Physics*, ed. R. Dornhaus, G. Nimtz, and W. Richter, Springer Tracts in Modern Physics (ed. G. Höhler), Vol. 78, Springer New York, pp. 157–164, 167, and 176 (1976).
85. E.D. Palik, ed., *Handbook of Optical Constants of Solids*, Academic Press, San Diego, pp. 564 and 593 (1985).
86. D.A. Long, *Raman Spectroscopy* (McGraw-Hill, New York), Section 3.4.2 (1977).
87. J. Serrano, J. Strempfer, M. Cardona, M. Schwoerer-Bohning, H. Requard, M. Lorenzen, B. Stojetz, P. Pavone, and W.J. Choyke, "Determination of the photon dispersion of zinc blende (3C) silicon carbide by inelastic X-ray scattering", Appl. Phys. Lett. **80**, 4360–4362 (2003).
88. P. Brüesch, *Phonons: Theory and Experiments II*, Springer Series in Solid State Sciences, Vol. 65, Springer, New York, p. 78 (1986).
89. A. Mooradian, "Raman spectroscopy of solids", in *Laser Handbook*, eds. F.T. Arecchi and E.O. Schulz-DuBois, North-Holland, Amsterdam, p. 1451 (1972).
90. Z.C. Feng, D. Talwar, and I. Ferguson, "Spectroscopic properties of cubic SiC on Si", in *Silicon Carbide – Materials, Processing and Devices*, eds. S.E. Sadow, N.S. Saks, D.J. Larkin, and A. Schöner, MRS Symp. Proc. Vol. 742, Materials Research Society, Pittsburgh, K2.14.1-6 (2003).

91. Y. Ishida, T. Takahashi, H. Okumura, and S. Yoshida, "Investigation of antiphase domain annihilation mechanism in 3C-SiC on Si substrates", *J. Appl. Phys.* **94**, 4676–4689 (2003).
92. P. Liaw and R.F. Davis, *J. Electrochem. Soc.* **131**, 3014 (1984).
93. D.N. Talwar, H. Ono, and Z.C. Feng, "Identification of intrinsic and radiation-induced defect centers in β -SiC", in *21st International Conference on the Physics of Semiconductors*, eds. P. Jiang and H.Z. Zheng, World Scientific, Singapore, pp. 1701–1704 (1992); D.N. Talwar and Z.C. Feng, "Vibration modes due to the nitrogen occupying Si and C sites in cubic silicon carbide", in *Silicon Carbides and Related Materials*, eds. M.G. Spencer, R.D. Devaty, and M. Rahman, *Inst. Phys. Conf. Ser.* No. 137, Institute of Physics Publishing, Bristol, pp. 283–286 (1994).
94. L. Patrick and W.J. Choyke, *Phys. Rev. B* **5**, 3253 (1972); "Localized vibrational modes of a persistent defect in ion-implanted SiC", *J. Phys. Chem. Solids* **34**, 565–567 (1973).
95. W. Windl, K. Karch, P. Pavone, O. Schütt, D. Strauch, W.H. Weber, K.C. Hass, and L. Rimai, "Second-order Raman spectra of SiC: experimental and theoretical results from *ab initio* phonon calculations", *Phys. Rev. B* **49**, 8764–8767 (1994).
96. W.J. Choyke, "Solid state spectroscopy and our understanding of SiC", in *Proc. 20th Colloquium Spectroscopicum International and 7th International Conf. on Atomic Spectroscopy*, Prague, p. 385 (1977).
97. D.W. Feldman, J.H. Parker, Jr., W.J. Choyke, and L. Patrick, *Phys. Rev.* **173**, 787 (1968).
98. K. Kunc, *Ann. Phys. (France)* **8**, 319 (1973–74); K. Kunc, M. Balkanski, and M.A. Nusimovici, *Phys. Stat. Sol. (b)* **72**, 229 (1975).
99. M. Hofmann, A. Zywiertz, K. Karch, and F. Bechstedt, "Lattice dynamics of SiC polytypes within the bond-charge model", *Phys. Rev. B* **50**, 13401–13411 (1994).
100. S.R. Nutt, D.J. Smith, H.J. Kim, and R.F. Davis, "Interface structures in beta-silicon carbide thin films", *Appl. Phys. Lett.* **50**, 203 (1987).
101. P. Pirouz, C.M. Chorey, and J.A. Powell, "Antiphase boundaries in epitaxially grown β -SiC", *Appl. Phys. Lett.* **50**, 221 (1987).
102. B.-T. Lee, D.-K. Kim, C.-K. Moon, J.K. Kim, Y.H. Seo, K.S. Nahm, H.J. Lee, K.-W. Lee, K.-S. Yu, Y. Kim, and S.J. Jang, "Microstructural investigation of low temperature chemical vapor deposited 3C-SiC/Si thin films using single-source precursors", *J. Mater. Res.* **14**, 24–28 (1999).
103. W.J. Choyke, "A review of radiation damage in SiC", in *Radiation Effects in Semiconductors 1976*, eds. N.B. Urli and J.W. Corber, *Inst. Phys. Conf. Ser.* No. 31, Institute of Physics, London, pp. 58–69 (1977).
104. Z.C. Feng, M.J. Bevan, W.J. Choyke, and S.V. Krishnaswamy, "A photoluminescence comparison of CdTe thin films grown by molecular beam epitaxy, metalorganic chemical vapor and UHV sputtered depositions", *J. Appl. Phys.* **64**, 2595–2600 (1988).
105. H. Itoh, M. Yosahito, I. Nashiyama, H. Okumura, S. Misawa, and S. Yoshida, "Photoluminescence of radiation induced defects in 3C-SiC epitaxially grown on Si", *J. Appl. Phys.* **77**, 837–842 (1995).
106. W.J. Choyke and L. Patrick, "Photoluminescence of radiation defects in cubic SiC: localized modes and Jahn-Teller effect", *Phys. Rev. B* **4**, 1843 (1971).

107. J.A. Freitas, Jr., S.G. Bishop, J.A. Edmond, J. Ryu, and R.F. Davis, "Photoluminescence spectroscopy of ion-implanted 3C-SiC grown by chemical vapor deposition", *J. Appl. Phys.* **61**, 2011–2016 (1987).
108. J.A. Freitas, Jr., S.G. Bishop, P.E.R. Nordquist, Jr. and M.L. Gipe, "Donor binding energies determined from temperature dependence of photoluminescence spectra in undoped and aluminum-doped beta SiC films", *Appl. Phys. Lett.* **52**, 1695–1697 (1988).
109. J.A. Freitas, Jr. and S.G. Bishop, "New deep acceptor in epitaxial cubic SiC", *Appl. Phys. Lett.* **55**, 2757–2759 (1989).
110. S.G. Bishop, J.A. Freitas, Jr., T.A. Kennedy, W.E. Carlos, W.J. Moore, P.E.R. Nordquist, Jr., and M.L. Gipe, "Donor identification in thin film cubic SiC", in *Amorphous and Crystalline Silicon Carbide*, eds. G.L. Harris and C.Y.-W. Yang, Springer Proceedings in Physics, Vol. 34, Springer, Berlin), pp. 90–98 (1989).
111. J.A. Freitas, S.G. Bishop, Jr., P.E.R. Nordquist, Jr., and M.L. Gipe, "Time-resolved photoluminescence studies of undoped and Al-doped cubic SiC", in *Amorphous and Crystalline Silicon Carbide and Related Materials II*, eds. G.L. Harris and C.Y.-W. Yang, Springer Proceedings in Physics, Vol. 43, Springer, Berlin, pp. 106–111 (1989).
112. S.G. Bishop and J.A. Freitas, Jr., "Photoluminescence characterization of cubic SiC grown by chemical vapor deposition on Si substrates", *J. Cryst. Growth* **106**, 38–46 (1990).
113. J.A. Freitas, Jr., P.B. Klein, and S.G. Bishop, "Photoluminescence excitation spectroscopy of cubic SiC grown by chemical vapor deposition on Si substrates", *Mater. Sci. Forum* **83–87**, 1195–1201 (1992).
114. W.J. Moore, J. Lin-Chung, J.A. Freitas, Jr., Y.M. Altaiskii, V.L. Zucz, and L.M. Ivanov, "Nitrogen donor excitation spectra in 3C-SiC", *Phys. Rev. B* **48**, 12289 (1993).
115. W.J. Moore, J.A. Freitas, Jr., and P.J. Lin-Chung, "Donors in cubic silicon carbide", *Solid State Commun.* **93**, 389–392 (1995).
116. D.N. Talwar and Z.C. Feng, "Tight-binding description for the bound electronic states of isolated single and paired native defects in β -SiC", *Phys. Rev. B* **44**, 3191–3198 (1991).
117. V. Nagesh, J.W. Farmer, R.F. Davis, and H.S. Kong, "Defects in neutron irradiated SiC", *Appl. Phys. Lett.* **50**, 1138–1140 (1987).
118. P. Zhou, M.G. Spencer, G.L. Harris, and K. Fekade, "Observation of deep levels in cubic silicon carbide", *Appl. Phys. Lett.* **50**, 1384–1386 (1987).
119. K. Zekentes, M. Kayiambaki, and G. Constantinidis, "Electron traps in β -SiC grown by chemical vapor deposition on silicon (100) substrates", *Appl. Phys. Lett.* **66**, 3015–3017 (1995).
120. C. Wang, J. Bernholc, and R.F. Davis, "Formation energies, abundances, and the electronic structure of native defects in cubic SiC", *Phys. Rev. B* **38**, 12752–12755 (1988).
121. W. Lu, K. Zhang, and X. Xie, "An electronic structure study of single native defects in beta-SiC", *J. Phys. Cond. Matter* **5**, 891 (1993).
122. Yu.M. Suleimanov, A.M. Grekhov, and V.M. Grekhov, "Vibronic structure of D₁ spectra of irradiated silicon carbide", *Sov. Phys. Solid State* **25**, 1060–1061 (1983).

123. H. Itoh, M. Yoshikawa, I. Nashiyama, S. Misawa, H. Okumura, and S. Yoshida, “Radiation induced defects in CVD-grown 3C-SiC”, IEEE Trans. Nucl. Sci. **37**, 1732–1738 (1990).
124. W.G. Spitzer, D.A. Kleinamn, and C.J. Frosch, “Infrared properties of cubic silicon carbide films”, Phys. Rev. **113**, 133–136 (1959).
125. R.T. Holm, P.H. Klein, and P.E.R. Nordquist, Jr., “Infrared reflectance evaluation of chemically vapor deposited β -SiC films grown on Si substrates”, J. Appl. Phys. **60**, 1479–1485 (1986).
126. Y.M. Lei, Y.H. Yu, L.L. Cheng, B. Sundaraval, E.Z. Luo, C.X. Ren, S.C. Zou, S.P. Wong, D.H. Chen, and I.H. Wilson, “Investigation and modeling of the infrared optical properties of direct current sputtered SiC films on silicon”, J. Appl. Phys. **88**, 3053–3058 (2000).
127. A. Romano-Rodriguez, A. Pérez-Rodriguez, C. Serre, J.R. Morante, J. Esteve, M.C. Acero, R. Kögler, W. Skorupa, M. Östling, N. Nordell, S. Karlsson, and J. Van Landuyt, Mater. Sci. Forum, **338–342**, 309–312 (2000).
128. Z.C. Feng, W.Y. Chang, S.J. Chua, J. Lin, and C.C. Tin, “Infrared optical investigation of 3C-SiC on Si”, in *Proceedings of the 25th International Conference on the Physics of Semiconductors*, Springer Proceedings in Physics, Vol. 87, Springer, Berlin, pp. 1559–1560 (2001).
129. Y.T. Hou, Z.C. Feng, S.J. Chua, M.F. Li, N. Akutsu, and K. Matsumoto, “Influence of Si-doping on the characteristics of GaN on sapphire by infrared reflectance”, Appl. Phys. Lett. **75**, 3117–3119 (1999).
130. S. Shokhovets, R. Goldhalm, V. Cimalla, T.S. Cheng, and C.T. Foxon, J. Appl. Phys. **84**, 1561–1566 (1998).
131. Z.C. Feng, S.J. Chua, G.A. Evans, J.W. Steeds, K.P.J. Williams, and G.D. Pitt, “Micro-Raman and photoluminescence study on n-type 6H-SiC”, Mater. Sci. Forum **353–356**, 345–348 (2001).
132. T. Yamada, K.M. Itoh, “Optical and electrical characterization of free-standing 3C-SiC films grown on undulant 6in Si substrates”, Mater. Sci. Forum **389–393**, 675–678 (2002).
133. T.S. Zheleva, O.-H. Nam, M.D. Bremser, and R.F. Davis, “Dislocation density reduction via lateral epitaxy in selectively grown GaN structures”, Appl. Phys. Lett. **71**, 2472–2474 (1997).
134. W.J. Choyke, H. Matsunami, and G. Pensl, eds., *Fundamental Questions and Applications of SiC* (part II), Phys. Stat. Solidi (a) **162**, No. 1 (1997); *Silicon Carbide: Recent Major Advances*, Springer, Berlin (2004).

Electron Paramagnetic Resonance Characterization of SiC

M.E. Zvanut

Electron paramagnetic resonance (EPR) spectroscopy is a powerful tool for studying the physical and chemical structure of point defects in crystalline semiconductors. Investigations throughout the past few decades have provided detailed descriptions of some of the most important intrinsic defects and impurities in silicon carbide. Several reviews summarize the significant findings. This chapter expands the scope of earlier work by focusing on EPR studies of as-grown electronic-grade SiC. Both intrinsic and extrinsic defects pertinent to devices are discussed. In particular, impurities used to produce n- and p-type wafers and those incorporated to yield semi-insulating SiC are reviewed. In addition, defects generated by ion implantation are also discussed. To avoid repetition of previously published reviews, the physical description of the defects is only briefly summarized. Rather, this chapter emphasizes the use of collaborative techniques to determine defect energy levels and electrical-passivation mechanisms. Overall, the chapter highlights the contribution of EPR to understanding the electrical, physical, and chemical processes important to technological applications of silicon carbide.

7.1 Introduction

Electron paramagnetic resonance (EPR) spectroscopy has been used since the fifties to study electronic materials such as Si, the II-VI semiconductors, and GaAs. EPR, or electron spin resonance (ESR) as it sometimes called, utilizes the absorption of microwaves by a point defect to determine the detailed electronic structure and symmetry. Since the signal obtained is a response to changes in magnetic dipole orientation (ie. a ‘spin-flip’), only paramagnetic defects may be detected. That is, the EPR signal intensity is proportional to the number of defects with unpaired electrons. The magnetic interactions among the electron, local environment and applied magnetic field enable one to paint a detailed picture of the chemical and physical structure of a defect.

For instance, from analysis of EPR spectra at various temperatures and orientations the boron acceptor in SiC is generally thought to substitute for Si at the hexagonal site with the hole situated primarily on a nearest neighbor C.

Many texts describe the theoretical basis and basic applications of EPR for a variety of semiconductor systems, including SiC [1–6]. The work presented below concentrates exclusively on the defects pertinent to device applications, and the description of the technique is limited to aspects that will enable the interested reader to determine the applicability of EPR to their problem. As a result, no information will be provided which enables a novice to measure spectra and interpret the results. Only the rudimentary steps needed to paint a picture of a defect from measured EPR spectra is presented. For details, the reader is referred to several excellent texts, particularly [1–3].

The chapter is divided into four sections. Section 7.1 contains the fundamentals of EPR spectroscopy necessary to appreciate the following discussions and assess the applicability of the technique to a variety of situations. The next two sections focus on specific point defects, with Sect. 7.2 covering intrinsic centers including those induced by growth and ion-implantation. Section 7.3 focuses on acceptor and donor impurities such as Al, B, and N, as well as the deep level impurities thought to cause electrical compensation. Note that throughout this chapter, the term ‘defect’ will be used to refer to both intrinsic centers, like dangling bonds and vacancies, and extrinsic centers such as impurities. Section 7.4 contains a few final concluding remarks about the prospects of further studies using EPR.

Before continuing, the reader should recognize the valuable contribution of several other types of magnetic resonance techniques. Electron nuclear double resonance (ENDOR), optically detected magnetic resonance (ODMR), and electrically detected magnetic resonance (EDMR), have been valuable tools for confirming the chemical and physical structure of point defects in SiC. More recently, spin echo and high magnetic field experiments have provided detailed pictures of a variety of centers. Of course, a complete, well-accepted description of any defect requires years of investigations and inclusion of non-magnetic resonance techniques as well. Although decades of SiC studies have produced libraries of literature covering a wide range of defects, the SiC substrates being produced today for electronic applications have yielded many new results. These are the focus of this chapter.

7.1.1 The Technique

As stated earlier, EPR senses the spin-flip caused by the presence of an external magnetic field at paramagnetic centers. This implies that only those defects with unpaired electrons will be detected. As seen throughout this chapter, rather than a limitation, focusing on defects with unpaired electrons is an advantage because by restricting detection to certain charge states, the change in charge state may be observed by monitoring the signal intensity due to a specific center. Furthermore, many of the technologically relevant

impurities and intrinsic defects are paramagnetic or may be excited to their paramagnetic state. The heart of the technique is illustrated in Fig. 7.1. The top portion shows the basic spectrometer consisting of the klystron or Gunn diode used to produce the microwave radiation, microwave bridge for setting the desired power, wave guides which transmit the radiation to the sample, and cavity resonator in which a particular mode of the microwave is stored. Because radiation of this wavelength is not easily varied, a fixed frequency is used, commonly 10 GHz. The sample is placed in the ‘bath’ of microwaves stored in the cavity, and a magnetic field is applied to create the condition necessary for absorption. Simply put, the applied magnetic field, B , splits the energy levels of the electron’s spin-up and spin-down states (the Zeeman Effect) (see Fig. 7.1 and [1–3]). Since the energy difference is proportional to B , ramping the magnetic field allows one to search for the field at which absorption of the microwave energy (E) at a specific defect will occur. The absorption detected in the external circuitry produces a signal shown in bottom portion of Fig. 7.1. In order to increase the signal-to-noise ratio so that the low number of paramagnetic centers typical of electronic materials may be observed, an oscillating magnetic field is super-imposed on the ramped field. As a result, the change in the absorption is detected, producing the derivative-like line shape shown in the figure.

EPR centers are generally characterized by a g -tensor as well as a number of other parameters reflecting the symmetry and chemical make-up of the defect. In the simplest case, the g -tensor is derived from the g -value (g) measured at each orientation of the sample with respect to the incident magnetic field:

$$B_0 = hv/g\mu_b ,$$

where B_0 is the value of applied magnetic field at resonance, h is Planck’s constant, v is the microwave frequency, and μ_b is the Bohr magneton. The g -value is basically the Lande free electron value shifted by an amount that depends on the local environment of the defect. Thus, each defect has a characteristic g -tensor. However, the g -value alone is not sufficient to describe an EPR center. The effect of the nuclear magnetic field, crystal field, and nearby paramagnetic defects may change the absorption energy. A full quantum mechanical treatment of their effect is given in [1–3]. Suffice it to say that by the application of theory to an intensive set of experimental data, a spectrum is interpreted in terms of a specific chemical impurity or intrinsic defect. In addition, angular dependence studies provide the local symmetry of the defect, and double integration of the EPR signal yields the number of centers.

To provide some feel for the interpretation of EPR spectra, two examples are provided: the shallow nitrogen donor and native carbon vacancy in SiC. Figure 7.2 shows the characteristic fingerprint of isolated N atoms at a cubic site: three evenly spaced lines of equal intensity. The arrows point to the three hyperfine lines arising from interaction of the applied and local magnetic fields with the nitrogen nuclei. The central line is distorted by the presence

Basis of EPR Spectroscopy

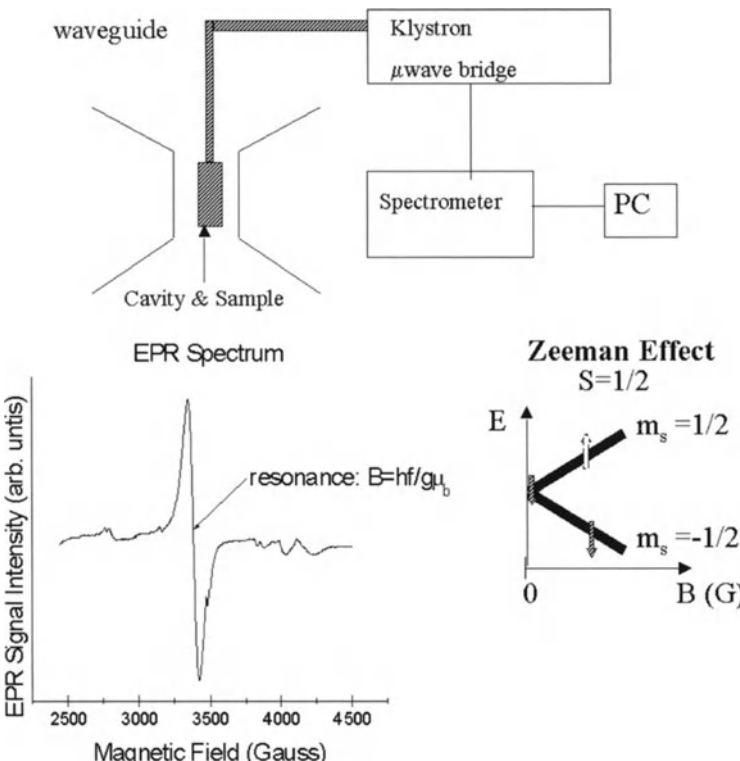


Fig. 7.1. *Top center:* schematic of EPR system. *Bottom right:* energy levels of spin- $\frac{1}{2}$ particle split by applied magnetic field B ; m_s represents the magnetic spin quantum number. *Bottom left:* typical EPR spectrum – the large signal at $B \sim 3400$ G represents the defect of interest. Smaller signals on the left and right arise from the background

of an additional, unrelated signal. The Zeeman energy at which the paramagnetic electron absorbs the incident radiation, E_z , is shifted by the interaction between the electron and the magnetic moment of the nitrogen nucleus (the hyperfine interaction). Since almost all nitrogen atoms have a nuclear spin of one, the Zeeman energy at every nitrogen has equal probability of being lowered ($m_I = -1$), increased ($m_I = +1$), or unaffected ($m_I = 0$) depending on the relative orientations of the electron and nuclear dipole moments. Thus, three lines of equal intensity are produced: one representing $E_z - E_{hf}$, one $E_z + E_{hf}$, and one E_z , where E_{hf} is hyperfine interaction energy. The magnetic field separation between the lines is proportional to E_{hf} . The g -value is

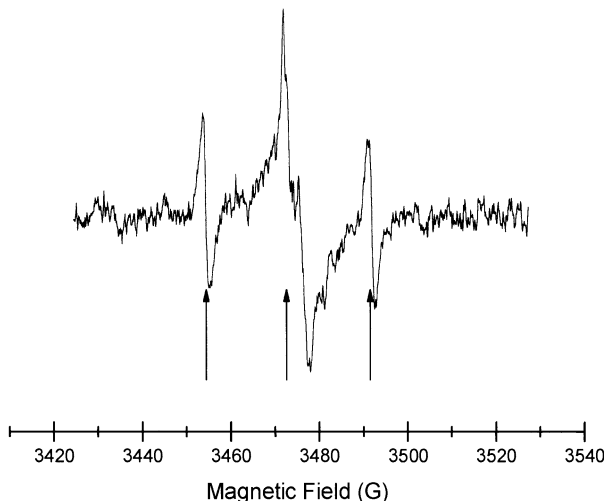


Fig. 7.2. EPR spectrum of nitrogen at the cubic site in 4H-SiC measured at 4 K. The arrows point to the three lines associated with the nitrogen impurity; the fourth signal is unrelated

obtained from the average B_0 of the outer two lines, or, in this case, B_0 of the central line.

From the above, it should be apparent that observation of the nuclear hyperfine lines is the key to determining the chemical origin of an EPR center. Unfortunately, not all impurities have isotopes with 100% abundant non-zero nuclear spin. In particular, only 4.5% of all Si atoms (^{29}Si) and a mere 1.1% of carbon atoms (^{13}C) are spin 1/2. Therefore, since E_{hf} for vacancies arises from neighboring atoms only, such defects in SiC have very low probability of being situated near a nucleus of non-zero spin. In these cases, the spectrum consists of a strong Zeeman line due to defects involving spin zero Si and C nuclei, and pairs of equally spaced smaller lines due to the very few defects involving spin 1/2 Si and C nuclei. The separation between the satellite lines is proportional to the hyperfine interaction energy. Figure 7.3 shows an EPR measurement of V_C with the magnetic field oriented along the c -axis. The spectrum is magnified to emphasize the position of the satellite lines, A and B, which arise from the spin 1/2 nearest neighbor Si nuclei. The relative integrated intensity of set A to the central lines is about 5% and that of set B is 15%. The outer set is attributed to those centers with one nearest neighbor spin 1/2 nucleus; the inner set to those in which any one of the three Si neighbors is spin 1/2. See sketch in upper left corner of figure. The larger separation between one pair of lines than the others is due to the stronger interaction energy between the vacancy and one 'special' nucleus. The situation for V_C is thought to arise from a slight distortion along the c -axis causing the Si along the [0001] direction to move from or towards the vacancy by an amount different from that of the three neighbors in the basal plane. Additional

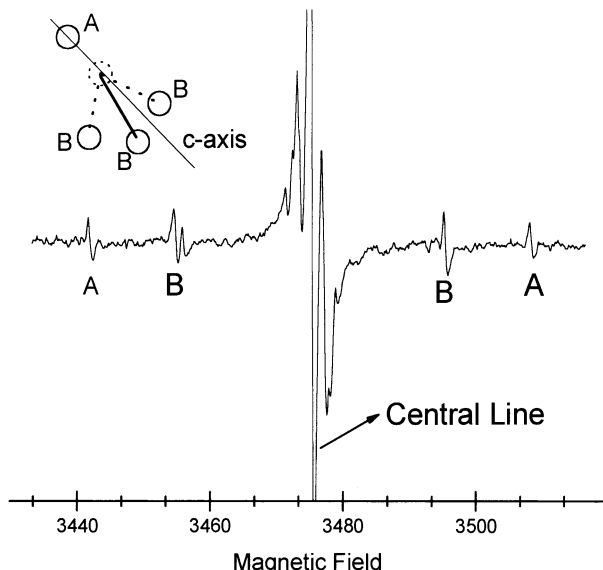


Fig. 7.3. EPR spectrum of V_C measured with the magnetic field parallel to the c -axis. The *central line* is truncated so that the satellite lines, A and B, may be more clearly seen. The *inset* shows a schematic of the carbon vacancy: the *dashed circle* represents the vacancy; the other four circles represent the Si nearest neighbors

measurements including temperature and angular dependence support this picture. In summary, detection of two sets of hyperfine lines with intensity equivalent to interactions with four Si atoms distinguished by two different energies paints a picture of a carbon vacancy slightly distorted along the c -axis. The charge state is concluded to be positive, consistent with the electron spin- $\frac{1}{2}$ nature of the EPR signal and observation of the spectrum in p-type and Si material only.

In addition to a physical description, EPR data may provide the total number of centers. This is accomplished by comparing the spectra of an unknown quantity of a defect with that obtained from a known quantity. Significantly, the EPR signal from the standard need not arise from the same defect or even a different defect in the same material. This convenience is afforded by the fact that the spin-flip probability is independent of the local environment. Common calibration standards include DPPH and the phosphorus signal in powdered n-type Si. In principle, the comparison can lead to an absolute number of spins with an accuracy of 50% with sensitivity as low as 10^{10} spins [3]. A couple of items to remember regarding the absolute spin measurement:

- 1) Only the paramagnetic state of any defect is being measured. For instance, the number of shallow boron acceptors on the hexagonal site may be calculated. However, the result is limited to acceptors that have captured the hole in the valence band. For this reason, EPR of shallow defects is often

performed at low temperature to more closely reflect the total number of acceptors. Compensation by deeper levels, an issue addressed later in this chapter, may further reduce the number of EPR-active boron sites. Although the amount of the impurity calculated from the acceptor signal will not include boron aggregates, boron complexes, or other forms of boron, different EPR signals may be related to these entities and measured separately.

- 2) Only the total number of centers is determined. Additional experiments are needed to find the spatial distribution of defects. When concentration is given in an EPR study, the centers are assumed to be uniformly distributed throughout the material unless otherwise stated.

Several EPR parameters used to obtain spectra affect the signal intensity. Microwave power and magnetic field modulation amplitude, common variables in any EPR measurement, are chosen to maximize detection while minimally distorting the line shape. In special cases, DC magnetic field ramp rate and modulation frequency may also be changed. Manipulation of ramp rate can lead to detection of signals not observed by conventional parameter settings. For example, the V_C - C_{Si} pair in SiC is detected using ‘fast passage’ conditions, a version of the standard measurement in which the ramp time for the DC magnetic field is shorter than the spin relaxation time constants, and the amplitude of the modulated magnetic field is sufficiently large [3]. Although special care must be taken in interpreting the total number of spins using this method, the approach is invaluable for detecting some defects [7].

7.1.2 Collaborative Techniques

Sometimes the paramagnetic state of a defect is induced by an external source. High energy particle irradiation has commonly been used; however, unless one is interested in radiation damage, the additional defects which are usually created during the procedure can confuse interpretation and minimize the relevance to technological applications. The interested reader may consult [4] for a review of radiation-induced defects. Below, optically and thermally-induced methods are discussed.

Optical illumination may excite the EPR active state in two different ways. Using low infrared wavelengths, diamagnetic ($S = 0$) centers may be excited to their triplet ($S = 1$) state where the $\Delta m_s = 1$ transitions within the $S = 1$ manifold may be seen. The spin state is deduced by the presence of $2S$ number of lines and the lower probability $\Delta m_s = 2$ transition ('half-field' lines). Recently, the carbon vacancy-carbon antisite (V_C - C_{Si}) pair was identified in high purity SI SiC using this method. Radiation such as near infrared, visible, or ultraviolet may ionize the defect by removing an electron to the conduction band or by exciting an electron from the valence band. This not only enables detection of previously compensated centers, but may lead to determination of the electrical level of the defect [8]. For instance, the

$V^{4+/5+}$ level was found to be 1.6 eV above the valence band edge, E_v , using photo-induced EPR [5]. More recently, the level for the carbon vacancy, V_C , was also reported.

The affects of heat treatment in various ambient may also be monitored with EPR when the temperature is sufficient to change the paramagnetic state of a center or remove the defect responsible for the EPR signal. An example of particular significance to the electronics community is the passivation of defects by hydrogen. The free electron of the hydrogen atom can react with a paramagnetic defect to form a non-EPR center. Heat treatment at the appropriate temperature may break the H-defect bond, thereby unveiling the EPR active state. The passivation of donors and acceptors, as well as carbon dangling bonds, is reviewed later in this chapter.

The defects pertinent to electronic-grade SiC are listed in column one of Table 7.1. Column 2 shows the minimum number of centers required for detection using a state of the art spectrometer such as the ESR EMX produced by Bruker Inc. The values are based on spectra recorded at the optimal temperature for detection, usually 4 K. The linewidth of the signal, which depends on sample quality and defect density, strongly affects detection capability. The sensitivity reported in the table was calculated using typical linewidths obtained from personal experience and observation of those reported in the literature, but it should be recognized that these may vary by as much as a factor of ten. The shallow boron linewidth, for instance, is reported from 0.1 G to as large as 1 G. The other major factor influencing sensitivity is the number of lines associated with a spectrum. The total electron spin and spin of neighboring nuclei split a resonance line by $2S$ and $2I + 1$, respectively. Thus, V^{3+} with electron spin 1 and nuclear spin 7/2 produces 16 lines at each site, greatly increasing the detection minimum. Many other factors affect sensitivity, so the numbers in column two should be viewed as ‘rule of thumb’ estimates only. Also listed in the table is the site at which the center is thought to reside. Those accompanied by a ‘?’ represent preliminary assignments. The references in the last column provide a detailed spectroscopic description of each defect.

Table 7.1. EPR centers commonly detected in electronic-grade as-grown 4H-SiC*

Defect	Sensitivity	Site	Reference
N	7×10^{11}	C – hex, cubic	[6]
P	5×10^{11}	Si – hex, cubic (?)	[38–41]
B	2×10^{12}	Si – hex, cubic	[6]
Al	2×10^{11}	Si – one line attributed to both sites	[6, 42]
V^{4+}	1×10^{13}	Si – hex, cubic	[52]
V^{3+}	2×10^{15}	Si – hex, cubic	[52]
V_C	4×10^{11}	Hex (?), cubic (?)	[25–28]

* Table assumes a maximum sensitivity of 10^{11} spins/1 G linewidth at 300 K

7.2 Intrinsic Defects

This section reviews two categories of intrinsic defects pertinent to electronic grade SiC. Specifically, EPR centers found in as-grown SiC and ion-implanted material are reviewed. Here, as well as in the next section, results obtained from the 4H polytype are emphasized. Thus, when not specified, ‘SiC’ means 4H-SiC. Otherwise, the polytype is noted.

7.2.1 As-Grown SiC

Until about five years ago, there were very few reports of defects in bulk as-grown hexagonal SiC. Generally, high energy radiation is employed to enhance the typically low number of intrinsic defects. Indeed, it is from irradiation studies that most of the detailed description of the intrinsic centers arises. As of this writing, two of the defects previously identified in irradiated samples have been identified in as-grown SiC wafers: a carbon vacancy-related center (V_C) and a carbon vacancy-carbon antisite pair (V_C-C_{Si}). In addition to these, several groups debate the origin of a third as a silicon antisite or a carbon vacancy located on different symmetry site than the one earlier identified. In as-grown material, the defects addressed below are seen exclusively in semi-insulating wafers suggesting that their paramagnetic charge state lies energetically deep within the band gap.

The carbon vacancy-related center in non-irradiated 4H-SiC was identified only recently by Zvanut and Konovalov [9, 10]. The spectroscopic features of the center match closely with those reported earlier in 2 MeV electron-irradiated material. From analysis of the relative intensities of the hyperfine lines and central line, Son and coworkers determined that the spectrum was due to a carbon vacancy-related center [11]. Recent theoretical calculations support that conclusion [12]. Observation of an EPR active state for the carbon vacancy is somewhat surprising because earlier theoretical calculations based on *ab initio* density functional theory and the local spin-density approximation predicted a negative correlation energy for V_C [13]. The results imply that the only stable states for the carbon vacancy are the doubly-positively charged state, the neutral state, and the doubly negatively charged state, all of which are non-paramagnetic. Nevertheless, several investigations support the identification of the defect as a carbon vacancy. Furthermore, the center is thought to be in the positive charge state because the defect has spin 1/2 and is not seen in n-type material.

Photo-induced EPR, a method in which the EPR signal is measured after exposure to selected photon energy, reveals a threshold for the decay of V_C at 1.5 eV [14]. Although the data may be interpreted in terms of an energy level for V_C as $E_v + 1.5$ eV or $E_c - 1.5$ eV, the authors assume the positive charge state for V_C and conclude that the results represent the $V_C(+/-)$ level at 1.5 eV above E_v [14]. Torpo and co-workers predict a defect level remarkably similar to the one revealed by photo-EPR; furthermore, they show that the

negative correlation energy may be eliminated by inclusion of a Madelung correction into the *ab initio* calculation [15]. The assignment of the defect level with respect to the valence band edge is further supported by the original photo-EPR measurements that produced a decay in the V_C signal intensity at 1.1 eV accompanied by an approximately equal increase in the boron signal at the same photon energy [9, 10]. Figure 7.4 shows the concentrations of V_C (\bullet) and B (\circ), relative to their respective maximum concentration, $[X]_{\max}$. Note that the maximum concentration of boron is approximately ten times that of V_C . If direct defect-to-defect charge transfer is assumed, the results are consistent with the 1.5 eV $V_C(+/0)$ level recently reported. The level is obtained by adding the (1.1 ± 0.2) eV V_C and B threshold energies to the known defect level for the boron acceptor ($0.3 - 0.4$ eV above E_v). Based on the results discussed above, it appears the plus-to-neutral transition energy of V_C is confirmed. However, photo-induced EPR measurements of several different as-grown SI SiC wafers show variations in the optical threshold for the EPR response of V_C from 0.7 to 1.5 eV [16, 17]. Thus, it appears that further work is required before the carbon vacancy level may be conclusively determined. Finally, it should be mentioned that Kalabukhova and coworkers performed photo-excitation and photo-quenching measurements on semi-insulating material [18]. They identify a spectrum, I_p , for which the wavelength dependence of the signal's decay after exposure to band gap illumination is consistent with the 1.5 eV defect level; however, the defect has a *g*-tensor which differs from that of V_C , and no further interpretation of the spectrum is provided.

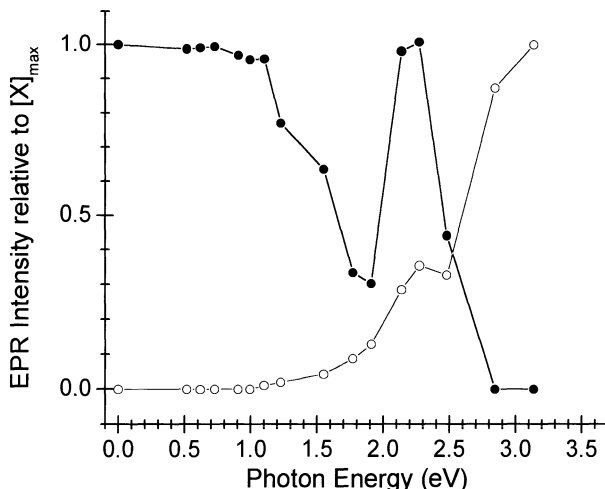


Fig. 7.4. Photoinduced EPR data obtained from as-grown 4H high-purity SI SiC. Filled circles, V_C ; unfilled circles, shallow boron acceptor. The intensity is measured relative to the maximum observed for each center; the total amount of boron is about ten times that of V_C .

The stability of the carbon vacancy is reported in several studies, all indicating that the defect survives temperatures of at least 1600 °C [19, 20]. High temperature annealing of nominally SI 4H-SiC changes the intensity of both V_C and the boron acceptor, but only after temperatures greater than 1000 °C in an Ar ambient. Figure 7.5 shows the concentration of carbon vacancies and boron acceptors as a function of anneal temperature. The data reveal a decrease in the carbon vacancy concentration and an increase in boron at about the same temperature, 1000 °C. Furthermore, within the factor of two experimental error typical of EPR absolute concentration calculations, a one-to-one exchange between B and V_C is observed in the temperature range of 1000–1400 °C. However, above 1400 °C the total amount of boron exceeds that of the carbon vacancies. The concentration of boron acceptors obtained after the 1700 °C anneal is about 10 times bigger than the initial concentration of V_C . After the final heat treatment, the EPR spectrum was measured while exposing the sample to light. Sub-band gap illumination (578 nm) of the 1700 °C annealed sample restored the V_C signal to the original intensity and increased the boron spectral lines. The arrows in Fig. 7.5 point to the concentrations measured after illumination. The photo-induced EPR results indicate that V_C and B increased by approximately the same amount and that thermal annealing did not annihilate the carbon vacancies in this sample.

The trend observed between 1000–1400 °C and the measurements made after exposure to sub-band gap light highlight several important results. First, carbon vacancies can compensate boron acceptors. Second, the gradual reduction of V_C above 1000 °C is caused by charge exchange with shallow boron acceptors in these samples. Furthermore, the annealing results combined with

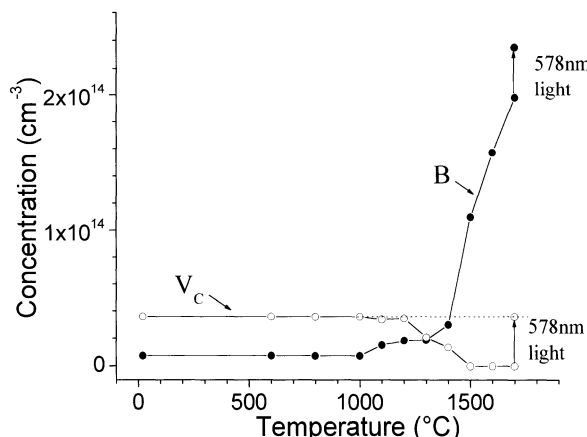


Fig. 7.5. Concentration of V_C (unfilled circles) and shallow B acceptor centers (filled circles) in 4H-SiC as a function of annealing in dry Ar at the specified temperature. Arrows show the increase of V_C and B signals during exposure to 578 nm light ([20], p. 446, Fig. 2)

the photo-induced EPR data taken after the 1700 °C anneal reveal that although heat treatment may change the charge state of V_C , the defect is thermally stable up to 1700 °C. However, it is cautioned that results like those shown in Fig. 7.5 are expected to depend on the amount of both extended and point defects in the crystal. Clearly, additional studies including annealing and photo-induced EPR on a wide variety of samples must be performed before the fundamental annealing kinetics of the carbon vacancy can be definitively established.

The near-midgap level measured for V_C might suggest that the carbon vacancy is the major contributor to the compensation of shallow acceptors and donors. However, the V_C concentration reported is no more than $5 \times 10^{14} \text{ cm}^{-3}$, about an order of magnitude less than reported for B acceptors or N donors in the same material [21]. Recently, Carlos and coworkers reported the observation of a carbon vacancy-carbon antisite pair ($V_C\text{-}C_{Si}$)⁺⁺ with sufficient concentration to electrically compensate most high purity SiC material [7]. The spectra was first seen by Vainer and Ill'in in as-grown lightly doped 6H-SiC:N, and later identified through EPR studies of neutron-irradiated n-type 6H-SiC [22, 23]. The spectral signatures, referred to as P6 and P7, reflect two different configurations of the defect. P6 is aligned along the *c*-axis, exhibits axial symmetry, and occupies both the cubic and hexagonal lattice sites. The symmetry of P7 is non-axial and appears to arise from the three basal bonds. Unlike the isolated carbon vacancy discussed earlier, the pair defect is observed only during excitation with near infrared light ($\sim 1 - 1.5 \text{ eV}$). This is because the defect has two ‘unpaired holes’ which make the total spin 1. Of the two states for this entity, $S = 0$ and $S = 1$, the $S = 0$ diamagnetic state is the lowest. The light, then, excites the defect to its paramagnetic triplet ($S = 1$) state where the EPR transitions occur.

The defect levels for the $V_C\text{-}C_{Si}$ pair have not been measured; however theoretical studies have determined which charge states should have levels in the band gap. The calculations show that only the double-plus and neutral states will exist because the pair exhibits a negative correlation energy [23]. That is, the energy required to capture two electrons at ($V_C\text{-}C_{Si}$)⁺⁺ is less than that required to capture just one electron. The negative correlation energy implies that the carbon vacancy-carbon antisite pair is an efficient compensating defect; thus, supporting the conclusion that the defect likely plays a major role in the compensation of SI SiC.

Several theoretical studies and one positron annihilation investigation suggest the existence of antisite defects in SiC [15, 24]. Recently, Son and coworkers identified a set of EPR lines in irradiated p-type SiC as an isolated silicon antisite (Si_C) [25]. However, earlier work in 2 MeV electron-irradiated 6H-SiC and more recent work in as-grown high purity 4H wafers indicates that the spectrum is due to a carbon vacancy-related center [26, 27]. The latter two studies suggest that this center and the previously discussed V_C may represent carbon vacancies situated on the two inequivalent lattice sites in 4H-SiC. Theoretical calculations of the electron-nuclear hyperfine energy support the

carbon vacancy assignment as does the nearly similar energy at which the centers are optically quenched, ~ 1 eV [27, 28]. Given the significant role played by vacancies and antisites in diffusion during high temperature annealing, clarification of this issue is of high importance.

Room temperature EPR studies of as-grown SiC wafers usually reveal an isotropic line with g values ranging between 2.0024 to 2.0026 in 4H-SiC [29, 30]. Comparison with similar EPR spectra in intentionally damaged and amorphous SiC suggests that the defect is a C-dangling bond. In [30], the defect was examined by first oxidizing SiC in steam at 1150 °C for 6 hours to eliminate the center. The samples were then heat treated in dry N₂ (99.999% pure) for 200 min at 900 °C. In all three polytypes, 3C, 6H, and 4H, the signal was quenched by the oxidation and regenerated by the heat treatment. The relative amplitude of the EPR signal measured during an isochronal annealing study of 3C (unfilled circles) and 6H-SiC (filled squares) is shown in Fig. 7.6. The maximum total number of centers is on the order of 10¹². The results were interpreted in terms of removal of hydrogen from a carbon dangling bond. The activation energy calculated from these data, (4.0 ± 0.3) eV, is consistent with the expected strength of a C-H bond, supporting the defect depassivation interpretation. After generating the C-dangling bond signal, samples were subjected to a series of anneals in forming gas (H₂/N₂) at temperatures up to 700 °C. Figure 7.7 shows the results for both the undoped 3C (unfilled circles) and p-type 6H-SiC (filled squares). The difference in energy required to re-passivate the centers is thought to be related to the dependence of hydrogen diffusivity on resistivity rather than polytype. In summary, the activation/passivation study suggest that the C-dangling bond in SiC may be ‘cured’ by a low temperature (< 700 °C) forming gas anneal but the passiva-

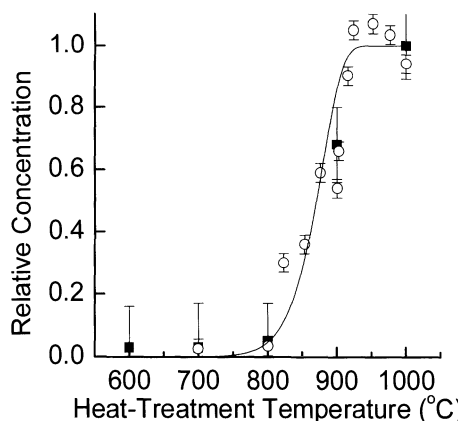


Fig. 7.6. Activation profile for the center in oxidized 3C-SiC epilayer samples (unfilled circles) and 6H-SiC (filled squares). The solid line represents a fit of the Arrhenius equation to the 3C-SiC data, from which an activation energy of (4.0 ± 0.3) eV is estimated ([30], p. 4122, Fig. 4)

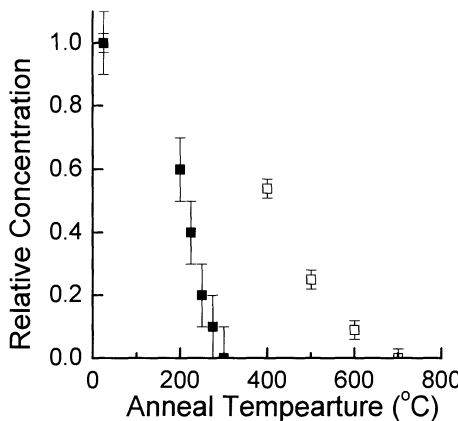


Fig. 7.7. The concentration of centers in oxidized, dry-heat-treated 6H- (*filled squares*) and 3C- (*unfilled squares*) SiC as a function of annealing temperature in forming gas (7% H₂ and 93% N₂) ([30], p. 4122, Fig. 5)

tion is not stable. Thermal treatments at temperatures greater than 800 °C release the hydrogen, regenerating the dangling bond defect.

The location of carbon dangling bonds is of critical importance for device applications. A defect in the SiC bulk or at the surface could have deleterious affects on any planar field-effect transistor. Furthermore, studies of metal-oxide semiconductors structures indicate that defects in the oxide and at the SiC/oxide interface will also affect device operation. Thus, the location of the centers discussed above was studied by a series of etching experiments [31]. First, the oxide was etched with a hydrogen fluoride (HF) solution. The EPR intensity did not change until all of the oxide had been removed indicating that the defects are located in the SiC or near the SiC/oxide interface. A similar result was found by Gerardi and coworkers [29]. The depth distribution below the SiC surface was measured using a series of oxidations to remove layers of SiC. Since the defect is known to be passivated by the oxidation process, the oxidized-etched samples were heat-treated in dry N₂ to reactive the centers. After each oxidation/heat treatment step, the number of centers was measured with EPR. The amount of centers observed after at least 1 μm of SiC was removed was within a factor of two of the original number of defects. This result indicates that the centers are not located at the abrupt SiC/SiO₂ interface, and that the C-dangling bond is distributed throughout the thickness of the wafer. However, a second explanation is offered by the authors. Recalling that the activation/passivation studies indicate that detection of the center involves out-diffusion of H and that the H diffusion rate should be very low, the authors suggest the reason the dangling bond center persists after removing SiC is because the oxidation itself generates the defect within a few monolayers of the SiC surface. Thus, the work offers two possible scenarios: the defects are incorporated throughout the bulk during

growth or they are generated near the surface during oxidation. Note that if the 10^{12} defects measured after each oxidation/heat treatment are distributed uniformly throughout the wafer, the density of these dangling bonds is less than $2 \times 10^{13} \text{ cm}^{-3}$. However, if the centers are generated during oxidation and only those within the maximum estimated 1 μm diffusion depth of hydrogen are seen, the density may be as high as 10^{16} cm^{-3} , similar to a typical doping concentration. Whichever situation applies, the presence of carbon-dangling bonds near the surface or distributed throughout the bulk should not be ignored in the analysis of defects affecting device performance.

Although V_C , $V_{C-\text{Cs}_i}$, and the debated second V_C (Si_c) are the only intrinsic centers identified in bulk as-grown SiC, it should be noted that most of the defects revealed by magnetic resonance studies of irradiated samples likely exist prior to irradiation. These include the negatively charged and neutral silicon vacancy and several types of complex defects involving H or other impurities. As high purity, high quality material becomes more readily available, such defects will no doubt be revealed and their complex interactions with the lattice thoroughly studied.

7.2.2 Implantation-Induced Defects

The most technologically important defect-related studies regarding ion-implantation into SiC are those involving dopant impurities such as N, Al, or B. The main focus of doping by implantation is formation of an abrupt implanted profile at specified depths below the surface of a homo-epitaxially grown layer of SiC. Unfortunately, EPR measurements of such samples cannot differentiate between the 500 μm -thick substrate and the $\sim 1 \mu\text{m}$ -thick epitaxial layer; thus direct information about an implanted epitaxial layer too thin to be removed from the substrate is not easily obtained. Discussed below are results from several related studies that may serve as a guide as to the type of defects that may be produced during implantation.

Barklie and coworker performed EPR on (0001) 6H-SiC implanted with 200 keV Ge ions at room temperature [32]. One isotropic resonance signal with varying line width and line shape is observed over a dose range of 10^{12} to 10^{15} cm^{-2} . The EPR spectrum is deconvoluted into two separate signals, one with a broad line-width indicative of several different types of isolated intrinsic defects and a narrow one most likely due to carbon dangling bonds. Below $3 \times 10^{14} \text{ cm}^{-2}$, the broad signal dominates; while beyond this value, the narrow one grows rapidly. Annealing studies of the broad signal show that the temperature dependence does not exhibit a simple Arrhenius behavior suggesting multiple activation energies due to the different types of defects such as V_{Si} and divacancies. The number of defects decreases by an order of magnitude by 500 °C, typical of radiation-induced intrinsic defects. The g value of the narrow signal seen at higher doses is similar to that observed in a-C and a-SiC; therefore, Barklie and coworkers attributed the resonance line to carbon dangling bonds. Its dominance at doses just below those required

for formation of a continuous buried amorphous layer is consistent with this assignment.

The second study pertinent to device production involves room temperature proton-implantation into n-type 6H and 4H-SiC [33]. Ions were accelerated to 12 MeV in order to specifically study the straggle region of implantation. At this energy, the protons penetrate the entire wafer, providing sufficient implanted material for a meaningful EPR study. After implantation, two types of defects are observed, the negatively charged silicon vacancy (V_{Si}^-) and the neutral silicon vacancy (V_{Si}^0). Interestingly, the EPR spectrum of V_{Si}^- at the cubic and hexagonal sites has the same EPR parameters indicating that the defect is site insensitive, but the two different sites are distinguished for V_{Si}^0 . Neither the dose dependence nor the temperature dependence is remarkably different for the two charge states of V_{Si} . The limited annealing studies performed indicate that the concentration of all implantation-induced centers are reduced by at least an order of magnitude after a 900 °C anneal. The results are similar for both polytypes.

The maximum total concentration of EPR centers was measured to be about $1.9 \times 10^{17} \text{ cm}^{-3}$ after a proton dose of 10^{16} cm^{-2} ; however, SRIM calculations predict that the density of defects created by implantation for this dose is $3.7 \times 10^{18} \text{ cm}^{-3}$. The authors argue that the discrepancy is due to the neglect of interstitial/vacancy interaction in the SRIM calculation. Interstitials created during room temperature implantation may capture the vacancy, thereby reducing the total number. A similar situation has been noted for implantation into n-type Si. It is also observed that after implantation, the samples become more resistive as indicated by the change in the EPR sensitivity [34]. This is consistent with the simultaneous observation of both charge states of the silicon vacancy. Theory predicts that the 0/- and -/- transitions are closer to mid-gap than the nitrogen donor which presumably dominates prior to implantation. Thus, the creation of intrinsic defects has lowered the Fermi level, producing more resistive material. The authors further support their conclusion by noting that the concentration of silicon vacancies is nearly equal to the nitrogen donor density.

Perhaps the study most directly related to device fabrication is that by Bratus and co-workers who studied the damage created by 150 keV Al^+ ions implanted in 6H-SiC at room temperature [35]. They implanted doses between 3×10^{13} to $5 \times 10^{16} \text{ cm}^{-2}$. Results from the lower doses are pertinent to production of such active regions as buried channels in charge coupled devices and counter-doping in metal oxide semiconductor field effect transistors. At the higher doses, the results may be used to understand the mechanisms involved in source and drain formation or contact improvement. EPR spectra reveal dose dependent line broadening effects similar to those seen during Ge^+ implantation. However, the maximum linewidth occurred at an Al^+ dose well below that required for amorphization; thus, rather than a reduction of crystallinity, the linewidth dependence on dose was attributed to dipolar and exchange effects resulting from communication between closely packed para-

magnetic species. Annealing at temperatures up to 1100 °C for ten-minute intervals reduced the defect density by about two orders of magnitude; however, no isolated Al impurities were detected. Rather, the signal observed was similar to one often attributed to broken Si and C bonds, as in the case of Ge⁺ implanted SiC. It remains to be seen whether implantation at higher temperatures typically used for device processing will eliminate the high density of dangling bonds found in these experiments and produce spectra characteristic of the substitutional Al acceptor.

7.3 Impurity-Related Defects

This section will first cover the shallow impurities pertinent to device applications, N, Al, and B. Then, the transition metals, primarily vanadium, will be discussed with respect to their potential role in compensation.

7.3.1 Shallow Impurities

Nitrogen is the only impurity commonly employed as an n-type dopant in SiC. In the 4H polytype, there are two electrical levels for the neutral-to-positive charge state transition, 0.521 eV and 0.918 eV below the conduction band edge, E_c , as measured by infra-red spectroscopy [36]. EPR spectra of 4H-SiC reveal two sets of three lines consistent with isolated nitrogen at a hexagonal and cubic site. In 6H-SiC, measurements at 120 GHz microwave frequency showed two centers with nearly the same g tensor and large hyperfine interaction, and a third with a different g tensor and barely resolved hyperfine lines [6]. Based on the assumption that the two cubic sites should exhibit the same symmetry and interatomic interactions, the pairs of triplets were assigned to the two cubic sites and the single, barely resolved set to the hexagonal site. This assignment has been extended to the 4H polytype where one of the pairs of triplets consists of well-resolved lines and the other three barely resolved lines. EPR measurements of partly compensated material reveals only the cubic site, implying that the hexagonal site represents the level closer to the conduction band since the EPR active state requires the presence of neutral nitrogen impurities [6]. Near band-gap illumination generates the characteristic lines of the hexagonal site, consistent with the position of the sites energetically close to the band edge.

The hopping conduction thought to occur in heavily doped material has been indirectly observed by EPR [37]. Studying a series of 6H-SiC wafers doped with 1×10^{17} to $6 \times 10^{18} \text{ cm}^{-3}$ N, Veinger and co-workers concluded that the changes observed in the EPR spectra were related to delocalization effects resulting from electron exchange. High field measurements, capable of resolving the EPR spectra of each lattice site, suggest that electron hopping between nitrogen sites dominates at high concentrations.

Several groups have studied the potential of phosphorus as a shallow donor in SiC. Veinger and separately, Kalabukhova first identified the EPR of phosphorus in 6-H SiC doped by neutron transmutation [38,39]. Two of the signals observed were attributed to P substituting for Si at the hexagonal and cubic lattice sites. The signal was also observed in P-ion implanted SiC [40]. Recently, Isoya and coworkers performed a systematic study of the effects of implantation energy, temperature, and annealing conditions on the shallow phosphorus centers [41]. In samples implanted at 3 MeV and 340 keV at temperatures between room temperature and 1200 °C, the only EPR signals observed are those due to the unintentionally incorporated nitrogen impurities and implantation damage. The amplitude of the latter decreases with increasing implantation temperature. After annealing at 1650 °C for 30 min in Ar, the samples show the characteristic spectra of isolated phosphorus donors. The amount of P donors, which did not vary with implantation temperature, was calculated to be less than 8% of the total implanted phosphorus ions. The small fraction of centers situated on the lattice sites is consistent with the limited success of n-type doping via phosphorus implantation. The remaining phosphorus ions may be associated with the P-related defects reported in SiC:P doped by means of neutron transmutation. However, no spectra similar to those reported by Kalabukhova or Veinger were reported in the more recent studies of ion-implanted material.

Aluminum is the p-type dopant of choice. In contrast to N and B, little is published about EPR-detection of the aluminum acceptor in SiC. The different symmetry sites have not been resolved, but it is known that Al, unlike B, exhibits an EPR response typical of an effective-mass like shallow acceptor [6]. Photoluminescence detected EPR (PL-EPR) results are consistent with the $E_v + 0.191$ eV level reported for the Al acceptor [6]. However, magnetic-circular dichroism EPR measurements determine the level to be somewhat deeper, 0.25 eV [6]. The concentration and temperature dependence of the Al EPR signal was reported recently by Gerardi [42]. The Al signal monotonically increases with hole concentration; however, only about one-tenth of the holes may be accounted for by the EPR active Al centers in these samples. Studies of the shape of the Al signal reveal additional interesting concentration affects. Intensity and linewidth changes as a function of temperature and concentration are interpreted in terms of site-to-site impurity hopping when the Al concentration is below $1 \times 10^{18} \text{ cm}^{-3}$. Above this value, a broad isotropic line typical of nearly free electrons emerges, prompting the authors to suggest that impurity band conduction dominates. Additional Al-related work involves passivation with H, a subject that will be addressed later in this section.

Although seldom an intentional p-type dopant, B is an omni-present species that provides much source of discussion and confusion. Like nitrogen, the impurities at different lattice sites are distinguished by their *g*-tensor and nuclear hyperfine energy. A detailed well-accepted model for the structure is not available; however, most agree that boron substitutes for Si at

both the cubic and hexagonal sites. The defect levels reported for 6H SiC have been predicted from PL-EPR spectroscopy. From these measurements, the nitrogen donor-boron acceptor luminescence (2.7 eV) and the conduction band-to-boron acceptor PL (2.8 eV) were clearly associated with the shallow boron resonance [6]. The energy level for the B(0/-) transition is situated 0.3 to 0.4 eV above E_v . A third PL response with onset at 2.4 eV is attributed to ‘deep’ boron, a name derived from the position of the energy level in the band gap about 0.3 eV above the acceptor boron level [6]. This broad yellow-green luminescence is thought to be associated with a magnetic resonance signal at $g \sim 2$ as well a characteristic level measured by deep level transient spectroscopy (DLTS) [6]. However, many investigators over the past 20 years have argued whether the electrical level at 0.6 eV, the broad green PL spectrum, and the magnetic resonance signal are manifestations of the same defect [43–45]. Tandem PL, EPR, and DLTS measurements show that the intensity of the $g \sim 2$ resonance, the yellow luminescence line, and DLTS spectrum exhibit the same trend when measured before and after annealing at 2350 °C [46]. Also, the signal amplitudes measured in different samples follow the same behavior. But this study is cursory and the relationship remains uncertain. Based on results of ENDOR experiments using ^{11}B diffused 6H-SiC, the EPR signal is attributed to a B-V_C pair [47,48]. Although optically detected magnetic resonance results are consistent with the B-V_C pair model, the physical structure of deep boron is far from confirmed [49].

Since hydrogen is present in almost all processing steps, including growth, the effect of atomic, ionic, and molecular hydrogen are continuously studied. In particular, hydrogen is known to electrically passivate donor and acceptor impurities. Gendron and coworkers, and separately Gerardi, studied the effects of hydrogen on the N, B, and Al EPR signals [29, 50]. In 6H n⁺ SiC doped with N and p-type samples doped with Al, the signal intensity of the respective dopants decreased by about 75% after exposure to hydrogen gas at 10 bar pressure held at temperatures between 1500 and 1700 °C for 10–20 hours. The amplitude of the boron acceptor signal observed in the p-type material was also reduced [50]. Later experiments on more lightly N-doped films ($N \sim 10^{17} \text{ cm}^{-3}$) revealed an apparent contradiction [51]. Similar hydrogenation produced little change in the N EPR signal. After SIMS studies confirmed that the result was not due to dopant density dependence of hydrogen penetration, the apparent contradiction was resolved by considering the amount of negatively charged H expected to be present in the material. By analogy to known situations in other semiconductors, it is suggested that H⁻ exists when the Fermi level is very high (n⁺ material) and H⁺ exists whenever the Fermi level is close the valence band (p-type material). Since H⁻ would be necessary to neutralize positively charged N donors, the effective decrease in passivation observed between heavily and more lightly N-doped SiC may be attributed to a decrease in the amount of ionized H readily available to react with the donors in the latter. Gerardi demonstrated, indirectly, similar phenomena for Al [29]. An attempt at re-activation by a 500 °C vacuum

anneal resulted in a decrease in the Al EPR signal instead of the expected increase. The authors suggest the introduction of unintentional hydrogen from the quartz ware; however, it is possible that the H^+ species initially present in the p-type samples continued to react with the ionized dopants during this low temperature heat treatment.

7.3.2 Transition Metal Impurities: Vanadium and Other Elements

Of the many transition metals identified in SiC by EPR, the most technological important is vanadium. Vanadium has long been recognized as a deep level defect capable of compensating unintentional acceptors and donors, thereby yielding semi-insulating substrates required for MESFET and HMET devices. Although today vanadium-doped wafers are challenged by the latest innovations in high purity material, for many devices the SI wafers formed by impurity doping remain a viable, and cheaper, alternative. The utility of this d^5 transition element lies in its ability to electrically passivate shallower defects by trapping both electrons and holes. When the vanadium concentration is adjusted appropriately, SiC wafers may be produced with resistivity as high as $10^7 \Omega \text{ cm}$ at 300°C .

In ideally pure SiC, four of the five vanadium valence electrons form tetrahedral bonds with the nearest neighbors. In ionic notation, this charge state is referred to as V^{4+} . The equivalent description using semiconductor terminology is neutral vanadium (V^0). An energy of about 1.6 eV must be absorbed by the impurity to release an electron to the conduction band and form V^{5+} . Thus, the $V^{4+/5+}$ (or equivalently, $V^{0/+}$) level is located at $E_c - 1.6 \text{ eV}$ and is referred to as the donor level. Likewise, if V^{4+} captures an electron to become V^{3+} , the level ($V^{4+/3+}$ or $V^{0/-}$) is the acceptor level. Note that both the donor and acceptor levels are referenced to the neutral charge state, as for donors and acceptors formed by column V and III elements in column IV semiconductors. In deference to the EPR literature, the ionic notation will be used throughout this discussion rather than traditional semiconductor language. Because vanadium has two different levels, one that acts as an acceptor and the other a donor, the impurity is called amphoteric.

The V^{4+} charge state is EPR active, with the extra electron of the d^5 outer shell serving as the paramagnetic entity. The hexagonal and cubic sites of 6H and 4H-SiC are identified by separate spectra, all reflecting the spin 1/2 nature of the center. Monitoring vanadium on the cubic site in 6H-SiC:Al (p-type) as a function of excitation wavelength, Maier and coworkers demonstrated that for the cubic site the $V^{4+/5+}$ level lies 1.6 eV above the valence band edge [5, 52]. In this study, the level for the hexagonal site was not determined. V^{3+} , a spin 1 center due to the presence of two ‘unpaired electrons’, was observed only in n-type material. Like V^{4+} , the V^{3+} spectrum has been observed on both the cubic and hexagonal sites in 4H and 6H material. Analysis of the V^{3+} ‘half-field’ lines reveals interactions with Si neighbors consistent with a description of the impurity as substitutional vanadium residing on a Si

lattice site [52]. Since the positive charge state is found exclusively in n-type SiC, the authors suggest that the $V^{3+/4+}$ level lies in the upper half of the band gap. A correlation of EPR and optical absorption results places the energy within 0.66 eV of E_c [53, 54] in 6H SiC and about 0.8 eV below E_c in 4H [54].

More recent photo-EPR studies of vanadium-doped semi-insulating SiC reveal transitions for both the acceptor and donor levels. Also, preliminary experiments relate the variation in the Hall-measured carrier activation energy with different relative amounts of the V^{4+} and V^{3+} charge states. For instance, in 4H vanadium-doped SI SiC with a carrier activation energy of 1.6 eV, dark EPR measurements show only V^{4+} . Optical excitation with photon energy larger than 1.5 eV increases the EPR signal intensity, converting V^{5+} to V^{4+} via capture of an electron from the valence band. Both the dark and photo-EPR measurements verify that the vanadium impurity is the predominate source of compensation in the SI SiC:V wafers with activation energy of 1.5 eV. In contrast, several different types of SiC:V wafers with a 1.1 eV activation energy reveal the presence of both V^{4+} and V^{3+} when measured in the dark. Here, photo-EPR reveals changes in the concentrations of both entities at energies of about 1 eV, consistent with the carrier activation energy. Determination of the location of the $V^{4+/3+}$ electronic level based on this data is ongoing. Although the exact nature of the species causing the activation energy shift from 1.5 eV to 1.1 eV has not yet been identified, the experiments show that vanadium remains the mechanism controlling carrier generation in the V-doped SI wafers in samples with a carrier activation energy of 1.1 eV. It should be noted that in the recent SI SiC EPR studies the vanadium transitions involve the hexagonal V^{4+} centers, unlike earlier studies which monitored only those on the cubic sites. Interestingly, an EPR signal identical to that of the cubic site reported earlier was not seen in the recent work; rather, a spectrum similar to but more complex than that reported by Maier and coworkers was measured. The role of the defects represented by this more complicated spectra remain to be assessed, but it may be the link to the variations found among activation energies in vanadium doped SI SiC.

Carlos and coworkers have also studied vanadium in SI 4H-SiC. In their samples, both V^{4+} and the shallow boron acceptor (B^0) were observed simultaneously at temperatures below 20 K [55]. In principle, since the energy of the $V^{4+/5+}$ transition is larger than that of the $B^{0/-}$, the ‘extra’ electron of V^{4+} should be captured by the boron acceptor; thus, V^{4+} and B^0 should never be observed simultaneously without any external excitation. The presence of these two species despite thorough attempts to remove all accidental sources of excitation such as room light indicates that the wafers were non-uniformly doped. This work reveals the potential of EPR to provide a contactless method of detecting local non-uniformities among donors and acceptors as well deep level compensating species.

In 1997, Baur, Kunzer and Schneider compiled a review of the EPR detected transition metal impurities in SiC [56]. Since that time, one group has

identified two additional impurities, Ta and W in as-grown 6H substrates grown by physical vapor transport [57]. Without illumination, the EPR spectra revealed two different centers. One was attributed to W^{5+} and the other tentatively assigned to Ta^{3+} . Band gap illumination quenched the spectral lines of both entities, indicating that W and Ta have electrical levels in the band gap of 6H-SiC. Comparison with theoretical studies and DLTS measurements suggests that a double donor level of W exists at $E_v + 1.94$ eV. The authors also mention that if the concentration of the tungsten could be controllably increased, the impurity may act as an efficient compensating center for SI SiC. In the present material, only 10^{14} cm^{-3} centers were observed, far below that usually required for effective compensation.

7.4 Concluding Comments

The previous pages have reviewed EPR studies of SiC thought to be pertinent to technological processes. The intrinsic defects observed to date in as-grown high-purity SI SiC were described and a variety of processes related to impurities in n-type, p-type, and compensated wafers were addressed. Several other issues should be mentioned regarding future magnetic resonance studies of SiC. First, in order to accurately describe any defect, the full symmetry of the center should be determined. Such studies require rotation of the sample about three mutually perpendicular axes, a situation difficult to realize when one is confined to millimeter-thick wafers. Thus, bulk electronic-grade samples would enhance our knowledge of many of the defects discussed above. The use of thicker pieces would also address another problem, signal-to-noise ratio. The high quality of the material now being produced for device applications severely minimizes the amount of point defects detectable by EPR. Often, the limited sample size afforded by the thin wafers is overcome by stacking several pieces; however, this can lead to misalignment of the crystal axes and produce artificially complicated line shapes.

Another problem that plagues many studies of defects in SiC is the similarity of the g -tensors found for many intrinsic EPR centers. This factor is inherent to SiC because the shift of g from the free-electron value is proportional to the spin-orbit coupling constant, a value that is small for both C and Si. Thus, several different intrinsic defects may be barely resolved at the typical measurement frequency of 10 GHz. Lately, this problem has been addressed by experiments employing frequencies as high as 240 GHz. Although the complexity of such experiments limits their potential as routine characterization methods, intensive studies have resolved spectra of several intrinsic defects in as-grown SI SiC and have provided valuable structural information [25, 27].

It is hoped that this review will highlight the significance of EPR for point defect studies and further the understanding of defect-related phenomena.

References

1. C.P. Poole, *Electron Spin Resonance: A comprehensive Treatise on Experimental Technique*, Interscience, New York (1967).
2. W. Gordy, in *Techniques of Chemistry*, ed. by W. West, Vol. 15, Wiley, New York (1980).
3. J.A. Weil, J.R. Bolton, and J.E. Wertz, "Electron Paramagnetic Resonance", Wiley, New York (1994).
4. L.A. de S. Balona and J.H.N. Loubser, "ESR in irradiated silicon carbide", *J. Phys. C* **3**, 2344 (1970).
5. K. Maier, J. Schneider, W. Wilkening, S. Leibenzeder, and R. Stein, "Electron spin resonance studies of transition metal deep level impurities in SiC", *Mater. Sci. Eng. B* **11**, 27–30 (1992).
6. S. Greulich-Weber, "EPR and ENDOR investigations of shallow impurities in SiC polytypes", *Phys. Stat. Sol. (a)* **182**, 95 (1997).
7. W.E. Carlos, E.R. Glaser, and B.V. Shanabrook, "Optical and magnetic resonance signatures of deep levels in semi-insulating 4H SiC", *Physica B* **340–342**, 151 (2003).
8. A defect level refers to the energy required to add an electron to a defect from the valence band or the energy emitted when an electron is excited from a defect to the conduction band. For example, $E(V^{4+}/V^{5+})$ is the energy necessary to add an electron to V^{5+} to create V^{4+} . The energy may be referenced to either the conduction band edge or valence band edge. The former would be written, $(E_c - E)$ and the latter, $(E + E_v)$ were E is the value of the energy in eV.
9. M.E. Zvanut and V.V. Konovalov, "The level position of a deep intrinsic defect in 4H-SiC studied by photo-induced electron paramagnetic resonance", *Appl. Phys. Lett.* **80**, 410 (2002).
10. V.V. Konovalov, M.E. Zvanut, J.R. Jenny, S.G. Müller, H. McD. Hobgood, and V. Tsvetkov, "Electron paramagnetic resonance studies of a carbon vacancy-related defect in as-grown 4H-SiC", *Physica B* **308–310**, 671 (2002).
11. N.T. Son, P.N. Hai, and E. Janzen, "Carbon vacancy-related defect in 4H and 6H SiC", *Phys. Rev. B* **63**, 201201 (2001).
12. M. Bockstedte, M. Heid, and O. Pankratov, "Signature of intrinsic defects in SiC: *Ab initio* calculations of hyperfine tensors", *Phys. Rev. B* **67**, 193102 (2003).
13. F. Bechstedt, A. Fissel, F. Furthmuller, U. Grossner, and A. Zywiertz, "Native defects and complexes in SiC", *J. Phys. Cond. Matter.* **13**, 9027–9037 (2001).
14. N.T. Son, B. Magnusson, and E. Janzen, "Photoexcitation-electron-paramagnetic-resonance studies of the carbon vacancy in 4H-SiC", *Appl. Phys. Lett.* **81**, 3945–3947 (2003).
15. L. Torpo, M. Marlo, T.E.M. Staab, and R.M. Nieminen, "Comprehensive *ab initio* study of properties of monovacancies and antisites in 4H-SiC", *J. Phys. Cond. Matter* **13**, 6203–6231 (2001).
16. V.V. Konovalova and M.E. Zvanut, unpublished work.
17. V.V. Konovalov and M.E. Zvanut, "Interactions between intrinsic defects and nitrogen/boron impurities in semi-insulating 4H SiC. EPR study", *J. Electron. Mater.* **31**, 351 (2002).
18. E.N. Kalabukhova, S.N. Lukin, A. Saxler, W.C. Mitchel, S.R. Smith, and J.S. Solomon, "Photosensitive electron paramagnetic resonance spectra in semi-insulating 4H SiC crystals", *Phys. Rev. B* **64**, 235202 (2001).

19. D. Alvarez, V.V. Konovalov, and M.E. Zvanut, "The interaction among defects during high temperature annealing of high purity SiC", "State-of-the-Art Program on Compound Semiconductors XXXVI and Wide Bandgap Semiconductors for Photonic and Electronic Devices and Sensors II," Electrochemical Society Conference Proceedings 2002-3, edited by R.F. Kopf, F. Ren, E.B. Stokes, H.M. Ng, A.G. Baca, S.J. Pearton, S.N.G. Chu, pp. 258–265, May 2002.
20. D. Alvarez, V.V. Konovalov, and M.E. Zvanut, "Effects of high temperature annealing on defects and impurities in as-grown semi-insulating 4H SiC", *J. Electron. Mater.* **32**, 444 (2003).
21. J.R. Jenny, S.G. Müller, A. Powell, V.F. Tsvetkov, H.M. Hobgood, R.C. Glass, and C.H. Carter, "High-purity semi-insulating 4H-SiC grown by the seeded-sublimation method", *J. Electron. Mater.* **31**, 366 (2002).
22. V.S. Vainer and V.A. Il'in, "Electron spin resonance of exchange-coupled vacancy pairs in hexagonal silicon carbide", *Sov. Phys. Solid State* **23**, 2126 (1981).
23. Th. Lingner, S. Greulich-Weber, and J.-M. Spaeth, "Structure of the silicon vacancy in 6H-SiC after annealing identified as the carbon vacancy-carbon antisite pair", *Phys. Rev. B* **64**, 245212 (2001).
24. A. Polity, S. Huth, and M. Lausmann, "Defect characterization in electron-irradiated 6H-SiC by positron annihilation", *Phys. Rev. B* **59**, 10603 (1999).
25. N.T. Son, P.N. Hai, and E. Janzen, "Silicon antisite in 4H SiC", *Phys. Rev. Lett.* **87**, 045502 (2001).
26. V.Ya. Bratus, I.N. Makeeva, S.M. Okulov, T.L. Petrenko, T.T. Petrenko, and H.J. von Bardeleben, "Positively charged carbon vacancy in 6H-SiC: EPR study", *Physica B* **308–310**, 621 (2001).
27. V.V. Konovalov, M.-E. Zvanut, J. van Tol, "240 GHz EPR studies of intrinsic defects in as-grown 4H SiC", *Phys. Rev. B* **68**, 012102 (2003).
28. M. Bockstedte, M. Heid, and O. Pankratov, "Signature of intrinsic defects in SiC: *ab initio* calculations of hyperfine tensors" *Phys. Rev. B* **67**, 193102 (2003).
29. G.J. Gerardi, E.H. Poindexter, and D.J. Keeble, "Paramagnetic centers and dopant excitation in crystalline silicon carbide", *Appl. Spectrosc.* **50**, 1428 (1996).
30. P.J. Macfarlane and M.E. Zvanut, "Characterization of paramagnetic defect centers in three polytypes of dry heat treated, oxidized SiC", *J. Appl. Phys.* **88**, 4122 (2000).
31. P.J. Macfarlane and M.E. Zvanut, "Effect of oxidation conditions on the concentration of carbon dangling bonds in oxidized 6H-SiC", *Mater. Sci. Forum* **338–342**, 1125 (1999).
32. R.C. Barklie, M. Collins, B. Holm, Y. Pacaud, and W. Skorupa, "An EPR study of defects induced in 6H-SiC by ion implantation", *J. Electron. Mater.* **26**, 137 (1997).
33. H.J. Von Bardeleben, J.L. Cantin, and I. Vickridge, "Proton-implantation-induced defects in n-type 6H- and 4H-SiC: an electron paramagnetic resonance study", *Phys. Rev. B* **62**, 10126 (2000).
34. The sensitivity of an EPR measurement is proportional to the cavity 'Q', the ratio of the amount of energy stored in the cavity to the energy lost to the walls and sample. In general, a more highly conducting semiconductor tends to lower the Q and decrease the sensitivity of the measurement. Typically, a standard is placed in the cavity along with the sample to monitor changes in 'Q'.

35. V.Ya. Bratus, T.T. Petrenko, H.J. von Bardeleben, E.V. Kalinina, A. Hallen, "Vacancy-related defects in ion-beam and electron irradiated 6H-SiC", *Appl. Surf. Sci.* **184**, 229–236 (2001).
36. W. Gotz, A. Schoner, G. Pensl, W. Suttrop, W.J. Choyke, R. Stein, and S. Leibenzeder, "Nitrogen donors in 4H-silicon carbide", *J. Appl. Phys.* **73**, 3332 (1993).
37. A.I. Veinger, "Investigation of the temperature and concentration dependences of the hyperfine structure of the EPR spectrum of silicon carbide", *Sov. Phys. Sem.* **1**, 14 (1967).
38. A.I. Veinger, A.G. Zabrodskii, G.A. Lomakina, and E.N. Mokhov, *Sov. Phys. Solid State* **28**, 917 (1986).
39. E.N. Kalabuknova, S.N. Lukin, and E.N. Mokhov, *Sov. Phys. Solid State* **35**, 361 (1993).
40. E.N. Kalabuknova, S.N. Lukin, E.N. Mokhov, M. Feege, S. Greulich-Weber, and J.-M. Spaeth, *Inst. Phys. Conf.* **137**, 215 (1993).
41. J. Isoya, T. Ohshima, A. Ohi, N. Morishita, and H. Itoh, "ESR characterization of activation of implanted phosphorus ions in silicon carbide", *Nucl. Instrum. Methods B* **206**, 965–968 (2003).
42. G.J. Gerardi, E.H. Poindexter, and D.J. Keeble, "Paramagnetic centers in Al-doped 6H-SiC: temperature ad concentration effects", *J. Appl. Phys.* **87**, 1914 (2000).
43. H. Kuwahara and S. Yamada, "Free-to-bound transition in β -SiC doped with boron", *Phys. Stat. Sol. (a)* **90**, 739 (1975).
44. S.G. Sridhara, L.L. Clemen, R.P. Devaty, W.J. Choyke, D.J. Larkin, H.S. Kong, T. Troffer, and G. Pensl, "Photoluminescence and transport studies of boron in 4H SiC", *J. Appl. Phys.* **83**, 7909.
45. M. Ikeda, H. Matsunami, and T. Tanaka, *Phys. Rev. B* **22**, 2842 (1980).
46. P.G. Baranov and E.N. Mokhov, "Electron paramagnetic resonance of deep boron in silicon carbide", *Semicond. Sci. Technol.* **11**, 489–494 (1996).
47. A.v. Duijn-Arnold, T. Ikoma, O.G. Poluektov, P.G. Baranov, E.N. Mokhov, and J. Schmidt, "Electronic structure of the deep boron acceptor in boron-doped 6H-SiC", *Phys. Rev. B* **57**, 1607–1619 (1998).
48. P.G. Baranov, E.N. Mokhov, A. Hofstetter, and A. Sharmann, "Electron-nuclear double resonance of deep-boron acceptors in silicon carbide", *JETP Lett.* **63**, 848 (1996).
49. N.G. Romanov, V.A. Vetrov, P.G. Baranov, E.N. Mokhov, and V.G. Oding, "Optical detection of magnetic resonance in boron-doped a-SiC", *Sov. Tech. Phys. Lett.* **11**, 483 (1985).
50. F. Gendron, L.M. Porter, C. Porte, and E. Bringquier, "Hydrogen passivation of donors and acceptors in SiC", *Appl. Phys. Lett.* **67**, 1253 (1995).
51. B. Theys, F. Gendron, C. Porte, E. Bringquier, and C. Dolin, "Hydrogen passivation of nitrogen in 6H-SiC", *J. Appl. Phys.* **82**, 6346 (1997).
52. K. Maier, H.D. Muller, and J. Schneider, "Transition metals in silicon carbide (SiC): vanadium and titanium", *Mater. Sci. Forum* **81–87**, 1183 (1992).
53. M. Kunzer, U. Kaufmann, K. Maier, and J. Schneider, "Magnetic circular dichroism and electron spin resonance of the A-acceptor state of vanadium, V^{3+} , in 6H-SiC", *Mater. Sci. Eng. B* **29**, 118 (1995).
54. J.R. Jenny, M. Skowronski, W.C. Mitchel, H.M. Hobgood, R.C. Glass, G. Augustine, and R.H. Hopkins, "Deep level transient spectroscopic and hall effect

- investigation of the position of the vanadium acceptor level in 4H and 6H SiC”, J. Appl. Phy. **68**, 1963 (1996).
- 55. W.E. Carlos, W.J. Moore, G.C.B. Braga, J.A. Freitas Jr., E.R. Glaser, and B.V. Shanabrook, “Contactless studies of semi-insulating 4H-SiC”, Physica A **308–310**, 691–694 (2001).
 - 56. J. Baur, M. Kunzer, and J. Schneider, “Transition metals in SiC polytypes, as studied by magnetic resonance techniques”, Phys. Stat. Sol. (a) **162**, 153 (1997).
 - 57. K. Irmscher, “Electrical properties of SiC: characterisation of bulk crystals and epilayers”, Mater. Sci. Eng. B **91–92**, 358 (2002).

Material Selection and Interfacial Reaction in Ohmic-Contact Formation on SiC

W. Lu, W.E. Collins, and W.C. Mitchel

Ohmic contacts are a necessary part of microelectronic devices. In this chapter, we review the materials used for ohmic contacts and their interfacial reactions and structures on n- and p-type SiC, discuss material selection for ohmic-contact formation on SiC and the mechanism of formation of such contacts, and summarize recent advances. The metals for ohmic contacts on SiC are classified by group as the periodic table, and the relationship between the chemical reactivity of the metal with SiC and ohmic-contact formation is presented. Most metals in group VIII are excellent for ohmic contacts on n-type SiC, and only silicides and carbon are formed. A group IIIA metal, Al, is the most effective material for ohmic-contact formation on p-type SiC, and forms carbides and Si on SiC. The metals in groups IVB–VIIB generally show good thermal stability on SiC, and both silicides and carbides are formed. Various compounds, including silicides, carbides, nitrides, borides, and composites, for ohmic contacts on SiC are summarized. The recent advances in improved contacts, in our understanding of the mechanism, and in forming ohmic contacts with high thermal stability are also summarized. The role of nanosize graphitic structures in ohmic contacts and the mechanism based on catalytic graphitization are presented. Finally, challenging issues such as interfacial structural characterization on the nanometer and atomic scales and high-stability ohmic contacts in oxidizing environments are discussed.

8.1 Introduction

Silicon carbide, SiC, is an attractive semiconductor due to its superior electrical, thermal, chemical, and mechanical properties, which include its wide band gap, high thermal conductivity, high breakdown field, high-saturation electron drift velocity, high chemical stability, high radiation resistance, and strong mechanical strength [1, 2]. These properties make SiC a promising material for next generation electronic devices for high power, high frequency, and high temperatures. Since SiC wafers became commercially available in the

early 1990's [1,2], many critical issues in SiC properties, material growth, and processes have been extensively investigated worldwide, and the momentum continues in improving materials and processes, and developing new devices.

Electron transfer on the semiconductor surface is a very important issue in device design and fabrication. The ohmic contact is a necessary part in the operation of all semiconductor electronic devices, in which an interconnection between metal and semiconductor exhibits linear or quasi-linear current-voltage characteristics. Ohmic contacts must be able to provide the necessary device current, and the voltage drop across the contact should be small compared to the voltage across the active device regions [3]. The applications of SiC devices in high power and high temperature require high quality ohmic contacts, including low contact resistivity for high current capability, high stability at high temperature, and high stability for long time operation in harsh environments.

Ohmic contacts on SiC have been investigated extensively in the past decade, various materials, including metals, alloys, silicides, carbides, and borides have been examined. A significant advance has been achieved, but good ohmic contacts on SiC are only formed on highly doped SiC and after annealing at high temperatures [2,4–8]. However, the formation of high quality ohmic contact on SiC is still currently one of the most critical issues in SiC technologies [9], and significant advances are needed for developing high performance devices. Importantly, the mechanism of ohmic contact formation has not been understood, and the material selection for ohmic contacts has been determined by the "trial and error" method.

Cole et al. [8] recently have provided a review on ohmic contacts on SiC in the sister book, which gave an excellent summary on ohmic contact performance of various metals and related materials. This chapter discusses the interfacial reactions on SiC and the challenging issues, and it is organized as following: a brief introduction of contact theory and the critical factors in forming ohmic contact on SiC are presented, followed by discussions of ohmic contact performance and their interfacial reactions between SiC and various groups of elements and different compound materials. Finally, the challenging issues in understanding the mechanism, recent advances, structural characterizations in the nanometer and atomic scales, and thermal stability are discussed.

8.2 Classical Theory and the Critical Factors in Ohmic Contact Formation on SiC

Since Braun [10] discovered the rectifying properties of semiconductors in 1874, the classical theory of electrical contacts on semiconductors has been well developed [11,12].

In an ideal metal/semiconductor contact, the work functions of the metal (ψ_m) and semiconductor (ψ_s) determine the contact nature [11–13]. In an

n-type semiconductor, the barrier for electron movements from the n-type semiconductor into the metal is $\psi_m - \psi_s$. The barrier to the reverse flow of electrons from the metal to the semiconductor is $(\psi_m - \chi_s)$, where χ_s is the electron affinity of the semiconductor.

Therefore, the Schottky barrier height (SBH) of the metal contact on an n-type semiconductor is:

$$\psi_{\text{SBH}} = \psi_m - \chi_s \quad (8.1)$$

and an ohmic contact is formed when $\psi_m < \chi_s$ for an n-type semiconductor.

For a p-type semiconductor, when $\psi_m < \psi_s$, the contact is rectifying and a barrier $(\psi_s - \psi_m)$ exists for hole flow from the semiconductor to the metal. The barrier to reverse flow is defined as:

$$\psi_{\text{SBH}} = E_G - (\psi_m - \chi_s) \quad (8.2)$$

and an ohmic contact is formed on p-type semiconductors when $\psi_m > \psi_s$ [11, 12].

The work function of the surface of a metal is defined as the difference in potential energy of an electron between the vacuum level and the Fermi level [14]. The work functions of most elements are listed in the Table 8.1 [15]. In the microelectronics industry, metals are widely used in almost every electrical device. The metals are required to have excellent conductivity, good mechanical properties, and chemical inertness. However, only a short list of metals is used in the electronic industry, such as Al, Ni, Co, Ti, Cu, and Au. As shown in Table 8.1, the work functions of these metals range from 4.2 to 5.2 eV.

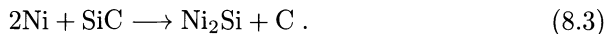
Table 8.1. Work functions (eV) of elements (from [15], with permission for reproduction from the American Institute of Physics)

IA	IIA	IIIB	IVB	VB	VIB	VIIIB	VIII		IB	IIB	IIIA	IVA	VA	VIA	VIIIA	VIIIA
H																He
Li	Be								B 4.45	C 5.0	N	O	F			Ne
2.9	4.98								Al 4.28	Si 4.85	P	S	Cl			Ar
Na	Mg															
2.75	3.66															
K	Ca	Sc	Ti	V	Cr	Mn	Fe	Co	Ni	Cu	Zn	Ga	Ge	As	Se	Kr
2.30	2.87	3.5	4.33	4.3	4.5	4.1	4.5	5.0	5.15	4.65	4.33	4.2	5.0	3.75		
Rb	Sr	Y	Zr	Nb	Mo	Tc	Ru	Rh	Pd	Ag	Cd	In	Sn	Sb	Sb	Xe
2.16	2.59	3.1	4.05	4.3	4.6		4.71	4.98	5.12	4.26	4.22	4.12	4.42	4.55	I	
Cs	Ba	La	Hf	Ta	W	Re	Os	Ir	Pt	Au	Hg	Tl	Pb	Bi	Po	At
2.14	2.7	3.5	3.9	4.25	4.55	4.96	4.83	5.27	5.65	5.1	4.49	3.84	4.25	4.22		Rn

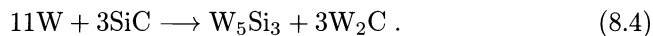
The work function of 6H-SiC is 4.75 eV and the electron affinity is 3.3 eV [16, 17]. According to (8.1), the work function of metals is required to be less than 3.3 eV to form an ohmic contact on n-type 6H-SiC. As shown in Table 8.1, only the IA, IIA, and IIIB metals have the work functions less than the electron affinity of SiC. Unfortunately, these metals are easily oxidized and have poor mechanical strength, and are not suitable for the microelectronic applications. In fact, there is no direct relationship between the work functions and ohmic contact formation on SiC. Therefore, the “trial and error” method has been used to search of the optimal ohmic contact materials, including metals, silicides, carbides, borides, and etc.

Several reviews have provided excellent summaries and described recent progresses in ohmic contacts on SiC [2, 4–8]. All metal/SiC structures, as deposited, show rectifying contact behavior, but many metal/SiC contacts become ohmic after thermal annealing. For example, the most commonly used metal for ohmic contact on n-type SiC is Ni, for which the work function is 5.15 eV as shown in Table 8.1. According to (8.1), a Ni/SiC contact should be rectifying, not ohmic. The most commonly used metal for ohmic contact on p-type SiC is Al, for which the work function is 4.28 eV. Again, the Al/SiC contacts should be rectifying, not ohmic. Excellent ohmic contacts of Ni/n-type SiC and Al/p-type SiC are formed after annealing around 1000 °C in vacuum or Ar gas [4–8]. Similar behavior also is observed for metal contacts on Si and other semiconductors [11].

At elevated temperatures, SiC becomes chemically reactive with most metals [5, 6]. Some metals, such as most of the group VIII metals, react with SiC to form silicides and carbon. For example:



Many metals, such as most of the group IIIB to VIIB metals, react with SiC to form stable carbides and silicides. For example, W reacts with SiC to form both carbides and silicides.



A few metals, such as Al, react with SiC to form carbides and Si.



Experimentally, chemical reaction between SiC and metals is necessary to form ohmic contact. In many studies [5, 6], the formation of silicides or carbides at high temperature has been assumed necessary for the formation of ohmic contacts on SiC. However, there are two issues that cannot be explained using this assumption: first, metals usually react with SiC at much lower temperatures than those required to activate ohmic contact. For example, as (8.3), Ni reacts with SiC to form Ni₂Si at 500 °C but the contact does not become ohmic until they are annealed at around 950 °C [5, 6]. Therefore, the

formation of the silicides on SiC by itself is not responsible for the formation of ohmic contacts. Second, the values of the work functions of silicides are similar to those of the metals, i.e., the assumption that the silicides phase is responsible for ohmic contact formation does not follow the Schottky-Mott limit. Similar issues also exist in the other two types of contacts as described in (8.4) and (8.5).

Kurtin et al. [18] have related the electrical contacting properties of different metals on semiconductor surfaces to a criterion of the type of bonding in the semiconductor. The covalent semiconductors are susceptible to Fermi level pinning and insensitive to work function differences between the metal and the semiconductor, while the ionic semiconductors are opposite. SiC is between the two extreme conditions, and the experimental data support the conclusion that the Fermi level on 6H-SiC is only partially pinned [5].

The surface preparation of SiC prior to metal deposition is worth to be mentioned. It is well known that SiC surface cleaning is very important to the as deposited electrical properties [4]. However, since reactions between the metal and SiC are necessary prior to ohmic contact formation, it is unlikely that the SiC surface after annealing still is contaminated, and the cleaning procedure is not a determining factor in ohmic contact formation. Usually, the RCA method to clean SiC is sufficient to produce repeatable ohmic contacts on SiC.

Many factors affect ohmic contacts on SiC such as the doping concentration, annealing temperatures, annealing times, annealing environments, SiC polytypes and polarity, surface preparation, film thickness, deposition method, measurement method, and etc. The TLM (transfer length method) is usually used for the measurement of specific contact resistivity [3]. Generally, the SiC polytype only affects the value of the specific contact resistivity due to the differences in the band gap, not the nature of the contacts and formation mechanism. Therefore, ohmic contacts in this chapter are discussed together with different SiC polytypes. It is generally agreed that the doping concentration, annealing temperatures, and contact materials are the most important factors in forming ohmic contact on SiC. In this review, only these parameters along with SiC polytype are listed, unless specified, in the discussion of ohmic contact behavior. Since a large amount of studies on ohmic contacts on SiC have been published in the last ten years, it is impossible to include every published work in this review, and only selected publications are cited.

8.3 Interfacial Reactions of Ohmic Contact Metals on SiC

8.3.1 Silicides and Carbon in Metal/SiC

The group VIII metals include Fe, Co, Ni, Ru, Rh, Pd, Pt, Ir, and Os. Most of them have been demonstrated to be suitable materials for ohmic contacts

on n-type SiC, and some of them also for p-type SiC. Since the metals in this group have a d-shell occupied by 6 to 10 electrons, the energy levels of such configurations change little on acceptance of electrons from carbon [19, 20]. Therefore, except for Fe [21], the interfacial structures for these metals on SiC after annealing consist of silicides and carbon, and carbides do not exist. Numerous studies have been published on the contact properties, chemical composition, and structures of metal/SiC for this group metals. Nevertheless, we still do not understand why one metal exhibits better ohmic contact material than another, and the ohmic contact mechanism of these metals on SiC is still unclear.

Ni has been the most extensively investigated metal, and it is generally accepted as the best ohmic contact material for n-type SiC. There are many reports that Ni form excellent ohmic contacts on SiC [22–28]. For examples, Crofton et al. [23] reported that the specific contact resistivity is less than $5 \times 10^{-6} \Omega \text{cm}^2$ on n-type 6H-SiC after annealing at 950 °C. Wan et al. [25] found that Ni contacts began to exhibit ohmic behavior on n-type 3C-SiC with the specific contact resistivity was $1.4 \times 10^{-5} \Omega \text{cm}^2$ after annealing at 1000 °C. Roccaforte et al. [27] reported that the specific contact resistivity was $3.9 \times 10^{-5} \Omega \text{cm}^2$ on n-type 6H-SiC with a doping concentration of $7.4 \times 10^{18} \text{ cm}^{-3}$ after annealing at 950 °C. Ohmic contact cannot be formed in Ni/n-SiC if the carrier concentration was lower than $5 \times 10^{17} \text{ cm}^{-3}$. Generally, an excellent ohmic contact ($< 10^{-5} \Omega \text{cm}^2$) in Ni/n-SiC is obtained on highly doped SiC ($> 10^{18} \text{ cm}^{-3}$) after annealing at 900 °C or above. Other experimental conditions, such as the use of vacuum or inert gas annealing environment, annealing time, SiC polytypes, surface preparation, and etc, affect the contact properties, but are not critical factors.

The interfacial structures of Ni/SiC have been extensively investigated. For example, Bächli et al. [29] examined thermally induced reactions of Ni film on 3C-SiC and provided an overview of the Ni/SiC structures at elevated temperatures. After annealing at 450 °C, carbon diffuses throughout the Ni film and forms a carbon-rich layer at the Ni surface with a thickness of a few nanometers. Ni silicide, Ni₃₁Si₁₂, starts to form and is the only phase detected at 500 °C. Since Ni₂Si is thermodynamically stable with SiC and carbon, which forms first at the surface and grows toward the SiC substrate, Ni₂Si and Ni₃₁Si₁₂ co-exist at 600 °C. At 700 °C, Ni₂Si is the only silicide in the film. The carbon distribution consists of three distinct layers: the first zone is a constant carbon concentration that extends from near the SiC/silicides interface through most of the film thickness. The second zone is a thin layer with deficiency of carbon near the surface, and the third zone is a thin graphite layer at the surface. Figure 8.1 shows the overall evolution of the reaction and film structure between Ni and SiC. Many studies using different techniques have provided similar results of Ni/SiC. Pai et al. [30] reported that Ni₃₂Si₁₂ and Ni₂Si were formed at 500–600 °C, and only Ni₂Si was found in the temperature range of 700–900 °C using X-ray diffraction (XRD) and ion backscattering spectroscopy. La Via et al. [31] found that only

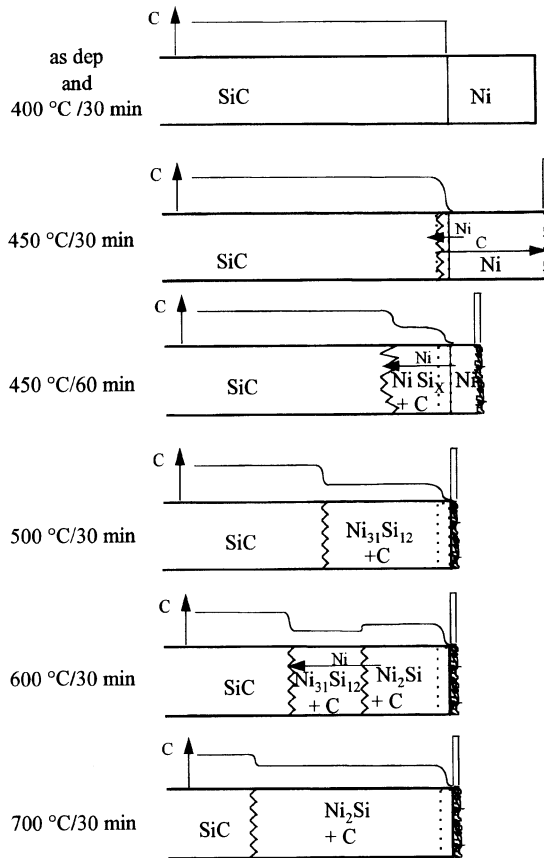


Fig. 8.1. Reaction between a 300 nm thick Ni film on the Si face of 3C-SiC. This sequence of sketches of the overall evolution summarizes the reaction and interfacial structure of Ni/SiC (from [29], with permission for reproduction from Elsevier)

Ni₂Si was found from 600 to 950 °C on 6H-SiC. The carbon precipitates has been dissolved in the silicide phase. Fujimura et al. [32] observed that δ-Ni₂Si and θ-Ni₂Si (high temperature phase of δ-Ni₂Si) were formed at the Ni/6H-SiC interface between 800 °C and 1150 °C using XRD. The activation energy of δ-Ni₂Si formation is 212 kJ/mol, which suggests that the diffusion of Ni through δ-Ni₂Si controls the rate of formation. Pécz et al. [33] examined the interfacial structures of Ni/4H-SiC after annealing using transmission electron microscopy (TEM). The reactions between Ni and SiC resulted in the formation of Ni silicides and a high number of voids at the interface. Marinova et al. [34] reported that carbon was in the graphite state and silicon was bonded predominantly to Ni resulting in Ni silicides X-ray photoelectron spectroscopy (XPS). Increase in graphite precipitation in the subsurface region of the contact layer leads to the degradation of the ohmic contact. Waldrop et al. [35]

found that C-face SiC reacted with Ni at 400 °C to form Ni silicides and carbon, while Si-face SiC started to react with Ni at 500 °C. Rastegaeva et al. [36] observed the formation of Ni silicides in the temperature range of 400–600 °C using XRD. It was observed that Ni_3Si_2 and Ni_2Si phases were formed in Ni/SiC on the C-face after annealing at 1000 °C. On the Si-face, only the Ni_2Si phase formed after annealing under the same condition. Kurimoto et al. [37] showed that the Ni silicides formed by annealing at above 500 °C using Raman spectroscopy. Ni_2Si phase was the primary phase near and above the temperature at which ohmic contacts are formed. Figure 8.2 shows that graphite clusters or defective graphite crystals were formed in Ni/SiC after annealing at 1000 and 1100 °C as observed by Raman spectroscopy. Graphitic carbon in Ni/SiC was formed at the temperature range when ohmic contact formation was formed.

Therefore, Ni silicides and carbon are the products of Ni and SiC reactions, and Ni carbides are not formed. All of the Ni react with SiC form Ni silicides prior to the formation of ohmic contacts. Ni/SiC is typical of many metal/SiC systems in that the chemical reactions forming various phases take place at temperatures lower than those required to activate ohmic contacts. Upon increasing the annealing temperatures to 900–1000 °C, rectifying behavior is converted to an ohmic contact without significant changes in the silicides phase. Since only Ni_2Si and carbon phases exist at the activation temperatures for ohmic contacts, Ni/SiC is a good prototype for investigating the interfacial structure and the mechanism of ohmic contacts on SiC.

Co has chemical and physical properties similar to Ni. Porter et al. [38] reported that Co forms ohmic contacts on n-type SiC with a carrier concentration of $3.2 \times 10^{18} \text{ cm}^{-3}$ after annealing in vacuum at 1000 °C. The specific contact resistivity was $2.5 \times 10^{-2} \Omega \text{ cm}^2$, which was much higher than that of Ni/SiC. The TEM images revealed that the contacts were composed of a mixture of CoSi and graphite, and all of the Co was consumed. The authors

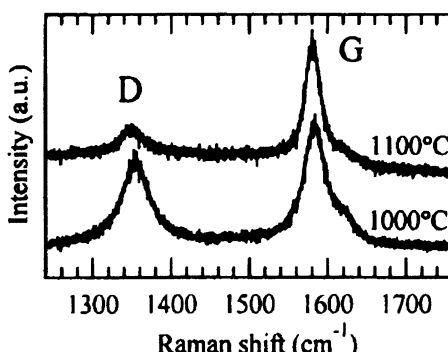


Fig. 8.2. Graphitic signals observed by Raman spectroscopy for Ni/SiC after annealing at 1000 and 1100 °C (from [37], with permission for reproduction from the American Institute of Physics)

speculated that the ohmic contact was formed due to defects created in the interface region from the reaction. Park et al. [39] investigated the Co/SiC interface reactions from 600 to 1000 °C. Co₂Si was formed at 700 °C as the first crystalline phase, and CoSi at 800 °C as the final stable phase. Free carbon moved to the top of the reacted Co silicides/SiC layer. Lim et al. [40, 41] observed that the sputtered Co film started to react with SiC to produce Co₂Si at 850 °C. At 1050 °C, Co₂Si and CoSi were found to co-exist, and carbon precipitates were found in the reaction zones. Above 1250 °C, only CoSi was observed with carbon precipitates having an oriented structure.

Pd films form ohmic contacts on p-type 4H-SiC after annealing at 600–700 °C [42]. The lowest specific contact resistivity was $5.5 \times 10^{-5} \Omega \text{ cm}^2$ after annealing at 700 °C when a very heavily doped p-SiC was used (the carrier concentration was at 10^{19} cm^{-3}). Kalinina et al. [43] reported that Pd formed ohmic contacts on p-type 4H-, 6H-, and 15R-SiC with a carrier concentration of $4 \times 10^{18} \text{ cm}^{-3}$. A specific contact resistivity of $4 \times 10^{-4} \Omega \text{ cm}^2$ was obtained after annealing at 600 °C. The interfacial structure of annealed Pd/SiC is similar to that of Ni/SiC. Pd carbides do not exist, and Pd₂Si and Pd₃Si phases are formed at 700 °C as shown by Auger electron spectroscopy (AES) [42]. At 600 °C, Pd₃Si is the dominating phase [43]. Pai et al. [30] found that Pd₃Si is formed at 500 °C, Pd₃Si and Pd₂Si co-exist after annealing at 700 °C, and only Pd₂Si is found from 700 to 900 °C using XRD. Veuillen et al. [44] found that a low coverage (0–20 Å thick) Pd film reacts with SiC to form Pd₂Si at room temperature under ultra-high vacuum. Annealing at 600 °C or higher temperatures resulted in the formation of Pd₂Si islands which partially covered the SiC surface and were surrounded by carbon. No other silicides were found. Bermudez [45] reported that the reaction products between Pd and SiC are Pd silicides with dissolved carbon. Lu et al. [46] found that Pd₂Si is formed from Pd/SiC at 300 °C, and Pd₂Si reacts with SiC to form PdSi at 500–600 °C on SiC. Chen et al. [47, 48] observed various Pd silicides (Pd_xSi, $x = 1, 2, 3$, and 4) after annealing at 425 °C.

Pt has a high work function at 5.65 eV [15], however, as deposited Pt has been reported to form ohmic contact on n-type SiC [49, 50]. The specific contact resistivity was $5 \times 10^{-5} \Omega \text{ cm}^2$ on Pt/3C-SiC with a carrier concentration of $\sim 10^{17} \text{ cm}^{-3}$ [49]. After annealing at 900 °C for 30 minutes, the contact was no longer ohmic. The authors speculated that the carbon at the interface resulting from the reaction between Pt and SiC was responsible for the non-ohmic behavior. Na et al. [50] reported that the as deposited Pt film showed ohmic contact on n-type 6H-SiC (the doping concentration was not specified). However, the ohmic contact was converted to rectifying behavior after annealing at 500 °C. At 900 °C, the Schottky barrier height was 1.37 eV. The authors speculated that donor-like traps developed in the sputtering process were responsible for reducing the barrier height to form ohmic contacts. The annealing process and the reaction between Pt and SiC reduced the interface density and led to defect-free interface, which resulted in the ohmic to rectifying conversion. Pt films also formed ohmic contacts on p-type SiC

using the focused ion beam direct-write deposition [52]. A two-step process was applied which included a focused ion beam surface modification and *in situ* direct-write metal deposition. The surface modification step incorporated a substantial Ga concentration within 15 nm of the SiC surface, resulting in a highly disordered interfacial layer and substantial reduction of the specific contact resistivity. A specific contact resistivity of $2.8 \times 10^{-4} \Omega \text{ cm}^2$ was obtained on p-type SiC ($1 \times 10^{19} \text{ cm}^{-3}$) and Pt deposition at 600°C . The interfacial structures of annealed Pt/SiC are similar to those of other VIII group metals on SiC, such as Ni, Co, and Pd. No evidence of interfacial reaction in Pt/SiC is found when the annealing temperature is below 650°C [51]. After annealing at 750°C , an interface composed of carbon and Pt_2Si is formed. Na et al. [50] reported that inter-diffusion takes place between Pt and SiC below 900°C . At 900°C , Pt_2Si is formed.

A specific contact resistivity of $4 \times 10^{-4} \Omega \text{ cm}^2$ was formed for Re films as deposited on n-type 3C-SiC with a carrier concentration of $\sim 10^{17} \text{ cm}^{-3}$, which decreased to $2.5 \times 10^{-4} \Omega \text{ cm}^2$ after annealing at 500°C . Ohmic contacts of Re films were improved on nitrogen implanted SiC [49].

Overall, in the VIII group metals, Ni is the best ohmic contact material for n-type SiC and Pd has potential for application to p-type SiC. However, due to low oxidation resistance, Ni and Pd are not the best choice for SiC devices required to operate at high temperature in air.

8.3.2 Silicides and Carbides in Metal/SiC

Some metals in the VIB, VB, and IVB groups have been examined as ohmic contact materials on SiC. Since the IVB to VIIIB metals have 2 to 5 electrons in the d-shell, they form strong chemical bonds with carbon to form thermal stable carbides [19, 20]. Generally, the advantages of these metals as ohmic contact materials are good thermal stability and oxidation resistance [53], but the disadvantages are that these metals require higher annealing temperatures for forming ohmic contacts on SiC and exhibit higher contact resistivity than those of the group VIII metals.

The group VIB metals include Cr, Mo, and W. W films as deposited form ohmic contacts on 3C-SiC with un-intentionally doping concentrations of $10^{17}\text{--}10^{18} \text{ cm}^{-3}$ with a specific contact resistivity of $10^{-3} \Omega \text{ cm}^2$ [26, 54]. Iliaidis et al. [52] reported that W films formed ohmic contacts on p-type SiC using the focused ion beam direct-write deposition. After a surface modification using a Ga focused ion beam and W deposition at 600°C , a specific contact resistivity of $2.5 \times 10^{-4} \Omega \text{ cm}^2$ was obtained on p-type SiC ($1 \times 10^{19} \text{ cm}^{-3}$). Edmond et al. [55] found that Cr formed ohmic contact with a specific contact resistivity of $7 \times 10^{-2} \Omega \text{ cm}^2$ on n-type 6H-SiC with a carrier concentration of $5 \times 10^{16} \text{ cm}^{-3}$ after annealing at 1250°C . Mo on SiC has similar contact properties to W [53]. Olowolafe et al. [56] reported that the specific contact resistivity was $4.08 \times 10^{-3} \Omega \text{ cm}^2$ for Mo film on p-type 6H-SiC with a doping concentration of about 10^{18} cm^{-3} after annealing at 1000°C in $\text{N}_2\text{-H}_2$.

However, Mo/SiC after annealing in N₂ at 1100 °C was non-ohmic, but after annealing in Ar at 1100 °C, it formed an ohmic contact with a specific contact resistivity of $4.73 \times 10^{-2} \Omega \text{ cm}^2$. These results indicate that annealing environments also have some effects on ohmic contact formation.

Cr, Mo, and W react with SiC to form silicides and carbides at high temperature. W is stable with SiC up to 950 °C, but forms W₅Si₃ and W₂C at 1100 °C [54]. Jacob et al. [26] reported that the W/SiC interface was stable after annealing at 900 °C. Kakanakova-Georgieva et al. [57] found that W carbide and silicides were formed at 1200 °C. Geib et al. [53] observed that W/SiC and Mo/SiC structures were stable after annealing at 850 °C and 800 °C, respectively, although W and Mo formed a very thin-mixed layer of metal carbide and silicates on SiC upon deposition at room temperature. Olowolafe et al. [56] reported that only inter-diffusion between Mo and SiC take place at 1000 °C, while no compounds formed. Hara et al. [58] observed a Mo₂C/Mo₅Si₃/SiC multilayer structure after annealing at 1200 °C. SiC polytypes and Mo deposition methods made no difference in the film composition after annealing.

The group VB metals include V, Nb, and Ta. Only Ta has been investigated for contact material on SiC. Ta formed an ohmic contact on n-type 3C-SiC as deposited with a specific contact resistivity of $5 \times 10^{-5} \Omega \text{ cm}^2$ with the carrier concentration at $\sim 10^{17} \text{ cm}^{-3}$ [49]. Olowolafe et al. [56] found that Ta formed ohmic contacts on p-type 6H-SiC with a doping concentration of about 10^{18} cm^{-3} after annealing at 1100 °C in N₂-H₂. The specific contact resistivity was $2.13 \times 10^{-3} \Omega \text{ cm}^2$, and TaSi₂ and carbon or Ta carbides were identified using Rutherford backscattering spectroscopy (RBS). A thin-mixed layer of Ta carbide and silicide on SiC interface was formed as deposited [53]. Above 400 °C, Ta reacts with SiC to form Ta silicide and carbide.

The group IVB metals include Ti, Zr, and Hf. Only Ti has been investigated for contact material on SiC. The most common use of Ti for ohmic contact is the addition with Al to improve morphology on p-type SiC [59], which is discussed in the next section.

Ti also forms ohmic contacts on n-type SiC [31, 60, 63]. La Via et al. [31] reported that Ti films formed ohmic contacts on n-type 6H-SiC with the doping concentrations of 10^{17} – 10^{18} cm^{-3} . The specific contact resistivity was 10^{-4} – $10^{-5} \Omega \text{ cm}^2$ after annealing at 900–1000 °C. Teraji et al. [63] reported that Ti films formed ohmic contact on n-type SiC (the carrier concentration was $5 \times 10^{17} \text{ cm}^{-3}$) when the SiC was immersed in boiling water for 10 minutes before deposition. The specific contact resistivity was $6 \times 10^{-3} \Omega \text{ cm}^2$ as deposited. The authors speculated that a monohydride might be formed on Si-face SiC in the boiling water and the density of interface states was reduced by the formation of an atomically flat interface, which they believed it necessary for ohmic contact formation in Ti/SiC. Ti even reacts with SiC as deposited at room temperature to form both TiC and TiSi_x [35]. Porter et al. [64] found that TiC and Ti₅Si₃ were formed at 700 °C and that the contact was rectifying on n-type 6H-SiC. As shown in Fig. 8.3, La Via

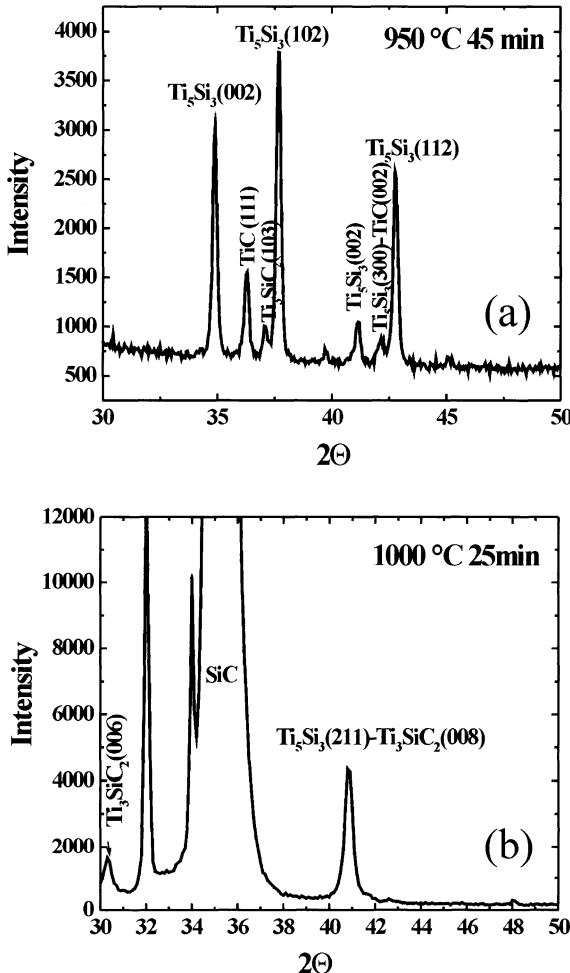


Fig. 8.3. XRD spectra of Ti/SiC after annealing at 950 °C (a) and 1000 °C (b) (from [31], with permission for reproduction from Elsevier)

et al. [31] found a double layer of TiC and Ti_5Si_3 formed at 900 and 950 °C, and Ti_3SiC_2 was observed only at 1000 °C. Touati et al. [60, 61] also observed that the Ti/SiC interface was stable below 700 °C. The cubic structure disilicide C49 TiSi_2 (high resistive crystal structure) formed at the interface in the temperature above 700 °C. From 700 to 900 °C, a mixture of metastable silicides phases such as TiSi , Ti_5Si_3 , and Ti_5Si_4 were also detected. The strong reduction of the contact resistivity has been traced back to the formation of the crystalline disilicide C49 TiSi_2 . Goesmann et al. [62] investigated the microstructure of Ti/SiC after annealing. Below 700 °C, the diffusion path from SiC to Ti is $\text{SiC}/\text{TiC}_{1-y}$ /two-phase $\text{Ti}_5\text{Si}_3 + \text{TiC}_{1-y}/\text{Ti}_3\text{Si}/\text{Ti}$. Between 800 to 1000 °C, the diffusion path is $\text{SiC}/\text{Ti}_3\text{SiC}_2/\text{Ti}_5\text{Si}_3$ /two-phase

$\text{Ti}_5\text{Si}_3 + \text{TiC}_{1-y}/\text{Ti}_3\text{Si}/\text{Ti}$, and the contact is rectifying. At 1200 °C, the diffusion path from SiC to Ti is $\text{SiC}/\text{Ti}_3\text{SiC}_2/\text{Ti}_5\text{Si}_3$ /two-phase $\text{Ti}_5\text{Si}_3 + \text{TiC}_{1-y}/\text{Ti}_5\text{Si}_3/\text{Ti}$, and the contact is ohmic. The ternary phase, Ti_3SiC_2 , at the interface was believed to be responsible for ohmic contact formation.

Therefore, Ti/SiC after annealing shows complex interfacial structures with several Ti silicides and carbides co-existing, and the interface is thermodynamically unstable at elevated temperatures. The structural complexity in the interface makes investigation of the mechanism of ohmic contact on Ti/SiC difficult.

It is worthwhile to note that the group IB metals (Cu, Ag, and Au) have very low chemical reactivity with carbon [65–68]. Since the d-shells in the IB metals are completed with electrons, the IB metals have weak interactions with carbon [19, 20]. No chemical reactions between SiC and Au or Ag take place at elevated temperatures. However, SiC decomposes into Si and C in Au/SiC structure and ohmic contacts were formed after annealing at 700 °C [65]. Au is commonly used as an oxidation barrier material on SiC due to the thermal stability.

8.3.3 Silicon and Carbides in Al/SiC and Al-Alloy/SiC

Al has been widely investigated as an ohmic contact material for SiC. It is generally accepted that Al/Ti alloy is the best material for ohmic contacts on p-type SiC [4–8]. Al reacts with SiC to form Al carbide (Al_4C_3) and elemental Si after annealing at 400 and 600 °C, and Al silicides are not formed [35].

Edmond et al. [55] reported that Al forms ohmic contacts on p-type SiC. The specific contact resistivity was $3.1 \times 10^{-2} \Omega \text{cm}^2$ on 6H-SiC with a carrier concentration of $1 \times 10^{16} \text{ cm}^{-3}$ after annealing at 877 °C. Jacob et al. [26] reported that ohmic contacts were formed as deposited on Al/3C-SiC with a carrier concentration of $\sim 10^{17} \text{ cm}^{-3}$. The specific contact resistivity was $2 \times 10^{-4} \Omega \text{cm}^2$, and increased to $10^{-3} \Omega \text{cm}^2$ measured at 400 °C.

Al film has poor oxidation resistance and exhibits rough surface after annealing. Therefore, Al-Ti alloys have been commonly applied for ohmic contacts on p-type SiC [69–74]. Nennewitz et al. [70] reported that ohmic contacts were not formed using Al/Ti alloy (20 nm/250 nm) on p-type 6H-SiC with the doping concentration between 10^{15} and 10^{17} cm^{-3} after annealing at 1050 °C. However, for a doping concentration at 10^{18} cm^{-3} , a specific contact resistivity of $\sim 10^{-2} \Omega \text{cm}^2$ was obtained after annealing at 550 and 1050 °C. Crofton et al. [71] reported that low specific contact resistivities of 10^{-5} – $10^{-6} \Omega \text{cm}^2$ were obtained for Al/Ti alloy (90/10 wt%) on p-type SiC with a high doping concentration of $1.3 \times 10^{19} \text{ cm}^{-3}$ after annealing at 1000 °C. A high Al/Ti ratio exceeding TiAl_3 stoichiometry was required to form ohmic contact on p-type SiC [72]. Recently, Crofton et al. [73] reported that Al-Ti alloy with 90 wt% Al showed the best ohmic contacts but had poor surface morphology after annealing. Ohmic contacts were not formed when Al is below 60 wt% in the alloy for p-type SiC with a doping concentration of $7 \times 10^{18} \text{ cm}^{-3}$ after

annealing at 1000 °C. The authors suggested that the Al/Ti alloy with 70 wt% represents the best Al/Ti composition to achieve the best ohmic contacts on p-type SiC. Thus, Ti does not improve the ohmic contact properties, but it does improve surface morphology. However, Johnson et al. [74] recently found the Ti concentration in Ti/Al film has little effect on ohmic contact formation. The lowest specific contact resistivity was $2.5 \times 10^{-4} \Omega \text{ cm}^2$ after annealing at 1000 °C on 4H-SiC with a doping concentration of $4.8 \times 10^{18} \text{ cm}^{-3}$, and only varied by a factor of four when the Ti wt% in the Al/Ti alloy ranged from 0 to 50%.

Mohney et al. [75] reported that 70 wt% Al in Ti-Al alloy exhibited good ohmic contact behavior and fairly good film uniformity. Only alloys with some amount of a liquid phase present at the annealing temperature formed an ohmic contact on p-type SiC. The surface morphology became quite smooth when the Al fraction was reduced to 60%. Pécz et al. [76] identified the structure of the annealed contact layer as a Ti_3SiC_2 layer on SiC, covered by a Al_3Ti layer using TEM. But the Al_3Ti phase was also to be found in contact with SiC on some areas at the interface. The authors suggested that Ti_3SiC_2 is a new promising ohmic contact material for p-type SiC, as shown in Fig. 8.4. It is worthwhile noting that Ti_3SiC_2 is the interface phase in Ti/SiC structure after annealing [62]. Therefore, the role of Al and Ti in Ti/Al alloy ohmic contacts on p-type SiC remains an interesting subject for further investigation.

Several other Al based alloys have been examined to improve ohmic contacts on p-type SiC. Olowolafe et al. [56] reported that a specific contact resistivity of $10^{-4} \Omega \text{ cm}^2$ was achieved for both Mo/Al and Ta/Al alloys on p-type 6H-SiC with a doping concentration of about 10^{18} cm^{-3} after annealing at 1100 °C. Nakatsuka et al. [77] reported that Co/Al alloys formed ohmic contacts on p-type SiC, but the specific contact resistivity was higher than that of Ti/Al. Konishi et al. [78] investigated Ni/Al and Ni/Ti/Al alloys for ohmic contacts on p-type SiC. Ni/Ti/Al films demonstrated excellent ohmic contacts for a doping concentration in 4H-SiC of $3.0 \times 10^{18} \text{ cm}^{-3}$. A specific contact resistivity of $6.6 \times 10^{-5} \Omega \text{ cm}^2$ was obtained after annealing at 800 °C. Ni/Al films showed a specific contact resistivity at $5 \times 10^{-3} \Omega \text{ cm}^2$ under the same annealing conditions as Ni/Ti/Al on SiC. The authors believed that the high reactivity of Ni with SiC reduces the ohmic contact formation temperature, Al acts as an acceptor in SiC, and Ti might reduce or prevent the formation of unreacted carbon atoms by forming Ti_3SiC_2 compounds at the interface. Ti_3SiC_2 with Ni_2Si , NiAl_3 , Ti_2Al , TiAl_2 , and TiAl_3 are found in the film when ohmic contact is formed. The carbon phase is believed to increase the contact resistivity. Ni/Ti/Al film also showed better surface morphology than Ti/Al film after annealing.

Al-based alloys have also been used for ohmic contact on n-type SiC. Hallin et al. [79] reported that the specific contact resistivity on Al/Ni/Al/n-4H-SiC was more than three times lower than that of Ni/SiC after annealing at 1000 °C. The Al layer between the Ni and the SiC is believed to prevent voids from forming at the interface and also to reduce the oxide on the SiC sur-

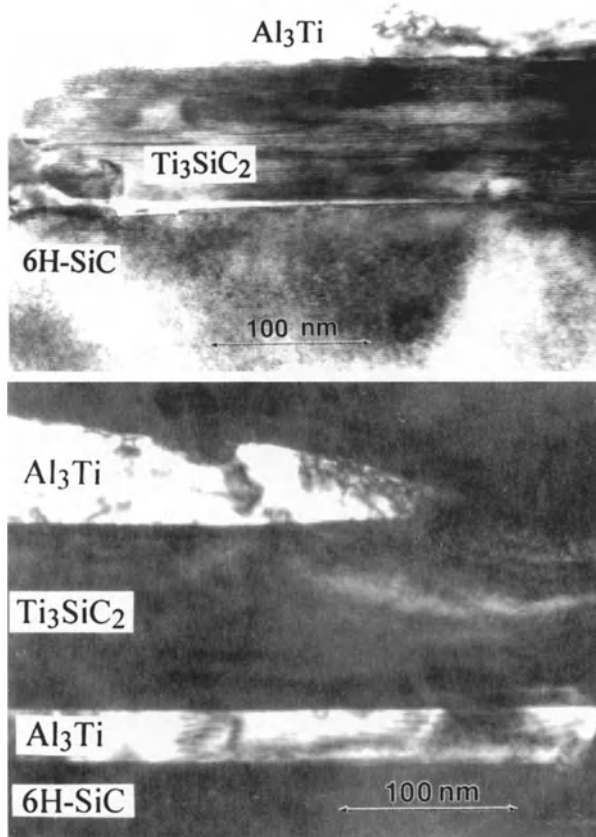


Fig. 8.4. Cross-sectional TEM images of Ti/Al/SiC after annealing at 900 °C. *Top*, the lattice spacing along the *c*-axis both in Ti_3SiC_2 and in 6H-SiC; *bottom*, the ternary layer between two layers of Al_3Ti (from [76], with permission for reproduction from Elsevier)

face. A specific contact resistivity of $1.8 \times 10^{-5} \Omega \text{cm}^2$ was found for Al/Ni/Al film on n-type 4H-SiC with a doping concentration of $1 \times 10^{19} \text{ cm}^{-3}$ after annealing at 1000 °C. Marinova et al. [80] used a Ni/Al alloy film on n-type 6H-SiC for ohmic contacts. The specific contact resistivity as deposited was $4.4 \times 10^{-4} \Omega \text{cm}^2$ for 6H-SiC with a doping concentration of $1 \times 10^{18} \text{ cm}^{-3}$. However, the contact became non-ohmic between 300 and 900 °C, but became ohmic after annealing at 1020 °C with a specific contact of $1.2 \times 10^{-4} \Omega \text{cm}^2$. Al reacted with SiC to form Si and Al_4C_3 , and also formed Al_2O_3 to reduce SiO_x at the interface at elevated temperatures. Ni diffused through the Al, Al_2O_3 and Al_4C_3 , while Al diffused towards the surface. NiSi , $\text{Ni}_3(\text{AlSi})_7$, and $\text{Ni}_{5.4}\text{AlSi}_2$ may be formed, and carbon was in the graphitic state after annealing at 1000 °C. Gao et al. [81] reported that Ti/Ni/Al composite films

Table 8.2. Metals forming ohmic contacts on n-type SiC

IA	IIA	IIIB	IVB	VB	VIB	VIIB	VIIIB		IB	IIB	IIIA	IVA	VA	VIA	VIIA	VIIIA	
H																He	
Li	Be								B	C	N	O	F			Ne	
Na	Mg								Al	Si	P	S	Cl			Ar	
K	Ca	Sc	Ti	V	Cr	Mn	Fe	Co	Ni	Cu	Zn	Ga	Ge	As	Se	Br	Kr
Rb	Sr	Y	Zr	Nb	Mo	Tc	Ru	Rh	Pd	Ag	Cd	In	Sn	Sb	Sb	I	Xe
Cs	Ba	La	Hf	Ta	W	Re	Os	Ir	Pt	Au	Hg	Tl	Pb	Bi	Po	At	Rn

Table 8.3. Metals forming Ohmic Contacts on p-type SiC

IA	IIA	IIIB	IVB	VB	VIB	VIIB	VIIIB		IB	IIB	IIIA	IVA	VA	VIA	VIIA	VIIIA	
H																He	
Li	Be								B	C	N	O	F			Ne	
Na	Mg								Al	Si	P	S	Cl			Ar	
K	Ca	Sc	Ti	V	Cr	Mn	Fe	Co	Ni	Cu	Zn	Ga	Ge	As	Se	Br	Kr
Rb	Sr	Y	Zr	Nb	Mo	Tc	Ru	Rh	Pd	Ag	Cd	In	Sn	Sb	Sb	I	Xe
Cs	Ba	La	Hf	Ta	W	Re	Os	Ir	Pt	Au	Hg	Tl	Pb	Bi	Po	At	Rn

as deposited were ohmic (10^{-2} – $10^{-3} \Omega \text{cm}^2$) on n-type 4H-SiC with a doping concentration of $7 \times 10^{18} \text{ cm}^{-3}$. After annealing at 1000°C , the specific contact resistivity was $4.5 \times 10^{-5} \Omega \text{cm}^2$. Ni₂Si and TiC were formed after annealing. The authors believed that the contact layer metal does not participate in creating the actual ohmic contact, but it improves the contact by reducing the interface oxide, reacting with carbon and also extending the distance for the fast diffusing Ni. Basak et al. [82] recently reported that Ti/Ni/Ti/Au film showed ohmic contact behavior on SiC at 750°C .

Tables 8.2 and 8.3 summarize the elements that have been demonstrated to form ohmic contacts on n-type and p-type SiC. As shown, the IVA and IVB to VIII elements form ohmic contacts on n-type SiC, while the IIIA and VIII metals form good ohmic contacts on p-type, as well as Ti, Ta, and Mo.

8.4 Compounds Used for Ohmic Contacts

8.4.1 Silicides

Metal silicides are the main products of metal and SiC reactions after annealing, and have been assumed responsible for ohmic contact formation on SiC. Some of the transition metal silicides have been examined as ohmic contact materials on both n- and p-type SiC. In the VIII group metals, Ni and Co silicides have been investigated. Lundberg et al. [83] investigated ohmic contact properties of CoSi_2 on SiC. The CoSi_2 film was deposited by sequential electron-beam evaporation. The specific contact resistivity was less than $3.0 \times 10^{-5} \Omega \text{cm}^2$ on n-type SiC after annealing at 900°C with a doping concentration of $1.4 \times 10^{19} \text{cm}^{-3}$, and showed no dependence on the current density within a range of 140 to $23\,000 \text{A/cm}^2$. CoSi_2 also formed ohmic contacts on p-type SiC as well [84]. The specific contact resistivity was less than $4.0 \times 10^{-6} \Omega \text{cm}^2$ on highly p-doped SiC (carrier concentration of $2 \times 10^{19} \text{cm}^{-3}$) after a two-step vacuum anneal at 500°C and 900°C . In the temperature from 22 to 200°C , the contact resistivity increased with temperatures. Aging at 1100°C in vacuum degraded the morphology and contact resistivity drastically.

NiSi_2 and Ni_2Si films have also been investigated for ohmic contact materials [24, 85, 86]. The specific contact resistivity was $3.6 \times 10^{-6} \Omega \text{cm}^2$ on highly n-doped SiC with a doping concentration of $2.5 \times 10^{19} \text{cm}^{-3}$ after annealing at 900°C [85]. Marinova et al. [24] examined $\text{Ni}_2\text{Si}/\text{SiC}$ on n-type SiC prepared by annealing Ni/Si/SiC and Si/Ni/SiC structures. After annealing at 950°C , a Ni_2Si film was formed. The specific contact resistivity was $\sim 10^{-4} \Omega \text{cm}^2$, and the Ni/Si/SiC had a slightly higher specific contact resistivity than that of Si/Ni/SiC . Carbon was found only on the interface, not in the silicides film. NiSi_2 films also formed ohmic contacts on n-type SiC after annealing at 950°C , and resulted in the same value of specific contact resistivity as Ni/SiC [86]. Ohmic contacts on p-type SiC using Ni silicides have not been reported.

TaSi_2 formed an ohmic contact on n-type 3C-SiC with a carrier concentration of $5 \times 10^{16} \text{cm}^{-3}$ after annealing at 850°C , not on p-type SiC [55]. Getto et al. [87] deposited titanium silicide (TiSi_x) on n-type epitaxial SiC layer with a carrier concentration of $5 \times 10^{18} \text{cm}^{-3}$. An ohmic contact was formed after annealing at 1000°C with a specific contact resistivity less than $8 \times 10^{-6} \Omega \text{cm}^2$. The ternary phase, Ti_3SiC_2 , was found at the interface of TiSi_2/SiC , in which is similar to Ti/SiC [62]. Capano et al. [88] recently reported that the C54- TiSi_2 and TiSi are observed following a $600^\circ\text{C}/30$ minutes and an $850^\circ\text{C}/30$ minutes annealing cycle when the Ti to Si layer thickness is 1:3. When the Ti to Si layer thickness is 1:1, Ti_5Si_3 and TiSi phases are formed after the same annealing cycle.

Although silicide films reduce the reactions between SiC and the film, no significant improvements in ohmic contact were observed. Annealing is still

required to form an ohmic contact, and the annealing temperatures are close to those for metal/SiC. Marinova et al. [24] compared ohmic contacts of Ni/SiC and Ni₂Si/SiC, and the specific contact resistivity of Ni₂Si/SiC was one order of magnitude higher than that of Ni/SiC. Pécz et al. [33] reported that Ni/Si films exhibited ohmic contact behavior on n-type SiC and the addition of a Si layer reduced the decomposition of SiC and the voids on the interface after annealing.

8.4.2 Carbides

Only TaC and TiC have been examined as ohmic contact materials for SiC [89–94], while TiC has been the most extensively investigated. Chaddha et al. [90,92] investigated TiC contacts on heavily doped n-type SiC. The processing temperature was very high: TiC film was synthesized by CVD using TCl₄ and C₂H₄ at 1260 °C. The specific contact resistivity was $1.30 \times 10^{-5} \Omega \text{cm}^2$ on 6H-SiC with a doping concentration of $4 \times 10^{19} \text{ cm}^{-3}$, and less than $6 \times 10^{-6} \Omega \text{cm}^2$ on 3C-SiC with a doping concentration of $2 \times 10^{19} \text{ cm}^{-3}$.

Lee et al. [91] have studied TiC as ohmic contact materials on n- and p-type SiC. TiC was prepared by Ti and C60 co-evaporations. Using highly doped n-type SiC ($1.3 \times 10^{19} \text{ cm}^{-3}$) and p-type ($> 10^{20} \text{ cm}^{-3}$), the as-deposited TiC film was good ohmic contact, and the lowest contact resistivity was $7.4 \times 10^{-7} \Omega \text{cm}^2$ at 200 °C for n-type SiC and $1.1 \times 10^{-4} \Omega \text{cm}^2$ at 25 °C for p-type SiC. Annealing at 950 °C did not improve the contact on n-type SiC, but the specific contact resistivity reduced to $1.9 \times 10^{-5} \Omega \text{cm}^2$ on p-type SiC. Since the doping concentration in p-type SiC is very high, even the as-deposited Ti/SiC formed ohmic contacts with specific contact resistivity at $\sim 10^{-4} \Omega \text{cm}^2$. Lee et al. [89,93] reported ohmic contacts from epitaxial TiC film on Al ion implanted 4H-SiC. A sacrificial silicon nitride (Si₃N₄) layer was deposited on the SiC prior to Al implantation in order to reach a high doping concentration at the surface while maintaining a low dose. The lowest specific contact resistivity of the TiC films prepared by the co-evaporation of Ti and C60 was $2 \times 10^{-5} \Omega \text{cm}^2$ after annealing at 500 °C, and TiC film was stable after annealing at 950 °C in vacuum.

Another carbide, TaC, has been investigated for the use as ohmic contacts on n-type SiC [94]. An ohmic contact was formed after annealing at 800 °C on 6H-SiC with a high doping concentration of $2.3 \times 10^{19} \text{ cm}^{-3}$. The specific contact resistivity of the TaC film was $2.1 \times 10^{-5} \Omega \text{cm}^2$ after annealing at 1000 °C. With Pt and Au overlayers, the specific contact resistivity was reduced to $7.4 \times 10^{-5} \Omega \text{cm}^2$ and $1.4 \times 10^{-6} \Omega \text{cm}^2$, respectively.

Transition metal carbides, like silicides and nitrides, have chemical inertness with SiC, oxygen resistance, and good electrical conductivity [95]. These materials have great potential in SiC based devices for high power and high temperature applications.

8.4.3 Nitrides

Among the transition metal nitrides, only Ti and W nitrides have been examined [57, 59, 86, 96–98]. TiN does not react with SiC, has excellent conductivity, and can be grown epitaxially with a small mismatch on SiC. Glass et al. [96] used ion-assisted reactive evaporation with low energy nitrogen ions to deposit TiN on n-type 6H-SiC with a doping concentration of $1.6 \times 10^{18} \text{ cm}^{-3}$. Prior to the deposition, the SiC was cleaned with 100 eV nitrogen ions for 2–5 minutes. TiN/SiC was ohmic as deposited, and the contact was stable after short period annealing at 550 °C. However, using different deposition methods, such as reactive evaporation (RE), and ion-assisted reactive evaporation (IARE) without pre-cleaning, as deposited Ti/SiC was rectifying [97]. The authors believed that the exposure of the SiC to low energy nitrogen ions results in (a) removing the surface contaminants, (b) disordering the crystalline surface, and (c) the formation of bonds between Si and N. The Si_3N_4 layer formed on the SiC surface by low energy nitrogen ions appears to be responsible for ohmic contacts. The insulating Si_3N_4 layer may free the Fermi level by passivating the SiC interface states. Iliadis et al. [98] used Ga focused ion-beam (FIB) surface modification and pulsed laser deposition to prepare TiN film on p-type SiC. The contact was ohmic and the specific contact resistivity was $2.8 \times 10^{-3} \Omega \text{cm}^2$ for TiN growth at room temperature on un-modified SiC with a doping concentration of $1 \times 10^{19} \text{ cm}^{-3}$, and $3.2 \times 10^{-4} \Omega \text{cm}^2$ on the surface modified SiC. With an ion dose and energy of $5.0 \times 10^{16} \text{ ions/cm}^2$ and 20 KeV, the specific contact resistivity was reduced to $4.4 \times 10^{-5} \Omega \text{cm}^2$ on SiC when an epitaxial TiN film was grown at 600 °C. An intermixed Si(Ga)C layer on the interface is believed to be responsible for the reduction in contact resistivity. Pécz [86] applied reactive magnetron sputtering to deposit an epitaxial TiN film at 700 °C on 3C- and 6H-SiC, and the contact was ohmic as deposited. The specific contact resistivity was $1.3 \times 10^{-3} \Omega \text{cm}^2$ on 6H-SiC with a doping concentration of $5 \times 10^{17} \text{ cm}^{-3}$. The TiN contact was stable in vacuum up to 1100 °C. Lee et al. [59] recently reported that TiN/Al film on p-type 4H-SiC only improves surface morphology, not ohmic contact, compared to Al/SiC and Ti-Ai/SiC.

Kakanakova-Georgieva et al. [57] reported that WN was thermally stable on SiC at 800 °C, which is similar to the thermal stability of pure W on SiC. WN film was prepared by reactive sputtering. After annealing at 1200 °C, nitrogen atoms desorbed, and W carbide and silicides formed. Pécz [86] also reported similar results for WN_x film prepared by reactive magnetron sputtering on n-type SiC with a doping concentration of $9.5 \times 10^{16} \text{ cm}^{-3}$. The WN_x films were stable at 800 °C but the contact was rectifying. After annealing at 1200 °C, W_5Si_3 and W_2C formed and the contact became ohmic.

TiN has a low work function (3.74 eV), and the nitrides usually have excellent oxidation resistances with stability in air up to 800 °C [95]. Therefore, the nitrides have advantages for applications in high temperature devices, but more investigations are needed to better understand the interfacial chemistry.

8.4.4 Borides

Oder et al. [99] examined metal borides, CrB_2 , W_2B , and TiB_2 , on p-type SiC. Ohmic contact behavior was observed after annealing at 1100°C on highly doped p-type SiC ($1.3 \times 10^{19} \text{ cm}^{-3}$). The specific contact resistivities for CrB_2 and W_2B were 8.2×10^{-5} and $5.8 \times 10^{-5} \Omega \text{cm}^2$, respectively. TiB_2 forms ohmic contacts with a high specific contact resistivity. Interfacial mixing occurs in TiB_2/SiC and $\text{W}_2\text{B}/\text{SiC}$ after annealing, not in CrB_2/SiC . A composite Au/ CrB_2/SiC structure also exhibits a good thermal stability at 300°C in vacuum.

8.4.5 Composite Structures

A composite film in this review is defined as a film composed of a non-metallic element (Si or C) with one or more metals. They are used to reduce the contact resistivity and to improve the surface morphology of the films. As discussed in the Sect. 8.4.1, the addition of Si layer prior to a metal film deposition is commonly used to produce metal silicide films on SiC. The silicides are formed before the contact becomes ohmic. In this section, the metals we discuss do not react (or low reactivity) with Si or C before the contact becomes ohmic.

Several such Si-based composite films have been investigated. Kakanakov, et al. [100] demonstrated that Al/Si composite films improve the contacts on p-type SiC. Ohmic contacts were formed for AlSi(2%)Ti(0.15%) film on p-type 4H-SiC with a doping concentration of $3-5 \times 10^{19} \text{ cm}^{-3}$ after annealing at 700°C . The lowest specific contact resistivity was $9.6 \times 10^{-5} \Omega \text{cm}^2$ after annealing at 950°C . Papanicolaou et al. [101] reported that Si/Pt films form ohmic contacts with a specific contact resistivity of $2 \times 10^{-4} \Omega \text{cm}^2$ on p-type 4H-SiC with $1 \times 10^{19} \text{ cm}^{-3}$ after annealing at 1100°C , which is comparable to the values obtained with conventional Al/Ti contacts. Jang et al. [102] reported that ohmic contacts using Pt/Si film with a specific contact resistivity at $2.89 \times 10^{-4} \Omega \text{cm}^2$ was formed on p-type 6H-SiC after annealing at 1100°C . The doping concentration was $7.0 \times 10^{18} \text{ cm}^{-3}$. A single phase, PtSi, was found at the interface after annealing. However, Olowolafe et al. [56] investigated the effects of Si interface layers on Ta contacts on p-type SiC. Ta/Si/SiC formed ohmic-like I-V characteristics on 4H-SiC with a doping concentration of $\sim 10^{18} \text{ cm}^{-3}$ after annealing at 1100°C in H_2-N_2 . The specific contact resistivity was high at $0.147 \Omega \text{cm}^2$ on Ta/Si/SiC, and $2.13 \times 10^{-3} \Omega \text{cm}^2$ on Ta/SiC on the same conditions.

Recently, the use of carbon films and carbon-based composite films for ohmic contacts on SiC have been reported [103–107]. Lu et al. [103, 104] demonstrated that the carbon films prepared by sputtering formed ohmic contacts on n-type 4H-SiC after annealing above 1050°C . The specific contact resistivity was between $10^{-3}-10^{-4} \Omega \text{cm}^2$ on 4H-SiC with a high doping concentration of $1.3 \times 10^{19} \text{ cm}^{-3}$ after annealing between 1050 and 1350°C ,

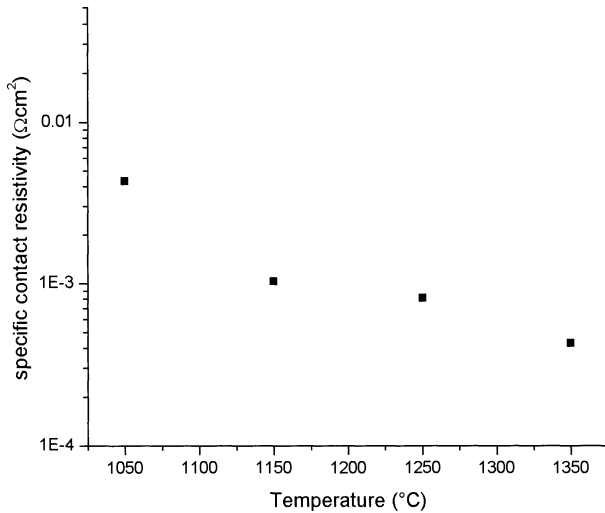


Fig. 8.5. Specific contact resistivities on carbon/SiC after annealing at various temperatures in Ar for 30 minutes (4H-SiC, n-type, Si face, 8° off-axis, and a doping concentration of $1.3 \times 10^{19} \text{ cm}^{-3}$) (from [104], with permission for reproduction from the Minerals, Metals, and Materials Society)

as shown in Fig. 8.5. Similar to metal/SiC contacts, the annealing temperature required for the formation of ohmic behavior in C/SiC increases with decreasing doping concentration.

Ni is a well-known graphitization catalyst and the lowest temperatures for Ni induced graphitization for various carbon structures, such as diamond, diamond-like amorphous carbon, graphite, and graphite-like amorphous carbon are in the range of 700 to 900 °C [108]. Lu et al. [106] have examined ohmic contact formation of Ni/C/SiC. Using a graphitized carbon interfacial layer between Ni and SiC. The ohmic contact properties were improved significantly. Figure 8.6 shows the I - V curves of Ni/SiC and Ni/C/SiC after annealing at 700 °C in Ar for two hours. As shown, the Ni/SiC sample exhibits rectifying behavior, while the Ni/C/SiC sample shows typical ohmic behavior. On highly doped SiC ($\sim 10^{19} \text{ cm}^{-3}$), the optimal conditions for the formation of ohmic contacts in the composite film was a 2.0 nm thick carbon film annealed at 700–800 °C in Ar for two hours. The specific contact resistivities were 10^{-6} – $10^{-7} \Omega \text{cm}^2$. For the Ni/C/SiC with moderate doping concentrations ($\sim 10^{17} \text{ cm}^{-3}$), the specific contact resistivities were around $10^{-5} \Omega \text{cm}^2$ after annealing at 900–1000 °C. Various metal/carbon/SiC [105] and Ni/C60/SiC [107] were investigated, and demonstrated the addition of interfacial carbon layer improves ohmic contact significantly, compared to the metal/SiC contacts.

An investigation of Ti/Al/C composite films on p-type SiC by Lu et al. [109] has found that the formation of nanometer scale graphitic structures at

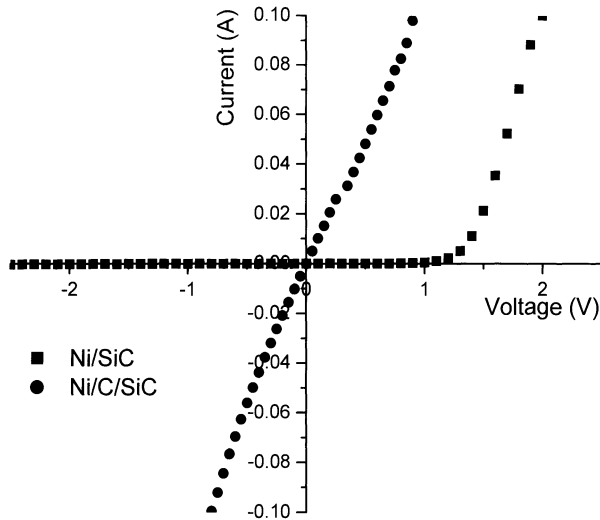


Fig. 8.6. Current–voltage curves for Ni/C/SiC and Ni/SiC after annealing at 700 °C in Ar for two hours (n-type, on-axis, Si face, and with a doping concentration of $3.1 \times 10^{19} \text{ cm}^{-3}$) (from [106], with permission for reproduction from Elsevier)

the SiC surface plays an important role in the formation of ohmic contacts on SiC. Zhao et al. [110] reported ohmic contacts with low contact resistivities (10^{-4} – $10^{-6} \Omega \text{cm}^2$) for Al films on the C-Al co-implanted SiC. This result is consistent with the conclusion of Lu et al. [109] that interfacial graphitic structures play an important role to the formation of ohmic contacts on SiC.

8.5 Recent Advances and Challenging Issues

8.5.1 Toward Understanding in the Ohmic Contact Mechanism

Due to structural complexity and multi-components in the films after annealing, the mechanisms for the formation of ohmic contacts on SiC have been an unsolved issue since the beginning of SiC research. It is generally agreed that there are no correlations between the work functions of the contact materials and ohmic contact properties, and no experimental evidences that the interface states on SiC are high enough to predetermine the contact properties. The classical contact theories of Schottky-Mott limit and Bardeen limit are unsuccessful to predict the formation of ohmic contact on SiC, and there are no ohmic contact mechanisms available for guiding the materials selection and structural design for electrical contacts on SiC. After the last ten years of intensive SiC research, unfortunately, not many advances in understanding the mechanisms have been made, and the “trial and error” method has been used in selecting contact materials. This is one of the most exciting but one of the most troublesome subjects in the field of wide band gap semiconductors.

There is some evidence that “interface pinning” takes place at as deposited metal/SiC interface [5, 63, 111, 112]. However, after high temperature annealing and chemical reactions between the metal and SiC, new interfaces are created. Experimentally, the routine cleaning methods, such as the RCA or the modified RCA methods seem to efficiently clean SiC prior to metal deposition. In metal/SiC rectifying contacts, a relationship between the metal work functions and the Schottky barrier height still somewhat exists and it is common to obtain ideality factors with values of near one in rectifying contacts [4]. Therefore, “interface pinning” seems not to be the dominant factor, and the Bardeen limit is not applicable in ohmic contacts on SiC in general.

The main issue in ohmic contacts on SiC is that there is no correlation between the work function of the contacting materials and the formation of ohmic contacts. In the last several years, the reactions between metals and SiC have been extensively investigated, and metal silicides or carbides have been studied as the main contacting components responsible for the ohmic contacts. It is a natural assumption since metal silicides or carbides are the main products of metal and SiC reactions, and they are good electrical conductive materials.

However, based on the assumptions that metals silicides may be responsible for the formation of ohmic contacts, the prediction on ohmic contact formation and improvements have not been successful. The reaction temperatures between metals and SiC are much lower than that of ohmic contact formation. For example, as discussed in the Sect. 8.3.1, Ni starts to react with SiC to form Ni silicides at 500 °C, which is much lower than the temperature to form ohmic contact for Ni/SiC [29]. The formation of metal silicides and carbides has not provided any direct evidences that lead to ohmic contact formation. Also, the values of work functions for most metal silicides are close to those of metals. For example, Ni₂Si is the only Ni silicides phase above 700 °C, the work functions of is about 4.55 eV [113]. According to the Schottky and Mott limit in (8.1), the contact between Ni₂Si and n-type SiC should be rectifying. In fact, rectifying behavior of Ni/SiC improves after annealing up to 800 °C [114].

Besides the silicide model discussed above, other models have been proposed to explain the formation of ohmic contacts on SiC. Konishi et al. [78] believed that the ohmic behavior of Ni/Al and Ni/Ti/Al alloys on p-type SiC were due to Al diffusion into the SiC and the subsequent formation of a heavily doped region at the interface. However, no experimental evidence of the Al diffusion was presented [78]. At temperatures near 1000 °C which contacts become ohmic, it is known that Al is very difficult to diffuse into SiC.

Mohney et al. [75] believed that the spike formation at the interface caused by the reaction of Al and SiC is necessary for ohmic contact formation on SiC. The SiC surface after removal of 200 nm 70 wt%Al in Ti/Al film annealed at 1000 °C showed a semicontinuous network of small pits, on the order of 100–600 nm in lateral dimension and a roughness of 12 nm. It is possible that current is transported primarily at the spikes because of an enhancement of

the electric field at these features and/or enhancement of the semiconductor doping at these locations. However, similar spike structures also were observed on the annealed Pd/SiC by Lu et al. [115]. The Pd/SiC after annealing at 400–600 °C showed only rectifying contacts.

The microstructures in annealed Ni on SiC have been extensively investigated and Ni/SiC interface is often therefore used as a prototype for investigating the mechanisms in the formation of ohmic contacts on SiC. Han et al. [116–118] recently re-examined these microstructures of Ni/SiC using several techniques. They found the work function of Ni₂Si to be higher than that of Ni by 0.36 eV, and concluded that Ni₂Si is not responsible for the formation of ohmic contact in Ni/SiC [117]. A graphite phase at the surface after annealing at 950 °C was attributed to carbon out-diffusion. The authors believed that the formation of carbon vacancies, acting as donors for electrons, plays a major role in the formation of the ohmic contacts through the reduction of the effective Schottky barrier height. Figure 8.7 shows the cross section TEM images of Ni/SiC after annealing at 800 and 950 °C [118]. A carbon phase was found near the interface. However, a significant amount of carbon still remained at the interface as seen in Fig. 8.7 using TEM. A strong graphite phase was formed as the ohmic contact was formed at 950 °C [116–118], but the effects of the structural evolution of the carbon phase around the temperature of the Schottky-ohmic conversion was not examined. Using Raman spectroscopy, Kunimoto et al. [37] found that the diffusion of Si atoms into the Ni layer may play a key role in forming ohmic contacts at above 900 °C. The formation of Ni silicides at the interface was not the key factor for the formation of ohmic contacts, and the nano-size graphite clusters or defective graphite crystals are formed after annealing at 1000 °C and 1100 °C in Ni/SiC, as shown in Fig. 8.2.

Based on the catalytic graphitization effects of various metals, a model for the formation of ohmic contacts has been proposed recently [105–107]. The model seems to provide a relationship between metal selection, annealing temperature, film morphology, and ohmic contact formation. The following section discusses the model.

8.5.2 Catalytic Graphitization Effects of Metals

The microstructural changes during graphitization include conversion of diamond-like (sp^3) to graphite-like (sp^2) carbon, re-arrangement of disordered carbon atoms to hexagonal graphitic layer structures, alignment of small graphitic flakes to larger planar structures, and formation of stacking structures with the neighboring layers [119]. Catalytic graphitization by metals was extensively investigated in the 1960's and 1970's [19, 20]. Catalytic graphitization refers to the enhancement of the crystallinity of the carbon involving chemical reactions between the un-graphitized carbon and the catalysts [19]. A generally accepted mechanism for catalytic graphitization is carbide formation-decomposition, in which amorphous carbon diffuses in

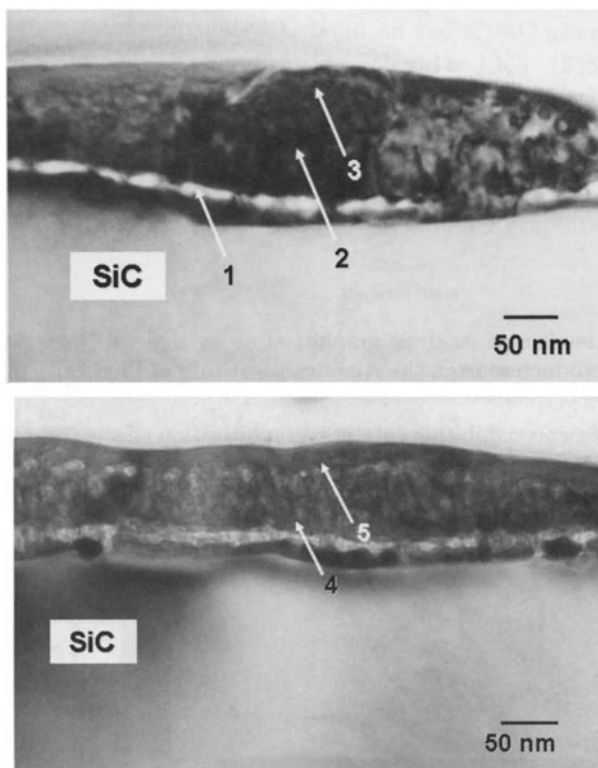


Fig. 8.7. Cross-sectional TEM image of Ni/SiC after annealing. *Top*, at 800 °C, and *bottom*, at 950 °C (from [118], with permission for reproduction from the American Institute of Physics)

the metal catalyst particles, forms carbides, and then the carbides decompose to form graphitized carbon. Another mechanism is carbon dissolution-precipitation which is controlled by the solubility of carbon in the metal. In both mechanisms, the driving force for the graphitization process is the decrease of the free energy by the conversion of amorphous carbon to graphitized carbon [120]. Figure 8.8 illustrates the carbide formation-decomposition graphitization process in metal catalytic graphitization mechanism. Based on this mechanism, the reactions and diffusion processes cause surface tension changes in the films and result in dynamic changes in the morphological features of the films. Table 8.4 lists the metals have shown as catalytic graphitization effects. As seen in the Table, most of the transition metals and some main group elements show catalytic graphitization activities. Comparing these to the metals which have been shown to form ohmic contacts on n- and p-type SiC in Tables 2 and 3. It can be concluded that all metals used as ohmic contact materials exhibit catalytic graphitization activities.

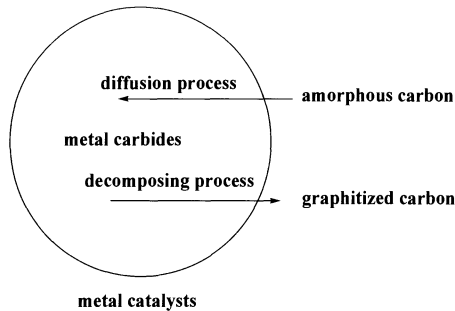


Fig. 8.8. Mechanism of catalytic graphitization by a metal (from [105], with permission for reproduction from the American Institute of Physics)

Table 8.4. Elements exhibiting catalytic graphitization effects (from [19], with permission for reproduction from Kluwer)

IA	IIA	IIIB	IVB	VIB	VIB	VIIIB	VIII		IB	IIB	IIIA	IVA	VA	VIA	VIIA	VIIIA	
H																He	
Li	Be								B	C	N	O	F			Ne	
Na	Mg								Al	Si	P	S	Cl			Ar	
K	Ca	Sc	Ti	V	Cr	Mn	Fe	Co	Ni	Cu	Zn	Ga	Ge	As	Se	Br	Kr
Rb	Sr	Y	Zr	Nb	Mo	Tc	Ru	Rh	Pd	Ag	Cd	In	Sn	Sb	Sb	I	Xe
Cs	Ba	La	Hf	Ta	W	Re	Os	Ir	Pt	Au	Hg	Tl	Pb	Bi	Po	At	Rn

There is overwhelming evidence that a carbon phase is found when ohmic contacts are activated on metal/SiC [4–8]. For example, Rastegaeva et al. [36] observed an enhancement of carbon at the Ni₂Si/SiC interface after annealing at 1000 °C, and speculated that the enrichment is a key factor in the formation of ohmic contact. However, some authors believed that the carbon phase degrades the ohmic contacts [4, 34].

Lu et al. [103, 104] have demonstrated that a carbon film forms ohmic contact on SiC. The as-deposited films are amorphous with an sp²/sp³ ratio of 1, and ohmic contacts were formed in carbon/SiC structures when the sp² carbon structures gradually increase at high temperatures. Raman spectra provide overall information on the structural evolution of the carbon films.

Figure 8.9 shows the deconvoluted G band on the C/SiC after annealing at 1050 and 1350 °C in Ar for 30 minutes. The D band at 1325–1335 cm⁻¹ is associated with disordered or defective hexagonal planar graphite structures [121]. The band at 1595 cm⁻¹ is close to the G band at 1582 cm⁻¹ [121] which involves the in-plane bond-stretching motions of pairs of graphitic (sp^2) carbon atoms on the basal plane of ideal graphite. The combination of the D and G bands is indicative of the presence of polycrystalline graphitic (sp^2) struc-

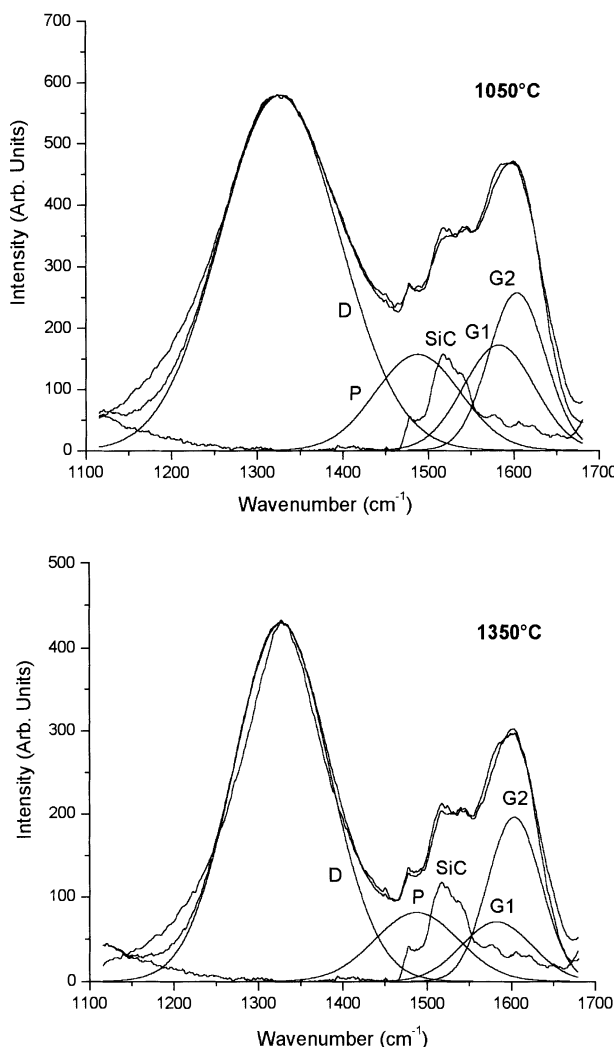


Fig. 8.9. The deconvoluted G band on the carbon/SiC films after annealing at 1050 and 1350 °C in Ar for 30 minutes (4H-SiC, n-type, 8° off-axis, Si face, and with a doping concentration of $2.0 \times 10^{18} \text{ cm}^{-3}$) (from [104], with permission for reproduction from the Minerals, Metals, and Materials Society)

tures. As shown, the sp^2 carbon structures consist of amorphous aromatic-like carbon, polyene-like carbon, and nano-size graphite flakes. Schottky contacts on C/SiC are converted to ohmic contacts after annealing. The concentration of nano-graphitic flakes relative to the aromatic-like and polyene-like carbon increases nearly linearly with annealing temperature. Stacked graphitic structures are not observed.

Figure 8.10 shows the size of the nano-graphitic flakes and the $I_{G2}/(I_{G1} + I_P)$ intensity ratio of carbon/4H-SiC with the doping concentration of $2.0 \times 10^{18} \text{ cm}^{-3}$. As seen in Fig. 8.10a, the size of the flakes is nearly constant at about 3.5 to 3.7 nm after annealing at various temperatures. The number of flakes formed can be estimated from the ratio of the intensity of the G2 band to the sum of the G1 and P bands, $I_{G2}/(I_{G1} + I_P)$ [121]. This ra-

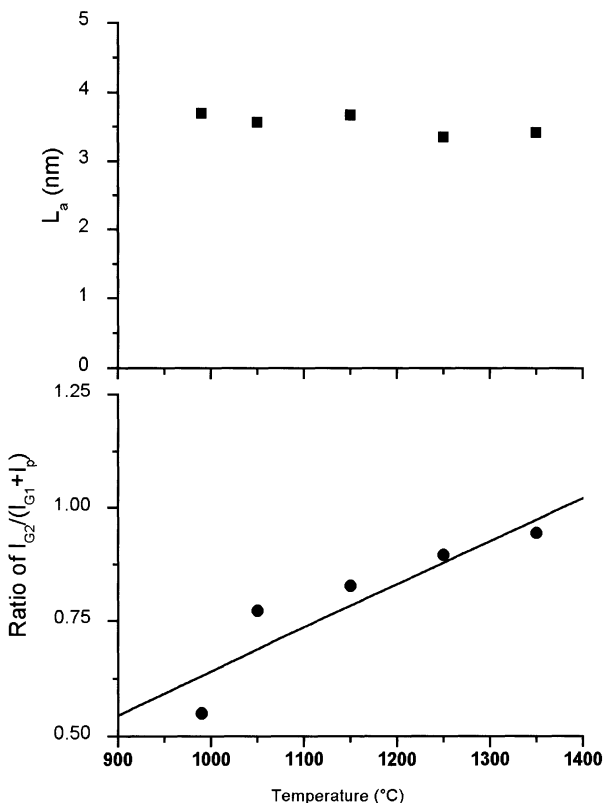


Fig. 8.10. Nanographic flakes on annealed carbon/SiC after annealing at various temperatures in Ar for 30 minutes (4H-SiC, n-type, 8° off-axis, Si face, and with a doping concentration of $2.0 \times 10^{18} \text{ cm}^{-3}$): (a) the size, L_a , of the graphite flakes as a function of annealing temperature, and (b) the ratio of the intensity of the G2 Raman line to the sum of the intensities of the G1 and P bands (from [104], with permission for reproduction from the Minerals, Metals, and Materials Society)

tio is plotted in Fig. 8.10b. The ratio increases nearly linearly with annealing temperature, and suggests that the amount of nano-graphitic flakes increases with annealing temperature at the expense of the amorphous aromatic sp^2 carbon (G1 band) and the polyene-like carbon. Ohmic contacts on SiC are formed when a sufficient amount of nano-graphitic flakes is formed.

Since Ni is an excellent graphitization catalyst, the catalytic graphitization effect on ohmic contacts on SiC was examined on Ni/C/SiC structures [105, 106]. As shown in Fig. 8.6, ohmic contacts formed on Ni/C/SiC after annealing at 700 °C. The graphitization process and graphitic related structures in the Ni/C/SiC after annealing were revealed by Raman spectroscopy, scanning electron microscopy (SEM), and atomic force microscopy (AFM). The results can be interpreted by the well-known catalytic graphitization mechanism [19, 20]. Therefore, it is likely that Ni acts as a graphitization catalyst and accelerates the graphitization process, and the formation of nano-graphitic flakes and related structures result in the formation of ohmic contacts on SiC. The catalytic graphitization effects of Ni accelerate the formation of the graphitic structures and lead to the formation of ohmic contacts.

Further, a C60 interfacial layer between a Ni film and SiC improves the ohmic contact properties significantly [107]. The C60 film was deposited on SiC by the Langmuir-Blodgett method prior to the Ni film deposition using DC sputtering. High quality ohmic contacts were formed on Ni/C60/4H-SiC structures after annealing at 800 °C in Ar for two hours. The specific contact resistivity was $1.17 \times 10^{-6} \Omega \text{cm}^2$ for a SiC with a doping concentration of $1.8 \times 10^{19} \text{ cm}^{-3}$. Raman spectra showed that the ohmic contacts formed after the C60 decomposed and converted to graphitic states. The simultaneous formation of ohmic contacts and the graphitic structures in the annealed Ni/C60/SiC is similar with that of Ni/C/SiC, for which the Ni catalytic graphitization effects play the determining role in forming the ohmic contacts. An interfacial carbon layer was also found to improve ohmic contacts on p-type SiC [109]. Using a Ti/Al/C/p-SiC structure, excellent ohmic contacts were formed on p-type SiC with one order magnitude lower doping concentration than it required for conventional Ti/Al/SiC structures.

Lu et al. [105] have proposed an ohmic contact mechanism based on metal catalytic graphitization activities. As shown in Tables 8.2–8.4, they concluded that ohmic contact formation on SiC is directly related to the formation of graphitic structures in metal/carbon/SiC structures. Metals studied included Ni, Co, Cr, NiCr, Ti, W, Mo, Al, and Au. In Fig. 8.11, ohmic contacts were formed for Ni/C, Co/C, Cr/C, and NiCr/C films on 4H-SiC (n-type, C-face, and a doping concentration of $1.8 \times 10^{19} \text{ cm}^{-3}$). Ni and Co are well known as excellent graphitization catalysts. Raman spectra showed that the formation of graphitic carbon is related to the formation of ohmic contacts in the annealed metal/carbon/SiC structures, as shown in Fig. 8.12. Figure 8.13 shows the deconvolution of D and G bands of the Co/C/SiC and NiCr/C/SiC samples after annealing at 800 °C in vacuum for two hours. As shown, the sp^2 carbons consist of several structures in Co/C/SiC and NiCr/C/SiC after an-

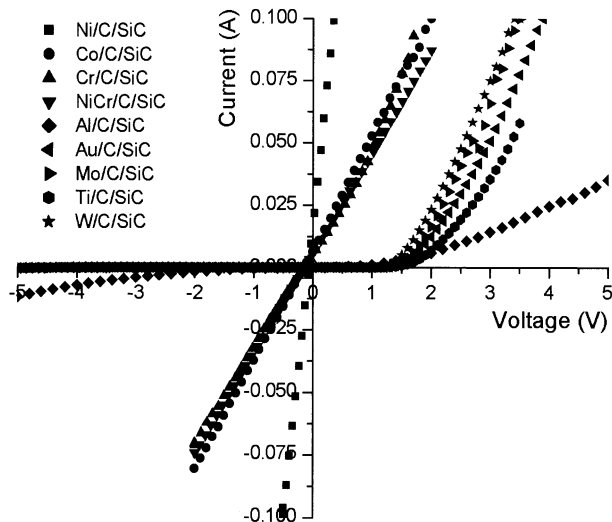


Fig. 8.11. Current–voltage curves of nine metal/carbon/4H-SiC samples after annealing at 800 °C in vacuum (n-type, C face, on-axis, and with a doping concentration of $3.1 \times 10^{19} \text{ cm}^{-3}$) (from [105], with permission for reproduction from the American Institute of Physics)

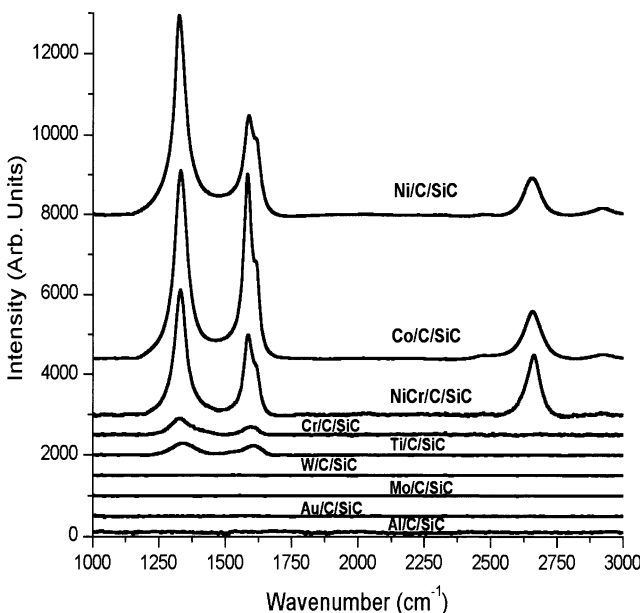


Fig. 8.12. Raman spectra of nine metal/carbon/4H-SiC samples after annealing at 800 °C in vacuum (n-type, C face, on-axis, and with a doping concentration of $3.1 \times 10^{19} \text{ cm}^{-3}$) (from [105], with permission for reproduction from the American Institute of Physics)

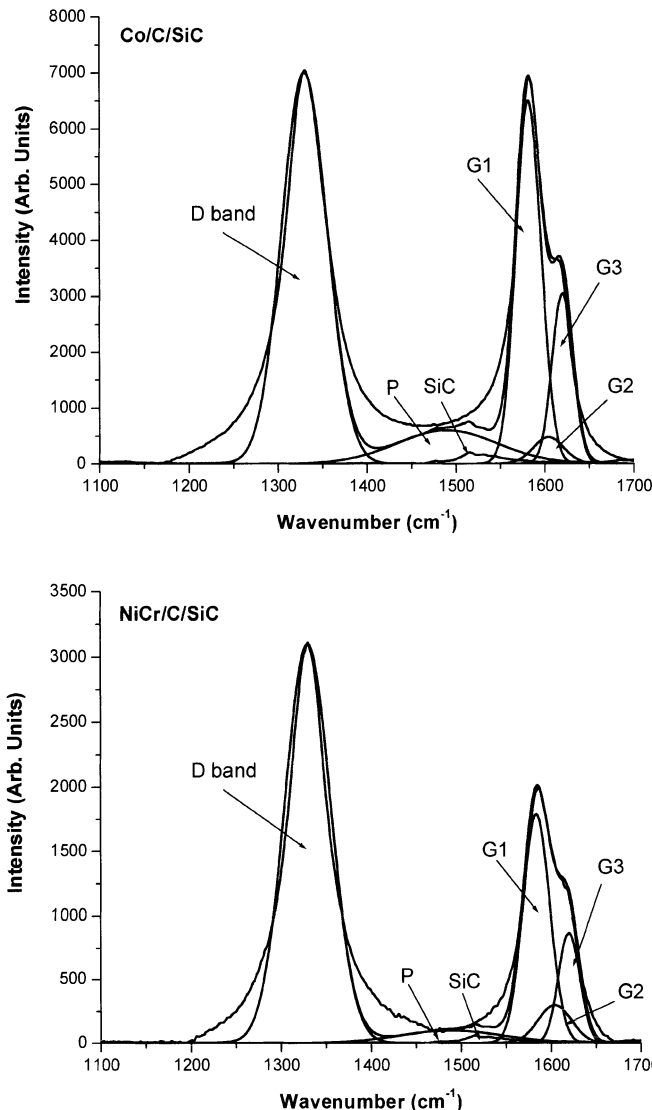


Fig. 8.13. The deconvolution of the D and G bands of Co/C/SiC and NiCr/C/SiC samples after annealing at 800 °C in vacuum for two hours. *Top*, Co/C/SiC, and *bottom*, NiCr/C/SiC (From [105], with permission for reproduction from the American Institute of Physics)

nealing: (a) amorphous aromatic sp^2 carbon clusters, (b) nano-size graphitic flakes, (c) Ni graphite intercalation compounds, and (d) the polyene-like carbons [105], which is similar to that of Ni/C/SiC structure [106].

Lu et al. [105] used the generally accepted catalytic graphitization mechanisms to explain the scanning electron microscopy (SEM) images, which

demonstrated a relationship between the catalytically reacted morphology and ohmic contact behavior. The conventional un-catalyzed graphitization process used for forming highly graphitized structures takes place in the temperature region of 2000–3000 °C [119], which is much to high for the conventional ohmic contact activation processes. However, it is known that some metals, such as Ni, Co, Fe, are excellent catalysts for graphitization at low temperatures, in the range of those used for ohmic contact activation on SiC. The morphology of the films became coarse, and many rounded features were formed. Ni/C/SiC formed the best ohmic contact, and had the roughest surface, in which the film broke and exhibited the rounded features. The diffusion of carbon and the reactions of carbide formation and decomposition in the metal particles caused changes in the surface tension and resulted in the rough surface with the rounded features. The more effective catalysts, the more dramatic changes in the morphology.

According to the mechanism as shown in Fig. 8.8, the catalytic graphitization process takes place after carbon diffuses into the metal particles and the carbides decompose. Two factors, the carbon diffusivity (or solubility) in the metal and the thermal stability of the carbide, determine the catalytic graphitization process. Carbon has the largest solubility in Ni and Co compared to other metals [123]. For example, carbon has a better solubility in Ni than Ti. When Ni and Ti are initially uniformly dispersed in the Ni₉₀Ti₁₀ alloy film on SiC, Ni-rich silicides and carbon are adjacent to the SiC surface as the first layer, while Ti as TiC is as the second layer after annealing [124]. Metal carbides, such as Ni₂C and Co₂C, are thermally unstable [122, 123]. Ni₂C and Co₂C decompose immediately to form graphitized carbon, and Ni/C/SiC and Co/C/SiC exhibit good ohmic contacts. Cr₃C₂ has small negative enthalpy and free energy. Therefore, Ni and Co are better graphitization catalysts and better materials for ohmic contacts than Cr.

It is interesting to note that the catalytic graphitization effect can explain many results in the literature. An example is metal/Si film for ohmic contacts on SiC. Annealing of metal/Si/SiC structures results in the formation of a carbon phase. Since Si is a graphitization catalyst [19, 20], the presence of Si could enhance the graphitization process at the interface. The same effect explains the formation of silicides film by the co-deposition method for ohmic contacts. The model of catalytic graphitization can explain the improvement in ohmic contact performance using Ni/Al and Ni/Ti /Al alloys reported by Konishi et al. [78]. Since Ni is very reactive with SiC producing carbon and Ni silicides, the carbon produced improves the ohmic contacts. It is worthwhile to mention that metal silicides also are graphitization catalysts. Iron and Cobalt silicides have catalytic activities and produce carbon nanotubes and nano-rods in the CVD process [125]. The graphitization model can also explain the experimental results of ohmic contact formation after laser irradiation reported by Eryu et al. [126] and Vlasov et al. [127], since graphitization process accelerates by laser irradiation.

Using the metal catalytic graphitization model to predict ohmic contact behavior of metals on SiC, several factors must be considered: (a) carbon diffusivity in the metal, (b) the thermal stability of carbides, and (c) the temperatures required for metal catalytic reaction.

8.5.3 Structural Characterizations at Atomic and Nanometer Scales

Although numerous investigations have been published on interfacial reactions and chemical composition of metals on SiC, the mechanisms involved in the formation of ohmic contacts on SiC have not been fully understood. It is commonly found that the overall film compositions on SiC consist of silicides, carbides, and/or carbon after annealing. However, due to the complexity of the interface after thermal annealing, it has been difficult to study the composite structures at nanometer and atomic scales. Also, the overall compositions before and after the activation of ohmic behavior in many metal/SiC structures usually are not significantly different. Therefore, the challenging issue is to better understand the interface structures, especially structural and electrical properties at nanometer and atomic scales in the multi-component structures.

The evolution from a “trial and error” method to “designing interface structures for the desired properties” on SiC is needed. To do so, the interfacial structures and electrical properties in the nano-meter and even atomic scales need to be understood in order to fully reveal the electrical contact mechanism. It has been realized that the interfacial structures of annealed metal/SiC at the atomic and nanometer scales at the interface play important roles in forming the ohmic contacts. A band structure change is also important [128] when the size of graphitic structural units is down to nanometers. The most difficult issue in understanding the mechanism of ohmic contact on SiC is to characterize the interfacial structures at the atomic and nanometer scales and correlate the results with electrical contact properties. However, currently available characterization techniques are very limited in producing such resolution in the nano-structural composites. Advances in fabrication of well-designed thin films with high uniformity in structures as well as novel characterization techniques are required to make structural characterizations possible. In addition, the knowledge of the reactivity, thermal stability, diffusivity, and electronic structures of each component at the interface are also important in designing a structure for ohmic contacts.

Only a few studies have been conducted on interfacial structures on the nano-meter scale. For example, Im et al. [129] investigated metal-SiC interface of Pd/SiC and Pt/SiC Schottky diodes using ballistic electron emission microscopy (BEEM). BEEM is able to provide local information on interface electronic properties at the nanometer scale, local hot electron degradation properties, and interfacial band structure. It was observed that an additional conduction band minimum (CBM) appears at ~ 0.14 eV above the lowest CBM in Pd/4H-SiC, and ~ 0.5 eV above the lowest CBM in Pd/15R-SiC.

An enhancement in ballistic transmittance by hot electron injection over regions was observed using BEEM. Hirai et al. [130] investigated the interface of Co/SiC using STM (scanning tunneling microscopy). Co reacts with Si at room temperature to form Co silicides and but does not react with carbon. On 6H-SiC (0001) 6×6 surface, Co deposition forms clusters.

The interactions between silicides, carbides, and carbon need to be better understood. Bermudez [45] reported that carbon dissolves in Pd silicides. Robin et al. [131] observed Pd graphite intercalation compounds in annealed Pd/SiC using STM. Lu et al. [105, 106] found that Ni graphite intercalation compounds in annealed Ni/SiC and Co/SiC using Raman spectroscopy. However, a challenging issue in characterization is not only to identify the structures of metal/graphite interacted compounds, but also to understand their electrical properties of these compounds.

The unit size of the structures needs to be measured at the atomic and nano-size scales. Lu et al. [103, 104] used Raman spectroscopy to estimate the unit size of various graphitic structures. It was found that two-dimensional nano-graphitic flakes with the size of 3–4 nm are accounted for ohmic contact formation in carbon/SiC structures, and also play an important role in metal/carbon/SiC. However, the limitation in size measurement using Raman spectroscopy is about 1–2 nm [121]. Therefore, novel measurement techniques with atomic resolution in these materials need to be developed.

8.5.4 Thermal Stability

Ohmic contacts with high thermal stability are required for the applications of SiC devices operated at high temperatures [132]. Important factors to consider include: (a) thermal stability of the thin film materials, (b) thermal stability between the film and SiC, and (c) thermal stability in an oxidizing environment. Multilayer films have been used to improve thermal stability. However, the “trial and error” method has been used in the search for an optimal composition and multilayer structures, due to the lack of a suitable theory for selecting materials.

Materials often used to form good ohmic contacts on SiC are Ni and Al, which oxidize easily, especially Al. Therefore, the common method is to use a chemically inert metal such as Au or W to cover the ohmic contact metal to prevent contact with oxygen. However, more reliable contacts on p-type SiC at high temperature above 400 °C need to be developed. Due to the easy oxidation of Al, new materials for p-type SiC need to be developed.

Most metals react with SiC at elevated temperatures. High melting temperature metals, such as W and Mo, form stable interfaces with SiC after annealing at 800 °C and 850 °C [53]. Some compound materials have also demonstrated excellent thermal stability on SiC. Kakanakova-Georgieva et al. [57] compared the thermal stability of W and WN films on SiC. WN can stand up to 800 °C. Chaddha et al. [90] reported that TiC forms ohmic contacts on SiC and is thermally and chemically stable at 1400 °C in H₂. Cole et al. [133, 134]

have examined the ohmic contact stability of Pt/Ti/WSi/Ni composite films on SiC in nitrogen. The structures were initially annealed at 1000 °C to form ohmic contacts. The thermal stability was then evaluated *via* pulsed/cyclic thermal fatigue and aging experiments at 650 °C in nitrogen. The 1000 °C annealed contact retained ohmic after 100 h of aging and was found to be chemically and microstructurally stable. Jang et al. [135] reported that the W/WC/TaC/SiC structures were stable after 1000 h in vacuum at 600 °C. Neither degradation of the specific contact resistivity nor reactions of the film with SiC were observed. At 1000 °C, the specific contact resistivity displayed a noticeable degradation, and significant oxygen incorporation between TaC and SiC was reported to be responsible for the degradation.

The most challenging issue is the thermal stability of ohmic contacts in an oxidizing environment at high temperatures. Shor et al. [136] reported that Ti/TiN/Pt/Au structures on n-type SiC exhibited limited deterioration of the ohmic contact properties after 20 h at 650 °C in air. The structures have a potential for use of in short-lifetime devices in the temperature range from 600 to 700 °C, and for long-lifetime devices in the temperature range from 400 to 500 °C. Okojie et al. [137] recently found that ohmic contacts of Ti/TaSi₂/Pt composite films on n-type SiC can withstand at 600 °C for 1000 h in air. As shown in Fig. 8.14, the interface of the Ti/TaSi₂/Pt film remains stable under the same conditions. However, thermal stable ohmic contacts on p-type SiC is still a major challenge to be overcome.

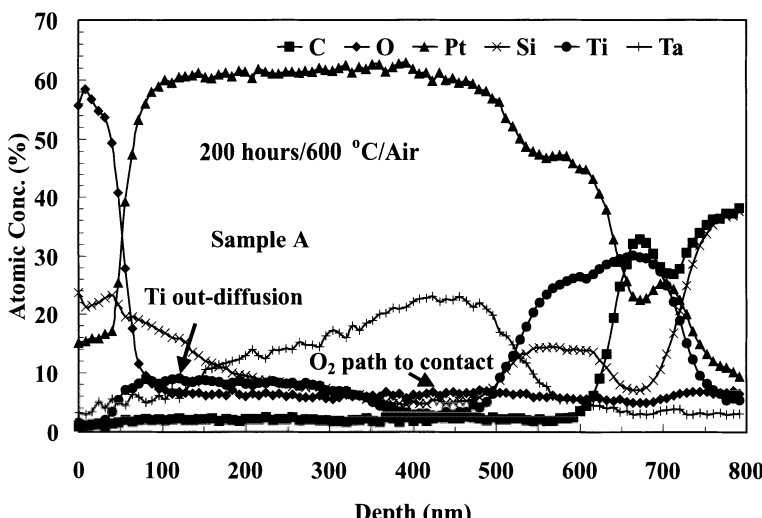


Fig. 8.14. AES depth profile of Ti (100 nm)/TaSi₂ (200 nm)/Pt (300 nm) on SiC after heat treatment at 600 °C in air (from [137], with permission for reproduction from the American Institute of Physics)

8.6 Conclusion

After extensive research in the last ten years, significant advances in ohmic contacts on SiC have been accomplished. Many metals, silicides, carbides, borides, and composites have been examined. Excellent ohmic contacts on n-type SiC and fairly good ohmic contacts on p-type SiC have been obtained after high-temperature annealing around 1000 °C and by using highly doped SiC. Advances have been made in improving the thermal stability of ohmic contacts on SiC recently. However, ohmic contacts with low contact resistivity on moderately/lightly doped SiC are still difficult to achieve. Contact materials for high thermal stability in oxidizing environments and for low contact resistivity on p-type SiC need to be developed. Although the mechanism for the formation of ohmic contacts on SiC has not been fully understood, some advances have been made on the basis of the formation of nanographitic structures, carbon vacancies, and spikes on SiC. It has been realized that nanosize graphitic structures play an important role in the contact properties. Since SiC is the most mature of the wide-bandgap semiconductors, the improvements in ohmic-contact technology will have a significant impact on high-power and high-temperature devices. The future prospects for greater advances suggest that SiC is not only a highly promising wide-bandgap semiconductor, but also an interesting subject for research in the areas of surface and interface sciences.

Acknowledgments

Two co-authors (W. L. and W.E. C.) acknowledge the supports from Missile Defense Agency (Grant No.: DAAD 19-02-1-0001) and NASA through the Fisk Center for Photonic Materials and Devices (Grant No.: NCC8-133). The authors would like to thank Prof. L.C. Feldman at Vanderbilt University for valuable discussions.

References

1. “SiC Materials and Devices”, Semiconductors and Semimetals, Vol. 52, ed. by Y.S. Park, Academic Press, San Diego (1998).
2. P.G. Neudeck, “SiC Technology”, The VLSI Handbook, ed. by W.-K. Chen, CRC Press, Boca Raton, pp. 6-1 (1999).
3. D.K. Schroder, “Semiconductor Materials and Device Characterization”, 2nd ed., Wiley, New York (1998).
4. V. Saxena and A.J. Steckl, in “SiC Materials and Devices”, Semiconductors and Semimetals, Vol. 52, ed. by Y.S. Park, Academic Press, San Diego, p. 77 (1998).
5. L.M. Porter and R.F. Davis, Mater. Sci. Eng. B **34**, 83 (1995).
6. J. Crofton, L.M. Porter, and J.R. Williams, Phys. Status Solidi (b) **202**, 581 (1997).

7. L.D. Madsen, *J. Electron. Mater.* **30**, 1353 (2001).
8. M.W. Cole and P.C. Joshi, in "Silicon Carbides: Materials, Processing and Devices", edited by Z.C. Feng and J.H. Zhao, Taylor and Francis, New York (2003).
9. J.A. Cooper, *Mater. Sci. Eng. B* **44**, 387 (1997).
10. F. Braun, *Pogg. Ann.* **153**, 556 (1874).
11. E.H. Rhoderick and R.H. Williams, "Metal-Semiconductor Contacts", 2nd ed., Clarendon Press, Oxford (1988).
12. H.K. Henisch, "Semiconductor Contacts", Clarendon Press, Oxford (1984).
13. S.M. Sze, "Physics of Semiconductor Devices", 2nd edition, Wiley, New York (1981), p. 304.
14. C. Kittel, "Introduction to Solid State Physics", 7th edition, Wiley, New York (1996).
15. H.B. Michaelson, *J. Appl. Phys.* **48**, 4729 (1977).
16. J. Pelletier, D. Gervais, and P. Pomot, *J. Appl. Phys.* **55**, 94 (1984).
17. M.J. Bozack, *Phys. Status Solidi (b)* **202**, 549 (1997).
18. S. Kurtin, T.C. McGill, and C.A. Mead, *Phys. Rev. Lett.* **22** 1433 (1969).
19. A. Ōya and H. Marsh, *J. Mater. Sci.* **17**, 309 (1982).
20. A. Ōya and S. Ōtani, *Carbon* **17**, 131 (1979).
21. K.M. Geib, C.W. Wilmsen, J.E. Mahan, and M.C. Bost, *J. Appl. Phys.* **61**, 5299 (1987).
22. V.A. Dmitriev, K. Irvine, M. Spencer, and G. Kelner, *Appl. Phys. Lett.* **64**, 318 (1994).
23. J. Crofton, P.G. McMullin, J.R. Williams, and M.J. Bozack, *J. Appl. Phys.* **77**, 1317 (1995).
24. Ts. Marinova, A. Kakanakova-Georgieva, V. Krastev, R. Kakanakov, M. Neshhev, L. Kassamakova, O. Noblanc, C. Arnodo, S. Cassette, C. Brylinski, B. Pecz, G. Radnóczki, and G. Vincze, *Mater. Sci. Eng. B* **46**, 223 (1997).
25. J. Wan, M.A. Capano, and M.R. Melchoch, *Solid-State Electronics* **46**, 1227 (2002).
26. C. Jacob, P. Pirouz, H.-I. Kuo, and M. Mehregany, *Solid-State Electronics* **42**, 2329 (1998).
27. F. Roccaforte, F. La Via, V. Raineri, L. Calcagno, and P. Musumeci, *Appl. Surf. Sci.* **184**, 295 (2001).
28. J.I. Noh, K.S. Nahm, K.C. Kim, and M.A. Capano, *Solid-State Electronics* **46**, 2273 (2002).
29. A. Bächli, M.-A. Nicolet, L. Baud, C. Jaussaud, and R. Madar, *Mater. Sci. Eng. B* **56**, 11 (1998).
30. C.S. Pai, C.M. Hanson, and S.S. Lau, *J. Appl. Phys.* **57**, 618 (1985).
31. F. La Via, F. Roccaforte, A. Makhtari, V. Raineri, P. Musumeci, and L. Calcagno, *Microelectronic Engineering* **60**, 269 (2002).
32. T. Fujimura, and S.-I. Tanaka, *J. Mater. Sci.* **34**, 235 (1999).
33. B. Pécz, G. Radnóczki, S. Casete, C. Brylinski, C. Arnodo, and O. Noblanc, *Diamond Relat. Mater.* **6**, 1428 (1997).
34. Ts. Marinova, V. Krastev, C. Hallin, R. Yakimova, and E. Janzén, *Appl. Surf. Sci.* **99**, 119 (1996).
35. J.R. Waldrop, and R.W. Grant, *Appl. Phys. Lett.* **62**, 2685 (1993).
36. M.G. Rastegaeva, A.N. Andreev, A.A. Petrov, A.I. Babanin, M.A. Yagovkina, and I.P. Nikitina, *Mater. Sci. Eng. B* **46**, 254 (1997).

37. E. Kurimoto, H. Harima, T. Toda, M. Sawada, M. Iwami, and S. Nakashima, *J. Appl. Phys.* **91**, 10215 (2002).
38. L.M. Porter, R.F. Davis, J.S. Bow, M.J. Kim, and R.W. Carpenter, *J. Mater. Res.* **10**, 26 (1995).
39. S.W. Park, Y.I. Kim, J.S. Kwak, and H.K. Baik, *J. Electron. Mater.* **26**, 172 (1997).
40. C.S. Lim, H. Nickel, A. Naoumidis, and E. Gyarmati, *J. Mater. Sci.* **30**, 3874 (1995).
41. C.S. Lim, H. Nickel, A. Naoumidis, and E. Gyarmati, *J. Mater. Sci.* **31**, 4241 (1996).
42. L. Kassamakova, R.D. Kakanakov, I.V. Kassamakov, N. Nordell, S. Savage, B. Hjörvarsön, E.B. Svedberg, L. Åbom, and L.D. Madsen, *IEEE Trans. Electron. Devices* **46**, 605 (1999).
43. E.V. Kalinina, G.F. Kholuyanov, A.V. Shchukarev, N.S. Savkina, A.I. Babanin, M.A. Yagovkina, and N.I. Kuznetsov, *Diamond Relat. Mater.* **8**, 1114 (1999).
44. J.Y. Veuillen, T.A. Nguyen Tan, I. Tsiaouassis, N. Frangis, M. Brunel, and R. Gunnella, *Diamond Relat. Mater.* **8**, 352 (1999).
45. V.M. Bermudez, *Appl. Surf. Sci.* **17**, 12 (1983).
46. W.J. Lu, D.T. Shi, A. Burger, and W.E. Collins, *J. Vac. Sci. Technol. A* **17**, 1182 (1999).
47. L.-Y. Chen, G.W. Hunter, P.G. Neudeck, and D. Knight, *J. Vac. Sci. Technol. A* **16**, 2890 (1999).
48. L.-Y. Chen, G.W. Hunter, P.G. Neudeck, G. Bansal, J.B. Petit, D. Knight, *J. Vac. Sci. Technol. A* **15**, 1228 (1997).
49. J.S. Chen, A. Bachli, M.-A. Nicolet, L. Baud, C. Jausaud, and R. Madar, *Mater. Sci. Eng. B* **29**, 185 (1995).
50. H.J. Na, J.K. Jeong, M.Y. Um, B.S. Kim, C.S. Hwang, and H.J. Kim, *Solid-State Electronics* **45**, 1565 (2001).
51. L.M. Porter, R.F. Davis, J.S. Bow, M.J. Kim, and R.W. Carpenter, *J. Mater. Res.* **10**, 2336 (1995).
52. A.A. Iliadis, S.N. Andronescu, W. Yang, R.D. Vispute, A. Stanishevsky, J.H. Orloff, R.P. Sharma, T. Venkatesan, M.C. Wood, and K.A. Jones, *J. Electron. Mater.* **28**, 136 (1999).
53. K. Geib, C. Wilson, R. Long, and C. Wilmsen, *J. Appl. Phys.* **68**, 2796 (1990).
54. L. Baud, C. Jausaud, R. Madar, C. Bernard, J.S. Chen, and M.A. Nicolet, *Mater. Sci. Eng. B* **29**, 126 (1995).
55. J.A. Edmond, J. Ryu, J.T. Glass, and R.F. Davis, *J. Electrochem. Soc.* **135**, 359 (1988).
56. J.O. Olowolafe, J. Liu, and R.B. Gregory, *J. Electr. Mater.* **29**, 391 (2000).
57. A. Kakanakova-Georgieva, Ts. Marinova, O. Noblanc, C. Arnodo, S. Cassette, and C. Brylinski, *Thin Solid Films* **337**, 180 (1999).
58. S. Hara, K. Suzuki, A. Furuya, Y. Matsui, T. Ueno, I. Ohdomari, S. Yoshida, S. Misawa, E. Sakuma, Y. Ueda, and S. Suzuki, *Jpn. J. Appl. Phys.* **29**, L394 (1990).
59. B.T. Lee, J.-Y. Shin, S.-H. Kim, J.-H. Kim, S.-Y. Han, and J.-L. Lee, *J. Electron. Mater.* **32**, 501 (2003).
60. F. Touati, K. Takemasa, and M. Saji, *IEEE Trans. Electron. Devices* **46**, 444 (1999).
61. F. Touati, M. Kiminori, and M. Saji, *J. Electron. Mater.* **28**, 186 (1999).

62. F. Goesmann, and R. Schmid-Fetzer, *Semicond. Sci. Technol.* **10**, 1652 (1995).
63. T. Teraji, S. Hara, H. Okushi, and K. Kajimura, *Appl. Phys. Lett.* **71**, 689 (1997).
64. L.M. Porter, R.F. Davis, J.S. Bow, M.J. Kim, R.W. Carpenter, and R.C. Glass, *J. Mater. Res.* **10**, 668 (1995).
65. D.E. Ioannou, N.A. Papanicolaou, and P.E. Nordquist, *IEEE Trans. Electron. Devices* **34**, 1694 (1987).
66. T. Hatayama, K. Kawahito, H. Kijima, Y. Uraoka, and T. Fuyuki, 2001 International Conference on Silicon Carbide and Related Materials, ThA3-2, Tsukuba, Japan, Oct. 28–Nov. 2, 2001.
67. D.W. Niles, H. Hochst, G.W. Zajac, T.H. Fleisch, B.C. Johnson, and J.M. Meese, *J. Vac. Sci. Technol. A* **6**, 1584 (1988).
68. Z. An, A. Ohi, M. Hirai, M. Kusaka, and M. Iwami, *Surf. Sci.* **493**, 182 (2001).
69. J. Crofton, P.A. Barnes, J.R. Williams, and J.A. Edmonds, *Appl. Phys. Lett.* **62**, 384 (1992).
70. O. Nennewitz, L. Spiess, and V. Breternitz, *Appl. Surf. Sci.* **91**, 347 (1995).
71. J. Crofton, L. Beyer, J.R. Williams, E.D. Luckowski, S.E. Mohney, and J.M. Delucca, *Solid State Electronics* **41**, 1725 (1997).
72. O. Nakatsuka, T. Takei, Y. Koide, and M. Murakami, *Mater. Trans.* **43**, 1864 (2002).
73. J. Crofton, S.E. Mohney, J.R. Williams, and T. Isaacs-Smith, *Solid State Electronics* **46**, 109 (2002).
74. B.J. Johnson, and M.A. Capano, *Solid State Electronics* **47**, 1437 (2003).
75. S.E. Mohney, B.A. Hull, J.Y. Lin, and J. Crofton, *Solid-State Electronics* **46**, 689 (2002).
76. B. Pécz, L. Tóth, M.A. di Forte-Poisson, and J. Vacas, *Appl. Surf. Sci.* **206**, 8 (2003).
77. O. Nakatsuka, Y. Koide, and M. Murakami, Proceedings of International Conference on Silicon Carbide and Related Materials 2001, S. Yoshida, S. Nishino, H. Harima, and T. Kimoto (Eds), Trans Tech Publications, Switzerland, 2002, p. 885.
78. R. Konishi, R. Yasukochi, O. Nakatsuka, Y. Koide, M. Moriyama, and M. Murakami, *Mater. Sci. Eng. B* **98**, 286 (2003).
79. C. Hallin, R. Yakimova, B. Pécz, A. Georgieva, Ts. Marinova, L. Kasamakova, R. Kakanakov, and E. Janzén, *J. Electron. Mater.* **26**, 119 (1997).
80. Ts. Marinova, R. Yakimova, V. Krastev, C. Hallin, and E. Janzén, *J. Vac. Sci. Technol. B* **14**, 3252 (1996).
81. Y. Gao, Y. Tang, M. Hoshi, and T.P. Chow, *Solid-State Electronics* **44**, 1875 (2000).
82. D. Basak, and S. Mahanty, *Mater. Sci. Engin. B* **98**, 177 (2003).
83. N. Lundberg, and M. Östling, *Solid-State Electronics* **38**, 2023 (1995).
84. N. Lundberg, and M. Östling, *Solid-State Electronics* **39**, 1559 (1996).
85. T. Nakamura, and M. Satoh, *Solid-State Electronics* **46**, 2063 (2002).
86. B. Pécz, *Appl. Surf. Sci.* **184**, 287 (2001).
87. R. Getto, J. Freytag, M. Kopnarki, and H. Oechsner, *Mater. Sci. Eng. B* **61–62**, 270 (1999).
88. M.A. Capano, J.K. Patterson, L. Petry, and J.S. Solomon, *J. Electron. Mater.* **32**, 458 (2003).
89. S.-K. Lee, C.-M. Zetterling, M. Östling, J.-P. Palmquist, and U. Jansson, *Microelectronic Engineering* **60**, 261 (2002).

90. A.K. Chaddha, J.D. Parsons, and G.B. Kruaval, *Appl. Phys. Lett.* **66**, 760 (1995).
91. S.-K. Lee, C.-M. Zetterling, M. Östling, J.-P. Palmquist, H. Höglberg, and U. Jansson, *Solid-State Electronics* **44**, 1179 (2000).
92. J.D. Parsons, G.B. Kruaval, and A.K. Chaddha, *Appl. Phys. Lett.* **65**, 2075 (1994).
93. S.K. Lee, C.-M. Zetterling, E. Danielsson, M. Östling, J.-P. Palmquist, H. Höglberg, and U. Jansson, *Appl. Phys. Lett.* **77**, 1478 (2001).
94. T. Jang, L.M. Porter, G.W.M. Rutsch, and B. Odekirk, *Appl. Phys. Lett.* **75**, 3956 (1999).
95. H.O. Pierson, "Handbook of Refractory Carbides and Nitrides", Noyes Publications, Westwood (1996).
96. R.C. Glass, L.M. Spellman, and R.F. Davis, *Appl. Phys. Lett.* **59**, 2868 (1991).
97. R.C. Glass, L.M. Spellman, S. Tanaka, and R.F. Davis, *J. Vac. Sci. Technol. A* **10**, 1625 (1992).
98. A.A. Iliadis, S.N. Andronescu, K. Edinger, J.H. Orloff, R.D. Vispute, V. Talyansky, R.P. Sharma, T. Venkatesan, M.C. Wood, and K.A. Jones, *Appl. Phys. Lett.* **73**, 3545 (1998).
99. T.N. Oder, J.R. Williams, S.E. Mohney, and J. Crofton, *J. Electron. Mater.* **27**, 12 (1997).
100. R. Kakanakov, L. Kassamakova, I. Kassamakov, K. Zekentes, and N. Kuznetsov, *Mater. Sci. Engin. B* **80**, 374 (2001).
101. N.A. Papanicolaou, A. Edwards, M.V. Rao, and W.T. Anderson, *Appl. Phys. Lett.* **73**, 2009 (1998).
102. T. Jang, J.W. Erickson, and L.M. Porter, *J. Electr. Mater.* **31**, 506 (2002).
103. W. Lu, W.C. Mitchel, C.A. Thornton, W.E. Collins, G.R. Landis, and S.R. Smith, *J. Electrochem. Soc.* **150**(3), G177 (2003).
104. W. Lu, W.C. Mitchel, C.A. Thornton, G.R. Landis, W.E. Collins, *J. Electron. Mater.* **32**, 426 (2003).
105. W. Lu, W.C. Mitchel, G.R. Landis, T.R. Crenshaw, W.E. Collins, *J. Appl. Phys.* **93**, 5397 (2003).
106. W. Lu, W.C. Mitchel, G.R. Landis, T. Crenshaw, and W.E. Collins, *Solid State Electronics* **47**, 2001 (2003).
107. W. Lu, W.C. Mitchel, G.R. Landis, T. Crenshaw, and W.E. Collins, *J. Vac. Sci. Technol. A* **21**, 1510 (2003).
108. M. Yudasaka, K. Tasaka, R. Kikuchi, Y. Ohki, S. Yoshimura, and E. Ota, *J. Appl. Phys.* **81**, 7623 (1997).
109. W. Lu, W.C. Mitchel, T. Crenshaw, G.R. Landis, and W.E. Collins, the 2003 MRS Spring Meeting, C2.9, San Francisco, CA, April 21–25, 2003.
110. J.H. Zhao, K. Tone, S.R. Weiner, M.A. Caleca, H. Du, and S.P. Withrow, *IEEE Electron Dev. Lett.* **18**, 375 (1997).
111. S. Hara, T. Teraji, H. Okushi, and K. Kajimura, *Appl. Surf. Sci.* **107**, 218 (1996).
112. S. Hara, T. Teraji, H. Okushi, and K. Kajimura, *Appl. Surf. Sci.* **117**, 394 (1997).
113. S.P. Murarka, "Silicides for VLSI Applications", Academic Press, New York (1983).
114. Q. Zhang and T.S. Sudarshan, *J. Electron. Mater.* **30**, 1466 (2001).

115. W. Lu, T.R. Crenshaw, W.E. Collins, P. Neudeck, G. Hunter, L. Feldman, and W.C. Mitchel, the 2001 Electrical Materials Conference, Notre Dame, IN, June 27–29, 2001.
116. S.Y. Han and J.-L. Lee, *J. Electrochem. Soc.* **149**, G189 (2002).
117. S.Y. Han, K.H. Kim, J.K. Kim, H.W. Jang, K.H. Lee, N.-K. Kim, E.D. Kim, and J.-L. Lee, *Appl. Phys. Lett.* **79**, 1816 (2001).
118. S.Y. Han, J.-Y. Shin, B.-T. Lee, and J.-L. Lee, *J. Vac. Sci. Technol. B* **20**, 1496 (2002).
119. D.B. Fischbach, in “Chemistry and Physics of Carbon”, Vol. 7, edited by P.L. Walker Jr., Marcel Dekker, New York (1971), p. 1.
120. W.L. Holstein, R.D. Moorhead, H. Hoppa, and M. Boudart, in “Chemistry and Physics of Carbon”, Vol. 18, edited by P.A. Thrower, Marcel Dekker, New York (1982), p. 139.
121. A.C. Ferrari, and J. Robertson, *Phys. Rev. B* **61**, 14095 (2000).
122. “CRC Handbook of Chemistry and Physics”, 64th edition, (CRC Press, Boca Raton, FL, 1983), p. D-51.
123. C.-M. Sung, and M.-F. Tai, *Int. J. Refractory Metals & Hard Materials* **15**, 237 (1997).
124. M. Levit, I. Grimberg, and B.-Z. Weiss, *J. Appl. Phys.* **80**, 167 (1996).
125. H.L. Chang, C.H. Lin, and C.T. Kuo, *Thin Solid Films* **420–421**, 219 (2002).
126. O. Eryu, T. Kume, K. Nakashima, T. Nakata, and M. Inoue, *Nucl. Instrum. Meth. B* **121**, 419 (1997).
127. I.I. Vlasov, A.A. Lyalin, E.D. Obraztsova, A.V. Simakin, and G.A. Shafeev, *Quantum Electronics* **28**, 673 (1998).
128. K. Nakada, M. Fujita, G. Dresselhaus, and M.S. Dresselhaus, *Phys. Rev. B* **54**, 17954 (1996).
129. H.-J. Im, B. Kaczer, J.P. Pelz, S. Limpijumnong, W.R.L. Lambrecht, and W.J. Choyke, *J. Electron. Mater.* **27**, 345 (1998).
130. M. Hirai, Y. Marumoto, M. Kusaka, M. Iwaqmi, T. Ozawa, T. Nagamura, and T. Nakata, *Appl. Surf. Sci.* **113/114**, 360 (1997).
131. K. Robbie, S.T. Jemander, N. Lin, C. Hallin, R. Erlandson, G.V. Hansson, and L.D. Madsen, *Phys. Rev. B* **64**, 155401 (2001).
132. P.G. Neudeck, R.S. Okojie, and L.-Y. Chen, *Proceeding of the IEEE* **90**, 1065 (2002).
133. M.W. Cole, P.C. Joshi, C.W. Hubbard, M.C. Wood, M.H. Ervin, and B. Geil, *J. Appl. Phys.* **88**, 2652 (2000).
134. M.W. Cole, P.C. Joshi, C. Hubbard, J.D. Demaree, and M. Ervin, *J. Appl. Phys.* **91**, 3864 (2002).
135. T. Jang, B. Odekirk, L.D. Madsen, and L.M. Porter, *J. Appl. Phys.* **90**, 4555 (2001).
136. J.S. Shor, R.A. Weber, L.G. Provost, D. Goldstein, and A.D. Kurtz, *J. Electrochem. Soc.* **141**, 579 (1994).
137. R.S. Okojie, D. Lukco, Y.L. Chen, and D.J. Spry, *J. Appl. Phys.* **91**, 6553 (2002).

Oxidation, MOS Capacitors, and MOSFETs

S. Dimitrijev, H.B. Harrison, P. Tanner, K.Y. Cheong, and J. Han

One of the most important advantages of SiC as a wide-energy-gap material is the high quality of the interface with its native oxide (SiO_2). It is this feature that is critical for the development of the most used semiconductor device – the metal–oxide–semiconductor field-effect transistor (MOSFET). This chapter presents the current understanding of the interface and near-interface defects in thermally oxidized SiC. Particular emphasis is placed on the characterization techniques, given that nonequilibrium conditions, which appear owing to wide energy gap of SiC, lead to qualitatively different results from the case where these widely used techniques are applied to Si structures. A special section is devoted to nitridation of SiC– SiO_2 interfaces as the most promising technique for achieving the device-quality interfaces required for commercial applications. Finally, the performance of some of the power MOSFETs fabricated on SiC is presented.

9.1 Introduction

Good *bulk* properties are sufficient for many useful applications of semiconductor materials. However, the dominant applications are critically dependent on both the *bulk* and the *surface* properties. It is the high density of surface defects that limits the application of many semiconductor materials with excellent bulk properties to niche applications.

There are two semiconductor materials – silicon and silicon carbide – that can have surface defects passivated to levels that are significantly lower than the achievable surface density of current carriers. The passivation utilizes silicon dioxide, the native oxide of both silicon and silicon carbide. The successful passivation of the silicon surface, developed during the 1960s, means that current carriers (electrons and holes) can move over the semiconductor surface. This effect enables the operation of the metal–oxide–semiconductor field-effect transistor (MOSFET) – an electronic switch that is suitable for the integration of complex electronic systems. Consequently, very large-scale integration

(VLSI) has been achieved in silicon during the enormous progress in electronic systems that we have witnessed over the past few decades.

Silicon carbide is a developing semiconductor material with bulk properties superior to silicon. In particular, it has wider energy gap, higher breakdown electric field, and higher thermal conductivity. To combine a passivated semiconductor surface with these superior bulk properties means to open up possibilities for device functions and applications that are not possible in silicon technology.

Although SiO_2 is the native oxide of SiC, initial attempts to passivate the surface of SiC with its native oxide could not provide a device-quality semiconductor-insulator interface. To a large extent this was due to the inferior material quality of the early wafers; however, there is also an inherent problem related to carbon release and clustering during the oxidation of SiC [1]. This problem is combined with very important issues related to the application of known characterization techniques. Because of the wide energy gap of SiC, nonequilibrium charge conditions can be retained for very long periods of time, making it very challenging to modify and apply characterization techniques that were developed for equilibrium conditions in silicon.

This chapter reviews the development of gate oxides on SiC, along with a review of the characterization techniques that have been used to support, and indeed enable, this development. A special section is devoted to nitrided gate oxides, as these gate oxides have demonstrated remarkable improvements in the quality of the oxide-semiconductor interface. The final section in the chapter provides an insight into the development of SiC-based power MOSFETs and the advantages that can be achieved by utilizing the superior bulk properties of SiC.

9.2 Gate Oxides on SiC

Before we consider gate oxides on SiC, it is useful to ask the question of the possible use of deposited dielectrics instead of a thermally grown oxide. One reason for this question comes from the demand for SiC power devices, where the maximum blocking voltage is often limited by the field in the dielectric, not by breakdown of the semiconductor. Thus the ideal insulator should have a dielectric constant comparable to or higher than that of the substrate, which is not the case with SiO_2 and SiC. The higher the dielectric constant, the lower the electric field in the insulator. As pointed by Lipkin et al. [2], a critical measure of a material's applicability as a gate dielectric is the product of its relative dielectric constant (ϵ) and its safe operating field (E_o). The ideal case would be when the product ϵE_o exceeds that of SiC. AlN and TiO_2 are amongst the insulators under investigation. However, the investigations of Lipkin et al. [2] regarding these particular dielectric materials show that best performance was accomplished only with insulators incorporating silicon dioxide. All others insulators suffer from significant leakage currents at high

temperature. It was then concluded that the good insulating properties of SiO_2 combined with its technological feasibility make it most suitable as a gate dielectric on SiC.

9.2.1 Gate Dielectric Requirements

There are two major requirements for the gate dielectric of MOS devices, namely high barriers for electron and hole injection and good oxide quality. The gate dielectric should have sufficiently high energy barriers to block the charge carriers (holes and electrons) between the channel and the gate of a MOSFET. The energy barriers for both electrons and holes in a semiconductor have to be high enough to prevent thermally stimulated injection. The energy band parameters for the interfaces of SiO_2 with Si and four SiC polytypes are illustrated in Fig. 9.1 [3]. The valence band offsets for thermal SiO_2 were calculated using $E_g = 8.9 \text{ eV}$. At room temperature, the theoretical barrier height for electron injection for Si and 3C-SiC MOS structures is 3.15 eV and 3.6 eV respectively, while it is reduced to 2.95 eV for 6H-SiC and to 2.7 eV for 4H-SiC. SiC MOS structures have shown an excessive temperature dependence of the Fowler–Nordheim (F–N) electron injection, which could seriously influence the application of SiC power MOSFETs at high temperature. Agarwal et al. [4] have reported an effective barrier height of 2.43 eV at room temperature for dry oxides thermally grown on n-type 4H-SiC. However, the barrier height is reduced to 2.11 eV at 150 °C and to 1.76 eV at 325 °C. Similarly, Bano et al. [5] reported an effective barrier height of about 2.5 eV at room temperature and of 2.0 eV at 300 °C.

From the point of view of injection reduction, the energy band diagram would be considered optimal if the conduction band offset were equal to the valence band offset [3]. As illustrated in Fig. 9.1, the band diagram of the SiO_2 –SiC interface is nearly symmetric. Consequently, the leakage current

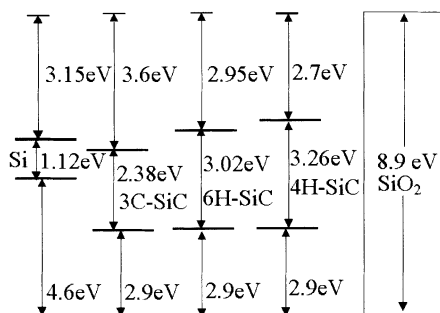


Fig. 9.1. Schematic energy band diagram of Si, 3C-SiC, 6H-SiC, 4H-SiC, and SiO_2 illustrating the conduction and valence band offsets for each of these materials with respect to SiO_2 [3] (with permission for reproduction from the American Institute of Physics)

in SiC MOS structures remains acceptably low, even at elevated temperatures [2, 4–6].

The gate oxide in MOS devices should have a high electric breakdown field to prevent leakage current via the gate. As demonstrated by Lipkin et al. [2], the breakdown strength at high temperatures for silicon dioxide is the highest for all dielectrics studied. The oxide quality is strongly affected by the perfection of the oxide–semiconductor interface. A smoother interface provides a better platform for the oxide to grow upon and establishes a well-arranged network of SiO_2 that has a high breakdown field. In addition to this, a smooth interface with few interface traps is vital to obtaining a high channel mobility in MOSFETs, as the scattering effect and trapping of the mobile carriers are minimized [7].

9.2.2 Interface and Near-Interface Traps

There exists a transition layer between SiO_2 and Si at the $\text{SiO}_2\text{--Si}$ interface [8, 9]. The properties of this disordered region are strongly related to the electrical properties of a Si MOS structure, as the presence of defects in this transition region leads to fixed charges and interface traps. Dangling bonds on surface Si atoms (P_b centers) represent the main source of interface states at the (111) $\text{SiO}_2\text{--Si}$ interface [9], which is structurally isomorphic to the oxidized Si faces of hexagonal SiC. As these defects appear because of structural mismatch between Si and the oxide [10], it is logical to expect their presence at $\text{SiO}_2\text{--SiC}$ interfaces as well. However, the interface states observed in as-oxidized SiC appear to be different from the well-studied P_b centers in at least two principal respects. First, they cannot be passivated with hydrogen [11–13]. Second, their electrical behavior is dissimilar to the well-known amphoteric character of the P_b centers at the (111) $\text{SiO}_2\text{--Si}$ interface [13].

In an attempt to explain the energy distribution and stability of the $\text{SiO}_2\text{--SiC}$ interface traps, it was suggested that they were related to carbon clusters with sp^2 -bonded fragments [13, 14]. Indeed, the presence of excess carbon at oxide–SiC interfaces was revealed by electron spectroscopy [15–18] and by electron spin resonance [3]. In addition, unidentified centers, believed to be related to C, were detected at the $\text{SiO}_2\text{--SiC}$ interface by electron paramagnetic resonance [19, 20]. Because these centers were activated by heating in a nonmoisturizing ambient and passivated in a moisturizing ambient, it was believed that C–H bonding was responsible for their characteristics [19]. The activation mechanism appears to be related to the release of hydrogen or some hydrogenous species from C bonds. Etching studies conducted with hydrofluoric acid indicate that the centers are located not in the SiO_2 , but rather in the SiC near the $\text{SiO}_2\text{--SiC}$ interface [19].

Clearly, the presence of carbon in SiC makes the interfacial chemistry of the oxidation of SiC more complicated than for Si and introduces C-related defects at the $\text{SiO}_2\text{--SiC}$ interface that do not appear at the $\text{SiO}_2\text{--Si}$ interface. There is substantial evidence that some of the excess carbon released during

thermal oxidation remains at or near the $\text{SiO}_2\text{--SiC}$ interface, either as isolated atoms or in the form of clusters [13]. Analysis of an as-oxidized $\text{SiO}_2\text{--4H-SiC}$ interface using atomic-force microscopy (AFM) images reveals the presence of nanometer-sized protrusions [15, 21]. These platelet-shaped inhomogeneities (Fig. 9.2) were suggested to be carbon protrusions formed during thermal oxidation of SiC. These residual carbon complexes have been identified as the main reason for the problems observed with the electronic properties of the $\text{SiO}_2\text{--SiC}$ interface and the gate oxide itself [22].

Another possible source of defects in $\text{SiO}_2\text{--SiC}$ MOS structures is the inherent defects in the oxide with energy levels within the SiC bandgap. Afanas'ev and Stesmans [23] reported on the existence of an H-complexed oxygen vacancy ($\text{O}_3\equiv\text{SiH HSi}\equiv\text{O}_3$) acting as an electron trap with an energy level at 3.1 eV below the SiO_2 conduction band. In addition to these inherent oxide defects, the energy of positively charged oxygen vacancy centers is predicted to be within the range of 4.3–5.0 eV below the SiO_2 conduction band [24]. Finally, the E'_γ -center related to the O-vacancy defects observed in $\text{SiO}_2\text{--SiC}$ structures [3] may also contribute to the interface trap distribution.

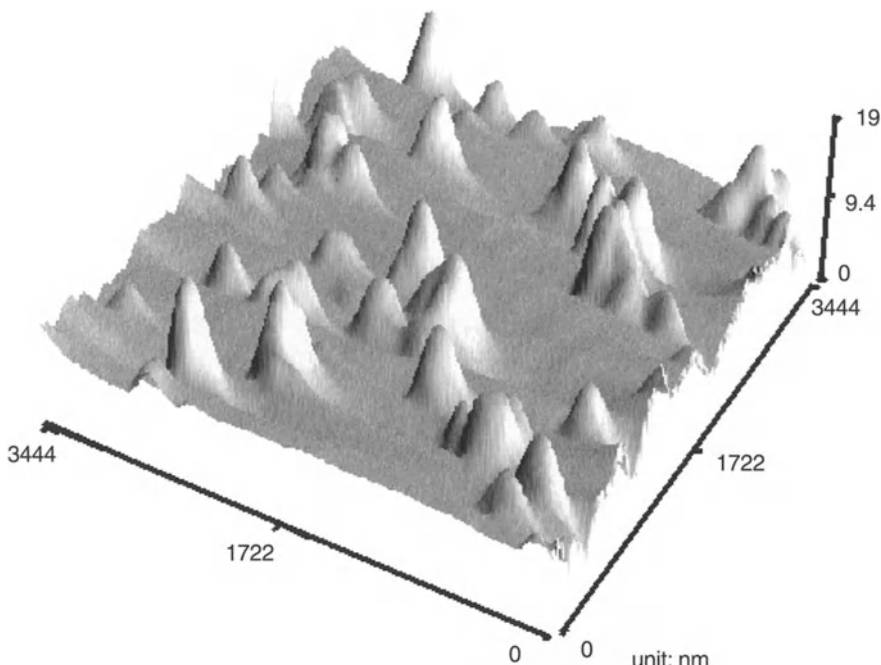


Fig. 9.2. Three-dimensional AFM image of an as-oxidized sample of 4H-SiC without an epilayer, after etching back the oxide to the SiC surface [21] (with permission for reproduction from IEEE)

9.2.3 Electrical Characterization of $\text{SiO}_2\text{--SiC}$ Interfaces

Owing to the wide energy gap of SiC, most of the SiC– SiO_2 interface traps are energetically located far from both band edges, so they cannot be detected by conventional Si– SiO_2 interface characterization methods at room temperature. This is because the response times of the deep SiC– SiO_2 interface traps increase exponentially with energy from the band edge so that the traps cannot follow the changes in the measurement signal. The interface traps located beyond 0.6 eV from the band edges are apparently inactive at room temperature [12]. This situation is similar to the electrical behavior of the Si– SiO_2 interface at low temperature (77 K) [25], implying that the techniques used for characterizing Si– SiO_2 interfaces at room temperature have to be used at high temperatures for characterizing $\text{SiO}_2\text{--SiC}$ interfaces. At high temperatures (500–650 K), the response times of interface traps are shortened, allowing the measurable range of interface traps to be widened significantly [26]. A number of techniques used commonly for characterizing Si– SiO_2 interfaces on MOS capacitors can be employed to characterize SiC– SiO_2 interfaces at elevated temperatures and are described below.

Terman's High-Frequency Capacitance–Voltage (HF $C\text{--}V$) Technique

This technique, conducted at room temperature, was initially proposed by Terman [27] to investigate the density of Si– SiO_2 interface traps. It has been employed by some researchers to measure a single-valued density of 6H-SiC– SiO_2 interface traps at high temperature from high-frequency $C\text{--}V$ measurements [28–32]. At a sufficiently high frequency, the interface traps respond to the slowly varying DC gate voltage but do not respond to the AC probe frequency. Hence, the interface traps do not contribute any capacitance, but induce additional charge that causes the HF $C\text{--}V$ curve to stretch out with respect to the gate voltage. The measured flat-band voltage shift from the ideal HF $C\text{--}V$ curve represents the effective density of interface traps that contains contributions not only from interface traps but also from oxide charge. At room temperature, this technique can measure less than 12% of the energy gap, compared with about 33% of the energy gap for measurements conducted at 300 °C [12]. Although it is the simplest and most straightforward technique, it suffers from inaccurate capacitance measurement and poor resolution [26].

Simultaneous High–Low Capacitance–Voltage (Hi–Lo $C\text{--}V$) Technique

This technique measures the high-frequency capacitance simultaneously with the quasi-static capacitance at high temperature. The high-frequency capacitance consists of the oxide and semiconductor depletion capacitances, whereas

the quasi-static capacitance contains additional capacitance from interface traps. The differences between the capacitances acquired at high and low frequencies, measured in the depletion region, provide a density profile of the interface traps [32]. It has been reported that the value of D_{it} measured by this technique is consistent and reliable [33]. In addition, this technique can eliminate any bias history effects arising from measuring the capacitance separately [26].

AC Conductance Technique

This technique, proposed by Nicollian and Goetzberger [34], measures the equivalent parallel conductance G_p of a MOS capacitor as a function of frequency f ($f = 2\pi/\omega$) at a fixed bias in the depletion region. The conductance, representing the loss mechanism caused by capture and emission of carriers at interface traps, is a measure of the interface-trap density. A profile of the interface-trap density can be obtained by varying the bias voltage. In order to adapt this technique to measure the SiC–SiO₂ interface-trap density, the measurements must be conducted at high temperature and the influence of surface potential fluctuations must be taken into consideration to avoid underestimating the density. This technique is considered the most sensitive, accurate, powerful, and widely used method to measure the interface-trap density, but it is a complicated and tedious technique, requiring extensive data acquisition and analysis.

Besides the measurements at high temperature listed above, there are a few alternative ways to measure the SiC–SiO₂ interface-trap density at room temperature that can provide reliable results. Examples are the photo-*CV* technique, the Hall effect technique, and the MOSFET subthreshold current technique.

Room Temperature Photo-*CV* Technique

Initially, the *C–V* curve is measured under a light-tight room-temperature condition by sweeping the voltage from accumulation to deep depletion. Under this condition, the SiC–SiO₂ interface-trap density does not respond to the DC bias. Then, the MOS capacitor is biased in deep depletion and is illuminated by UV light, which generates minority carriers in excess of the thermal-equilibrium concentration. Immediately after the light is switched off, a positive-bias sweep is initiated, resulting in a constant capacitance, well above the inversion level. In the depletion region, minority carriers are retained at the interface traps owing to their deep energy levels in the energy gap. When the traps start to capture majority carriers, an *interface-state ledge* is observed. There should be a considerable voltage shift from the initial *C–V* curve that was measured in the dark environment for high interface-trap densities, as shown in Fig. 9.3a [35]. The ledge (which corresponds to the voltage shift) is used to deduce the total interface-trap density. A second hysteresis is

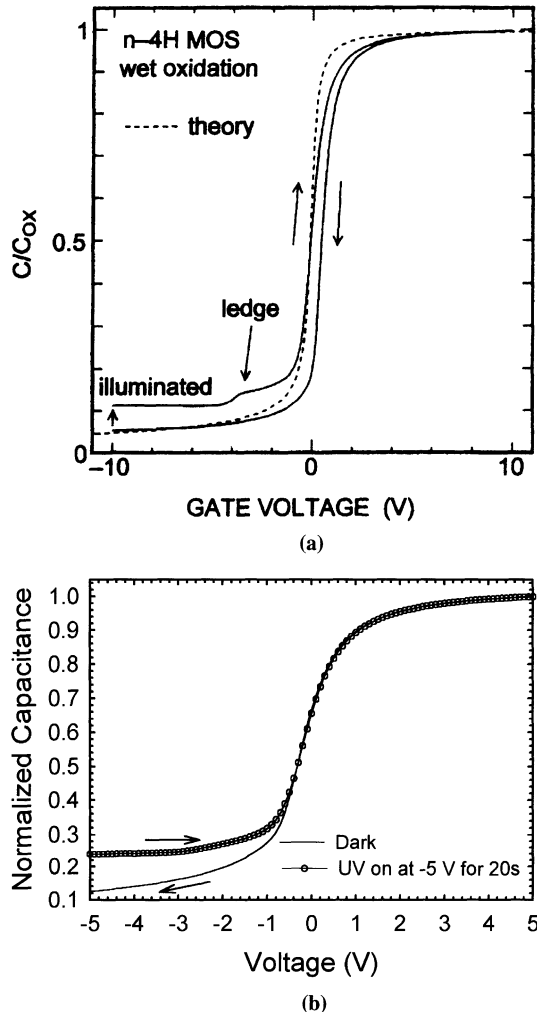


Fig. 9.3. HF $C-V$ curves for a MOS capacitor on 4H-SiC obtained using the room-temperature photo- $C-V$ technique, with an oxide grown (a) by wet oxidation, exhibiting a considerable interface-state ledge [35], and (b) in 10% N_2O , showing no interface-state ledge [36] (with permission for reproduction from IEEE)

also observed beyond the interface-state ledge, which is due to near-interface traps adjacent to the interface traps [12].

The sensitivity of this technique is questionable, as the interface-state ledge does not exist for samples with a high-quality SiC– SiO_2 interface (Fig. 9.3b) [36]. Therefore, this technique is only suitable for analyzing samples with high interface-trap densities.

Hall Effect Technique

This technique was first applied to obtain the interface-trap density near the band edges in silicon MOS devices [37], utilizing MOS Hall bars to measure the electron transport in the MOS inversion layer, which was affected by electron trapping. Experimental data for the interface-trap density in a 4H-SiC MOS sample characterized by this technique and by the quasi-static-frequency $C-V$ technique are compared in Fig. 9.4 [38], and the correlation between the two methods is reasonable. Although the two techniques are comparable, the Hall effect technique is preferable for characterizing the interface-trap density in enhancement mode MOSFETs, as the interface-trap density near the band edge of interest can be directly measured from a Hall structure fabricated on the same substrate as the MOSFETs. For example, an n-channel MOSFET is built on a p-type substrate, and by using this technique, the interface-trap density near the conduction band edge can be obtained. In contrast, $C-V$ techniques using a p-type MOS structure provide the interface-trap density near the valence band edge.

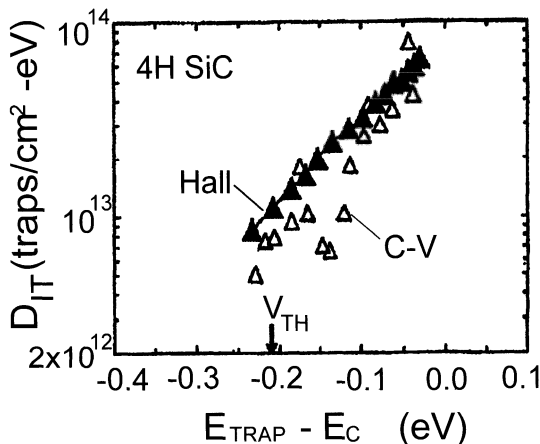


Fig. 9.4. Hall effect measurements of D_{it} in a 4H-SiC MOS sample compared with low-frequency $C-V$ measurements [38] (with permission for reproduction from the American Institute of Physics)

MOSFET Subthreshold Current Technique

In addition to the above-mentioned techniques that utilize MOS structures to determine the interface-trap density, MOSFET structures are also commonly used to measure the interface-trap density from their subthreshold current. When the transfer characteristic is represented as a semilogarithmic plot

($\log I_D$ versus V_{GS}), the slope of the plot, which is defined as the subthreshold swing (S), corresponds to the interface-trap density in the weak-inversion region [39, 40]. S is given by

$$S = \frac{dV_{GS}}{d(\log I_D)},$$

and the interface-trap density is then correlated with S by [41]

$$D_{it} = \frac{1}{q} \left(\frac{qS}{2.3kT} - 1 \right) C_{ox} - C_D,$$

where C_{ox} and C_D are the capacitances of the oxide and the depletion layer, T is the absolute temperature, q is the elementary charge, and k is Boltzmann's constant. C_D can be evaluated by solving the Poisson equation for the substrate doping concentration, which can be extracted from an HF $C-V$ measurement on an MOS capacitor, and it can be approximated by [42]

$$C_D = \frac{C_{ox}}{1 + \epsilon_o W / \epsilon_s t_{ox}},$$

where ϵ_o and ϵ_s are the permittivities of the oxide and silicon carbide, respectively, W is the depletion layer width, and t_{ox} is the oxide thickness.

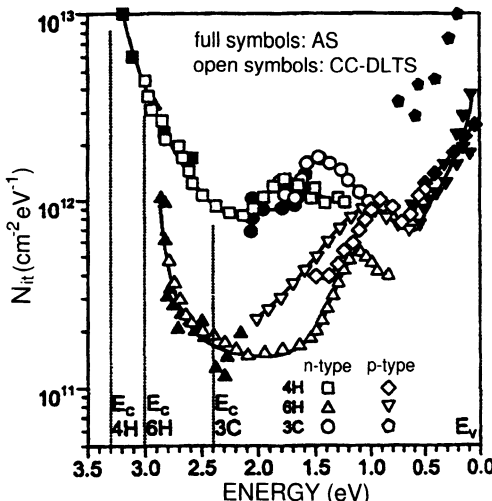


Fig. 9.5. Energy distribution of the interface-trap density for 3C-, 4H-, and 6H-SiC MOS structures measured using AS (full symbols) and CC-DLTS (open symbols). The origin of the energy scale is at the top of the SiC valence band; the dotted lines mark the conduction band energies in various SiC polytypes [43] (with permission for publication from Trans Tech Publications)

Other Techniques

Besides the above-mentioned techniques, there are a number of exotic techniques used to characterize SiC–SiO₂ interface traps, such as temperature-dependent admittance spectroscopy (AS) and constant-capacitance deep-level transient spectroscopy (CC-DLTS) (Fig. 9.5) [43]. The former technique is able to measure the traps very near to the band edge, whereas the latter technique covers a wider measurable range deep inside the energy band.

9.2.4 Electrical Characterization of Defects Near the SiO₂-SiC Interface

Low-Temperature CV Technique

Near-interface traps can be evaluated by analyzing C–V curves ($f = 1$ kHz) at room temperature (330 K) and low temperature (77 K) for a MOS structure with a biasing that shifts from accumulation toward depletion in fixed-step

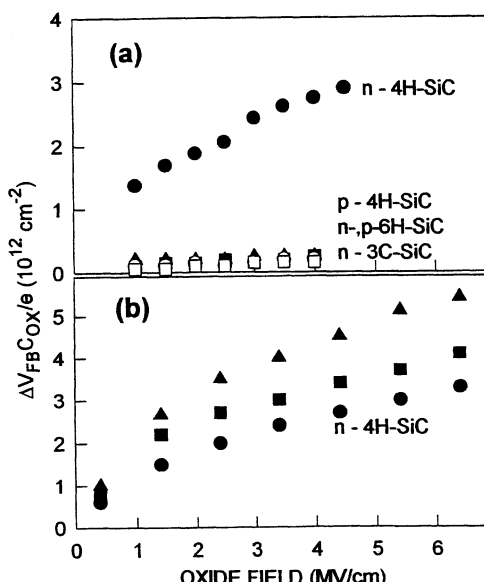


Fig. 9.6. Density of trapped charges determined by the low-temperature C–V technique as a function of the maximum electric field applied to the oxide. (a) SiC MOS structures with ~ 100 nm thick dry oxides grown on 4H- (circles), 6H- (squares), and 3C-SiC (triangles) substrates, n-type (filled symbols) and p-type (open symbols), at a measurement temperature of 130 K; (b) n-type 4H-SiC MOS structures with 50 nm thick oxides grown at 1120 °C in dry O₂ (●), in Ar + H₂O (■), and in O₂ + 2% H₂ (▲), at a measurement temperature of 77 K; e is the elementary charge [44] (with permission for publication from the American Institute of Physics)

increments. The shift of the C - V curves measured from accumulation to depletion at 77 K with respect to those measured at 300 K can be related to the density of electrons or holes (depending on the type of substrate) that are trapped near the interface. When the sample is heated back to 300 K, the C - V curves return to their initial room temperature condition [44]. Figure 9.6 compares the densities of trapped electrons measured for different polytypes and substrate conductivities with oxides grown under different conditions.

Slow-Trap Profiling Technique

This technique directly measures the current due to electron trapping or electron release from the traps by stepping the gate voltage in small increments [45]. A positive voltage step causes a positive displacement current spike, which, in the absence of a leakage current, produces a positive current even at negative gate voltages. Similarly, a negative voltage step causes a negative displacement current spike. These current spikes occur even without near-interface traps; however, they are typically shorter than 30 ms. Any current that lasts well beyond the expected RC constant of the circuit is due to near-interface trapping mechanisms. Dividing the current by the sample area, the electron charge q , and the value of the voltage step gives the near-interface trap density in $\text{cm}^{-2} \text{s}^{-1} \text{V}^{-1}$. Figure 9.7 shows an example of a slow-trap profile – a profile of the trap density as a function of energy and response time. The near-interface trap density per unit area (N_{st} in cm^{-2}) can also be obtained by numerical time and voltage integrations of the profile obtained.

9.2.5 Processing Techniques for Improvement of Interface Quality

The advancement of SiC MOS device technology is attributable to the successful development of commercially available bulk SiC substrates and the improvement in SiC epitaxial growth techniques [46–50]. However, this advancement has been hindered by imperfections in SiO_2 –SiC interfaces that can considerably deteriorate the performance of MOS devices. In addition to the improvements in the quality of bulk substrates by epitaxial techniques, technologies to improve the quality of interfaces are necessary. There are two techniques that have demonstrated significant reductions in the densities of interface and near-interface traps and subsequent improvements in device performance, such as a higher oxide breakdown field and channel mobility. These two techniques are ultraviolet–ozone cleaning of the substrate before oxidation [3] and gate oxide nitridation [51]. The results related to the latter technique are reviewed in Sect. 9.3.

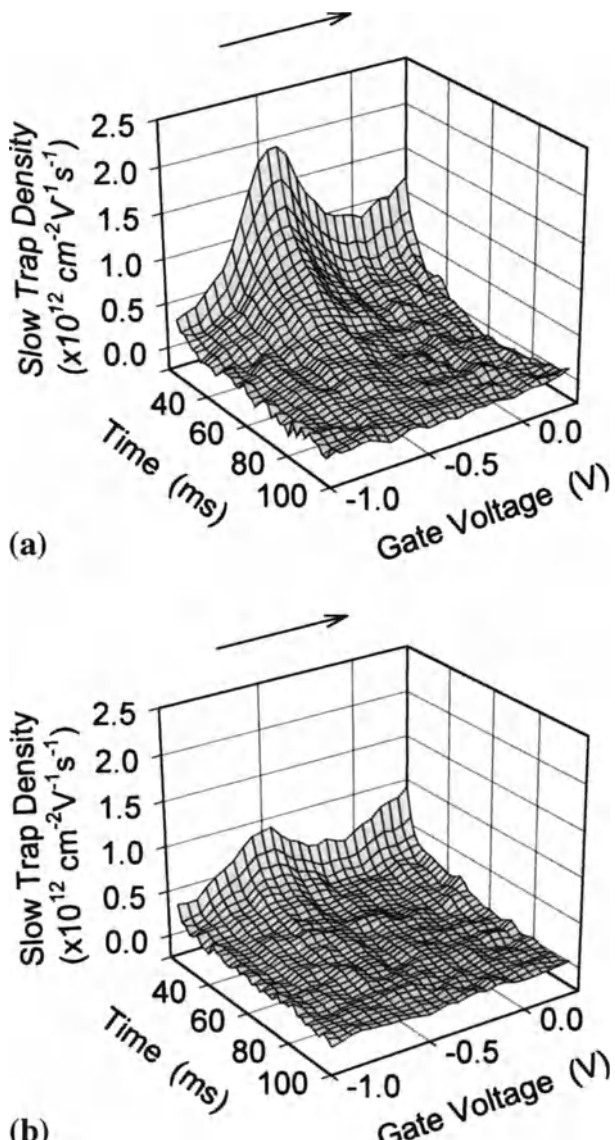


Fig. 9.7. Slow-trap profiles of ultrathin oxides grown on n-type SiC by dry oxidation: (a) without annealing and (b) with NO annealing. The time axis begins at 20 ms [45] (with permission for reproduction from Elsevier)

9.3 Nitrided Gate Oxides

9.3.1 Effects of Nitrogen at the $\text{SiO}_2\text{--SiC}$ Interface

Nitridation is involved in at least two sets of mechanisms at the $\text{SiO}_2\text{--SiC}$ interface: (1) creation of strong $\text{Si}\equiv\text{N}$ bonds that passivate interface traps due to dangling and strained bonds, and (2) removal of carbon and the associated complex silicon–oxycarbon bonds [52].

The mechanisms leading to the creation of strong $\text{Si}\equiv\text{N}$ bonds are completely analogous to the case of the $\text{SiO}_2\text{--Si}$ interface [53, 54]. In the case of both the $\text{SiO}_2\text{--Si}$ and the $\text{SiO}_2\text{--SiC}$ interfaces, there are dangling Si bonds that are passivated by N, and strained Si–O bonds that are replaced by strong $\text{Si}\equiv\text{N}$ bonds during the nitridation. In both cases, the creation of these bonds improves the reliability of the oxide gate [30, 55, 56]. An important difference in the case of SiC is that not only is the reliability improved by the strong $\text{Si}\equiv\text{N}$ bonds but also the initial interface-trap density is significantly reduced. This interface-trap reduction is analogous to the well-established interface-trap reduction in Si due to creation of Si–H bonds (interface passivation). This hydrogen-based passivation is not effective in the case of SiC – it leads not to a net reduction of the interface-trap density [23, 57] but just to a shift of their energy levels away from the midgap. The reason for that is the wider energy gap of SiC, particularly the 4H polytypes, which encompasses the energy levels of Si–H bonds. In contrast, the energy levels of the much stronger $\text{Si}\equiv\text{N}$ bonds are outside the energy gap of SiC, meaning that they are electrically passive defects [58].

The second role of nitridation is related to removal of carbon from the interface [52, 59, 60]. Most of the carbon atoms released by oxidation of a SiC substrate react with the existing oxygen to create CO molecules that diffuse out of the oxide [13]. However, some of the released carbon atoms accumulate into carbon clusters [13], which act as interface traps themselves [61] and cause the appearance of complex silicon oxycarbon compounds at the interface [62]. Nitridation not only passivates the carbon-related interface traps [61] but also can remove interstitial carbon, as well as carbon from already formed clusters [52, 59, 60]. As a result, nitrided $\text{SiO}_2\text{--SiC}$ interfaces are free from complex silicon oxycarbon defects.

9.3.2 Physical Characteristics of Nitrided $\text{SiO}_2\text{--SiC}$ Interfaces

Figure 9.8 compares the SIMS profiles of nitrogen and oxygen through the oxide–semiconductor interface for oxides grown on both Si and SiC substrates and nitrided in NO. It can be seen that the nitrogen distribution relative to the interface is exactly the same in both cases, but the percentage of N is greatly reduced in the case of SiC [21].

The question, then, is how the nitrogen is bonded at the oxide–SiC interface. Figure 9.9 compares XPS spectra for Si 2p at the interfaces of dry

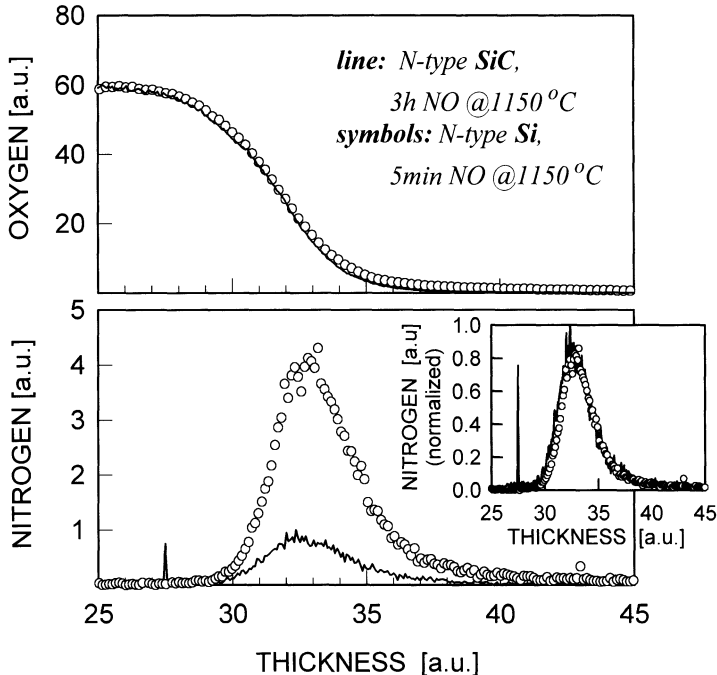


Fig. 9.8. Normalized SIMS profiles of oxygen (*top*) and nitrogen (*bottom*) in nitrided oxides on Si (*symbols*) and SiC (*lines*). The nitrogen peak shape and position are the same relative to the oxygen profiles [21] (with permission for reproduction from IEEE)

oxides on 4H-SiC samples annealed in argon and NO [62]. The argon-annealed sample has a broader and more complex peak than has the NO-annealed sample. A similar difference was also seen in the oxygen and carbon peaks. This indicates that NO annealing of the oxide creates a cleaner interface with less suboxide compared with annealing in an inert gas such as argon. There is also evidence that $\text{Si}\equiv\text{N}$ bonding occurs at the interface in NO-annealed oxides on SiC, as demonstrated in Fig. 9.10, which shows the N 1s peak at 397.8 eV. This is very close to the energy of the $\text{Si}\equiv\text{N}$ bonding in silicon nitride.

Another physical effect of nitridation is smoothing of the interface, as shown in the atomic force microscope images of Fig. 9.11. Removal of the dry oxide and nitrided oxide layers revealed a significantly smoother SiC surface in the nitrided case, with a mean square roughness of 0.1322 nm, compared with 0.5778 nm for the dry oxide [63]. This is thought to be due to the more efficient carbon removal during oxide growth in the nitrided case and hence reduced formation of carbon clusters at the interface.

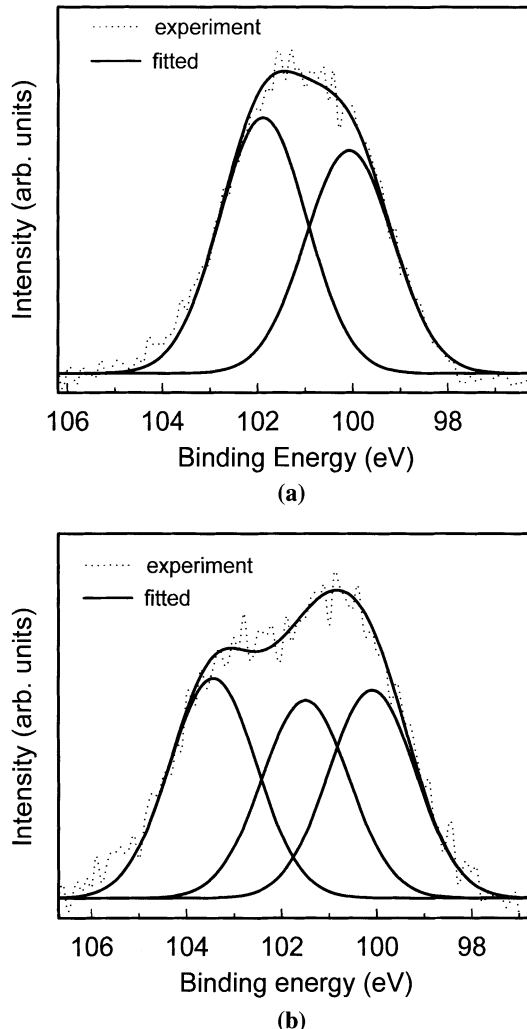


Fig. 9.9. (a) Si 2p XPS spectrum at an NO-annealed SiO₂/SiC interface. (b) Si 2p XPS spectrum at an Ar-annealed SiO₂/SiC interface [62] (with permission for reproduction from the American Institute of Physics)

9.3.3 Electrical Characteristics of MOS Capacitors with Nitrided Gate Oxides

Having discussed the physical effects of nitridation on the oxide–SiC interface, we now look at the benefits to the electrical properties of the oxide and its interface with SiC. A major hurdle to be overcome in the development of a viable SiC MOSFET is the reduced channel mobility caused by high densities of interface and near-interface traps. As the different polytypes have differing energy gaps, the energy levels of traps with respect to the energy gap mean

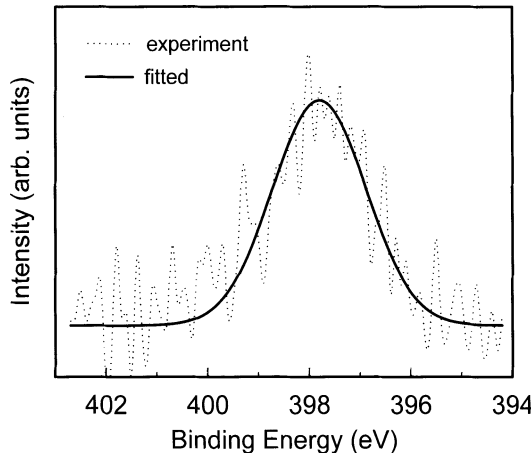


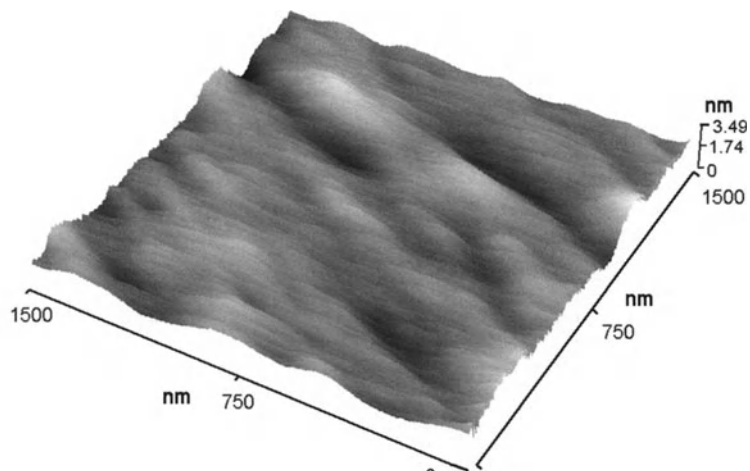
Fig. 9.10. N 1s XPS spectrum at the interface of an NO-annealed sample indicating the existence of Si≡N bonds [62] (with permission for reproduction from the American Institute of Physics)

that they are electrically active in some polytypes but not in others [64]. For instance, traps with energies just below the conduction band of 4H-SiC are not active in the case of 3C-SiC as they are placed above the conduction band edge, as shown in Fig. 9.12 [60].

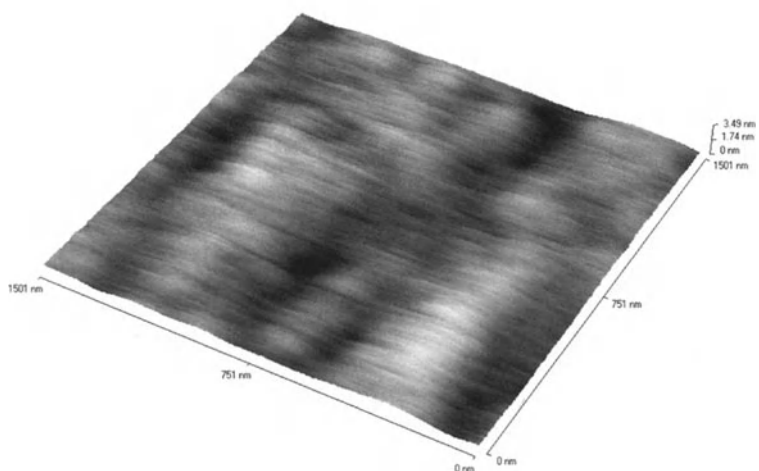
Various studies have linked certain physical defects to the energy location of traps in the energy gap. Traps in the lower half of the energy gap are thought to be related to carbon compounds [65]. Near to the conduction band of 4H-SiC, high densities of predominantly near-interface traps are thought to be responsible for the poor inversion layer mobility in lateral MOSFETs when standard wet and dry oxidation processes are used. Afanas'ev et al. studied NO- and N₂O-nitrided oxides on 4H-SiC and their effects on fast and slow interface traps [60]. They found that fast interface traps were reduced over the entire energy gap in both cases, owing to removal of carbon clusters, as seen in Fig. 9.13.

9.3.4 Channel-Carrier Mobility in MOSFETs with Nitrided Gate Oxides

Many studies have shown that nitrided gate oxides produce superior MOSFET characteristics, such as lower on-resistance as a consequence of improved channel mobility, higher gate breakdown voltages, and more practical threshold voltages. In the case of inversion-type MOSFETs on 4H-SiC, Das et al. showed that NO nitridation resulted in a fourfold decrease in both the fixed oxide charge and the interface traps in the nitrided oxide compared with a dry oxidation followed by a low-temperature wet anneal, as seen in Fig. 9.14 [66]. The nitridation process produced a low-field electron mobility of 28 cm²/Vs,



(a)



(b)

Fig. 9.11. AFM topography for (a) dry oxide and (b) nitrided oxide. The root mean square roughness are 0.5778 nm and 0.1322 nm, respectively (with permission for reproduction from Trans Tech Publications)

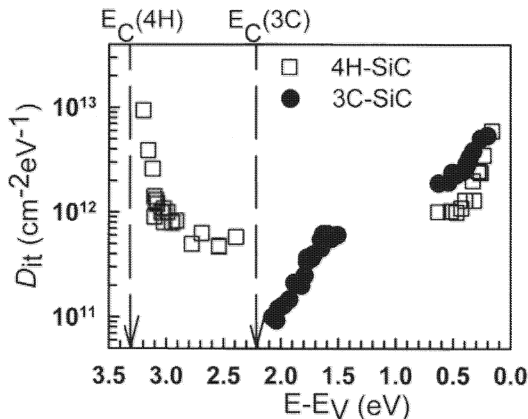


Fig. 9.12. Interface-trap densities as a function of energy for identically processed 3C-SiC(001) and 4H-SiC(1120) MOS capacitors [60] (with permission for reproduction from the American Institute of Physics)

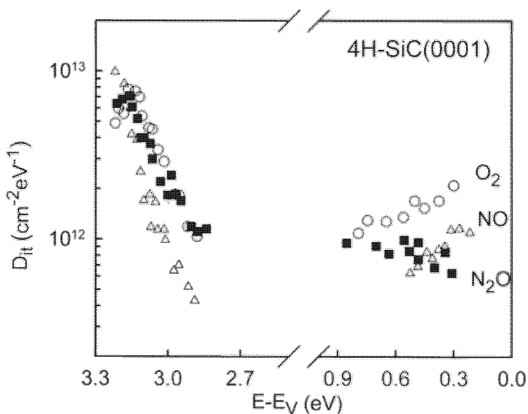


Fig. 9.13. Energy distribution of 4H-SiC/SiO₂ interface states obtained from AC conductance measurements on samples with oxides grown at 1300 °C in dry O₂ (circles) or 10% N₂O (squares), and at 1175 °C in NO (triangles) [60]

which was uniform across the wafer, independent of channel orientation in the *c*-plane, and only slightly reduced by the presence of an ion implanted p-well.

The output characteristics of a 4H-SiC enhancement mode n-channel MOSFET fabricated by Schorner et al. with an NO-nitrided gate oxide are shown in Fig. 9.15 [67]. The transfer characteristics appear in Fig. 9.16, and from this were extracted the values of the low-field mobility of 48 cm²/Vs and of the threshold voltage of 0.6 V [67].

A similar result was obtained by Chung et al. in a study of NO annealing with various gate oxidation processes on 4H-SiC [68, 69]. The nitridation

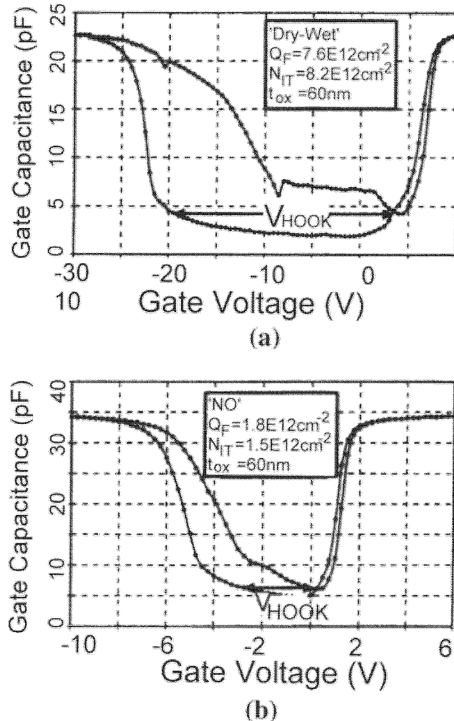


Fig. 9.14. Capacitance–voltage measurements on (a) “dry–wet” MOSFET and (b) “NO” MOSFET showing the reduced interface charge and trapping due to the post-oxidation NO annealing [66] (with permission for reproduction from Trans Tech Publications)

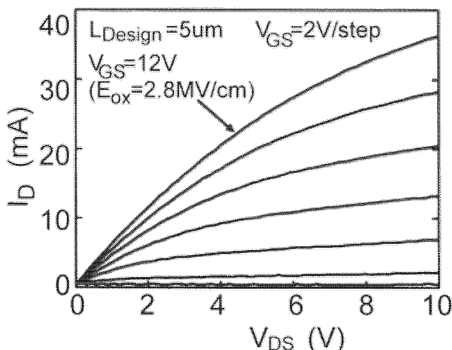


Fig. 9.15. Output characteristics of a 4H-SiC enhancement mode n-channel MOSFET with a designed length of $5 \mu\text{m}$ (substrate doping $N_A - N_D = 6 \times 10^{14} \text{ cm}^{-3}$) [67] (with permission for reproduction from the American Institute of Physics)

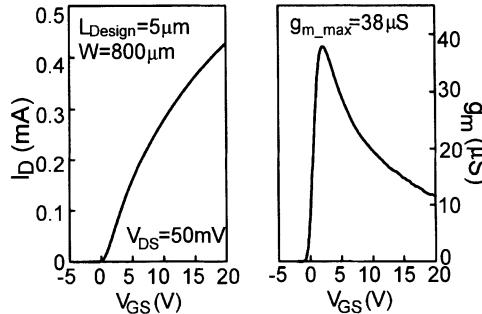


Fig. 9.16. (a) Transfer characteristics of the 4H-SiC enhancement mode n-channel MOSFET and (b) the corresponding transconductance [67] (with permission for reproduction from the American Institute of Physics)

process resulted in an eightfold decrease in the interface-trap density near the conduction band edge and a tenfold increase in the field effect channel mobility to a value of $35 \text{ cm}^2/\text{Vs}$. Nitridation was also seen to produce a lower temperature dependence of the field effect mobility and a significantly reduced threshold voltage shift at higher temperatures.

9.4 Power MOSFETs

Although oxide on SiC has been studied since the early 1960s, the first SiC MOSFETs were only successfully realized 15 years ago on the cubic polytype [70]. These pioneering devices, obtained with the 3C polytype, suffered from high leakage current and did not show any clear saturation regime. Later on, Shibahara et al. [71], followed by Kong et al. [72], reported n-channel SiC MOSFETs with a clear saturation regime even at high V_{DS} . These early results were all obtained with the 3C polytype, grown on either Si or SiC. These devices, limited by the presence of structural defects, inherent in the crystal growth method used, nevertheless had much better high-temperature properties than those of Si devices. Inversion-mode p-type MOSFETs have also been fabricated and were reported to be poorer than their n-type counterparts [73]. With the availability of the first single-crystal wafers at the beginning of the 1990s, MOSFETs have also been fabricated on other polytypes such as 6H-SiC [25, 74–76], 4H-SiC [76, 77], 15R-SiC [39], and 3C-SiC [78]. These latest results have undeniably demonstrated not only the feasibility of SiC MOSFETs but also their excellent suitability for power applications.

As first pointed out by Baliga [79], the specific on-resistance of the drift region increases rapidly with increasing blocking voltage. This is due to the fact that, in order to increase the breakdown voltage, the designer has to reduce the doping level of the drift region and to increase its thickness, which results in a high on-state voltage. This is best demonstrated by the fundamental analysis by Baliga [80], where the relationship between the specific

on-resistance of the drift region and the semiconductor material properties is expressed as

$$R_{\text{on,sp(ideal)}} = \frac{4BV^2}{\varepsilon_s \mu E_c^3},$$

where BV is the breakdown voltage, ε_s is the dielectric constant, μ is the carrier mobility, and E_c is the critical electric field for breakdown. The denominator of this expression is better known as Baliga's figure of merit (BFOM) for power devices. One important prediction given by this equation is that wide-energy-gap semiconductors (with high critical electric fields) are expected to have much lower specific resistances in the drift region. This has provided a very strong motivation for the development of power MOSFETs in SiC.

9.4.1 Device Structures

The motivating factors for the development of vertical SiC power MOSFETs are a very low specific on-resistance, fast switching, and superiority over Si IGBTs in the 600–2000 V range. Vertical SiC MOSFETs are made either by a double-diffused MOS, or “DMOS”, process, or by a trench-gated, or “UMOS”, process. The DMOS structure, commonly used for Si power devices, is extremely difficult to fabricate because diffusion in SiC is negligible even at high temperatures (1600 °C). Because UMOS relies on epitaxy, it is thus much easier to fabricate the UMOS structure in SiC. However, SiC UMOSFETs suffer some critical disadvantages related to their particular MOS structure. They have poor oxide uniformity due to the trench structure [81]. The presence of a higher interface-trap density on the sidewalls diminishes the overall device performance. The high electric field is increased at the corners of the UMOS trench, restricting its breakdown voltage [82–84]. Inversion-channel mobilities in UMOS devices have been reported to be lower than those in planar SiC MOSFETs. Because of the lower barrier heights for electron injection in the 4H-SiC–SiO₂ polysilicon system, Fowler–Nordheim carrier injection occurs across the gate oxide. Still, the UMOS structure offers inherent advantages over the DMOS structure. It has a smaller pitch and a lower potential $R_{\text{on,sp}}$ owing to the absence of the JFET region.

The use of accumulation-mode MOSFETs, known as ACCUFETs, was suggested to circumvent the problems associated with the high field in the gate oxide and the poor inversion layer mobilities in the channels of the DMOS and UMOS structures. In this device, an n-type layer is epitaxially grown on a p-base region, the thickness and the doping concentrations of these two layers being adjusted so that the n-epitaxial layer is fully depleted at zero gate voltage. When a positive gate voltage is applied, an accumulation-layer channel is formed at the interface between the n-epitaxial layer and the gate oxide.

9.4.2 Performance of Power SiC MOSFETs

The higher critical electric field of SiC compared with Si allows the use of much greater doping concentrations and thinner layers for a given voltage compared with what is necessary in the case of Si devices. This should result in a much smaller specific on-resistance $R_{\text{on,sp}}$.

Although the very low diffusion coefficients in SiC have motivated the fabrication of UMOSFETs, the performance of these devices is still limited by premature oxide breakdown and low inversion layer mobility. Early results on vertical power MOSFETs (UMOSFETs) fabricated on SiC [82, 85] suffer from a high specific on-resistance ($38 \text{ m}\Omega \text{ cm}^2$) for a maximum breakdown voltage of only 260 V. A double-implant MOS (DIMOS) process was used to ameliorate the high-field stressing encountered by conventional SiC UMOS transistors. As a result, the blocking voltage of this double-implanted MOSFET (DIMOSFET) was increased to up to 760 V [86]. Sugawara and Asano [87] have reported a 4H-SiC UMOSFET with a high breakdown voltage of up to 1.4 kV; however, the specific on-resistance is still too high ($R_{\text{on,sp}} = 311 \text{ m}\Omega \text{ cm}^2$). Lateral double-implanted MOSFETs fabricated on an insulating 4H-SiC substrate have demonstrated record-high blocking voltages of 2.6 kV [88]. A 6H-SiC triple-ion-implanted MOSFET has been reported to have a blocking voltage of 1800 V [89]. This device has $R_{\text{on,sp}} = 82 \text{ m}\Omega \text{ cm}^2$ at $V_{\text{DS}} = 50 \text{ mV}$ and $V_{\text{GS}} = 10 \text{ V}$. This specific on-resistance is an order of magnitude lower than that of a silicon DMOSFET of the equivalent blocking capability.

For the first time, the performance of SiC power MOSFETs exceeded the theoretical limits of silicon devices with the introduction of the first SiC ACCUFET [90–92]. Onda et al. [90] have developed a 6H-SiC trench MOSFET on (0001) C-face wafers with a MOS structure consisting of epitaxially grown n-type SiC trench sidewall layers. It features an on-state resistance as low as $23.84 \text{ m}\Omega \text{ cm}^2$ with a blocking voltage of more than 450 V. By using a buried p⁺ layer to shield the channel region (in order to circumvent the problems associated with gate oxide rupture and poor channel conductance), Shenoy and Baliga [91] obtained devices with a blocking voltage of 350 V and a specific on-resistance of $18 \text{ m}\Omega \text{ cm}^2$, close to the simulated $15 \text{ m}\Omega \text{ cm}^2$, at room temperature, for a gate bias of only 5 V using 6H-SiC. This measured specific on-resistance is also within 2.5 times the value calculated for the epitaxial drift region. When implemented in 4H-SiC, however, the ACCUFET had a larger $R_{\text{on,sp}} = 3200 \text{ m}\Omega \text{ cm}^2$, which decreased with increasing temperature ($R_{\text{on,sp}} = 128 \text{ m}\Omega \text{ cm}^2$ at 450 K). Tan et al. [92] reported an improved UMOS ACCUFET with a blocking voltage of 850 V while maintaining a low on-resistance of $27 \text{ m}\Omega \text{ cm}^2$. Recently, Linewih et al. [93] reported a new ACCUFET structure for high-power applications. It utilizes a fully depleted n-channel epilayer, grown on a p-base epilayer, to achieve normally-off operation. A trench region is implanted to create an n-type path that connects the n-channel epilayer (accumulation channel) to the underlying n drift re-

gion. This novel structure is believed to provide the highest figure of merit for power devices.

References

- V.V. Afanas'ev, "SiC/SiO₂ interface defects", in *Defects in SiO₂ and Related Dielectrics: Science and Technology*, eds. G. Pacchioni, L. Skuja, and D.L. Griscom, Kluwer Academic, Dordrecht, p. 529 (2000).
- L.A. Lipkin and J.W. Palmour "Insulator Investigation on SiC for Improved Reliability", IEEE Trans. Electron Devices **46**, 525–529 (1999).
- V.V. Afanas'ev, M. Bassler, G. Pensl, M.J. Schulz, and E.S. von Kamienski, "Band offsets and electronic structure of SiC/SiO₂ interfaces", J. Appl. Phys. **7**, 3108–3113 (1996).
- A.K. Agarwal, S. Seshadri, and L.B. Rowland, "Temperature dependence of Fowler–Nordheim current in 6H- and 4H-SiC MOS capacitors", IEEE Electron Device Lett. **18**, 592–594 (1997).
- E. Bano, T. Ouisse, P. Lassagne, T. Billon, and C. Jaussaud, "High temperature dependence of Fowler–Nordheim emission tunneling current in (6H) and (4H) SiC MOS capacitors", *Proceedings of the International Conference on SiC and related Materials*, Kyoto, Japan, 18–21 September 1995, Conference Series No. 142, Institute of Physics, Bristol, pp. 733–736 (1996).
- S. Nakamura, H. Kumagai, T. Kimoto, and H. Matsunami, "Breakdown fields along various crystal orientations in 4H-, 6H- and 3C-SiC", Mater Sci. Forum **389–393**, 651–654 (2002).
- S. Suzuki, S. Harada, R. Kosugi, J. Senzaki, and K. Fukuda, "Correlation between inversion channel mobility and interface traps near the conduction band in SiC MOSFETs", Mater Sci. Forum **389–393**, 1045–1048 (2002).
- E.H. Nicollian and J.R. Brews, *MOS Physics and Technology*, Wiley, New York (1982).
- C.R. Helms and E.H. Poindexter, "The silicon–silicon-dioxide system: its microstructure and imperfections", Rep. Prog. Phys. **57**, 791–804 (1994).
- A. Stesmans, "Structural relaxation Pb defects at the (111) Si/SiO₂ interface as a function of oxidation temperature: the Pb–generation–stress relationship", Phys. Rev. B **48**, 2418–2423 (1993).
- V.V. Afanas'ev, M. Bassler, G. Pensl, and M.J. Schulz, "Intrinsic SiC/SiO₂ interface states", Phys. Stat. Sol. (a) **162**, 321–337 (1997).
- J.A. Cooper, Jr., "Advances in SiC MOS technology", Phys. Stat. Sol. (a) **162**, 305–320 (1997).
- V.V. Afanas'ev, A. Stesmans, and C.I. Harris, "Observation of carbon clusters at the 4H-SiC/SiO₂ interface", Mater. Sci. Forum **264–268**, 857–860 (1998).
- G. Pensl, V.V. Afanas'ev, M. Bassler, M. Schadt, T. Troffer, J. Heindl, H.P. Strunk, M. Maier, and W.J. Choyke, "Electrical properties of silicon carbide polytypes", Inst. Phys. Conf. Ser. **142**, 275–278 (1996).
- B. Hornetz, H.-J. Michel, and J. Halbritter, "ARXPS studies of SiO₂–SiC interfaces and oxidation of 6H SiC single crystal Si-(001) and C-(001) surfaces", J. Mater. Res. **9**, 3088–3091 (1994).
- V.R. Vathulya, D.H. Wang, and M.H. White, "On the correlation between the carbon content and the electrical quality of thermally grown oxides on p-type 6H-silicon carbide", Appl. Phys. Lett. **73**, 2161–2163 (1998).

17. P. Martensson, F. Owman, and L.I. Johansson, "Morphology, atomic and electronic structure of 6H-SiC(0001) surfaces", *Phys. Stat. Sol. (b)* **202**, 501–514 (1997).
18. Y. Hijikata, H. Yaguchi, M. Yoshikawa, and S. Yoshida, "Composition analysis of SiO₂/SiC interface by electron spectroscopic measurements using slope-shape oxide films", *Appl. Surf. Sci.* **184**, 161–166 (2001).
19. P.J. Macfarlane and M.E. Zvanut, "Generation and annealing characteristics of paramagnetic centers in oxidized 3C-SiC and 6H-SiC", *J. Electron. Mater.* **28**, 144–147 (1999).
20. N.T. Son, W.M. Chen, J.L. Lindström, B. Monemar, and E. Janzén, "Carbon-vacancy related defects in 4H- and 6H-SiC", *Mater. Sci. Eng. B* **61–62**, 202–207 (1999).
21. P. Tanner, S. Dimitrijev, H.-F. Li, D. Sweatman, K.E. Prince, and H.B. Harrison, "SIMS analysis of nitrided oxides grown on 4H-SiC", *J. Electron. Mater.* **28**, 109–112 (1999).
22. V.V. Afanas'ev, "Electronic properties of the SiO₂/SiC interfaces", *Microelectron. Eng.* **48**, 241–248 (1999).
23. V.V. Afanas'ev and A. Stesmans, "H-complexed oxygen vacancy in SiO₂: energy level of a negatively charged state", *Appl. Phys. Lett.* **71**, 3844–3846 (1997).
24. A.X. Chu and W.B. Fowler, "Theory of oxide defects near the Si–SiO₂ interface", *Phys. Rev. B* **41**, 5061–5075 (1990).
25. S.T. Sheppard, M.R. Melloch, and J.A. Cooper, Jr., "Characteristics of inversion-channel and buried-channel MOS devices in 6H-SiC", *IEEE Trans. Electron Devices* **41**, 1257–1259 (1994).
26. J.N. Shenoy, M.K. Das, J.A. Cooper, Jr., M.R. Melloch, and J.W. Palmour, "Effect of substrate orientation and crystal anisotropy on the thermally oxidized SiO₂/SiC interface", *J. Appl. Phys.* **79**, 3042–3047 (1996).
27. L.M. Terman, "An investigation of surface states at a silicon/silicon oxide interface employing metal–oxide–silicon diodes", *Solid-State Electron.* **5**, 285–299, (1962).
28. P.T. Lai, J.P. Xu, and Y.C. Cheng, "Interface properties of NO-annealed N₂O-grown oxynitride", *IEEE Trans. Electron Devices* **46**, 2311–2314 (1999).
29. P.T. Lai, J.P. Xu, and C.L. Chan, "Effects of wet N₂O oxidation on interface properties of 6H-SiC MOS capacitors", *IEEE Electron Device Lett.* **23**, 410–412 (2002).
30. J.P. Xu, P.T. Lai, C.L. Chan, B. Li, and Y.C. Cheng, "Improved performance and reliability of N₂O-grown oxynitride on 6H-SiC", *IEEE Electron Device Lett.* **21**, 298–300 (2000).
31. S. Chakraborty, P.T. Lai, J.P. Xu, C.L. Chan, and Y.C. Cheng, "Interface properties of N₂O-annealed SiC metal oxide semiconductor devices", *Solid-State Electron.* **45**, 471–474 (2001).
32. M.R. Melloch and J.A. Cooper, Jr., "Fundamentals of SiC-based device processing", *MRS Bull.*, March, 42–47 (1997).
33. J.N. Shenoy, G.L. Chindalore, M.R. Melloch, J.A. Cooper, Jr., J.W. Palmour, and K.G. Irvine, "Characterization and optimization of SiO₂/SiC metal–oxide–semiconductor interface", *J. Electron. Mater.* **24**, 303–309 (1995).
34. E.H. Nicollian and A. Goetzberger, "The Si–SiO₂ interface-electrical properties as determined by the metal–insulator–silicon conductance technique", *Bell. Syst. Tech. J.* **46**, 1055–1133 (1967).

35. H. Yano, F. Katafuchi, T. Kimoto, and H. Matsunami, "Effects of wet oxidation/anneal on interface properties of thermally oxidized SiO₂/SiC MOS system and MOSFET's", IEEE Trans. Electron Devices **46**, 504–510 (1999).
36. K.Y. Cheong and S. Dimitrijev, "MOS capacitor on 4H-SiC as a nonvolatile memory element", IEEE Electron Device Lett. **23**, 404–406 (2002).
37. F.F. Fang and A.B. Fowler, "Transport properties of electrons in inverted silicon surfaces", Phys. Rev. **169**, 619–631 (1968).
38. N.S. Saks, M.G. Ancona, and R.W. Rendell, "Using the Hall effect to measure interface trap densities in silicon carbide and silicon metal–oxide–semiconductor devices", Appl. Phys. Lett. **80**, 3219–3221 (2002).
39. R. Schörner, P. Friedrichs, and D. Peters, "Detailed investigation of N-channel enhancement 6H-SiC MOSFETs", IEEE Trans. Electron Devices **46**, 533–541 (1999).
40. Y. Zeng, A. Softic, and M.H. White, "Characterization of interface traps in the subthreshold region of implanted 4H and 6H-SiC MOSFETs", Solid-State Electron. **46**, 1579–1582 (2002).
41. D.K. Schroder, *Semiconductor Material and Device Characterization*, Wiley, New York (1998).
42. R.F. Pierret, *Semiconductor Device Fundamentals*, Addison-Wesley, Reading (1996).
43. G. Pensl, M. Bassler, F. Ciobanu, V.V. Afanas'ev, H. Yano, T. Kimoto, and H. Matsunami, "Traps at the SiC/SiO₂-interface", Mater. Res. Soc. Symp. Proc. **640**, H3.2.1–H3.2.11 (2001).
44. V.V. Afanas'ev, A. Stesmans, M. Bassler, G. Pensl, and M.J. Schulz, "Shallow electron traps at the 4H-SiC/SiO₂ interface", Appl. Phys. Lett. **76**, 336–338 (2000).
45. S. Dimitrijev, P. Tanner, and H.B. Harrison, "Slow-trap profiling of NO and N₂O nitrided oxides grown on Si and SiC substrates", Microelectron. Reliab. **39**, 441–449 (1999).
46. H. Morkoc, S. Strite, G.B. Gao, M.E. Lin, B. Sverdlov, and M. Burns, "Large-band-gap SiC, III–V nitride, and II–VI SnSe-based semiconductor device technologies", J. Appl. Phys. **76**, 1363–1398 (1994).
47. D.J. Larkin, "An overview of SiC epitaxial growth", MRS Bull., March, 36–41 (1997).
48. V.A. Dmitriev and M.G. Spencer, "Fabrication technology: growth and doping", in *Semiconductors and Semimetals*, Vol. 52, 21–75 ed. Y.S. Park, Academic Press, San Diego (1998).
49. J.P. Bergman, H. Jakobsson, L. Storasta, F.H.C. Carlsson, B. Magnusson, S. Sridhara, G. Pozina, H. Lendenmann, and E. Janzén, "Characterisation and defects in silicon carbide", Mater. Sci. Forum **389–393**, 9–14 (2002).
50. A.R. Power and L.B. Rowland, "SiC materials-progress, status, and potential roadblocks", Proc. IEEE. **90**, 942–955 (2002).
51. S. Dimitrijev, H.B. Harrison, P. Tanner, K.Y. Cheong, and J. Han, "Properties of nitrided oxides on SiC", in *Recent Major Advances in SiC*, eds. W.J. Choyke, H. Matsunami, and G. Pensl, Springer, Berlin (2003).
52. P. Jamet, S. Dimitrijev, and P. Tanner, "Effects of nitridation in gate oxides grown on 4H-SiC", J. Appl. Phys. **90**, 5058–5063 (2001).
53. P.J. Tobin, Y. Okada, S.A. Ajuria, V. Lakhota, W.A. Feil, and R.I. Hedge, "Furnace formation of silicon oxynitride thin dielectrics in nitrous oxide (N₂O): the role of nitric oxide (NO)", J. Appl. Phys. **75**, 1811–1817 (1994).

54. Z.Q. Yao, H.B. Harrison, S. Dimitrijev, D. Sweatman, and Y.T. Yeow, "High quality ultra thin dielectric films grown on silicon in a nitric oxide ambient", *Appl. Phys. Lett.* **64**, 3584–3586 (1994).
55. H.F. Li, S. Dimitrijev, and H.B. Harrison, "Improved reliability of NO-nitrided SiO₂ grown on p-type 4H-SiC", *IEEE Electron Device Lett.* **19**, 279–281 (1998).
56. H.B. Harrison, H.F. Li, S. Dimitrijev, and P. Tanner, "Nitrogen in ultra thin dielectrics", in *Fundamental Aspects of Ultrathin Dielectrics on Si-based Devices*, Vol. 47, 191–215, eds. E. Garfunkel, E. Gusev, and A. Vul, Kluwer Academic, Dordrecht, (1996).
57. E.S. von Kamienski, E.A. Golz, and H. Kurz, "Effect of Ar and H₂ annealing on the electrical properties of oxides of 6H SiC", *Mater. Sci. Eng. B* **29**, 131–133 (1995).
58. P. Jamet, S. Dimitrijev, and P. Tanner, "Passivation of the oxide/4H-SiC interface", *Mater. Sci. Forum* **389–393**, 973–976 (2002).
59. P. Jamet, S. Dimitrijev, and P. Tanner, "Indications for nitrogen-assisted removal of carbon from SiO₂–SiC interface", *Mater. Sci. Forum* **353–356**, 655–658 (2001).
60. V.V. Afans'ev, A. Stesmans, F. Ciobanu, G. Pensl, K.Y. Cheong, and S. Dimitrijev, "Mechanisms responsible for improvement of 4H-SiC/SiO₂ interface properties by nitridation", *Appl. Phys. Lett.* **82**, 568–570 (2003).
61. G.Y. Chung, C.C. Tin, J.R. Williams, K. McDonald, M. Di Ventra, S.T. Pantelides, L.C. Feldman, and R.A. Weller, "Effect of nitric oxide annealing on the interface trap densities near the band edges in the 4H polytype of silicon carbide", *Appl. Phys. Lett.* **76**, 1713–1715 (2000).
62. H.-F. Li, S. Dimitrijev, D. Sweatman, H.B. Harrison, P. Tanner, and B. Feil, "Investigation of nitric oxide and Ar annealed SiO₂/SiC interfaces by X-ray photoelectron spectroscopy", *J. Appl. Phys.* **86**, 4316–4321 (1999).
63. K.Y. Cheong, S. Dimitrijev, and J. Han, "Effects of initial nitridation on the characteristics of SiC–SiO₂ interface", *Mater. Sci. Forum* **433–436**, 583–586 (2003).
64. R. Schörner, P. Friedrichs, and D. Peters, "Detailed investigation of N-channel enhancement 6H-SiC MOSFETs", *IEEE Trans. Electron Devices* **46**, 533–541 (1999).
65. M. Bassler, G. Pensl, and V. Afanas'ev, "‘Carbon cluster model’ for electronic states at SiC/SiO₂ interfaces", *Diamond Relat. Mater.* **6**, 1472–1475 (1997).
66. M.K. Das, G.Y. Chung, J.R. Williams, N.S. Saks, L.A. Lipkin, and J.W. Palmour, "High-current, NO-annealed lateral 4H-SiC MOSFETs", *Mater. Sci. Forum* **389–393**, 981–988 (2002).
67. R. Schörner, P. Friedrichs, D. Peters, D. Stephani, S. Dimitrijev, and P. Jamet, "Enhanced channel mobility of 4H-SiC MOSFETs fabricated with standard power MOSFET technology and gate-oxide nitridation", *Appl. Phys. Lett.* **80**, 4253–4256 (2002).
68. G.Y. Chung, C.C. Tin, J.R. Williams, K. McDonald, R.K. Chanana, R.A. Weller, S.T. Pantelides, L.C. Feldman, O.W. Holland, M.K. Das, and J.W. Palmour, "Improved inversion channel mobility for 4H SiC MOSFETs following high temperature anneals in nitric oxide", *IEEE Electron Device Lett.* **22**, 176–178 (2001).
69. G.Y. Chung, J.R. Williams, C.C. Tin, K. McDonald, D. Farmer, R.K. Chanana, S.T. Pantelides, O.W. Holland, and L.C. Feldman, "Interface state density and

- channel mobility for 4H-SiC MOSFETs with nitrogen passivation”, *Appl. Surf. Sci.* **184**, 399–403 (2001).
70. Y. Kondo, T. Tkahashi, K. Ishii, Y. Hayashi, E. Sakuma, S. Misawa, H. Daimon, M. Yamanaka, and S. Yoshida, “Experimental 3C-SiC MOSFET”, *IEEE Electron Device Lett.* **7**, 404–406 (1986).
 71. K. Shibahara, T. Saito, S. Nishino, and H. Matsunami, “Fabrication of inversion-type n-channel MOSFETs using cubic-SiC on Si(100)”, *IEEE Electron Device Lett.* **7**, 692–693 (1986).
 72. H.S. Kong, J.W. Palmour, J.T. Glass, and R.F. Davis, “Temperature dependence of the current–voltage characteristics of metal–semiconductor field-effect transistor in n-type beta-SiC grown via chemical vapor deposition”, *Appl. Phys. Lett.* **51**, 442–444 (1987).
 73. D.B. Slater, Jr., L.A. Lipkin, G.M. Johnson, A.V. Suvorov, and J.W. Palmour, “NMOS and PMOS high temperature enhancement-mode devices and circuits in 6H-SiC”, *Inst. Phys. Conf. Ser.* **142**, 805–808 (1996).
 74. J.B. Casady, J.D. Cressler, W.C. Dillard, R.W. Johnson, A.K. Agarwal, and R.R. Siergiej, “Direct current characterization of depletion-mode 6H-SiC MOSFET’s from 294 to 723 K”, *Solid State Electron.* **19**, 777–784 (1996).
 75. J.N. Pan, J.A. Cooper, Jr., and M.R. Melloch, “Thin-oxide silicon-gate self-aligned 6H-MOSFET’s fabricated with low-temperature source/drain activation anneal”, *IEEE Electron Device Lett.* **18**, 349–351 (1997).
 76. S. Sridavan and B.J. Baliga, “Inversion layer mobility in SiC MOSFET’s”, *Mater. Sci. Forum* **264–268**, 997–1000 (1998).
 77. K. Ueno, R. Asai, and T. Tsuji, “4H-SiC MOSFETs utilizing the H₂ surface cleaning technique”, *IEEE Electron Device Lett.* **19**, 244–246 (1998).
 78. J. Wan, M.A. Capano, M.R. Melloch, and J.A. Cooper, Jr., “N-channel 3C-SiC MOSFET on silicon substrate”, *IEEE Electron Device Lett.* **23**, 482–484 (2002).
 79. B.J. Baliga, “Trends in power semiconductor devices”, *IEEE Trans. Electron Device* **43**, 1717–1731 (1996).
 80. B.J. Baliga, “Semiconductors for high voltage vertical channel field effect transistors”, *J. Appl. Phys.* **53**, 1759–1764 (1982).
 81. J.N. Shenoy, *Basic MOS Studies for Silicon Carbide Power Devices*, PhD Thesis, Purdue University (1996).
 82. J.W. Palmour, S.T. Allen, R. Singh, L.A. Lipkin, and D.G. Waltz, “4H-silicon carbide power switching devices”, *Proc. Sixth Int. Conf. Silicon Carbide and Related Materials*, pp. 813–816 (1995).
 83. N. Ramungul, R. Tyagi, A. Bhalla, T.P. Chow, M. Ghezzo, J. Kretchmer, and W. Hennessy, “Design and simulation of 6H-SiC UMOS FET and IGBT for high-temperature power electronics applications”, *Proc. Sixth Int. Conf. Silicon Carbide and Related Materials*, pp. 773–776 (1995).
 84. A.K. Argawal, “1.1 kV 4H-SiC power MOSFETs”, *IEEE Electron Device Lett.* **18**, 586–588 (1997).
 85. J.W. Palmour, J.A. Edmond, H.S. Kong, and C.H. Carter, *Conf. Ser. on SiC and Relat. Mater.* **137**, 499–502, Institute of Physics Publishing, Bristol (1994).
 86. J.N. Shenoy, J.A. Cooper, Jr., and M.R. Melloch, “High-voltage double-implanted power MOSFET’s in 6H-SiC”, *IEEE Electron. Device Lett.* **18**, 93–95 (1997).
 87. Y. Sugawara and K. Asano, “1.4 kV 4H-SiC UMOSFET with low specific on-resistance”, *Proc. Int. Conf. Power Semicondor Devices*, pp. 119–123 (1998).

88. J. Spitz, M.R. Melloch, J.A. Cooper, Jr., M.A. Capano, "High-voltage (2.6 kV) lateral DMOSFETs in 4H-SiC", IEEE Electron Device Lett. **19**, 100–102 (1998).
89. D. Peters, R. Schörner, P. Friedrichs, J. Völkl, H. Mitlehner, and D. Stephani, "An 1800 V triple implanted vertical 6H-SiC MOSFET", IEEE Trans. Electron Devices **46**, 542–548 (1999).
90. S. Onda, R. Kumar, and K. Hara. "SiC integrated MOSFETs", Phys. Stat. Solidi A **162**, 369–388 (1997).
91. P.M. Shenoy and B.J. Baliga, "The planar 6H-SiC ACCUFET: a new high-voltage power MOSFET structure", IEEE Electron Device Lett. **18**, 589–591 (1997).
92. J. Tan, J.A. Cooper, Jr., and M.R. Melloch, "High-voltage accumulation-layer UMOSFETs in 4H-SiC", 56th Annual Device Research Conference, Digest, pp. 88–89 (1998).
93. H. Linewih, S. Dimitrijev, C.E. Weitzel, and H.B. Harrison, "Novel SiC accumulation-mode power MOSFET", IEEE Trans. Electron Devices **48**, 1711–1717 (2001).

4H-SiC Power-Switching Devices for Extreme-Environment Applications

Z. Luo, T. Chen, D.C. Sheridan, and J.D. Cressler

The behavior of 4H-SiC power diodes under radiation exposure and related issues are investigated and reviewed in this chapter. The fundamentals of power diodes and radiation are introduced. The DC performance of unterminated SiC junction barrier Schottky (JBS) diodes and Schottky barrier diodes (SBDs) under gamma radiation shows the significant tolerance of SiC diodes to gamma radiation exposure. The breakdown voltage increase after gamma radiation is ascribed to changes in the SiC/SiO₂ interface. Investigation of SiC MOS capacitors confirmed this effect. NO passivation is shown to effectively improve the SiC/SiO₂ interface and the interface charge density even after gamma irradiation. Both the DC and the AC performance of SiC JBS/SBDs under high-dose proton irradiation were also investigated. SiC JBS devices show a degradation of series resistance (R_S) and improvements of reverse leakage current and blocking voltage after high-fluence proton exposure. The AC performance after proton irradiation shows that SiC JBS diodes are very effective in minimizing switching losses for high-power applications, even under high levels of radiation exposure, indicating superior radiation hardness for SiC switching diodes. We conclude that SiC power devices hold much promise for power-switching systems operating in a radiation environment.

10.1 Introduction

Silicon Carbide (SiC) is one of the most promising candidates for power semiconductor devices. As can be seen in Table 10.1, SiC has a wide bandgap (E_G) of larger than 3 eV, three times larger than Si. Compared to Si, SiC enjoys an order of magnitude improvement in critical field strength (E_C), twice the saturation velocity (V_{sat}), and three times the thermal conductivity (μ). Baliga's figure-of-merit (BFOM) [1] suggests that SiC should have more than an order of magnitude theoretical advantage over Si for unipolar power devices (e.g., Schottky-barrier diodes, and MOSFETS). Among over 200 polytypes of SiC,

Table 10.1. Parameters of power semiconductor materials

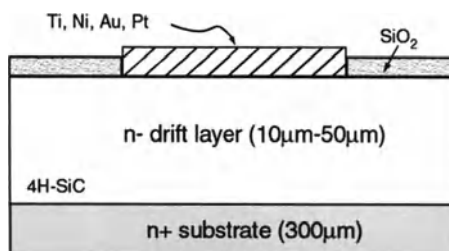
Material	E_G (eV)	ϵ_r	μ_n (cm ² /Vs)	E_C (MV/cm)	λ (W/cm s)	BFOM
Si	1.12	11.8	1350	0.3	1.5	1
GaAs	1.4	12.8	8500	0.4	0.5	15.6
3C-SiC	2.2	9.6	900	1.2	4.5	33.4
4H-SiC	3.26	10	650 370	2.0	4.5	130
6H-SiC	3.00	9.7	370 50	2.4	4.5	110

the 4H-SiC orientation is typically preferred for power switching devices because of the availability of the bulk material, its higher mobility, and reduced mobility anisotropy.

SiC-based devices are also very attractive for harsh environments for both military and space-based applications due to both their fast switching speeds and their ability to operate in the high temperature environment, and under high levels of radiation. Currently, the literature on radiation effects in SiC devices is very limited and mostly focuses on terrestrial particle detector systems. SiC radiation detectors with considerable hardness to various radiation types have been reported [2–4]. 4H-SiC neutron detectors, for instance, have been demonstrated with no significant degradation of detection efficiency after neutron fluences up to 1×10^{17} n/cm². Devices based on 6H-SiC have shown negligible degradation of device characteristics for gamma radiation doses up to 100 Mrad, but showed significant degradation with neutron irradiation for fluences in excess of 1×10^{16} n/cm². The present work addresses active device applications for radiation-rich applications such as space electronics.

10.1.1 Fundamentals of Power Schottky Barrier Diodes

A typical SiC Schottky diode structure is shown in Fig. 10.1. Several important parameters, such as Schottky barrier height, current-voltage ideality factor, specific on-resistance, breakdown (blocking) voltage, and reverse leakage current, should be known in order to fully characterize a Schottky diode. Based on

**Fig. 10.1.** Schematic cross section of a SiC Schottky diode

thermionic emission theory, under moderate bias, the forward current-voltage characteristics are given by [1]:

$$V_F = \frac{n k T}{q} \ln \left(\frac{J_F}{A^* T^2} \right) + \phi_b + R_{on} J_F , \quad (10.1)$$

where n is the ideality factor. For a perfectly ideal device, n equals to unity (a pure exponential). Normally, however, n is larger than unity and typically a device with $n \sim 1.0 - 1.3$ is acceptable for Schottky devices. The parameter A^* is Richardson's constant, whose value is:

$$A^* = 4\pi m^* q k^2 / h^3 . \quad (10.2)$$

For 4H-SiC, A^* is calculated to be $146 \text{ A K}^{-2} \text{ cm}^{-2}$ using $m^* = 0.2m_0$ and 6 conduction band minima.

In (10.1), ϕ_b is the Schottky barrier height, and R_{on} is the “on-resistance” due to the drift region, which can be calculated as:

$$R_{on} = \frac{t_{epi}}{q \mu_n N_D} = \frac{4 V_{BR}^2}{\varepsilon_s \mu_n E_C^3} , \quad (10.3)$$

where t_{epi} is the drift layer thickness, N_D is the drift layer doping concentration, V_{BR} is the ideal parallel-plate breakdown voltage for the given drift layer, and E_C is the critical field strength. In reality, we usually use R_s to replace R_{on} in (10.1), because contributions from the substrate and backside ohmic contacts must also be taken into account in addition to the drift layer resistance.

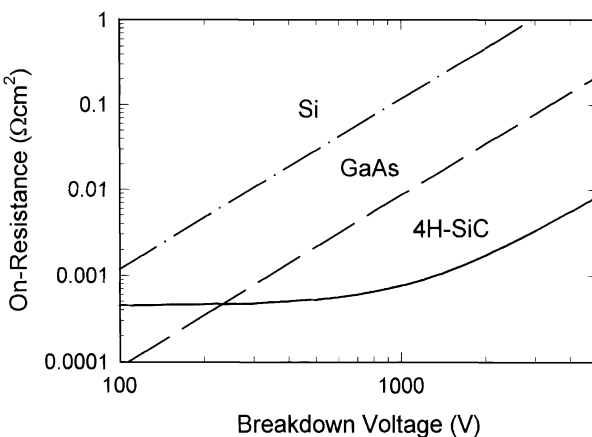


Fig. 10.2. Device on-resistance versus ideal breakdown voltage for different power device semiconductor materials. SiC shows a much smaller R_{on} than do Si and GaAs for the same breakdown voltage

Since the critical field strength of SiC is an order of magnitude larger than for Si, the drift region can be fabricated much thinner, resulting in an almost $30\times$ decrease in on-resistance. This fact represents the primary advantage of SiC over Si for power device applications, since lower resistance directly translates to improved switching efficiency. A plot of breakdown voltage versus on-resistance for Si, SiC, and GaAs is shown in Fig. 10.2 [5].

Another important parameter for Schottky diodes is the reverse leakage current. The primary mechanisms for the leakage currents are thermionic emission, field emission, thermionic field emission, generation in the depletion region, and material defects [6]. Breakdown voltage, or blocking voltage, is clearly also very important for a power device applications, and optimization of breakdown voltage for SiC diodes will be discussed below.

10.1.2 The Fundamentals of Radiation

In a general sense, radiation represents energy in motion, either in the form of high-speed particles (e.g., cosmic rays) or electromagnetic waves (e.g., gamma rays). In many applications, electronic devices and circuits are necessarily exposed to a hostile radiation environment. The kinds of particles encountered, their energy, and their spectral distribution impinging on a electronic device, strongly depend on the system application. In nuclear research, for instance, high energetic neutrons and photons are primarily released. For many space satellite applications, on the other hand, protons and other charged particles such as electrons are predominantly present in the radiation belts generated by solar flares and subsequently trapped in Earth's magnetic field [7]. Other space conditions might involve alpha particle or gamma radiation. With respect to performance degradation of semiconductor devices, the damage due to radiation is mainly due to ionization damage, displacement damage, and single event effects. The primary displacement damage degradation effects are increased resistivity or even type inversion for high-resistivity Si, increased dark current in junction devices and charge-coupled devices, and reduced minority carrier lifetime in bipolar devices [8].

The energy deposited per gram of material is called the radiation “dose” and is expressed in rads or Grays. For Si, for instance, $1.0\text{ rad} = 100\text{ erg/g} = 6.24 \times 10^{13}\text{ eV/g}$, and $1.0\text{ Gray} = 1.0\text{ J/kg} = 100\text{ rads}$. It is clear from this definition that the energy loss also depends on the mass and density of the target, so that one typically speaks about “rad(Si)” as a preferred energy unit for evaluating radiation tolerance.

Another basic radiation unit is particle “flux,” the particle density impinging on the material per unit area per unit time. The integrated flux over the given exposure time is called the “fluence,” and is expressed in particles/cm².

10.2 SiC Power Diode Structures

10.2.1 SBD, pn and JBS diodes

Among the different kinds of power switching diodes, the Schottky Barrier Diode (SBD) has faster switching speeds compared to pn diode, because of the lack of minority charge storage. SBD typically suffer from high reverse leakage current, however [9]. Leakage current in power diodes can cause several unwanted effects at both the device and circuit level. These currents can contribute to switching losses, or even increase intrinsic temperatures, resulting in potential reliability concerns. On the other hand, pn diodes provides much smaller leakage currents, but their switching speed is typically worse than SBDs because of stored charge. The Junction Barrier Schottky (JBS) diode represents a logical compromise between the SBD and pn diode structures. The JBS structure is simply composed of a Schottky diode with closely spaced p⁺ regions inside the active Schottky diode area. As seen in Fig. 10.3a, at forward bias, Schottky diode current flows between the p⁺ regions so that the forward voltage drop can be very small. Under reverse voltage, however, the p⁺ depletion regions spread out and pinch off the narrow Schottky regions at certain (tunable) reverse voltage, effectively shielding the Schottky interface and hence reducing the higher inherent leakage of the SBD (Fig. 10.3b). Con-

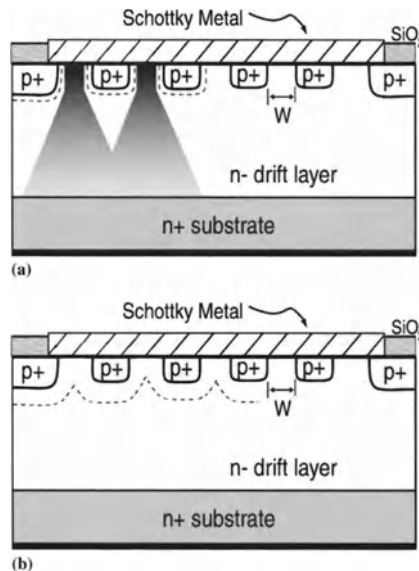


Fig. 10.3. Junction barrier diode structure. (a) Under forward bias, current flows between p⁺ regions, improving the voltage drop of the pn structure. (b) Under reverse bias, the p⁺ regions shield the Schottky interface from the high electric field, decreasing reverse leakage of the Schottky structure

sequently, JBS diodes offer the attractive Schottky-like on-state and switching characteristics, while preserving the attractive pn-like off-state characteristics.

In order for JBS diodes to work properly under both forward and reverse conditions, the spacing between the p⁺ regions must be carefully optimized. A smaller JBS spacing, for instance, can result in a reduction of peak interface field (improved reverse leakage) but also an increased forward resistance, which can result in a current constriction between the p⁺ regions. Our simulations show that the pinch resistance can add as much as 1 V to the diode's forward voltage drop at 100 A/cm². Therefore, the desired JBS structure must be carefully optimized according to application requirement, and maintain the best tradeoff between low forward voltage drop and reduced leakage current. This design space is best understood via calibrated numerical simulations.

10.2.2 Edge Termination for Power Diodes

In terms of reverse blocking capability, SiC clearly has many advantages. Theoretically, a SiC diode with a 50 μm drift layer thickness doped at $1 \times 10^{14} \text{ cm}^{-3}$ should be able to block about 7000 V, which is far more higher than the 1 kV blocking ability of a Si diode with an identical structure (Fig. 10.4). In practice, however, the ideal breakdown voltage can never be approached in reality because of the premature breakdown occurring at the device edges. As the depletion layer spreads away from the main pn or Schottky junction, a three-dimensional cylindrical depletion layer forms at the device periphery. This creates increased field crowding at the device edge, as shown

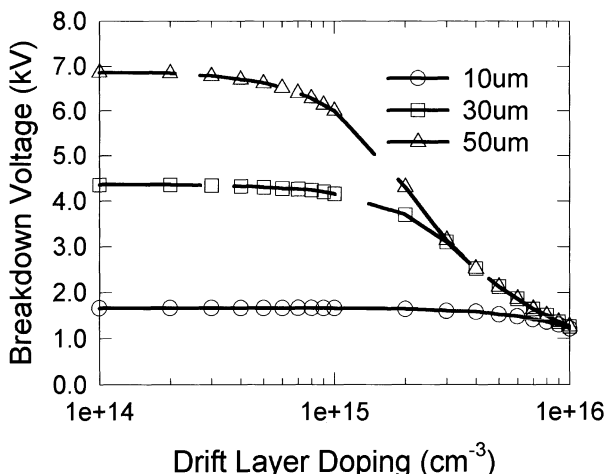


Fig. 10.4. Ideal breakdown voltage of SiC diode as a function of drift layer doping and thickness. A SiC diode with a 50 μm drift layer thickness doped to $1 \times 10^{14} \text{ cm}^{-3}$ should be able to block up to 7000 V. Reprinted from [15] with permission from Elsevier

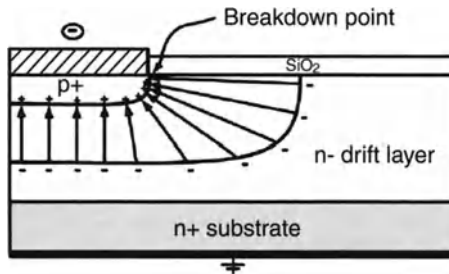


Fig. 10.5. Field crowding due to junction curvature effects at the edge of a pn diode structure under reverse bias

on Fig. 10.5. Compared to Si devices, SiC devices have more deviation from the 1-D ideal breakdown voltage. The small radius of junction curvature to critical depletion region width (x_j/W_{cpl}) ratio results in a significantly enhanced edge field and hence lowers the intrinsic device breakdown voltage to approximately 30% of the ideal value. Specialized edge termination structures must therefore be used to minimize this effect and increase the planar junction breakdown voltages to near ideal values. Effective SiC edge termination is thus critical in order to obtain the maximum breakdown voltage and the corresponding minimum on-resistance.

Edge Termination Techniques

Different types of edge termination commonly used in Si power devices have been investigated for SiC devices, including field plate extensions [10], high resistivity implanted layers [11], Junction Terminal Extentions (JTE) [12,13], and guard rings [14, 15].

Among these termination techniques, field plate techniques (Fig. 10.6) are very sensitive to the condition of SiC/SiO₂ interface and require thick, high quality oxide layers to reduce the high oxide fields. Thus, field plate extensions are generally used only for moderate voltage SiC power devices. High-resistivity implanted layers suffer from large leakage current density even at low reverse bias voltages, due to implant damage in the implanted edges.

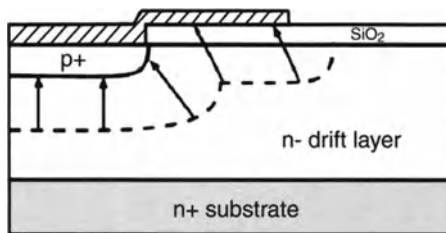


Fig. 10.6. Field plate termination

The JTE technique (Fig. 10.7) is theoretically the most effective termination technique for improving the ideality of SiC power devices, and has received significant recent attention. Unlike most junction-related termination techniques, JTE methods are independent of junction depth, and therefore are highly desirable in SiC devices because of the low dopant diffusivity in SiC. However, JTE structures require precise control on net activated dopant charge, which may greatly vary with the annealing ambient, temperature, and dopant species. The JTE approach also needs additional processing steps in order to form the JTE zones and may increase the reverse leakage due to implantation.

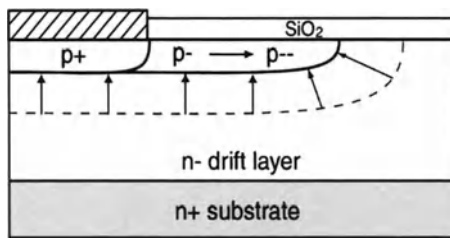


Fig. 10.7. Junction terminal extension

The floating guard ring structure (Fig. 10.8) is quite attractive as an effective means of planar edge termination. Guard ring structures reduce the amount of field crowding at the main junction by spreading the depletion layer through lower potential floating p⁺ rings. Guard rings can be usually formed simultaneously with the main junction or anode contact, thus saving processing steps. The disadvantage of guard ring approach, however, is that the ring width and spacing need to be precisely designed in order to be effective, and hence requiring tedious numerical simulations.

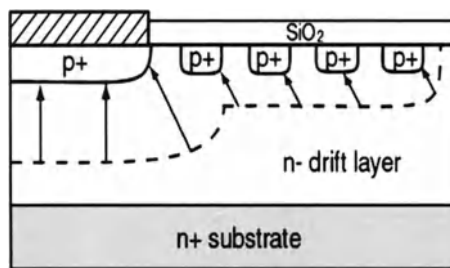


Fig. 10.8. Floating guard ring structure

Guard Ring (GR) Structure Optimization

As mentioned above, although GR structures represent an attractive means of edge termination for SiC power diodes, numerical optimization is required [15]. Here, we illustrate this process using the MEDICI [16] numerical simulator.

To determine the optimum guard ring spacing, the simulations use an iterative process by which a single ring is first optimized, then additional rings are added, and subsequently re-optimized. Figure 10.9 illustrates the dependence of the breakdown voltage on the spacing for a single guard ring. It is obvious from this graph that the exact spacing of the guard rings can have a significant effect on the obtained breakdown voltage. For a single ring, the optimum junction-to-ring spacing in this case is 2.5–3.0 μm . An increase in spacing shifts the peak field to the edge of the main junction, resulting in a lower breakdown voltage, and thus stresses the importance of establishing a robust numerical solution strategy for practical device design. If the spacing is decreased, the peak electric field is maintained at the ring edge, but the electric field shielding of the main junction is diminished and the breakdown voltage is lowered.

Table 10.2 lists the optimized spacing for a 1–4 GR design. When adding more consecutive rings, the simulated optimum spacing of the previous optimized design is no longer valid because of the increased spreading of the depletion layer and the resultant perturbation of the electric field profile. Additional rings added at constant spacing push the peak electric field closer to the main junction, requiring a decrease in the spacing of the innermost rings. The optimized profile corresponds to a 10 μm epitaxial layer with $N_D = 1 \times 10^{15} \text{ cm}^3$, $S_1 = 1.5 \mu\text{m}$, $S_2 = 1.5 \mu\text{m}$, $S_3 = 2.0 \mu\text{m}$, and $S_4 = 2.5 \mu\text{m}$. According to the simulations, a properly designed GR structure can achieve 84% of the ideal

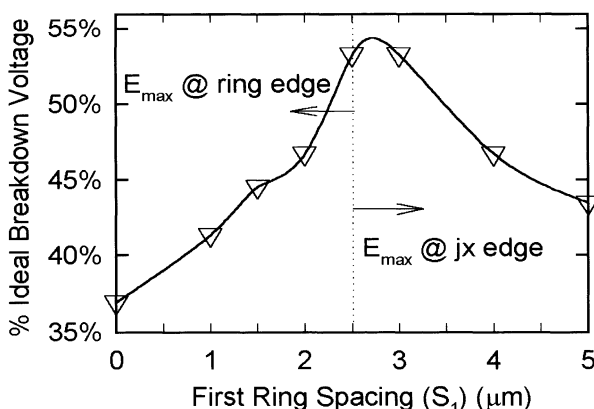


Fig. 10.9. Optimization of the first ring spacing in a guard ring structure. Reprinted from [15] with permission from Elsevier

breakdown voltage. Experimental results reached 76% of the ideal breakdown voltage, validating the optimization methodology described.

Table 10.2. Simulated optimum ring spacing for 4H-SiC diodes with $r_j/W_{\text{CPP}} = 0.05$ and a ring width of 5 μm

Rings	S_1 (μm)	S_2 (μm)	S_3 (μm)	S_4 (μm)	% Ideal	V_{BR}
1	3	—	—	—	52%	
2	2	3	—	—	68%	
3	2	2.5	3	—	74%	
4	1.5	1.5	2	2.5	84%	

10.3 Device Fabrication

10.3.1 Fabrication of SBD/JBS Diodes with Guard Ring Termination

As mentioned above, the JBS diode structure and the guard ring termination can be formed simultaneously using a single ion implantation step. Throughout this chapter, all of the diode results are for guard-ring terminated diodes.

The major fabrication steps for SiC SBD/JBS diodes with guard ring termination investigated in this work include: alignment marks formation, junction formation, oxide passivation formation, and contact formation. Since during the fabrication procedure SiC must experience extremely high processing temperatures ($> 1600^\circ\text{C}$), the deposition of metal as alignment marks cannot hold up under further processing, and thus alignment marks must be formed using RIE trench etching.

The low dopant diffusion capability of SiC makes it impossible to form junctions using traditional solid-state diffusion, and thus ion implantation is the only viable method to form selective n or p-type planar junctions. Because of the high temperatures required for low-damage implants, deep selective area implant masks must be formed using a metal implantation mask that will not chemically react to the underlying SiC layer during implantation. A thick Mo layer was sputter-deposited to perform as an effective mask. Figure 10.10 is a picture of a Mo implant mask for a JBS structure with 7 guard rings. Before implantation, the implantation profile needs to be optimized using TRIM calculations. After high-temperature implantation, annealing of the sample is necessary for activation. To improve the profile, a special technique used during the annealing is to load samples into a SiC annealing chamber consisting of a SiC pillbox on a carbon strip heater, where the sample is completely enclosed with a SiC overpressure to prevent silicon and carbon sublimation during annealing. This approach has drastically increased the

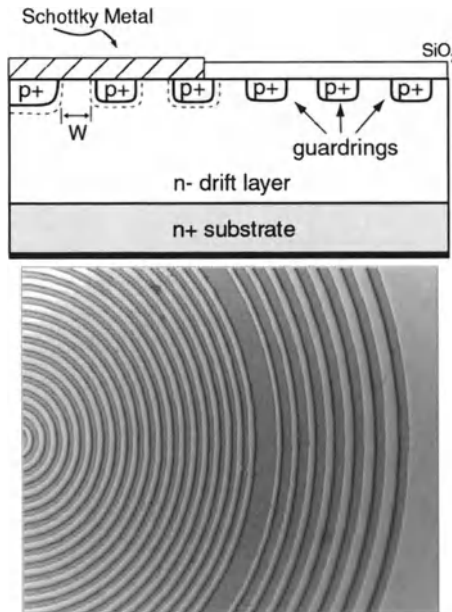


Fig. 10.10. Schematic cross section and top-view photograph of a JBS diode with guard ring structure

quality of the surface morphology compared to a comparable anneal without a SiC overpressure performed on similar samples.

After annealing, the oxide passivation needs to be performed. Three thermal oxidation steps are required to form the thick oxide required for effective device passivation: a thin sacrificial oxide to remove any residual implantation particles and surface damage and its removal; a second thin thermal oxidation layer providing the basis for the following thick passivation layer; and a thick SiO_2 layer formed by deposition of polysilicon subsequent reoxidization. The reason for obtaining SiO_2 by reoxidizing the deposited polysilicon layer is that the oxidation rate of SiC is too low, and direct growth of a thick passivation layer is impractical.

Contact formation involves both a backside n-type ohmic contact and a front-side Schottky contact. For good ohmic contacts, annealing after metal deposition is necessary. Schottky contact can be formed without any annealing. To decrease final contact resistance, Au and Ti overlayers were deposited directly onto the Ni Schottky contact.

10.3.2 Fabrication of SiC MOS Capacitors

The key steps for fabrication of the SiC MOS capacitors investigated in this work include: careful surface cleaning, high quality, thin-layer oxidation, passivation, and contact formation. After cleaning the SiC samples, they were

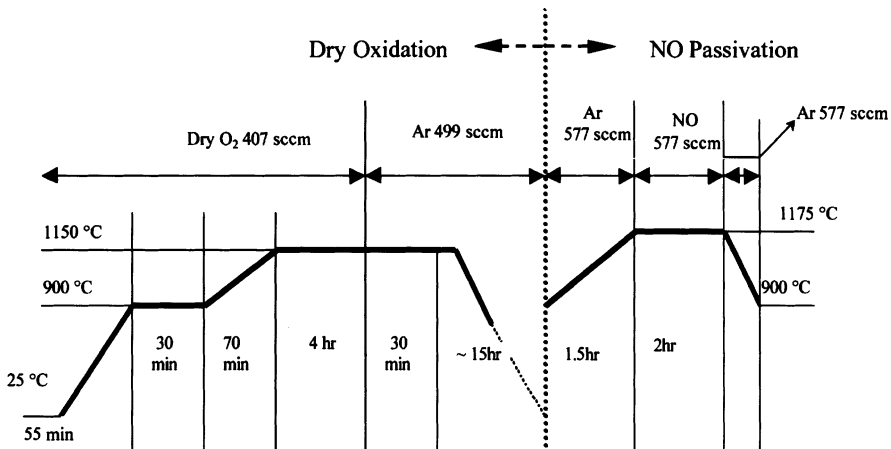


Fig. 10.11. Oxide growth and passivation for SiC MOS structure. Reprinted from [25] with permission from Elsevier

immediately loaded into a double-walled oxidation furnace in an argon atmosphere at room temperature for oxidation. Figure 10.11 shows the details of the oxidation and NO passivation process for the SiC MOS capacitors. As will be seen below, NO passivation was used to obtain a better-quality oxide on SiC (i.e., lower interface state density). The last fabrication step is to deposit the gate contact. Gate metals (100 nm Mo + 100 nm Au) were deposited onto the oxide by conventional sputtering techniques to form the final MOS capacitor structure. All MOS capacitors were circular in shape, with diameters of 70, 200 and 340 μm .

10.4 Radiation Effects in SiC Power Switching Diodes and Capacitors

The fabricated SiC SBD/JBS diodes and MOS capacitors were exposed to different radiation conditions and the effects on their operational characteristics investigated. The SiC die were placed in ceramic DIP chip carriers for radiation exposure. Gamma irradiation was performed at room temperature in a gamma cell 220 ^{60}Co irradiator at the Naval Surface Warfare Center in Crane, IN. Dose rates were approximately 200 rad(Si)/s and were verified using thermo-luminescent dosimeters (TLD). Proton irradiation was performed using 62.5 MeV protons to a total fluence of $5 \times 10^{13} \text{ p/cm}^2$ at the Crocker Nuclear Laboratory Cyclotron Facility at the University of California at Davis. During the irradiation, the device terminals were electrically floating.

10.4.1 SiC SBD Under Gamma Irradiation

Under high dose gamma irradiation, SiC SBD typically show superior radiation hardness [17]. The dc performance of SiC Schottky diodes in a high gamma dose radiation environment demonstrates the exceptional potential for SiC in extreme environment electronics.

To characterize dc performance of the SiC SBDs under gamma irradiation, devices with different Schottky metal contacts were irradiated to doses of up to 4 Mrad (SiC). Afterwards, I - V characteristics were measured but show no evidence of radiation-induced degradation. Figure 10.12 shows typical I - V characteristics of these diodes before and after each radiation dose. Figure 10.13 is the corresponding barrier height for different metal contact extracted from Fig. 10.12. Observe that there is no observable degradation in the I - V characteristics after a total dose of 1 Mrad. The measured Schottky barrier height remains relatively constant for all three Schottky metals at each dose. The maximum standard deviation is only 0.02. The extracted ideality factor for each diode type also remained approximately constant at 1.09, 1.03, and 1.27 for the Ti, Mo and Ni Schottky diodes, respectively.

Reverse leakage current measurements were performed up to 100 V on all diodes and the reverse leakage also remained unaffected by the radiation exposure. The breakdown voltage, however, for each diode type, increased significantly after a total radiation dose of 4 Mrad. As shown in Fig. 10.14, for the Ti SBDs, the breakdown voltage increased an average of 195 V (234 V for the Mo Schottky diodes, and 157 V for the Ni Schottky diodes). During the measurement of the breakdown voltage, it was observed that although the absolute breakdown voltage increased, the post-irradiated diodes suffered from significant breakdown “walk-out” when the applied voltage reached to

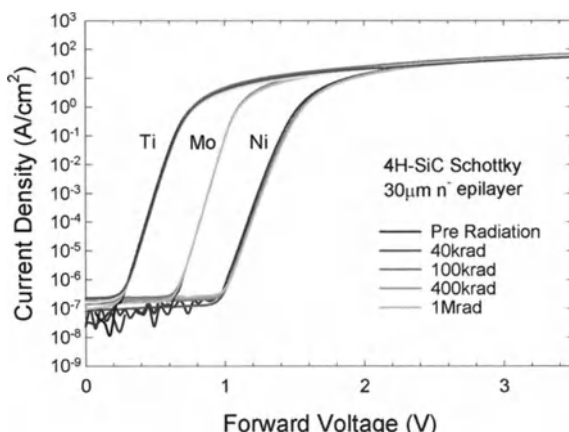


Fig. 10.12. Forward current–voltage characteristics of Schottky diodes before and after gamma irradiation. Reprinted from [17] with permission from IEEE

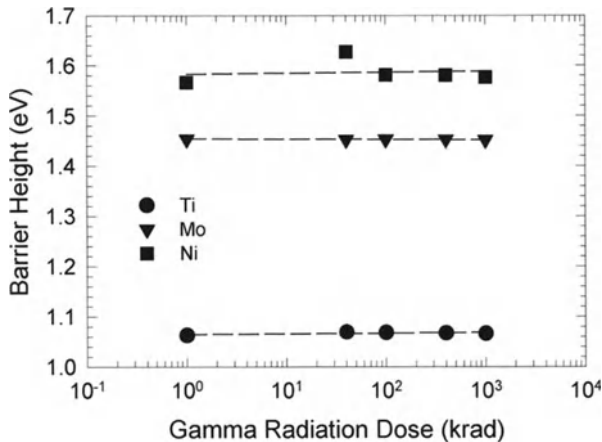


Fig. 10.13. Extracted barrier height as a function of gamma radiation dose. Reprinted from [17] with permission from IEEE

near the initial pre-radiation breakdown voltage. This “walk-out” effect has been previously observed in high-voltage diodes under non-irradiation circumstances and was attributed to excess charge in the surface passivation layer, leading to oxide charging and increased surface fields [18]. To confirm this in SiC, both experimental measurements and simulations on surface charge change is compared and the results explained via the net increase of breakdown voltage after gamma irradiation.

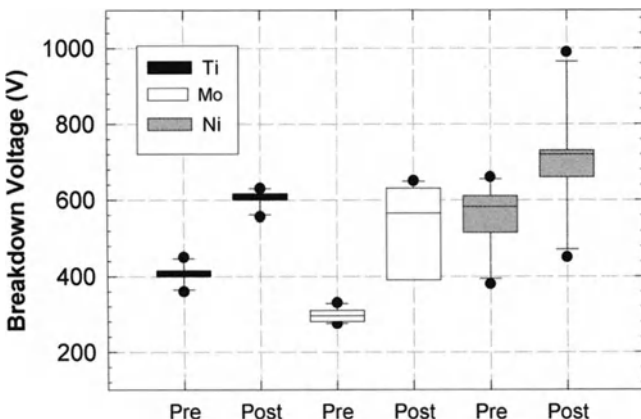


Fig. 10.14. Measured breakdown voltages for three different Schottky metals, before and after 4 Mrad gamma irradiation. Reprinted from [17] with permission from IEEE

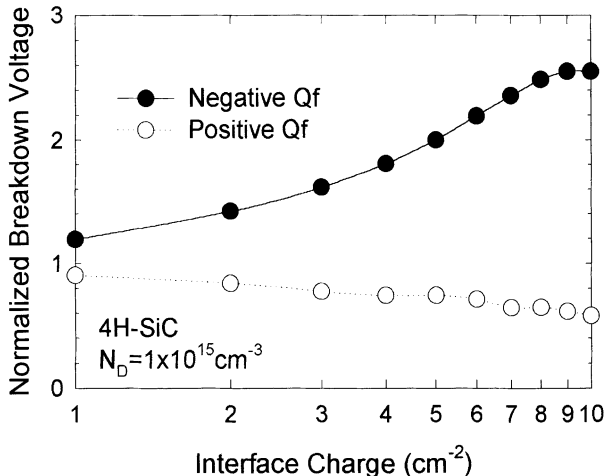


Fig. 10.15. Simulated change in breakdown voltage for both positive and negative interface charge. Reprinted from [17] with permission from IEEE

In high-voltage planar devices, negative surface charge has been shown to increase the depletion layer spreading, thus reducing the field crowding effects at the device edge and improving the breakdown voltage. As will be shown below, the gamma radiation response of MOS capacitors also suggests that gamma radiation introduces negative surface charge (in contrast to Si, which is inevitably positive). Using the MEDICI [16] numerical simulator, the breakdown voltage for the SiC planar diode structure was calculated for both increasing negative and positive surface charge, as shown in Fig. 10.15. The simulated $V_{BR} - Q_{eff}$ relationship supports the fact that negative surface charge enhances the depletion layer's spreading, while positive surface charge restricts the spreading on the other hand. The breakdown voltage was simulated for both pre- and post radiation diodes. In comparison to the measured breakdown data, the simulated breakdown voltage for the pre-radiation diodes with a N_{eff} of $-1.67 \times 10^{12} \text{ cm}^2$ was 840 V, while the post-radiation diodes with a N_{eff} of $-3.26 \times 10^{12} \text{ cm}^2$ was 1040 V (Fig. 10.16). The 200 V increase in breakdown voltage correlates very well with the measured average increase of 195 V. The differences between the simulated and measured breakdown voltage may be attributed to either inexact impact ionization coefficients or significant variation in epitaxial doping concentration used in the simulations.

10.4.2 Gamma Irradiation of SiC MOS Capacitors

Analysis of the drift region resistance indicates that SiC MOSFETs should be able to outperform even bipolar silicon devices at blocking voltages up to 10 kV [19]. The ability of SiC to oxidize and form SiO_2 also in principle

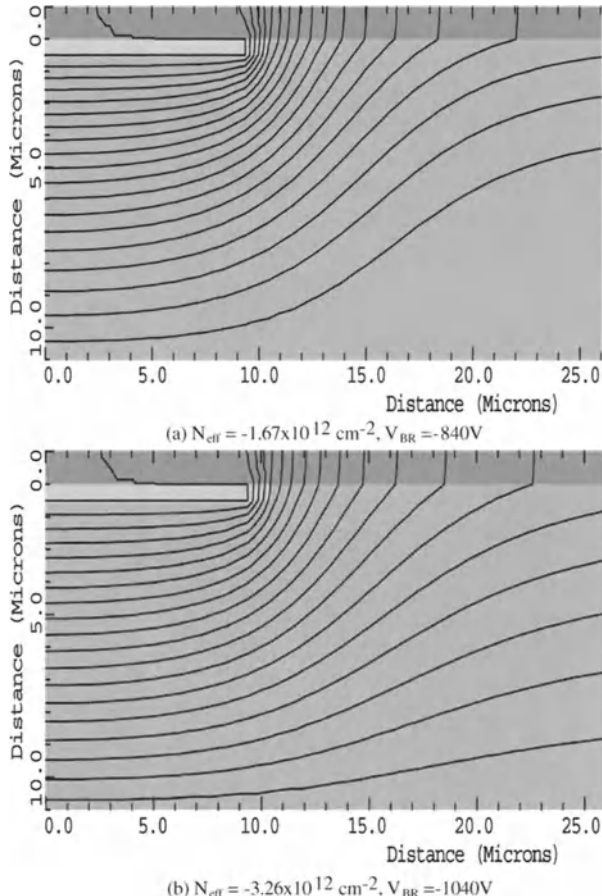


Fig. 10.16. Simulated breakdown voltage for different negative interface charges, corresponding to both the pre- and the post-gamma-radiation condition. A negative increase of interface charge leads to improvement of the field crowding at device edges. (a) corresponds to a pre-radiation diode, $N_{\text{eff}} = -1.67 \times 10^{12} \text{ cm}^{-2}$, $V_{\text{BR}} = -840 \text{ V}$; (b) corresponds to a post-radiation diode, $N_{\text{eff}} = -3.26 \times 10^{12} \text{ cm}^{-2}$, $V_{\text{BR}} = -1040 \text{ V}$

allows compatibility with standard silicon-based fabrication processes, providing a strong motivation for research on SiC-based power MOSFET structures. In this section we address the radiation response of SiC MOS structures. The MOS capacitor has the advantage of simplicity of fabrication and of analysis. Fabrication of the MOS capacitor uses the same processing used in fabricating the integrated circuit. Therefore, the MOS capacitor provides direct measurement and monitoring of the MOS system as it would be applied in the integrated circuit.

By using both high frequency $C-V$ and quasi-static $C-V$ measurements, we can quantitatively analyze the SiC/SiO₂ interface for both pre- and post radiation conditions. These measurements allow one to obtain the interface density (D_{it}) and total effective oxide charge (Q_{eff}), which includes the oxide fixed charge (Q_{fix}), interface charge (Q_{it}), oxide trapped charge (Q_{ox}), and mobile ion charge (Q_{mo}). Since in the case of SiC Q_{eff} is very high (compared to Si), it represents the main component of the measured Q_{eff} .

The effective oxide charge can be calculated as:

$$Q_{eff} = C_{ox}(W_{MS} - V_{FB}) , \quad (10.4)$$

where W_{MS} is the work function difference between the metal and 4H-SiC and V_{FB} is the flat band voltage. Assuming the interface states do not follow the applied high-frequency signal at 100 kHz, the measured $C-V$ characteristics then does not include the effect of interface states. Thus the difference between high-frequency $C-V$ and quasi-static $C-V$ gives the interface state density D_{it} [20]:

$$D_{it} = \frac{1}{q} \left[\left(\frac{1}{C_{QS}} - \frac{1}{C_{ox}} \right)^{-1} - \left(\frac{1}{C_{HF}} - \frac{1}{C_{ox}} \right)^{-1} \right] . \quad (10.5)$$

Typical $C-V$ curves for the n-type SiC MOS and the p-type SiC MOS capacitors before and after a total dose gamma exposure of 4 Mrad are shown in Figs. 10.17 and 10.18, respectively. For the p-type SiC MOS capacitors, the gamma radiation resulted in large negative CV shift, corresponding to a net positive effective charge increase, and the charge increase was calculated to be $5.73 \times 10^{12} \text{ cm}^{-2}$. Conversely, the n-type MOS capacitors exhibited a positive

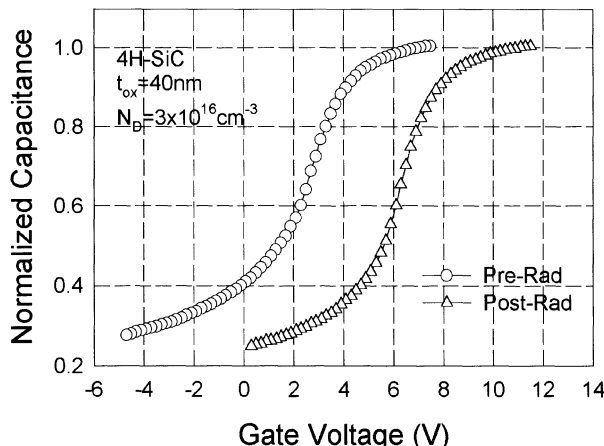


Fig. 10.17. $C-V$ characteristics of n-type 4H-SiC MOS capacitors before and after 4 Mrad gamma irradiation. Reprinted from [17] with permission from IEEE

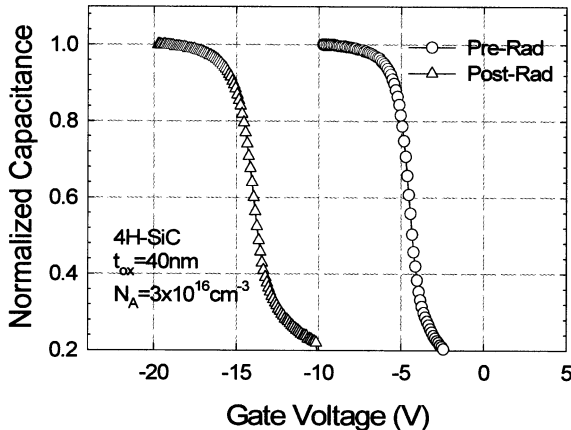


Fig. 10.18. C – V characteristics of p-type 4H-SiC MOS capacitors before and after 4 Mrad gamma irradiation. Reprinted from [17] with permission from IEEE

CV shift and a net negative Q_{eff} increase, from $1.67 \times 10^{12} \text{ cm}^{-2}$ to an average of $3.26 \times 10^{12} \text{ cm}^{-2}$. The interface traps in the upper half of the bandgap are donor like and those in the lower half of the bandgap are acceptor like. Therefore both positive and negative Q_{eff} are possible depending on epitaxial layer doping type [21, 22]. As indicated above, these N_{eff} changes were subsequently applied in our breakdown simulations and theoretically explained the experimental breakdown increase observed in the switching diodes.

It was shown that oxides on n and p-type 4H-SiC degrade differently under high dose gamma irradiation. The results of “Hi-Lo” analysis of the C – V measurements for both n- and p-type MOS capacitors is shown in Fig. 10.19 and Fig. 10.20, respectively. For p-type material, the interface state density decreased slightly away from the valence band edge after irradiation. On the other hand, for the n-type MOS oxide interface, the trap density at $E_C - E = 0.1 \text{ eV}$ slightly increased from $2.05 \times 10^{13} \text{ eV}^{-1} \text{ cm}^{-2}$ to $3.37 \times 10^{13} \text{ eV}^{-1} \text{ cm}^{-2}$.

The increased surface charge observed in the SiC MOS structures after irradiation presents a reliability concern for SiC power devices, and the field-effect mobility could be very low due to high resultant interface state density. Further research on SiC oxide physics and passivation methods are needed to address these issues in order to improve the SiC/SiO₂ interface for SiC power MOSFET applications.

Although SiC MOSFETs are quite attractive in power electronics, the development of SiC MOSFETs has been impeded by the low value of effective carrier mobility typically achieved in the FET channel. The low mobility is directly linked to interface states at the SiO₂/SiC interface that either trap and/or scatter carriers. Obtaining a high-quality oxide with low interface state and oxide trap densities has proven to be challenging because of the resid-

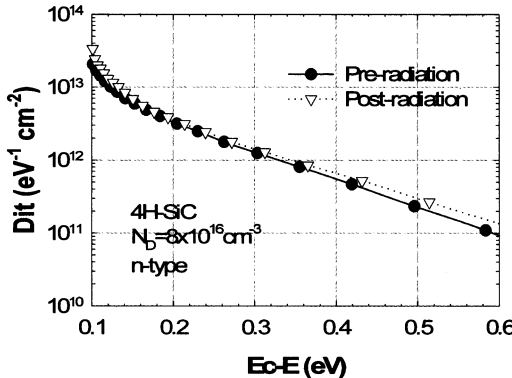


Fig. 10.19. Interface state density of n-type 4H-SiC MOS capacitors before and after 4 Mrad gamma irradiation. Reprinted from [17] with permission from IEEE

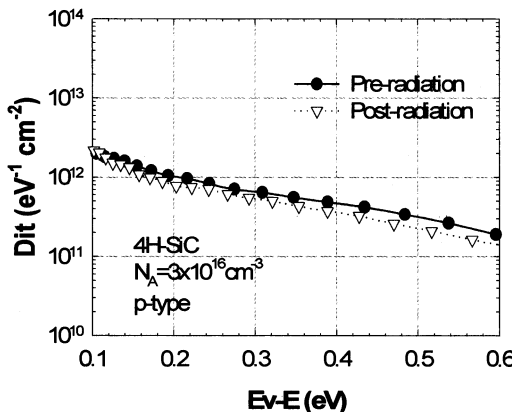


Fig. 10.20. Interface state density of p-type 4H-SiC MOS capacitors before and after 4 Mrad gamma irradiation. Reprinted from [17] with permission from IEEE

ual carbon on the growth interface, as well as off-axis epitaxial layers that have rough surface morphologies [23]. It has been proven that appropriate high-temperature passivation in nitric oxide (NO) significantly decrease interface states and increase the effective channel mobility [24]. The reliability of SiC/SiO₂ interface with NO passivation after gamma irradiation will be discussed in this section [25]. n-type 4H-SiC was used to fabricate the SiC MOS capacitors and Mo was the metal used for contact here.

Figure 10.21 shows typical C-V result for pre-radiation n-type SiC MOS capacitors both with and without NO passivation. Observe that there is a positive flat-band shift for the NO-passivated MOS capacitors, indicating the introduction of negative charge due to NO passivation. The C-V curves for samples without passivation demonstrate more distinct frequency dispersion

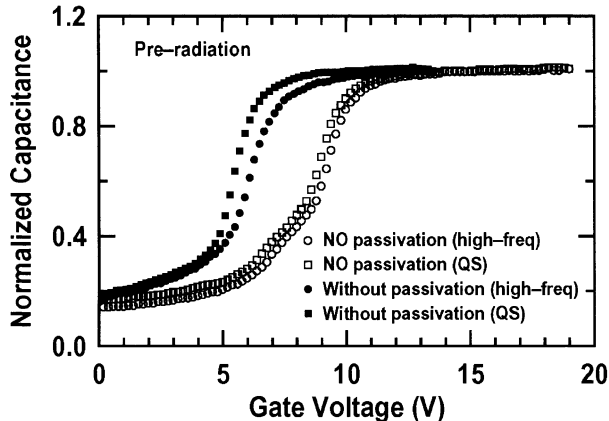


Fig. 10.21. The influence of NO passivation on the C - V characteristics of n-type MOS capacitors. Reprinted from [25] with permission from Elsevier

between high-frequency C - V and quasi-static C - V at the onset of depletion. This behavior is evidence of a higher D_{it} located close to the conduction band edge. Figure 10.22 shows the C - V curves of the NO-passivated 4H-SiC capacitors both before irradiation and after four different gamma doses, and Fig. 10.23 shows the counterpart C - V curves for the 4H-SiC capacitors without passivation. By comparing Figs. 10.22 and 10.23, we see that at fixed dose, the NO passivated samples have a positive flat-band shift compared to those without passivation. This is consistent with the results shown in Fig. 10.21 for the pre-irradiation samples. Both unpassivated and passivated MOS capaci-

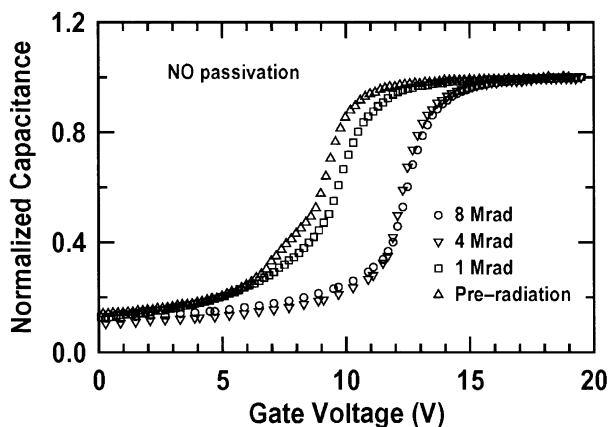


Fig. 10.22. The C - V characteristics of NO-passivated n-type MOS capacitors before and after gamma irradiation. Reprinted from [25] with permission from Elsevier

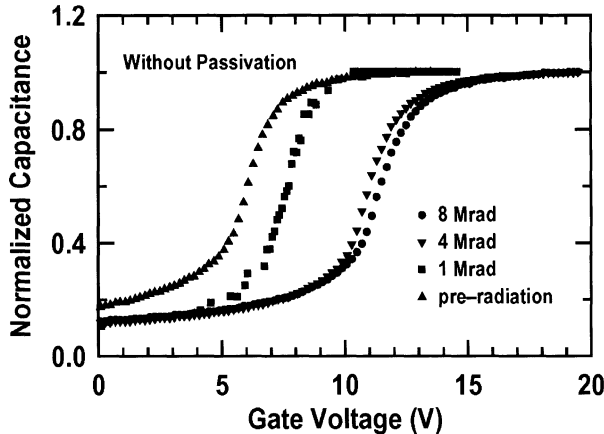


Fig. 10.23. The C - V characteristics of unpassivated n-type MOS capacitors before and after gamma irradiation. Reprinted from [26] with permission from Elsevier

tors show a positive shift of C - V , corresponding to negative interface charge increase.

The calculated effective oxide charge density as a function of radiation dose is shown in Fig. 10.24. The variation of Q_{eff} after irradiation for both NO passivated and unpassivated oxides is similar. Q_{eff} increases slightly when the radiation dose is less than 1 Mrad, and then the increase becomes obvious between 1 Mrad and 4 Mrad doses, indicating faster radiation induced oxide charge generation. However, Q_{eff} achieves a saturation value when the radiation dose is higher than 4 Mrad. It has been suggested that in SiC/SiO₂, two types of charge compensation can result in radiation-hard oxides [25].

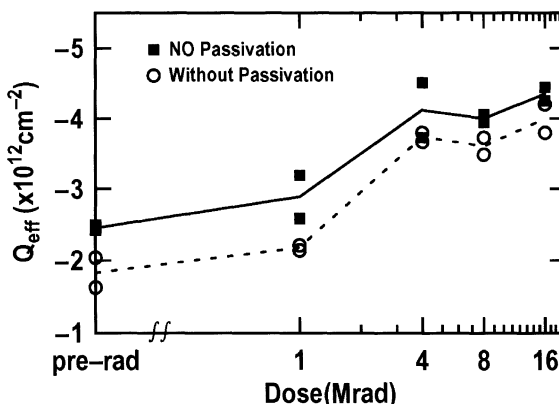


Fig. 10.24. The effective oxide charge as a function of dose for both passivated and unpassivated n-type MOS capacitors

First, negatively charged interface states compensate the radiation-introduced trapped holes. Second, the fixed negative interface charge can compensate the positive oxide charge. In the case of SiC, both forms of compensation may contribute to the saturated oxide charge density at high radiation doses.

The extracted interface state densities for both NO passivated and unpassivated capacitors are summarized in Fig. 10.25 and Fig. 10.26. Figure 10.27 shows the interface state density at fixed energy $E_C - E = 0.2$ eV for various dose. The comparison between Figs. 10.25 and 10.26 confirms that NO passivation produces a significant decrease of D_{it} in oxides on SiC, as widely

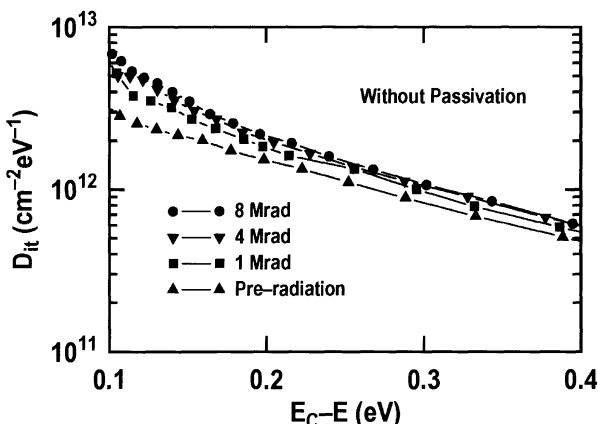


Fig. 10.25. Interface state density for 4H-SiC MOS capacitors without passivation for different gamma radiation doses. Reprinted from [25] with permission from Elsevier

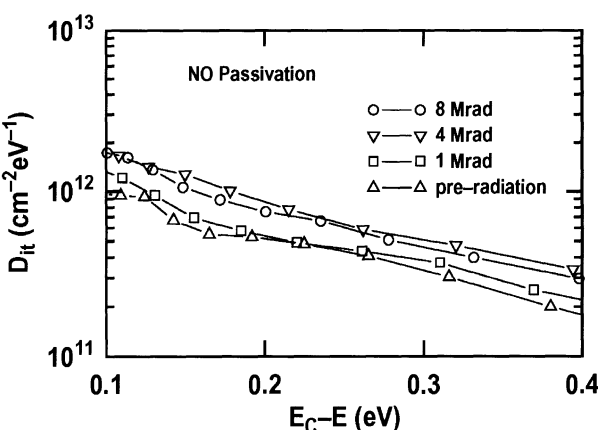


Fig. 10.26. Interface state density for 4H-SiC MOS capacitors with NO passivation for different gamma radiation doses. Reprinted from [25] with permission from Elsevier

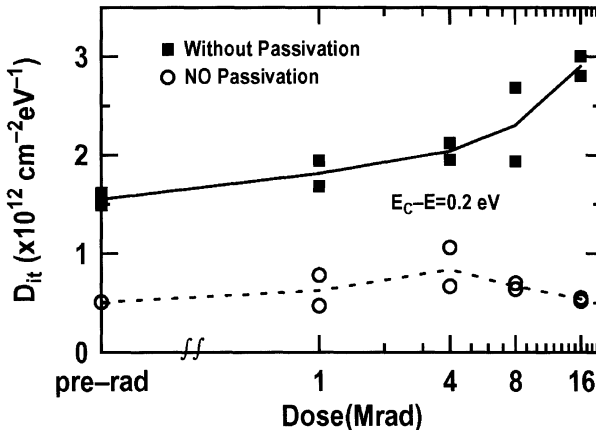


Fig. 10.27. Interface state density as a function of gamma radiation dose for both passivated and unpassivated n-type MOS capacitors. Reprinted from [25] with permission from Elsevier

reported. This also agrees with the relative bigger frequency dispersion of the $C-V$ curve for the pre-radiation sample without passivation. D_{it} of NO passivated MOS capacitors decreases by about 3–4 times at each fixed dose. As shown in Fig. 10.27, D_{it} for both passivated and unpassivated samples increases slightly with gamma dose until 4 Mrad. When the radiation dose is higher than 4 Mrad, D_{it} for unpassivated samples continues to increase, while that for the passivated samples has a very slight change. The physical reason for different D_{it} variation for passivated and unpassivated samples remains unclear. It can be concluded that NO passivation effectively eliminated the

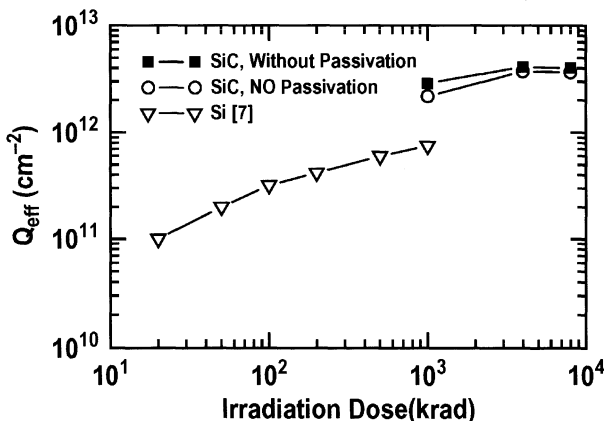


Fig. 10.28. Measured Q_{eff} of both passivated and unpassivated SiO_2/SiC , compared with values for Si SOI technology, as a function of radiation dose. Reprinted from [25] with permission from Elsevier

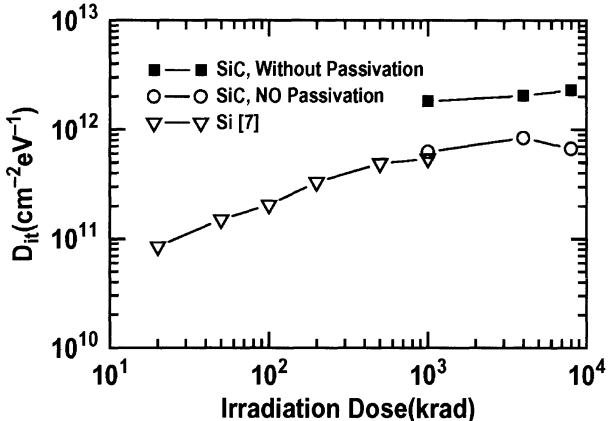


Fig. 10.29. Extracted D_{it} of both passivated and unpassivated SiO_2/SiC , compared with values for Si SOI technology, as a function of radiation dose. Reprinted from [25] with permission from Elsevier

interface states and traps which is radiation-sensitive. This suggests that NO passivation is a good technique for the improvement of SiC MOSFET reliability under gamma irradiation.

For comparison, the radiation dose dependence of the absolute value of Q_{eff} for the present SiO_2/SiC gate oxides and a buried oxide from a Si SOI technology [27] are shown in Fig. 10.28. We can see that while the net total charge in SiO_2/SiC is larger than that of SiO_2/Si , the relative change of Q_{eff} from pre-radiation values is far smaller for SiC. A similar comparison for D_{it} is shown in Fig. 10.29. Observe that at 1 Mrad, the NO-passivated SiO_2/SiC films are comparable to those of the Si SOI technology, and substantially better than for the unpassivated oxides. These results suggest that if adequate passivation techniques can be developed to push D_{it} in SiC down to Si-like levels, a similar radiation tolerance might potentially be expected for SiO_2/SiC interface-based devices.

10.4.3 SiC SBD/JBS Diodes Under Proton Irradiation

In addition to gamma radiation, proton radiation also plays an important role in space power electronics. Proton irradiation has been known as an effective doping method in some materials such as GaAs [28]. The increase of resistance after proton radiation has been reported in diodes made with these materials. Proton and electron irradiation has also been reported to lead to the formation of both donor and acceptor deep centers in 6H-SiC [29]. Here we discuss both the dc and ac response of 4H-SiC SBD/JBS diodes to proton irradiation. In order to have a fair comparison, a commercial Si p-i-n ultra-fast switching diode (UF1007) [30] was also exposed to proton irradiation and compared with the irradiated SiC diodes.

The structures discussed here include SiC SBD with 7 guard rings and different SiC JBS structures with 7 guard rings. All of the diodes are 100 μm diameter, and the width between the junctions in the JBS structures were 3 μm , 4 μm , and 5 μm .

DC Performance Under Proton Irradiation

Unlike after gamma irradiation shown above, the dc characteristics of 4H-SiC SBD/JBS diodes show distinct changes after proton irradiation. Both SiC SBD and JBS diodes show similar a response to proton irradiation. Figure 10.30 shows typical forward DC characteristics of a JBS diode with 3 μm JBS ring spacing and 7 guard rings termination, both before and after $5 \times 10^{13} \text{ p/cm}^2$ proton irradiation. As can be seen, the low-injection region of the J - V curve shows little change after irradiation, suggesting that proton exposure does not degrade the Schottky contact of the device (i.e., the barrier remains unchanged at around 0.94 eV). Using (10.1), the series resistance can also be obtained from J - V curves. The J - V comparison here shows that the series resistance and forward voltage drop dramatically increases at higher currents due to proton-induced series resistance. In the case of the JBS diode shown, the series resistance R_s increases dramatically from 25 Ω (pre-rad) to 12.1 M Ω (post-rad). This result is surprising, given that previous research showed little degradation after gamma radiation, even up to 100 Mrad total dose, and suggests that SiC device behavior depends strongly on the radiation type. Three factors can potentially account for the added resistance after proton irradiation. First, there is an added contact resistance from the metal itself. In order to eliminate potential contact resistance changes, Kelvin contact (force bias on one probe and measure on the other probe) measurements

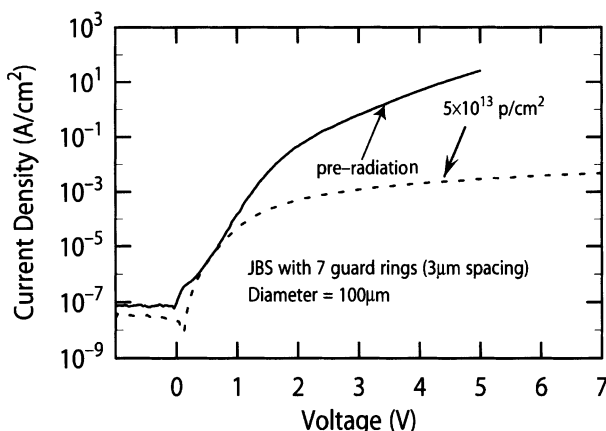


Fig. 10.30. Forward current–voltage characteristics of the seven-guard-ring-terminated 4H-SiC JBS diode, before and after proton exposure

were used to re-measure the J - V characteristics of the JBS diode. The resistance obtained in this case was $R_s = 7.2 \text{ M}\Omega$. A measurement of resistance of the metal itself shows a increase from several to 15Ω for pre-radiation samples to $1.2\text{--}2.2 \text{ k}\Omega$ for post-radiation samples. The relative resistance change of metal suggest that proton exposure has changes the surface chemistry of the metal, which might be similar to the changes on SiGe HBTs due to proton exposure, but it is too small to explain the net resistance change.

The second potential factor for the observed R_s increase could be a decrease in doping level due to displacement effects. Displacement damage can de-ionize dopant impurities and/or introduce traps into SiC, thereby leading to an increase in series resistance from the bulk of the wafer. The effective doping change due to displacement damage can be measured using C - V method. From the C - V measurements on the SBD, we obtained $2\text{--}5 \times 10^{14} \text{ cm}^{-3}$ epieffective doping level, down from a starting value of $1\text{--}2.5 \times 10^{15} \text{ cm}^{-3}$ in the active region of the device (i.e., reverse bias can only probe a finite volume of the wafer). This suggests that proton-induced dopant de-ionization also plays a role in the resistance increase after proton exposure. Another possibility is the radiation-induced change in the carrier mobility, although this is difficult to quantify. A combination of these three factors is believed to lead to the observed dramatic increase of R_s .

Figure 10.31 is the enlarged portion of the J - V characteristics of the same JBS diode from 1.5 V to 2.5 V , comparing it to a standard terminated SBD diode. As we discussed above, both SBD and JBS diodes present similar forward-mode performance, before and after radiation. To show the influence of p^+ region on the radiation response, the forward voltage drop at a fixed current density (10^{-3} A/cm^2 in this case) for different spacings both before and after irradiation is shown in Fig. 10.32. The voltage drop after irradiation is much higher than that before irradiation for different spacings of the JBS

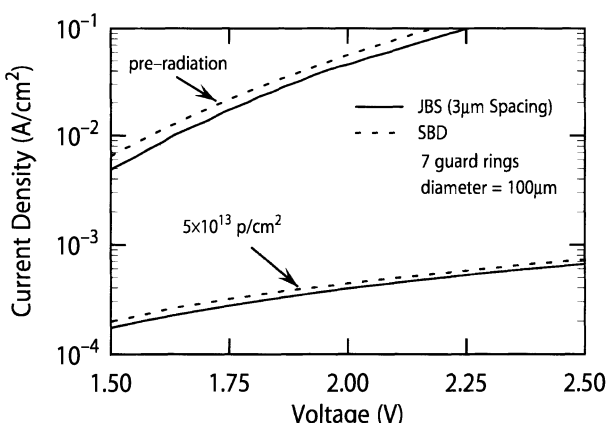


Fig. 10.31. Enlarged J - V characteristics of the seven-guard-ring-terminated 4H-SiC JBS and SBD diodes ($100 \mu\text{m}$ diameter), before and proton exposure

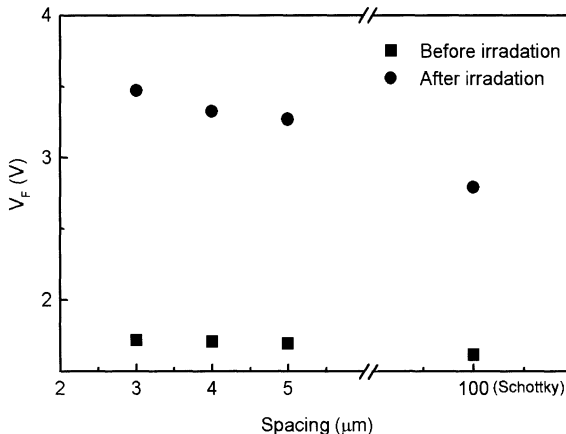


Fig. 10.32. Measured forward voltage drop versus spacing before and after proton irradiation; p^+ width = 5 μm

structure. We also observe a more obvious increase of the forward voltage drop as the spacing decreases for the post-radiation diodes, and is due to the decrease in the effectiveness of JBS structure itself. The effective doping change leads to a decrease of the active area and thus decreases the effectiveness of current collection under forward bias. As discussed above, this is reasonable, because as the effective doping decreases, the depletion region of the p-n structure expands. Thus the effective area of Schottky region is smaller, leading to higher forward voltage drop and a severe serial resistance increase. MEDICI simulations were used to confirm this hypothesis. According to the simulations, the current at high injection shows a decrease of almost 2 orders of magnitude with doping change from 1×10^{15} to $2 \times 10^{14} \text{ cm}^{-3}$ for the JBS structure. For an ideal Schottky diode, however, the decrease is within one order of magnitude. If the SBD is a small diode with guard ring at the edge, the influence of the p^+ guard ring can also cause a dramatic decrease of the current at high injection. Thus, we can conclude that at low doping, the JBS structure is not as effective at improving the forward current-voltage characteristics. Since all of the diodes measured for the proton radiation experiment were of only 100 μm diameter, the influence of the p^+ region to the $I-V$ characteristics of these diodes cannot be neglected.

For comparison to these SiC $J-V$ results, Fig. 10.33 shows the $I-V$ characteristics of the commercial Si p-i-n diode (area and type of termination structure are unknown). Interestingly, a significant series resistance increase after proton exposure is also observed, which is presumably also due to dopant de-ionization. On the other hand, the Si p-i-n diode shows a very strong degradation in the low-bias region, consistent with the expected radiation-induced G/R center production and lifetime changes in the device epi region.

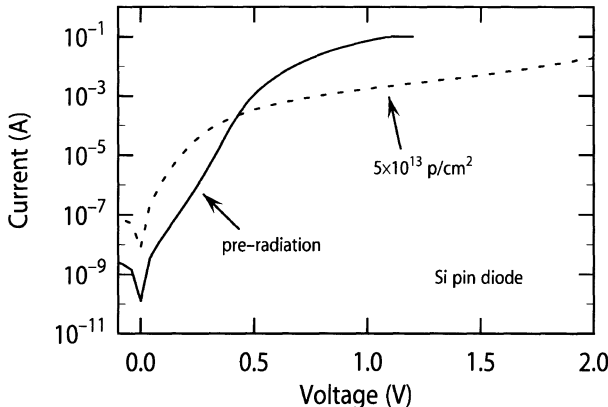


Fig. 10.33. Forward current–voltage characteristics of the Si p–i–n diode before and after proton exposure

At low reverse voltage, the reverse current of the SiC diodes decreased after radiation, as shown in Fig. 10.34, which is opposite to the expected degradation observed in the Si diode (Fig. 10.35). The reverse current density of the SiC diodes decreases from 1.6×10^{-7} A/cm² to 7×10^{-8} A/cm² at 10 V. For the Si diodes, on the other hand, the current dramatically increases from 6.8×10^{-9} A to 1.4×10^{-7} A at 10 V, consistent with radiation-induced G/R center production and hence lifetime reduction. For the SiC, this result is actually consistent with an earlier report using EBIC which indicated that electron irradiation could have a pronounced annealing effect on carrier lifetime in 6H-SiC epi [31], although this has not been observed before using protons. Low effective doping level due to proton irradiation also could also

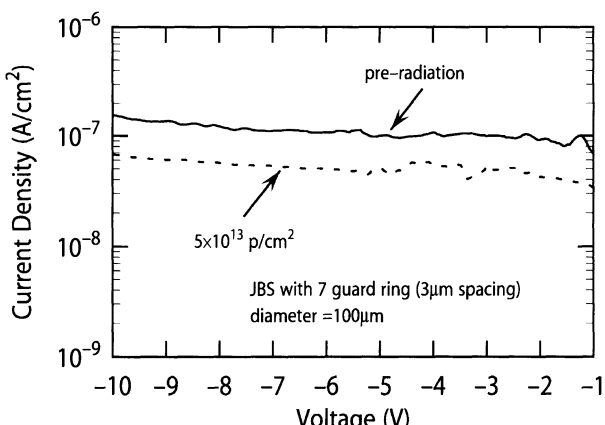


Fig. 10.34. Reverse current–voltage characteristics of the terminated 4H-SiC JBS diode before and after proton exposure

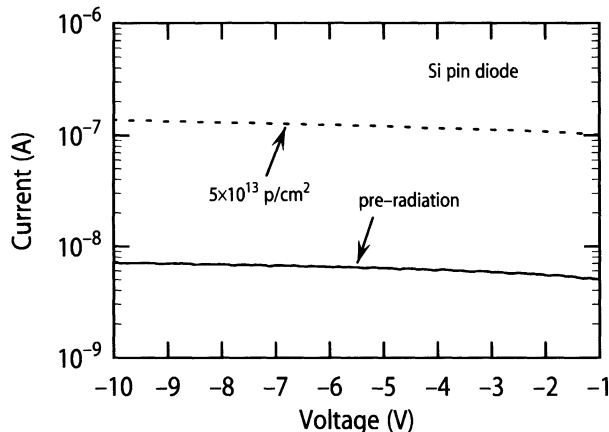


Fig. 10.35. Reverse current–voltage characteristics of the Si p–i–n diode before and after proton exposure

influence the reverse current at low reverse voltage in that the JBS diode has wider depletion area in the junction at the same voltage, which means smaller Schottky area. This is important especially at low reverse voltage, given that Schottky area could still contributes leakage current at low reverse voltage.

The breakdown voltage actually increases in these SiC JBS diodes after proton exposure, showing a similar trend to SiC diodes after gamma exposure. For the Si p–i–n diode, however, the breakdown voltage has no obvious change with irradiation and remains around 1300 V. Figure 10.36 shows the radiation-induced change in breakdown voltage as a function of number of guard rings used in the termination structure in SiC diodes. A significant im-

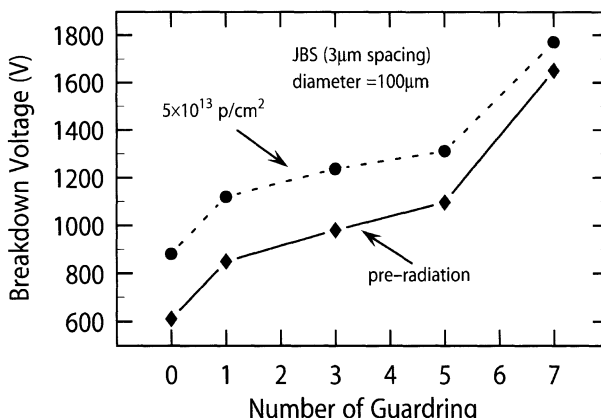


Fig. 10.36. Comparison of measured breakdown voltage of the JBS diode before and after irradiation as a function of the number of guard rings used in the edge termination

provement can be observed in Fig. 10.36 (the average increase in breakdown voltage is 220 V). Clearly, the effect is not strongly dependent on the number of rings, although a gradual saturating trend at higher number of guard ring is observed. A peak blocking voltage got here is 1780 V after $5 \times 10^{13} \text{ p/cm}^2$ proton exposure.

As shown above, a similar breakdown voltage increase in unterminated SiC SBD diodes after gamma radiation was observed and was later attributed that to an increase of negative surface charge in the SiO_2/SiC passivation layer. Given the similar observed trends to the blocking voltage, a similar explanation is plausible here, even though the radiation type is different. In addition, the dopant de-ionization which caused series resistance increase would also improve the breakdown voltage, and thus it is likely that a combination of both effects is operative here. Using calibrated MEDICI simulations [16], the breakdown voltage for the planar diode structure was calculated for both surface charge changes as well as doping level changes. The simulation results suggest that a doping change from $1 \times 10^{15} \text{ cm}^{-3}$ to $5 \times 10^{14} \text{ cm}^{-3}$ would cause a 200 V breakdown increase, while a negative charge change increase from $-1.67 \times 10^{-12} \text{ cm}^{-2}$ to $-3.24 \times 10^{-12} \text{ cm}^{-2}$ would cause a similar increase. Further experiments involving proton exposure of MOS capacitors will be needed to understand exactly how the SiC/Si_2 interface responds to proton irradiation.

AC Performance Under Proton Irradiation

A SiC device with 1/10th the blocking layer thickness and 10 times the doping concentration of a comparable Si device ideally should yield the same blocking ability as a Si device. This should not only improve the specific on-resistance (i.e., reduce the losses), but also improves the switching speed of SiC devices. We have made measurements of the reverse recovery behavior of both irradiated SiC and Si diodes. The circuit for measuring the reverse recovery current of a power diode is shown in Fig. 10.37. In this test circuit, the device under test (DUT) is connected as a freewheeling diode in parallel with an inductive load. When the gate pulse falls, the drain voltage rises and the stored inductor current must dissipate through the freewheeling DUT for a time t_{off} . Since switched mode power supplies are generally used in a continuous mode, the t_{off} is not long enough for all the inductor current to be dissipated. Hence, the MOSFET begins to turn on at the end of falling edge of t_{off} , and the DUT must change from a fully on-state to a blocking mode in order to support the on state voltage of the drain. It is in this short time frame that the significant portion of the reverse losses due to the reverse recovery currents occur. The di/dt for the DUT is controlled by the inductive load. All of the comparisons here were made at $I_F = 0.5 \text{ A}$ and $di/dt = 12$.

SiC JBS diodes have a negligible reverse recovery current compare to Si p-i-n diode, greatly improving their losses for high-power switching circuits (Fig. 10.38). Graphs in Figs. 10.38–10.40 were printouts from oscilloscope.

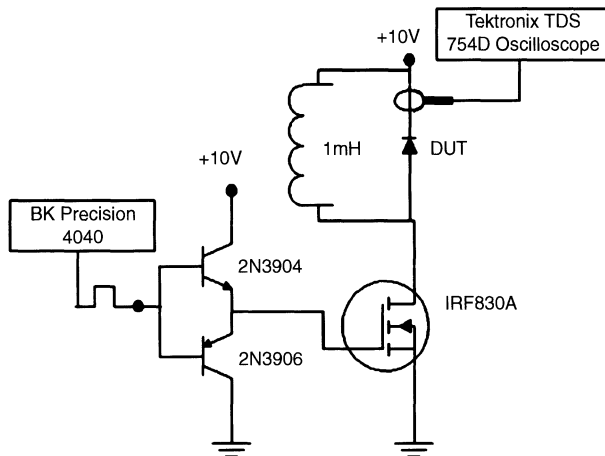


Fig. 10.37. Schematic of the test circuit used in the reverse-recovery-transient measurements

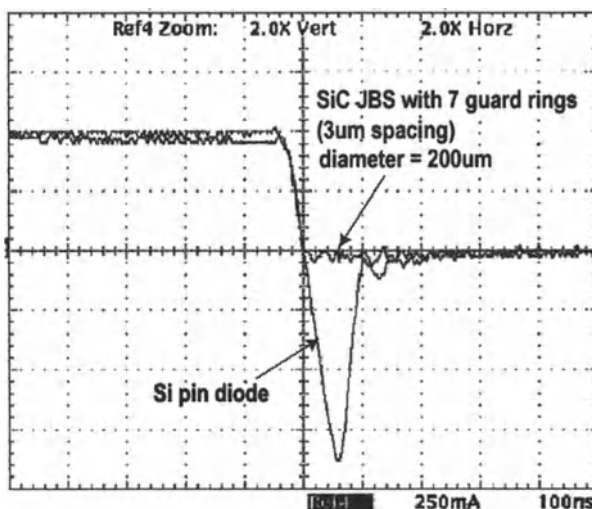


Fig. 10.38. Reverse recovery transient waveforms, comparing the SiC JBS and Si p-i-n diodes, *x*-axis for time in 100 ns/unit and *y*-axis for current in 250 mA/unit

x-axis denotes the time with 100 ns per unit and *y*-axis does the current with 250 mA per unit (units are divided by dashed lines in the figures). In the Si p-i-n structure, charge storage is far more important than junction capacitance. The observed reverse recovery current is primarily due to minority carrier storage (determined by the carrier lifetime). The JBS diode, however, is a majority carrier device (like the SBD), and hence has negligible carrier storage and is dominated by junction capacitance only under high-injection

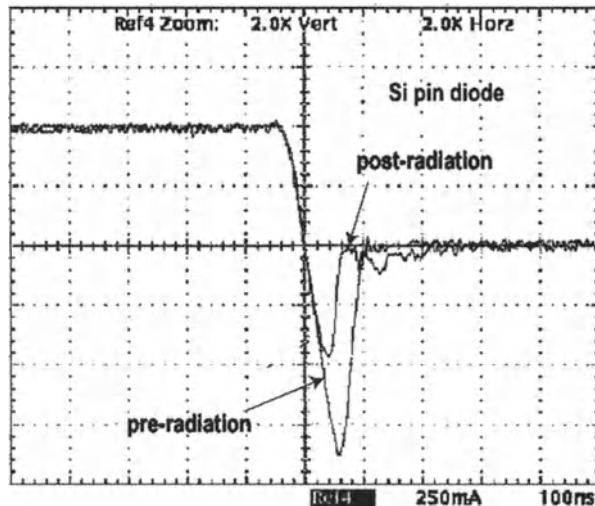


Fig. 10.39. Reverse recovery transient waveforms, comparing the pre- and post-irradiated Si p-i-n diodes, x -axis for time in 100 ns/unit and y -axis for current in 250 mA/unit

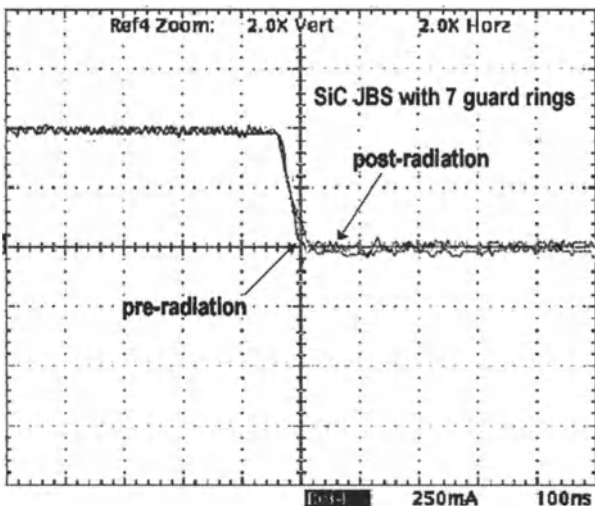


Fig. 10.40. Reverse recovery transient waveforms, comparing the pre- and post-irradiated SiC JBS diodes, x -axis for time in 100 ns/unit and y -axis for current in 250 mA/unit

currents. The reverse recovery current in the Si diode is huge in comparison to that of the SiC diode. As shown in Fig. 10.38 for pre-irradiation, the Si p-i-n diode has a reverse recovery current peak ($I_{rr,max}$) of 930 mA and reverse recovery time (t_{rr}) of 101 ns, while for the SiC JBS diode, $I_{rr,max}$ is only 62 mA and with a t_{rr} of 38 ns.

After irradiation, the Si p-i-n diode yields a significantly decreased reverse recovery current, as shown in Fig. 10.39. Both $I_{rr,max}$ and t_{rr} dramatically decrease from 930 mA and 101 ns to 480 mA and 69 ns, respectively. This indicates that the minority lifetime strongly decreases after proton exposure, consistent with the reverse leakage current observations. However, there is little change after irradiation for the SiC diodes, although a trend of increased $I_{rr,max}$ and t_{rr} with proton exposure was observed. For the particular terminated SiC JBS diode shown in Fig. 10.40, $I_{rr,max}$ remains the same at 62 mA while t_{rr} increased from 38 ns to 44 ns after proton exposure. Since the current storage is so small, to accurately compare the reverse recovery current for pre- and post-radiation condition, it is necessary to perform the measurement at higher blocking voltage and di/dt . Clearly, however, JBS diodes do exhibit attractive power switching performance even after high-fluence proton irradiation.

10.5 Summary

4H-SiC JBS/SBD diodes are attractive candidates for power-switching applications, and their behavior under radiation exposure has been investigated. Unterminated SiC JBS/SBDs exhibit significant tolerance to gamma radiation exposure. The $I-V$ characteristics remain almost unchanged, and the breakdown voltage increases; this is ascribed to changes in SiC/SiO₂ interface. Investigation of SiC MOS capacitors confirmed this effect. NO passivation was also shown to effectively improve the SiC/SiO₂ interface, and the interface charge density reaches a level comparable to that obtained with Si SOI technology even after gamma irradiation.

After proton radiation, the DC performance of SiC JBS/SBDs shows a drastic increase in the series resistance, which is due to the combination of an increase in the contact resistance, displacement-damage-induced dopant deionization, and a change of the mobility in the device. In comparison with a Si control diode, the low-voltage reverse current decreased after radiation, surprisingly. Similar breakdown voltage increases to those obtained with gamma exposure were observed, and are presumably due to the same mechanism. Finally, the AC performance after proton irradiation shows superior radiation hardness for SiC switching diodes. We conclude that SiC power devices hold much promise for power-switching systems operating in a radiation environment.

Acknowledgments

The authors are grateful to C. Ellis, J.R. Williams, S. Clark, R. Reed, P. Marshall, G. Niu, and H. Brandhorst for their contributions to this work, and the Auburn University CSPAE, NASA-GSFC, DTRA, and Navy Crane for their support.

References

1. B.J. Baliga, *Power Semiconductor Devices*, Boston: PWS Publishing Co., 1995.
2. S. Seshadri, R. Dulloo, F. Ruddy, J. Seidel, and L. Rowland, "Demonstration of an SiC neutron detector for high-radiation environments", IEEE Trans. Electron Devices **46**, 567–571, 1999.
3. J. McGarrity, F. Mclean, W. Delancey, J. Palmour, C. Carter, J. Edmond, and R. Oakley, "Silicon carbide JFET radiation response", IEEE Trans. Nucl. Sci. **39**, 1974–1981, 1992.
4. T. Ohshima, M. Yoshikawa, H. Itoh, Y. Aoki, and I. Nashiyama, "gamma-Ray irradiation effects on 6H-SiC MOSFET", Mater. Sci. Eng. B **61–62**, 480–484, 1999.
5. David C. Sheridan, *Ph. D thesis*, Electrical and Computer Engineering Department, Auburn University, 2000.
6. E.H. Rhoderick, R.H. Williams, "Metal-semiconductor contacts", Oxford University Press, New York 1988.
7. E.G. Stassinopoulos and J.P. Raymond, "The space radiation environment for electronics", Proc. IEEE **76**, 1423–1442, 1988.
8. E.A. Gutierrez, D.M.J. Deen, and C.L. Claeys, "Low Temperature Electronics", Chap. 4, Academic Press, San Diego 2001.
9. K.J. Schoen, J.M. Woodall, J.A. Cooper Jr., and M.R. Melloch, "Design considerations and experimental analysis of high-voltage SiC Schottky barrier rectifiers", IEEE Trans. Electron Dev. **45**, 1595–1604, 1998.
10. Q. Wahab, T. Kimoto, A. Ellison, C. Hallin, M. Tuominen, R. Yakimova, A. Henry, J.P. Bergman, and E. Janzen, "A 3 kV Schottky barrier diode in 4H-SiC", Appl. Phys. Lett. **72**, 445–447, 1998.
11. D. Alok, B.J. Baliga, "SiC device edge termination using finite area argon implantation", IEEE Trans. Electron Dev. **44**, 1013–1017, 1997.
12. S. Ortolland, M.L. Locatelli, D. Planson, J.P. Chante, and A. Senes, "Comparison between aluminum and boron-doped junction termination extensions for high voltage 6H-SiC planar bipolar diodes", Mater. Sci. Forum **264–268**, 1045–1048, 1998.
13. D. Peters, R. Schorner, K.H. Holzlein, and P. Friedrichs, "Planar aluminum-implanted 1400 V 4H-silicon carbide p–n diodes with low on resistance", Appl. Phys. Lett. **71**, 2996–2997, 1997.
14. M.S. Adler, V.A.K. Temple, A.P. Ferro, R.C. Rustay, "Theory and breakdown voltage for planar devices with a single field limiting ring", IEEE Trans. Electron Dev. **24**, 107–113, 1977.
15. D.C. Sheridan, G. Niu, J.N. Merrett, J.D. Cressler, C. Ellis, and C.-C. Tin, "Design and fabrication of planar guard ring termination for high-voltage SiC diodes", Solid State Electron. **44**, 1367–1372, 2000.

16. *MEDICI 2-D semi. device simulator, Avant! Corp., Palo Alto, CA*, 1999.
17. D.C. Sheridan, G. Chung, S. Clark, and J.D. Cressler, “The effects of high-dose gamma irradiation on high-voltage 4H-SiC Schottky diodes and the SiC–SiO₂ interface”, *IEEE Trans. Nucl. Sci.* **48**, 2229–2232, 2001.
18. R. Stengl and E. Falck, “Surface breakdown and stability of high-voltage planar junctions”, *IEEE Trans. Electron Dev.* **38**, 2181–2188, 1991.
19. B.J. Baliga, “High voltage silicon carbide devices.” *Mater. Res. Soc. Symp. Proc. 512, Wide-Bandgap Semiconductors for High Power, High Frequency and High Temperature*, eds. S. DenBaars, J. Palmour, M. Shur, and M. Spencer, 77–89, 1998.
20. D.K. Schroder, *Semiconductor Material and Device Characterization*. London: Wiley, 1998.
21. H. Yano, T. Kimoto, H. Matsunami, M. Bassler, and G. Pensl, “MOSFET performance of 4H-, 6H-, and 15R-SiC processed by dry and wet oxidation”, *Mater. Sci. Forum* **338–342**, 1109–1112, 2000.
22. H.F. Li, S. Dimitrijev, D. Sweatman, and H.B. Harrison, “Effect of NO annealing conditions on electrical characteristics of n-type 4H-SiC MOS capacitors”, *J. Electron. Mater.* **29**, 1027, 2000.
23. G.Y. Chung, C.C. Tin, J.R. Williams, K. McDonald, M. Di Ventra, S.T. Pantelides, “Effect of nitric oxide annealing on the interface trap densities near the band edges in the 4H polytype of silicon carbide”, *Appl. Phys. Lett.* **76**, 1713–1715, 2000.
24. G.Y. Chung, C.C. Tin, J.R. Williams, K. McDonald, P.K. Chanana, R.A. Weller, S.T. Pantelides, L.C. Feldman, O.W. Holland, M.K. Das, and J.W. Palmour, “Improved inversion channel mobility for 4H-SiC MOSFETs following high temperature anneals in nitric oxide”, *IEEE Electron Dev. Lett.* **22**, 176–178, 2001.
25. T.B. Chen, Z.Y. Luo, J.D. Cressler, T.F. Isaacs-Smith, J.R. Williams, G.Y. Chung, and S. Clark, “The effects of NO passivation on the radiation response of SiO₂/4H-SiC MOS capacitors”, *Solid State Electron.* **46**, 2231–2235, 2002.
26. Z. Shaneld, G.A. Brown, A.G. Revesz, H.L. Hughes, “A new MOS radiation-induced charge: negative fixed interface charge”, *IEEE Trans. Nucl. Sci.* **39**, 303–307, 1992.
27. F.T. Brady, J.T. Chu, S.S. Li, and W. Krull, “A study of the effects of processing on the response of implanted buried oxides to total dose irradiation”, *IEEE Trans. Nucl. Sci.* **37**, 1995–2000, 1990.
28. D.C. Look and J.R. Sizelove, “Defect production in electron-irradiated n-type GaAs”, *J. Appl. Phys.* **62**, 3660–3664, 1987.
29. A.M. Strel’chuk, A.A. Lebedev, V.V. Kozlovski, N.S. Savkina, D.V. Davydov, V.V. Solov’ev, and M.G. Rastegaeva, “Doping of 6H-SiC pn structures by proton irradiation”, *Nucl. Instrum. Methods B* **147**, 74–78, 1998.
30. <http://www.diodes.com/datasheets/ds25002.pdf>
31. W.A. Doolittle, A. Rohatgi, R. Ahrenkiel, D. Levi, G. Augustine, and R.H. Hopkins, “Understanding the role of defects in limiting the minority carrier lifetime in SiC”, *Mater. Res. Soc. Symp. Proc. 483, Power Semiconductor Materials and Devices*, eds. S.J. Pearton, R.J. Shul, E. Wolfgang, F. Ren, S. Tenconi, 197–202 (1997).

SiC Nuclear-Radiation Detectors

N.B. Strokan, A.M. Ivanov, and A.A. Lebedev

The properties and perfection of SiC films are related to aspects of their application in various kinds of devices. In particular, interest in using SiC as a detection medium in the registration and spectrometry of nuclear radiation is reviving.

At present, intensive investigations of the parameters of the transport of nonequilibrium charge carriers in SiC films are being carried out. Diode and transistor-type detector structures have been successfully tested in physical and technological applications. High radiation and chemical hardness of the detectors have been demonstrated.

11.1 Introduction

Strictly speaking, SiC-based semiconductor detectors of various kinds of nuclear radiation cannot be called devices of a new type. Indeed, even in the first attempts to replace the gas in ionization chambers with a more condensed semiconducting medium, made in the 1960s, SiC-based detectors occupied a prominent place [1–3]. However, SiC lagged noticeably behind the “competing” materials in the dynamics of its improvement in those years.

On the one hand, high-perfection crystals of monatomic Ge and Si were created and the technology of compensation of the residual acceptor conductivity with a donor impurity of lithium was developed. On the other hand, materials with large atomic numbers were obtained (the compounds HgI_2 and $CdTe$, and $CdZnTe$ solid solutions). These ways proved to be more effective for the spectrometry and detection of nuclear radiation. Various designs of silicon detectors (including detectors with multiple elements) were developed to the greatest extent by taking advantage of planar technology. As a result, the interest in silicon carbide was temporarily diminished.

Among the studies of SiC that were carried out in the 1970s, mention should be made of the successful introduction of the acceptor impurity beryllium into n-type crystals [4–6]. Detectors with beryllium-compensated conduc-

tivity successfully operated as neutron and fission-fragment counters directly in a reactor channel, with their working capacity retained up to 600 °C.

In recent years, the interest in silicon carbide as a material for detectors has been revived to a noticeable extent, and we make an attempt to describe the present state of affairs in what follows.

11.2 Detector Material Properties

Semiconductor detectors of nuclear radiation are, as a rule, fabricated in the form of reverse-biased p⁺-n (or n⁺-p) or p⁺-i-n⁺ diode structures. The space-charge region (SCR) serves as the working volume, and the p⁺ and n⁺ regions act as electrodes. Decelerating nuclear particles (quanta) create ionization in the semiconductor, producing tracks formed by nonequilibrium electron–hole pairs. Separation of charge carriers in the electric field of the SCR and their subsequent drift toward the electrodes give rise to a current pulse in the recording circuit, as in the case of an ionization chamber. The amount of charge created is strictly related to the particle energy. Therefore, in the case of complete charge transport to the electrodes, the charge is a measure of this energy.

To successfully implement the above mechanism, the starting material used to fabricate detectors must possess a certain combination of properties. These are the following: a low impurity concentration (resulting in an extended SCR); bipolar conduction (the absence of charge accumulation, which would distort the electric field); a large carrier drift length (carrier transport with high charge collection efficiency (CCE)); a wide bandgap, ensuring weak thermal generation of carriers (low noise); and the possibility of fabrication of high-voltage diode structures. Since the tracks occupy only a minor part of the detector volume, a high local uniformity of carrier transport conditions is necessary for the pulses to be identical.

As regards modern SiC, the above set of requirements is met rather satisfactorily. The standard level of the impurity concentration in lightly doped epitaxial layers is 5×10^{14} – 10^{15} cm⁻³. This gives SCR = 30 μm at a voltage of 500 V. The lifetimes, on the order of hundreds of nanoseconds for the less mobile holes, combined with the high value of the saturation drift velocity, ensure a CCE of nearly 100%. The radiation hardness and chemical stability of SiC, and also the possibility of device operation at temperatures of hundreds of degrees Centigrade are particularly attractive.

It may be concluded that the recent advances in the control of the properties of silicon carbide make it possible to commence the designing of detectors and to perform tests in relation to the detection and spectrometry of various kinds of nuclear radiation.

In turn, a study of the “counting” and electrical characteristics of detector structures can determine the parameters of SiC governing the structural perfection of the material. Among the techniques employed for studying

the electrical characteristics, mention should be made of the well-developed deep-level transient spectroscopy (DLTS) and electron-beam-induced current (EBIC) techniques.

11.3 Detection of Short-Range Particles

11.3.1 Measurement of SiC Detectors

Most studies analyzing silicon carbide as a detection medium have been done on 4H- or 6H-SiC epitaxial films with a net doping concentration of $\sim 10^{15} \text{ cm}^{-3}$. The film thickness was about $10 \mu\text{m}$, i.e. was comparable to the deceleration length of short-range ions. Single-crystal SiC wafers $\sim 300 \mu\text{m}$ thick, doped to a level of $(3.0 - 6.0) \times 10^{18} \text{ cm}^{-3}$, served as substrates. The rectifying contact was, as a rule, fabricated as a Schottky barrier by magnetron sputtering of Ni [7] or by deposition of a thin, 1000 \AA thick film of gold [8]. A schematic diagram of the diode is shown for this case in Fig. 11.1 [8].

It is convenient to use, as a heavily ionizing radiation, alpha particles produced in the natural decay of ^{241}Am , with an energy of 5.48 MeV and a range of $18 \mu\text{m}$ in SiC. The nonequilibrium charge induced by the alpha particles was recorded with the use of standard spectrometric equipment, including a charge-sensitive preamplifier, amplifier-shaper, precision pulse generator, and multichannel analyzer calibrated using a precision silicon detector. The shape, average amplitude, and full width at half maximum (FWHM) of the spectra were determined in the studies.

A typical dependence of the average signal amplitude on the detector bias is shown in Fig. 11.2 for a $10 \mu\text{m}$ thick film [9]. Here, alpha particles with a range of $\sim 20 \mu\text{m}$, produced by a ^{244}Cm source, were used, i.e. the particles penetrated the film and the ionization corresponded to a virtually linear

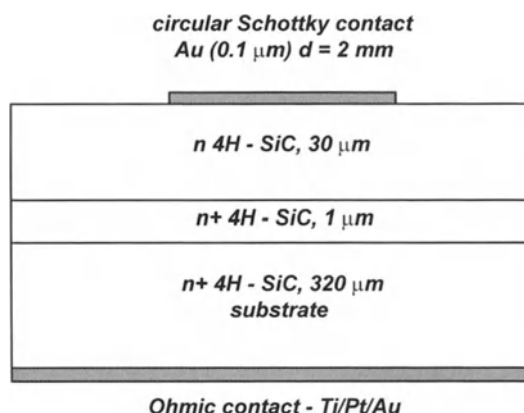


Fig. 11.1. Schematic illustration of the detector studied in [8] (with permission for reproduction from Elsevier)

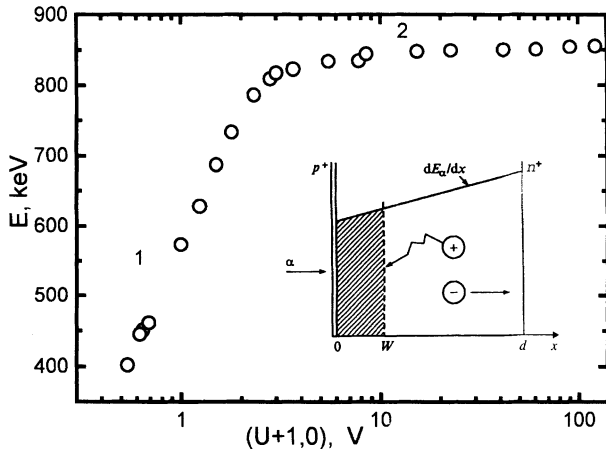


Fig. 11.2. Experimental dependence of the signal amplitude on the bias voltage applied to a detector: 1, before, and 2, after total depletion. The *inset* shows the geometry used in the analysis of the diffusion; W is equal to SCR [9] (with permission for reproduction from Nauka)

portion of the Bragg curve. Figure 11.2 shows two stages of rise in the signal, with different rates. Apparently, these portions correspond to biases U before and after full depletion of the structure. When the electric-field region occupies only a part of the n-base, the charge transfer includes, together with carrier drift in the field region, also hole diffusion in the base. The diffusion, which is slower than the drift, leads to significant loss of charge via carrier recombination. To a first approximation, the signal grows in proportion to the value of $\text{SCR} = W \sim U^{1/2}$.

When depletion is achieved and the field region extends across the entire film, only carrier drift occurs. Since the field effectively separates electrons and holes, the loss of charge is determined in this case by localization at trapping centers, rather than by recombination. In the process, those centers which capture carriers for a time longer than the time of pulse formation by the recording apparatus (on the order of microseconds) manifest themselves. The signal amplitude increases because of the growing drift velocity. Finally, charge transport can be considered complete in the saturation region.

A similar behavior of the signal amplitude ($\sim U^{1/2}$) was observed in [8], in which the SCR could only be made as wide as $9.9 \mu\text{m}$, even though the film thickness was $30 \mu\text{m}$. It is indicative that no significant transformation of the shape of the amplitude spectrum was observed with increasing average amplitude (Fig. 11.3, [8]).

The above data make it possible to determine the important parameters of SiC when used as a detection medium. These are the average energy ε for electron-hole pair formation; the diffusion length of holes $L_D = (D\tau_0)^{1/2}$; the degree of uniformity of their lifetime, $\Delta\tau/\tau_0$, in the base of the diode structure;

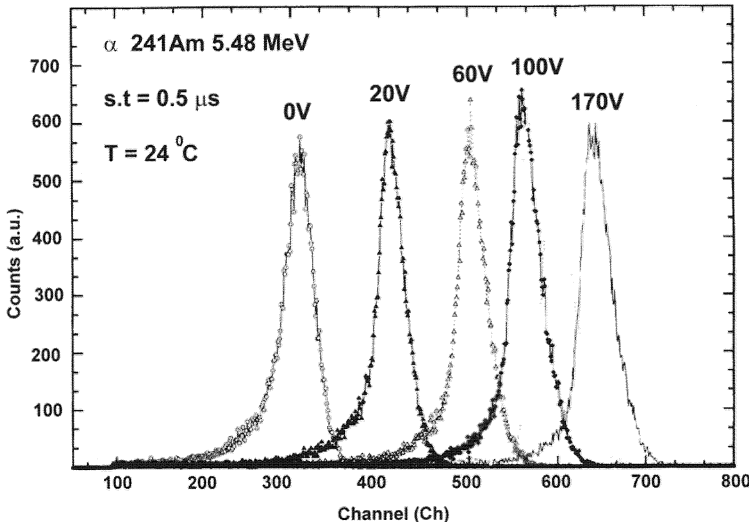


Fig. 11.3. Response of a 4H-SiC detector to 5.48 MeV ^{241}Am alpha particles impinging on the Schottky contact at the applied bias voltages indicated. Replotted using original data from Fig. 3 of [8] (with permission for reproduction from Elsevier)

and the lifetimes of carriers before their capture in the course of drift in the SCR. Here, D is the diffusion coefficient, and τ_0 is the average lifetime.

11.3.2 Determining the Average Energy per Electron–Hole Pair

To find ε , it is necessary to know the energy introduced into the film. For this purpose, the results of mathematical modeling of the deceleration of an alpha particle by means of the TRIM software were invoked [10]. By use of the Bragg ionization curve dE_a/dx obtained, it was found from the data in Fig. 11.2 that $E = 2.112$ MeV is released in the film, whose thickness ($d = 10 \mu\text{m}$) was found from capacitance measurements.

As already noted, the recorded signal is proportional to the charge $Q_0 = eN$ introduced by the particle, where N is the number of electron–hole pairs formed and e is the elementary charge. This yields the proportionality $N = E/\varepsilon = E_{\text{sat}}/\varepsilon_{\text{Si}}$, where E_{sat} is the saturation energy taken from experiment (Fig. 11.2, [9]); ε_{sat} was evaluated, from the calibration of the analyzer with a silicon detector, to be equal to ε_{Si} (3.62 eV). In this way, a value $\varepsilon = 8.84$ eV was obtained for the data in Fig. 11.2. As shown below, the ε value can be refined by analyzing the diffusion–drift transport.

11.3.3 Determining the Hole Diffusion Length

The diffusion–drift transport was considered for the case of stationary carrier generation, uniform over the sample volume, in [11, 12]. It should be noted

that stationary excitation changes the occupancy of deep levels. In carrier generation by single alpha particles, carrier diffusion occurs under the conditions of equilibrium filling, which may be manifested in the values of the diffusion length L_D obtained.

To take into account the dependence on the coordinates of the concentration of carriers generated by alpha particles, a simplification is introduced by assuming that dE_a/dx is a linear function of x . Then $dE_\alpha/dx = G(x) = 1 + bx$, with normalization to 1 at $x = 0$. The charge deficit $\lambda = 1 - Q/Q_0$ is calculated (see [13]) by a formula valid for $(d - W)/L_D > 2$:

$$\lambda = \frac{\int_W^d G(x - W) (1 - \exp((W - x)/L_D)) d(x - W)}{d(1 + 0.5bd)} . \quad (11.1)$$

Here, Q is the recorded charge, $Q_0 = d(1 + bd/2)$. For $G(x) = 1$, (11.1) gives the known result

$$\frac{Q}{Q_0} = \frac{W + L_D}{d} . \quad (11.2)$$

The expression $\lambda(W, L_D, d)$ is cumbersome and lacks clearness. However, it allows us to fit for the function $\lambda(W)$ with respect to two parameters $-L_D$

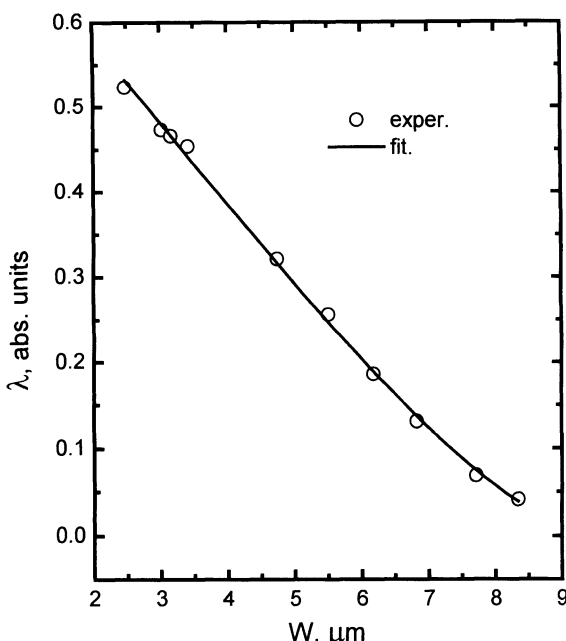


Fig. 11.4. Dependence of the signal deficit on the SCR boundary. Circles, experiment; line, fitting [9] (with permission for reproduction from Nauka)

and d (Fig. 11.4). In this case, λ was calculated from the data in Fig. 11.2 as $\lambda = (E_{\text{sat}} - E)/E_{\text{sat}}$, and W was found from capacitance measurements. As a result, a value $L_D = 2.42 \mu\text{m}$ was obtained and the d value was refined. Fitting gave $d = 9.76 \mu\text{m}$, which yielded a refined average energy for pair formation $\varepsilon = 8.6 \text{ eV}$. The last value is close to the result $\varepsilon = 8.4 \text{ eV}$ obtained in [14].

11.3.4 Shape of Amplitude Spectrum for Diffusion and Its Relationship to the Hole Lifetime τ

The use of alpha particles makes it possible to find the nonuniformity of τ over the film area [15]. The tracks of alpha particles are formed by dense bunches of electron-hole pairs with diameter on the order of $10 \mu\text{m}$. Therefore, the charge generated by each particle reflects the transport conditions in a microscopic volume. The chaotic incidence of particles on the detector reveals the statistics (over the sample area) of the lifetime τ , which is the parameter most sensitive to structural imperfections. As a result, the shape of the amplitude spectrum is related to the nonuniformity of τ .

Calculation of the Spectrum Shape

The amplitude spectrum is plotted in the coordinates $dN/dq = f(q)$, where dN is the number of pulses in the amplitude range dq , and the q values are normalized to the charge Q_0 introduced. To construct the spectrum in accordance with [15], the identity $dN/dq = (dN/d\tau)(d\tau/dq)$ was written and the problem was reduced to the shape of the distribution of τ and the type of the function $q = f(\tau)$. The function $dN/d\tau$ was taken in the form of a Gaussian distribution with variance σ :

$$\frac{dN}{d\tau} = \frac{\exp \left[-(\tau - \tau_0)^2 / 2\sigma^2 \right]}{\sqrt{2\pi}\sigma}. \quad (11.3)$$

This assumption is justified by the fact that the Gaussian function is the most probable under conditions of minor deviations of the parameter from the mean value $|\tau - \tau_0| < \tau_0$. Also, the FWHM of the spectrum of τ values was introduced as $\Delta\tau = 2.35\sigma$. For simplicity, the generation was assumed to be uniform across the film thickness, and then the type of $d\tau/dq$ was found in accordance with (11.2). This gives a system equations in which the numerical multipliers have been discarded:

$$\frac{dN}{dq} = \sqrt{\frac{\tau}{\tau_0}} \exp \left[\frac{-(\tau/\tau_0 - 1)^2}{0.362(\Delta\tau/\tau_0)^2} \right], \quad (11.4)$$

$$q = \left(W + L_D \sqrt{\tau/\tau_0} \right) / d. \quad (11.5)$$

It can be seen from (11.4), (11.5) that the dimensionless parameters of the spectra are W/d , L_D/d , and $\Delta\tau/\tau_0$. These parameters affect the spectrum shape differently. For example, W/d only shifts the peak position, leaving the spectrum width unchanged. Conversely, the nonuniformity of τ affects only the width. The value of L_D/d affects the spectrum as a whole. Figure 11.5 [9] illustrates the transformation of the charge signal spectrum on varying $\Delta\tau/\tau_0$. It can be seen that, up to a relative nonuniformity of 50% ($\Delta\tau/\tau_0 = 0.5$), the spectra are symmetric. When $\Delta\tau/\tau_0$ increases to 1, asymmetry arises because of an extended low-amplitude portion appearing on the left wing of the spectrum. However, the FWHM is described by a linear function over the entire range of $\Delta\tau/\tau_0$ values (see the inset of Fig. 11.5).

Plotting the linewidth as a function of L_D/d shows that this dependence is also linear, with a slope proportional to $\Delta\tau/\tau_0$. Combining these dependences gives a numerical coefficient of ~ 0.5 for the FWHM of the spectral line:

$$q_2 - q_1 = 0.48 \frac{\Delta\tau}{\tau_0} \frac{L_D}{d} . \quad (11.6)$$

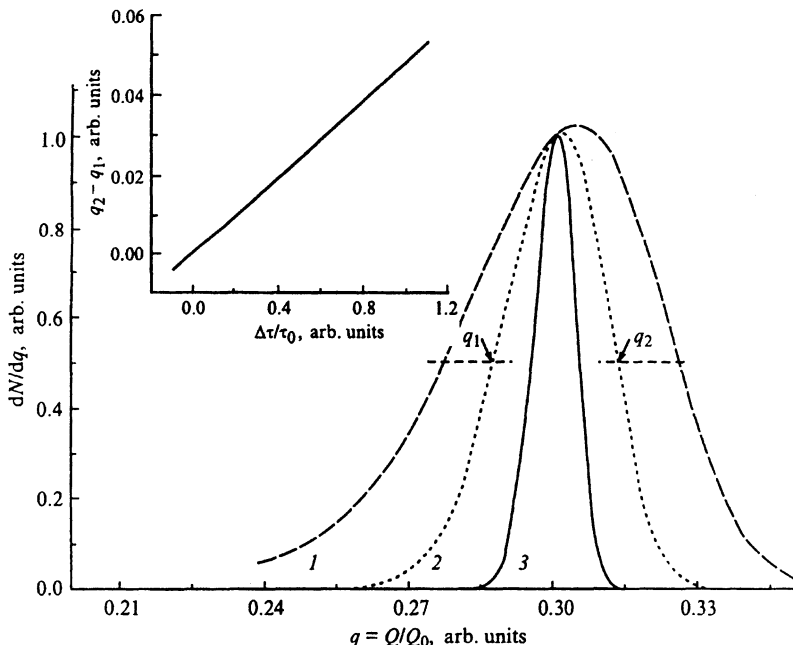


Fig. 11.5. Shape of amplitude spectrum for different nonuniformities of the lifetime. $\Delta\tau/\tau, \%$: 1–100, 2–50, 3–20. $W/d = 0.2$, $L_0/d = 0.1$. The *inset* shows the width of the spectral line (FWHM) as a function of $\Delta\tau/\tau$ [9] (with permission for reproduction from Nauka)

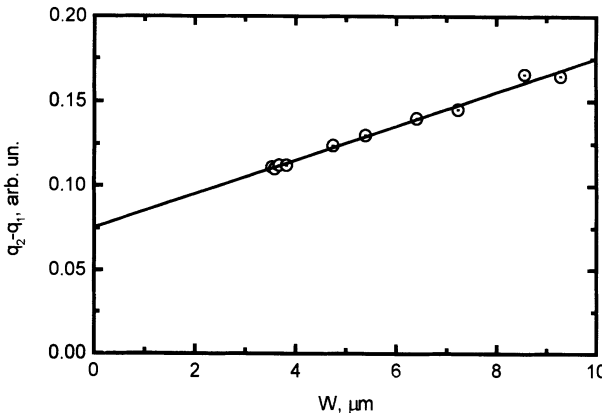


Fig. 11.6. Experimental dependence of the width of the spectrum on the extent of the field region. The value of the width for $W = 0$ corresponds to fluctuations in the course of diffusion of holes [9] (with permission for reproduction from Nauka)

It can be seen that the linewidth is independent of W/d , i.e. it is not affected by the bias voltage. This is apparent since fluctuations of the recorded charge are related to the stage of carrier diffusion.

Experiment

The shape of the amplitude spectrum was measured on films with $L_D = 2.4 \mu\text{m}$ and $d = 9.76 \mu\text{m}$. Figure 11.6 [9] shows how the width of a line normalized to the charge introduced depends on the width of the field region W . The increase in linewidth with W contradicts (11.6) and indicates that a certain contribution to the fluctuations of the resulting amplitude comes from carrier drift in the field region. As follows from Fig. 11.6, the dependence $(q_2 - q_1) = f(W)$ is linear, and, therefore, its extrapolation to $W = 0$ gives the $q_2 - q_1$ value for the case of diffusion transport.

The value $q_2 - q_1 = 0.075$ thus obtained makes it possible to find, using (11.6), the value of $\Delta\tau/\tau_0$; this is equal to $(0.075/0.48)(d/L_D) = 0.6$, or 60%, which, incidentally, corresponds to the average carrier lifetime uniformity in detector-grade silicon. It was mentioned above that, in [8], the FWHM remained constant when the detector bias was varied. This should be related to a higher uniformity of charge transfer in the SCR of the film.

11.3.5 Drift Transport and Carrier Capture Times

Calculation

After full base depletion is achieved, the field distribution and the carrier generation profile are of the type shown in the inset of Fig. 11.7 [9]. Here, the

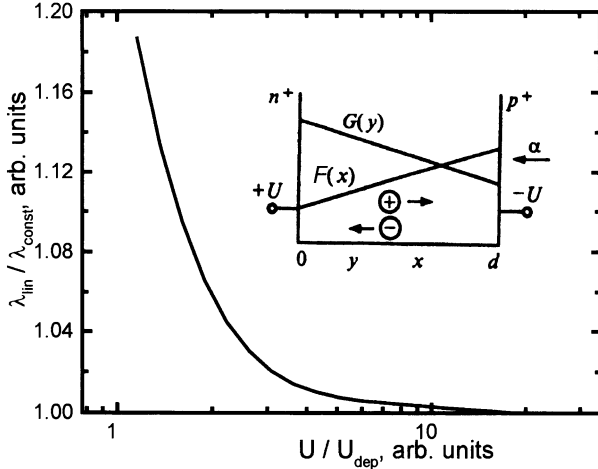


Fig. 11.7. Holes charge loss after total depletion of the detector structure. λ_{const} and λ_{lin} correspond to a constant or linear electric field, respectively. The inset shows the geometry of the detector with linear functions for charge generation $G(y)$ and electric field strength $F(x)$ [9] (with permission for reproduction from Nauka)

geometric layout of the experiment is similar to that used in [16], where carrier drift in a linearly varying field was considered for the case of generation at an arbitrary point y . In the case of a SiC detector, account should be taken additionally of the nonuniform nature of generation, and the average detected charge should be found for the conditions specified.

For this purpose, some calculation needs to be done. First, the carrier concentration has to be found as a function of the coordinates for carrier generation at an arbitrary point y . Further, the charge $q(y)$ induced on the electrodes has to be determined and, finally, its average value has to be determined, taking account of the generation profile $G(y)$.

The above operations can be written for holes as

$$p(x) = G(y) \exp \left(- \int_y^x \frac{dx}{\mu \tau_h F} \right), \quad (11.7)$$

$$q(y) = \frac{1}{d} \int_y^d p(x) dx, \quad (11.8)$$

$$\bar{q} = \frac{\int_0^d G(y) q(y) dy}{d(1 - k/2)}. \quad (11.9)$$

Here the electric field strength $F(x) = a + \rho x$, where $\rho = (4\pi/\chi)\rho_0$, χ is the dielectric constant, ρ_0 is the space charge density, $G(y) = 1 - k(y/d)$,

$Q_0 = d(1 - k/2)$, μ is the hole mobility, and τ_h is the lifetime of holes till their localization at trapping centers.

For simplicity, the capture is considered to be weak and described by the linear term of the expansion of the exponential in the form

$$p(x) = G(y) \left(1 - \int_y^x \frac{dx}{\mu \tau_h F} \right). \quad (11.10)$$

In this case, the solutions have a clear form in the case of a uniform field $F(x) = \text{const}$ and equiprobable generation $G(y) = 1$, namely

$$q(y) = (1 - y/d) \left[1 - \frac{d - y}{2\mu \tau_h F} \right], \quad (11.11)$$

$$\bar{q} = 0.5 \left(1 - \frac{d}{3\mu \tau_h F} \right). \quad (11.12)$$

Similar expressions are valid for electrons. A linear type of field makes the above relations more complex by introducing a logarithmic dependence on the voltage (see [16]). To account for the resulting discrepancies, the ratio of the losses of charge caused by localization for the cases of a linear (λ_{lin}) and a uniform (λ_{const}) dependence of the field on the coordinate is presented in Fig. 11.7. The curves were plotted using the formula

$$\lambda_{\text{lin}}/\lambda_{\text{const}} = 1.5U_*^2 \left[1 - 0.5 \left(\frac{U_*^2 - 1}{U_*} \right) \ln \frac{U_* + 1}{U_* - 1} \right], \quad (11.13)$$

where U_* is the ratio between the voltage applied to the structure and the voltage for full depletion, V_{dep} . It can be seen from Fig. 11.7 that the difference between the amounts of loss disappears at $U/U_{\text{dep}} > 10$. This is indicative that the expressions for the charge transported by electrons and holes are identical in the case of uniform generation.

If the generation is nonuniform across the film thickness, different formulas are obtained for electrons and holes. The expressions for the charge losses by capture lose their clarity and have the form

$$\begin{aligned} \lambda_h = \frac{0.25d^2}{(1 - k/2)V_{\text{dep}}(\mu\tau)_h} & \left\{ U_* + \frac{k}{3} - \frac{k}{4}(U_* + 1)(2 - U_*) \right. \\ & \left. - \frac{U_*^2 - 1}{2} \left[1 + \frac{k}{4}(U_* - 1) \right] \ln \frac{U_* + 1}{U_* - 1} \right\}, \end{aligned} \quad (11.14)$$

$$\begin{aligned} \lambda_e = \frac{0.25d^2}{(1 - k/2)V_{\text{dep}}(\mu\tau)_e} & \left\{ U_* - \frac{k}{3} - \frac{k}{4}(U_* - 1)(2 - U_*) \right. \\ & \left. - \frac{U_*^2 - 1}{2} \left[1 - \frac{k}{4}(3 - U_*) \right] \ln \frac{U_* + 1}{U_* - 1} \right\}. \end{aligned} \quad (11.15)$$

Despite being cumbersome, (11.14) and (11.15) make it possible to find the carrier lifetimes τ_e and τ_h by using the values of those lifetimes as fitting parameters.

Experiment

The data in Fig. 11.2 will be used here as an example of the analysis of charge losses measured in the drift mode. These data allow us to plot the losses as a function of voltage (see Fig. 11.8) for comparison with a calculation by (11.14) and (11.15). The value of V_{dep} was set at 6.7 V on the basis of capacitance measurements. The lifetimes τ_e and τ_h were varied. The smallness of the rms deviation served as a criterion for agreement between the calculated and experimental data. This quantity was found to be much smaller with (11.14) when losses of holes predominate. The value $\tau_h = 35$ ns obtained in this case is shorter than the lifetime $\tau_h = 62$ ns obtained from diffusion transport (see Fig. 11.4, $L_D = 2.42 \mu\text{m}$). Such a difference can be attributed to different occupancies of trapping centers. Diffusion occurs under conditions of equilibrium level occupancy, whereas drift proceeds under nonequilibrium conditions, when the trapping center occupancy is markedly lower.

Conclusion

The above results mainly reflect the methodological possibilities of the analysis of diffusion-drift transport of nonequilibrium charge. Expressions describing the charge deficit and the shape of the amplitude spectrum have been derived analytically (with certain assumptions made). These expressions serve

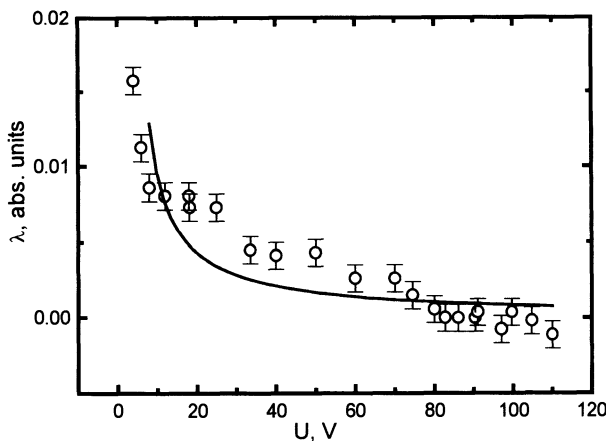


Fig. 11.8. Holes charge loss as a function of detector bias. Circles, experiment; line, fitting, with $V_{dep} = 6.7$ V, $\tau_h = 35$ ns [9] (with permission for reproduction from Nauka)

Table 11.1. Energy levels, density, and related impurities for the trapping centers detected by DLTS and ICTS [17]

	S0	S1	S2	S3	S4	S5
E (eV)	0.10	0.19	0.32	0.91	0.40*	0.75*
N_T (cm^{-3})	2×10^{11}	8.9×10^{12}	6×10^{11}	2.2×10^{13}	4.5×10^{12}	1.4×10^{13}
Related impurity	Nitrogen	Chromium			Vanadium	

* At the Au epitaxial-SiC interface.

as a basis for determining the transport parameters: the carrier lifetimes in drift through the SCR, the diffusion length of minority carriers in the base, and the extent of lifetime nonuniformity over the film area.

In [17], the charge collection properties of 4H-SiC Schottky diodes were determined using the semiconductor-device drift-diffusion analysis program DESSIS [18]. In [17], higher-quality films were used, and values of 500 ns and 95 μs for the hole and electron lifetimes, respectively, were obtained.

The nature of carrier trapping centers was studied in [17] by means of DLTS and isothermal capacitance transient spectroscopy (ICTS). By comparing DLTS and ICTS findings, the characterization of the trap levels can be performed very accurately, and also shallow levels, not detectable by DLTS, can be reliably investigated. This can be seen from Table 11.1 ([17]), which summarizes the energy levels, concentration, and possible nature of trapping centers.

To conclude this section devoted to particle detection, it may be stated that modern SiC films reliably demonstrate a level of drift transport parameters that ensure that the CCE is close to unity. The problem to be solved is further purification to remove impurities, allowing further extension of the SCR. However, recent results in this field are rather promising. For example, a reproducible net concentration level of $(1-3) \times 10^{13} \text{ cm}^{-3}$ was achieved in [19]. The total trap concentration could be made as low as $4.7 \times 10^{11} \text{ cm}^{-3}$. Such a material will allow fabrication of solid-state detectors of the “fully depleted type” for short-range particles.

11.4 Spectrometry of X-Ray Radiation

The experiments with alpha particles are of the radiation detection type, since the range of alpha particles exceeds the film thickness. Under these conditions the particle energy is not liberated entirely in the working volume of a detector. The results obtained by Bertuccio et al. [20] on the spectrometry of X-rays with a quantum energy $E_\gamma < 60 \text{ keV}$ are of interest in this connection. The dominating mechanism of photoabsorption in this energy range is that of transfer of the entire quantum energy to an electron. Even though the ranges of photoelectrons grow nonlinearly with

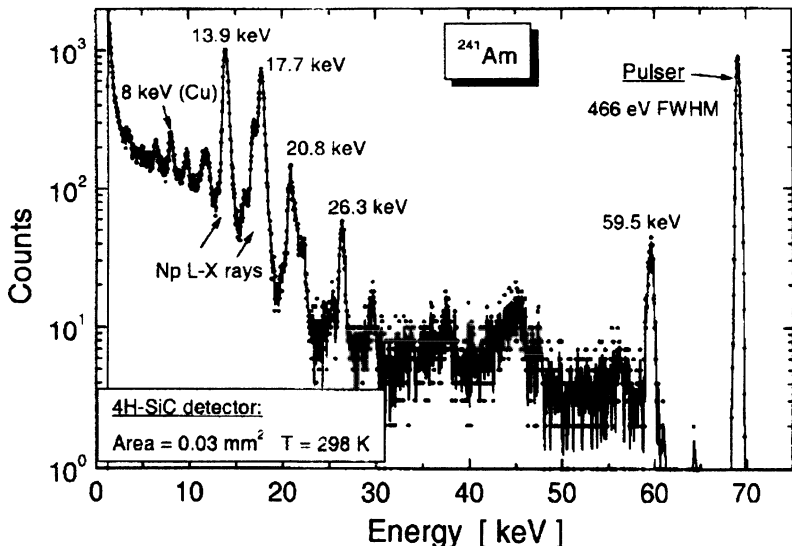


Fig. 11.9. ^{241}Am X- γ -ray spectrum acquired at room temperature with an SiC detector. An energy resolution of 466 keV FWHM was measured on the pulser line [20] (with permission for reproduction from IEEE)

increasing energy ($\sim E_{\beta}^{1.4}$), they do not exceed $10 \mu\text{m}$ here. Therefore, their energy will be completely absorbed in the SCR of the detector (especially at $E_{\gamma} < 20 \text{ keV}$); this situation is characteristic of the spectrometric mode.

The study employed n-type 4H-SiC films manufactured by CREE Research Inc. [21], with a net doping concentration and thickness of $9 \times 10^{14} \text{ cm}^{-3}$ and $70 \mu\text{m}$, respectively. Single-crystal heavily n-doped 4H-SiC wafers were used as substrates. A Schottky barrier of diameter 2 mm was created on the epitaxial layer using a special technology [8]. Reverse current measurements were performed at $300\text{--}380 \text{ K}$ up to 200 V . The mean electric field strength was 170 kV/cm . The authors of [20] emphasize that 4H-SiC epitaxial detectors show current densities more than two orders of magnitude lower than those of Si detectors (from 5 pA/cm^2 at room temperature).

Figure 11.9 presents an observed X-ray spectrum acquired with a small detector area (0.03 mm^2). The detector was biased at 300 V ($W = 18 \mu\text{m}$). This value was a result of a compromise between a high CCE and a moderate contribution of excess noise.

It can be seen that the characteristic energies of the ^{241}Am source are clearly resolved. The energy scale retains linearity over the entire range of $8.0\text{--}59.5 \text{ keV}$. Account should, however, be taken of the pronounced distortion of the line intensities with increasing photon energy. This is due to the fast decrease in the detection efficiency, caused by the small value of W . Making W larger would not only reduce the intensity distortions, but also diminish the

detector capacitance (for a constant area). The latter would result in a lower noise level.

11.5 Response of SiC Detectors to Electron and Photon Irradiation

In this section, the response of epitaxial SiC detectors to electron and photon irradiation is characterized in order to assess the potentialities of this material as a material for on-line radiation dosimeters. The samples were exposed to 22 MeV electron and 6 MV photon beams in the dose range 1–10 Gy at a dose rate of 2.7 Gy/min, which is of interest for radiotherapy [22]. The photon beam (6 MV) was obtained using 6 MeV electrons from a linear accelerator. The authors of [22] compared the possibilities of SiC, silicon, and CVD diamond dosimeters. It was found that, under these conditions, the sensitivity of silicon dosimeters degrades and falls by 35% after irradiation with 20 MeV electrons to a dose of 3 kGy.

By virtue of its polycrystalline nature, CVD diamond is characterized by a pronounced nonuniformity of properties, affecting its spatial resolution. Moreover, to stabilize the dosimeter sensitivity, it is necessary to carry out procedure called “pumping”. This can be done by irradiating the material with a 50 kV X-ray tube to a typical dose of 10 Gy [23].

The best results were obtained with Schottky diodes fabricated on 4H-SiC epitaxial wafers manufactured by CREE. The net concentration in the epitaxial layer was $2.2 \times 10^{15} \text{ cm}^{-3}$, and the layer thickness was 30 μm . Diodes were tested as radiation dosimeters with electron and photon beams. The reverse bias was 150 V. The collected charge was a linear function of the absorbed dose induced by 22 MeV electrons (dose range 1–10 Gy), with a slope of 16.37 nC/Gy.

The current induced by exposure to 6 MV photons (dose rate 2.1–6.5 Gy/min) was linear too, with a slope of $3.5 \times 10^{-10} \text{ A min/Gy}$. The active depth of the detectors was determined as the sum of the SCR = 8.5 μm and the diffusion length = 12.2 μm = $\sqrt{2.98 \text{ cm}^2/\text{s}} \times 500 \text{ ns}$. A minority carrier lifetime of 500 ns was obtained as a preliminary result [17].

However, the use of a semi-insulating bulk 6H-SiC (230 μm thick) sample with sandwich contacts resulted in poor sensitivity to electrons. This could be attributed to the large number of structural defects. The presence of recombination centers made the CCE value lower, and micropipes increased the dark leakage current.

The summary table (Table 11.2), comparing the characteristics of dosimeters of different kinds, suggests that epitaxial SiC-based diodes show promise as radiation dosimeters.

Table 11.2. Comparison of the sensitivity and the sensitivity per unit volume of one of the SiC epitaxial dosimeters with those of commercial (Scanditronix) Si dosimeters and of two CVD diamond dosimeters recently reported in the literature [22]

Dosimeter	Voltage (V)	Active volume (mm ³)	Sensitivity (nC/Gy)	Sensitivity/volume [nC/(Gy mm ³)]
Silicon*	Unbiased	0.295	150	509
CVD diamond	50	3.7	690	190
CVD diamond	400	4.7	420	90
SiC	150	0.06	16.4	273

* The silicon dosimeter was preirradiated to 10 kGy with 20 MeV electrons so that further irradiation did not affect the sensitivity much.

11.6 SiC Detectors for High-Energy Physics Experiments

In designing experiments with a hard radiation load at future high-luminosity colliders (such as the Large Hadron Collider at CERN), SiC, naturally, was among the materials considered. Its possibilities as a material for tracking detectors were studied in [24].

The authors of [24] used a 310 µm thick semi-insulating 4H-SiC substrate from CREE. The contacts on the front and back sides were ohmic. Figure 11.10 [24] shows a cross section of a pad detector with a guard-ring structure. Good-quality detectors show, between -500 and +500 V, a linear rise in the dark current with increasing bias voltage. On the basis of the slope of this dependence, the substrate resistivity was found to be $5.1 \times 10^{10} \Omega \text{ cm}$.

In order to evaluate the possibility of using SiC in tracking detectors for high-energy physics experiments, the response signal to quasi-minimum-ionizing particles (MIPs) from a ⁹⁰Sr source (for which the maximum energy of beta particles is 2.2 MeV) was measured. A Si detector was placed behind the SiC detector and signals with energy $\geq 1 \text{ MeV}$ were selected using a gate circuit.

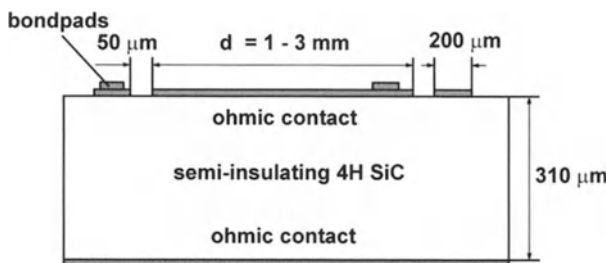


Fig. 11.10. Geometry of a detector formed from semi-insulating 4H-SiC [24] (with permission for reproduction from Elsevier)

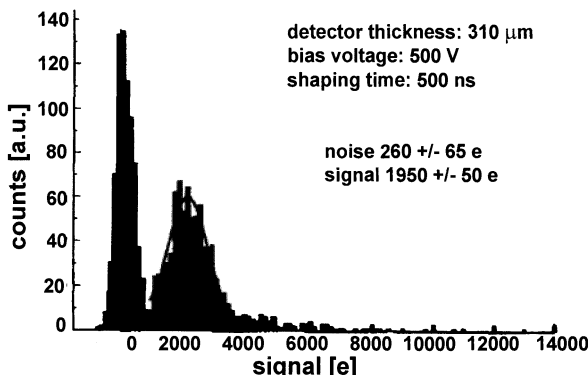


Fig. 11.11. Signal response of a 310 μm thick detector due to quasi-MIPs from a ^{90}Sr source, taken directly (for 60 s) after applying a bias voltage of 500 V [24] (with permission for reproduction from Elsevier)

The tracks of such electrons contained 17 000 e/h pairs, which exceeded the signal from real MIPs by only 8%. Figure 11.11 [24] shows the signal measured directly (for 60 s) after applying the bias voltage. It can be seen that the signal and noise spectra are clearly resolved, but the authors of [24] mention two adverse effects.

First, the maximum CCE of the detector is only $\sim 12\%$. Second, the signal amplitude falls in the course of time with a time constant of 14.2 min. These facts point to a low carrier lifetime and the involvement of deep levels in the formation of the electric field.

A radiation hardness test, performed using 8 GeV protons with a fluence of up to $4.16 \times 10^{14} \text{ cm}^{-2}$, showed a decrease in CCE by about 23%. The time constant of the exponential decay was reduced to 3.6 min. Simultaneously, tests showed an increase in the substrate resistivity by a factor of 3.

It should be emphasized that [24] was the first attempt to fabricate particle detectors based on semi-insulating 4H-SiC. The observed instability and comparatively low CCE are to be related to the insufficient perfection of the material at that time (~ 1998). It should be recalled that a low CCE for electrons in semi-insulating SiC was also observed in [22].

11.7 Operation of SiC Detectors in a Reactor Channel

This problem is related to the monitoring of the operation of a reactor. Characteristically, its solution is based simultaneously on the radiation and temperature hardness and the chemical stability of SiC.

As far back as the 1960s, good agreement was observed in neutron flux measurements between flux profiles measured in a low-power reactor with a p-n SiC diode coated with ^{235}U and flux profiles determined using con-

ventional gold foil activation techniques [25]. It was also established that SiC diodes can detect alpha particles after being subjected to a considerable thermal-neutron fluence of $6 \times 10^{15} \text{ cm}^{-2}$. For fast neutrons ($> 1 \text{ MeV}$), the fluence may be as high as $\sim 10^{17} \text{ cm}^{-2}$ [26]. In [6], SiC detectors demonstrated approximately five times higher radiation hardness, compared with silicon devices, in the detection of ^{233}U fission fragments directly in a reactor channel. It was proposed to measure neutron spectra with SiC diodes equipped with a set of ^{233}U , ^{234}U , ^{235}U , ^{238}U , ^{232}Th , and ^{239}Pu radiators.

The advances in recent years in the field of high-purity SiC crystal growth make it possible to solve the problem of measuring a mixed neutron/gamma field [27, 28].

The authors of [27, 28] used a matrix of 22 Schottky diodes 200 or 400 μm in diameter. The diodes could be connected in parallel, to make the total area larger. A lithium fluoride layer placed adjacent to the detector surface served as a converter. This enabled counting of neutrons by means of tritons (^3H), in accordance with the reaction $^6\text{Li}(n,\alpha)^3\text{H}$. Figure 11.12 [28] presents a spectrum of amplitudes of signals from gamma quanta and generated tritons. It can be seen that the shape of the spectrum makes it possible to distinguish these kinds of radiation. Figure 11.13 [28] presents profiles of neutrons and gamma quanta as a function of the distance from the reactor centerline. The measurements were made with 12 diodes connected in parallel. A counting time of 30 min was employed for each measurement, and the neutron and gamma count rates were obtained simultaneously.

The reactor power was raised to 290 W. This corresponded to an epicadmium neutron fluence rate of up to $3 \times 10^7 \text{ cm}^{-2}\text{s}^{-1}$ and to a gamma dose rate of 0.6–234 krad · Si h $^{-1}$. A linear response was obtained with the detector. Also, the detector showed a high level of precision for both neutrons

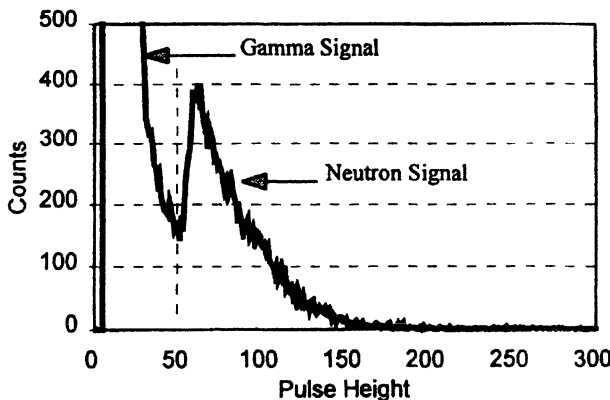


Fig. 11.12. Typical pulse height spectrum acquired with a SiC Schottky detector (bias = -25 V) in a mixed neutron/gamma field. Gamma and neutron counts are separable on the basis of pulse height, so that both levels can be monitored in a single measurement [28] (with permission for reproduction from IEEE)

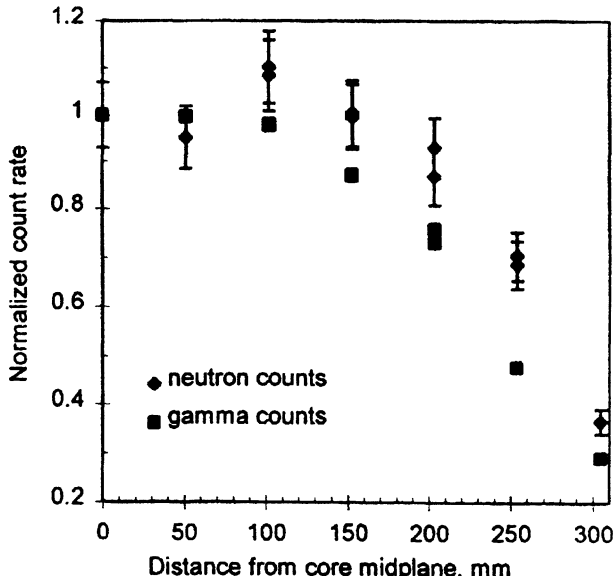


Fig. 11.13. Axial neutron and gamma profiles in an irradiation tube as a function of distance from the core midplane during a reactor shutdown [28] (with permission for reproduction from IEEE)

and gamma rays. These levels were 1.9% and better than 0.6%, respectively. Thus, the ability of an SiC detector to measure neutron and gamma radiation at levels comparable to those encountered for a spent fuel assembly was demonstrated.

11.8 Radiation Hardness of the SiC Detectors

11.8.1 Introduction

The question of radiation hardness was considered in all of the above sections. The investigations of radiation defects cover a wide range. This range is indicated by some reports presented at the recent international conference ICSCRM2001 held in Tsukuba, Japan, in which defects generated by electron beams [29], neutron fluxes [30], and gamma radiation [31] were studied. In this section, the emphasis is placed upon problems related to high-energy physics. In addition to the experiments described in Sect. 11.6, studies were also carried out with lightly doped SiC films and at high doses.

At present, experiments are under development at CERN's Large Hadron Collider, where the detectors should be operational for at least ten years. In these experiments, the doses of detector irradiation with relativistic particles are within the limits 2×10^{14} – $5 \times 10^{15} \text{ cm}^{-2}$, depending on the detector position relative to the point of beam collision [32].

Under these conditions, serious problems arise with technologically well-developed silicon detectors even at doses of $\sim 10^{14} \text{ cm}^{-2}$. First, the dissipated power increases dramatically (the reverse current and the depletion voltage of the structure grow). Second, the efficiency of nonequilibrium charge transport falls, and, correspondingly, the signal amplitude decreases. Recently, the efficiency of cooling of a silicon detector and control over the field profile through dosed carrier injection from the contact have been studied (CERN RD39 collaboration) [33]. The fact that the handling of silicon detectors is becoming more complicated is stimulating a search for materials with higher radiation hardness.

11.8.2 Experimental Procedure

The effect of 8 MeV proton fluences of up to $2 \times 10^{16} \text{ cm}^{-2}$ on 6H-SiC was studied in [34]. Under irradiation, the room-temperature free-electron concentration in the layer decreases, while the total charge of ionized impurities $|N_D^+ - N_A^-|$, measured at a temperature $T = 650 \text{ K}$, increases. This means that irradiation leads to formation of deep centers in the upper half of the bandgap, which capture electrons from shallow donors. These deep centers (for example, the R-center, with an ionization energy of $\sim 1.2 \text{ eV}$) are ionized at high temperature, but they do not contribute to $|N_D^+ - N_A^-|$ measured at 300 K, because their recharging time is about two weeks at this temperature.

It has also been established that, under similar conditions, SiC p⁺-n structures maintain their CCE for the detection of short-range ions (alpha particles) after irradiation with 8 MeV proton fluence of up to $8 \times 10^{15} \text{ cm}^{-2}$ [35].

In another study [36], the radiation hardness of SiC Schottky diodes was analyzed under conditions of irradiation corresponding to the application of these diodes as detectors of relativistic particles. The first 1 GeV proton fluence was chosen to be $\sim 3 \times 10^{14} \text{ cm}^{-2}$, which is half an order of magnitude higher than the “critical” fluence for silicon detectors. The second dose chosen was $9.8 \times 10^{14} \text{ cm}^{-2}$.

The SiC detectors used in [36] were Schottky diodes 600 μm in diameter, fabricated by magnetron sputtering of Ni onto the surface of 6H-SiC epitaxial films grown by vacuum sublimation epitaxy [37]. The film doping profile was inhomogeneous, with a carrier concentration varying from $\sim 5 \times 10^{14} \text{ cm}^{-3}$ at the surface to $\sim 8 \times 10^{15} \text{ cm}^{-3}$ at a depth of $\sim 7 \mu\text{m}$. Such a distribution of $(N_D^+ - N_A^-)$ creates a “pulling field” in the space-charge region. This increases the effective diffusion length of carriers [38].

The samples were irradiated with a 1 GeV proton beam extracted from the synchrocyclotron at the St. Petersburg Institute of Nuclear Physics at Gatchina. The long-burst operation mode was used for the irradiation to ensure a time-uniform exposure. The particle detection efficiency of the SiC diode structures was measured using alpha particles from a ²⁴⁴Cm source. The recorded energies (or the nonequilibrium charge created in the SiC) were determined by analyzing the signal amplitude as a function of the reverse bias

applied to the diode. Data on the capacitance of the structure were used to determine the real size of the sensitive region and the diffusion length of holes. The parameters and concentrations of deep levels were calculated from data furnished by DLTS.

11.8.3 Experimental Results

Figure 11.14 shows a typical dependence of the measured energy E on the reverse bias U for three structures. These dependences $E(U)$ were analyzed, proceeding from the fact that the charge generated in SiC by an alpha particle is strictly calibrated.

According to the Bragg ionization curve, the energy loss is strictly related to the length of the sensitive region of the detector W_{eff} . The Bragg curve obtained from the TRIM software was used and was approximated (with the exception of its peak region) by a cubic polynomial in W_{eff} . Correspondingly, the calculated energy $E_{\text{th}}(W_{\text{eff}})$ released along the path W_{eff} was described by a fourth-order polynomial. The W_{eff} values were obtained by solving numerically the equation $E = E_{\text{th}}(W_{\text{eff}})$, where E is the measured quantity, with an accuracy better than $0.025 \mu\text{m}$. Figure 11.15 presents the $W_{\text{eff}}(U)$ dependence obtained as described above. Adding 1.5 V to the bias voltage took the contact potential difference across the Schottky barrier into account. At 100 V , W_{eff} exceeds $7 \mu\text{m}$, being equal to the sum of the SCR width W and the hole diffusion length L_D :

$$W_{\text{eff}} = W + L_D . \quad (11.16)$$

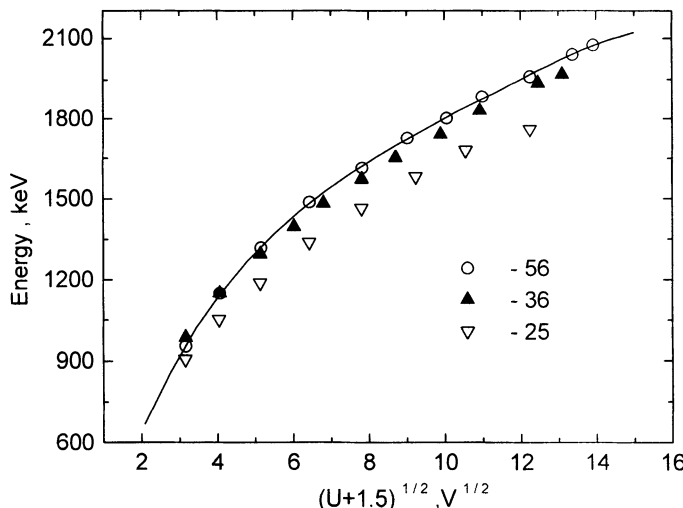


Fig. 11.14. Energy released by an alpha particle in the sensitive region of the structure versus reverse bias for three as-grown samples (56, 36, 25) [36] (with permission for reproduction from Elsevier)

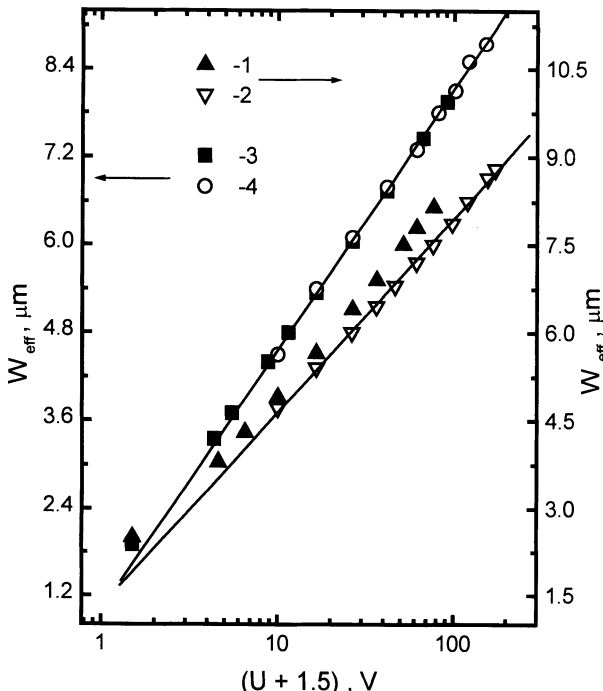


Fig. 11.15. Effective width of the sensitive region of the structure versus reverse bias. Samples: “1” and “2” represent sample 36; “3” and “4” represent sample 56; “2” and “4” represent as-grown samples; and “1” and “3” represent samples after proton irradiation with a fluence of $2.7 \times 10^{14} \text{ cm}^{-2}$ [36] (with permission for reproduction from Elsevier)

To distinguish the contributions to W_{eff} from the W and L_D terms, the dependence of the capacitance C on the bias U was measured. The stray capacitance starts to be significant for small-area structures: to exclude this error, the following expression was used for $W_{\text{eff}}(C)$

$$W_{\text{eff}} = \frac{A}{C - P_1} + P_2 , \quad (11.17)$$

where A is a constant related to the area of the structure, and P_1 and P_2 correspond to the stray capacitance and L_D . Figure 11.16 shows a numerical fit, obtained using (11.17), to the experimental data measured for samples before and after proton irradiation to a fluence of $2.7 \times 10^{14} \text{ cm}^{-2}$. The values of L_D obtained are (1.66 ± 0.08) and $(1.2 \pm 0.1) \mu\text{m}$, respectively. Table 11.3 summarizes the changes in L_D and W_{eff} for five samples [39].

Table 11.4 presents the trap parameters of the deep centers before and after the first irradiation, as determined by DLTS. It can be seen that only the concentration of the R-centers changes significantly, and no new centers appear. Since the R-centers are presumably associated with vacancies (see,

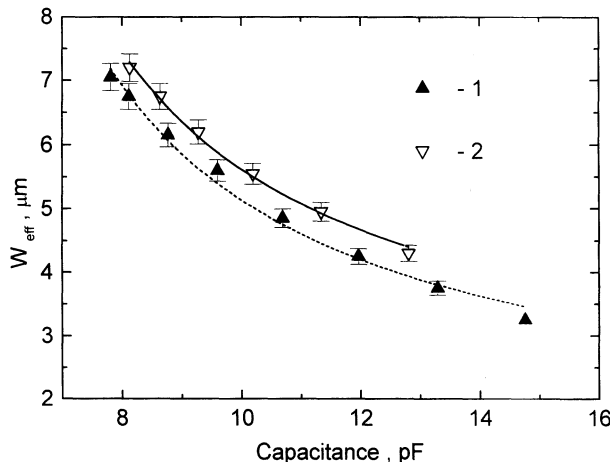


Fig. 11.16. Effective width of the sensitive region of the structure versus measured capacitance for sample 25. Points, experiment; lines, approximation by (11.9). 1, irradiated sample; 2, as-grown sample [36] (with permission for reproduction from Elsevier)

Table 11.3. Diffusion length and the effect of irradiation on the size of the sensitive region [39]

Sample	L_D , μm, before irradiation	L_D , μm, after irradiation	Variation of W_{eff}
25	1.66	1.21	Decreasing
36	1.80	1.24	Increasing
46	0.78	0.61	Constant
55	0.92	—	Decreasing
56	1.00	0.38	Constant

Table 11.4. Deep centers according to DLTS data [39]

Type of center	$E_c - E_t$, eV	Concentration, cm^{-3}	
		Before irradiation	After irradiation
E1/E2	0.35–0.4	$(1-2) \times 10^{13}$	$(1-2) \times 10^{13}$
R	1.1–1.2	$< 5 \times 10^{12}$	5×10^{13}

e.g., [34]), the rate of their introduction can be estimated from the number of initially formed vacancies. A computer simulation by the TRIM software shows that the number ratio of vacancies is 110:1 for proton energies of 8 MeV and 1 GeV.

However, the experiment gave an approximately 400 times lower concentration of R-centers. Thus, the result expected in terms of the model of primary defects differs markedly from the concentration of “final” defects formed in the physicochemical processes in the SiC. This fact indicates that the defect

formation processes at 8 and 1 GeV are not identical. Apparently, this is due to the two orders of magnitude difference in the energies transmitted to the primary-knock-on Si and C atoms.

The overall fluence of irradiation with relativistic protons was $1.3 \times 10^{15} \text{ cm}^{-2}$. This fluence caused certain changes in the characteristics of the structures. (1) The room temperature capacitance at a frequency of 1 kHz became voltage-independent. (2) At elevated temperatures (490 K and 600 K) the capacitance changed with voltage, showing higher absolute values compared with the fluence proton $2.7 \times 10^{14} \text{ cm}^{-2}$. (3) The space charge distribution became more uniform, i.e. there occurred additional doping in the silicon carbide sample.

The absence of a $C(U)$ dependence indicated the appearance of a high-resistance base as a result of compensation. This must lead to a decrease in the detector signal in the partial-depletion mode because of the slow relaxation of the base [40]. However, as demonstrated in [41], the relaxation of the base is markedly accelerated in the case of alpha particle penetration through the structure because of the presence of a substantial concentration of nonequilibrium carriers in the particle track.

Indeed, as also in [41], the dependence of W_{eff} as a function of $(U + 1.5)^{1/2}$ was linear. Unfortunately, the quantity L_D , found from a linear approximation to this dependence, has a value of nearly zero, on average for different samples.

Figure 11.17 shows the charge collected in the detector after the first and second irradiation. The voltage that needs to be applied to the structure after the second irradiation for collecting the same amount of charge as that measured after the first irradiation is approximately three times higher. This indicates that higher electric field strengths are necessary for collecting the same amount of charge, because the drift velocity of the carriers was not saturated. The relative resolution (FWHM, %) is characterized by a decreasing depen-

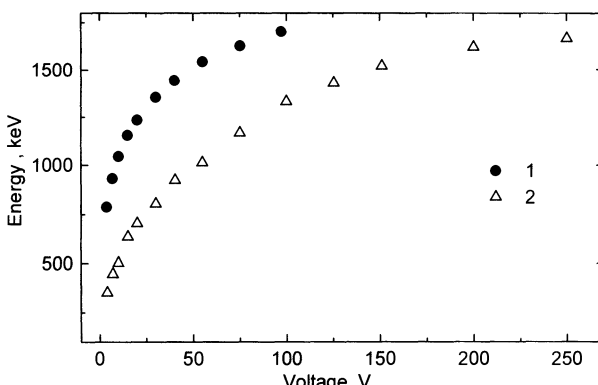


Fig. 11.17. Signal in energy units versus voltage for sample 73. Fluence: 1, $3 \times 10^{14} \text{ cm}^{-2}$; 2, $1.3 \times 10^{15} \text{ cm}^{-2}$ [36] (with permission for reproduction from Elsevier)

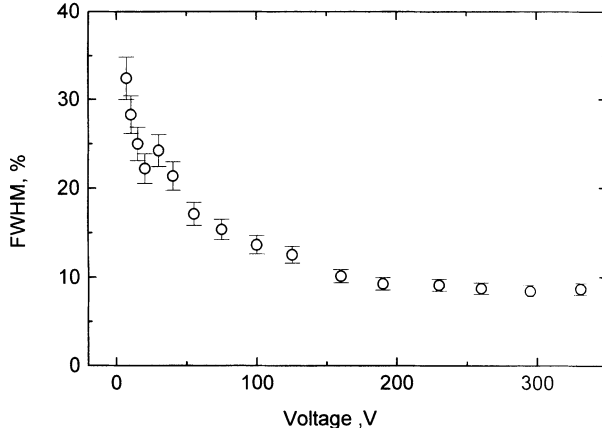


Fig. 11.18. Energy resolution (FWHM) versus applied voltage. Sample 46, proton fluence $1.3 \times 10^{15} \text{ cm}^{-2}$ [36] (with permission for reproduction from Elsevier)

dence on voltage, i.e. the relative resolution improves with increasing field strength and W_{eff} (Fig. 11.18). This is due to the improvement of the charge transport conditions that occurs when the signal amplitudes are grouped together around the average value. The spectrum shape is not altered, remaining Gaussian.

11.8.4 Estimation of the Drift Parameters

The data presented in Figs. 11.15–11.17 allow estimation of how W_{eff} and L_D change after the first irradiation. The L_D value averaged over nine samples is $0.9 \mu\text{m}$, and L_D varies within a range of no more than 30% (with the exception of sample no. 56). The deviations from the initial W_{eff} values are even less significant. The range of variation of W_{eff} can be judged directly from Figs. 11.16 and 11.17.

The hole drift length in an electric field of strength F can be found as follows

$$L_F^p = \mu\tau F = L_D^2 \frac{Fe}{kT}. \quad (11.18)$$

Here k is the Boltzmann constant, T is the absolute temperature, and μ and τ are the carrier mobility and lifetime, respectively. Assuming $F = 10^5 \text{ V/cm}$ and $L_D = 1 \mu\text{m}$, $L_F^p = 400 \mu\text{m}$ for holes at room temperature was obtained after the first irradiation. The electron drift length L_F^n could be evaluated using the data of [38], where $(\mu\tau)_n = 7 \times 10^{-9} \text{ cm}^2/\text{V}$ was obtained in the unipolar electron transport mode for 8 MeV protons with a fluence of $8 \times 10^{15} \text{ cm}^{-2}$. Assuming that R-centers are responsible for the decrease in the lifetime, and introducing a correction to the $(\mu\tau)_n$ value to account for the number of R-centers formed after the first irradiation, $L_F^n \leq 1 \text{ cm}$ was obtained for the

conditions of the experiment. Thus, the carrier drift lengths are quite satisfactory for detectors with an SCR several hundred micrometers long.

After the second irradiation, with a fluence of $1.3 \times 10^{15} \text{ cm}^{-2}$, the trend in the variation of N_{eff} is preserved, and the value of L_D decreases. However, the SiC structures retain properties sufficient for effective carrier transport. The initial signal amplitudes can be achieved. The energy resolution, which characterizes the uniformity of the carrier transport conditions throughout the detector volume, remains high.

As regards the nature of the radiation defects introduced, comparison of the results of [36] with the data reported in [34], where 8 MeV protons were used for irradiation, indicates that the proton energy has no significant effect on the spectrum of centers formed upon irradiation. The R-centers, with energies 1.1–1.2 eV below the bottom of the conduction band, still play an essential role.

Concerning the characteristics of the detectors, irradiation with a proton fluence of $\sim 3 \times 10^{14} \text{ cm}^{-2}$ can be regarded as a threshold for radiation-induced modification of the properties of SiC. At this irradiation stage, neither conductivity compensation in the material nor any significant shortening of the carrier lifetime is observed. However, fluences of $\sim 10^{15} \text{ cm}^{-2}$ lead to compensation in the neutral base of the structure and impair the carrier lifetimes.

11.9 Signal Amplification

In the above, high values of parameters characterizing carrier transport in SiC were established and examples of the successful use of SiC detectors in accomplishing a number of topical tasks were presented. It will be recalled that the diode structures remain operative up to 500–600 °C [5, 42]. However, the main problem still associated with the detectors is the narrow width of the working zone, W_{eff} . This is particularly important in the detection of penetrating ionizing radiation. It is of interest in this connection to find out whether it is possible to obtain a signal stronger than that produced by the energy originally released in the W_{eff} zone, i.e. to achieve “internal” charge amplification.

11.9.1 Principle of “Through-Conducting Channel”

This principle was formulated in the late 1950s for semi-insulating films with monopolar conduction. In [35], a similar situation was modeled for $p^+ - n - n^+$ structures based on 6H-SiC films. The films had an initial concentration of uncompensated donors ($N_D^+ - N_A^-$) = $4.5 \times 10^{16} \text{ cm}^{-2}$ at a layer thickness of several micrometers. The structures were, additionally, irradiated with 8 MeV protons to a dose of $8 \times 10^{15} \text{ cm}^{-2}$. This led to strong conductivity compensation, with the resistivity of the films becoming $5 \times 10^9 \Omega \text{ cm}$. The effect of the “through-conducting channel” was studied by means of alpha spectrometry.

A mode in which alpha particles penetrate through a semi-insulating film to which a forward bias U_{for} is applied was investigated in [43, 44]. It was assumed that the lifetime of nonequilibrium holes is short because of the high concentration of trapping centers. In this case, holes are localized at the centers, becoming immobile. On the other hand, because the forward bias U_{for} is applied, the contacts do not limit the current, and transport of mobile electrons through a track shunting the sample and through the external circuit is possible. Thus, a “through-conducting channel” appears in the semi-insulating film, with the transferred charge exceeding that created by ionization, q , by a factor $(\mu F \tau / d)$:

$$Q = \frac{q\mu F \tau}{d} = \frac{q\tau}{t_{\text{dr}}} , \quad (11.19)$$

where μ and τ are the mobility and lifetime of electrons, F is the electric field strength, and $t_{\text{dr}} = d/\mu F$ is the time of transit through the film.

The experimental dependence $Q(U_{\text{for}})$ in [35] was linear in accordance with (11.19) and corresponded to $\mu\tau = 7 \times 10^{-9} \text{ cm}^2/\text{Vs}$. Thus, the amplification factor was 1.7. It will be recalled that the above example refers to a film with a high concentration of structural defects and a correspondingly low $\mu\tau$. Therefore, the experiment described elucidates the principle of amplification, rather than giving its achievable value.

11.9.2 Amplification in a Triode Structure

Charge amplification, also by a factor τ/t_{dr} , can be obtained in a triode structure [45, 46]. This situation was modeled in [47], where p-type 6H-SiC films played the role of the base region in a structure grown on an n⁺ substrate by vacuum sublimation [37]. The net concentration of impurities ionized at room temperature was $N_A - N_D = 2.8 \times 10^{15} \text{ cm}^{-3}$ at a film thickness of $\sim 10 \mu\text{m}$. A Schottky barrier fabricated by depositing Ni by magnetron sputtering served as the second electrode.

The structures were studied in a floating-base mode, with alpha particles (produced by a ²⁴⁴Cm source) incident on the Schottky barrier side. The alpha particles had an energy of 5.8 MeV and a range in SiC of 20 μm . The nonequilibrium charge appearing in the base corresponded (taking account of the Bragg curve for ionization losses) to absorption of approximately one-third of the above energy. The structures were connected in series with a load resistance and a bias source. The signal from the alpha particles was recorded using a charge-sensitive preamplifier. The shape of the signal spectrum and the average amplitude were determined as a function of applied voltage by means of the conventional amplitude analysis technique. All measurements were done at room temperature under fore-vacuum conditions.

Experimental Results

Capacitance measurements demonstrated that the p–n⁺ junctions of the structure were not identical. The Schottky barrier corresponded to an “abrupt” junction, whereas the transition to p-type conduction at the n⁺ substrate was gradual. Therefore, two connection polarities were tested, with either the p–n⁺ junction of the substrate or the Schottky barrier serving as the collector.

Figure 11.19 [48] shows the dependence of the signal (E) on the voltage (U) applied to the structure for the case when the p–n⁺ junction with the substrate served as the collector. It can be seen that the steep rise in the signal at $U \leq 50$ V gives way to a sublinear dependence with an apparent tendency toward leveling off. It is important to note that the signal exceeds the energy released by an alpha particle in the base. However, this excess is only by a factor of two, i.e. no substantial amplification is observed. This behavior of the signal is probably related to the low carrier lifetime in the emitter (Schottky barrier).

The spectral line shape is Gaussian. The ratio of the spectrum width to the average amplitude demonstrates a slight increase as a function of U (see Fig. 11.20). The FWHM value of $\sim 10\%$ indicates a sufficiently high uniformity of charge transport conditions in the film.

In the case when the Schottky barrier plays the role of the collector, the $E(U)$ dependence becomes superlinear. The signal corresponds to a value of about 80 MeV, whereas the initial value for the energy released by an alpha

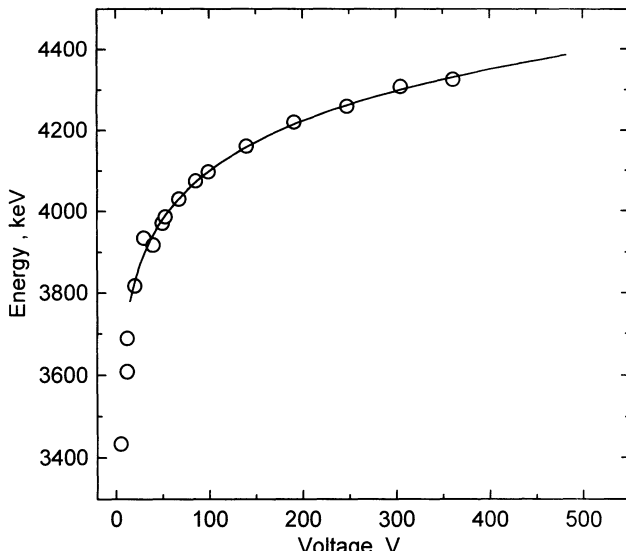


Fig. 11.19. Signal from an alpha particle versus voltage applied to the transistor structure. The role of the collector is played by the p–n⁺ junction with the substrate [48] (with permission for reproduction from Elsevier)

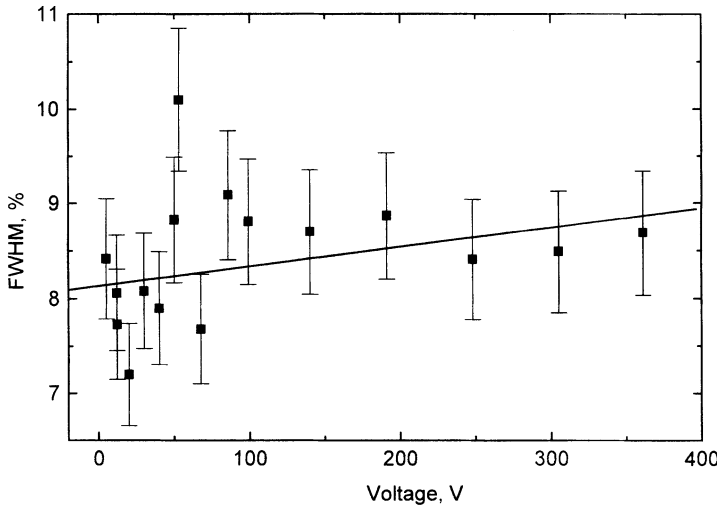


Fig. 11.20. Width of the spectral line (FWHM) versus the voltage applied to the transistor structure. The role of the collector is played by the p–n⁺ junction with the substrate [48] (with permission for reproduction from Elsevier)

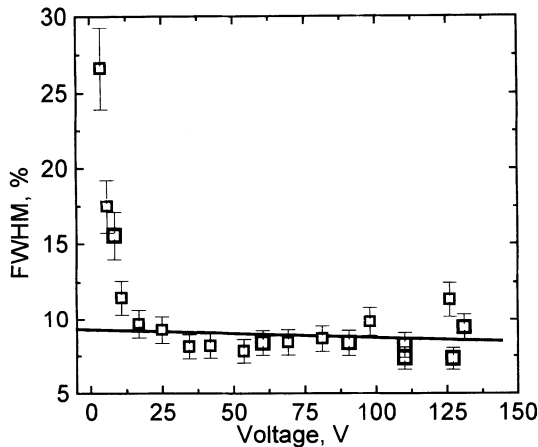


Fig. 11.21. Width of the spectral line (FWHM) versus the voltage applied to the transistor structure. The Schottky barrier plays the role of the collector [48] (with permission for reproduction from Elsevier)

particle is close to 2 MeV. Similarly to the first case, the shape of the spectrum is Gaussian. Characteristically, the pronounced scatter of the amplitudes observed at low voltages ($U \leq 15$ V) tends with increasing voltage to a constant FWHM value of $\sim 9\%$ (see Fig. 11.21), virtually equal to that mentioned above. It is also noteworthy that the constant ratio of the spectrum width to the average spectrum amplitude indicates linear amplification of both “large” and “small” portions of the initially introduced charge.

Phototransistor Model

The observed amplification was described in terms of the phototransistor model [47]. Minority carriers (electrons in the present case) formed in the base by deceleration of an alpha particle diffuse toward the emitter and collector junctions, being involved in drift caused by the respective fields (see, e.g., [45]). Nonequilibrium holes find themselves in a potential well, charging it positive relative to the emitter. The change in the emitter–base potential difference makes the electron flux injected by the emitter stronger.

To describe the effect quantitatively, account was taken of the fact that the primary current of the phototransistor is amplified by a factor $(1 - \alpha_T)$, where α_T is the base-transport factor for electrons. Note that this expression is valid under the assumption that the emitter efficiency is unity. The expression for α_T was taken from [49] for the case of transport of the charge injected into the base on applying a δ -pulse of voltage to the emitter–base junction. Then

$$\alpha_T = \frac{(d - W) / L_D}{sh[(d - W) / L_D]} . \quad (11.20)$$

Here d , W , and L_D are the film thickness, the width of the SCR at the collector junction, and the diffusion length of electrons, respectively.

In considering the initially created charge, only carriers entering the collector were taken into account. It was assumed that the entire nonequilibrium electron charge created by an alpha particle in the W region drifts toward the collector. The contribution from the electron diffusion toward the SCR boundary was described in [47] by the expression

$$(d - W) \exp\left(-\frac{d - W}{L_D}\right) . \quad (11.21)$$

The following expression was then obtained for the signal (in energy units):

$$E = 0.2 \frac{W + (d - W) \exp[-(d - W)/L_D]}{1 - [(d - W) / L_D] / \{sh[(d - W) / L_D]\}} , \quad (11.22)$$

where the coefficient $0.2 \text{ MeV}/\mu\text{m}$ accounts for the specific energy loss in the initial portion of the Bragg curve.

Equation (11.22) is convenient for approximating experimental data, with d and L_D used as parameters. Since the experiment gives the dependence $E(U)$, the U values were recalculated to obtain W , on the basis of known impurity concentration of $2.8 \times 10^{15} \text{ cm}^{-3}$ and the fact that the junction at the Schottky barrier is abrupt. Figure 11.22 presents the results of fitting the dependence described by (11.22) to data obtained for two samples. Noteworthy features are the rather long electron diffusion lengths ($L_D = 8.85$ and $5.85 \mu\text{m}$) and the fact that d virtually coincides with the actual film thickness. The accuracy of fitting is characterized by the values $d = (8.53 \pm 0.09) \mu\text{m}$ and $1/L_D = (0.171 \pm 0.005) 1/\mu\text{m}$, obtained for sample N2.

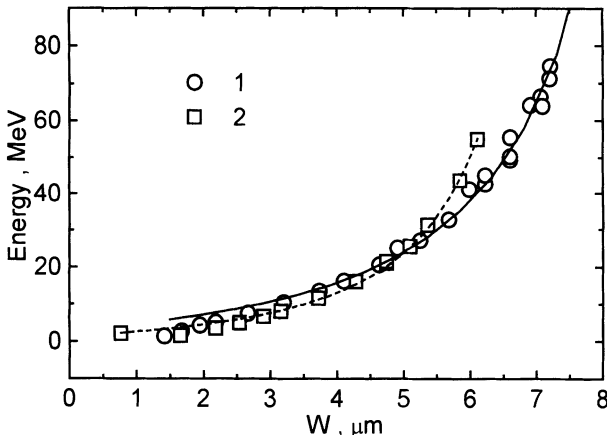


Fig. 11.22. Signal from an alpha particle versus the space-charge region at the collector junction (Schottky barrier). *Points*, experiment; *lines*, approximation by (11.11) with the fitting parameters $L_D = 8.85$ and $5.85 \mu\text{m}$; film thickness $d = 10.75$ and $8.53 \mu\text{m}$ for samples 1 and 2, respectively [48] (with permission for reproduction from Elsevier)

Conclusion

Thus, it has been shown [47, 48] that internal amplification by a factor of ~ 50 times can be achieved in short-range particle detectors based on “pure” SiC films. This can be done in comparatively easy-to-fabricate structures with a Schottky barrier as the collector. In terms of the materials science, the experiments with particle detection revealed that the nonuniformity of the diffusion-drift carrier transport parameters in the films does not exceed 10%.

It is advantageous in practical terms that large signals can be obtained for short-range ions in such applications as neutron flux measurements, after reaction of neutrons with light elements of the type $^{10}\text{B}(\text{n},\alpha)^7\text{Li}$ and $^6\text{Li}(\text{n},\alpha)^3\text{H}$.

As regards penetrating radiation (e.g., X-rays), it is rather important that the possibility of markedly raising the effective SCR width of a detector arises. For example, Fig. 11.23 shows the dependence of the current induced by an X-ray tube with an accelerating voltage of 20 kV [50]. A rise in the current by a factor of ~ 35 with increasing detector bias, similar to that in Fig. 11.22, is clearly seen. It would be expected that similar charge amplification would be observed for single quanta in the X-ray range (see [20], devoted to spectrometry of low-energy X-ray quanta). The internal amplification can markedly improve the signal-to-noise ratio of the electronic circuit. This is important for SiC in view of the high average energy for electron-hole pair generation in this material.

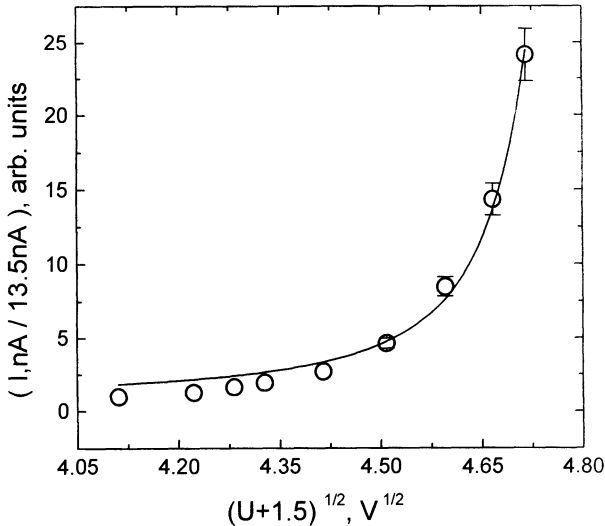


Fig. 11.23. Dependence of the current induced by an X-ray tube with an accelerating voltage of 20 kV versus the voltage applied to the transistor structure. The values of the current are normalized to 13.5 nA, the initial point accepted. Circles, experiment; solid lines, approximation. The Schottky barrier plays the role of the collector [50] (with permission for reproduction from Nauka)

11.10 Summary

This description of the results of using SiC as a detector material has two aspects. First, the unique possibilities of SiC detectors for performing tasks in physics and technology have been described. The principal examples of the application of such detectors were given. Second, the connection between the detector characteristics and the essential material parameters was set out. Some methods for determination of the properties of SiC from detector characteristics were described.

It may be concluded that the recent progress in the techniques for producing high-perfection SiC films (with a net concentration of impurities of $10^{14}\text{--}10^{15}\text{ cm}^{-3}$ and a density of pipe defects of about $1/\text{cm}^2$) has put SiC in the category of “detection media”. Beyond doubt, the investigations of the properties of SiC should be taken further, and various configurations of detectors should be designed too.

References

1. R.V. Babcock, S.L. Ruby, F.D. Schupp, and K.H. Sun, *Miniature Neutron Detectors*, Westinghouse Electrical Corp. Materials Engineering Report No. 5711-6600-A (1957).

2. R.V. Babcock and H.C. Chang, "SiC neutron detectors for high-temperature operation", Int. Atom. Energy Symp. Proc. **1**, 613 (1963).
3. R.V. Babcock, *Radiation Damage in SiC*, Westinghouse Research and Development Center Document No. 64-8C2-432-P1 (1964).
4. V.A. Tikhomirova, O.P. Fedoseeva, and G.F. Kholuyanov, "Properties of ionizing-radiation counters made of SiC doped by diffusion of beryllium", Sov. Phys. Semicond. **6**, 957–959 (1972).
5. V.A. Tikhomirova, O.P. Fedoseeva, and G.F. Kholuyanov, "Detector characteristics of a SiC detector prepared by the diffusion of beryllium", Atomnaya Energiya **34**, No. 2, 122–124 (1973).
6. V.A. Tikhomirova, O.P. Fedoseeva, and V.V. Bolshakov, "SiC detectors as fission-fragment counters in reactors", Izmeritel'naya Teknika **6**, 67–68 (1973).
7. A.A. Lebedev, N.S. Savkina, A.M. Ivanov, N.B. Strokan, and D.V. Davidov, "Epitaxial 6H-SiC layers as detectors of nuclear particales", Mater. Sci. Forum **338–342**, 1447–1450 (2000).
8. F. Nava, P. Vanni, C. Lanzieri, and C. Canali, "Epitaxial silicon carbide charge particle detectors", Nucl. Instrum. Methods A **437**, 354–358 (1999).
9. A.A. Lebedev, N.S. Savkina, A.M. Ivanov, N.B. Strokan, and D.V. Davidov, "6H-SiC epilayers as nuclear particale detectors", Semiconductors **34**, 243–249 (2000).
10. J.F. Ziegler (ed.), *Ion Implantation Science and Technology*, Academic Press, Orlando (1984).
11. R.A. Logan and A.G. Chynoweth, "Charge multiplication in GaP p–n-junction", J. Appl. Phys. **33**, 1649–1654 (1962).
12. V.V. Makarov, "Distribution of the electron–hole pair generation density under bombardment of SiC by electrons with energy 20 keV", Sov. Phys. Semicond. **9**, 1098–1101 (1975).
13. I.N. Il'yashenko and N.B. Strokan, "Carrier lifetime in α -particle tracks for diffusion–drift transport in Si", Semiconductors **30**, 167–170 (1996).
14. M. Rogalla, K. Runge, and A. Soldner-Rembold, "Particle detectors based on semi-insulating silicon carbide", Nucl. Phys. B. **78**, 516–520 (1999).
15. N.B. Strokan, "Determination of the uniformity of the carrier lifetime in a material from the profile of the amplitude spectrum of an ion detector", Techn. Phys. Lett. **24**, 186–188 (1998).
16. V.K. Eremin, S.G. Danengirh, N.B. Strokan, and N.I. Tisnek, "Influence of the space charge on the semiconductor detector characteristic", Sov. Phys. Semicond. **8**, 556–561 (1974).
17. F. Nava, P. Vanni, G. Verzellesi, A. Castaldini, A. Cavallini, L. Polenta, R. Nipoti, and C. Donolato, "Charged particle detection properties of epitaxial 4H-SiC schottky diodes", Mater. Sci. Forum **353–356**, 757–762 (2001).
18. *DESSIS-6.0 Reference Manual*, ISE Integrated Systems Engineering AG, Zurich, (Switzerland).
19. T. Kimoto, S. Nakazawa, K. Fujihira, T. Hirao, S. Nakamura, Y. Chen, K. Hashimoto, and H. Matsunami, "Recent achievements and future challenges in SiC homoepitaxial growth", Mater. Sci. Forum **389–393**, 165–170 (2002).
20. G. Bertuccio and R. Casigaghi, "Study of silicon carbide for X-ray detection and spectroscopy", IEEE Trans. Nucl. Sci. **50**, 175–185 (2003).
21. CREE Research, Inc., Durham, NC 27713, USA.

22. M. Bruzzi, F. Nava, S. Russo, S. Sciortino, and P. Vanni, "Characterisation of SiC detectors response to electron and photon irradiation", *Diamond Relat. Mater.* **10**, 657–661 (2001).
23. P. Bergonzo, D. Tromson, C. Mer, B. Guizard, F. Foulon, and A. Brambilla, "Particle and radiation detectors based on diamond", *Phys. Stat. Sol. (a)* **185**, 167–181 (2001).
24. M. Rogalla, K. Runge, and A. Soldner-Rembold, "Particle detectors based on semi-insulating SiC", *Nucl. Phys. B (Proc. Suppl.)* **78**, 516–520 (1999).
25. R.R. Ferber and G.N. Hamilton, *Silicon Carbide High Temperature Neutron Detectors for Reactor Instrumentation*, Westinghouse Research and Development Center Document No. 65-1C2-RDFCT-P3 (1965).
26. A.R. Dulloo, F.H. Ruddy, and J.G. Seidel, *Radiation Response Testing of SiC Semiconductor Neutron Detectors for Monitoring Thermal Neutron Flux*, Westinghouse Science and Technology Report No. 97-9TK1-NUSIC-R1 (1997).
27. F.H. Ruddy, A.R. Dulloo, J.G. Seidel, S. Seshadri, and L.B. Rowland, "Development of a silicon carbide radiation detector", *IEEE Trans. Nucl. Sci.* **45**, 536–541 (1998).
28. A.R. Dulloo, F.H. Ruddy, J.G. Seidel, C. Davison, T. Flinchbaugh, and T. Daubenspeck, "Simultaneous measurement of neutron and gamma-ray radiation levels from a TRIGA reactor core using silicon carbide semiconductor detector", *IEEE Trans. Nucl. Sci.* **46**, 275–279 (1999).
29. S. Kanazawa, M. Okada, T. Nozaki, K. Shin, S. Ishihara, and I. Kimura, "Radiation induced defects in p-type silicon carbide", *Mater. Sci. Forum* **389–393**, 521–524 (2002).
30. S. Kanazawa, M. Okada, J. Ishii, T. Nozaki, K. Shin, S. Ishihara, and I. Kimura, "Electrical properties in neutron-irradiated silicon carbide", *Mater. Sci. Forum* **389–393**, 517–520 (2002).
31. K.K. Lee, T. Ohshima, and H. Itoh, "Radiation response of p-channel 6H-SiC MOSFETs fabricated using pyrogenic conditions", *Mater. Sci. Forum* **389–393**, 1097–1100 (2002).
32. G. Lindstrom, M. Moll, and E. Fretwurst, "Radiation hardness of silicon detectors – a challenge from high-energy physics", *Nucl. Instrum. Methods A* **426**, 1–15 (1999).
33. E. Verbitskaya, M. Abreu, V. Bartsch, W. Bell, P. Berglund, and J. Bol, "Optimization of electric field distribution by free carrier injection in silicon detectors operated at low temperatures", *IEEE Trans. Nucl. Sci.* **49**, 1–6 (2002).
34. A.A. Lebedev, A.I. Veinger, D.V. Davydov, V.V. Kozlovskii, N.S. Savkina, and A.M. Strelchyk, "Doping of n-type 6H-SiC and 4H-SiC with defects created with a proton beam", *J. Appl. Phys.* **88**, 1 (2000).
35. A.A. Lebedev, N.B. Strokan, A.M. Ivanov, D.V. Davydov, and V.V. Kozlovskii, "Thin heavily compensated 6H-SiC epilayers as nuclear particle detectors", *Mater. Sci. Forum* **353–356**, 763–766 (2001).
36. M. Ivanov, N.B. Strokan, D.V. Davidov, N.S. Savkina, A.A. Lebedev, Yu.T. Mironov, G.A. Ryabov, and E.M. Ivanov, "Radiation hardness of SiC based ions detectors for influence of the relative protons", *Appl. Surf. Sci.* **184**, 431–436 (2001).
37. N.S. Savkina, A.A. Lebedev, D.V. Davydov, A.M. Strel'chuk, A.S. Tregubova, C. Raynaud, J.-P. Chante, M.-L. Locatelli, D. Planson, J. Milan, P. Godignon, F.J. Campos, N. Mestres, J. Pascual, G. Brezeanu, and M. Badila, "Low-doped

- 6H-SiC n-type epilayers grown by sublimation epitaxy”, Mater. Sci. Eng. B **77**, 50–54 (2000).
- 38. M.M. Anikin, N.I. Kuznecov, A.A. Lebedev, N.S. Savkina, A.L. Sirkin, and V.E. Chelnokov, “Current deep level spectroscopy in 6H-SiC p-n-structure with pulling field”, Fiz. Tekh. Poluprovodn. **28**, 456–460 (1994).
 - 39. A.M. Ivanov, N.B. Strokan, D.V. Davidov, N.S. Savkina, A.A. Lebedev, Yu.T. Mironov, G.A. Ryabov, and E.M. Ivanov, “Radiation hardness of SiC ion detectors to affect relativistic protons”, Semiconductors **35**, 481–484 (2001).
 - 40. V. Eremin, N. Strokan, E. Verbitskaya, and Z. Li, “The development of transient current and charge techniques for the measurement of effective impurity concentration in the space charge region of p-n-junction detectors”, Nucl. Instrum. Methods A **373**, 388 (1996).
 - 41. N.B. Strokan, A.A. Lebedev, A.M. Ivanov, D.V. Davydov, and V.V. Kozlovskii, “Special features of alpha-particale detection with semi-insulating 6H-SiC films”, Semiconductors **34**, 1386–1390 (2000).
 - 42. G. Violina, P. Shkreby, E. Kalinina, G. Kholujanov, V. Kossov, R. Yafaev, A. Hallen, and A. Konstantinov, “Silicon carbide detectors of high energy particles”, Third International Seminar on Silicon Carbide and Related Materials, May 24–26, Novgorod, Russia, p. 125 (2000).
 - 43. S.M. Ryvkin, “Pulse formation mechanism in semiconductor crystalline counters”, J. Techn. Phys. **26**, 2667–2683 (1956).
 - 44. N.A. Vitovskiy, P.I. Maleev, and S.M. Ryvkin, “Mechanism of creation of pulses in crystal detectors under conditions of a through-conducting channel”, J. Techn. Phys. **28**, 460–469 (1958).
 - 45. S.M. Ryvkin, *Photoelectric Effects in Semiconductors*, Consultants Bureau, New York (1964).
 - 46. A. Rose, *Concepts in Photoconductivity and Applied Problems*, Interscience Publishers, New York (1963).
 - 47. A.A. Lebedev, N.B. Strokan, A.M. Ivanov, D.V. Davydov, N.S. Savkina, E.V. Bogdanova, A.N. Kuznetsov, and R. Yakimova, “Amplification of the signal in triode structures of ion detectors based on 6H-SiC epitaxial films”, Appl. Phys. Lett. **79**, 4447–4449 (2001).
 - 48. N.B. Strokan, A.M. Ivanov, D.V. Davydov, N.S. Savkina, E.V. Bogdanova, A.N. Kuznetsov, and A.A. Lebedev, “Triode structure of ion detector based on 6H-SiC epitaxial films”, Appl. Surf. Sci. **184**, 455–459 (2001).
 - 49. A.A. Grinberg, “Calculation of transient processes in semiconductor triodes”, Solid State Phys. **1**, 31–43 (1959).
 - 50. N.B. Strokan, A.M. Ivanov, M.E. Boiko, N.S. Savkina, A. M. Strel’chuk, A.A. Lebedev, and R. Yakimova, “Silicon carbide transistor structures as detectors of weakly ionizing radiation”, Semiconductors **37**, 65–69 (2003).

Index

- 15R-SiC 14, 15, 80, 92–94, 99, 100
2H-SiC 15, 63–83, 162
3C-SiC 14, 15, 63–83, 92, 93, 161, 162,
180, 200, 209–267, 361, 376
4H-SiC 14–16, 33, 36, 38, 41, 44, 52, 53,
63–83, 92–96, 107–109, 113, 116,
143, 150, 292, 293, 347, 353, 359,
361, 363, 367, 376, 377, 384, 391,
392
6H-SiC 14–16, 28, 43–46, 52, 53, 63–83,
92–104, 111, 113, 125, 142, 251,
376, 398, 402
- ab initio 63, 64, 68, 76, 79, 81, 83, 164,
165, 172
absorption 75, 212
acceptor 7, 16, 36, 39, 43, 54, 75, 162,
282, 284–287, 293–297
acoustic 79, 82
amorphization 193, 292
anisotropy 74
annealing 287–295, 306–338, 359, 363,
382, 384, 385, 402
antisite 259, 285, 288
argon 212, 359
atomic force microscopy (AFM) 98,
359
axial strain 224, 227
- back-folding 80, 82
Baliga’s figure of merit (BFOM) 366,
375
ballistic electron emission microscopy
(BEEM) 72
- band gap 2, 14, 16, 38, 43, 64, 70–73,
89, 92, 248, 285–287, 293–295, 297,
307, 324, 375, 392
band structure 63, 64, 70–74, 76–79
barrier height 305, 311, 325, 366, 377
bonding energy 63–67
Born effective charges (BEC) 76
boron 282–287, 294, 295
bound exciton 215, 247
breakdown voltage 90, 365–367, 375
Brillouin zone 64, 70, 75, 76, 82, 173,
185
Burgers vector 98, 100, 103
- capacitance 432, 434
carbide 320
carbon 346
carbon vacancy 259, 279, 282–289
catalytic 326, 327
catalytic graphitization 326
cell 65, 76
characterization 39, 42, 44, 45, 47, 49,
211, 267, 335, 345, 346, 350, 355
chemical vapor deposition (CVD) 38,
41, 209–212
compensation 278, 283, 288, 293, 298,
411, 434
composite 322
conduction band 64, 70–73, 79, 83,
283, 293–295, 347, 361, 365, 377,
394
contact 382, 384, 386, 387, 399
crystal field 64, 74, 75, 163, 278

- crystal growth 5, 8, 10–12, 14, 17, 19, 22–25, 27, 28, 32–34, 39, 48, 49, 54, 123, 212
 crystal quality 251, 411, 412
 crystal structure 63–66, 83
 crystallography 65, 141
 cubic site 65, 279, 293, 297
 cubic site (K-site) 280, 294, 295
 current-voltage 377, 387
 cyclotron resonance (CR) 73
 d-shell electron 308, 312
 Debye temperature 177, 187, 198
 deep level 38, 54, 162, 278, 295, 430–432
 deep level transient spectroscopy (DLTS) 295, 423, 432
 defect 8, 9, 14–16, 18, 21, 23, 24, 28, 30, 31, 33, 37–40, 42–45, 47–50, 53–55, 162, 278, 345, 348, 349, 355, 361, 365, 378
 density functional theory (DFT) 63–66, 76
 device 30, 32, 34–37, 39, 44, 47, 49, 50, 52–55, 63, 70, 345, 346, 356, 365–367, 375
 diamond structure 66, 164
 dielectric constant 76, 346, 366
 diffusion length 416, 431
 dislocation 11, 12, 16, 17, 23, 28, 30, 31, 33, 44–47, 49, 50, 55, 98, 105, 152, 251, 254
 dissociation 100, 103, 104
 divacancy 259
 donor 7, 16, 34, 38, 43, 54, 72, 278–284, 288, 292–298, 392, 398
 donors 162
 doping 9, 10, 16, 34, 38–41, 43, 52, 54, 73, 307, 377, 400
 dynamic matrix 76
 dynamical matrix 173, 174
 edge dislocation wall 105
 edge termination 380–383
 effective mass 64, 73–75
 electron paramagnetic resonance (EPR) 162, 287–298
 electron spin resonance 287–298
 energy gap 214, 345, 346, 350, 358, 361
 epitaxy 2, 30, 52, 90, 109, 252, 383, 389, 393
 etch pit 47, 49, 50, 105, 107, 111, 115
 exchange interaction 67
 exciton 215, 247
 Fermi level 292, 295, 305
 first principle 76
 force constant 76, 77
 Fowler–Nordheim (F–N) electron 347
 free energy 64, 68–70, 77
 Frenkel pair 166
 frozen phonon method 76
 full width half maximum (FWHM) 42, 104, 105
 fundamental property 63
 gate oxide 346, 366
 general gradient approximation (GGA) 63
 GGA 66, 67
 graphitization 323, 326–328
 graphitization mechanism 327, 328
 Green’s function 161, 165, 166, 177, 178
 Grüneisen parameter 161, 163–165, 199
g-value 279, 280, 290, 291
 Hall effect 351, 353
 Hamiltonian 230
 heat transfer 129
 hexagonal 3, 4, 14, 15, 28, 30, 47, 63–70, 74, 75, 79, 80, 91, 92
 hexagonal site 278, 281, 293
 hexagonality 65–67
 high purity 283, 288, 291, 296, 298
 hydrogen 289, 291, 294–296
 hyperfine interaction 281, 282, 293
 image force 101
 impact ionization 389
 implantation 291, 292, 384
 impurity 283–297
 inelastic X-ray scattering 75, 80, 163, 198
 inequivalent lattice site 288
 infrared 75, 77, 78, 81, 163, 164, 261
 interface trap density 354, 356, 391
 interfacial reaction 303–338

- interstitial 183
- intrinsic defect 162, 279, 285, 291, 295
- ionization 378, 389
- irradiation 283, 285, 291, 378, 386
- lattice 2, 30, 42, 44, 63–68, 70, 74–76
- lattice distortion 165, 171, 183
- lattice relaxation 165, 171
- lattice vibration 63, 64, 66–68, 75, 76, 163
- LDA 64, 66, 67, 69–72, 74–76, 78–80
- LDA band structure 72, 73
- leakage current 346–348, 356, 365, 378–381, 387, 403
- LED 90, 96
- Lely method 92, 94, 95, 104, 109, 125
- lifetime 378, 402, 407, 417–422
- linear response theory 76
- LO-TO splitting 76–78, 185, 199
- local density approximation (LDA) 63
- low angle grain boundary 37, 44, 53, 91, 101, 104, 199
- low temperature 214, 355
- luminescence 110
- macrodefect 13, 18, 28, 147
- magnetic circular dichroism 139
- mass transfer 8, 26
- MESFET 37, 39, 52, 90
- metal-oxide-semiconductor (MOS) 90, 109, 347–356, 360, 366
- metastable 92
- micropipe 14, 16, 18, 28, 29, 31, 36, 37, 39, 41, 44–47, 49, 50, 53–55, 91, 96, 98, 105, 109, 152
- mobility 92, 109, 348, 356, 360–366, 376, 392, 393, 400, 420, 421, 435
- modeling 70, 127
- mosaicity 105, 107, 109
- near-interface trap 348, 352, 356
- neutron scattering 75, 81
- nitridation 345, 356, 358, 359, 365
- nitride 210, 321
- nitrogen 7, 8, 16, 34, 35, 37–39, 41, 43, 191, 279–281, 292–295, 358
- nonequilibrium 345, 346
- nucleation 3, 5–7, 11–13, 15–18, 21, 22, 32, 33, 40, 95–99, 104, 113
- off-axis 15, 115
- ohmic 385
- ohmic contact 303–338
- optical phonon 216
- optically detected magnetic resonance 278, 295
- oxidation 289–291, 345–349, 356, 358, 361, 363, 385, 386
- oxidation resistance 312
- oxycarbon 358
- passivation 284, 289–295, 345, 346, 358, 393
- phonon 64, 68–70, 75–81
- phonon density 184
- phonon density of states 68, 69, 77, 198
- phonon dispersion 64, 68, 76, 77, 79–82, 163, 174, 184, 198
- phonon dispersions 77
- phonon frequency 68, 75, 76, 79, 80, 82, 164
- phonon replica 215, 247
- phosphorus 282, 294
- photoelastic effect 109
- photoluminescence (PL) 284–288
- photoluminescence excitation (PLE) 256–258
- phototransistor 437–440
- physical vapor transport (PVT) 16–18, 21, 28, 30, 32, 33, 36, 38, 40, 55, 125
- point defect 54, 166, 278, 288, 298
- polarity 94, 307
- polaron 73
- polytype 5, 8, 9, 14–16, 27, 31, 33, 34, 36, 42, 44, 49, 50, 55, 63–80, 91, 99, 106, 162–165, 307, 347, 356–361, 365, 367, 375
- polytypism 91, 162, 163
- pseudo-potential 64, 67
- quasi-harmonic theory 68
- Raman 75, 77, 78, 81, 154, 163, 164
- Raman imaging 154
- Raman spectroscopy 216, 232–246, 310, 326
- reciprocal space 104

- reliability 358, 379, 392
 repulsive interaction 101
 rigid-ion model 165, 172, 173, 198
 Rutherford backscattering (RBS) 222
 scanning electron microscopy (SEM)
 44, 331, 333
 scattering 75, 80, 81
 Schottky 39, 43, 53, 376–379, 385, 387,
 392, 413, 438
 Schottky barrier height 305, 325
 Schottky-Mott limit 324
 screw dislocation 11, 12, 30, 31, 44, 46,
 55, 98, 101, 105
 secondary ion mass spectrometry
 (SIMS) 221, 358
 secular equation 226
 semi-insulating 2, 36, 37, 52, 54, 285,
 286, 296, 297
 sensitivity 45
 SiC-SiO₂ interface 355, 356, 381, 391
 silicide 307, 312
 silicon 315
 silicon carbide (SiC) 63–83, 161, 303,
 345–367
 simulation 64, 96, 126
 slow-trap profiling technique 356
 specific heat 161, 164, 175, 198
 specific on-resistance 376
 spin 278–283, 285, 288, 297, 298
 spin-orbit splitting 231
 spin-orbit coupling 64, 74
 stability 64, 67, 83, 336
 stacking 64, 65, 79, 80, 82, 92
 stacking fault 16, 30, 44, 47, 51, 54, 55,
 91, 111
 step bunching 13, 17, 18, 101
 stoichiometric 9, 10
 strain 9, 42, 44, 45, 102, 108, 109, 114
 stress 49, 154
 subgrain boundary 91, 98, 104, 107
 sublimation 3–9, 14, 18, 22, 27–30, 32,
 34, 35, 37, 38, 40, 52, 90, 93–95, 98,
 124
 substrate 2, 5, 11, 28–30, 37, 39, 46,
 52–54, 163, 377
 supercell 76
 supersaturation 6, 9, 11, 15, 17, 18, 22,
 30, 33
 surface diffusion 26
 surfactant 93
 synchrotron white beam X-ray topo-
 graphy (SWBXT) 45, 46,
 98
 thermal conductivity 2, 38, 52, 55, 90
 thermal expansion 161, 163, 165, 175,
 199
 thermal stress 18, 21, 23, 155
 thermodynamic stability 64, 70
 thermodynamics 68, 127
 transmission electron microscopy
 (TEM) 28, 44, 47, 106, 111, 309
 tungsten 298
 UV 351
 UV irradiation 110
 vacancy 167
 valence band 64, 70, 74, 75, 282–286,
 295, 297, 347, 392
 vanadium 296, 297
 vibrational mode 161
 void 98, 100
 warpage 104
 work function 304, 307, 391
 X-ray diffraction (XRD) 43, 163, 308
 X-ray photoelectron spectroscopy
 (XPS) 358
 X-ray rocking curve 42, 104, 105
 X-ray topography 111
 Zeeman 279–281
 zone-folding 81

Springer Series in
MATERIALS SCIENCE

Editors: R. Hull R. M. Osgood, Jr. J. Parisi H. Warlimont

- 10 **Computer Simulation of Ion-Solid Interactions**
By W. Eckstein
 - 11 **Mechanisms of High Temperature Superconductivity**
Editors: H. Kamimura and A. Oshiyama
 - 12 **Dislocation Dynamics and Plasticity**
By T. Suzuki, S. Takeuchi, and H. Yoshinaga
 - 13 **Semiconductor Silicon**
Materials Science and Technology
Editors: G. Harbecke and M. J. Schulz
 - 14 **Graphite Intercalation Compounds I**
Structure and Dynamics
Editors: H. Zabel and S. A. Solin
 - 15 **Crystal Chemistry of High-T_c Superconducting Copper Oxides**
By B. Raveau, C. Michel, M. Hervieu, and D. Groutt
 - 16 **Hydrogen in Semiconductors**
By S. J. Pearton, M. Stavola, and J. W. Corbett
 - 17 **Ordering at Surfaces and Interfaces**
Editors: A. Yoshimori, T. Shinjo, and H. Watanabe
 - 18 **Graphite Intercalation Compounds II**
Editors: S. A. Solin and H. Zabel
 - 19 **Laser-Assisted Microtechnology**
By S. M. Metev and V. P. Veiko
2nd Edition
 - 20 **Microcluster Physics**
By S. Sugano and H. Koizumi
2nd Edition
 - 21 **The Metal-Hydrogen System**
By Y. Fukai
 - 22 **Ion Implantation in Diamond, Graphite and Related Materials**
By M. S. Dresselhaus and R. Kalish
 - 23 **The Real Structure of High-T_c Superconductors**
Editor: V. Sh. Shekhtman
 - 24 **Metal Impurities in Silicon-Device Fabrication**
By K. Graff 2nd Edition
 - 25 **Optical Properties of Metal Clusters**
By U. Kreibig and M. Vollmer
 - 26 **Gas Source Molecular Beam Epitaxy**
Growth and Properties of Phosphorus Containing III-V Heterostructures
By M. B. Panish and H. Temkin
 - 27 **Physics of New Materials**
Editor: F. E. Fujita 2nd Edition
 - 28 **Laser Ablation**
Principles and Applications
Editor: J. C. Miller
 - 29 **Elements of Rapid Solidification**
Fundamentals and Applications
Editor: M. A. Otooni
 - 30 **Process Technology for Semiconductor Lasers**
Crystal Growth and Microprocesses
By K. Iga and S. Kinoshita
 - 31 **Nanostructures and Quantum Effects**
By H. Sakaki and H. Noge
 - 32 **Nitride Semiconductors and Devices**
By H. Morkoç
 - 33 **Supercarbon**
Synthesis, Properties and Applications
Editors: S. Yoshimura and R. P. H. Chang
 - 34 **Computational Materials Design**
Editor: T. Saito
 - 35 **Macromolecular Science and Engineering**
New Aspects
Editor: Y. Tanabe
 - 36 **Ceramics**
Mechanical Properties, Failure Behaviour, Materials Selection
By D. Munz and T. Fett
 - 37 **Technology and Applications of Amorphous Silicon**
Editor: R. A. Street
 - 38 **Fullerene Polymers and Fullerene Polymer Composites**
Editors: P. C. Eklund and A. M. Rao
-

Springer Series in
MATERIALS SCIENCE

Editors: R. Hull R. M. Osgood, Jr. J. Parisi H. Warlimont

- 39 **Semiconducting Silicides**
Editor: V. E. Borisenko
- 40 **Reference Materials
in Analytical Chemistry**
A Guide for Selection and Use
Editor: A. Zschunke
- 41 **Organic Electronic Materials**
Conjugated Polymers and Low
Molecular Weight Organic Solids
Editors: R. Farchioni and G. Grossi
- 42 **Raman Scattering
in Materials Science**
Editors: W. H. Weber and R. Merlin
- 43 **The Atomistic Nature
of Crystal Growth**
By B. Mutaftschiev
- 44 **Thermodynamic Basis
of Crystal Growth**
 $P-T-X$ Phase Equilibrium
and Non-Stoichiometry
By J. Greenberg
- 45 **Thermoelectrics**
Basic Principles
and New Materials Developments
By G. S. Nolas, J. Sharp,
and H. J. Goldsmid
- 46 **Fundamental Aspects
of Silicon Oxidation**
Editor: Y. J. Chabal
- 47 **Disorder and Order
in Strongly
Nonstoichiometric Compounds**
Transition Metal Carbides,
Nitrides and Oxides
By A. I. Gusev, A. A. Rempel,
and A. J. Magerl
- 48 **The Glass Transition**
Relaxation Dynamics
in Liquids and Disordered Materials
By E. Donth
- 49 **Alkali Halides**
A Handbook of Physical Properties
By D. B. Sirdeshmukh, L. Sirdeshmukh,
and K. G. Subhadra
- 50 **High-Resolution Imaging
and Spectrometry of Materials**
Editors: F. Ernst and M. Rühle
- 51 **Point Defects in Semiconductors
and Insulators**
Determination of Atomic
and Electronic Structure
from Paramagnetic Hyperfine
Interactions
By J.-M. Spaeth and H. Overhof
- 52 **Polymer Films
with Embedded Metal Nanoparticles**
By A. Heilmann
- 53 **Nanocrystalline Ceramics**
Synthesis and Structure
By M. Winterer
- 54 **Electronic Structure and Magnetism
of Complex Materials**
Editors: D. J. Singh and
D. A. Papaconstantopoulos
- 55 **Quasicrystals**
An Introduction to Structure,
Physical Properties and Applications
Editors: J.-B. Suck, M. Schreiber,
and P. Häussler
- 56 **SiO_2 in Si Microdevices**
By M. Itsumi
- 57 **Radiation Effects
in Advanced Semiconductor Materials
and Devices**
By C. Claeys and E. Simoen
- 58 **Functional Thin Films
and Functional Materials**
New Concepts and Technologies
Editor: D. Shi
- 59 **Dielectric Properties of Porous Media**
By S.O. Gladkov
- 60 **Organic Photovoltaics**
Concepts and Realization
Editors: C. Brabec, V. Dyakonov, J. Parisi and
N. Sariciftci